

DEVELOPMENT AND APPLICATION OF PHOTSENSITIVE BIORESINS FOR 3D BIOFABRICATION STRATEGIES

FROM VOLUMETRIC PRINTING TO TWO-PHOTON STEREOLITHOGRAPHY



DISS. ETH NO. 28943

**DEVELOPMENT AND APPLICATION OF PHOTSENSITIVE
BIORESINS FOR 3D BIOFABRICATION STRATEGIES:
FROM VOLUMETRIC PRINTING TO TWO-PHOTON
STEREOLITHOGRAPHY**

A thesis submitted to attain the degree of

DOCTOR OF SCIENCES

(Dr. sc. ETH Zurich)

presented by

RICCARDO RIZZO

BSc University of Trieste, Biological Sciences and Technology
MSc University of Trieste, Medical Biotechnology

born on *13.02.1994*

Citizen of Italy

accepted on the recommendation of

Prof. Dr. Marcy Zenobi-Wong, examiner

Prof. Dr. Cole A. DeForest, co-examiner

Prof. Dr. Yu Shrike Zhang, co-examiner

2023

“I love fools’ experiments. I am always making them.”

Charles Robert Darwin

to my wife and my family

Abstract

Tissue Engineering is an interdisciplinary research field that brings together the principles of biology, chemistry, material science and engineering to repair and regenerate tissues and organs. In the thirty years from its foundation, tissue engineering has grown exponentially by embracing and fostering innovations from the most disparate research fields. In recent years, advances in three-dimensional (3D) biofabrication technologies had played a major role opening new, unprecedented avenues towards the generation of tissues and organs that accurately resemble native structure and function.

In particular, the use of light to control the biofabrication processes in a remote, contact-less fashion is playing an increasingly important role. Light offers a highly versatile trigger to drive various photochemical reactions, from the formation of chemical bonds to their breakage. For example, it can span from UV to near-infrared wavelengths, thus targeting different photochemical processes and with implications for cytotoxicity and tissue penetration. Light can also be generated from various sources, like highly coherent laser beams or non-coherent LED illumination. In addition, the flexibility given by the broad range of possible optical manipulations has enabled light-based biofabrication of tissue constructs with resolution and size ranging from nanometers to centimeters.

This dissertation presents a series of works focused on exploiting the power of light for tissue engineering applications. At first, a comprehensive overview of this rapidly evolving field is offered to capture state-of-the-art and future directions. An optimized click-based photoresin is then introduced for the first time for use with a novel biofabrication method called volumetric printing (VP), resulting in unprecedented printing speed and promising biological outcomes. In a second study, optical manipulation of the photoresin was investigated to combine VP and high resolution two-photon ablation (2PA), resulting in the first hybrid printing featuring VP. Complex, multiscale 3D organotypic vasculature-like models with resolution down to $\sim 2 \mu\text{m}$ were generated using this method, opening new avenues for highly precise microtissue on-a-chip technologies.

Another novel light-based method developed in the lab, termed Filamented Light (FLight) biofabrication, was instead exploited to generate articular cartilage constructs with characteristic zonal architecture. Leveraging FLight capabilities in generating unidirectional, highly aligned microfeatures, anisotropic deposition of collagen fibrils typical of superficial and deep-zone of articular cartilage was induced. Infant chondrocytes embedded in tailored photoresin drove excellent tissue maturation with cartilage-like extracellular matrix composition and mechanical properties.

In another study, aligned tissue maturation was obtained using a method based on a simple mechanical sizing procedure. By pressing a homogeneous hydrogel through a grid with variable opening sizes, highly anisotropic macroporous constructs featuring aligned guidance cues were produced and exploited to direct aligned muscle tissue maturation.

The photochemical reactions presented in the first part of the dissertation are based on the generation of free-radicals to trigger the desired chemical reaction. To bypass the production of potentially harmful radicals, a radical-free (RF) approach based on a photouncaging mechanism is introduced in a following study. RF strategy was shown to have superior biocompatibility and to be suitable for high resolution two-photon stereolithography (2P-SL), thus paving the way for a paradigm shift in light-based biofabrication towards radical-free approaches.

In another study, a similar photouncaging mechanism was exploited to enable spatiotemporal controlled immobilization of bioactive signals in 3D matrices. This approach, termed two-photon patterning (2PP), allows the interrogation of bioactive signals role in tissue morphogenesis and its potential was first demonstrated with the guidance of peripheral neuron axons.

Lastly, an antibacterial biomedical adhesive based on chitosan is presented. The biocompatible and clinically compliant transglutaminase-based crosslinking was combined with chitosan electrostatic binding to negatively charged tissues. Such biomedical adhesive strategy can offer an attractive alternative to suturing in several circumstances. Finally, the dissertation closes with a summary of the contributions and an outlook.

Riassunto

L'ingegneria tissutale è un campo di ricerca interdisciplinare che riunisce i principi di biologia, chimica, scienza dei materiali e ingegneria per riparare e rigenerare organi e tessuti. A trent'anni dalla sua fondazione, l'ingegneria tissutale è cresciuta in modo esponenziale assimilando e promuovendo innovazioni dei campi di ricerca più disparati. Negli ultimi anni, i progressi nelle tecnologie di biofabbricazione tridimensionale (3D) hanno svolto un ruolo fondamentale nel creare soluzioni senza precedenti per la generazione di tessuti e organi che riproducano accuratamente struttura e funzioni native.

In particolare, l'uso della luce permette di controllare i processi di biofabbricazione a distanza e senza contatto e sta assumendo un ruolo sempre più importante in questo campo. La luce è un mezzo estremamente versatile per innescare varie reazioni fotochimiche, dalla formazione di legami chimici alla loro rottura. Ad esempio, può spaziare dalle lunghezze d'onda dell'UV a quelle del vicino infrarosso, innescando così diversi processi fotochimici e con implicazioni relative a citotossicità e capacità di penetrazione nei tessuti. La luce può anche essere generata da varie fonti, come fasci laser altamente coerenti o illuminazione LED non coerente. Inoltre, la flessibilità data dall'ampia gamma di possibili manipolazioni ottiche ha permesso la biofabbricazione di costrutti tissutali con risoluzione e dimensioni che vanno dai nanometri ai centimetri.

Questa tesi presenta una serie di lavori incentrati sullo sfruttamento della luce per applicazioni di ingegneria tissutale. Nella prima parte viene offerta una panoramica completa di questo campo in rapida evoluzione per cogliere lo stato dell'arte e le direzioni di ricerca future. Viene poi introdotta per la prima volta una fotoresina ottimizzata basata sulla chimica a scatto da utilizzare con un nuovo metodo di biofabbricazione chiamato stampa volumetrica (VP), la quale ha permesso di raggiungere una velocità di stampa senza precedenti e promettenti risultati biologici. In un secondo studio, la manipolazione ottica di una fotoresina è stata studiata per combinare la VP e l'ablazione a due fotoni ad alta risoluzione (2PA), ottenendo così il primo esempio di stampa ibrida con VP. Con questo metodo sono stati generati complessi modelli 3D di vasi sanguigni di varie dimensioni fino ad una risoluzione di $\sim 2 \mu\text{m}$, aprendo così a nuove possibilità per tecnologie di microtessuti su chip ad alta precisione.

Un altro metodo innovativo basato sulla luce e precedentemente sviluppato nel nostro laboratorio, denominato biofabbricazione a luce filata (FLight), è stato invece sfruttato per generare costrutti di cartilagine articolare con una caratteristica architettura a zone. Sfruttando le capacità di FLight di generare microfilamenti unidirezionali e altamente allineati, abbiamo indotto la deposizione anisotropa di fibrille di collagene tipiche della zona superficiale e profonda della cartilagine articolare. I condrociti infantili incorporati in una fotoresina

ottimizzata per questa applicazione, hanno indotto un'eccellente maturazione del tessuto con composizione della matrice extracellulare e proprietà meccaniche simili a quelle della cartilagine nativa.

In un altro studio, la maturazione anisotropa di tessuti è stata ottenuta con un metodo basato su una semplice procedura di ridimensionamento meccanico. Premendo un idrogel omogeneo attraverso una griglia con aperture di dimensioni variabili, sono stati prodotti costrutti macroporosi altamente anisotropi che sono stati sfruttati per promuovere la maturazione di tessuto muscolare allineato.

Le reazioni fotochimiche presentate nella prima parte della tesi si basano sulla generazione di radicali liberi per innescare la reazione chimica desiderata. Per evitare la produzione di radicali potenzialmente dannosi, in uno studio successivo viene introdotto un approccio privo di radicali (RF) basato su un meccanismo di rilascio foto-attivato di capsule fotosensibili. La strategia RF ha dimostrato di avere una eccellente biocompatibilità e di essere applicabile alla stereolitografia a due fotoni ad alta risoluzione (2P-SL), aprendo così la strada a un cambiamento di paradigma nella biofabbricazione basata sulla luce verso approcci privi di radicali.

Un simile meccanismo di fotoincapsulamento è stato sfruttato in un altro studio per consentire l'immobilizzazione spazio-temporalmente controllata di segnali bioattivi in matrici 3D. Questo approccio, denominato modellazione a due fotoni (2PP), consente di esaminare il ruolo dei segnali bioattivi nella morfogenesi dei tessuti e il suo potenziale è stato dimostrato per la prima volta con la crescita controllata di assoni di neuroni periferici.

Infine, viene presentato un adesivo biomedico antibatterico a base di chitosano. La reticolazione biocompatibile e clinicamente conforme basata sulla transglutaminasi è stata combinata con il legame elettrostatico del chitosano ai tessuti con carica negativa. Questo adesivo biomedico può offrire una valida alternativa alla sutura in diverse circostanze. La tesi si chiude in ultimo con un riassunto dei risultati e prospettive future.

Contents

CHAPTER 1: Introduction	1
1.1. Hydrogels: The Cornerstone of Tissue Engineering.....	2
1.2. Engineering the Extracellular Matrix (ECM)	3
1.3. Hydrogels: an Overview	5
1.3.1. Hydrogel Forming Polymers.....	6
1.3.1.1. Natural Polymers	6
1.3.1.2. Synthetic Polymers	7
1.3.2. Crosslinking Mechanisms	8
1.3.2.1. Chemical Crosslinking	8
1.3.2.2. Physical Crosslinking.....	9
1.3.2.3. Dynamic Crosslinking.....	10
1.4. 3D Biofabrication	11
1.5. Organization of the Work	14
CHAPTER 2: Light-Based Biofabrication	15
Abstract.....	16
2.1. Introduction.....	17
2.1.1. Skin.....	19
2.1.2. Blood Vessels	19
2.1.3. Bone.....	21
2.1.4. Liver.....	21
2.1.5. Heart	22
2.2. Photoactivated Material Toolbox.....	23
2.2.1. Light-Induced Crosslinking.....	23
2.2.1.1. Photoinitiated Chain-Growth Radical Polymerization.....	23
2.2.1.2. Photoinitiated Step-Growth Polymerization.....	26
2.2.1.3. Photomediated Redox Crosslinking	30
2.2.2. Water-Soluble Photoinitiators (PIs).....	31
2.2.2.1. Single-Photon Initiators (1PIs).....	31
2.2.2.2. Two-Photon Initiators (2PIs).....	35
2.2.3. Photodegradation and Photouncaging Reactions.....	38
2.2.3.1. Nitroaryl Groups	40

2.2.3.1.2. Nitrodibenzofuran (NDBF).....	41
2.2.3.1.3. 2-(2-Nitrophenyl)propoxycarbonyl (NPPOC).....	41
2.2.3.2. Coumarin.....	41
2.2.4. Common Photosensitive Bioinks and Bioresins.....	42
2.2.4.1. Gelatin.....	42
2.2.4.2. Hyaluronic Acid.....	44
2.2.4.3. Polyethylene Glycol (PEG).....	45
2.2.4.4. Alginate.....	46
2.2.4.5. Collagen.....	47
2.2.4.6. Poly(Vinyl Alcohol) (PVA).....	47
2.2.5. Biocompatibility of Photoactive Systems.....	48
2.3. 3D Deposition Bioprinting.....	50
2.3.1. Extrusion Bioprinting.....	50
2.3.1.1. Principles of Extrusion Bioprinting.....	50
2.3.1.1.1. Rheological Properties for Printability.....	51
2.3.1.1.2. Material Strategies for Extrusion Bioprinting.....	52
2.3.1.1.3. Embedded Printing.....	53
2.3.1.1.4. Rapid UV Crosslinking.....	55
2.3.1.1.5. Nanoparticle/Nanofibril Inks.....	55
2.3.1.1.6. Self-Healing Bioinks.....	56
2.3.1.1.7. Granular Bioinks.....	56
2.3.1.1.8. Hardware Advances for Extrusion Bioprinting.....	58
2.3.1.2. Applications.....	60
2.3.1.3. Limitations and Outlook.....	64
2.3.2. Droplet-Based Bioprinting.....	66
2.3.2.1. Principles of Droplet-Based Bioprinting.....	66
2.3.2.1.1. Hardware.....	67
2.3.2.1.2. Bioink Considerations for Droplet-Based Printing.....	68
2.3.2.1.3. Crosslinking Methods.....	70
2.3.2.1.4. Photoactivated Bioinks in Droplet-Based Bioprinting.....	72
2.3.2.2. Applications.....	74
2.3.2.2.1. HT Screening and Patterning.....	74
2.3.2.2.2. Tissue Implants.....	75
2.3.2.3. Limitations and Outlook.....	77
2.4. Vat Polymerization Bioprinting.....	79

2.4.1. Projection VP	80
2.4.1.1. Principles of Projection VP	80
2.4.1.1.1. Hardware	80
2.4.1.1.2. Resolution	84
2.4.1.1.3. Considerations for Bioprinting Cells in a Vat	86
2.4.1.1.4. Bioresins for Projection VP	87
2.4.1.2. Applications	92
2.4.1.3. Limitations and Outlook	95
2.4.2. Two-Photon SL	97
2.4.2.1. Principles of 2P-SL	97
2.4.2.1.1. 2P Absorption	97
2.4.2.1.2. Instrument Setup and Fabrication Parameters	99
2.4.2.2. 2P-Microfabrication Applications	105
2.4.2.2.1. Bond Formation in Microfabrication	105
2.4.2.2.2. Bond Cleavage in Microfabrication	116
2.4.2.3. 2P-Microfabrication Limitations and Outlook	120
2.4.2.4. 2P-Patterning Applications	122
2.4.2.4.1. Bond Formation in Patterning	123
2.4.2.5. 2P-Patterning Limitations and Outlook	131
2.5. Outlook	132
CHAPTER 3: Volumetric (Bio)Printing	136
Abstract	137
3.1. Introduction	138
3.2. Results and Discussion	140
3.3. Conclusion	147
3.4. Experimental Section	147
3.5. Supporting Information	150
3.5.1. Supplementary Methods	150
CHAPTER 4: Multiscale Hybrid Printing	160
Abstract	161
4.1. Introduction	162
4.2. Results and Discussion	163
4.2.1. Refractive Index: How to Limit Self-Focusing Effect	163
4.2.2. Towards Defect-Free Volumetric Printing (VP)	164
4.2.3. Optical Setup: Impact on Microdefects and Resolution	167

4.2.4. Hybrid Printing: Combining Volumetric Printing (VP) with Two-Photon Ablation (2PA).....	168
4.2.5. Printing of Complex Organotypic Multiscale Models	170
4.3. Conclusion	173
4.4. Experimental Section/Methods	173
4.5. Supporting Information.....	176
CHAPTER 5: FLight Biofabrication	179
Abstract.....	180
5.1. Introduction.....	181
5.2. Results and Discussion.....	181
5.2.1. Design of FLight Photoresins for Cartilage Regeneration.....	181
5.2.2. FLight Hydrogels Characterization.....	183
5.2.3. Tissue Maturation	184
5.3. Conclusions and Future Work.....	188
5.4. Materials and Methods	189
CHAPTER 6: Microstrands for Tissue Alignment	193
Abstract.....	194
6.1. Introduction.....	195
6.2. Materials and Methods	196
6.3. Results and Discussion.....	201
6.3.1. Sizing Process and Choice of the Material	201
6.3.2. Macroporosity and Percolation	204
6.3.3. Computational Modeling and Cell Viability	206
6.3.4. 3D Physical Guidance of Oriented Cell Maturation.....	209
6.4. Conclusions.....	212
6.5. Supporting Information.....	213
CHAPTER 7: Radical-Free Biofabrication.....	217
Abstract.....	218
7.1. Introduction.....	219
7.2. Results and Discussion.....	220
7.2.1. Design, Synthesis and Characterization of RF Crosslinker.....	220
7.2.2 RF Photocrosslinking.....	221
7.2.3 Cellular Response to Absence of Reactive Oxygen Species (ROS).....	224
7.2.4 2P-SL (Bio)Printing.....	227
7.3. Conclusion	230
7.4. Experimental Section	230

7.5 Supporting Information.....	236
CHAPTER 8: Two-Photon Patterning	243
Abstract.....	244
8.1. Main Text.....	245
8.2. Supporting Information.....	257
CHAPTER 9: Enzymatically Crosslinkable Chitosan Adhesive	274
Abstract.....	275
9.1. Main Text.....	276
9.2. Supporting Information.....	284
CHAPTER 10: Conclusions & Outlook	294
Acknowledgements	300
References	301
Curriculum Vitae	352

CHAPTER 1

Introduction

Three-dimensional bioprinting is a vast and exponentially growing research area in tissue engineering that encompasses knowledge varying from chemistry and biology to engineering and material science. Before embarking into the details of the research projects discussed in this dissertation, this introductory chapter offers a concise overview of some fundamental concepts of tissue engineering, hydrogel formation and bioprinting methods with particular emphasis on those aspects that will be later found throughout the thesis.

1.1. Hydrogels: The Cornerstone of Tissue Engineering

In 1993, the term Tissue Engineering made its first appearance with a pioneering article from Robert Langer and Joseph Vacanti.¹ This new research field brought together the principles of biology and engineering aiming to repair and regenerate tissues and organs. In the 30 years from its foundation, tissue engineering has grown exponentially and constantly evolved, embracing and fostering innovations from the most disparate research fields.²⁻¹³

The general paradigm is summarized in Figure 1.1A, with highly porous scaffolds composed of biodegradable polymers serving as cell transplant devices.¹ Autologous primary and stem cells can be isolated directly from patients via biopsies to limit immunological rejection. In particular, stem cells and induced pluripotent stem cells can be used to target different cell lineages, thus overcoming the expansion limit of primary cells.¹⁴⁻¹⁵ Current molecular biology offers a range of well-established protocols to isolate, induce and differentiate human cells as well genetic engineering tools to precisely edit their genome (i.e., CRISPR/Cas9).¹⁶⁻¹⁸ Vendors, on the other hand, offer a broad range of human cell types together with optimized culture media, making tissue engineering of diverse tissues more accessible. The step of *in vitro* tissue maturation has also notably evolved, with the development of sophisticated bioreactors,¹⁹⁻²³ well-defined and time-controlled culture media composition,²⁴⁻²⁹ and a series of precise imaging techniques to monitor tissue development.³⁰⁻³³ Organoids, self-organized 3D tissues derived from stem cells, are also playing an increasingly important role both in the understanding of tissue development and its regeneration.³⁴⁻⁴¹

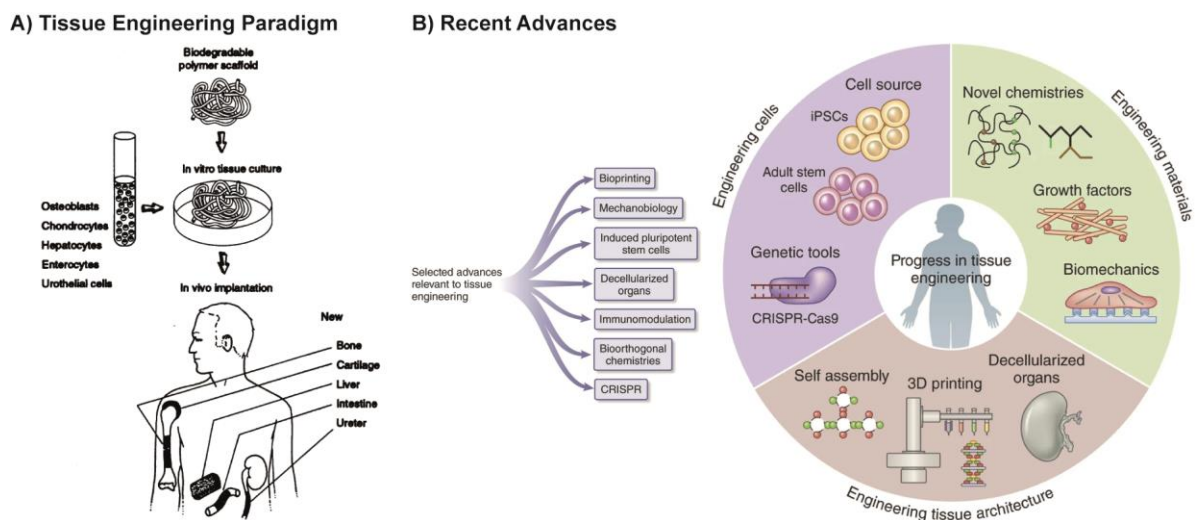


Figure 1.1 | A) General concept of tissue engineering as first described in 1993. A polymeric scaffold is used to support tissue formation by the embedded cells during *in vitro* culture. Matured tissues/organs can be implanted *in vivo* to restore impaired functions. B) In the following decades, a number of advances became available, from cell sources to genetic engineering and methods to manufacture 3D tissue constructs. Figure A and B were adapted with permission from ref.¹ and ref.², respectively.

This dissertation mostly focuses on the third element of this paradigm, the scaffold. Defined as biocompatible 3D porous matrices to biologically and physically support cells in their tissue maturation process, scaffolds represent the cornerstone of tissue engineering. Profiting from extensive literature and profound knowledge in polymer physics, polymer chemistry and material science, it is now becoming possible to precisely design tissue-specific matrices.⁴²⁻⁴⁴ Beside the possibility to choose from a wide variety of synthetic and natural polymers as well as chemical modifications, a major step-forward toward the design of functional artificial matrices was represented by three-dimensional (3D) bioprinting.⁴⁵ Recent blooming of biofabrication strategies have spawned the range of available options to precisely manufacture tissues and organs architectures, thus making it possible to generate complex cell-laden matrices with patient specific designs.

A key role in this direction has been played by hydrogels, high-water content 3D polymer networks acting as artificial matrices. Their first appearance in the literature dates back to 1960,⁴⁶⁻⁴⁷ but it is from the 90s that their biophysical and biochemical properties were applied in tissue engineering for their similarities to the native extracellular matrix (ECM). In the next sections of this introductory chapter, the ECM characteristics and how they can be engineered with hydrogels are discussed followed by an overview of the most promising biofabrication strategies.

1.2. Engineering the Extracellular Matrix (ECM)

The ECM is a dynamic, complex network of biomaterials that provides support for cells within tissues.⁴⁸ It plays a crucial role in tissue structural integrity, cellular spatial organization and by presenting biophysical and biochemical signals it regulates several aspects of cell behaviours.⁴⁹⁻⁵⁰ It is nowadays widely accepted that the functions of ECM signals are at least as important as soluble signals in governing cell processes such as differentiation, spreading, migration, proliferation and polarity.^{49, 51-53}

Therefore, one of the key steps towards the tissue engineering Holy Grail, that is the generation of functional tissues and organs, is the synthesis of engineered matrices resembling native ECM. Native ECM is highly tissue specific in its composition and topology.⁵⁰ However, it is fundamentally made of water, cell-secreted fibrous proteins (i.e., collagens and elastins), glycoproteins (i.e., laminins and fibronectins) and glycosaminoglycans (GAGs) (i.e., hyaluronan, chondroitin sulfate, dermatan sulfate), most of which found as covalently bound to core proteins forming large macromolecular elements known as proteoglycans (Figure 1.2).⁴³ Collagens provide tissue stability and cell-adhesion sites. Fibronectin binds to cell surface receptors, bioactive molecules and other structural components of the matrix, providing biophysical and biochemical integration of cells and ECM. Large negatively charged proteoglycans can also associate with cellular receptors and act as space filling component. Cells can interact with the ECM structural and bioactive

components through various surface receptors that can transmit mechanical forces or biological signals intracellularly, activating transduction pathways eventually regulating gene expression.

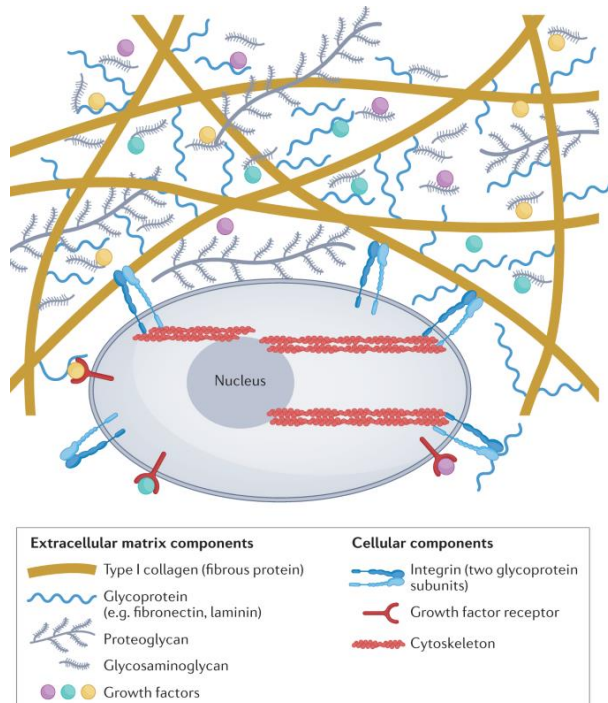


Figure 1.2 | Illustration of ECM components and their interaction with a cell. Figure reproduced with permission from ref.⁴³.

The proportion of these components and their structural organization can confer very different mechanical properties.⁵⁴ In articular cartilage for example, collagen fibrils assume various orientation at different depth of the tissue.⁵⁵⁻⁵⁷ In the superficial layer they are found to be parallel to the surface, thus better protecting the joint from shear forces, while in the deep layer they orient vertically, providing resistance to compressive forces. In Chapter 5, a novel strategy to obtain such characteristic architecture is discussed.

Due to its composition, ECM exhibits time-dependant mechanical properties (viscoelastic behaviour) and its stiffness can span between several order of magnitudes, from tens of pascals in the brain to gigapascals in the bone.^{43, 58} The fibrous architecture of natural ECM results in a highly porous network, with macropores in the range of a few to tens of micrometers. Network porosity plays a crucial role in facilitating cell spreading, migration as well as nutrient diffusion and matrix deposition.⁵⁹⁻⁶⁰ A method to generate macroporous constructs for 3D physical guidance of tissue maturation is presented in Chapter 6. Finally, ECM is continuously remodelled by the embedded cells with secretion of new matrix and enzymatic digestion of the existing one. Therefore, ECM is not only tissue-specific in its composition and architecture, but also dynamically evolving during tissue development, injuries, diseases or aging.⁶¹⁻⁶⁴

In a nutshell, mimicking ECM is not a challenge for which one solution is good for all tissues. Each one requires an accurately designed engineered ECM, with defined and possibly dynamic structural, mechanical and biological properties. Although ECMs extracted from tumours (i.e., Matrigel) and decellularized tissues are widely explored material platforms to mimic such complex environment,⁶⁵⁻⁶⁸ hydrogels represent to date the most appropriate solution in the effort to design artificial matrices in a controlled, reproducible and tunable manner.⁶⁹ Over the past 60 years publications including the term “hydrogel” have exponentially increased, reflecting the wide range of potential applications of these materials and the tremendous progress in their understanding and design (Figure 1.3).⁷⁰ Thanks to their characteristics, hydrogels can be used in the biomedical field in a variety of forms – implantable, injectable or sprayable- and applied to diverse applications, from drug and cell delivery, to adhesives (see Chapter 9), coatings or to regenerate human tissues.⁷⁰⁻⁷⁶

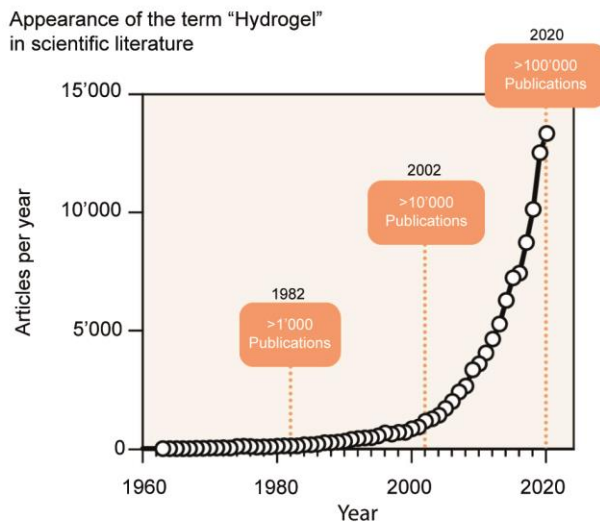


Figure 1.3 | Growth of publication per year referencing hydrogels. Adapted with permission from ⁷⁰

1.3. Hydrogels: an Overview

Their utility and translational potential is doubtless, but what makes hydrogel technology so unique? In this section, a brief smattering of hydrogels, from definition to design criteria, is offered as an introduction to relevant terms and concepts that will be encountered in the dissertation.

Hydrogels are part of a broader class of materials that can be grouped under the term *soft matter*.⁷⁷⁻⁷⁸ Since most biological systems are composed of soft matter (ECM), hydrogels represent an ideal material for tissue engineering applications. The definition of *soft* comes from a critical property of this class of materials, that is the energy landscape of intermolecular interactions. For soft matter, weak intermolecular interactions on

the scale of $\sim 1 k_B T$ ($\sim 4 \times 10^{-21}$ J at 25°C) are predominant, leading to interesting dynamic and adaptive behaviours under minimal “physiological” stimuli (temperature, mechanical stimuli). As a comparison, hard materials such as metals and ceramics have interaction energies in the order of ~ 10 - $100 k_B T$, making thermal energy ($k_B T$) at physiological temperature and mechanical stimuli not sufficient to induce deformations. Beside weak interactions, in polymer networks (ECM, hydrogels), strong intermolecular forces are present in the form of physical or covalent bonds defining crosslinking points between polymer chains and adding a broad range of elastic and viscoelastic properties.⁷⁹⁻⁸¹

In the past decades, the increased understanding of polymers and polymer network physics helped to uncover fundamental relations governing macroscopic hydrogel properties. The nature of polymers (i.e., monomer composition, chain length, architecture, functionality) and crosslinking (i.e., mechanism, density) defines hydrogel properties such as elasticity, stiffness, toughness, swelling, cell-interactions and porosity. Thanks to the development of more and more precise models,^{77, 82-83} as well as a tremendous volume of experimental work, it is nowadays possible to rationally design a hydrogel system for specific applications.^{43, 84-86}

In this thesis, different kinds of polymers and crosslinking mechanisms have been used to form a diverse range of hydrogels (i.e., soft or stiff, bioactive or bioinert, fast or slow gelling) for applications ranging from light-based bioprinting (Chapters 3-8) to biological adhesives (Chapter 9). In the following sub-sections, an overview of the polymers and crosslinking mechanisms used to form hydrogels is presented. For a more detailed description of materials and chemistries used in this dissertation, the reader should refer to specific Chapters or the extensive review on light-based biofabrication proposed in Chapter 2.

1.3.1. Hydrogel Forming Polymers

Polymers are the hydrogels’ building blocks. Parameters such as molecular weight, functionality, hydrolytic stability, reversible association dynamics and presence of cell-instructing cues play a fundamental role in defining hydrogel biophysical and biochemical properties.^{42-43, 87} Therefore, the choice of the starting material(s) is a pivotal aspect in the design of an engineered ECM and can lead to very different outcomes. Hydrogel networks are commonly categorized as natural- or synthetic-based referring to the source of the polymeric constituent.

1.3.1.1. Natural Polymers

Natural polymers have the great advantage of being native ECM components, therefore intrinsically possessing bioactive cell-instructive motifs and biodegradation properties.⁸⁸⁻⁸⁹ On the other hand, as natural polymers originate from a biological source, immunogenicity and batch to batch variability represents an inherent limitation. Natural polymers can be generally categorized as protein-based and polysaccharide-based.

As composed of saccharides or amino acids building blocks, they possess multiple functional groups (i.e., amines, thiols, carboxylic acids) that can serve as reaction sites for chemical modifications (Figure 1.4). Collagen, the most abundant fibrous proteins in mammals, and its denatured form, gelatin, are among the most widely utilized naturally-derived polymers for tissue engineering purposes.⁹⁰⁻⁹⁴ Gelatin, in particular, represents an inexpensive, off-the-shelf product that retains some key properties of its source material (collagen) such as high biocompatibility, cell-adhesion sites and enzyme-mediated biodegradation potential.⁹⁵⁻⁹⁶ As it does not retain the supramolecular fibril structure of collagen, gelatin shows the reverse solution-to-gel transition as collagen, making it necessary to chemically modify it to obtain hydrogel formation at physiological temperature ($\sim 37^\circ\text{C}$). In this dissertation, gelatin has been widely explored as a material platform for light-mediated biofabrication (see Chapters 3-6). Other natural polymers from various sources such as hyaluronic acid (HA), alginate and chitosan have also been widely exploited in the past decades for tissue engineering applications. HA and alginate were for example found to be excellent materials for cartilage (see Chapter 6),⁹⁷⁻¹⁰² and neural (see Chapter 8) tissue engineering,¹⁰³⁻¹⁰⁴ while chitosan (see Chapter 9) has been mainly adopted for its cationic and intrinsically antibacterial properties.¹⁰⁵⁻¹⁰⁶

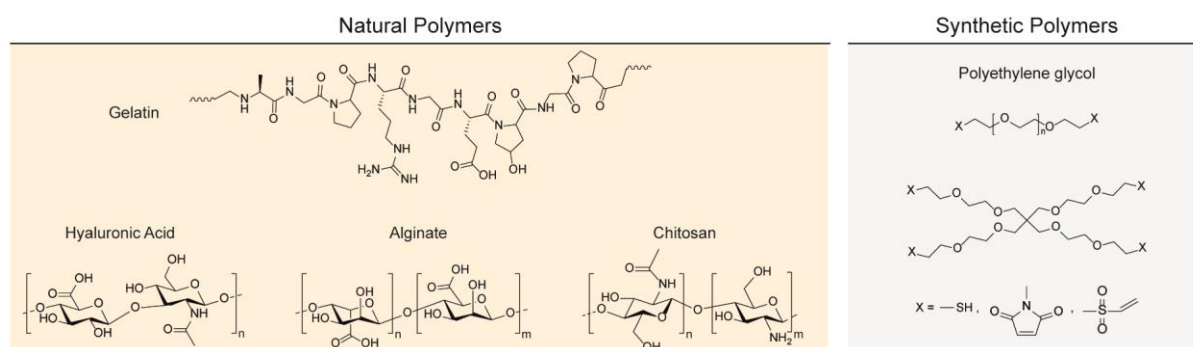


Figure 1.4 | Chemical structure of the main natural and synthetic polymers that will be later found in this dissertation.

1.3.1.2. Synthetic Polymers

In contrast to natural polymers, synthetic polymers do not commonly exhibit intrinsic bioactive properties, but offer higher processing flexibility and lower immunological concerns.¹⁰⁷⁻¹⁰⁸ They can be tailored for specific applications by changing their molecular weight, composition and architecture (i.e., linear or branched).^{44, 109} They can therefore be synthesized to match specific design requirements such as crosslinking or degradation kinetic, stiffness and cell-adhesion properties. Representative synthetic polymer in tissue engineering are poly(vinyl alcohol) (PVA), poly (N-isopropylacrylamide) (PNIPAM) and polyethylene glycol (PEG). PEG arguably represents the most widely used biocompatible synthetic polymer in tissue engineering (Figure 1.4).¹⁰⁹⁻¹¹¹ Its simple polyether structure renders it hydrophilic, antifouling and bioinert. Although it lacks bioactivity, PEG can be easily chemically modified and therefore decorated with the desired cell-

instructive molecules and peptides.¹¹² It can be found as off-the-shelf product in several architectures, from linear to multi-arm, and with a wide variety of end-chain reactive groups, from acrylate to norbornene/thiol and alkyne/azide, to name a few (Figure 1.4). PEG hydrogels have been therefore generated using various crosslinking mechanisms, from light- to enzymatic-based. In the context of this dissertation PEG was mainly used as a crosslinker in the form of linear or multi-arm thiolated PEG (PEGSH) for crosslinking based on thiol-norbornene photoclick reaction (Chapter 3, Chapter 5) and thiol-Michael addition (Chapter 7).

Overall, the current broad palette of polymers and possible chemical modifications provide a powerful tool for the rational design of hydrogels with tailored properties targeting tissue-specific extracellular environments.

1.3.2. Crosslinking Mechanisms

In addition to the choice of the hydrogel forming polymers, the design of an engineered artificial ECM with certain properties, such as stiffness, stability, gelation kinetic or stress-relaxation is strongly dependent on the crosslinking mechanism.¹¹³⁻¹¹⁵ Crosslinking can be simply defined by the formation of links between polymer chains. The so-called gelation – transition from polymeric solution into polymer network - occurs when the links formed between polymer chains reach an extent at which the system can no longer be identified as composed of multiple chains, but as a single macromolecular entity (polymer network). The gelation can occur via various mechanisms, generally distinguished as chemical or physical crosslinking.

1.3.2.1. Chemical Crosslinking

The formation of covalent bonds can be attained with several reaction mechanisms. To date, the most promising strategies can be divided into click reactions, enzymatic crosslinking and light triggered free-radical crosslinking. Compared to physical crosslinking, the presence of chemical bonds usually determines higher mechanical properties and enhanced stability of the polymer network.

Click-chemistry. Click-chemistry is a term, introduced in 2001 by Barry Sharpless and co-workers, to define a family of modular reactions that occurs fast, with high selectivity and stereo-specificity, high yield and with non-toxic end products.¹¹⁶ The introduction of such efficient form of chemistry has represented a major breakthrough in various sectors and was recently recognized with the 2022 Nobel Prize in Chemistry to Barry Sharpless, Carolyn Bertozzi and Morten Meldal. Until relatively recent, research on click-based hydrogels have focused almost exclusively on copper catalysed alkyne-azide cycloaddition.¹¹⁷ Today, the term click-chemistry includes an increasingly large family of reactions that can fall under this description.¹¹⁸⁻¹¹⁹ Of particular interest for biological application, where copper raises serious cytotoxicity concerns, a series of copper-free click-chemistries are now adopted to form hydrogels including for example Diels-Adler

cycloaddition,¹²⁰⁻¹²³ strain promoted alkyne-azide cycloaddition (SPAAC),¹²⁴⁻¹²⁵ oxime ligation,¹²⁶⁻¹²⁷ and Michael type-addition.¹²⁸⁻¹³¹ In the context of this work, thiol-Michael addition was exploited as a crosslinking mechanism for radical-free light-mediated biofabrication (Chapter 7).

Photocrosslinking. Light-mediated crosslinking in tissue engineering and 3D bioprinting is a fast-growing field which has also driven the (and adapted to) advances in light-based technologies. Upon light absorption, a photoinitiator molecule generates initiating radical species which then trigger the photocrosslinking mechanism. The palette of photochemical reactions includes free-radical polymerizations and step-growth polymerization mechanisms.¹³² As it represents the focus of this dissertation, an in-depth discussion on photocrosslinking mechanisms and photoactivated materials can be found in dedicated chapter (Chapter 2).

Enzyme-mediated crosslinking. Enzymes work in our body at physiological conditions and generally high substrate-specificity, making them an attractive alternative for many biomedical applications to avoid potential toxicity of chemicals, radicals, or reactions by-products.¹³³⁻¹³⁵ On the other hand, enzymatic catalytic activity can be significantly affected by small variations in temperature, pH or accessibility of the substrates.¹³⁵ Some examples of enzymes commonly used for hydrogel crosslinking are transglutaminase,¹³⁶⁻¹³⁸ tyrosinase,¹³⁹ sortase A,¹⁴⁰ and peroxidases.¹⁴¹ Transglutaminases (TGs) are a broad family of enzymes that catalyse the reaction between the free amine group of a lysine and the carboxamide group of a glutamine introducing an isopeptide bond.¹⁴² Factor XIII, a plasma transglutaminase responsible for the formation of the fibrin cloth in the coagulation cascade, has been used for the site-specific formation of various hydrogels.^{98, 104} In this dissertation a FXIII-crosslinkable hyaluronic acid (HA-TG) was used in the context of neural tissue engineering (Chapter 8) and a FXIII-crosslinkable chitosan derivative was developed to generate an in situ gelling antibacterial cartilage adhesive (Chapter 9). Another attractive enzyme-mediated crosslinking is offered by Sortase A, a transpeptidase extracted from gram-positive bacteria with high substrate specificity.¹⁴⁰ The enzyme recognition motifs (LPXTG) are cleaved between threonine and glycine residues to form a thioester bond with a terminal oligoglycine. Sortase A has shown good biocompatibility, no immune response when implanted *in vivo* and has the intrinsic advantage of being orthogonal to mammalian tissues.¹⁴⁰ In this thesis, sortase A was used to selectively immobilize bioactive cues in biological 3D matrices (Chapter 8).

1.3.2.2. Physical Crosslinking

Physical crosslinking occurs under mild conditions via non-covalent bonds including ionic/electrostatic interactions (i.e., alginate), hydrogen bonding (i.e., ureidopyrimidinone-based), hydrophobic interactions (i.e., LCST/UCST-based) and host-guest (i.e., cyclodextrin, cucurbituril-based) interactions.^{113, 115, 143-148} Due to the low-energy, non-covalent nature of these bonds, physical gels are generally softer than the chemically-crosslinked ones, but show intrinsic reversible, stimuli-responsive and self-healing properties.¹⁴⁹⁻¹⁵⁰

Amongst the most widely used non-covalent crosslinking strategies in tissue engineering, the ionic crosslinking of alginate and the thermal gelation of collagen and gelatin have played a central role.¹⁵¹⁻¹⁵³ Alginate is a bioinert and biocompatible linear polysaccharide composed of irregular blocks of mannuronic and guluronic acid residues (Figure 1.4). In the presence of divalent cations such Ca^{2+} , guluronic-rich blocks associate forming the so-called egg-box junctions.¹⁵⁴ In this work, the physical gelation of alginate was exploited for cartilage (Chapter 5) tissue engineering. On the other hand, collagen and gelatin undergo (opposite) thermal dependent structural rearrangement which can lead to hydrogel formation. Gelatin reversible physical crosslinking was exploited to form thermal sensitive hydrogels desirable for VP (Chapters 3 and 4) and a sizing-based printing method (Chapter 6).

1.3.2.3. Dynamic Crosslinking

In recent years, both chemical and physical crosslinking have been investigated for the formation of dynamic matrices. The use of reversible or dynamic crosslinking represents a promising approach to capture the dynamic nature of the ECM.¹⁵⁵⁻¹⁵⁷ A first, well studied strategy to move away from static hydrogels used enzymatically cleavable peptide sequences (i.e., MMP), but although it can resemble biodegradation of native ECM, this strategy leads to potentially undesired bulk hydrogel degradation over time. Beside proteolytic degradation, cellular remodelling of the ECM also happens due to dynamic physical linkages of the constituent fibres due to energy dissipation via stress-relaxation and rearranging of the matrix fibrous architecture. Several reversible chemistries, although mainly incorporated into non-fibrillar matrices, have shown promising results in capturing such crucial aspects.¹⁵⁸ Adaptable networks can be formed via physical interactions (i.e., host-guest, electrostatic) or via chemical bonds profiting from dynamic equilibrium of covalent linkages such as imine, hydrazone or oxime bonds.¹⁵⁹⁻¹⁶¹ Maintaining the bulk properties of the hydrogel while on the molecular level bonds are dynamically break and reform, is foreseen to play a central role in the development of the new generation of engineered ECMs. Also, given the diverse properties attainable with chemical and physical crosslinking, in the last decade an emerging trend in hydrogel research is represented by the combination of the two methods. Combining elastic and dissipative hydrogels can for example result in a significant increase in network toughness.¹⁶²⁻¹⁶⁴ In this dissertation, a double network that combined thiol-norbornene photoclick chemistry and alginate ionic crosslinking was investigated for cartilage tissue engineering (Chapter 5).

1.4. 3D Biofabrication

As described above, hydrogels can be designed as artificial matrices to support embedded cells and promote tissue (re)generation. However, to fully recapitulate tissues complexity, also micro and macrostructures should be attained. Biofabrication is a class of manufacturing processes in which hydrogel-forming biomaterials, bioactive molecules and living cells are combined and synergize to generate 3D functional constructs with tissue/organ-like structural organization.^{45, 165-169} Including biological components increases exponentially the complexity of these manufacturing processes when compared to non-biological ones. In fact, the accurate choice of material and crosslinking method should be optimized for a determined tissue and also match the technical requirements of the printing method (i.e., viscosity, transparency). Moreover, the integrity of the cellular component should be considered. For example, mechanical or thermal stress, long printing times, exposure to external stimuli (i.e., chemical, radicals, UV) can all have detrimental effect on cell viability and gene expression, thus hindering the regeneration potential.¹⁷⁰⁻¹⁷⁶

A typical workflow for 3D biofabrication starts with the image acquisition of the targeted tissue/organ, for example via computed tomography (CT), magnetic resonance (MRI) or two-photon imaging (Figure 1.5). These images are then used to reconstruct a 3D model compatible with the desired printing method/s. Alternatively, 3D models can be generated directly with a CAD software, nowadays also implementing sophisticated artificial intelligence functionalities (i.e., Chapter 4 design of organotypic vasculature models).

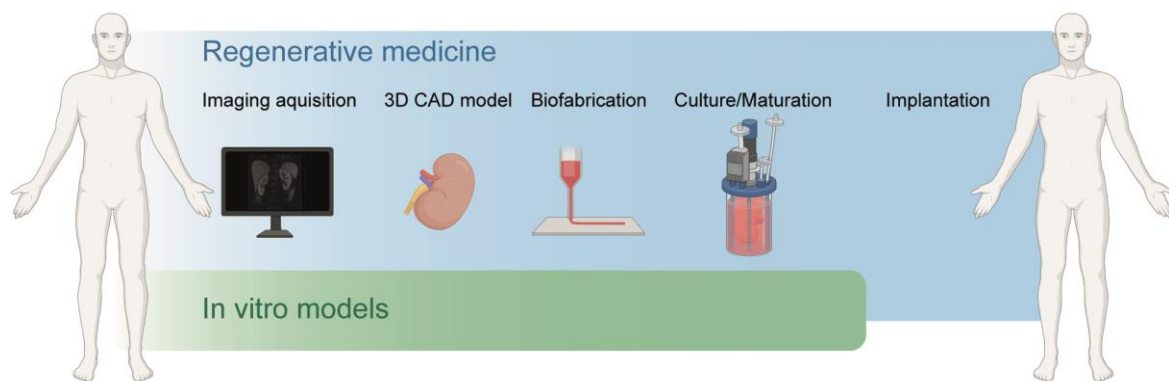


Figure 1.5 | Workflow for 3D biofabricated tissues and organs which can be exploited for regenerative medicine purposes (implants) or *in vitro* models (i.e., organ-on-a-chip). Adapted with permission from ⁴⁵

The biofabrication of the 3D anatomic model can then be achieved using various techniques which can be generally classified as deposition-based (i.e., extrusion or droplet/inkjet bioprinting) or vat-based (projection/scanning laser stereolithography or volumetric printing) (Figure 1.6).^{132, 177-178} Deposition-based methods rely on a layer-by-layer sequential deposition of drops (droplet/inkjet) or filaments (extrusion) of materials. In droplet printing controlled volumes of materials formed by either thermal or acoustic forces are

ejected and precisely delivered onto desired locations.¹⁷⁹⁻¹⁸⁰ For extrusion bioprinting a material possessing shear thinning and shear recovery properties is extruded through a nozzle to generate the 3D architecture in a layer-by-layer fashion either by pneumatic, piston or screw-driven extrusion.^{165, 177, 181-182} Due to its ease of use, scalability and cost-effectiveness, extrusion bioprinting became the most widely adopted biofabrication method. Amongst the numerous adaptations and developments of this printing method, the extrusion of sacrificial material in supporting gels gained particular interest in recent years with FRESH (freeform reversible embedding of suspended hydrogels),¹⁸³⁻¹⁸⁶ and SWIFT (sacrificial writing into functional tissues).³⁵

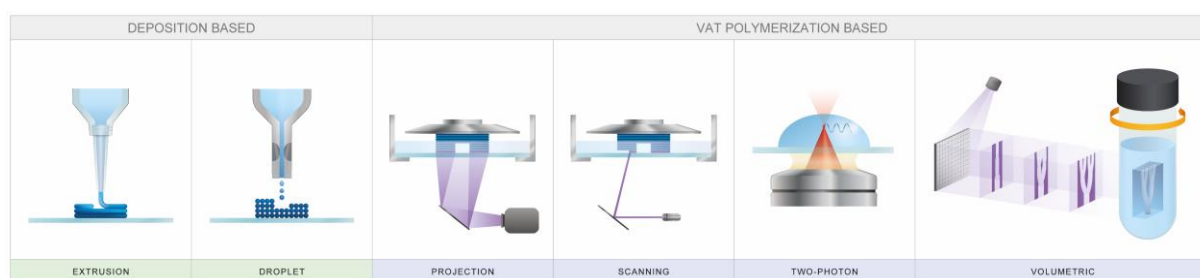


Figure 1.6 | Biofabrication methods classified as deposition-based (extrusion and droplet) and vat-polymerization based (projection, scanning one- and two-photon stereolithography and volumetric printing). Figure adapted with permission from ¹³² and ¹⁸⁷.

Although extrusion remains the most widely recognized example of 3D printing, this term was first described in 1986 by Charles W. Hull for a methodology known as stereolithography.¹⁸² Stereolithography is a light-mediated printing method in which layers of materials contained in a vat are sequentially cured to form a 3D structure (Figure 1.6).¹³² With the development of faster and more biocompatible photocrosslinking chemistries, vat-based stereolithography has been successfully exploited as a bioprinting method.¹³² As it can be easily manipulated with optics, the use of light as crosslinking trigger makes it possible to have unprecedented resolution with tightly focused lasers as in two-photon stereolithography (2P-SL), large build volumes as in digital light projection (DLP) or fast layer-less biofabrication as in volumetric printing (VP). An extensive review on light-mediated biofabrication and photoactivated materials is found in Chapter 2.

The bioprinted tissue is then matured *in vitro* and eventually implanted in the patient to restore the impaired function. However, the path toward clinical translation still presents key challenges (Figure 1.7).^{2, 177, 188-190} These include for example the printing of multimaterial/multicellular large, organ-size constructs with high cell density and spatial heterogeneity. In order to print large construct with high cell density, the isolation and expansion of a large number of cells, without affecting their phenotype, is necessary. Large organ-size constructs require also vascularization for a sufficient exchange of nutrients and oxygen and eventually anastomosis with the patient's blood circulation. Upon implantation, engineered constructs need to be tolerated by the host to avoid deleterious immune responses. Finally, for a controlled and standardized workflow, strategies to validate the structure fidelity and functions of the biofabricated tissues and organs are

necessary. A similar workflow, not including implantation step, can also be applied to the biofabrication of *in vitro* models (i.e., organs-on-a-chip)(Figure 1.5). Developed as a side branch of microfluidics, organ-on-a-chip technology aims to recapitulate tissue architecture and function in a chip, thus creating models particularly suited for high throughput applications ranging from drug screening to disease modelling.^{13, 191} In Chapter 4, a hybrid printing strategy to generate complex vasculature networks for potential on-a-chip applications is described.

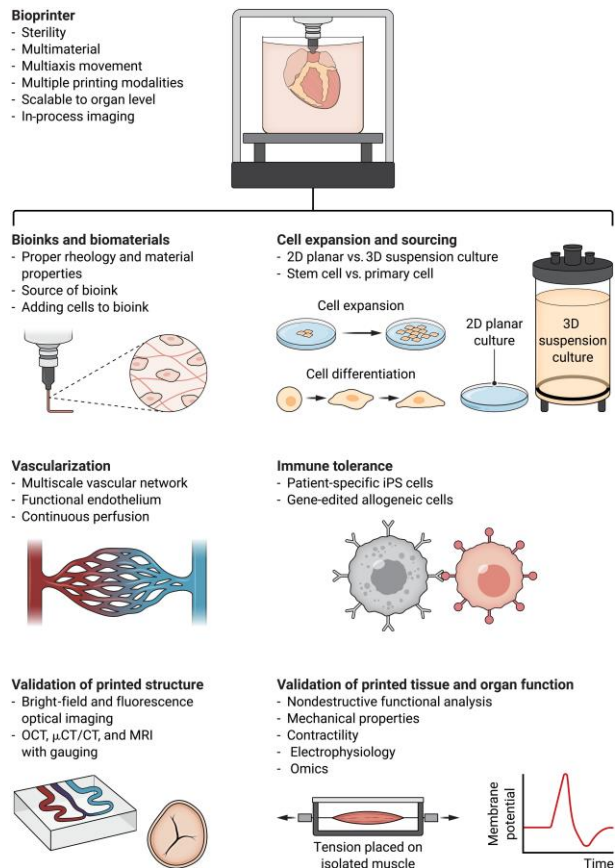


Figure 1.7 | Challenges and requirements for biofabrication of tissues and organs. Reproduced with permission from¹⁸⁸

Overall, despite the fact that engineering functional tissues is an extremely complex task with multifaceted challenges that remain to be addressed, the rapidly advancing 3D biofabrication field is showing promising results.^{13, 188-190} In this dissertation, contributions towards this end goal are mainly focused on the development of biocompatible and high performance photoresins for volumetric printing (VP) and two-photon lithography (2P-SL).

1.5. Organization of the Work

A comprehensive review of the main topic of this dissertation, photoactivated materials and light-mediated 3D biofabrication, is presented in Chapter 2. Then, Chapter 3 reports on the use photoclick chemistry in VP. Progress in VP and its combination with two-photon ablation (2PA) is discussed in Chapter 4. A novel light-based technique to generate aligned tissues named FLight is exploited in Chapter 5 for cartilage tissue engineering. Another approach to obtain tissue alignment based on mechanical sizing is then presented in Chapter 6. In Chapter 7, a chemical strategy based on one and two-photon-triggered uncaging mechanism is exploited to achieve photocrosslinking in a radical-free (RF) fashion. A similar two-photon uncaging mechanism is also explored in Chapter 8 to immobilize cell-instructive cues in 3D matrices at user-defined locations. Finally, Chapter 9 describes synthesis and characterization of a novel enzymatically crosslinkable chitosan adhesive. The dissertation closes with an overview of the contributions and an outlook.

CHAPTER 2

Light-Based Biofabrication

A Review

Chapter 2 offers a comprehensive review on photoactivated materials and light-based biofabrication strategies. The following chapters, mostly discussing research projects revolving around the use of light as a remote, contact-less trigger for photochemical reactions, leverage the knowledge of state-of-the-art techniques, materials and current limitations presented in this extensive work.

MANUSCRIPT

Guiding Lights: Tissue Bioprinting Using Photoactivated Materials

Mihyun Lee†, Riccardo Rizzo†, František Surman†, and Marcy Zenobi-Wong†

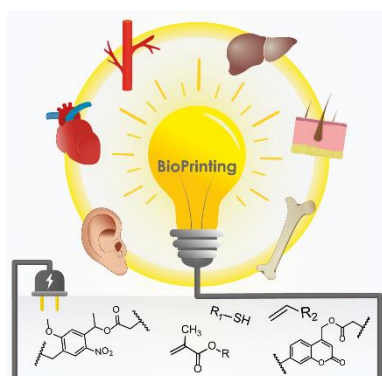
Chemical Reviews **2020** 120 (19), 10950-11027

DOI: 10.1021/acs.chemrev.0c00077

†Equal contributions in alphabetical order.

Reprinted with permission from Chem. Rev. 2020, 120, 19, 10950–11027, Copyright © 2020, American Chemical Society

Abstract



Photoactivated materials have found widespread use in biological and medical applications and are playing an increasingly important role in the nascent field of three-dimensional (3D) bioprinting. Light can be used as a trigger to drive the formation or the degradation of chemical bonds, leading to unprecedented spatiotemporal control over a material's chemical, physical, and biological properties. With resolution and construct size ranging from nanometers to centimeters, light-mediated biofabrication allows multicellular and multimaterial approaches. It promises to be a powerful tool to mimic the complex multiscale organization of living tissues including skin, bone, cartilage, muscle, vessels, heart, and liver, among others, with increasing organotypic functionality. With this review, we comprehensively discuss photochemical reactions, photoactivated materials, and their use in state-of-the-art deposition-based (extrusion and droplet) and vat polymerization-based (one- and two-photon) bioprinting. By offering an up-to-date view on these techniques, we identify emerging trends, focusing on both the chemistry and instrument aspects, thereby allowing the readers to select the best-suited approach. Starting with photochemical reactions and photoactivated materials, we then discuss principles, applications, and limitations of each technique. With a critical eye to the most recent achievements, the reader is guided through this exciting, emerging field, with special emphasis on cell-laden hydrogel constructs.

2.1. Introduction

Life on earth has evolved diverse mechanisms to harness the power of sunlight. Accordingly, the natural world is replete with examples of how living organisms interact with light to store energy, catalyze reactions, detect the external environment, and actuate. In addition to these natural examples, the discovery of light-emitting and light-sensing proteins¹⁹²⁻¹⁹⁵ has revolutionized biotechnology, resulting in disease treatment (photodynamic therapy)¹⁹⁶⁻¹⁹⁸ and control of cellular processes at an unprecedented level of spatial and temporal resolution. The conformational changes of membrane receptors, in particular the channelrhodopsins, have established the field of optogenetics¹⁹⁹⁻²⁰¹ and allow spatiotemporal control of neuronal activity²⁰¹ but also control of gene expression of multiple cell types²⁰² and migration.²⁰³ Recent biotechnological developments make possible light-induced editing of the genome by CRISPR-Cas9 photouncaging.²⁰⁴ By putting photolabile cages on molecules such as peptides, drugs, second messengers, mRNA, and ATP, one can render a whole host of cellular processes light-activatable at the subcellular level.

The power of light is increasingly used not only to control the cells behavior, but also to more intelligently design their 3D biomimetic extracellular environment. Through the connection of photoactivated biomaterials with bioprinting methods, cellular scaffolds are being printed that have complexity not previously obtained. Examples include: (1) printing/guiding at the resolution of micrometer-sized biological structures such as capillaries²⁰⁵⁻²⁰⁶ and neurites,²⁰⁷ (2) printing multimaterial and multicellular constructs,²⁰⁸⁻²¹⁰ (3) controlled patterning of biological cues in the matrix,²¹¹⁻²¹³ and (4) changes in mechanical properties at subcellular spatial resolution.^{205, 214-215} Promisingly, there is an increasing number of examples where bioprinted constructs have shown enhanced functionality compared to conventional homogeneous tissue-engineered environments.²¹⁶ The hope for the field is that these tissues could one day be used as living replacements to regenerate injured or diseased tissues and organs and as predictive high-content screening platforms for drugs.

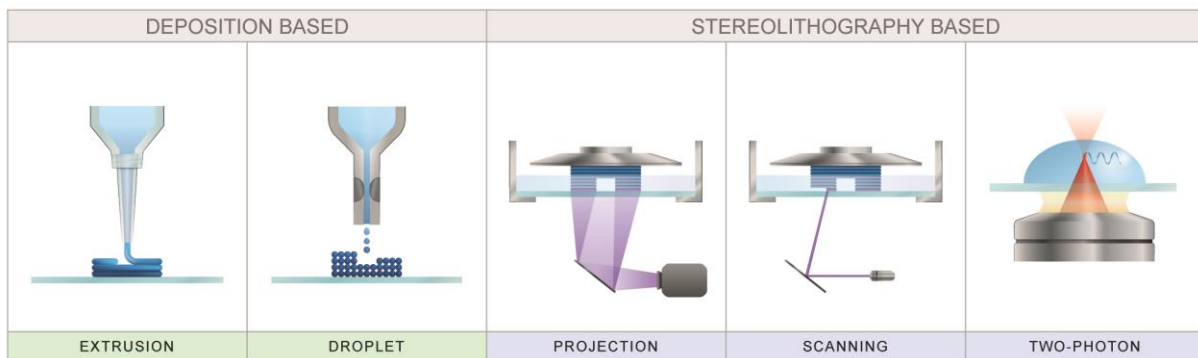


Figure 2.1 | Bioprinting modalities can be divided into deposition- and vat polymerization-based techniques.

Living tissues and organs display a hierarchical organization, and it has been postulated that this organization can be recapitulated by the length scales of various chemical/material reactions and biofabrication techniques.²¹⁷ Not all of the biological length scales (from atomic, molecular, macromolecular, cellular, cellular functional unit, tissue, organ, to an organism) can be replicated by current bioprinting techniques, however, certain length scales are possible (Figure 2.1, Table 2.1). For example, the extrusion bioprinting is an excellent method for printing tubular structures of several hundred microns in diameter, as this is the dimension of the bioink strand, which is extruded through the printer's nozzle.²¹⁸ Vat polymerization (VP) bioprinting, on the other hand, is a method in which a structure is solidified from a vat of photosensitive resin through controlled exposure to light. The method can be performed at very high resolution, suitable even for manipulating properties of the extracellular environment at subcellular resolution.^{124, 213, 219} In Table 2.1, we summarize the basic features of four bioprinting methods (extrusion bioprinting, droplet-based bioprinting, and projection/scanning and two-photon VP) that have profited most from the power and utility of photoactivated materials. General features of these methods, including feature size, maximum structure size, cost, and applicability for multimaterial printing or high throughput (HT) applications are shown.

Table 2.1 | Comparison of deposition bioprinting techniques (green) and vat polymerization bioprinting techniques (blue).

	DEPOSITION		VAT POLYMERIZATION	
	Extrusion printing	Droplet printing	Projection VP	Two-photon stereolithography
Max. structure size	cm	cm	cm	mm
Average time to print 1 cm³ block	20 min	N.A.	1 hr	Days
Typical feature size	100-600 μm	50-500 μm	25 - 150 μm	100 nm – 1 μm
Multimaterial	***	****	*	*
High throughput	**	****	**	*
Typical viscosity of ink/resin	10,000 Pa·s	<15 mPa·s ^d <200 mPa·s ^b	10 – 5000 mPa·s ^c <90,000 mPa·s ^d	Viscosity-independent
Cost of device (\$)	30-250k	5k	30k-50k	90k – 500k

^aInkjet printing ^bMicro-valve printing ^cConventional VP ^dVolumetric VP

To select the right printing method for the desired application, it can be useful to understand the hierarchical organization of tissues and organs. Tissues are typically defined as an aggregation of cells with similar structure and function. These cell groups can be categorized as falling under one of four types: connective, epithelial, muscle, or nerve.²²⁰ Higher-level tissues, however, can also be composite in nature, being made up of cell groups from more than one category. For example, muscle tissue can contain epithelial type cells in its vessels and connective tissue in the peri-, epi-, and endomysia as well as innervation.²²¹ In another example, vascular

tissue and lymphatic tissue are composed of a single layer of endothelium (a specialized type of epithelial cells) together with smooth muscle and adventitia (a type of connective tissue).²²² Tissues can vary greatly in their cellular density, ranging from ~ 9000 cells/mm³ in tissues like cartilage²²³ to $\sim 150\,000$ cells/mm³ in solid epithelial organ tissues such as liver.²²⁴ Organs can also be typed based on different criteria. For example, they can be ordered according to geometrical complexity, ranging from flat, tubular, hollow, to solid organs.²²⁵ Flat organs, such as cartilage²²³ and cornea,²²⁶ are avascular and contain just one or a few cell types. Most organs contain all four types of tissues. Figure 2.2 shows the important anatomical features of different types of organs that have been of interest in the biofabrication field.

2.1.1. Skin

Skin is a complex flat organ consisting of epidermis (epithelium), which is supported by an underlying dermis (connective tissue)²²⁷ (Figure 2.2). As an epithelial tissue, epidermis provides key barrier, secretion, and protection functions. This tissue is primarily cellular with the packing density of cells around 35 cells/100 μm^2 .²²⁸ An epithelial cell is polarized, with its basal domain/membrane facing the extracellular matrix (ECM) of the basement membrane, the apical side of the cell facing the lumen, and tight-junction-mediated contacts to neighboring cells laterally. Biofabrication of skin analogues has been considered relatively straightforward due to its 2D-like flat structure. A skin-mimetic construct with two characteristic layers of epidermis and dermis has been successfully biofabricated by an extrusion bioprinter (Figure 2.2, skin example).²²⁹ However, the *in vivo* functionality of skin is also supported by glands, sensory neurons, immune cells, and hair follicles, which have complex microarchitectures and functions that are traditionally hard to mimic and still remain challenging. In particular, hair follicles have been the subject of tissue engineering and biofabrication approaches.²³⁰

2.1.2. Blood Vessels

Blood vessels, tubular organs, have a branching structure (Figure 2.2), where large arteries with a diameter of several millimeters branch into narrower arterioles (diameter 5–100 μm) and then to capillaries (diameter 5–10 μm).²²² All structures of the macro/microcirculation are lined by a single layer of endothelial cells. All vessels except capillaries are enveloped by a circular layer of smooth muscle cells (tunica media) and an outer layer of innervated connective tissue (tunica externa).²²² The arterioles play a particularly important role in vasodilation and regulation of blood pressure. This general layered organization is also seen in more complex hollow organs like bladder, stomach, and esophagus, where the barrier, secretion, transport, and sensing properties of the epithelium play an important role in the function of the organ. One approach to printing narrow blood vessels with micrometer resolution is to make use of two-photon stereolithography (2P-SL).²⁰⁶ Branched 3D microvasculature geometries were printed in native collagen. The endothelial layer was

formed by HUVECs seeding after washing the uncrosslinked collagen from the vessel lumen (Figure 2.2, artery example).

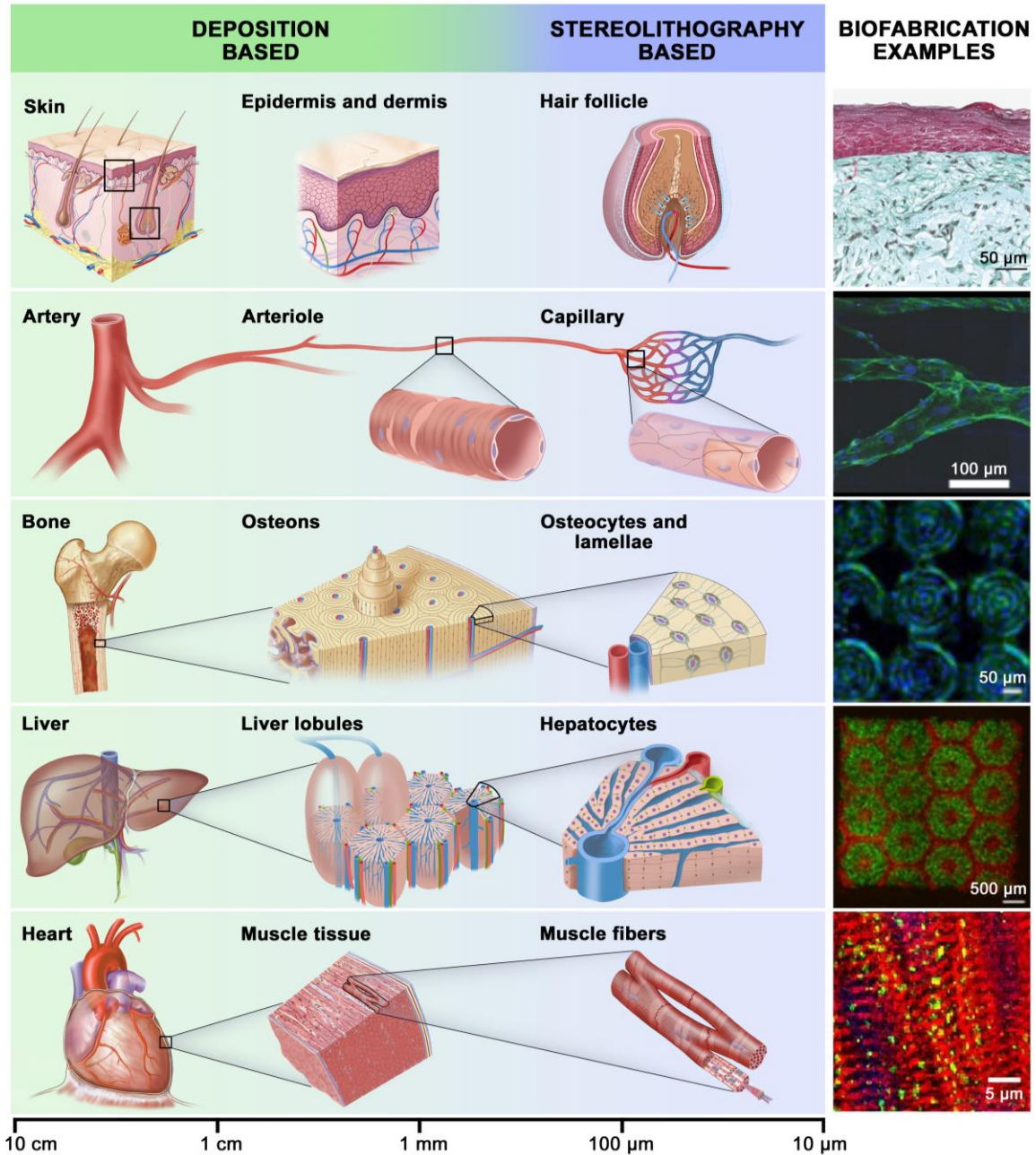


Figure 2.2| Hierarchical organization of flat (skin), tubular (artery), and solid (bone, liver, heart) organs of the body and relevant examples from the biofabrication literature. Skin: Adapted from with permission ref 39. Copyright 2016 Wiley-VCH. Artery: Adapted with permission from ref 15. Copyright 2016 Wiley-VCH. Bone: Adapted with permission from ref 47. Copyright 2019 Elsevier Ltd. Liver: Adapted with permission from ref 50. Copyright 2016 US National Academy of Sciences. Heart: Adapted with permission from ref 19. Copyright 2016 Elsevier Ltd.

2.1.3. Bone

Compact or cortical bone is a mineralized connective tissue with outstanding toughness due to its arrangement of collagen and hydroxyapatite mineral nanocrystals.²³¹ The composition and ultrastructural architecture of the 3D ECM not only lend the mechanical strength^{48,232} but also provide the embedded cells with signaling and biophysical cues.²³³ The tissue is organized into functional units called osteons (Figure 2.2). Osteons arise during the remodeling of the diaphysis of long bones.²³⁴ Bone-resorbing osteoclast cells tunnel their way into bone, bringing blood vessels with them. Bone-forming osteoblasts then deposit layers of lamellar bone (osteoid) along the surface of the channels, incrementally narrowing the central channel, leaving only the small blood vessel to nourish the osteon. Osteoblasts, which are entrapped in the normal mineralized lamella, become osteocytes, which themselves are connected by a network of cytoplasmic synapses, filling channels called canaliculi.²³⁵ Osteon-like concentric microgrooved patterns were created by combining photolithography with melt-casting (Figure 2.2, bone example). Microgrooved polycaprolactone surface patterns induce the corresponding cellular morphology and arrangement. Also, the surface exhibited suppressing of osteoclastogenic differentiation of RAW264.7 cells and modulated the secretion of osteoclastogenic cytokines by mesenchymal stem cells (MSCs). Osteoclast formation and activity created pathological conditions to delay the process of bone repair.²³⁶

2.1.4. Liver

Solid organs such as the liver and the heart have also been of interest to the biofabrication field. In the liver, the parenchymal tissue is organized into hexagonal-shaped lobules, the functional repeating unit of the liver.²³⁷ Each lobule is a mini-filtration system in which blood from the hepatic artery and portal vein enters the lobule at its outer spokes and passes by the hepatocytes before exiting through the central vessel. The hepatocytes are polarized based on exposure to gradients in nutrients, oxygen, and morphogens.²³⁸ Lobule-mimetic hexagonal structures have been successfully biofabricated using projection VP with multimaterials and multiple cell types (Figure 2.2), where enhanced hepatic cellular functions were confirmed compared to 2D or single-cell type culture.²³⁹ Still, most biofabricated structures so far retain very simplified features compared to the native tissue in terms of layer numbers, cell types, and the presence of perfusable vessels. Furthermore, with the current VP technique, it is difficult to achieve HT biofabrication of such microarchitectures requiring high resolution, which should be addressed if one aims to replace a whole organ or large piece of tissue with bioprinted one.

2.1.5. Heart

The heart, composed primarily of cardiac muscle, is a highly cellular contractile tissue, again with hierarchical organization.²⁴⁰ The cardiac muscle or myocardium is embedded between the epi- and endocardium layers. The myocardium is composed of single cells, the myocytes, which are around approximately 100 μm in length and are joined together at their long ends by intercalated discs, structures that ensure tight connectivity and synchronized contractility of the tissue. The cytosol of myocytes is filled with myofilaments, themselves composed of sarcomeres, the basic contractile unit of muscle. In biofabrication of this organ, scaffolds to help achieve alignment myotubes are critical. One approach has been to use bioprinting to extrude hydrogel strands, which then guide the seeded cells to form oriented, contractile cardiac tissue (Figure 2.2, heart example).²¹⁰

In addition to microarchitectures, solid organs have, by necessity, developed a complex arborization of blood vessels, lymphatics, and neural “stromata”. Metabolically active cells can be no more than a few hundred micrometers away from the nearest capillaries (the size of most “functional units”) due to the diffusion distance of oxygen.²⁴¹ This organic structure of solid organs is challenging to achieve by any engineering method, and thorough knowledge of the complex and interdependent pathways and crosstalk involved in organ morphogenesis is important. In addition to the significant challenge of engineering tissues of this spatial complexity, epithelial solid organs have a very high density, with multiple cell types, making tissue engineering very challenging from a metabolic demand perspective. We believe that photoactivated biomaterials and bioprinters of increasing sophistication will enable the engineering of tissues and organs that mimic their native counterparts to the extent that they can be used in clinical settings.

The goal of this review is to provide an overview of the light-based biofabrication toolbox, which consists of photochemistries, photoactivated polymers, and bioprinting technologies (Figure 2.1). In the photochemistry section, we restrict ourselves primarily to those reactions, which can be performed in water, are relatively fast, and occur under physiological conditions, allowing for cell encapsulation without significant cytotoxicity. For the polymers, we concentrate on hydrogels, which are three-dimensionally crosslinked hydrophilic polymer networks that can absorb large amounts of water without dissolution and provide an excellent mimic of native extracellular environments of cells. For the bioprinting methods, we focus on the most common deposition-based bioprinting methods (extrusion and droplet printing) and vat polymerization-based bioprinting methods (one-photon and two-photon) (Figure 2.1). We discuss which photochemistry, polymer, and technology combination is appropriate to achieve a desired print quality and resolution and which combinations are compatible with the specific biological demands of the embedded cells. Finally, we adopt quite a broad definition of the word “printing”, namely as an automated process in which cells, materials, and biological cues are drawn onto a 3D canvas according to a predesigned (computer) model. In this analogy,

the palette consists of photoactivated polymers, cells, and biological molecules, and we refer to these materials as **bioinks** when used in deposition-based bioprinting and **bioresins** for vat polymerization-based bioprinting. The “paintbrushes” are the printers, which can draw 3D structures using photoactivated formation of chemical bonds and erase material from the drawing by means of photoactivated cleavage of bonds.

2.2. Photoactivated Material Toolbox

From a biomaterial chemistry perspective, photochemical reactions can either lead to the formation of new bonds (photo-crosslinking) or the cleavage of existing bonds (photodegradation). The constructive and destructive nature of photoactivatable compounds allows for the biofabrication of biomaterials with predetermined microstructure to modulate hydrogel stiffness,²⁴² to degrade hydrogel to obtain high precision patterns in mechanical properties²⁴³ or to specifically immobilize/remove biochemical cues.²⁴⁴ By doing so, hydrogels able to mimic the native ECM can be achieved. Light-induced biofabrication of tissue models is also dependent on the appropriate selection of hydrogel precursors, photoinitiators (PIs), and light dosage. The following section will survey various photochemical processes and materials and their applicability in 3D bioprinting technologies for cell-laden hydrogels.

2.2.1. Light-Induced Crosslinking

Using light in 3D bioprinting techniques is already well established, perhaps most widely in preparing crosslinked hydrogels containing viable cells.^{167, 245} There is a broad range of photoactivated groups that, upon light stimulus, either form molecules with unpaired valence electrons called radicals or undergo an internal electronic activation, allowing them to react. Crosslinking based on radical polymerizations has found widespread usage in 3D bioprinting, as radicals are, contrary to ionic species, stable in aqueous physiological conditions and tolerant to hydrophilic compounds. Other possible strategies for light-induced crosslinking are cycloaddition reactions such as Diels–Alder reactions or 1,3-dipolar cycloaddition. Depending on the polymerization mechanism, crosslinking can proceed either through a chain-growth (Figure 2.3A) or step-growth process (Figure 2.3B).²⁴⁶

2.2.1.1. Photoinitiated Chain-Growth Radical Polymerization

The radical polymerization consists of three main steps: radical generation and initiation, propagation, and termination. Radical generation occurs under light irradiation, in which a PI absorbs light and undergoes a photochemical reaction to generate radical species, which initiates the polymerization of vinyl monomers.²⁴⁷ Monomers have been developed based on a wide range of functional groups including (meth)acrylate, (meth)acrylamide, and vinyl ester (Figure 2.3A). Generally, it is accepted that the reactivity of

vinyl monomers toward radical polymerization decreases from acrylate > acrylamide > vinyl ester \approx vinyl carbonate > methacrylate > methacrylamide.²⁴⁸ Among these, most frequently used are methacryloyl monomers, which are esters or amides derived from methacrylic acid having a polymerizable double bond at the α,β -unsaturated carbonyl position. They are usually prepared by esterification using acryloyl chloride or anhydride reacting with hydroxyl or amino groups of natural polymers.

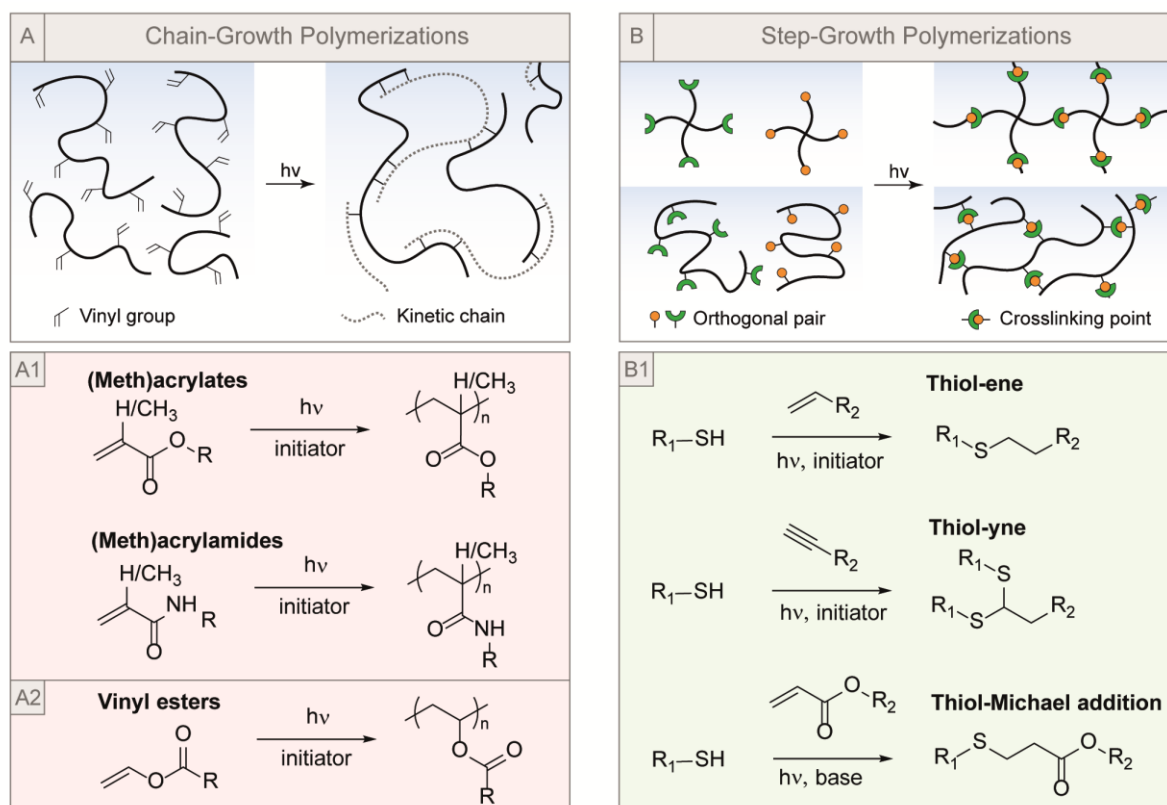


Figure 2.3 | Schematic representation of (A) chain-growth and (B) step-growth formation of the polymer network. Examples of “constructive” photochemical reactions to form and functionalize hydrogels by 3D biofabrication techniques: (A1) (meth)acrylates and (meth)acrylamides; (A2) vinyl esters. (B1) thiol-ene, thiol-yne, and thiol-Michael addition

Among the attractive features of photoinitiated radical polymerizations are their robustness, their relatively simple execution accessible by nonexperts, and a diverse array of commercially available monomers that can be utilized. Although it provides high reaction rates and tolerance to impurities, the photoinitiated radical polymerization of high-molecular-weight macromonomers, such as hyaluronic acid methacrylate (HA-MA) and gelatin-methacryloyl (Gel-MA), is associated with several characteristic features. Among them are oxygen inhibition,²⁴⁹⁻²⁵¹ reaction diffusion-controlled kinetics,²⁵²⁻²⁵³ volume relaxation and stress development, and heterogeneity of the polymer network.

First, the vulnerability of propagating radicals to react with molecular oxygen-forming unreactive peroxides, thus inhibiting the polymerization, remains a significant drawback.²⁴⁹⁻²⁵¹ For example, the amount of oxygen dissolved in acrylate monomers is on the order of 10^{-3} mol/L. In contrast, the concentration of propagating radicals is on the order of 10^{-8} mol/L.²⁵⁴ Several strategies have been applied to mitigate the inhibitory effect of physiological oxygen to the radical polymerization process. Among them, *N*-vinylpyrrolidone (NVP) has been employed as a water-soluble comonomer together with an organic photocatalyst eosin Y to form hydrogels under atmospheric conditions and low-intensity visible radiation. NVP was reported to significantly reduce the oxygen inhibition time, increase the rate of polymerization, and the final monomer conversion for the synthesis of hydrogels.²⁵⁵⁻²⁵⁶ Recently Aguirre-Soto et al. proposed that the reduction in oxygen inhibition is due to the complexation between NVP and eosin Y, which enhances the rate of photoinduced electron transfer to the co-initiator triethanolamine, while two oxygen molecules are consumed in this event.²⁵⁵

Another approach takes advantage of thiol reactivity to reduce oxygen inhibition. While peroxy radicals incorporated into polymer chains are not reactive toward monomer addition and propagation, they are reactive toward hydrogen abstraction from a thiol functional group.²⁵⁷⁻²⁵⁸ The generated thiyl radical can then undergo addition reactions with monomers to form thioether bonds and carbon-centered radicals that are able to propagate further. This approach applied to hydrogel formation uses multifunctional thiols in conjunction with multifunctional (meth)acrylates. Crosslinking occurs by a mixed-mode polymerization mechanism, where competition exists between the chain-growth homopolymerization of the (meth)acrylate and the step-growth mechanism of a thiol-ene polymerization.^{250,259}

Second, radical photo-crosslinking is defined by reaction diffusion-controlled kinetics. The mobility of macroradical chain ends is strongly limited, so that the only way for radical sites to move is through the propagation reaction of unreacted double bonds, so-called reaction diffusion.²⁶⁰ Thus, termination can occur only by propagation reactions. The photopolymerization of multifunctional vinyl monomers leads to a considerable amount of unreacted double bonds. In the context of 3D bioprinting, the complete functional group conversion and oxygenated conditions are critical for the viability of living cells in the crosslinked polymer network. Moreover, radical species' reactivity in the crosslinked polymer network is locally driven by diffusion (trapped carbon radicals) and results in high microstructural heterogeneity. It was observed that radical photopolymerization of multifunctional monomers produces a heterogeneous network containing highly crosslinked regions (microgel domains) as well as less densely crosslinked regions.²⁶¹ Because of the inhomogeneous network architecture, which is created during the radical curing process, the resulting hydrogel materials show shrinkage stress that could lead to deformation or mechanical failure of the construct.²⁶²

Another drawback is that the formation of the highly crosslinked hydrogel can lead to volume relaxation of the polymer toward their equilibrium specific volume. The process of volume relaxation can occur at a longer than or similar time scale to polymerization kinetics and is accompanied by volume shrinkage and stress development. Volume shrinkage behavior is significant for applications such as 3D bioprinting where shape- and volume-fidelity of the printed construct are important.²⁶³⁻²⁶⁴

2.2.1.2. Photoinitiated Step-Growth Polymerization

Thiol–ene Reactions. Highly efficient reactions of thiols with reactive carbon–carbon double bonds (enes) have demonstrated tremendous applicability in hydrogel network formation from photo-crosslinkable materials.²⁶⁵⁻²⁶⁶ Thiols (Figure 2.4 (1)) react with alkenes (2) by radical-mediated or base-catalyzed reactions. The radical-mediated thiol–ene reaction requires a PI to generate a radical initiator species (3) that abstracts the hydrogen radical from the thiol to form a thiyl radical (4). Then, the thiyl radicals attack the double bond of the alkene, generating a carbon-centered radical (5), which then abstracts the hydrogen radical from another thiol to regenerate the thiyl species, thus repeating the cycle. Thiol–ene hydrogel networks are formed rapidly and quantitatively under ambient conditions. Moreover, they produce polymer networks that are highly uniform with reduced shrinkage and mechanical stress.²⁶⁷ In contrast to conventional radical chain-growth polymerization, thiol–ene step-growth polymerization is insensitive to oxygen inhibition. All of these properties make thiol–ene reactions suited for hydrogel formation in the presence of cells and biological materials.²⁶⁸ A potential drawback for crosslinking is that the thiol–ene reaction cannot be considered strictly bioorthogonal. Specifically, the presence of a thiol-containing natural amino acid, cysteine (abundance 1.7%)²⁶⁹ may be able to generate thiyl radicals, which can compete during crosslinking. However, several cell types have been successfully encapsulated into thiol–ene hydrogels, including human MSCs,²⁷⁰ fibroblasts,²⁷¹⁻²⁷² fibrosarcoma,²⁷¹ and pancreatic beta-cells.²⁷³

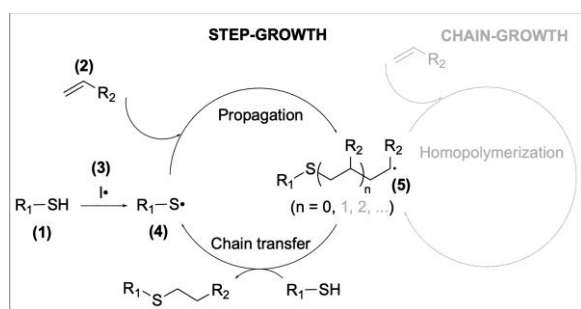


Figure 2.4 | Schematic of step-growth and chain-growth modes of photoinitiated thiol–ene reactions. The gray shading of the chain-growth mechanism denotes the competitive nature of thiol–ene reactions, which occur in a predominantly stepwise mechanism.

Thiol–ene hydrogels are prepared by covalent crosslinking of macromers containing thiols and alkenes. Reactive groups are introduced on macromers by a reaction with functional groups commonly found on

natural and synthetic polymers, including amines, carboxylic acids, aldehydes, and reduced disulfides. The choice of the alkene species also influences the polymerization mechanism. Norbornene, vinyl sulfones, vinyl ethers, and maleimides moieties have been increasingly utilized due to the incapability of their carbon-centered radical to homopolymerize through the chain-growth mechanism (Figure 2.4, gray shading).²⁷⁴⁻²⁷⁵ In such systems, the network formation proceeds only by step-growth mechanisms (Figure 2.4). Although a judicious selection of thiol–ene reactants and conditions can minimize side reactions, thiol-functionalized macromers can react with each other to form disulfides.²⁷⁶

Recently, Chu et al. identified that the presence of encapsulated chondrocytes alters the formation of PEG hydrogels by chain-growth radical polymerization and thiol–ene crosslinking.²⁷⁷ It is hypothesized that chondrocytes interact and deplete propagating radicals and thiol crosslinker before hydrogel formation. Hence, hydrogel immediately surrounding the chondrocyte resulted more loosely crosslinked than the bulk hydrogel, leading to the development of a stiffness gradient around the cell.

Thiol–yne Reactions. Reactions between thiols and alkynes are conceptually similar to thiol–ene reactions. The main difference is that alkyne is difunctional and can react with two thiol molecules to form a dithioether.²⁷⁸

Thiol-Michael Addition. The thiol-Michael addition is one of the most widely used click reactions in polymer science. The light-mediated approach was introduced by Xi et al., where the base, a primary amine, was caged using a photolabile group 2-(2-nitrophenyl)propyloxycarbonyl (NPPOC). Upon irradiation with 320–390 nm, the amine is released and exhibits catalytic activity. Although thiol–yne and thiol-Michael addition have similar advantages as thiol–ene reactions, both have yet to be realized in 3D biofabrication settings.²⁷⁹

Although photoinitiated radical reactions are the most widely employed crosslinking mechanism of hydrogel fabrication technologies, crosslinking can also be achieved with reagents that have innate photochemical activity, without the need for a PI. Although yet to be realized in 3D biofabrication technologies, these reactions represent fast crosslinking strategies. Among these are photostrain-promoted azide–alkyne cycloadditions, tetrazole–alkene, and tetrazine–alkene cycloadditions.²⁸⁰

Photo-Strain-Promoted Azide–Alkyne Cycloadditions (Photo-SPAAC). Cycloadditions comprise a broad and versatile class of reactions in which unsaturated molecules combine to form a cyclic adduct. They have been successfully applied to prepare injectable and cell encapsulating hydrogels.²⁸¹ Photo-SPAAC relies on photochemical decarbonylation of cyclopropanones to produce cyclooctynes (Figure 2.5A). Cyclopropanone-caged dibenzocyclooctynes are hydrolytically stable²⁸² and do not react with organic azides. Upon irradiation using 350 nm wavelength light, cyclopropanones release carbon monoxide to form cyclooctyne, which undergoes strain-promoted cycloaddition with azides. The photouncaging of

cyclopropenone is characterized by high quantum efficiency in aqueous physiological conditions. Hence, the photo-SPAAC has been applied for labeling proteins.²⁸³ It was also demonstrated that a SPAAC click reaction could be triggered by two- and three-photon excitation of cyclopropenone-caged dibenzocyclooctyne using infrared (IR) lasers of wavelength 690 and 1050 nm, respectively.²⁸⁴

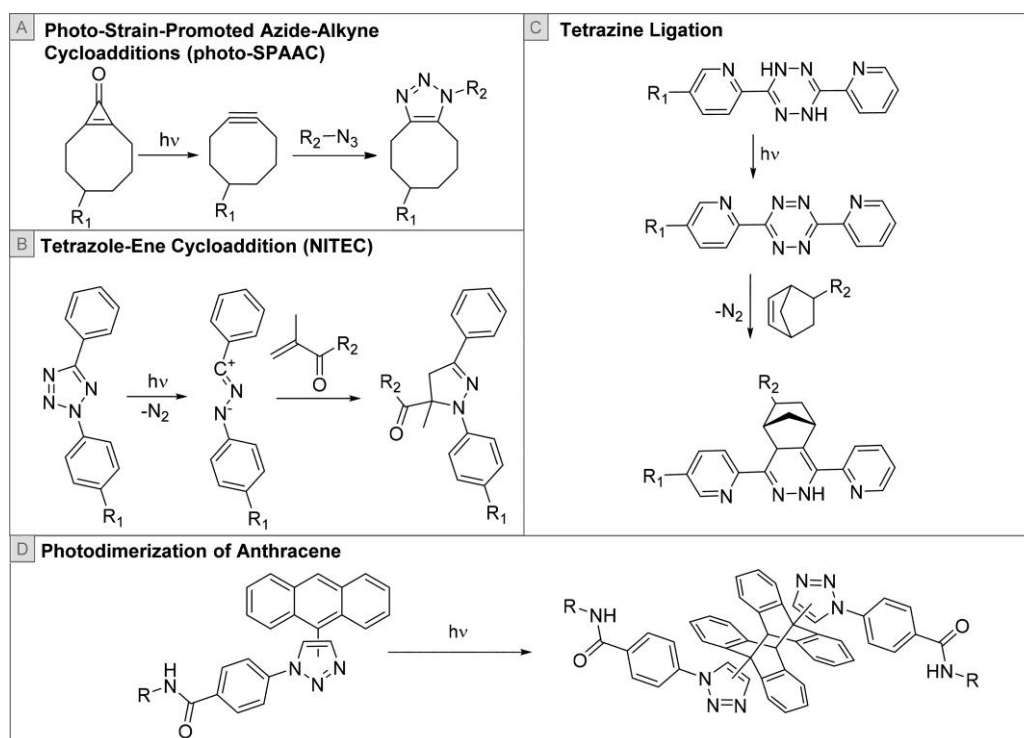


Figure 2.5 | General photoinduced click chemistry reactions. (A) Photo-strain-promoted azide–alkyne cycloadditions (photo-SPAAC), (B) tetrazoleene cycloaddition (NITEC), (C) tetrazine ligation, and (D) photodimerization of anthracene.

Nitrile Imine-Mediated Tetrazole–Ene Cycloaddition (NITEC). NITEC is a prominent example of orthogonal ligation chemistry (Figure 2.5B). Tetrazoles can be photoactivated, generating a highly reactive nitrile imine intermediate, which undergoes 1,3-dipolar cycloaddition reactions with various electron-deficient olefins (alkenes) to form a stable pyrazoline-based covalent linkage.²⁸⁵

Tetrazole to imine conversion can be triggered with low-power UV lamps, LED lights, or laser beams. Photoinduced NITEC ligations have been applied to selectively label alkene-containing proteins *in vitro*^{286–287} and *in vivo*^{288–289} without apparent toxicity. NITEC was used as catalyst-free crosslinking chemistry to prepare hydrogels from tetrazole- and methacrylate-functionalized four-arm PEG.²⁹⁰ The fast reaction rate and irreversible nature of the click reaction allowed hydrogel formation within minutes. Elegant work by Yu et al. designed water-soluble naphthalene-based tetrazoles that could be activated by 2P excitation at 700 nm.²⁹¹ Two-photon-triggered NITEC reactions were employed to perform fluorescence imaging of

microtubule dynamics in living Chinese hamster ovary cells that were pretreated with fumarate-modified docetaxel.

Table 2.2 | Advantages and Disadvantages of the Chemical Crosslinking Strategies Outlined in Section 2.2.1

Crosslinking Strategies	Advantages	Disadvantages
Radical Polymerization	<ul style="list-style-type: none"> • Ease of synthesis and robustness • Diverse array of functional monomers • High tolerance of polar functional groups compared to ionic polymerizations 	<ul style="list-style-type: none"> • Oxygen inhibition • Toxicity of unreacted groups • Radicals damaging to biological materials • Heterogeneous hydrogel networks
Thiol Conjugations	<ul style="list-style-type: none"> • Rapid crosslinking • Oxygen tolerance • Tunable reaction kinetics • Low natural abundance of cysteine reduces cross-reactivity with biomolecules • Homogeneous hydrogel networks 	<ul style="list-style-type: none"> • Potential for thiol exchange • Maleimides undergo hydrolysis • Oxidation to disulfides over time • Side reaction with amines • Not bioorthogonal, potential reaction with cysteine
photo-SPAAC	<ul style="list-style-type: none"> • Highly efficient photouncaging in water • No added catalyst needed • Gelation time of bicyclononyne-azide <1 min⁹³ 	<ul style="list-style-type: none"> • Laborious synthesis of alkynes • Cyclooctynes undergo side reaction with thiols
NITEC	<ul style="list-style-type: none"> • High selectivity • No added catalyst needed • Gelation time of tetrazole-acrylate groups in minutes¹⁰² 	<ul style="list-style-type: none"> • Thermodynamic equilibrium between open azide form and preferred tetrazole form.
Tetrazine Ligation	<ul style="list-style-type: none"> • High selectivity and bioorthogonality • Gelation time of tetrazine-<i>trans</i>-cyclooctene groups <2 s¹¹⁰ 	<ul style="list-style-type: none"> • Tetrazine instability
Photodimerization of Anthracene	<ul style="list-style-type: none"> • Bioorthogonal • Single type of functional group for crosslinking • No added catalyst needed • Gelation time in minutes¹⁰⁷ 	<ul style="list-style-type: none"> • Synthesis of functional anthracene is multiple step process
photo-CuAAC	<ul style="list-style-type: none"> • Bioorthogonal • Dark polymerization allows for shorter light exposure 	<ul style="list-style-type: none"> • Copper catalyst cytotoxicity
Tyramine Oxidation	<ul style="list-style-type: none"> • Single type of functional group for crosslinking 	<ul style="list-style-type: none"> • Not bioorthogonal, potentially reacts with tyramine or tyrosine

Tetrazine Ligation. First introduced in 2008, the reaction of *s*-tetrazines with alkene derivatives, referred to as tetrazine ligation, has emerged as one of the most potent chemistries in the bioorthogonal toolbox (Figure 5C).²⁹²⁻²⁹³ The reaction proceeds rapidly at room temperature in aqueous and organic solvents, produces high yields of product, and is chemoselective and bioorthogonal. To achieve spatial control, it was possible to use light and photoredox catalysts to generate reactive tetrazine from an unreactive dihydrotetrazine (dHTz)

precursor.²⁹⁴ Truong et al. reported hydrogel formation using tetrazine and norbornene functionalized four-arm PEG. Tetrazine groups were generated in situ by photo-oxidation of dHTz in physiological conditions and irradiation with red light (625 nm, 10 mW/cm²) in the presence of methylene blue as a photosensitizer. Upon oxidation, gel formation was reported to occur within minutes. Table 2.2 compares the main features of chemistries used for hydrogel formation.

Photodimerization of Anthracene. While the materials containing cinnamate and coumarines dimerize upon UV irradiation by $[2\pi + 2\pi]$ cycloaddition, anthracene photodimerization proceeds by a $[4\pi + 4\pi]$ cycloaddition mechanism (Figure 2.5D). Compared to the formation of a cyclobutane ring by $[2\pi + 2\pi]$ cycloaddition, anthracene undergoes photocycloaddition to give cyclooctane-type dimers. Consequently, the dimer of anthracene is less strained and more stable. Typically, irradiation by 365 nm light is used to induce the photocycloaddition of unsubstituted anthracene. The reaction does not require a catalyst and does not generate any byproduct or radicals that might damage cells. The presence of substituent on anthracene was used to enhance the photosensitivity under visible-light irradiation. Placing an electron-rich substituent group on the anthracene (Figure 2.5D) significantly red-shifted the light absorption compared to unsubstituted anthracene. This concept has been applied by Truong et al., where visible light irradiation (400–500 nm) drove a cycloaddition of anthracene groups covalently attached to four-arm PEG chains, which enabled hydrogel formation.²⁹⁵

2.2.1.3. Photomediated Redox Crosslinking

Photoinduced-Copper-Catalyzed Azide–Alkyne Cycloadditions. Photo-CuAAC are both orthogonal and efficient, and considerable effort has been made to render CuAAC chemistry light sensitive. Photo-CuAAC involves the in situ generation of Cu(I) via the photomediated process. PIs are introduced to the system to evoke the reduction of Cu(II) to Cu(I), which is needed to catalyze azide–alkyne cycloaddition (Figure 2.6A).²⁹⁶

Tyramine Oxidation. While the tyramine crosslinked hydrogels are generally formed through a reaction with hydrogen peroxide and horseradish peroxidase (HRP), hydrogel production using light was reported as well. The photochemical process is usually initiated using photosensitizers such as riboflavin, water-soluble metal complex tris(2,2'-bipyridyl)-ruthenium(II) chloride hexahydrate [Ru(II)(bpy)₃]Cl₂ or Eosin-Y (Figure 2.6 B). Loebel et al. studied single and two-photon crosslinking of tyramine-substituted hyaluronate using laser light at 488 and 710 nm, respectively.²⁹⁷ Photorheometry showed gelling properties in minutes, and using 2P-SL, predefined micropatterns were produced.

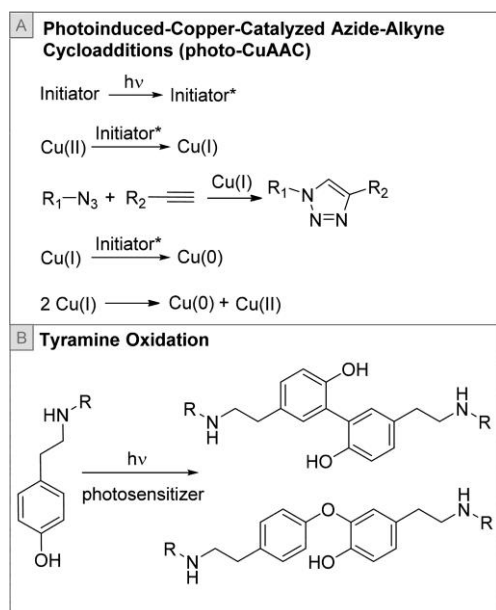


Figure 2.6 | Photomediated redox crosslinking*. (A) photoinducedcopper-catalyzed azide–alkyne cycloadditions (photo-CuAAC). (B) tyramine oxidation.

2.2.2. Water-Soluble Photoinitiators (PIs)

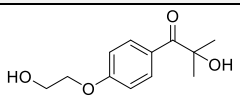
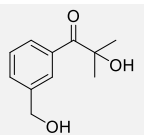
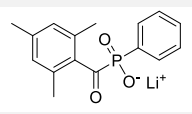
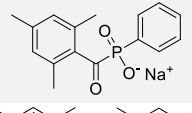
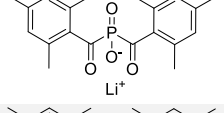
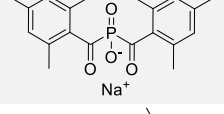
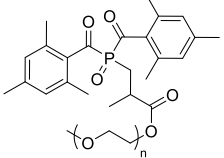
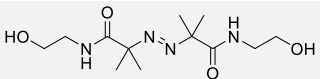
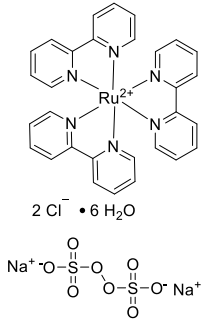
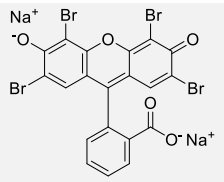
2.2.2.1. Single-Photon Initiators (1PIs)

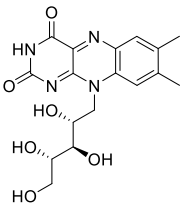
PI is a critical component to start the photocuring because most monomers alone do not produce initiating species with a sufficient quantum yield upon light exposure. Interest in PIs began after the progress of industrial photopolymerization in the late 1970s.²⁹⁸ The vast majority of industrial processes utilize oil-soluble PIs and their stable emulsions when aqueous dispersibility is required. However, the development of novel materials for biological and medical applications generated a strong demand for truly water-soluble PIs.²⁹⁹ This section aims to review progress in water-soluble PIs and presents criteria for evaluating and selecting PIs for use in biofabrication.

The critical requirements for PIs for hydrogel biofabrication in the presence of living cells are (1) aqueous solubility, (2) low cytotoxicity, (3) high efficiency in generating radicals by visible light and low-intensity light sources, and (4) excellent reactivity toward monomers. In conformity with the first law of photochemistry, high efficiency in generating free radicals can be achieved only when the absorption spectrum of a PI largely overlaps with the irradiation profile of the utilized light source. Table 2.3 summarizes the physicochemical properties of several water-soluble PIs used in 3D bioprinting. 1PIs are classified by the radical-generating mechanism into *Norrish Types I* and *II* photolysis (Figure 2.7A,B).³⁰⁰⁻³⁰² Upon irradiation, type I PIs undergo a homolytic bond cleavage to form two radicals that initiate the polymerization (Figure 2.7A). Type

II PIs undergo a bimolecular reaction in which the excited triplet state of a PI reacts with an auxiliary molecule (hydrogen donor), thereby producing an initiating radical (see an example of eosin Y initiation) (Figure 2.7B).

Table 2.3 | Chemical Structures of Common Water-Soluble PIs Used in 3D Biofabrication Techniques

PI	Chemical Structure	Water solubility (g/L)	λ_{\max} (nm)	ϵ_{\max} ($M^{-1} \text{ cm}^{-1}$)	Ref.
I2959		5	328 365	296 5	303
APi-180		74	329	97	303
LAP		47	365 380 405	218 191 30	303
Na-TPO		29	380	250	303
BAPO-OLi		54	383	197	303
BAPO-ONa		60	383	256	303
PEG-BAPO		1.38	390	450	298
VA-086		45	375	30	304
Ru(bpy) ₃ /SPS		10	450	14600	305
Eosin Y		1	515 516	69800 86500	306-307

Riboflavin		0.06-1.2	374 449	10300 12100	308-309
------------	---	----------	------------	----------------	---------

One of the first and still the most commonly used water-soluble 1PI is the α -hydroxyketone 2-hydroxy-1-[4-(2-hydroxyethoxy)phenyl]-2-methyl-1-propanone (I2959, Table 2.3). However, its major drawback is limited molar absorptivity at wavelength 365 nm ($\epsilon \approx 5 \text{ M}^{-1} \text{ cm}^{-1}$),³¹⁰ resulting in the need for high concentrations to fabricate hydrogels. Although water-solubility of I2959 (5 g/L)³¹⁰ is adequate for many applications, the structural analogue 2-hydroxy-1-[3-(hydroxymethyl)phenyl]-2-methyl-1-propanone (APi-180, Table 2.3) offers much higher solubility in water but has an absorption spectrum peaking at 329 nm. Increasing use by the bioengineering field of new monochromatic light sources (LED, laser diodes) emitting in the 365–405 nm range created a strong demand for water-soluble PIs absorbing in a similar range. Monoacylphosphine oxides (MAPOs), originally used exclusively for organic formulations, provide sufficient photosensitivity at wavelengths in the 380–450 nm range. Their water-soluble analogues were conveniently prepared by treatment of the oil-soluble PI ethyl phosphinate with lithium or sodium iodide providing the water-soluble phenyl(2,4,6-trimethylbenzoyl)phosphinate salts (LAP) and Na-TPO. Both offer an excellent water solubility, especially LAP (47 g/L), which considerably exceeds that of I2959.³¹⁰ Furthermore, LAP absorbs at 365 nm with a molecular extinction coefficient, ϵ , of $218 \text{ M}^{-1} \text{ cm}^{-1}$, while the ϵ of I2959 is only $5 \text{ M}^{-1} \text{ cm}^{-1}$, which implies that LAP can be used at considerably lower concentrations than I2959 with reduced cytotoxic effects.³¹⁰ Therefore, owing to favorable cytotoxicity and visible light absorption, LAP has become the first choice in state-of-the-art water-soluble PIs for 3D biofabrication.²⁹⁸ Another class of phosphinate-type PIs is bisacylphosphine oxides (BAPO), which have absorption spectra that are even more red-shifted than those of MAPO PIs. Especially for UV-LED light sources with peak emissions at 385, 395, and 405 nm, BAPO-type PIs provide suitable absorption properties. However, the synthesis of BAPO-type PIs is more demanding than for MAPO compounds. Corresponding, water-soluble alkali metal salts are accessible in a two-step procedure.³⁰³ The BAPO derivative can be esterified with polyethylene glycol (PEG) to provide a liquid, nonionic water-soluble PI.²⁹⁸

Another class of PIs is azo compounds. Their excitation results in a photofragmentation of the weakest C – N bond and release of a nitrogen molecule. Photochemically induced elimination of nitrogen from aliphatic azo compounds is accompanied by the formation of alkyl radicals, which initiate radical polymerization (Figure 2.7C). Commercially available water-soluble PI 2,2'-Azobis[2-methyl-N-(2-hydroxyethyl)propionamide] (also known as VA-086) was used in 3D bioprinting of Gel-MA with 365 nm light source.³¹¹

Recently, a growing interest in the use of Ru^{II} complexes for metal-catalyzed radical polymerizations has given rise to the design of an efficient ruthenium PI that can be activated under visible light. Irradiation of the water-soluble metal complex tris(2,2'-bipyridyl)-ruthenium(II) chloride hexahydrate [Ru(II)(bpy)₃]²⁺ together with sodium persulfate leads to the triplet charge transfer state of Ru. In the presence of sulfate anions, the Ru-excited state deactivates by electron transfer reactions, leading to Ru^{III} species and SO₄ radicals, which eventually leads to crosslinking reactions.^{305, 312}

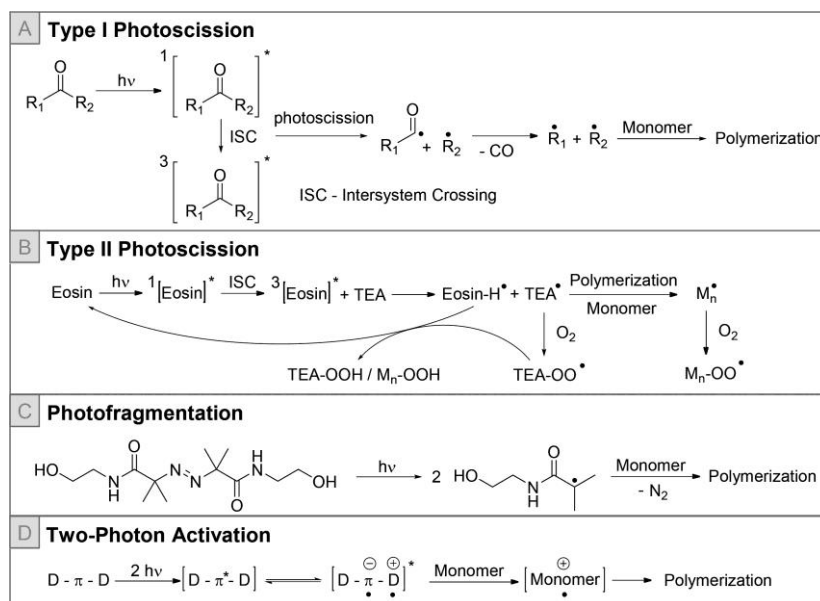


Figure 2.7 | Examples of photoinitiating mechanisms type I and type II photocission, photofragmentation, and two-photon activation.

A variety of PI systems containing dyes (e.g., eosin Y, riboflavin) have been described for 3D bioprinting. In these systems, it has been proposed that radicals are formed in the interaction of the excited dye in the presence of electron donors such as tertiary amines.³¹³⁻³¹⁴ Eosin Y is excited by green light to its singlet state, from which it undergoes intersystem crossing (ISC) to its triplet state. Then it is reduced by triethanolamine (TEA), and subsequent proton transfer generates two radicals, which initiates the polymerization. *N*-Vinylpyrrolidone (NVP) has been employed as a comonomer in the eosin-mediated synthesis of hydrogels to aid in reducing oxygen inhibition and enhancing the rate of radical polymerization and the final conversion.²⁵⁵ The riboflavin–TEA photoinitiating system has significant absorbance in the 300–500 nm range, and biocompatibility is significantly higher than the conventional I2959. However, it was found to be less efficient for 2P-polymerization.³¹⁴

Various initiating strategies have been developed in order to accelerate the printing speed. In a recent study,³¹⁵ a hybrid semiconductor/gold nanoparticle (CdS-Au) PI was developed for rapid 3D printing. This new type of PI generates radicals in the presence of dissolved oxygen through photocatalysis, and the

generated reactive oxygen radicals could induce photopolymerization of water-soluble acrylamide monomers. The CdS-Au had a very high molar extinction coefficient ($\sim 10^7 \text{ M}^{-1} \text{ cm}^{-1}$ at 385 nm), which is 11 orders of magnitude higher than that of I2959 ($0.0003 \text{ M}^{-1} \text{ cm}^{-1}$ at 385 nm) and therefore led to faster and more complete photopolymerization than the I2959 system. Still, biocompatibility and cytotoxicity of the PI have to be studied.

2.2.2.2. Two-Photon Initiators (2PIs)

In recent decades, two-photon stereolithography (2P-SL) has garnered a great deal of attention due to the possibility of fabricating 3D structures of complex chemical and physical hierarchy reminiscent of natural materials.³¹⁶ 2P-SL takes advantage of the nonlinear nature of two-photon absorption (2PA), which confines photochemical crosslinking of the material to small laser focal volume and allows structures to be fabricated with unprecedented spatiotemporal resolution. In contrast to single-photon absorption, 2PIs absorb two photons simultaneously, which allows the use of low energy near-infrared (NIR) light. The advantages of NIR light are improved depth penetration in tissue and less harm to living cells compared to UV light.³¹⁷

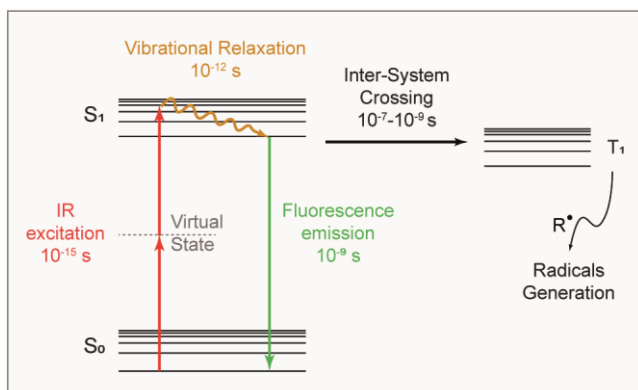


Figure 2.8 | Jablonski diagram of PI radical generation and competing fluorescence decay process (green). After the simultaneous absorption of two photons (red arrows), the excited PI decay through an intersystem crossing to the triplet state (T_1). From this state, PIs can generate radical species which trigger photochemistry reactions.

Several factors affect the design and application of PIs for 2P-polymerization. The first requirement is a large 2PA cross-section of the initiator. The 2PA absorption cross-section (σ^{2PA}) is measured in Göppert–Mayer units (GM, $1 \text{ GM} = 10^{-50} \text{ cm}^4 \text{ s/photon}$) and quantifies a probability of 2PA at a wavelength of interest.³¹⁸ From the excited state, the PI can either decay through ISC to a long-lived triplet state (T_1) from which radical active species can be generated (Figure 2.8) or decay through a fluorescence emission to the ground singlet state (S_0) (see Figure 2.8). Therefore, only a portion of the absorbed energy is used to trigger photochemical reactions with the generation of free radicals. Fluorescence represents the most relevant competing process but also other deactivation pathways such as cis–trans isomerization can take place,

reducing the efficiency of the PI.³¹⁹ The σ^{2PA} can be measured by direct methods (i.e., nonlinear transmission and χ -scan³²⁰) or indirect methods (i.e., 2P excited fluorescence).³¹⁹

In principle, molecules with a π -conjugated system typically exhibit 2PA activity. The molecular structure design of 2PI to improve the 2PA properties has been focused on the enhancement of the intramolecular charge transfer by the extending π -conjugated system and using strong electron-donating and electron-accepting groups. These can be classified into symmetric (A- π -A, D- π -D) and nonsymmetric (D- π -A) molecules, in which D stands for an electron donor, A stands for an acceptor, and they are linked by a π -conjugate bridge (Figure 2.7D).³¹⁹

New, highly efficient, and water-soluble 2PIs developed by Liska's group have met the increasing demand for 2P-polymerization of 3D hydrogels (Table 2.4). These include the benzylidene cycloketone-based 2PIs named G2CK, E2CK, and P2CK, which have carboxy groups to ensure water solubility.³²¹ Recently, a supramolecular water-soluble initiator WI was prepared through host-guest interactions, where host molecules 2-hydroxypropyl- β -cyclodextrins encompassed hydrophobic PI 2,7-bis(2-(4-pentaneoxy-phenyl)-vinyl)anthraquinone. The resulting supramolecular 2P initiator WI has a $\sigma^{2PA} \sim 200$ GM at the wavelength of 780 nm.³²²

One of the main problems with using 2P-SL in the presence of cells is the diffusion of the 2PI from the ECM into the cell's cytosol, where they exhibit considerable cyto- and phototoxicity. Liska and colleagues synthesized macromolecular 2PI HAPI, where the MGABA initiator precursor was linked to a hyaluronan backbone. It was demonstrated that the macromolecular nature of HAPI hinders the cellular translocation and exhibits superior biocompatibility compared to reference PI E2CK. Moreover, 3D hydrogel structures containing living cells were produced by the 2P-polymerization of Gel-MA at high scanning speeds of 100 mm/s.³²³

Three water-soluble benzylidene cyclanone dyes with cyclobutanone (T1), cyclopentanone (T2), and cyclohexanone (T3) moieties were designed and synthesized and their photophysical properties were investigated in water.³²⁴⁻³²⁵ Benzylidene cyclanone dyes were modified with four sodium carboxylate groups to achieve water solubility. The maximum σ^{2PA} of T1-T3 in water was determined as 567 GM, 808 GM, and 231 GM at 820 nm and 3D nanopatterns based on 2P-polymerization of bovine serum albumin (BSA), water-soluble acrylic ester monomer (SR610), and hyaluronic acid derivative (HA-GM) were successfully biofabricated using these 2PIs. The distinct disadvantage of the benzylidene cyclanone 2PI is their severe cytotoxicity at concentrations used for 2P-polymerization.

Table 2.4 | Chemical Structures of Typical Water-Soluble Photoinitiators Used in 2P-Microfabrication.

2PI	Chemical Structure	λ_{abs} nm	ϵ_{max} $\text{M}^{-1} \text{cm}^{-1}$	$\lambda_{2\text{P}}$ nm	$\sigma^{2\text{PA}}$ GM^{a}	Ref.
G2CK		-	-	800	163	321
E2CK		471	3.5	800 830	201 480	321, 326
P2CK		506	5.5	800	176	321
WI		290	-	750	282	322
HAPI		466	3.5	840	400	326
T1		522	2.87	820	567	324
T2		513	5.5	820	808 604 ^b , 1032 ^c	324, 325
T3		478	4.94	820	231	324

WSPI		423	4.9	730 800	360 120	327- 328
DAS		370	2.0	800	40	329

^a2P absorption cross section values in water, 1 GM = 10⁻⁵⁰ cm⁴ s/photon. ^bnonlinear transmission (NLT) method. ^cTwo-photon-excited fluorescence method.

Systematic investigations of the relationship between molecular structure and 2PA properties in various solvents were performed for chromophores based on the distyrylbenzene framework.³²⁷ One successful example of rational 2PI design is a distyrylbenzene chromophore with subsequent quaternization using trimethylamine, which affords the water-soluble molecule 1,4-bis(4-(*N,N*-bis(6-(*N,N,N*-trimethylammonium) hexyl)amino)-styryl)-2,5-dimethoxybenzene tetraiodide (WSPI).³²⁸ In an aqueous medium, WSPI showed $\sigma^{2PA} \sim 360$ GM at the wavelength of 730 nm. This initiator was used for the first time for 2P-polymerization in the formulation containing up to 80% of water and a living organism (*Caenorhabditis elegans*) as a real-time biocompatibility sensor. Large σ^{2PA} enabled the production of 3D microstructured scaffold from PEG-diacrylates (PEG-DA) with a fast scanning speed of 10 mm/s under laser power of 140 mW.

Recently, Tromayer et al. developed the first photocleavable water-soluble azoinitiator for 2P-polymerization, transcending the limitations of charge transfer π -conjugated PI.³²⁹ Novel tetrapotassium 4,4'-(1,2-ethenediyl)bis[2-(3-sulfophenyl)diazenesulfonate] (DAS) showed lower σ^{2PA} of around 40 GM at a wavelength of 800 nm compared to the established 2PI P2CK. Although DAS was used at double the concentration compared to P2CK due to lower σ^{2PA} , it supports to date the highest scanning speed up to 1 m/s, and the threshold power of 2P-polymerization was 45–100 mW.

2.2.3. Photodegradation and Photocaging Reactions

Using light offers many unique means of reaction control, such as selective irradiation wavelength, timing, and spatial restriction of the light exposure to control the photochemical reaction. It is particularly useful for precise conjugation of bioactive molecules (e.g., growth factors (GFs), signaling proteins, and morphogens) within the hydrogels.³³⁰ Immobilization of bioactive molecules (patterning) allows for modulation of cell fate determination, cell phenotype, or cell-material interactions. Furthermore, photoactivated materials can enhance cellular systems guidance into 3D microenvironments found in physiological tissues.^{213, 331}

Photocaging refers to the photolysis of the caged compound (Figure 2.9A). Specifically, photoremovable protecting groups (PPGs) have been applied to on-demand activate substrates within the hydrogel for reactions with proteins^{244, 332} or to liberate functional chemical groups on polymer chains, such as thiols, enabling their further click-reaction with a target (bio)molecule.^{211, 333-335} Therefore, this approach has found widespread application to photopattern biomolecules. The selection criterion for the PPG to be used depends on the application. Generally, an ideal PPG used in a cell-laden biomaterial should have (1) strong light absorption at wavelengths above 365 nm to avoid cell photodamage, (2) stability and solubility in physiological environments, (3) transparent photochemical byproducts to avoid competitive absorption, (4) low cytotoxicity, and (5) photoreaction with high quantum yield or efficiency for release.³³⁶

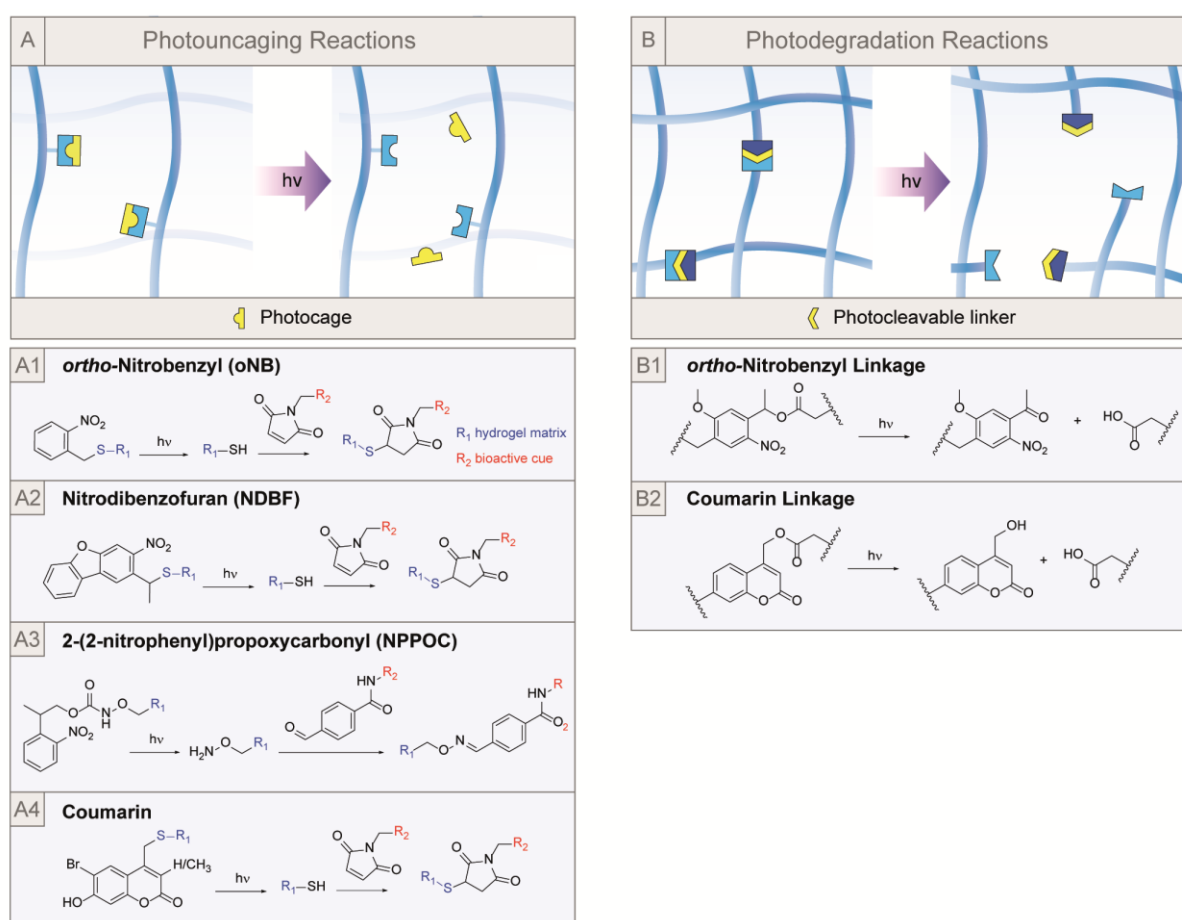


Figure 2.9 | Schematic illustration of photomediated uncaging and degradation of photoactive hydrogels. Examples of (A) photocaging and (B) photodegradation reactions.

One of the methods to fabricate photodegradable hydrogels is to incorporate a PPG into the crosslinks within the hydrogel network. Upon light irradiation, photolabile linkers are cleaved, and hydrogel degrades (Figure 2.9B). Consequently, the reduction in the number of crosslinks in the polymer network results in softening

(e.g., lower stiffness, porosity) of the hydrogel or its complete dissolution. The preparation of hydrogels incorporating photodegradable groups is achieved by the conjugation of photolabile molecules to a polymer chain-end and subsequent polymer crosslinking. Also, a crosslinking reaction could occur by a photopolymerization, such as using acrylates³³⁷⁻³⁴¹ or using click chemistry.^{124, 205, 342-343} This section will focus on the chemistry of photosensitive functional groups and trends for their use in light-responsive soft matter.

2.2.3.1. Nitroaryl Groups

2.2.3.1.1. ortho-Nitrobenzyl (oNB). Among the known PPGs, oNB derivatives (Figure 2.9A1) have emerged as the most commonly employed in biological applications. The mechanism of photolysis of oNB has been investigated by time-resolved spectroscopy.³⁴⁴⁻³⁴⁵ After light absorption, the excited singlet state of oNB is followed by an ISC to its triplet state. Then, the primary photochemical process is an intramolecular hydrogen transfer from the *o*-alkyl substituent to the nitro group, which is followed by the formation of the *aci*-nitro tautomer. Subsequently, the *aci*-nitro intermediate rearranges to the nitroso derivatives (*o*-nitrosobenzaldehyde or nitroso ketone) and release of the original uncaged compound occurs (Figure 2.10). Various substituents at the benzylic position of oNB affect the spectral properties of the chromophore. The most suitable strategy to obtain oNB derivatives with a red-shifted absorption band is to introduce either an electron-withdrawing group at the para position or electron-donating group at the meta position. In this way, the absorption maximum of oNB can be shifted from 345 to 420 nm.³⁴⁶⁻³⁴⁷

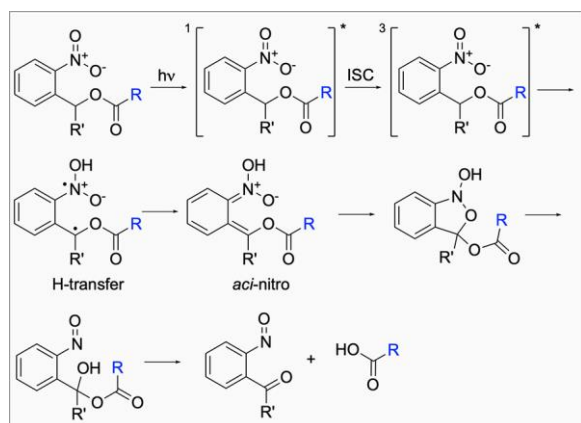


Figure 2.10 | Reaction mechanism of the uncaging process of oNB caged carboxylic acid bearing compound.

oNB can also be cleaved by 2PA.³⁴⁸⁻³⁴⁹ 2PA cross-section of oNBs protecting groups have been reported in the range of 0.015–0.065 GM at 750 nm, which is below the limit of 0.1 GM for efficient biological utilization.³³⁶ Only recently, Lunzer et al. demonstrated a strategy to enhance the two-photon induced photocleavage reaction in oNB-based hydrogels.³⁴¹ In their report, the formed hydrogel was treated with a

water-soluble two-photon active chromophore, cyclic benzylidene ketone-based molecule, which acted as a photosensitizer, i.e., efficiently absorbing two photons and then transferring the energy to oNB linkers. This modular system was proved to be biocompatible in the presence of encapsulated cells.

2.2.3.1.2. Nitrodibenzofuran (NDBF). To increase the absorbance at a longer wavelength, oNB aromatic core was extended to NDBF. Irradiation of NDBF (Figure 2.9A2) with 365 nm light or 2P excitation at 800 nm resulted in efficient deprotection. NDBF was shown to be efficient for thiol caging, circumventing the undesired isomerization of coumarin caged thiol to the dead-end product upon photolysis.³⁵⁰

2.2.3.1.3. 2-(2-Nitrophenyl)propoxycarbonyl (NPPOC). Deprotection efficiency was considerably improved by placing substituents on the aromatic ring of the oNB group. NPPOC (Figure 2.9A3), oNB homologue, was involved as a photocage of the alkoxyamine-modified substrate. The resulting NPPOC-photocaged alkoxyamine was subsequently reacted with aldehyde functionality via photomediated oxime ligation.³⁵¹ Using this approach, Farahani et al. created a cell-laden hydrogel with a spatially photopatterned protein.¹²⁷ To this end, the protein functionalized with photocaged alkoxyamines was introduced to the hydrogel network containing benzaldehyde-end groups. Upon UV light irradiation, the uncaged alkoxyamines formed stable oxime linkages with aldehyde moieties.

2.2.3.2. Coumarin

A general mechanism of the coumarin group photorelease is summarized in Figure 2.11. After initial light absorption, relaxation takes place to the lowest excited singlet state. Heterolytic C–X bond cleavage occurs through the intermediate, tight ion pair of coumarinylmethyl cation, and leaving group conjugate base. The coumarinylmethyl cation reacts with the solvent to generate a stable coumarinylmethyl product. The liberated leaving group is unstable and undergoes slow decarboxylation.³³⁴

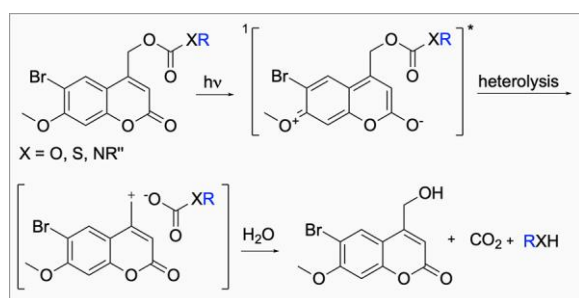


Figure 2.11 | Mechanism of photorelease of coumarin-caged compounds.

From a biological perspective, coumarin (Figure 2.9A4) PPG is suitable for cell-laden hydrogels because the photodegradation produces nontoxic byproducts.³⁵² Furthermore, coumarin PPG exhibits larger σ^{2PA} than oNB, providing efficient multiphoton cleavage of coumarin-based hydrogels.^{336, 347, 353} Similarly to oNB

groups, there is a growing interest and demand for alternative photolabile molecules with a red-shifted absorption spectrum allowing for visible light-triggered photocleavage.³⁵⁴⁻³⁵⁵ For example, Truong et al. recently obtained a photodegradable PEG hydrogel with photocleavable benzoquinone linkers.³⁵⁶ The synthesis of the hydrogel was achieved via thio-bromo click reaction between star-PEG end-functionalized with bromoquinone and thiol groups. The photocleavage was induced by irradiation with blue light (400–500 nm) and consisted of two subsequent processes, photoreduction of quinone and thermal trimethyl locking closure. The complete gel dissolution was obtained after 10 min of irradiation.

2.2.4. Common Photosensitive Bioinks and Bioresins

In the field of biofabrication, definitions of “bioinks” and “biomaterial inks” for deposition bioprinting were recently proposed. Bioinks are defined as “a formulation of cells suitable for processing by an automated biofabrication technology that may also contain biologically active components and biomaterials”.³⁵⁷ For VP methodologies, we propose the use of the term “bioresins” to refer to the precursor solution containing cells from which objects are polymerized. Materials used for the formulation of bioinks are hydrogel precursors (monomers, macromers, oligomers) that can be (photo)crosslinked to form a hydrogel. Hydrogels have attractive features for use in tissue engineering and regenerative medicine, such as biocompatibility and biodegradability, and importantly, many of them are able to mimic the native ECM milieu. By doing so, cell attachment, spreading, growth, infiltration, differentiation, and signaling can be controlled, allowing hydrogels to mature into functional tissue analogues. Hydrogel biomaterials, including gelatin, hyaluronic acid, alginate, PEG, and their use as photo-crosslinkable bioinks will be discussed in this section.

2.2.4.1. Gelatin

Gelatin is produced by the denaturation of collagen, which is a major component of natural ECM. It is highly biocompatible, contains Arg-Gly-Asp (RGD) cell-binding motifs, is enzymatically degradable by metalloproteases, and is inexpensive and generally recognized as safe (GRAS) by the Food and Drug Administration (FDA). Therefore, gelatin has become the most common material used in bioprinting. However, gelatin has an upper critical solution temperature (UCST) of around 30 °C,³⁵⁸ meaning it is water-soluble above this temperature and forms hydrogel only at lower temperatures than its UCST. Gelatin is therefore not stable at physiological or cell culture conditions but can be chemically modified and crosslinked to form a stable hydrogel.

Gelatin contains several modifiable functional groups (hydroxyl, amino, and carboxylic groups) from parent collagen amino acids and ornithine, which is formed after collagen denaturation.³⁵⁹ Crosslinking occurs by (photo)polymerization of reactive functional groups, typically methacryloyl, which are immobilized onto the gelatin backbone. Gelatin-methacryloyl (Gel-MA) can be reproducibly prepared by the reaction of gelatin with

methacrylic anhydride (MAA) (Figure 2.12A). Gel-MA contains both methacrylate and methacrylamide groups because hydroxyl groups as well as amino groups are reactive toward MAA. Highly substituted Gel-MA after long reaction times contains higher amounts of methacrylates compared to Gel-MA with a lower degree of functionalization (DF).³⁶⁰⁻³⁶² Abbreviation Gel-MA is sometimes incorrectly referred to as gelatin methacrylate, which is misleading as amino groups are more reactive toward MAA, and the majority of methacryloyl groups are thus methacrylamides. Methacrylamide groups on Gel-MA are hydrolytically more stable than methacrylate groups. It was shown that gelatin methacrylamide could be completely decoupled from Gel-MA through selective hydrolysis of methacrylate groups.³⁶³

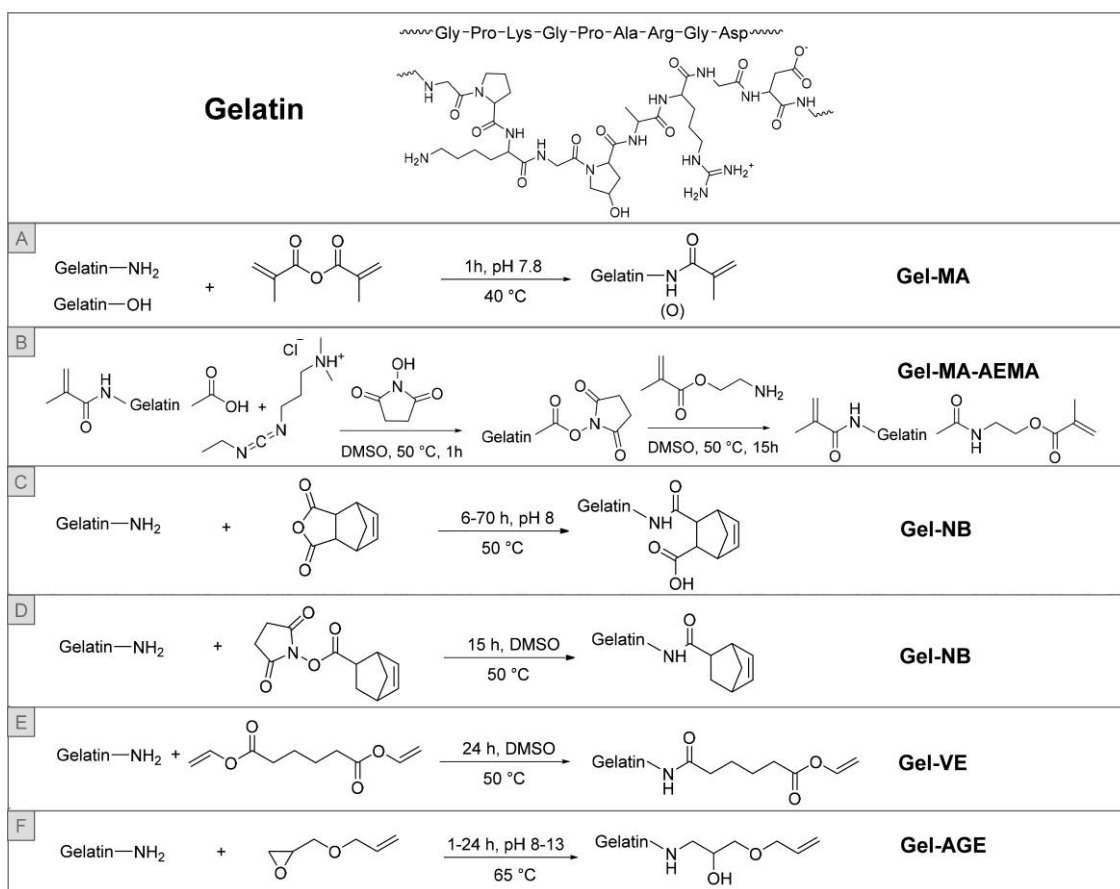


Figure 2.12| Overview of preparation methods of different photo-crosslinkable gelatins. (A) Gelatin methacryloyl (Gel-MA). (B) Gelatin methacryloyl amino ethoxy methacrylate (Gel-MA-AEMA).¹⁷⁷ (C) Gel-norbornene (Gel-NB) synthesized via reaction with carbic anhydride.³⁶⁴ (D) Gel-NB synthesized via reaction with 5-norbornene-2-carboxylic acid. (E) Gel-vinyl ester (Gel-VE).³⁶⁵ (F) Gelatin-allyl glycidyl ether (Gel-AGE).³⁶⁶

Hydrogels of purely gelatin methacrylamide were more compliant than those of Gel-MA. Another approach to enhance the mechanical properties of gelatin is to modify both amino and carboxylic groups sequentially. Van Hoorick et al. developed gelatin where first, primary amines were converted to methacrylamides, and subsequently, carboxylic groups were activated and additional methacrylates were introduced using amino

ethoxy methacrylate (AEMA) (Figure 2.12B).³⁶⁷ As a result, faster crosslinking kinetics, lower swelling ratios, and higher stiffness have been achieved, which expands the possibilities of gelatin for 2P polymerization. Activated carboxylic groups of Gel-MA may also be used as a handle to covalently introduce biological functionalities. In this respect, Gel-MA was functionalized with the neurotransmitter dopamine to obtain a crosslinkable functional gelatin derivative suitable to print scaffolds enhancing neuronal differentiation of neural stem cells.³⁶⁸

Gelatin derivatives for step-growth-based crosslinking approaches have also been reported.³⁶⁴ The most common step-growth crosslinking chemistry applied for gelatin derivatives is thiol–ene photoinitiated click chemistry. Thiol–ene photo-crosslinkable gelatin contains an alkene functionality such as norbornene (Figure 2.12C,D), vinyl ester (Figure 2.12E), vinyl sulfone, allyl ether (Figure 2.12F), or acrylate. Conversely, gelatin may be functionalized with thiols, which are crosslinked using an alkene crosslinker (PEG methacrylate (PEG-MA),³⁶⁹ Gelatin-norbornene (Gel-NB)³⁶⁴). Allyl groups were introduced onto gelatin by the reaction of allyl glycidyl ether (AGE) with primary amines.³⁶⁶

2.2.4.2. Hyaluronic Acid

Hyaluronic acid (HA) is a naturally derived, nonsulfated glycosaminoglycan comprised of repeating disaccharide units of *N*-acetyl-d-glucosamine and d-glucuronic acid. HA is an unbranched, anionic polysaccharide having a large molecular weight ($\sim 10^4$ – 10^7 Da). It has widespread clinical use in orthopedics as a treatment for osteoarthritic joint pain, in ophthalmology to treat dry eye disease, and in plastic surgery as a dermal filler.³⁷⁰ HA is a dominant component of the ECM of many tissues and has a role in regulating cell growth, migration, and differentiation.³⁷¹ Moreover, HA has inherent biological functions, such as binding affinity to the cell surface receptor CD44 and degradability by mammalian enzymes.³⁷² Because of its biological features, hydrogels built from HA are being used to engineer many tissues, including cartilage, heart, blood vessels, nerves, and skin.^{373–375} Naturally, HA has become one of the most prominent biomaterials used in 3D biofabrication. It contains several functional groups (primary and secondary hydroxyl, or carboxylic groups) in the backbone, which can be used to introduce photoreactive moieties (e.g., methacrylates, vinyl esters, norbornenes) (Figure 2.13).

The most common chemical modifications consist of the methacrylation of primary hydroxyl groups through a reaction with MAA^{376–377} (Figure 2.13A) or glycidyl methacrylate^{378–379} (Figure 2.13B). Many other HA-based bioinks (i.e., HA-VE, HA-NB)^{380–382} with various cell types have been reported to date.³⁸³

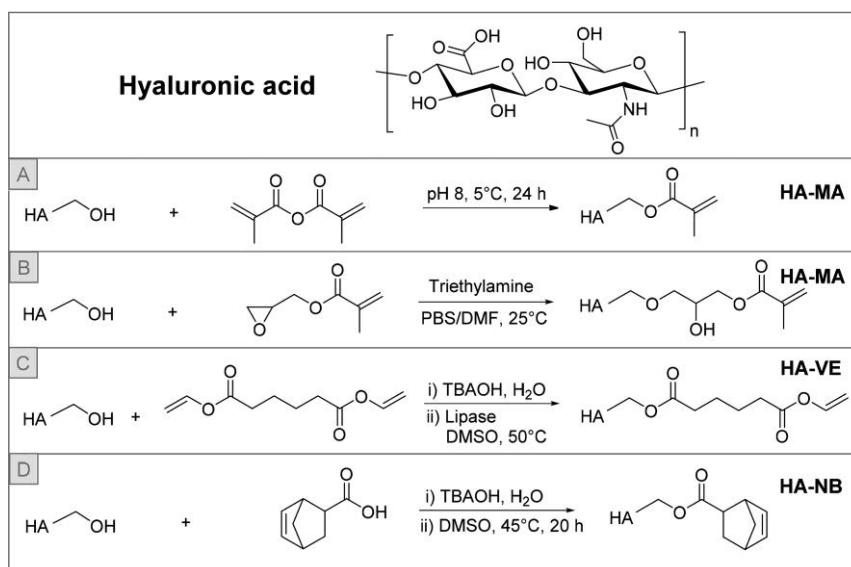


Figure 2.13 | Overview of preparation methods of different photo-crosslinkable HA. (A) HA methacrylate (HA-MA) prepared using MAA.³⁷⁶⁻³⁷⁷ (B) HA methacrylate (HA-MA) prepared using glycidyl methacrylate.^{378, 384} (C) HA-vinyl ester (HA-VE). (D) HA-norbornene (HA-NB).³⁸⁰⁻³⁸²

2.2.4.3. Polyethylene Glycol (PEG)

PEG is the most widely used synthetic hydrophilic polymer in biomedical applications including surface modification,³⁸⁵ drug delivery,³⁸⁶ tissue engineering,^{86, 387} and 3D biofabrication.³⁸⁸ Compared to natural polymers, PEG can be synthesized with targeted molecular weight and architecture, such as linear (Figure 2.14A) or branched structures (Figure 2.14B) and with defined chain end groups.

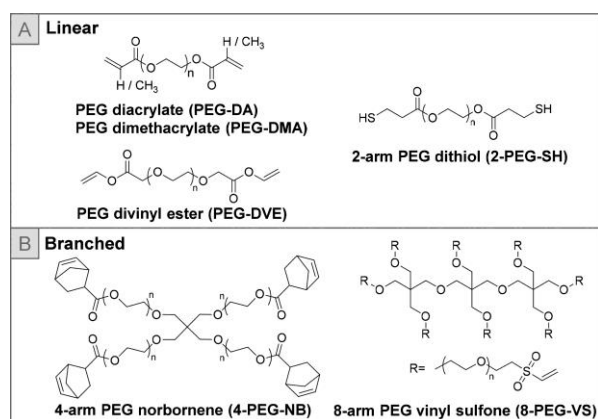


Figure 2.14 | Examples of photo-crosslinkable PEG. (A) Linear derivatives PEG-diacrylate (PEG-DA) and dimethacrylate (PEGDMA)^{216, 389-391} PEG-dithiol (2-PEG-SH),³⁹² and PEG-divinyl ester (2-PEG-DVE)³⁹³. (B) Branched derivatives PEG-norbornene (2-PEGNB)^{272, 392} and PEG-vinyl sulfone (2-PEG-VS).³⁹⁴⁻³⁹⁵

Although PEG-based hydrogels do not exhibit intrinsic biological activity due to the antifouling nature of PEG chains,³⁹⁶ they can be tailored to specific applications through incorporation of RGD peptides for cell adhesion or MMP-cleavable peptides for proteolytic degradation.³⁹⁷ Among the PEG-based bioinks, PEG-diacrylate (PEG-DA) and dimethacrylate (PEG-DMA),^{216, 389-391} PEG-divinyl ester (2-PEG-DVE),³⁹³ PEG-dithiol (2-PEG-SH),³⁹² PEG-norbornene (2-PEG-NB),^{272, 392} and PEG-vinyl sulfone (2-PEG-VS)³⁹⁴⁻³⁹⁵ have been utilized for light-induced 3D biofabrication methods.

2.2.4.4. Alginate

Alginate is a water-soluble, negatively charged polysaccharide biopolymer isolated from brown seaweed. It has a linear structure and consists of two types of monosaccharide residues as a repeating unit, namely 1,4-linked β -d-mannuronic acid (M) and α -l-guluronic acid (G). Typically, a hydrogel state with alginate is generated through ionic crosslinks between the carboxylic acid moieties and divalent cations (such as calcium, strontium, or barium). However, ionic gelation is reversible, and when ions are released, the gel may dissolve. Thus, alginate was adapted for photopolymerization.

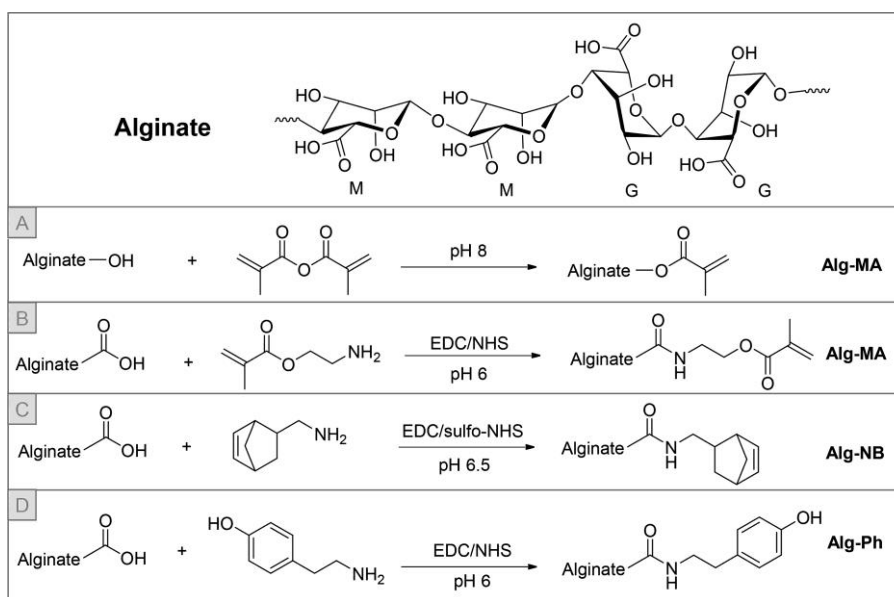


Figure 2.15 | Overview of preparation methods of different photo-crosslinkable alginates. (A,B) Alginate methacrylate (Alg-MA).³⁹⁸ (C) Alginate-norbornene (Alg-NB).³⁹⁹ (D) Alginate-phenyl (Alg-Ph).⁴⁰⁰⁻⁴⁰¹

The principal groups for alginate derivatization are the two hydroxyl groups and one carbonyl group present per monosaccharide residue. Similar to other polysaccharides, photopolymerizable methacrylate derivative (Alg-MA, Figure 2.15A) can be synthesized by the reaction of secondary hydroxyl groups with MAA.³⁹⁸ Another strategy is to functionalize the carboxylic group with aminoethyl methacrylates (Figure 2.15B).⁴⁰² Alginate can also be functionalized with norbornene, a reactive substrate for the radical thiol-one

reaction (Alg-NB, Figure 2.15C).³⁹⁹ Alginate functionalized with phenyl groups (Alg-Ph, Figure 2.15D) for oxidative photo-crosslinking was prepared via carbodiimide-mediated condensation of the carboxyl groups of alginate and primary amino groups of tyramine.⁴⁰⁰⁻⁴⁰¹

2.2.4.5. Collagen

Collagen is a main structural protein in the ECM and is thus naturally an attractive scaffold material for tissue engineering. Collagen is composed of triple helices, which self-assemble into fibrillar hierarchical structures providing mechanical strength, viscoelastic properties, bioactive adhesion sites, and biodegradability.⁹¹ It has been used as a bioink material in 3D printing and crosslinked mainly using temperature or pH change.⁴⁰³⁻⁴⁰⁴ However, thermal crosslinking is a lengthy process, and therefore, combining collagen with other polymers reduces the time for gelation and allows the use of collagen in 3D printing.³⁸⁹ Collagen has also been chemically modified by photo-crosslinkable (meth)acryloyl groups (Col-MA, Figure 2.16).⁴⁰⁵⁻⁴⁰⁸ Functionalization is mostly performed using amino groups of lysine and hydroxylysine residues, which react with activated esters, MAA, or glycidyl acrylate (Figure 2.16). However, reaction conditions often require careful optimization to avoid undesirable gelation during modification. Functionalization of collagen may cause loss of the fibrillar structure and the concomitant reduction of desirable features such as bioactivity and biodegradability.⁴⁰⁹

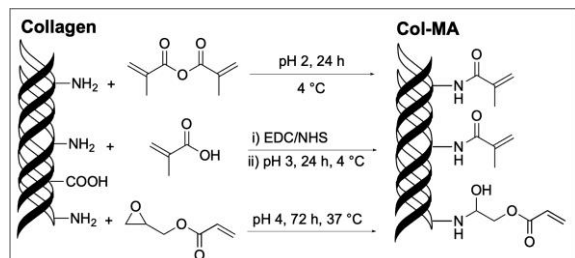


Figure 2.16 | Schematic of photo-crosslinkable collagen methacryloyl (Col-MA) synthesis.⁴⁰⁵⁻⁴⁰⁷

2.2.4.6. Poly(Vinyl Alcohol) (PVA)

PVA is a hydrophilic polymer synthesized by hydrolysis of poly(vinyl acetate). It is widely used in the pharmaceutical industry because of its biocompatibility, and many PVA-based applications are FDA approved. Recently, Qin et al. introduced novel cell-responsive PVA hydrogels made by 2P polymerization.⁴¹⁰ To manufacture a hydrogel microstructure, PVA was functionalized with norbornene (PVA-NB) (Figure 2.17A) for the subsequent thiol–ene reaction. This system allowed the rapid photochemical construction of 3D cell-instructive hydrogel by NIR light at high resolution. Anseth and co-workers have developed photopolymerizable PVA acrylate macromonomers (PVA-A) (Figure 2.17B) with varying degrees of reactive acrylate groups.⁴¹¹ Pendant hydroxyl groups of PVA were reacted with acrylate-

terminated ester anhydride. Another approach employs MAA to introduce methacrylate groups on the PVA backbone (Figure 2.17C).⁴¹²

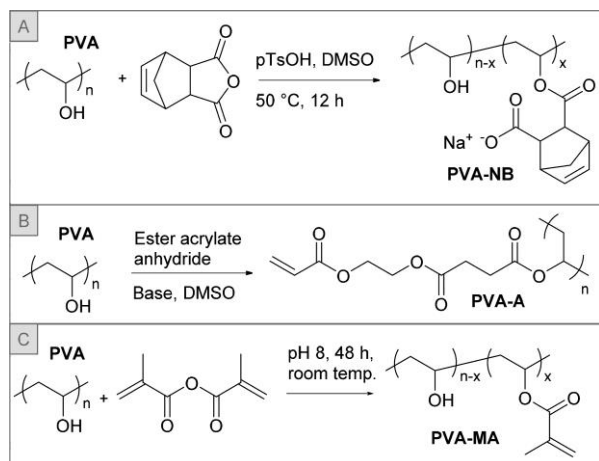


Figure 2.17 | Schematic of photo-crosslinkable PVA. (A) PVA-norbornene.⁴¹⁰ (B) PVA-acrylate.⁴¹¹ (C) PVA-methacrylate.⁴¹²

2.2.5. Biocompatibility of Photoactive Systems

During 3D biofabrication, cells are directly exposed to several factors, including the hydrogel precursors, PIs, radicals, light at different wavelengths and intensity, and the crosslinked hydrogel network itself. Although light irradiation might have various effects on a living organism, it is now widely used in the presence of cells for a range of biomedical applications.^{197, 413} It is generally accepted that visible (400–700 nm) and infrared (700–1000 nm) wavelengths are not detrimental to living cells, although prolonged irradiation might generate heat.⁴¹⁴ One of the targets of photodamage is cellular DNA. UV-B (280–315 nm) wavelength might be absorbed by cellular DNA and induce deleterious effects, such as the reduction in cell growth and survival or change in protein expression.⁴¹⁵ It has been found that long-wave UV-A (315–400 nm) wavelengths are less efficient in causing direct DNA damage. Recently, Ruskowitz et al. demonstrated that low doses of 365 nm UV light needed to induce thiol–ene gelation did not cause deleterious effects to hMSCs. Neither proliferation rates nor protein expression were affected. Moreover, apoptosis was not induced after exposure to varying intensity of 365 nm light. In contrast, exposure to lower wavelength UV light (254 nm) decreased proliferation, initiated pro-apoptotic pathways, and changed protein production.¹⁷⁰

The ability of living cells to survive 3D biofabrication is dependent not only on irradiation wavelength, time, and intensity but also on hydrogel formation chemistry.¹⁷¹ Free radicals generated during photopolymerization are known to oxidize cellular lipid bilayer or cause oxidative stress to cellular DNA.^{273, 416-417} Recently, Wong et al. investigated first only the effects of low-dose, near-UV light (300–425 nm) on hMSC function and found no significant change in global gene expression after multiple exposures totaling

25 min at 3.5 mW/cm².¹⁷¹ In contrast, cells exposed to radical photopolymerization exhibit significant differences in gene expression, which include genes related to the DNA damage. They found gene expression changes due to the presence of free radicals, not to long-wave UV exposure. In another study, exposure to only 365 nm irradiation without radical species for less than 10 min at 10 mW/cm² was considered cytocompatible.⁴¹⁸ These results are motivating the field to use and further explore nonradical-based crosslinking chemistries for hydrogel formation in the presence of living cells.

As discussed in previous sections, natural or synthetic polymers are functionalized to introduce photopolymerizable groups to induce their photo-crosslinking. However, radical-based crosslinking shows the occurrence of numerous (up to 25%) unreacted residual monomer groups⁴¹⁹⁻⁴²⁰ (acrylates or methacrylates), which become entrapped within the hydrogel structure and upon hydrolysis exhibit potential cytotoxic effects. Various acrylic monomers show a cytotoxic effect on the cell viability of, i.e., HeLa S3 cells with a range of maximal inhibitory concentration (IC₅₀) values from 0.01 to 3.70 mmol/L.¹⁷² In contrast, methacrylates are considerably less cytotoxic than acrylates with similar substituents. Widely used as a synthetic hydrogel precursor, PEG-DMA showed a higher IC₅₀ value (10.28 mmol/L) in HeLa S3 cells than IC₅₀ of acrylic monomers. Although methacrylate-based systems are the most prevalent photopolymerizable moiety, alternative vinyl esters can also undergo photopolymerization and exhibit low cytotoxicity. Compared to methacrylate and especially acrylate monomers, the corresponding vinyl esters conclusively demonstrate considerably lower cytotoxicity and ability to support growth of MC3T3-E1 osteoblastic cells.⁴²¹ Further, upon hydrolysis of vinyl ester moieties, the major degradation product is biocompatible PVA and unpolymerized vinyl ester groups hydrolyze to acetaldehyde, which can be metabolized *in vivo* into acetic acid.

Bryant et al. investigated the cytocompatibility of several PIs using the fibroblast cell line NIH/3T3 and encapsulated chondrocytes.¹⁷³ Of the initiators investigated, I2959 was found to cause the lowest level of toxicity on NIH/3T3 fibroblast cell line at concentrations <0.5% (w/w), light intensities 6 mW/cm² at 365 nm, and polymerization times up to 10 min. Also, it was demonstrated that chondrocytes survive the photoinitiation process of PVA hydrogel formation using conditions 0.05% (w/w) I2959, 8 mW/cm² at 365 nm light, and a 10 min exposure time. Another study evaluated the cellular toxicity of I2959 on six different mammalian cell populations: human fetal osteoblasts, bovine chondrocytes, rabbit corneal epithelial cells, human MSCs, goat MSCs, and human embryonic germ cells.^{174, 422} Different cell types have diverse susceptibility to radical-induced toxicity of identical PI concentration and light exposures. A range of I2959 concentrations (0.03–0.1% (w/v)) was well tolerated by all cell types studied.

To increase aqueous solubility, other initiators with improved cytocompatibility, such as MAPO and BAPO salts, have become state-of-the-art. The water-soluble initiator LAP has very low cytotoxicity (LC₅₀ 3.1

mmol/L) with fibroblasts encapsulated in a gelatin hydrogel. It was shown that cell survival for fibroblasts encapsulated in LAP-initiated PEG-DA hydrogels was 95% using the concentration of LAP 0.22 mM (0.0065% w/v).⁴¹⁷ Also, BAPO initiators show very low cytotoxicity, hence making phosphinate PIs an ideal choice for biofabrication.^{303, 417}

2.3. 3D Deposition Bioprinting

Bioprinting methodology and biomaterial development has exploded, and this review concentrates largely on advances published in recent years. Traditionally, the bioprinting space has been dominated by “deposition” approaches in which material is placed on a printbed with 3D automated control. Two common examples of this type of biofabrication are extrusion bioprinting and droplet-based bioprinting (Figure 2.1). Both of these have profited highly from photoactivated materials, but some of the major advantages with other types of crosslinking are also included for completeness. The reader is referred to excellent recent reviews on these topics.^{157, 168, 180, 423-424}

2.3.1. Extrusion Bioprinting

2.3.1.1. Principles of Extrusion Bioprinting

Extrusion bioprinting, also called robotic printing, direct ink writing (DIW), or contact bioprinting, is currently the most widely used 3D bioprinting method. Its popularity is due to its ability to rapidly produce centimeter-sized, cell-laden constructs, as well as to the commercial availability of low cost bioprinters and an increasing array of bioinks available for purchase from multiple vendors. The method is based on the flow of a continuous strand of biopolymer material out of a nozzle whose exit diameter is commonly in the range of ~100–600 μm . When printing at an average speed of ~10 mm/s, centimeter-sized constructs are achievable in less than an hour. During extrusion printing, the polymeric strands are stacked on top of each other in a layer-by-layer fashion to construct the 3D element. There is generally continuous contact between the material flowing out of the nozzle and the material on the printbed, except when the nozzle is retracted for repositioning, during which the flow out of the nozzle is momentarily interrupted. Flow is initiated by pressure in most bioprinters, although syringe pumps have been used. A progressing cavity pump can be used for increased accuracy of bioink flow and precision of the final printed object.⁴²⁵ Extrusion bioprinting is analogous to the popular fused deposition modeling (FDM) printing, where the thermoplastic filament is heated to the melting temperature, T_m , of the polymer and strands of melted polymer are extruded out of the hot end and stacked in a layer-by-layer fashion. In both cases, a computer-aided design (CAD) digital model of format .stl or .amf is sliced or converted to the machine language G-code. G-code is the most widely used numerical programming language to achieve automated control of machine tools and 3D printers.

Commercial extrusion bioprinters are configured so that either the build plate or the printhead/printing cartridge provides the movement in x , y , z , or a combination thereof (Figure 2.18). Although the basic function of all extrusion printers is similar, certain printers can be upgraded to allow hybrid biofabrication (i.e., extrusion combined with melt electrowriting). Printing into a support bath might profit from a build plate which is stationary. Likewise, methods where the amount of deposited material is continuously monitored could benefit from a stationary stage. On the other hand, in the case of a heavy print head with a significant amount of inertia, accurate printing might be better achieved by moving the buildplate and keeping the printhead fixed.

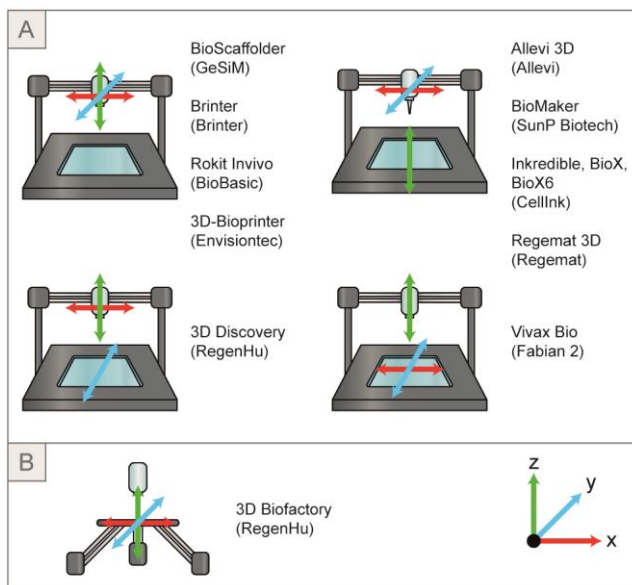


Figure 2.18 | Various configurations of extrusion bioprinters showing movement of the build plate and printhead/bioink cartridge in x (red), y (blue), and z (green) directions. (A) Cartesian printers. (B) Delta Printers.

2.3.1.1.1. Rheological Properties for Printability. The accuracy and reliability of extrusion bioprinting is largely dependent on the ability of the bioink to flow on demand, whereas the mechanical integrity of the print is dependent on the degree of layer–layer adhesion. Layers of uncrosslinked hydrogel fuse easily, but the layers will tend to flow and reduce print fidelity, whereas crosslinking each layer sequentially might lead to better shape retention but less interlayer adhesion. In FDM, stop–start–stop of the flow is guaranteed by the rapid and precise melting and solidification of the material. Integrity of the printed product results from a certain amount of molecular entanglement between the layers, which is achieved as the hot layer slightly melts the cold layer below.⁴²⁶ Reproducing this level of control over the flow properties in bioprinting is much more difficult to achieve as hydrated polymers crosslink slowly, allowing gravity and surface tension to distort the printed object. This rheological challenge of extrusion bioprinting has been referred to as a “race against instabilities”.¹⁸⁵

To obtain a more in-depth understanding of the flow and viscoelastic behavior of bioinks and acellular biomaterial inks, standard rheological tests are carried out as a general method for evaluating printability. First, polymeric solutions have either Newtonian or non-Newtonian properties, where the latter is further categorized into shear thickening (increasing viscosity with increasing shear rate) and shear thinning (decreasing viscosity with increasing shear rate), and their respective time-dependent versions are known as rheopecty and thixotropy. Shear thinning is a feature of most bioinks which reduces shear stress applied to cells within the bioink. Second, shear recovery, which determines the return of a material to the elastic state, is often measured. Third, the yield/flow point specifies when a solid starts flowing or the transition point from a viscoelastic solid to a viscoelastic fluid. The reader is referred to recent papers on rheological printability for more information. ^{157, 427-429}

2.3.1.1.2. Material Strategies for Extrusion Bioprinting. The three most common crosslinking strategies used in extrusion bioprinting are (1) light-induced crosslinking of photoactivatable polymers (chain-growth and step-growth polymerization), (2) ionic crosslinking, often using alginate, and (3) temperature-based crosslinking through use of thermosensitive polymers like gelatin. Methacryloyl derivatives of gelatin, ⁴³⁰ collagen, ⁴³¹ elastin, ⁴³² chitosan, ⁴³³ chondroitin sulfate, ⁴³⁴ and dECM ⁴³⁵ can be used as extrusion bioinks whose printed structure can be crosslinked by light.

Although less common than bioinks based on photoinitiated chain-growth radical polymerization, the increasing use of bioinks based on step-growth thiol-ene click chemistry is a noteworthy trend in extrusion bioprinting. Thiol-ene clickable bioinks made from poly(glycidol), ⁴³⁶ gelatin, ³⁶⁶ and alginate ³⁹⁹ have recently been published. Yeh et al. formed step-growth hydrogels using a photo thiol-ene reaction between norbornene-functionalized poly(glycerol sebacate) and pentaerythritol tetrakis(3-mercaptopropionate), which yielded 3D-printable structures and impressive deformational behavior. ⁴³⁷ Other semisynthetic bioinks based on thiol-ene reactions include photocurable PEG-DA and thiolated fibrinogen fragments ²¹⁶ and methacryloyl collagen with thiolated HA. ³⁸⁹ A bioink containing equimolar thiol/ene ratio of Gel-NB and thiolated gelatin was printed with adipose-derived stem cells (ADSCs). When benchmarked against Gel-MA, the thiol-ene bioink better promoted adipogenic differentiation, likely due to the more homogeneous polymer network and/or the large and bioactive thiol crosslinker. ⁴³⁸ Finally, in a comparison of 10% w/v Gel-NB and 10% w/v Gel-MA, and LAP and I2959 as PI, the more rapid crosslinking with the combination of LAP (at 365 nm) and Gel-NB allow printing of tall (20 mm) structures. ⁴³⁹

Rendering a biopolymer light-sensitive through methacrylation or other means results in a loss of viscoelasticity, ^{218, 440-442} which has serious consequences for its ability to be bioprinted. In certain types of bioprinting discussed later in this review, i.e., droplet and vat polymerization, the loss of viscosity is

auspicious, as low-viscosity materials are beneficial. However, for extrusion printing, special methods are needed to avoid the postprinting flow of the bioink (Figure 19).


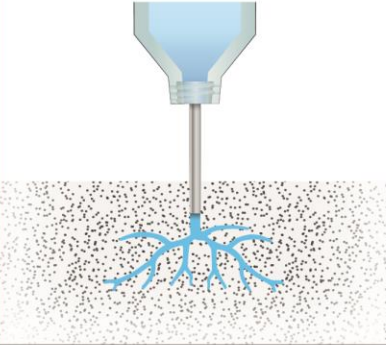
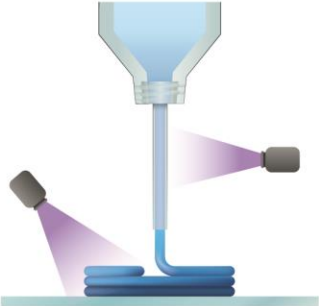
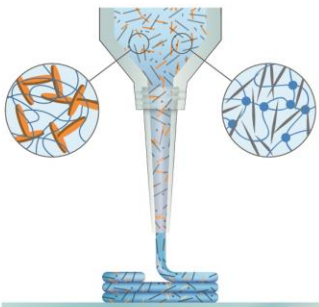
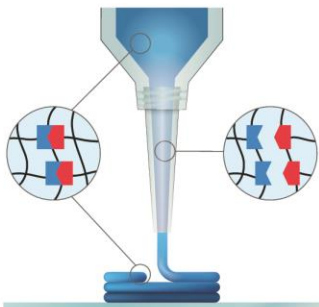

PROBLEM	SOLUTION	
		
LOW VISCOSITY	EMBEDDED PRINTING	UV CROSSLINKED
SOLUTION		
		
NANOPARTICLES / NANOFIBRILS	SELF-HEALING	JAMMED / ENTANGLED

Figure 2.19 | Common strategies to achieve good extrusion printability.

2.3.1.1.3. Embedded Printing. The search for ideal bioinks is akin to finding a “sweet spot” that combines excellent printing fidelity with a biological environment that robustly supports the embedded cells. Several strategies have been devised in recent years to achieve this. Extrusion of bioinks or biomaterial inks into a shear thinning fluid bed is one method to overcome the need for self-supporting bioinks (Figure 2.19). The method, called embedded printing, uses a support material which is solid at low shear stress but flows under conditions of high shear stress (i.e., in the vicinity of the moving nozzle). For example, 0.2% (w/v) Carbopol ETD 2020 is a nonthixotropic granular material that undergoes local shear thinning fluidization near the nozzle without perturbing adjacent regions and undergoes rapid recovery.¹⁸⁵ This allows previously

“unprintable” structures to be made (Figure 2.20A). For bioprinting applications, the support bath is often made of a slurry of gelatin particles.



Figure 2.20 | Examples of embedded printing. (A) Photo-crosslinkable poly(vinyl alcohol) is “written” in a granular bed consisting of Carbopol polymer (left), and in water after removal of the support (right). (B) Highly concentrated collagen bioink is extruded into a bath of coaservated gelatin microparticles according to a human heart scaled to neonatal size. (C) Scaffold-free pure cellular bioink is printed into a bath of oxidized, methacrylated alginate slurry with a 27-gauge needle (scale bar: 600 μm). (D) Pluronic sacrificial inks are printed into a bath of cell aggregates, leaving channels in high cell density constructs after removal of Pluronic (scale bars: 50 μm (top row) and 500 μm (middle and bottom rows)). (A,D) Adapted with permission from ref ¹⁸⁵ and ref ³⁵, respectively. Copyright 2015 and 2019 by the authors. Some rights reserved; exclusive licensee American Association for the Advancement of Science. Distributed under a Creative Commons Attribution NonCommercial License 4.0 (CC BY-NC) <http://creativecommons.org/licenses/by-nc/4.0/>. (B) Adapted with permission from ref ⁴⁴³. Copyright 2019 by the authors. Some rights reserved; exclusive licensee American Association for the Advancement of Science. (C) Adapted with permission from ref ⁴⁴⁴. Copyright 2019 The Royal Society of Chemistry.

Photoactivated HA-MA with 0.1% (w/v) PI I2959 could be printed into the support, UV crosslinked, after which the support could be melted away. ⁴⁴⁵ A 20 μm resolution of this technique has recently been achieved by replacing the slurry particles with highly uniform gelatin microparticles made by coacervation (Figure 2.20B). ¹⁸⁶ Interestingly, the gelatin microbeads of the support material were incorporated into the printed structure, giving it natural porosity once the gelatin had been eluted at 37 $^{\circ}\text{C}$. ⁴⁴⁶ Additional biomaterials that have been used for embedded printing include slurries of agarose ⁴⁴⁷ and gellan, ⁴⁴⁸ but most interesting, with respect to the topic of this review, is the approach using a support material made of photoactivated alginate (oxidized and methacrylated). ⁴⁴⁴ Bioinks composed of high-density solutions of MSCs could be printed into an alginate support bed, and the alginate was then UV crosslinked into a porous “mold” that could support the development of the cellular structure ⁴⁴⁴ (Figure 2.20C). In a reverse configuration, the support bath can be filled with cell aggregates from induced pluripotent stem cell (iPSC)-derived cells in which sacrificial

pluronic channels were printed. This approach allowed the biofabrication of “vascularized” tissues with cell densities approaching that of solid epithelial organs (Figure 2.20D).³⁵

2.3.1.1.4. Rapid UV Crosslinking. Other methods to increase printability capitalized on rapid crosslinking to prevent flow and improve print fidelity. By exposing each layer to UV light (Figure 2.19) (or spraying CaCl_2 on alginate prints⁴⁴⁹ or H_2O_2 on tyramine-modified prints⁴⁰⁰), one can stabilize each layer before printing the next⁴⁵⁰⁻⁴⁵¹ and therefore print taller structures without sagging.⁴⁵² In another approach, “precrosslinking” by light exposure of Gel-MA and HA-MA bioinks was used to improve their rheological properties and printability.^{450, 453} Also, exposure of HA-MA or HA-NB to UV light as it is ejected from a transparent glass capillary tube could increase the resolution of the print as well as protect cells from shear stress.^{382, 451} By optimizing the UV intensity and the length of the capillary, good printing resolution was obtained for low viscous precursors of Gel-MA (5% w/v), HA-MA (2.5% w/v), PEG-DA (5% w/v), and HA-NB (2% w/v).⁴⁵¹ Here, it was possible to print multimaterial cell-laden filaments using a core–shell nozzle and alternating the on–off status of the core and sheath flow. Finally, the polymer content of Gel-MA bioinks could be reduced even further through coextrusion with alginate with coaxial nozzles (see section on Hardware Advances and Figure 2.22). Recently, double-network stiff hydrogel components from PEG-DA and alginate were printed alongside cell-laden softer printed strands to give soft tissue grafts more stability.⁴⁵⁴

For completeness, soft and fluidic biomaterial precursors can be cofabricated with a much stiffer material, often a thermoplastic-like poly caprolactone (PCL), which then relaxes the need for self-supporting, perfectly printable inks. PCL filaments have been printed alongside those of ECM particle-containing inks,⁴⁵⁵ whereas de Ruijter has taken advantage of a technique known as melt electro-writing (MEW) for reinforcement.⁴⁵⁶ Advances in the MEW scaffolding have achieved impressive deformational and structural properties, and their stability often circumvents the need for bioprinting at all as the hydrogel is often injected or cast into the scaffold.⁴⁵⁷⁻⁴⁵⁹

2.3.1.1.5. Nanoparticle/Nanofibril Inks. Another common strategy for printing low concentrations of photoactivated materials like Gel-MA is through the addition of nanoparticles and nanofibers, which afford the material a higher yield stress and shear thinning properties (Figure 2.19). Recently, as little as 1% Gel-MA was printed with excellent resolution using the addition of (2,2,6,6-tetramethylpiperidin-1-yl)oxidanyl (TEMPO)-treated nanocellulose.⁴⁶⁰ The resolution of these scaffolds was improved by dripping 45 mM CaCl_2 onto the constructs during printing, which was thought to interact with the carboxylic groups of the cellulose nanofibrils. Viscosity-enhancing components that have been added to bioinks include laponite,⁴⁶¹ graphene oxide,⁴⁶² and carbon nanotubes.⁴⁶³⁻⁴⁶⁴ In fact, the addition of nanoparticles is of significant importance for the field, as it is an effective method for both contributing to shear thinning and for bringing additional functionality into the bioink. For instance, carbon nanotubes and metal nanowires can

render materials conductive, which could benefit electrically active tissues like cardiac and neural tissue.⁴⁶⁵⁻⁴⁶⁶ Nanosilicates have affinity binding to GFs, drugs, and other morphogens important in maintaining the viability of the cells and their ion release can support the osteogenic phenotype.⁴⁶⁷ Cidonio et al. showed that both osteogenesis and angiogenesis were enhanced in laponite–Gel-MA bioinks compared to Gel-MA alone, due to interactions between the GFs with the laponite.⁴⁶¹ In addition to the aforementioned nanoparticles with intrinsic shear thinning properties, recent studies demonstrated the use of nonshear thinning solid silica nanoparticles (ca. 40 nm in diameter) as a rheology enhancer via induction of electrostatic or dynamic covalent interactions between nanoparticles and polymer matrix.⁴⁶⁸⁻⁴⁶⁹ The rheological properties of such nanocomposite bioinks can be manipulated to a great extent by controlling the size, concentration of nanoparticles and, more importantly, the type of interactions between nanoparticles and polymers.⁴⁶⁸⁻⁴⁶⁹ The function of these nanoparticles was to serve as a mechanical reinforcement and mechanism to dissipate mechanical energy.⁴²³

2.3.1.1.6. Self-Healing Bioinks. In an effort to reproduce the flow properties necessary for bioprinting, it is suggested that materials crosslinked with reversible bonds could rapidly self-heal and be a promising strategy for producing extrusion bioprinting materials (Figure 2.19).⁴²³ These bioinks can be of the supramolecular type, based on noncovalent interactions (i.e., electrostatic, hydrophobic, hydrogen, and guest–host interactions) or can take advantage of reversible/exchangeable covalent bonds (i.e., boronate ester, imine, hydrazone).^{149,470} Although these reactions do not involve light, photoactivated materials have indeed been critical to enhancing properties of the final construct. As an example, Highley et al. utilized guest–host interactions in a bioink composed of hyaluronan modified by adamantine and cyclodextrin for both the extruded ink as well as for support bed.¹⁸⁴ The G–H interactions provided initial stability, but for long-term stability, a secondary network based on HA–MA was crosslinked with UV light. In a second approach, which did not require postprint crosslinking, Kim et al.⁴⁷¹ combined oxidized HA (OHA), a soluble glycol chitosan (GC) and adipic acid dihydrazide (ADH) for a self-healing bioink based on a competitive formation of imine bond (aldehyde of OHA and primary amine of GC) and acylhydrazone bonds between OHA and ADH. OHA and HA directly modified with ADH could also produce a self-healing and printing hydrogel, which could be additionally stiffened and patterned with HA functionalized with norbornene plus a tetrathiol and PI.⁴⁷² Taking advantage of noncovalent interactions between hydroxydopamine and proteins, Shin et al. showed that modification of ECM components with gallol moieties, an aromatic ring containing three hydroxyl groups, could form hydrophobic interactions that enhanced the short-term shear-thinning properties of the material, printing fidelity, and adhesion to tissue surfaces.⁴⁷³

2.3.1.1.7. Granular Bioinks. Typical bulk hydrogels have pore sizes in the range of 10–100 nm, and in addition to limited transport of oxygen, nutrients and waste products of these materials, the embedded cells

are dependent on protease- or hydrolytic-dependent cleavage of the polymer network to gain space for proliferation, migration, and ECM deposition. The introduction of interconnected macroporosity/supermacroporosity (macroporosity is defined here as pore sizes between 50 nm to 10 μm and supermacroporosity between 10 and 500 μm) has been shown to support formation of neurons, establishment of capillary beds, and proliferation and formation of cellular networks.⁴⁷⁴⁻⁴⁷⁶ Structures printed from macroporous bioinks would be able to benefit from the superior cell infiltration, spreading or migration which have been observed in structured hydrogel environments.⁴⁷⁷ The temporal control of polymerization afforded by photoactivated materials can play an important role. Macroporous bioinks were first reported based on aqueous phase separation that occurs between two immiscible aqueous phases of Gel-MA and poly(ethylene oxide)(PEO), where cells were loaded in the Gel-MA phase.⁴⁷⁸ Once the phase-separated bioink was stabilized by photo-crosslinking, the PEO was subsequently removed, leaving porous structures which highly promoted cell spreading. Perhaps an even more robust method to create macroporous materials uses granular microgels. These materials have excellent mass transport properties due to the interconnected void space between the microgels (see excellent reviews^{477, 479-480}). For example, the Khademhosseini group used microfluidic-assisted Gel-MA beads, which were annealed together with additional UV light exposure to form a high content Gel-MA material with excellent viability of the seeded human umbilical vein endothelial cells (HUVECs).⁴⁸¹ In a similar manner, the Segura group generated PEG microgels using microfluidics and then annealed the spheres together with UV (as well as activated Factor XIII (FXIIIa) or click chemistry).⁴⁸² Cells within these so-called microporous annealed particle (MAP) gels demonstrated excellent cell spreading, proliferation, and network formation compared to smaller-pore bulk gels, and the material showed improved *in vivo* wound healing in mice.⁴⁷⁴ The same group has also used tetrazine–norbornene click reactions to tune the interaction strength between microgels and by extension the stiffness of the microgel scaffold.⁴⁸³ Using colloidal interactions to form structured hydrogels, Nair et al. found that the vasculogenesis could be tuned based on the structure of the porous void fraction.⁴⁷⁶ They were able to demonstrate the formation of a network of dense and interconnected endothelial cell (EC)-lined capillaries within the colloidal macrostructured gels. Recently, Caldwell et al. showed the importance of porosity on cell behavior.⁴⁸⁴ They compared MSC-seeded macroporous scaffolds made from large ($\sim 190 \mu\text{m}$), medium ($\sim 110 \mu\text{m}$), and small ($\sim 14 \mu\text{m}$) spherical microgels and found that the large spheres significantly induced the cytokine secretion.⁴⁸⁴

Auspiciously, “soft jammed” granular microgel materials exhibit shear thinning and/or self-healing properties that make them particularly suitable for extrusion bioprinting (Figure 2.19). Being composed of already crosslinked materials, granular bioinks also have an inherent resistance to flow. For example, Highley et al. used a microfluidic-based approach to make jammed bioinks also containing cells, although the stability of these structures was weak and required the presence of a support gel.⁴⁷⁹ Xin et al. used electrospaying to

create PEG microbeads that were printable and could be annealed using thiol–ene click chemistry.³⁹² Composite bioinks containing microgels suspended in a continuous medium has also been reported. Song et al. used microgels from 10% gelatin to achieve shear thinning bioinks and suspended these microgels in a 3% gelatin solution that could later be stabilized by transglutaminase.⁴⁸⁵ Methods to produce microgels have also been an area of active research with “in-air” production of microgels achievable with faster rates and without the oil phase.⁴⁸⁶

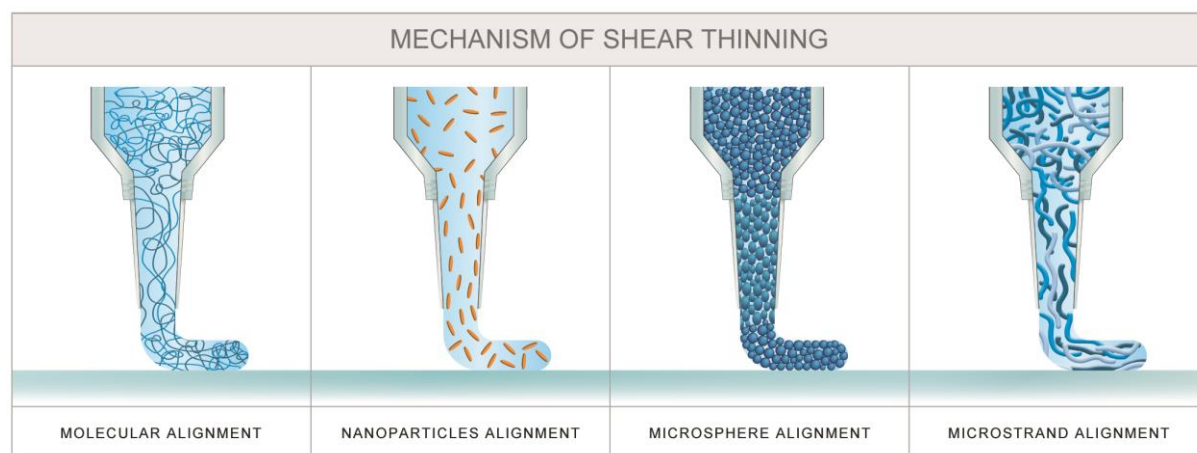


Figure 2.21 | Theoretical mechanisms of shear thinning in the nozzle of extrusion bioprinters.

Recently, methods to produce uniform elongated, high-aspect-ratio microgels have also been produced with greater potential to influence cell alignment and migration compared to spherical microgels.⁴⁸⁷⁻⁴⁸⁸ Kessel et al. showed that elongated gel microstrands were also applicable to extrusion bioprinting (Figure 2.19).⁴⁸⁹ High-aspect ratio HA-MA microstrands entangled, producing a printed construct with greater stability compared to spherical granular gels. The microstrand constructs did not need to be secondarily crosslinked, and the properties of the printed bioink could be adjusted by the time of exposure of the bulk gel to UV light. An added advantage is the alignment of the microstrands along the printing direction which contributed to the formation of anisotropic structures and alignment of cells.⁴⁸⁹ The mechanism of shear thinning in the nozzle of extrusion printers using entangled inks is illustrated in Figure 2.21, along with our current understanding of how molecules, nanoparticles, and microgels align and/or deform during flow. In each of these examples, stabilization of the structures by photoactivated materials can be advantageous.

2.3.1.1.8. Hardware Advances for Extrusion Bioprinting. One of the powerful aspects of extrusion bioprinting is the biological relevance of the dimension of the strands which are deposited. These strands can be deposited in patterns reminiscent of the vascular branching,⁴⁹⁰ and channels can be formed within hydrogels when the deposited material is a sacrificial bioink.⁴⁹¹⁻⁴⁹³ Other approaches to directly bioprint vascular structures have taken advantage of coaxial needles to print hollow structures from low

concentrations of photoactivated materials. For instance, by placing low viscosity Gel-MA ($\sim 0.08 \text{ Pa}\cdot\text{s}$), cells, and alginate in the core of the nozzle and CaCl_2 in the sheath component, it was possible to reduce the Gel-MA concentration to 4.5%⁴⁵³ (Figure 2.22A). Liu et al. were able to further reduce the Gel-MA concentration to 2.5% by polymerizing a core of Gel-MA, CaCl_2 , and cells within a sheath of alginate.⁴⁹⁴ Interestingly, two-material “Janus” type strands can also be made where the inner core of the coaxial extruders is fed via a *y*-junction microfluidic head (Figure 2.22B). Costantini et al. also printed coaxial Janus strands of PEG-fibrinogen, alginate, and I2959, where one-half of the core contained CaCl_2 myogenic cells and the other half BALB/3T3 fibroblasts.²¹⁶ Finally, triple coaxial nozzles can be used to print tubular structures where CaCl_2 is placed in both the outer sheath and inner core⁴⁹⁵ (Figure 2.22C) or when the inner core contains CaCl_2 in a fugitive Pluronic ink, which diffuses to crosslink two outer alginate-containing sheath layers (Figure 2.22D).^{209, 496} Some disadvantages of the coaxial vessels are their possible collapse and poor adhesion to adjacent strands. Recently, it has been suggested that more uniform endothelialisation of channels can be achieved by adding endothelial cells to sacrificial core gelatin strands that are printed alongside photoactivated sheath materials. As the gelatin liquefies, the released cells are shown to evenly cover the inner surface of channels.⁴⁹³

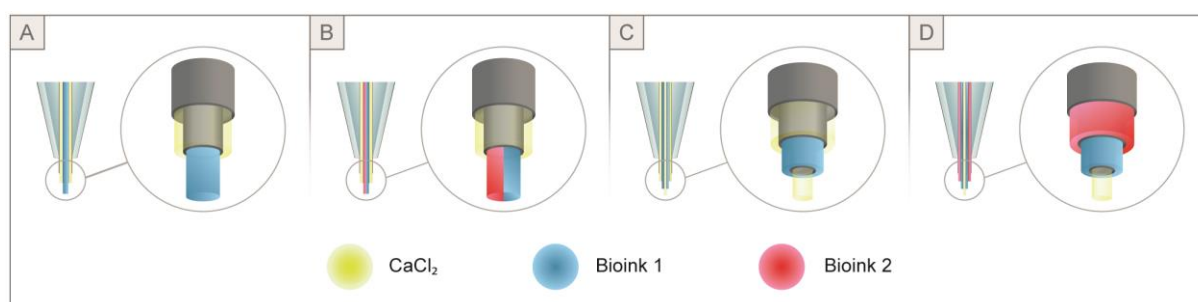


Figure 2.22 | Coaxial nozzles can be used to print low concentrations of photoactivated materials by adding alginate, which rapidly crosslinks in the presence of CaCl_2 . (A) A solid strand of bioink can be rapidly crosslinked with CaCl_2 in the sheath.²¹⁰ (B) A Janus arrangement allow printing of two bioinks within a single strand.²¹⁶ (C) Hollow structures can be printed using triple coaxial nozzles.⁴⁹⁴⁻⁴⁹⁵ (D) Two-layered hollow structures can be printed with triple coaxial nozzles (25G/18G/15G), where the core material is CaCl_2 -containing Pluronic.^{209, 496}

Recent hardware advances have also improved resolution of the method, one area in which extrusion bioprinting does not compare favorably to other techniques. For example, Kenics mixing elements were placed prior to the exit of the nozzle, creating complex “chaotic” patterns of multimaterials in the printed strands (Figure 2.23A).⁴⁹⁷ Although most commercial extrusion bioprinters have multiple print heads allowing two or more bioinks to be used, switching between print heads is often cumbersome, slow, and disrupts the print flow. The introduction of microfluidic print heads was a natural evolution to rapidly switch the flow of bioinks in accordance with the order and volume of each material needed for the multimaterial print.⁴⁹⁸⁻⁵⁰⁰ Capillaries from up to seven different reservoirs have been merged into a single print head, where

the actuation of valves and pressure allows continuous flow during the switching.⁴⁹⁹ A similar approach switched the flow between small nozzles that were bundled into one large nozzle.⁵⁰¹ Finally, to further increase the size and complexity of printed structures, the concept of parallel printing, also termed voxelated printing, has recently been published (Figure 2.23B).⁵⁰² Hardware advances are making possible the printing of new types of bioinks which need to be mixed just prior to exiting the nozzle or where particles like cells can be concentrated at the tip.⁴⁹⁸ Finally, the incorporation of “lab-on-a-tip”-type diagnostics could be used to expand the functionality of extrusion bioprinting.

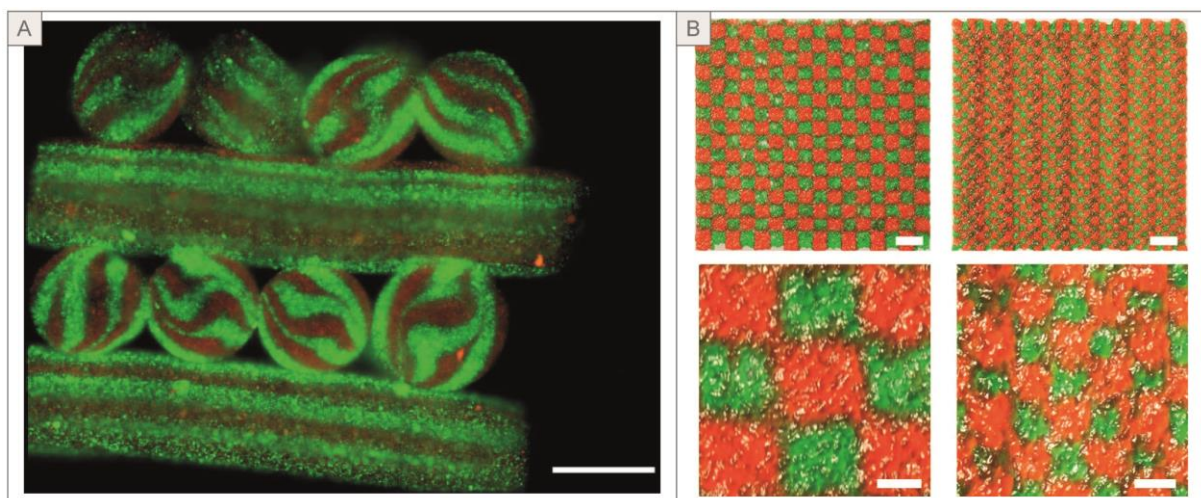


Figure 2.23 | Examples of (A) chaotic printing with a Kenics mixture in the nozzle (scale bar: 1 mm), and (B) parallel “voxelated” printing of gelatin using eight print heads and very rapid switching of the flow (scale bar top row, 8 mm; scale bar bottom row, 2 mm). (A) Adapted with permission from ref⁴⁹⁷. Copyright 2020 IOP. (B) Adapted with permission from ref⁵⁰¹. Copyright 2019 Society for Laboratory Automation and Screening.

2.3.1.2. Applications

Extrusion bioprinting has been applied to almost every cell and tissue type. However, the great majority of applications are at an early stage, and there is no bioprinted product currently on the market. Because of the large body of current literature, we have restricted ourselves to just a few illustrative examples of situations where bioprinted constructs have made significant advances in mimicking the properties of native tissues. Given the resolution of extrusion bioprinting, the method has been optimal for the production of tubular structures and channels, and in particular, the study of the interactions between channels. For example, Song et al.²⁴³ made channels using a sacrificial G–H bioink that was printed into a support bath. The support could be stabilized postprinting by a UV-triggered thiol–ene reaction. After endothelialisation of the channels, another channel releasing angiogenic factors was used to create signaling gradients, which induced sprouting of capillary structures into the support bed medium (Figure 2.24A).²⁴³ With this system, one could study the effect of shape and curvature on the process of vascular sprouting. In a second example, adjacent PEO–

pluronic sacrificial channels were printed into a bed of gelatin–fibrin, and after removal of the sacrificial material, proximal tubular ECs were perfused into one channel and glomerular microvascular ECs into the adjacent one (Figure 2.24B).⁵⁰³ The authors observed perfusion of albumin and glucose out of the proximal tubule into the vascular lumen, indicating that complex transport processes reminiscent of reabsorption process in kidneys could be modeled.

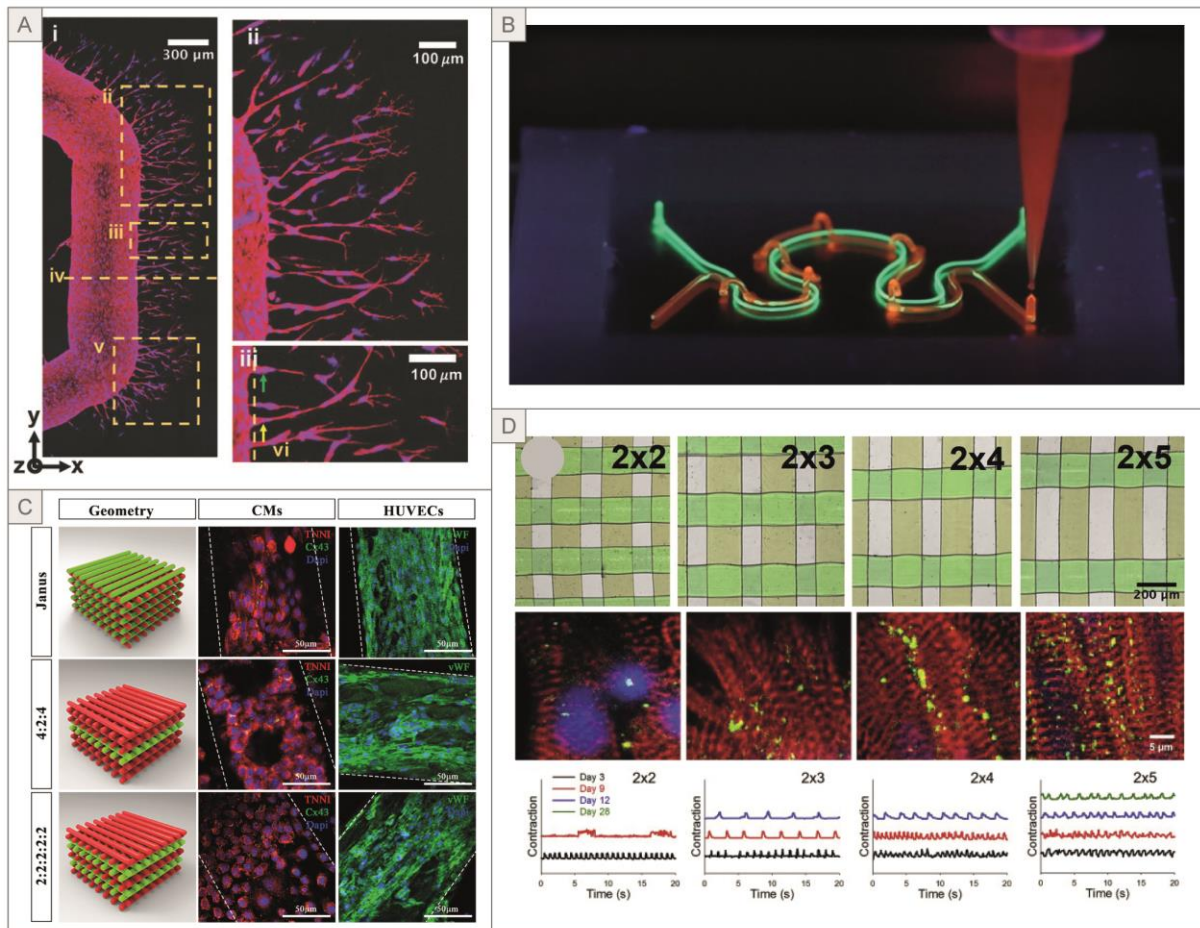


Figure 2.24 | Examples of extrusion bioprinting applications. (A) Vascular sprouting was influenced by the curvature of the channel. (B) Proximal tubule epithelial cells (green channel) were printed in close proximity of glomerular microvascular endothelial cells (red channel) as an *in vitro* model of renal reabsorption. (C) Cardiomyocytes and HUVECs were printed within a single strand (Janus) or in alternating layers (scale bar: 50 μm). (D) Contractile endothelialized myocardium was printed using an alginate/Gel-MA bioink, which was later seeded with cardiomyocytes. Long-term 28-day contractility was achieved when a 2×5 aspect ratio grid was used. (A) Adapted with permission from ref ²⁴³. Copyright 2018 Wiley-VCH. (B) Adapted with permission from ref ⁵⁰⁴. Copyright 2019 Springer Nature. (C) Adapted from ref ⁵⁰⁵. Distributed under the Creative Commons Attribution License. (D) Adapted with permission from ref ²¹⁰. Copyright 2016 Elsevier Ltd.

Extrusion bioprinting has also been used to study the importance of spatial interaction distance between cell types. For example, Maiullari et al. combined HUVECs and iPSC-derived cardiomyocytes⁵⁰⁵ to recreate

some of the complex inhomogeneities of cardiac tissue (Figure 2.24C). They found that the maturation of cells in bioprinted materials was superior to that of bulk gels, largely due to the printed macroporosity and improved mass transport. Additionally, they found staining of α -sarcomeric actin, which is indicative of aligned cardiomyocytes, was promoted in the printed samples and much reduced in bulk, nonprinted gels. In particular, the greatest *in vivo* alignment of the cardiomyocytes was found when the two cell types were printed within the same strand (called Janus geometry) using a microfluidic head, and the effect was diminished when the two cell types were printed in alternating layers (Figure 2.24C). In another study, anisotropic functional myocardium was extrusion bioprinted with an alginate/Gel-MA bioink containing 1×10^7 HUVECs/mL and I2959 in the core of a nozzle with CaCl_2 flowing in the sheath of the coaxial extruder. The aspect ratio of the grid ranged from 2×2 , 2×3 , 2×4 to 2×5 , and maximum cell alignment was found in the 2×5 configuration (Figure 2.24D).²¹⁰

Another strength of extrusion bioprinting is the ability to precisely position two or more cell types to better mimic their *in vivo* distribution. While these examples do not use light-activated materials, they could be adaptable to the materials described in this review. Derr et al. used extrusion bioprinting to manufacture skin equivalents (SEs) consisting of connective tissue dermis and epithelial epidermis.⁵⁰⁶ The bioink for the dermis was composed of fibrinogen, collagen type I, gelatin, and elastin combined with human dermal fibroblasts. Using the microvalve of the bioprinter, laminin/entactin was jetted onto the dermal surface, followed by extrusion of the neonatal dermal epithelial keratinocytes, which formed a complete monolayer after 14 days. The SEs showed good functionality with intact “outside in” and “inside out” barrier function,⁵⁰⁶ as confirmed by cadherin staining of the epidermal cells and collagen VII staining of the basement membrane (Figure 2.25A). In another recent example, the Cho group, who has pioneered the use of soluble ECM extracts to improve biological functionality of bioprinting materials, used a triple coaxial nozzle to position ECs on the inner surface of their biofabricated vessels and smooth muscle cells on the exterior (Figure 2.25B). The biofabricated grafts were patent in an *in vivo* rat model and stable endothelialisation and maturation of the smooth muscle layer were observed.²⁰⁹

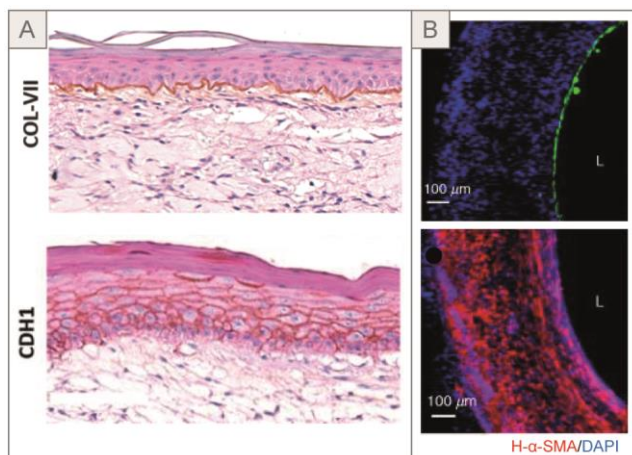


Figure 2.25 | Applications of multicellular extrusion bioprinting. (A) Bioprinted skin substitutes have barrier function with staining for basement membrane protein type VII collagen and cadherin-1 (CHD1). (B) Triple coaxial extrusion bioprinted vascular graft with single layer of endothelial cells facing the lumen and an exterior layer of smooth muscle cells. Left: Adapted with permission from ref ⁵⁰⁶. Copyright 2019 Mary Ann Liebert, Inc. Right: Adapted with permission from ref ²⁰⁹. Copyright 2019 AIP Publishing LLC.

Finally, a unique feature of extrusion bioprinting is its ability to align proteins and molecules along the printing direction, thus providing cells within the printed structure with important topological/guidance cues. In these cases, the shear stress, which is often thought to be a detrimental factor, can be beneficial in increasing alignment of the structures. Kim et al. used a 5% collagen bioink, which, when printed at a speed of 10 mm/s and using a 100 μm nozzle diameter, allowed sufficient alignment of the collagen to orient human ADSCs, H9C2 cardiac muscle cells, and MC3/3-E1 bone cells. ⁴⁰⁴ Interestingly, the application of 50 mM glycine and 150 mM KCl was critical to support the fibril formation of the collagen (Figure 2.26A). In a related application, collagenous bioinks derived from decellularized corneal ECM were extruded with 20G, 25G, and 30G nozzles, which increased the alignment of the collagen fibrils compared to a nonprinted control. The embedded keratocytes showed increasing cellular alignment as seen by f-actin staining but also increased expression of α -smooth actin at the highest gauge needle, where shear stress is highest (Figure 2.26B). ⁵⁰⁷ This increased expression is a sign of myofibroblast differentiation, a process associated with reduced corneal transparency. Fibrin can also align during extrusion as demonstrated by a study using a bioink containing fibrinogen, HA, and factor XIII. Strands were printed into a bath containing thrombin and PVA, which could stabilize the fibrin in an aligned orientation. Embedded primary Schwann cells could then align along the fibrin microstrands (Figure 2.26C). ⁵⁰⁸

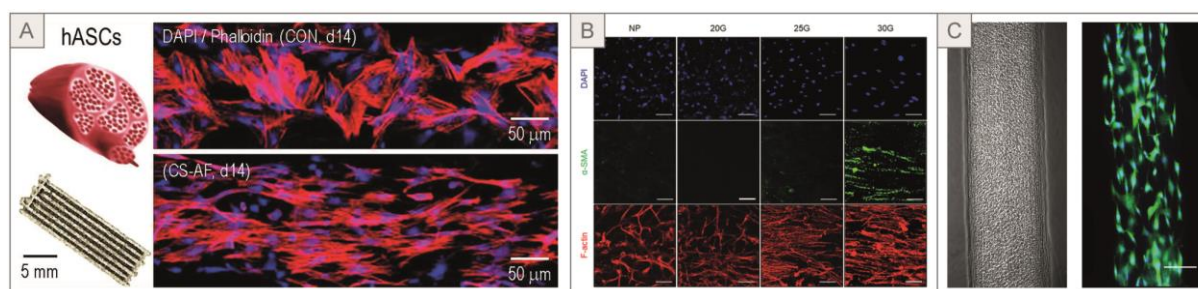


Figure 2.26 | Examples of cellular alignment according to the print direction. (A) Human adipose-derived stem cells align along fibrillated collagens. (B) In a corneal model, keratocytes were printed in bioink consisting of decellularized corneal extracellular matrix. Using nozzles of decreasing diameter, there was increasing alignment of the collagen fibers compared to nonprinted (NP) control. The smallest 30G nozzle however causes upregulation of α -smooth muscle actin (scale bar: 50 μ m). (C) Primary Schwann cells aligned according to bioprinted fibrin-HA strands (scale bar: 100 μ m). (A) Adapted with permission from ref ⁴⁰⁴. Copyright 2019 Elsevier BV. (B) Adapted with permission from ref ⁵⁰⁷. Copyright 2019 IOP Publishing Ltd. (C) Adapted with permission from ref ⁵⁰⁸. Copyright 2016 Elsevier BV.

2.3.1.3. Limitations and Outlook

Despite the substantial output of research using extrusion techniques and advances to produce good phenotypic models, extrusion bioprinting suffers from certain disadvantages. Looking toward the translation of bioprinted products to the clinics, it is important to bear in mind certain potential limitations of the method. First, extrusion has inherently limited resolution, and printing of cell-laden bioinks with good viability requires the use of nozzle diameters of several hundred micrometers. In reality, the diameter of the strand can be even larger due to exudate swelling. The printed strands are therefore an order of magnitude larger than the dimension of an average cell, making control of cellular and subcellular environment of individual cells not possible. Another potential limitation related to extrusion through the small nozzle size is the possible deleterious effects of shear stresses and extensional strains on cells as they are mixed into viscous bioinks and during their entry into and out of the nozzle. Shear stress can reduce cell viability, but it can also alter proliferation capacity and phenotypic expression of the cells, ^{507, 509} where simple live/dead assays may give an incomplete picture of the state of the cells after printing.

Perhaps a second restriction of the technique relates to the difficulty in controlling the flow of bioinks, which makes reproducibility and accuracy problematic to achieve. The strand must hold its shape until it is crosslinked, but it must also coalesce with the under- and overlying strands so that the part has good integrity. The rheological window, which allows these seemingly contradictory behaviors, is quite narrow. Multiple factors can affect the rheological properties of the bioink, including the mixing process, the DF, molecular weight of the polymer, and the addition of cells. To complicate the situation further, many bioinks may relax or have thixotropic or time-dependent shear thinning behavior, meaning the print process could change within a cartridge of bioink or from cartridge to cartridge. ⁵¹⁰ In practice, these viscosity variations may be

compensated by manual tuning of the printing process, particularly the printing pressure and speed. Given that there is a range of printing parameters, the amount of material that is actually deposited on the build plate, and hence the number of cells in the cellular product, can vary substantially.

Print fidelity of layer-by-layer hydrogel objects is more difficult, as hydrogels often undergo unpredictable dimensional changes. As has been observed in the deposition of strands by FDM, the profile of the strand is circular as it exits the nozzle, but as the strand is deposited, it makes a 90° turn. Once deposited, its cross-sectional dimension is more ellipsoid (wider in width than height). The sagging of the z direction is difficult to predict and increases with the number of layers. Therefore, the z error (programmed line thickness minus the actual line thickness) will result in changes in the distance between the nozzle tip and printed layer, which in extreme cases causes the nozzle to trail through the ink or the strand to break up. Again, manual adjustments to the printer are often necessary, when the number of printed layers exceeds around ten.

To improve print fidelity and keep the strand from flowing, a rapid cessation of flow postprinting is often achieved by exposure of UV light after each layer, which allows much taller structures to be printed (Figure 2.27).⁴⁵² Layer-by-layer crosslinking, however, can affect the layer–layer adhesion and/or cause a gradient in mechanical stiffness. Because the UV light can penetrate hundreds of micrometers into the printed construct depending on the optical properties of the material, the initial layers are exposed to more UV light than the upper layers. Postprinting of the entire construct has advantages in terms of construct integrity, but a disadvantage is that the z -error increases with increasing weight of the overlying layers.

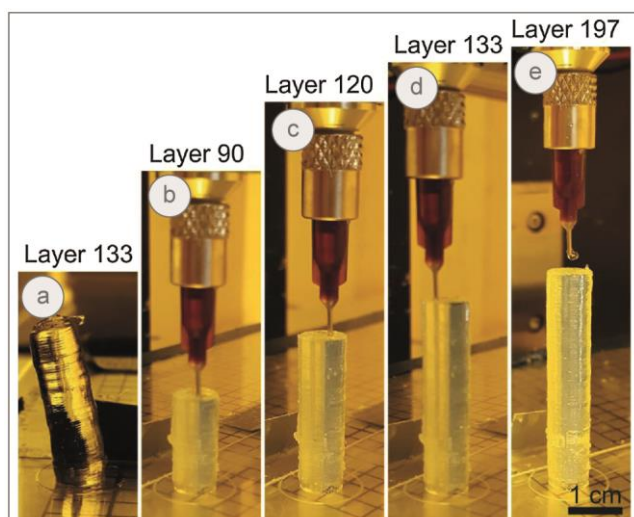


Figure 2.27 | Light-mediated printing of tall structures. PEG-DA was printed without crosslinking (a) and with crosslinking between layers (b–e), the latter of which allow the printing of tall structures but diminished the layer–layer adhesion strength. Adapted with permission from ref⁴⁵². Copyright 2017 Elsevier BV.

Currently, bioprinting of tens or hundreds of identical products necessary for *in vitro* screening and for toxicology and safety studies for regulatory purposes is challenging. The fidelity of the printed construct compared to the original.stl file needs to be assessed prior to submission to regulatory authorities.⁵¹¹ To assess print fidelity, algorithms have been developed, but improvements on both the processing of bioinks and the hardware to detect and correct printing errors are required.

Despite these limitations, extrusion bioprinting has unique advantages compared to its competitors. It is the only biofabrication technique which can create truly anisotropic properties,⁴⁸⁹ as the flow of the material can be used to effectively align fibrils, microgels, and by implication, cells. To benefit from this phenomenon, nonplanar slicing software,⁵¹² and curvilinear printing⁵¹³ could be harnessed to exploit the natural anisotropy of tissues or organs, replacing arbitrary layer-by-layer slicing. Extrusion bioprinting explicitly benefits from high-yield stress, viscous materials, thus the functionality of extrusion bioinks can be augmented through the addition of multifunctional nanoparticles and high cell densities in ways not possible for other techniques. Extrusion bioprinting excels in multimaterial applications and many of the most exciting advances have come on the hardware side (parallel printing,⁵⁰² chaotic printing,⁴⁹⁷ Janus printing²¹⁶). Finally, for clinical-sized grafts, extrusion bioprinting outperforms all other techniques and is the method of choice for replicating tubular structures like small caliber vessels and nerves found in the human body.

2.3.2. Droplet-Based Bioprinting

2.3.2.1. Principles of Droplet-Based Bioprinting

Droplet-based bioprinting originated from inkjet printing, which had been widely used for 2D printing of inks onto papers for decades. A conventional inkjet printer prints text or graphics by jetting ink droplets from an orifice, depositing them on a paper followed by a drying process. In 1994, the first inkjet-based 3D printer was brought to the market by Solidscape,¹⁸² where heated liquid wax droplets were deposited on a substrate and rapidly solidified by cooling to build a 3D construct in a layer-by-layer fashion. Later, starch- and plaster-based ink materials came on to the market, and finally in 2000, a 3D inkjet printer called Quadra (Objet Geomerics Ltd., currently a branch of Stratasys Ltd.), utilizing photoactivated materials as inks, became commercially available. The 3D inkjet printing technique, in combination with photoactivated inks and light-mediated solidification, is also known as multijet or polyjet 3D printing, which is widely used for general rapid prototyping as well as manufacturing 3D parts.⁵¹⁴ Since then, inkjet-based 3D printers have expanded their applications to other fields, including the deposition of living cells to build 3D cellular constructs. As the field grows, diverse droplet-based bioprinting methods have been developed, such as microvalve and acoustic-droplet-ejection bioprinting.¹⁷⁹ Since inkjet and microvalve bioprinting have been widely adopted for directly building cell-laden constructs (Figure 2.28), these two techniques and their use in combination with

photoactivated bioinks are discussed in this section. A comprehensive overview of general droplet-based bioprinting can be found in a recent review paper.¹⁷⁹

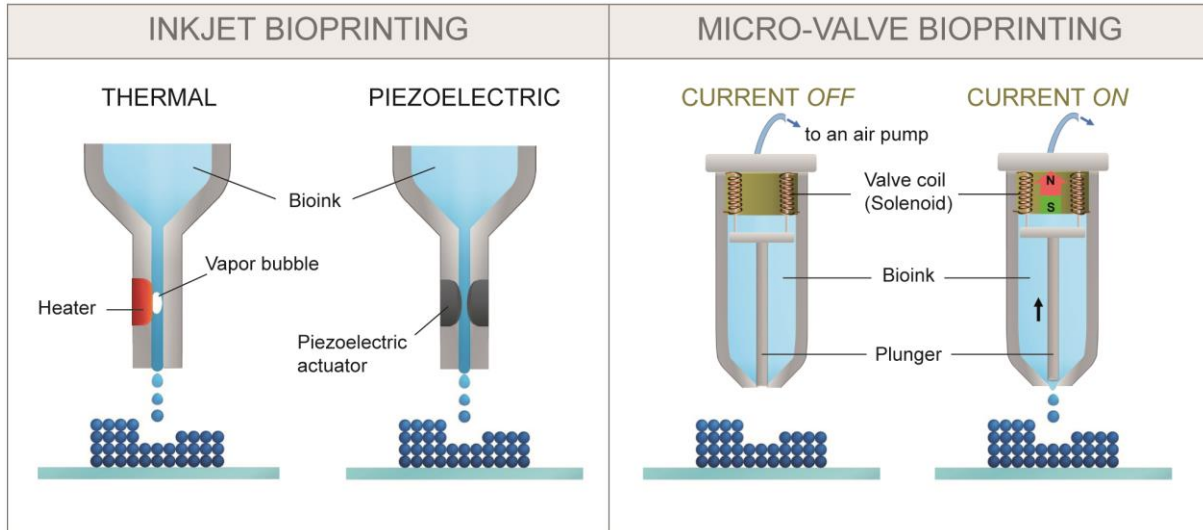


Figure 2.28 | Mechanisms of generation of droplets in drop-on-demand bioprinting. Left: In inkjet bioprinting, ejection of an ink drop is induced by pressure generated through either formation of vapor bubbles upon heating (thermal) or displacement of a piezoelectric actuator (piezoelectric). Right: In microvalve bioprinting, a droplet is ejected when the solenoid coil induces magnetic fields which pull the plunger upward and open the orifice. Because the ink in a cartridge is under pneumatic pressure at all times, when the orifice is opened, droplets can be ejected.

2.3.2.1.1. Hardware. There are two different modes of droplet-based printing: continuous jetting printing (CJP) and drop-on-demand (DOD) printing.⁵¹⁵ In CJP, an ink is continuously ejected and spontaneously breaks into droplets due to Rayleigh–Plateau instability, which describes the tendency of a continuous liquid stream to minimize the surface area of the stream by forming droplets.⁵¹⁶ The generated droplets are electrically conductive so that electric or magnetic fields can position them at the intended position. Droplets not used for printing are collected and recirculated. Conversely, in DOD printing, individual droplets are jetted on demand. In bioprinting applications, the DOD mode is preferred over CJP because it avoids ink recirculation, something which can raise the risk of contamination as well as waste valuable bioink material, and the DOD printing does not require electrical conductivity of the bioink. DOD printing typically involves the following three steps: (1) generation of droplets, (2) deposition of droplets on a substrate, and (3) layer-by-layer solidification.

In inkjet printing, droplet generation can be induced by thermal, piezoelectric, or electrostatic mechanisms, with thermal and piezoelectric-based bioprinters being the most widely adopted^{180, 517} (Figure 2.28). In thermal bioprinting, the jetting of a droplet is powered by pressure generated through rapid formation and collapse of an air bubble during rapid heating and cooling of a resistor. In piezoelectric bioprinting, the

displacement of a piezoelectric actuator generates pressure to eject the fluid. Thermal bioprinters are relatively cheap compared to piezoelectric ones. However, the local temperature of the ink can increase up to 300 °C for a few microseconds, which could limit material types to the ones resistant to thermal degradation.⁵¹⁸ In contrast, piezoelectric bioprinters are relatively expensive but compatible with a wider range of materials without any of the risks caused by high temperature compared with thermal bioprinters. For bioprinting cell-laden constructs, both bioprinters have been extensively utilized. The typical volume of droplets generated by the inkjet printers ranges from 1 to 100 pL, with a typical diameter of 10–100 μm. The rate of droplet generation is up to 30 kHz.^{179, 517}

In addition to inkjet printing, microvalve bioprinting is another DOD printing method widely adopted for biofabrication. A microvalve bioprinter generates ink droplets on demand by controlling the movement of a plunger by a solenoid coil (Figure 2.28). When a voltage pulse is applied, the solenoid coil induces magnetic fields, which pulls the plunger upward and opens the orifice. The bioink in a cartridge is under pneumatic pressure at all times, and thus when the orifice is opened and the pressure is high enough to overcome the viscosity and surface tension of the bioink, droplets are ejected. In this way, droplets can be generated at a few kHz, and the typical range of orifice diameters is 100–300 μm, which generates larger droplets (100–600 μm) compared to the thermal or piezoelectric inkjet bioprinter. However, it is more tolerant to viscous bioinks (1–200 mPa·s) compared to inkjet bioprinters.^{179, 519}

2.3.2.1.2. Bioink Considerations for Droplet-Based Printing. In addition to hardware, physical properties of a bioink should meet certain criteria to facilitate droplet-based bioprinting. In particular, surface tension, viscosity, and density are important parameters. A detailed physical description about printing fluids is suggested in the study by Jang et al.⁵²⁰ Briefly, one can predict printability of a fluid using the following equation proposed by Fromm:

$$Z = \frac{1}{Oh} = \frac{\sqrt{\gamma\rho l}}{\eta} = \frac{\sqrt{We}}{Re} \quad (2.1)$$

where Oh = Ohnesorge number, γ = surface tension of a fluid, ρ = density of a fluid, l = characteristic dimension (the radius of the printer orifice), η = viscosity of a fluid, We = Weber number, Re = Reynolds number.

For inkjet printing, a study based on numerical modeling suggested that a material with a Z value (the reciprocal of Ohnesorge number) between 1 and 10 is printable.⁵²¹ Later, a slightly different range of Z values ($4 < Z < 14$) was suggested, which was determined experimentally using a piezoelectric inkjet printer.^{520, 522} For a fluid with a Z value smaller than 1, too-high shear stress by high viscous fluid results in too much viscous dissipation to form a droplet, whereas a fluid with a Z value larger than 10 would form a main drop accompanied with small satellite droplets. For microvalve printing, this range could differ from inkjet

printing. Choi et al. reported that fluid with a Z value between 0.23 and 84.77 was able to form stable droplets and be printed using a custom-made microvalve printer.⁵²³ Ejection of a fluid with a low Z value (<1) was enabled by increasing the pneumatic pressure up to 200 kPa to overcome viscosity dissipation, and a backflow stopper helped with preventing liquid backflow and forcing the liquid to move forward. Printing a fluid with a high Z value (>14) was achieved by optimizing printing pressure and droplet velocity to avoid the formation of long filament-shaped droplets and satellite droplets. They claimed that the optimization could be done within a wider range of pressure and velocity compared to inkjet printing because the microvalve printer had a lower minimum velocity requirement (0.63 m/s) than an inkjet printer (1.4 m/s). However, Schulkes reported that a fluid with the Ohnesorge number (Oh) larger than 1 (i.e., $Z < 1$) forms a stable filament rather than a droplet, which implies that stable droplet-based printing with an ink having a low Z value close to this limit would be challenging.⁵²⁴

For a bioink droplet, viscosity is often the most important parameter in determining printability because most bioinks are based on biocompatible aqueous solutions; so there are no significant differences in surface tension (20–70 mJ/m²) or density (~ 1000 kg/m³) between bioinks, but viscosity can vary greatly. The typical viscosity of bioinks for a DOD inkjet bioprinter is <15 mPa·s⁵¹⁷ and for a microvalve bioprinter <200 mPa·s. In addition to the physical properties of a bioink, the travel speed of the droplet should be optimized, where the speed needs to be high enough to overcome the surface tension at the orifice and at the same time low enough to prevent the droplet from splashing on a substrate.⁵²⁵

In addition to the successful ejection of a droplet from the orifice, interactions between droplets and the receiving substrate are important for quality printing. The shape of a droplet is affected by substrate properties such as hydrophobicity and roughness. For printing continuous strands, the spacing between droplets should be also adjusted to form a uniform line. The conditions for printing stable droplets or strands using an inkjet printer have been intensely investigated both theoretically and experimentally.⁵²⁶⁻⁵²⁹ Soltman et al. demonstrated that the shape of a printed line depends mainly on spacing between droplets, lengths of delay (time between ejection of drops, $1/\text{frequency}$), and temperature for a given droplet volume.⁵²⁶ In this study, an aqueous ink of a conductive polymer, poly(3,4-ethylenedioxythiophene)/poly(styrenesulfonate)(PEDOT/PSS, 1.3 w/w%) was deposited onto a glass slide coated with poly(4-vinylphenol). Depending on the drop spacing and delay, the deposited droplets along a line exhibited different behaviors (Figure 2.29). When the spacing between droplets was greater than the droplet diameter, no coalescence occurred and isolated droplets were formed. As the distance decreased, the droplets coalesced to form a uniform line, yet a further decrease in spacing led to bulging along the line. The delay and temperature are important parameters that affect evaporation of liquid in a drop and thus drop volumes. For example, a shorter delay will lead to less evaporation than a longer delay, yielding larger drops, which require more spacing to form a uniform line than smaller drops. Indeed, for a given drop spacing, a

shorter delay resulted in bulging, whereas a prolonged delay led to formation of a uniform line. The width of a printed line is affected by the surface contact angle of the deposited ink drop as well as the size of a drop. A hydrophilic substrate will induce a higher degree of droplet-spreading than a hydrophobic one, which results in larger widths of printed lines. This tendency was experimentally demonstrated by Smith et al.⁵³⁰ using a silver-containing ink, where 358 and 82 μm of line widths were obtained on a glass (contact angle 5.9°) and a Teflon (contact angle 58°) substrate, respectively. Overall, material properties, drop coalescence, delay, drop volume, and drop–substrate interactions determine resolution of DOD printing.

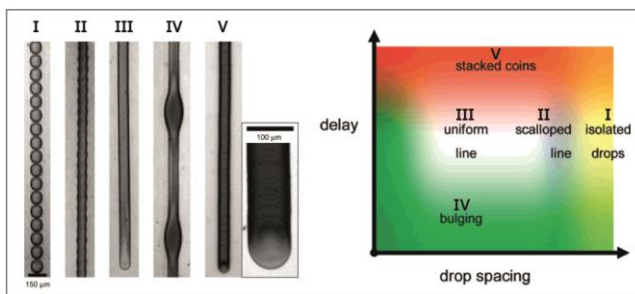


Figure 2.29 | Photographs of printed strands with respect to delay and drop spacing (left) and schematic representation of printed strand behavior at an intermediate temperature (right). Uniform lines (III, in the middle of the scheme) can be obtained with optimized drop spacing and delay (see white area). Adapted from ref.⁵²⁶.

2.3.2.1.3. Crosslinking Methods. After the deposition of droplets, crosslinking immediately follows (Figure 2.30, top). In addition to photo-crosslinking, various crosslinking chemistries have been adopted for droplet-based bioprinting including ionic⁵³⁰⁻⁵³¹ (e.g., Ca^{2+}), chemical⁵³² (e.g., protamine, poly-l-lysine), enzymatic⁵³³⁻⁵³⁴ (e.g., horseradish peroxidase (HRP), transglutaminase), and thermal crosslinking.⁵³⁵⁻⁵³⁶ For each type of crosslinking chemistry, several different methods of droplet printing have been demonstrated (Figure 2.30, bottom). For ionic, enzymatic, or chemical crosslinking, solidification can be induced by sequential deposition of bioink followed by another type of ink containing crosslinking agents. For example, iPSCs were successfully printed by sequentially depositing an ink composed of alginate and a bioink comprised of cells and CaCl_2 crosslinking solution.⁵³¹ Despite the fragility of iPSCs, the viability of printed cells showed no significant difference from nonprinted cells (>80%), implying high cytocompatibility of the printing method. In another system, a 3D cell-laden construct was printed by sequential printing of two inks, one composed of phenolic hydroxyl (Ph)-modified polymer and HRP and the other of Ph-modified polymer and hydrogen peroxide.⁵³³ Crosslinking between Ph moieties on gelatin or alginate was induced when the second ink, containing hydrogen peroxide, was printed on top of the layer printed using the first ink, with HRP.

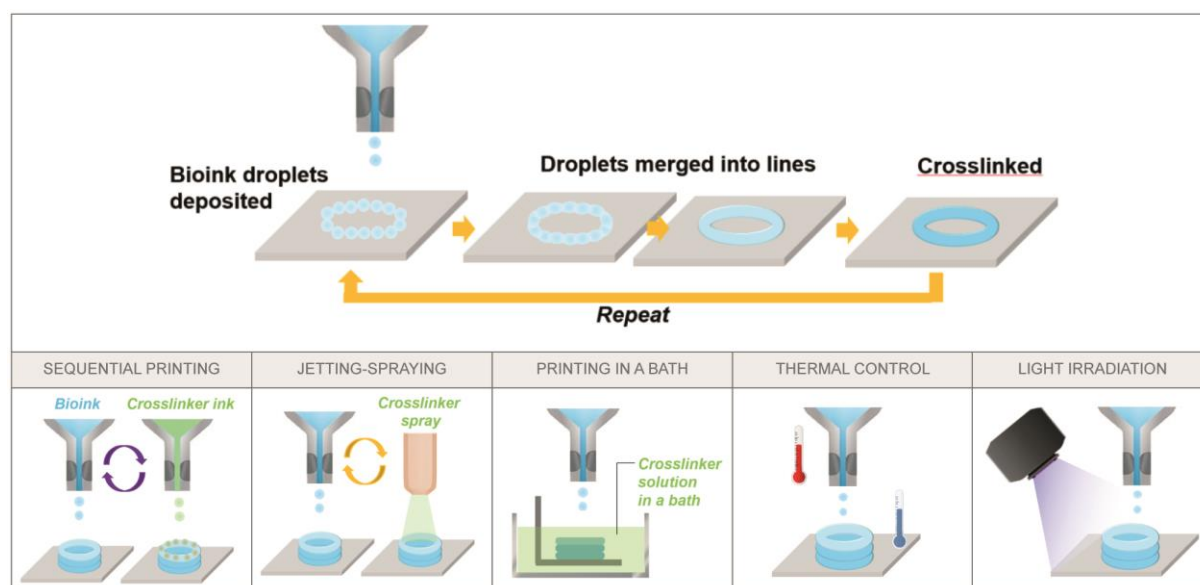


Figure 2.30 | General procedure of droplet-based printing (top) and different methods of crosslinking (bottom).

A jetting-spraying method is an approach where each deposited layer was spray-coated with crosslinkers, which is suitable for ionic or chemical crosslinking. Yoon et al. demonstrated that the method is compatible with various crosslinking agents, including CaCl_2 , thrombin, protamine, poly-L-lysine, and chitosan oligosaccharide.⁵³² In addition, a centimeter-scale cell-laden hydrogel was biofabricated with high printing fidelity at high printing speed (75 mm/s), which was attributed to the fast crosslinking made possible by the sprayed crosslinker mist. Similar to extrusion printing, printing in a bath has also been used for droplet-based printing. One common system is to print an alginate-based bioink into a bath filled with CaCl_2 solution. For instance, cell-laden vessel-like structures were generated by printing 1% alginate solution into a bath filled with a CaCl_2 solution.⁵³⁷ The solution provided a buoyant force as well as fast crosslinking so that vascular structures with overhangs were achieved. Because droplet-based printers are only compatible with inks having low viscosity, some studies have utilized approaches where a bioink composed of cells and low viscosity crosslinker is printed in a bath filled with un-crosslinked hydrogel precursor solution. In the study by Cui et al., a bioink comprised of thrombin/ Ca^{2+} and cells was printed into a fibrinogen biopaper to form fibrin channels.⁵³⁸ The printed endothelial cells (ECs) were aligned inside the fibrin channel and proliferated to form confluent layers in 21 days. In another approach, stabilization of ejected droplets was induced by self-assembly of lipid monolayers on the surface of droplets.⁵³⁹ Droplets of an aqueous ink were printed in a bath filled with oil, where lipid molecules are self-assembled on droplet surfaces and the deposited droplets were further stabilized by lipid–lipid interactions between droplets to form stable bilayers. The droplets in resulting printed constructs were highly cohesive, providing the constructs with structural integrity. In the follow-up study, the method enabled biofabrication of cellular constructs where multiple cell types were patterned with the minimum feature size of ca. 200 μm .⁵⁴⁰

A few thermoresponsive polymers have been explored as a bioink or biomaterial ink for droplet-based printing. Blaeser et al. printed thin-walled cylindrical structures by ejecting agarose ink kept at 39 °C into a bath containing fluorocarbon support liquid at 20 °C.⁵³⁶ In another study, a poly(*N*-isopropylacrylamide-*co*-2-(*N,N*-dimethylamino)-ethyl acrylate) bioink was printed onto a substrate at 37 °C to generate arrays of aggregates of ECs, which eventually were fused to each other.⁵⁴¹ Thermal crosslinking requires high concentrations of polymers for fast crosslinking, which hinders thermoresponsive polymers from being used as a sole bioink for droplet-based bioprinting. Instead, the thermal crosslinking is often used in combination with other crosslinking methods to obtain additional mechanical stability after printing. For instance, a bioink comprised of CaCl₂ and cells was printed into a mixture of alginate and collagen.⁵³⁰ Ionic crosslinking of alginate provided fast crosslinking during printing to maintain the printed structure, and the printed construct was further mechanically stabilized by inducing thermal crosslinking of collagen in the incubator at 37 °C for 3–5 h.

Lastly, light-induced crosslinking has been utilized to solidify cell-laden constructs. In most studies in droplet bioprinting, photo-crosslinking was induced by continuous irradiation on the printing stage (Figure 2.30, bottom). One needs to be careful not to expose the cartridges to the light throughout the printing procedure, which would cause undesirable crosslinking and clogging of the orifice. The photo-crosslinking method has several advantages over other crosslinking modes in droplet-based bioprinting. Compared to sequential printing or jetting-spraying methods, photo-crosslinking does not require a separate step for applying crosslinker, which could reduce the printing time. In addition, a wide range of materials could be used as photoactivated bioinks through conjugation of photoactive moieties to polymers, whereas ionic or thermal crosslinking is only relevant to a limited range of materials (e.g., gelatin, alginate). Furthermore, one could obtain additional structural stability by irradiating a printed construct after printing. For this, photo-crosslinking is often used in combination with other crosslinking chemistries. For example, in the study by Biase et al.,⁵⁴² a mixture of pluronic-diacrylate, eosin Y, and TEA was printed onto a substrate at room temperature to induce thermal crosslinking during printing, which was followed by photo-crosslinking by light irradiation after printing.

2.3.2.1.4. Photoactivated Bioinks in Droplet-Based Bioprinting. Most photoactivated bioinks developed for droplet-based printing are based on PEG-DMA or Gel-MA. The bioinks for droplet-based printing are limited by the requirement of low viscosity to avoid clogging. PEG-DMA, in general, has low viscosity and is easy to functionalize, which makes it attractive for droplet-based printing. In addition, compared to Gel-MA, mechanical properties of PEG-DMA gels are more tunable and suitable for printing mechanically robust constructs. For example, compressive moduli of printed constructs using 10% and 20% (w/v) PEG-DMA inks were 37 and 395 kPa, respectively.⁵⁴³ On the other hand, PEG itself does not provide any biological cues, which often leads to reduced viability or cellular functions of printed cells. To address the issue, efforts

have been made to enhance biological properties of PEG-DMA-based bioinks. In the study by Gao et al.,⁵⁴⁴ acrylated RGD and MMP-sensitive peptides were added to PEG-DMA. This ink was used to bioprint hMSCs within a layer-by-layer 3D tissue using a thermal inkjet bioprinter. The bioprinted hMSCs were then cultured in either a chondrogenic or osteogenic environment. hMSCs printed using the ink with acrylated peptides exhibited better mechanical maturation and higher chondrogenic or osteogenic marker expression compared to those printed using the ink without peptides. The same research group also reported a bioink composed of PEG-DMA and hydroxyapatite particles, which promoted formation of bone-like tissue during 21 days of in vitro culture.⁵⁴⁵

Gel-MA-based bioinks are more biologically active compared to PEG-DMA due to the presence of bioactive amino acid sequences such as RGD. However, Gel-MA is usually too viscous for inkjet or microvalve printing, and the one with low DF even forms a gel at room temperature. Therefore, Gel-MA solution at low concentrations (<5 wt %⁵⁴⁶⁻⁵⁴⁷) has been used as bioink to avoid any risks of clogging. Several approaches have been explored to improve properties of Gel-MA-based bioinks for droplet-based printing. In general, methacrylation interrupts physical crosslinking of gelatin, resulting in decreased viscosity. Therefore, for droplet-based printing, gelatin with high DS is desirable due to its low viscosity. However, high DS also leads to a high degree of crosslinking of gelatin and thus the formation of a stiff gel. To independently control the photo-crosslinking and viscosity of Gel-MA, Hoch et al. synthesized methacrylated and acetylated gelatin.⁵⁴⁸ The viscosity of GM10 (Gel-MA synthesized by adding 10-fold excess of MAA to gelatin) is suitable for inkjet printing (~ 6.7 G mPa·s at 37 °C for 15 wt % solution). However, the formed hydrogel retained a high storage modulus (~ 55 kPa for 15 wt % solution), indicating formation of a stiff gel. Acetylated- and methacrylated gelatin had viscosity as low as that of GM10 (~ 5.2 mPa·s at the same condition) but formed a soft gel ($G' \sim 25$ kPa for 15 wt %). Another approach to controlling the mechanical properties of Gel-MA-based bioinks is to add PEG-DMA.⁵⁸⁸ A bioink comprised of 10 wt % PEG-DMA and 1.5 wt % Gel-MA was successfully printed using a thermal inkjet bioprinter, and the compressive modulus of a bioprinted construct was ca. 40 kPa.

Compared to the other biofabrication techniques, droplet-based printing is highly compatible with multimaterial printing. Similar to extrusion-based printing, a droplet-based printer can have multiple printheads, each of which contains a cartridge filled with a bioink and single or multiple nozzles. In addition, droplet-based printing allows deposition of multimaterials in a single droplet. For example, arrays of droplets having varying ratios of PEG-DMA to Gel-MA have been printed using a microvalve bioprinter, which was used to study cellular response to different ECM compositions.⁵⁴⁹⁻⁵⁵⁰ To generate such arrays, droplets of Gel-MA were deposited with increasing volume followed by deposition of PEG-DMA with decreasing volume, resulting in the generation of arrays of droplets with the same volume. The resultant dual-material

droplets exhibited homogeneous opaqueness, even though the degree of mixing of two materials in a droplet was not further studied. The method of printing multimaterials without additional mixing is possible because of the low viscosity of bioinks used in droplet-based printing. However, to date, this approach has not been fully exploited to bioprint a 3D construct with multimaterial bioinks.

2.3.2.2. Applications

Droplet-based bioprinting allows for the generation of complex arrays/patterns of drops containing cells and/or biologics for HT screening as well as tissue engineering. In addition, several types of tissue analogues such as cartilage, bone, and vessels have been biofabricated using this technique in combination with photoactivated bioinks.

2.3.2.2.1. HT Screening and Patterning. Generation of droplets with varying compositions can be achieved by depositing different types of bioinks on a spot of varying volume. For example, in the study by Ma et al.,⁵⁴⁹ an array of droplets with varying ratios of Gel-MA to PEG-DMA was bioprinted using a microvalve bioprinter. Specifically, a Gel-MA bioink (5 wt %) containing human periodontal ligament stem cells was first deposited with decreasing droplet volume. The volume of a droplet was controlled by varying the duration of valve opening between 1–5 ms. Subsequently, a PEG bioink (10 wt %) containing the same cells was deposited on the same array of Gel-MA droplets to achieve Gel-MA:PEG-DMA ratios of 5:0, 4:1, 3:2, 2:3, 1:4, and 0:5. The bioprinted stem cells exhibited highest viability as well as greatest spreading area in the condition with the highest Gel-MA ratio (5:0), and as the ratio of Gel-MA in a drop decreased, the viability and spreading area also decreased (Figure 2.31). In a follow-up study,⁵⁵⁰ the same screening platform was used to find the optimal bioink composition for supporting *in vitro* osteogenic differentiation of human periodontal ligament stem cells, where the bioink composed of Gel-MA and PEG-DMA at a ratio of 4:1 was chosen, considering both biological properties and mechanical stability. The selected bioink with the cells was injected to an alveolar bone defect in a Sprague–Dawley rat and led to the better healing of the defect compared to the same hydrogel without cells or a saline solution. Even though both studies only utilized Gel-MA and PEG-DMA, the approach holds great promise for HT screening of various biologically active materials.

In addition, droplet-based printing allows the generation of micropatterns of biomolecules or cells. This strategy becomes powerful when the patterns are printed onto functional substrates. For example, microarrays of transfected cells with a spot diameter of ca. 500 μm were generated by seeding cells on the plasmid micropatterns printed by a piezoelectric inkjet printer.⁵⁵¹ To achieve local deposition of cells on the patterns, the glass substrate was first functionalized with PEG, followed by printing using an ink composed of a plasmid (encoding two different fluorescent proteins, Venus and mCherry) and ECM proteins. When

cells were seeded on the printed micropatterns on the PEG-functionalized substrates, the cells selectively attached to the patterns.

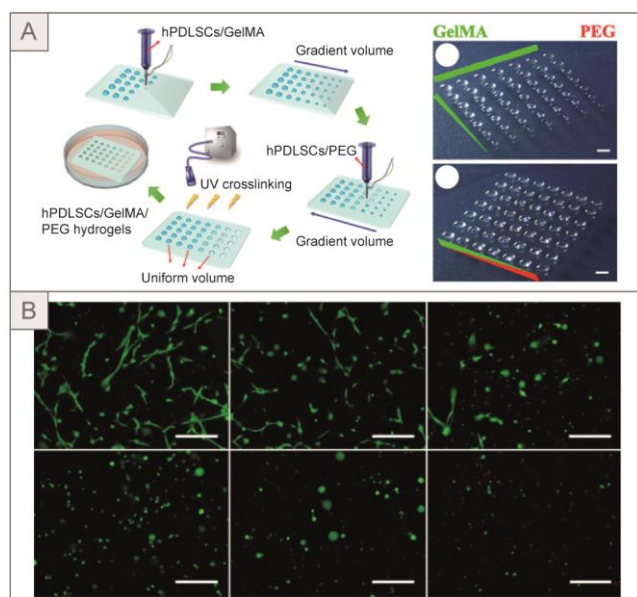


Figure 2.31 | (A) Bioprinted arrays of cell-laden hydrogel drops with varying ratios of Gel-MA and PEG-DMA for HT screening. (B) Live/dead staining images of cells in printed gels with a Gel-MA (5 wt %)/PEG-DMA (10 wt %) at ratios of 5/0, 4/1, 3/2 (top, left to right), 2/3, 1/4, 0/5 (bottom, left to right) (scale bars: 200 μm). Adapted with permission from ref ⁵⁴⁹. Copyright 2015 IOP Publishing Ltd.

The generated arrays could be a platform for functional analyses of specific genes on cells based on cell phenotypes. In a recent study by Jia et al.,⁵⁵² patterning of biomolecules such as fibronectin and GFs on biomimetic nanofibrous matrices was demonstrated. Droplets were printed onto six different electrospun fibrous matrices composed of PCL and collagen. The printing resolution was affected by the wettability of the matrices as well as fiber organization, where higher wettability led to a larger printing area and isotropic or anisotropic fiber orientations resulted in round or oval shapes of droplets, respectively. By optimizing the materials and printing conditions, arrays of spots with high resolution ($25 \pm 10 \mu\text{m}$) were printed on the matrices. Using the optimized conditions, transforming growth factor beta 1 (TGF- β 1) was printed on the PCL/collagen electrospun fibrous mat. The amount of TGF- β 1 deposited on each microspot was controlled by changing the number of printed layers of the TGF- β 1 solution (100 ng/mL), where the layer numbers were varied from 1 to 10. As a result, the expression of a myofibroblastic differentiation (α -smooth muscle actin, α -SMA) increased with the amounts (i.e., layers) of deposited TGF- β 1 on a microspot.

2.3.2.2.2. Tissue Implants. Photoactivated bioinks in droplet-based printing have been mainly studied for printing cartilage and bone analogues. Cui et al. developed a PEG-DMA-based bioink containing human chondrocytes (at 5×10^6 cells/mL) and I2959 (at 0.05%).⁵⁴³ The bioink was directly printed onto an ex vivo

osteocondral plug with cartilage lesion (4 mm diameter, 2 mm depth) using a thermal inkjet bioprinter (Figure 2.32A). Because of the low viscosity of the ink, cells in a cast gel sedimented, resulting in inhomogeneous cell distribution, whereas bioprinting with simultaneous layer-by-layer photopolymerization led to the formation of a gel having homogeneously distributed cells.

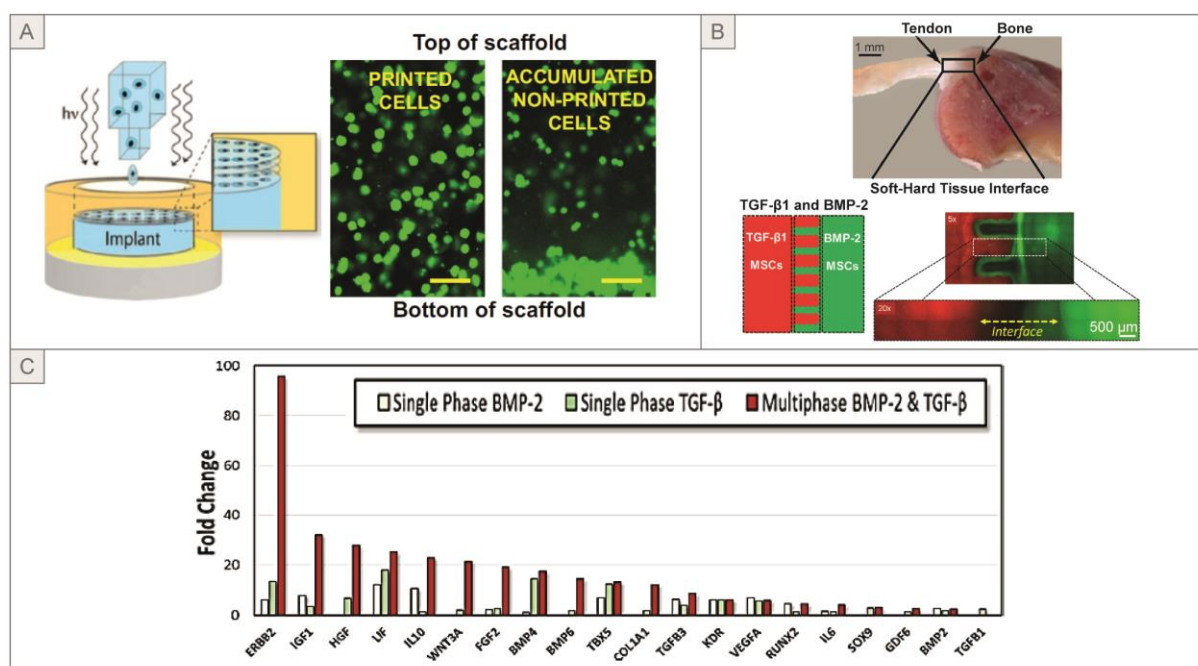


Figure 2.32 | Droplet-based bioprinting of cartilage analogues. (A) Left: Schematic of bioprinting onto an ex vivo osteochondral plug. Right: Distribution of cells (green) throughout a printed (left) or cast (right) scaffold (scale bars: 100 μ m). (B) Biomimetic fibrocartilage analogues bioprinted by a microvalve printer. The region stained as red contains TGF- β 1 and MSCs and the green region contains bone morphogenetic protein 2 (BMP-2) and MSCs. (C) Expression of chondrogenic and osteogenic marker genes by the cells in printed constructs containing BMP-2 or TGF- β only (single phase) or both (multiphase) after 36 days of in vitro culture. (A,B) Adapted with permission from ref ³⁸⁸. Copyright 2013 The Royal Society of Chemistry. (B,C) Adapted from ref ⁵⁴⁶

Bioprinted chondrocytes in a 10% PEG-DMA bioink underwent in vitro maturation, where increased gene expression of collagen II and aggrecan was observed after six weeks of culture compared to the gels cultured for two weeks. Furthermore, the in situ printed gel was well integrated into the osteochondral plug, resulting in significantly increased interface failure stress after six weeks of in vitro culture. In the follow-up study, they demonstrated that addition of Gel-MA to the PEG-DMA bioink led to enhanced biological activities of printed cells. ³⁸⁸ Then 1.5 w/v% of Gel-MA was added to a PEG-DMA bioink (10 w/v%) containing hMSCs (at 6×10^6 cells/mL), and a cylindrical construct (with 4 mm diameter, 4 mm height) was printed onto the osteochondral plug (Figure 2.32A, left). As confirmed in the previous study, cells were uniformly distributed throughout the printed construct, but casting of the same bioink resulted in sedimentation of cells (Figure 2.32A, right). With Gel-MA present in the bioink, printed cells showed enhanced expression of marker genes

for chondrogenesis or osteogenesis when cultured in chondrogenic or osteogenic media, respectively. In another study, biomimetic patterning of growth factors was achieved using a microvalve bioprinter.⁵⁴⁶ Then 5% Gel-MA-based bioinks containing MSCs and growth factors were used to bioprint a fibrocartilage analogue connecting tendon and bone (Figure 2.32B). To recapitulate the microenvironment of native tissue, two different bioinks containing either BMP-2 or TGF- β 1 were printed as an interlocking structure (Figure 2.32B). For comparison, two types of single-phase hydrogels (containing BMP-2 or TGF- β 1 without patterning) were prepared as well. As a result, the expression of marker genes for both osteogenesis and chondrogenesis was enhanced after 36 days of *in vitro* culture compared to single phase hydrogels (Figure 2.32C). In addition, genes related to tendon or muscle were also upregulated in the fibrocartilage model.

2.3.2.3. Limitations and Outlook

As addressed in the previous section, droplet-based bioprinting has several advantages over other bioprinting techniques, including high compatibility with multimaterial printing as well as ease of HT arrays for screening. In addition, it has higher resolution and greater control over the deposition pattern compared to extrusion-based printing. However, there are critical drawbacks which impede wide application of the technique for biofabrication.

First, the small range of possible viscosities greatly limits the types and concentrations of materials which can be used, which in turn limits the properties of printed constructs. Polymers with high molecular weight or high concentrations cannot be used for droplet-based printing, and thus it is difficult to print mechanically robust constructs.⁵⁵³ Furthermore, clogging can easily occur even with a bioink with low viscosity, if the duration of printing is long. For applications requiring a bioink with high viscosity, one could choose to use the microvalve bioprinter, which is compatible with materials with higher viscosity rather than thermal or piezoelectric inkjet printers. Other types of droplet-based printers could be an option for printing high viscosity bioinks without losing resolution or with higher resolution than inkjet printers. For example, an electrohydrodynamic (EHD) jet bioprinter can print an ink with maximum viscosity of ca. 3000 mPa·s⁵⁵⁴ due to the different mechanism of droplet generation in EHD jetting. An EHD jet bioprinter generates droplets using an electric field between the conductive build substrate and the orifice, which is typically metal-coated. The ink in a syringe forms a meniscus at the orifice by back pressure, and when high voltage is imposed, a droplet of the ink is pulled out of the orifice and ejected. This “pulling from outside” mechanism allows for printing with higher resolution (orifice diameter >100 μ m) with high-viscosity inks compared to the inkjet or microvalve printing, where pressure change in a syringe pushes an ink and ejects a drop. However, the use of EHD jet printers for printing cells has not yet been either intensely studied or optimized. Considering that most cell-laden constructs have been printed using inkjet or microvalve bioprinters to date, use of other types

of droplet-based printer, including EHD jet printers, could solve some of the issues in current droplet-based bioprinting.

In general, droplet-based printing is not suitable for printing with a bioink with high cell concentrations (typically $\sim 1 \times 10^6$ cells/mL), partly due to possible clogging and partly due to an increase in viscosity upon the addition of cells.⁵⁵⁵ In addition, the small diameters of the orifices of droplet printers (10–150 μm) are not compatible with printing large cell aggregates or microcarriers. The low viscosity of bioinks can also cause sedimentation of cells when printing large constructs, leading to an inhomogeneous distribution of cells. Additionally, because the technique is noncontact printing that involves the flight of droplets, the printing condition should be carefully adjusted to prevent droplets containing cells from drying or crosslinking during flight.

Other concerns about droplet-based bioprinting are possible damage to proteins and/or cells by high shear stress and/or heat. The viability of cells bioprinted using a thermal inkjet printer depends on the type of cells. For example, Chinese hamster ovary cells and primary motoneurons had viability higher than $\sim 90\%$,⁵⁵⁶ whereas adult human dermal microvascular endothelial cells (HMVECs), primary cells known to be highly sensitive to manipulation, resulted in 75% of cells apoptotic at 24 h postprinting.¹⁷⁵ In addition, in a later study, overexpression of angiogenic heat shock proteins by printed HMVECs was observed, which could be useful for capillary formation of printed tissue as the authors claimed. However, there also exist the risks of uncontrolled activation of other functional heat shock proteins.⁵⁵⁷⁻⁵⁵⁹ Recently, thermal inkjet printing was also associated with upregulation of oncogenic pathways, increased phosphorylation of kinases, and large-scale alternation in gene expression of breast cancer cells.¹⁷⁶

Piezoelectric inkjet printing can also lead to mechanical stress-induced cell death. In particular, printing at high power and/or high vibration frequencies can cause damage to the cell membranes. Saunders et al. reported that the viability of bioprinted fibroblasts decreased with the printing voltage, where 98% and 94% viability were observed for cells printed at 40 and 80 V, respectively.⁵⁶⁰ Furthermore, compressive mechanical stress caused by high vibration frequencies during piezoelectric inkjet printing can lead to denaturation of proteins. In the study by Nishioka et al., only 40% of HRP remained active after printing at a compression rate of $5.48 \times 10^4 \mu\text{m}^3/\mu\text{s}$, and the amount of damaged enzyme was reduced with decreasing the compression rate.⁵⁶¹ For microvalve bioprinting, high shear stress-induced cell death has been reported.^{531,562} Viability of printed endothelial cells was greatly affected by pneumatic pressure, where $\sim 60\%$ and $\sim 85\%$ live cells were found after printing at ~ 276 kPa (40 psi) and ~ 35 kPa (5 psi), respectively.⁵⁶² In the same study, the diameter of nozzles in a range of 150–400 μm only slightly affected viability. In addition, a long nozzle length (24.4 mm) led to lower viability of printed human embryonic stem cells (ca. 70%) compared to viability (ca. 90%) of the cells printed with a short nozzle length (8.9 mm). Therefore, in droplet-

based bioprinting, the printing conditions and methods should be carefully chosen according to the purpose of bioprinting. More importantly, the impact of droplet-based printing process on various biological activities should be further investigated.

In most droplet-based bioprinting with light-based crosslinking, the light is irradiated on the entire stage throughout the whole printing process, which could lead to overcuring of layers deposited earlier as well as cellular damage of overexposed cells. Therefore, the light penetration and curing depth along with light exposure to the cells in different layers during printing should be comprehensively studied for deposition-based printing, which will be important in particular for printing large cell-laden constructs.

Nevertheless, droplet-based bioprinting has distinct advantages over other bioprinting techniques when generating HT arrays, printing with multimaterials, and precisely positioning bioink drops at picoliter resolution. We envision that one could achieve droplet-based biofabrication of clinically relevant HT screening systems in addition to 3D tissue architectures by exploring new material/chemistry combinations and resolving the method's current limitations.

2.4. Vat Polymerization Bioprinting

Vat polymerization (VP) printing produces 3D objects by selective light irradiation of photoactivatable materials to induce localized curing of liquid materials called resins, which fill a vat. VP printing was first developed and patented by 3D Systems in 1987,¹⁸² where the term “stereolithography (SL)” was first proposed as a method for fabricating solid objects through layer-by-layer printing of photocurable materials. The SL was demonstrated using a laser beam, which thereafter has been heavily used for the printing of acellular structures out of epoxy or acrylic monomer-containing resins. Since the 2000s, the development of materials, including biocompatible, water-soluble PIs, and bioactive–photoactive materials such as Gel-MA, led to application of the technique for the bioprinting of cell-laden structures. In particular, the number of publications with a focus on printing cells with SL has increased sharply since 2010.

In addition, advanced light exposure techniques such as digital light processing (DLP) and two-photon SL have evolved, providing high printing speed and/or resolution. In recent bioprinting research, the new technologies have been favored over traditional laser-based SL (commonly known as SLA), and therefore this section mostly focuses on DLP (projection) VP and 2P-SL, including key working principles and important bioprinting applications as well as current limitations of these techniques.

2.4.1. Projection VP

Projection VP, also known as DLP VP, is a manufacturing technique based on spatially controlled irradiation, where light is transmitted through a digital photomask. In traditional single photon laser-based VP, also called SLA, a focused laser is guided by a scanning mirror to selectively induce crosslinking in a photo-crosslinkable material. The use of a focused laser provides high resolution. However, the point-by-point scanning of each layer is time-consuming and may ultimately lead to a reduction in cell viability and increased cell sedimentation when printing tall structures. For these reasons, projection VP has been preferred over laser-based VP in recent bioprinting studies. Recent advances in hardware, software, and material development allowed the achievement of fast and high quality bioprinting using projection VP. In particular, resolution and printing speed have been dramatically improved in two state-of-the-art projection VP systems: continuous liquid interface printing (CLIP) and volumetric printing (Figure 2.33).

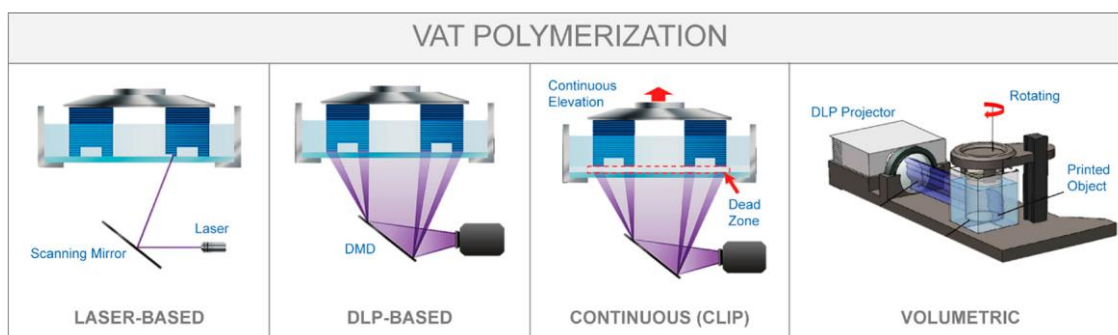


Figure 2.33 | Laser SL and different types of projection VP. Volumetric VP: Adapted with permission from ref ⁵⁶³. Copyright 2019, by the authors, some rights reserved; exclusive license American Association for the Advancement of Science.

2.4.1.1. Principles of Projection VP

In this section, the traditional VP printing method is described first, followed by emerging printing methods, namely CLIP and volumetric printing.

2.4.1.1.1. Hardware. The essential components of projection VP printers are a light source, a DLP device, a projection lens, a vat, and a z -movement motor and controller. LEDs and UV lamps are commonly used as light sources, occasionally in combination with filters, to selectively transmit specific wavelengths. From the source, UV light travels through a DLP device capable of directing the light. DLP devices can be classified as liquid crystal displays (LCDs) or as digital micromirror devices (DMDs). A DMD is an array of micromirrors made of highly reflective aluminum. Each mirror has an “on” and an “off” state characterized by its tilting angle, where the “on” state directs the light to the plane of printing and the “off” state transmits the light to a light-absorber (Figure 2.34A). A typical tilting angle is ± 12 degrees, where conventionally $+12$ degrees determines the “on” state and -12 degrees the “off” state.⁵⁶⁴ Each mirror in a DMD array

corresponds to a pixel. Compared to LCDs, DMDs allow higher UV transmittance efficiency, faster switching of patterns, and smaller pixel size,⁵⁶⁵ which makes it preferred over LCDs in bioprinting.

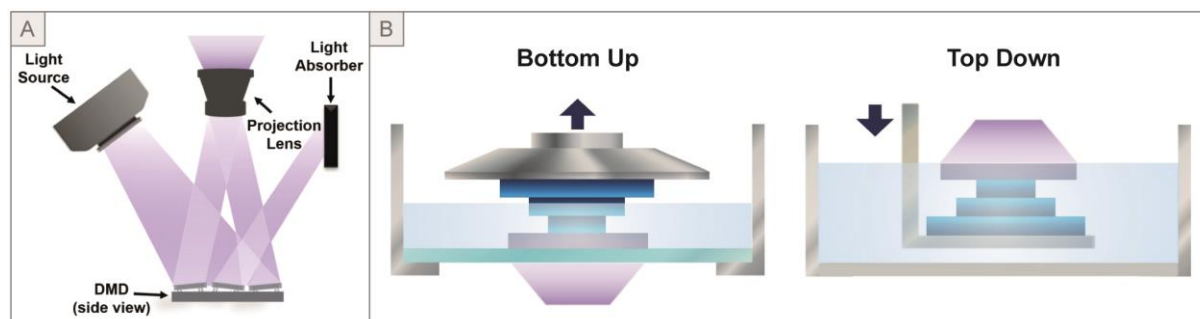


Figure 2.34 | Working principles and components of projection VP. (A) The schematic of a DMD-based DLP device. A light reflected on an “on” state micromirror is transmitted to the projection lens and eventually to the plane of printing, whereas an “off” state micromirror transmits a light to the light absorber. (B) Two different configurations of z -movement in layer-by-layer projection VP. In the bottom-up configuration, the printing stage moves up and photo-crosslinking occurs at the bottom of a vat, whereas in the top-down configuration the stage moves down and photo-crosslinking happens at the air–liquid interface.

When light is reflected on an “on” state micromirror, it passes through a projection lens and is focused on the plane of printing. Light reaching the build plane initiates the polymerization of photoactivated bioresins in the vat. Once a layer is crosslinked, the build platform moves up or down to allow the fresh resin to fill the space between the object being printed and the build plane, followed by repositioning for printing a new layer with a defined layer height (Figure 2.35A). Typically, the layer height is in the range of 25–100 μm in projection VP bioprinting. There are two possible configurations of the stage movement in the z -direction. Depending on this configuration, bioprinting is performed using a bottom-up or a top-down approach (Figure 2.34B). In the bottom-up configuration, light is transmitted from the bottom of the vat and the build platform moves up from the bottom of the vat after printing each layer. In the top-down configuration, crosslinking occurs at the top surface of the vat and the build plane moves down after printing each layer. In a top-down setting, the size of a printed construct is limited by the depth of a vat, and radical-based photo-crosslinking at the surface of a vat can be greatly inhibited by oxygen from the air. For these reasons, most bioprinting applications use a bottom-up configuration.

For bioprinting purposes, many laboratories have developed customized printing equipment by installing a DLP device on a laser-based SL printer such as SLA 250 from 3D systems (Rock Hill, South Carolina, US) or assembling it from an LED light, a DMD chip, aligning optics, and a movable stage. A few commercial DLP printers have been used for printing with bioresins such as Perfactory 3 mini (EnvisionTec, Gladbeck, Germany) and desktop DLP 3D printer M-ONE (Makex, Zhejiang, China). Recently, several DLP bioprinters have also become available, including Lumen X (Cellink, Gothenburg, Sweden) and Cellbricks (Cellbricks, Berlin, Germany).

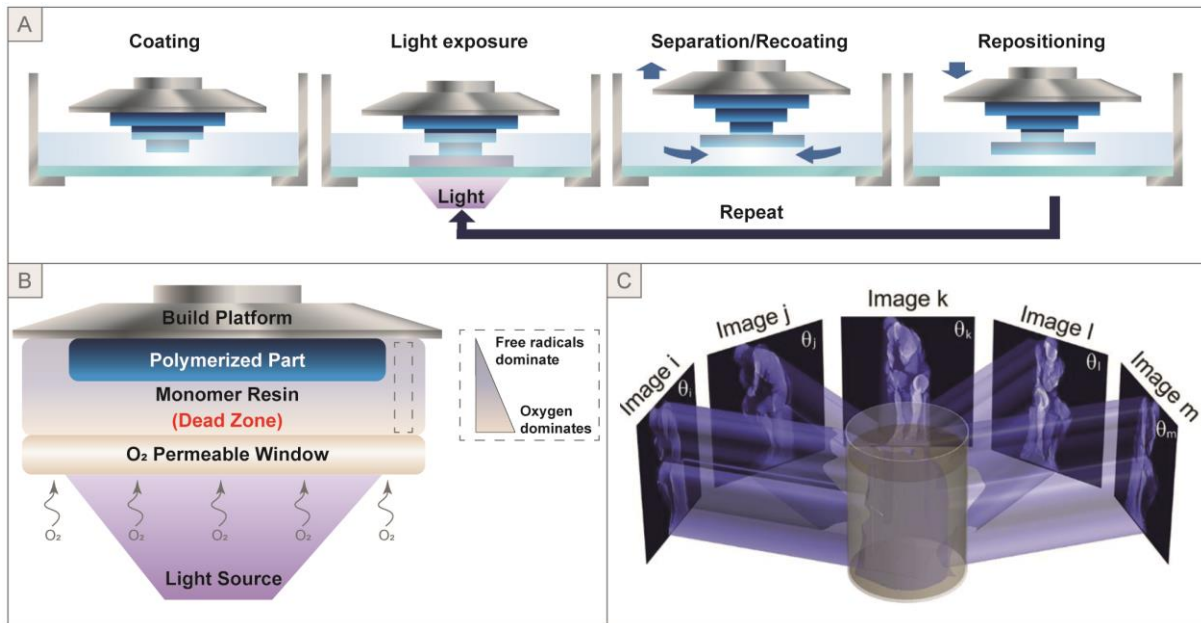


Figure 2.35 | Working principles of projection VP. (A) General process for layer-by-layer projection VP. (B) Schematic of the working principle of O₂ inhibition-based CLIP. Dead zone is created by diffused oxygen from an O₂-permeable window, which inhibits radical-mediated polymerization, allowing the continuous movement of the build platform and generation of 3D objects. (C) Schematic of volumetric printing. A bath filled with a resin is illuminated by a projection at multiple angles. Photo-crosslinking occurs at a region where the cumulative dose of irradiation is above the threshold. (B) Adapted from ref ⁵⁶⁶. (C) Adapted with permission from ref ⁵⁶³. Copyright 2019, by the authors, some rights reserved; exclusive license American Association for the Advancement of Science.

The main limitation of the traditional layer-by-layer method is associated with the slow speed of bioprinting in the vertical (z) direction. Because of this, most cell-laden constructs bioprinted by this method have relatively large x - y dimensions compared to heights. In VP bioprinting, printing speed can be calculated by considering the exposure/crosslinking time per layer and the time for separation, recoating, and repositioning of the stage after each layer. Although exposure times range between 3–40 s, actual printing time is largely influenced by the washing and recoating steps. Lim et al. reported a printing time of 1.5 h to print a 5 mm \times 5 mm \times 5 mm cube (z -step size of 50 μ m and a bioresin comprised of Gel-MA, PVA-MA, and Ru/SPS initiating system ⁴¹²). In this experiment, the irradiation time per layer was only 10 s but the time for printing a layer was 54 s. Similarly, in another study, ³¹³ the reported printing speed was 2 min/layer where a mixed PEG-DA and Gel-MA bioresin was used with the eosin Y/TEA/NVP initiating system.

A new technique called CLIP has recently been introduced to overcome the limitations of VP printing. In CLIP, radical-induced photo-crosslinking is inhibited in a “dead zone” created by oxygen ⁵⁶⁶⁻⁵⁶⁷ diffused from a gas permeable window (Figure 2.35B). In this dead zone, photoexcited photoinitiators or free radicals are quenched by oxygen or peroxides, and therefore solidification of a resin does not occur, which allows for the

simultaneous movement of the build platform, photopolymerization, and recoating. The thickness of the dead zone was adjusted by controlling the type of gas (dead zone thickness: oxygen > air > nitrogen) as well as the photon flux, where the higher photon flux resulted in the thicker dead zone. This method allows for continuous elevation of the printing platform without the necessity for multistep procedures as in the traditional approach (Figure 2.35), resulting in accelerated printing speed. Complex constructs of tens of centimeters in size were printed at 25–100 mm/h with a vertical resolution (i.e., slicing thickness of a digital model) of several tens of micrometers. Furthermore, the continuous printing significantly reduces the staircasing effect and produces an object with much smoother surface compared to laser- or DLP-based VP.

Continuous printing can be achieved by choosing different types of inhibitors instead of oxygen. Beer et al.⁵⁶⁸ demonstrated another continuous VP printing method using two-color lights, one initiating photopolymerization and the other inhibiting the reaction. In this study, bis[2-(*o*-chlorophenyl)-4,5-diphenylimidazole] (*o*-Cl-HABI) was utilized as a PI, which generates lophyl radicals upon UV irradiation to inhibit radical-mediated polymerization, thereby creating a dead zone adjacent to the illumination window. Camphorquinone was chosen as a second type PI to induce photo-crosslinking by irradiation of visible light. However, the CLIP technique has not yet been demonstrated in the presence of cells.

The principle of inhibition allowed for printing genuinely layer-less 3D objects by a printing technique called volumetric or tomographic printing.⁵⁶³ This printing method is based on a computational reconstruction of projection images from cross-sectional scans of a 3D digital model. The computational reconstruction is the reverse process of computed tomography in medical imaging. Using this technique, projection images are generated using an established tomography algorithm at different angles from 0 to 360 deg.⁵⁶⁹⁻⁵⁷⁰ A bath containing a photoactivated resin is illuminated by light through each projection at different angles (Figure 2.35C), and then photo-crosslinking is induced at a region where the cumulative dose of irradiation is above a threshold. In principle, the level of this threshold can be adjusted by doping the resin with oxygen. Technically, light illuminates in a single direction through a dynamic photomask and the chamber filled with a resin is rotating (Figure 2.33). The printing principle allows for printing with a resin with high viscosity (up to 90 000 mPa·s) or precrosslinked solid resin. However, printing with a resin with low viscosity might lead to deteriorated printing resolution due to possible local flow disturbance of the resin in a rotating printing chamber. The simultaneous photo-crosslinking in 3D significantly accelerated the printing process, where a centimeter-scale construct was produced within one minute. Even though it has not been demonstrated yet, the principle could be applied to nonradical based systems by utilizing other types of molecules instead of oxygen, which inhibits photopolymerization of the system to a certain extent. Furthermore, the method has been proven to be compatible with cell-laden bioresins.⁵⁷¹ Centimeter-scale cell-laden constructs were bioprinted using a Gel-MA bioresin with the LAP initiating system. The bioprinted chondroprogenitor cells showed viability higher than 85% and increasing metabolic activity over 1 week. Considering the

demonstrated printability and the cytocompatibility, the volumetric VP printing holds great promise to become a leading bioprinting technique in the near future.

2.4.1.1.2. Resolution. The lateral resolution of projection VP mainly depends on the DMD type and illuminating area. For a given number of micromirrors (i.e., pixels) of a DMD, illumination of a large area results in larger pixel sizes and reduced resolution (Figure 2.36).

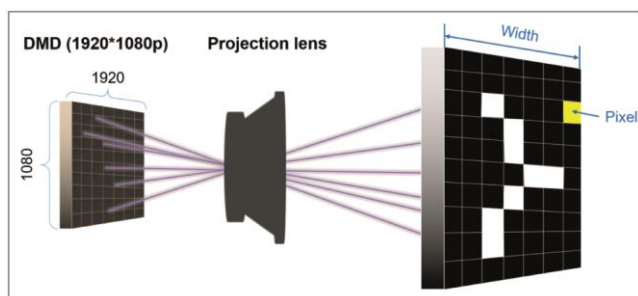


Figure 2.36 | Lateral resolution of projection VP. Each micromirror corresponds to a pixel, therefore for a given size of a DMD (typically 1920×1080), the lateral printing resolution decreases with increasing the projection area.

For example, for a DMD with 1080p ($1920\text{p} \times 1080\text{p}$) when the desired width of an object is 100 mm, the lateral resolution will be $\sim 52 \mu\text{m}$ (100 mm divided by 1920). The vertical resolution depends on the light penetration depth and thus is affected by type and concentration of photoinitiators, irradiation dose, photoactive moieties, and light-absorbing additives.⁵⁷² The thickness of a polymerized layer (e) can be calculated as:

$$e = \frac{1}{c\alpha} \ln\left(\frac{t}{t_0}\right), \quad t_0 = \frac{T}{acF_0} \quad (2.2)$$

where α = Napierian coefficient of molar extinction of PI ($\text{L}\cdot\text{mol}^{-1}\cdot\text{cm}^{-1}$), c = concentration of PI, t_0 = threshold irradiation required to start the polymerization, t = irradiation time, T = irradiation threshold value (photons/ m^3), and F_0 = light flux arriving on the surface (photons/ $\text{m}^3 \text{ s}$).

Equation 2.2 suggests that the vertical resolution of VP printing could be improved by reducing the irradiation time close to the crosslinking threshold, which will result in thinner layer heights. Second, the use of a PI with a high extinction coefficient at a high concentration will generate thin, crosslinked layers. When printing cells, both irradiation conditions and PI type/concentration cannot be widely varied because of cytocompatibility issues. Therefore, the third strategy, the addition of photoabsorbers, will be useful to efficiently control the penetration depth. Photoabsorbers in a bioresin will increase the threshold for photo-crosslinking, and thus the light can be confined at the illuminated surface, leading to a small crosslinked layer thickness. The confined photoactivation will also prevent overcuring of neighboring precured layers. In fact, several biocompatible photoabsorbers have been successfully demonstrated to effectively enhance

bioprinting. Sakai et al.⁵⁷³ developed an alginate-based bioresin for projection VP bioprinting with a visible light projector. High printing fidelity was achieved by adding a visible light absorber, Acid Red, to the bioresin comprised of an alginate derivative and $[\text{Ru}(\text{bpy})_3]^{2+}$ /SPS initiating system (maximum absorption at ~ 450 nm). Without the photoabsorber, the printed construct had a poorly defined structure, whereas the addition of 0.06 w/v % Acid Red to the resin significantly improved the printing quality (Figure 2.37A). An increased concentration of Acid Red (0.08 w/v %) led to decreased printing quality compared to the resin with 0.06 w/v %, which is attributed to inefficient photo-crosslinking due to excess light absorption by Acid Red. Acid Red did not compromise high cell viability ($>90\%$) of the bioresin. For the same initiating system, Ponceau 4R, a biocompatible food dye, was used as another visible light absorber in combination with a bioresin composed of PVA-MA and Gel-MA to improve printing quality.⁴¹² Addition of Ponceau 4R (1 wt %) resulted in decreased curing depths, which eventually prevented overcuring during printing and thus significantly improved the quality of printing (Figure 2.37B). Other types of food dyes have recently been identified as efficient photoabsorbers for an LAP initiating system, which allowed for generation of complex vascular structures in monolithic hydrogels using a projection VP printer.⁵⁷⁴ Among several tested candidates, tartrazine was chosen as a photoabsorber because of its light absorption range matching to the light of the printing system (405 nm) and its hydrophilicity, which makes it easy to wash out the chemical after printing. Production of various entangled vascular networks in transparent hydrogels including PEG-DA and Gel-MA was demonstrated using a resin containing the food dye photoabsorber (Figure 2.37C). The lowest voxel resolution was 50 μm . In addition, primary hMSCs were successfully bioprinted using the bioresin composed of PEG-DA and Gel-MA containing the photoabsorber, and the printed cells maintained high viability and osteogenic differentiation potentials.

The presence of light-scattering components such as micro-/nanoparticles can affect both lateral and vertical resolution.⁵⁷⁵⁻⁵⁷⁷ Scattering within a resin results in decreased lateral resolution because scattered light can induce uncontrolled photopolymerization in the neighboring region. On the other hand, similar to the effect of light-absorbing additives, light-scattering in a resin leads to reduced penetration depth, resulting in enhanced vertical resolution. This trend has been well studied in a report by Sun et al. using the Monte Carlo ray tracing method for ceramic microparticle-containing resins irradiated with a laser at 364 nm.⁵⁷⁷ They showed that the curing depth of a resin increases with the particle sizes (in a range of 0.3–1 μm), whereas the curing radius decreases with the particle sizes, which was attributed to the stronger light scattering by the particles with a diameter (0.3 μm) close to the wavelength of the light (0.364 μm). In the same study, other particle properties, including refractive index and absorption coefficient, were also shown to affect the resolution.

In practice, the curing depth (C_d) can be determined from the following empirical equation:⁵⁷⁸

$$C_d = D_p \ln \frac{E}{E_c} \quad (2.3)$$

where D_p = light penetration depth, E = irradiation dose per area, and E_c = threshold irradiation dose to start the photo-crosslinking. The calculation of the curing depth is an important first step in determining optimal settings for the VP printing system.

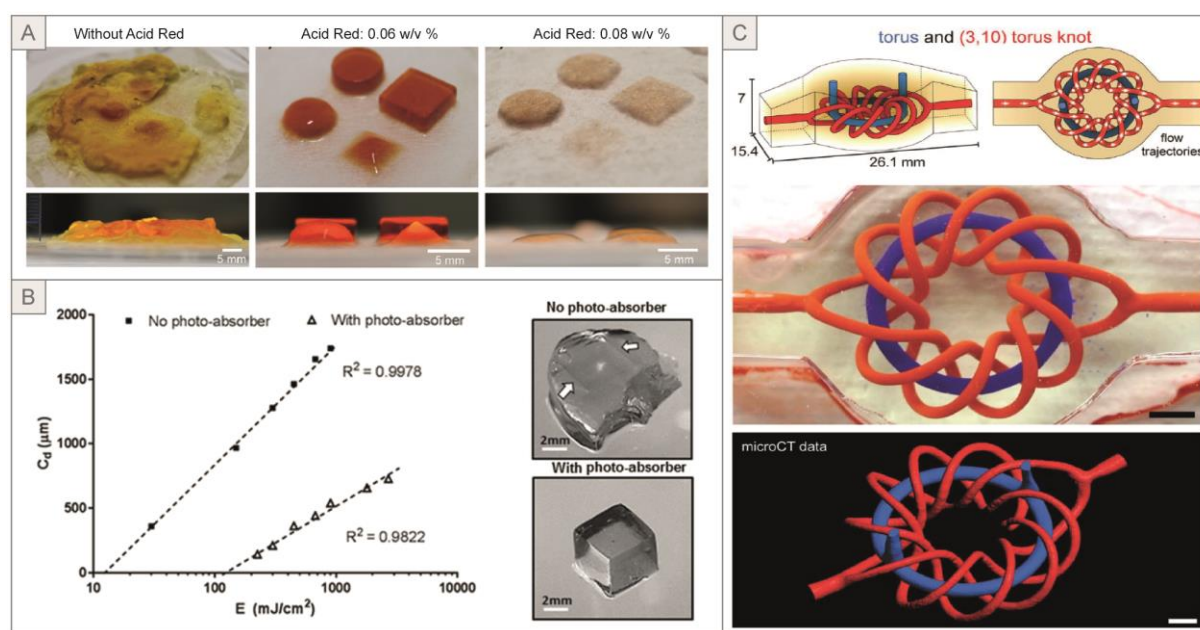


Figure 2.37 | 3D-printed hydrogels using photoactivated resins with/without photoabsorbers. (A) Printed hydrogels using an alginate-based resin containing different amounts of Acid Red (0, 0.06, or 0.08 w/v%). (B) Curing depth (C_d) of a resin composed of PVA-MA and Gel-MA with/without Ponceau 4R according to light intensity, and photographs of printed gels using each resin. (C) 3D design of a complex vascular structure, and a photograph and microCT scan of the printed vascularized hydrogel (20 wt % PEG-DA) based on the 3D design (scale bar: 3 mm). (A) Adapted from ref ⁵⁷³. Copyright 2018 American Chemical Society. (B) Adapted with permission from ref ⁴¹². Copyright 2018 IOP Publishing Ltd. (C) Adapted with permission from ref ⁵⁷⁴. Copyright 2019 by the authors, some rights reserved; exclusive licensee American Association for the Advancement of Science.

2.4.1.1.3. Considerations for Bioprinting Cells in a Vat. As discussed in section 2.2, materials and chemistries play an important role in the printing of cell-laden structures to keep the cells viable and functional. Because VP bioprinting is a nozzle-free process, cells are less likely to be damaged during the printing process compared to deposition-based bioprinting. However, cell sedimentation could be an issue when printing large constructs, which would result in an inhomogeneous distribution of cells throughout a construct. Indeed, Chan et al. observed cell sedimentation during printing using a bioresin composed of PEG-DA (700 Da, 20 w/v%) and fibroblasts (2×10^6 cells/mL) ⁵⁷⁹ (Figure 2.38, left). The sedimentation occurred during printing in a vat with a top-down configuration, where the vat was filled with the bioresin at the start of the printing without further mixing during printing. The issue was resolved by printing using a bottom-up configuration, where fresh bioresin is added after printing each layer (Figure 2.38, right).

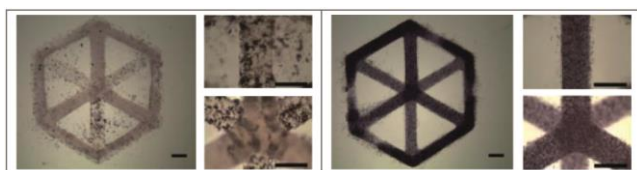


Figure 2.38 | Microscopic photographs of cell-laden hydrogels with (left) and without (right) cell sedimentation (scale bars: 1 mm). Adapted with permission from ref ⁵⁷⁹. Copyright 2010 The Royal Society of Chemistry.

In some studies, buoyancy-modifying components were added to control the viscosity of the bioresin and prevent cell sedimentation. Lin et al. added Percoll, colloidal silica nanoparticles coated with polyvinylpyrrolidone, to a PEG-DA bioresin (4 kDa, 10 w/v %) to obtain a homogeneous distribution of human ADSCs in a printed gel. ⁵⁸⁰ They suggested the optimal Percoll concentration to achieve the most homogeneous cell distribution was 37.5 v/v %. In another study, however, a much lower-concentration (6.5 v/v %) Percoll was used for the same purpose with a PEG-DA bioresin (1 kDa, 15 w/v %) containing HUVECs (2×10^6 cells/mL). In addition to Percoll, small amounts of HA-MA (0.5 w/v %) with high MW (700 kDa) were used to provide a PEG-DA bioresin with buoyant forces. ⁵⁸¹ Lim et al. confirmed that bioprinting using a bioresin composed of PVA-MA/Gel-MA (10 wt %/1 wt %) and hMSCs (5×10^6 cells/mL) produced a construct with homogeneous cell distribution. ⁵⁸² The result was attributed to the high viscosity of the bioresin (ca.13 mPa·s) as well as gentle movement of the printing platform during the normal printing process.

2.4.1.1.4. Bioresins for Projection VP. Several aspects should be considered when formulating a bioresin for projection VP. First, for a successful rerecoating process, the viscosity of a bioresin should not be too high. Hinczewski et al. reported that the highest viscosity to ensure sufficient layer recoating is 5 Pa·s. ⁵⁸³ Simultaneously, the viscosity of the bioresin should prevent cell sedimentation. In a study by Kim et al., ⁵⁸⁴ cells dispersed in 10% Gel-MA solution with a viscosity of 3 mPa·s eventually sedimented after 1 h without any mixing. However, if the same solution was slowly added in the vat after each layer, cells were homogeneously distributed throughout the printed construct. Similarly, Lim et al. reported that the gentle movement of the printing vat prevented cells from sedimenting in the bioresin (viscosity ~ 13 mPa·s). ⁴¹² In volumetric printing, however, a bioresin with high viscosity (up to 90 000 mPa·s) or crosslinked hydrogels should be used, because printing is performed in a rotating chamber. A too-low viscosity of the bioresin would lead to fluctuations and perturbations that would prevent photo-crosslinking at specific positions in 3D.

The choice of photo-crosslinking chemistry also plays an important role in projection VP bioprinting. To date, Gel-MA or PEG derivatives in combination with a PI, I2959, or LAP have been most intensely used for printing cell-laden constructs using projection VP. Recently, several visible light-initiating systems have

been adopted for projection VP-based bioprinting primarily to improve biocompatibility. For example, eosin Y initiating system has been used in combination with Gel-MA.⁵⁸⁵ The composition of the bioresin was 15 w/v % Gel-MA, 0.02 mM eosin Y, 0.2 w/v % TEA, 74 nM NVP and fibroblasts (at 8×10^6 cells/mL). The bioresin was printed into a grid structure using a DLP printer with the wavelength range of 480–600 nm. However, the time for crosslinking one layer during printing was 2 min, which is relatively slow compared to other photoinitiating systems. The same research group also studied a bioresin utilizing the VA086 photoinitiating system with a light wavelength of 405 nm.⁵⁸⁶ A cell-laden structure was printed using a bioresin comprised of 10 w/v% Gel-MA, 1 w/v% VA-086, and fibroblasts with a laser-based VP printer at 3 mm/s. The viability of the bioprinted cells was >90% at day 3, which is higher than usually reported for bioresins involving I2959 as a photoinitiator.

As for materials, PEG derivatives (PEG-DA, PEG-DMA) have been widely used in early studies. However, the recent trend in bioprinting has noticeably moved toward more biologically active materials such as Gel-MA. As described in the previous sections, PEG derivatives have general advantages in terms of tunable mechanical properties, ease of functionalization, and biocompatibility. However, they also have some issues that have been addressed in several studies. In the study by Raman et al.,⁵⁸⁷ a bioresin based on PEG-DMA-1 kDa allowed for DLP printing of feature sizes down to 3 μm , whereas the smallest feature size with a bioresin of PEG-DA-3.4 kDa was 30 μm , which was attributed to a higher degree of swelling of the bioresin with higher molecular weight compared to the one with lower molecular weight. However, the viability of bioprinted fibroblasts in this study was higher for the PEG-DA-3.4 kDa bioresin (ca. 93%) than that of the PEG-DMA-1 kDa (ca. 70%). The study implies that the molecular weight of PEG should be carefully chosen in consideration of the desirable resolution and cell types for each specific application. Another concern regarding the use of PEG-based bioresins is the lack of biological cues, which often leads to low viability of bioprinted cells. To improve this aspect, PEG has been modified with bioactive peptides⁵⁷⁹ or used in combination with biologically active molecules. For example, the addition of Gel-MA to a PEG-DA-based DLP resin led to improved viability of bioprinted cells from 60% for a PEG-DA-only resin to 85% for the resin composed of 50% PEG-DA and 50% Gel-MA.³¹³

Various Gel-MA-based bioresins have been reported for DLP bioprinting.⁵⁸⁸ In some studies, the biological activity of Gel-MA-based bioresins were further enhanced by the addition of functional materials. For example, Yu et al. showed that the addition of dECM enhanced biological activities of bioprinted cells by providing direct bioactive signals present in ECM.⁵⁸⁹ They prepared a bioresin composed of Gel-MA and heart or liver dECM and confirmed that both bioprinted cells better expressed tissue-specific markers compared to the Gel-MA-only bioresin. Another approach to improve the biocompatibility of a bioresin is to control porosity to enhance the diffusion of oxygen, nutrients, and cellular waste. Using the same porous Gel-MA resin described in the extrusion bioprinting section, the macroporous gel with the ratio of 4:1 (Gel-

MA:PEG, v/v) had smaller pore sizes ($24.8\ \mu\text{m}$) than the one with the ratio of 1:1 ($58.7\ \mu\text{m}$).⁴⁷⁸ The Gel-MA bioresin with higher porosity led to enhanced viability, spreading, and proliferation of bioprinted cells at day 7 compared to the one with lower porosity (Figure 2.39A).

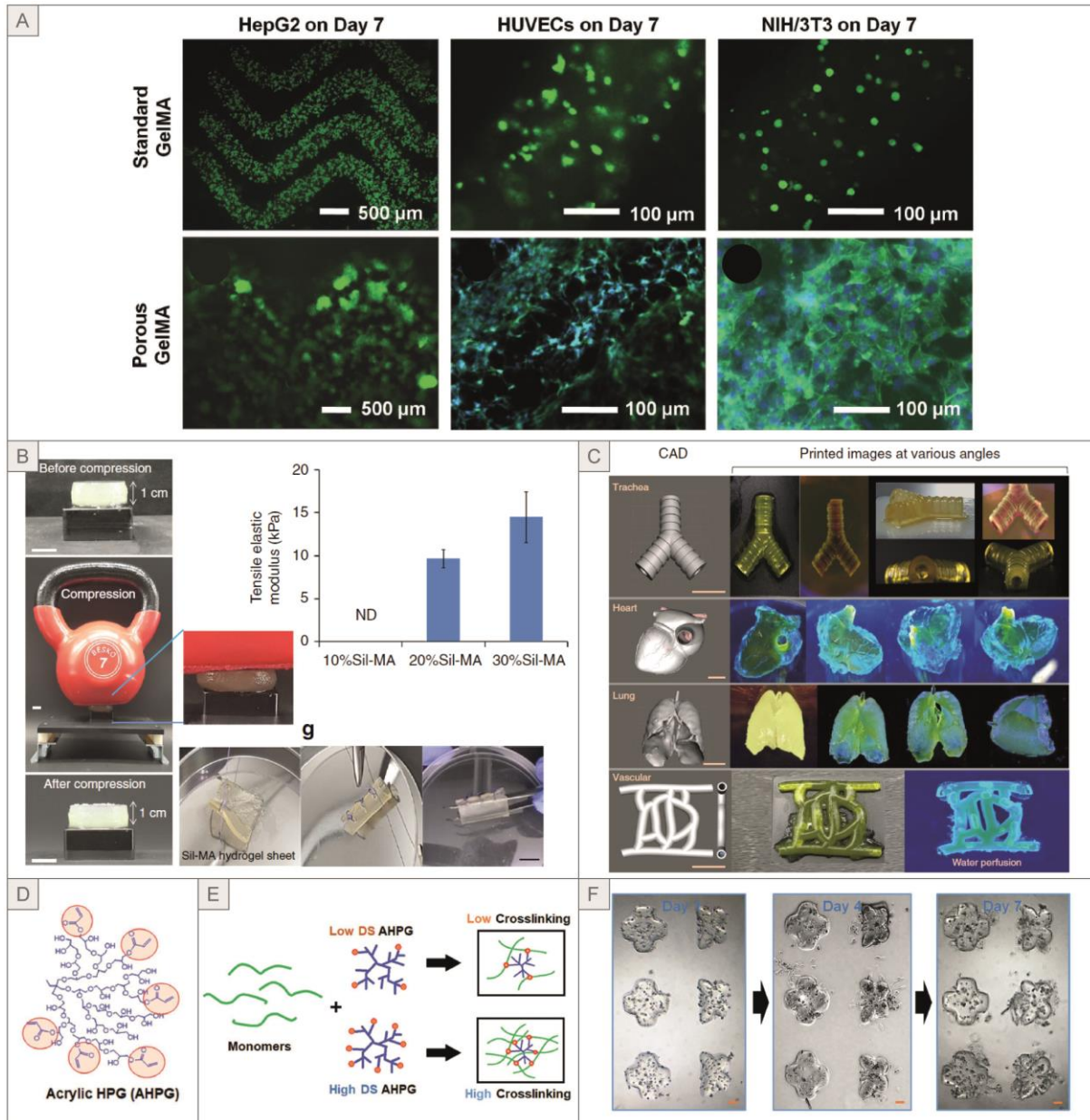


Figure 2.39 | Bioprinted hydrogels using functional resins and DLP bioprinters. (A) Fluorescence images of three different types of bioprinted cells using standard or porous Gel-MA resin after 7 days of in vitro culture. F-Actin and nuclei were stained as green and blue. (B) Photographs of printed Sil-MA gels before and after compression and a printed sheet-shaped gel sutured to form a tubular structure. Tensile modulus of Sil-MA gels with different concentrations (10%, 20%, 30%) (scale bars: 1 cm). (C) Various 3D constructs printed using the Sil-MA resin (scale bars: 1 cm). The vascular structure was perfused with water (blue color). (D) Chemical structure of AHPG. (E) Schematic of formulation of AHPG-based resins with controlled degrees of crosslinking. (F) Structural stability of

bioprinted microgels using an AHPG/Gel-MA bioink at days 1, 4, and 7 (scale bars: 100 μm). (A) Adapted with permission from ref⁴⁷⁸. Copyright 2018 Wiley-VCH. (B,C) Adapted from ref⁵⁸⁴. Copyright 2018 Springer Nature. (D–F) Adapted with permission from ref⁵⁹⁰. Copyright 2019 Wiley-VCH.

Although the majority of recent studies in the literature use PEG or gelatin-based bioresins for VP bioprinting, other functional polymers could provide desirable properties for bioresins. For instance, HA-MA-based bioresins were utilized to bioprint ECs where bioactivity of HA supported the proliferation of ECs and vascularization.^{591–592} More recently, glycidyl methacrylate-conjugated silk fibroin (Sil-MA) was synthesized and used in a DLP bioprinter.⁵⁸⁴ The mechanical properties of the Sil-MA bioresin were tuned by controlling the concentration (10–30%), where 30% polymer concentration exhibited very high mechanical strength (910 kPa at break) due to the intrinsic tensile strength of silk fibroin (Figure 2.39B). In addition, the Sil-MA bioresin showed good printability, which enabled printing of various biological structures (trachea, heart, lung, vasculature) (Figure 2.39C).

A recent study synthesized an acrylated hyperbranched polyglycerol (AHPG) (Figure 2.39D) as a crosslinker for various photosensitive polymers including PEG monoacrylate, polyacrylamide (PAAm), and Gel-MA, providing tunable mechanical properties.⁵⁹⁰ The degree of acrylation of AHPG was tunable over a wide range (10–70%) due to its hyperbranched nature (Figure 2.39E). The mechanical properties of gels were controlled using AHPG with different degrees of acrylation and molecular weight. For instance, 20% PEG monoacrylate gels had an elastic modulus ranging from ~ 5 to ~ 60 kPa. The synthesized AHPGs in general retained low cytotoxicity (viability $>80\%$), and arrays of cell-laden microgels were successfully bioprinted using a DLP bioprinter and bioresin composed of Gel-MA and AHPG (Figure 2.39F).

In principle, printing multimaterials using a VP-based bioprinter is possible by using different bioresins for each layer. For example, Ma et al.⁵⁹¹ biofabricated a liver analogue by depositing different bioresins containing hepatic progenitors (in Gel-MA) or supporting cells (HUVECs and ADSCs in the mixture of Gel-MA and HA-MA) in the same layer using a customized DLP bioprinter (Figure 2.40A). As a result, different types of cells were positioned in a liver lobule-like hexagonal structure, which led to enhanced *in vitro* maturation of the hepatic progenitor cells. However, this method is only applicable for printing thin constructs of a few layers because the process is extremely labor-intensive as it required manual supply of bioresins to each layer and washing steps. For this reason, the printed liver analogue in the study had only one layer. To print multimaterials more efficiently than the manual method, microfluidics-enhanced projection VP systems have been established by several groups.^{208, 593–594} Miri et al. developed an automated multimaterial biofabrication system based on four microfluidic inlets coupled to a printing chamber (Figure 2.40B).²⁰⁸ In this system, for printing a layer, a bioresin is supplied to the fluidic chip, followed by light irradiation and subsequent washing. The device enabled the biofabrication of a cell-laden skeletal muscle

model and a tendon-to-bone insertion model, both composed of multimaterials and multiple cell types (Figure 2.40C). Liu et al. reported another type of microfluidic device combined with a printing chamber.⁵⁹³ They developed a variable height micromixer (VHM), a microfluidic channel-based mixing device that can be combined with a DLP printer to print cell-laden hydrogels (Figure 2.40D). Three different types of VHMs with varying numbers of repeating units (1×1 units, 3×3 units, 9×9 units) were prepared and tested for mixing efficiency, where the VHM with a 9×9 unit had highest complexity of geometry with highly varying local z -heights (Figure 2.40D). As a result, the VHM with more complex geometry (9×9 units) provided more efficient mixing at a low flow rate ($320 \mu\text{L}/\text{min}$) compared to the VHM with simple geometry (1×1 units), which required a much higher flow rate ($2.4 \text{ mL}/\text{min}$) to obtain sufficient mixing. Combined with a DLP printer, cell-laden hydrogels were biofabricated by supplying Gel-MA and the cell suspension into two separate inlets that were subsequently mixed in the VHM and photo-crosslinked in the printing chamber. The VHM device enables possible in situ adjustment of the resin composition within a layer or during printing, allowing biofabrication of more complex architecture.

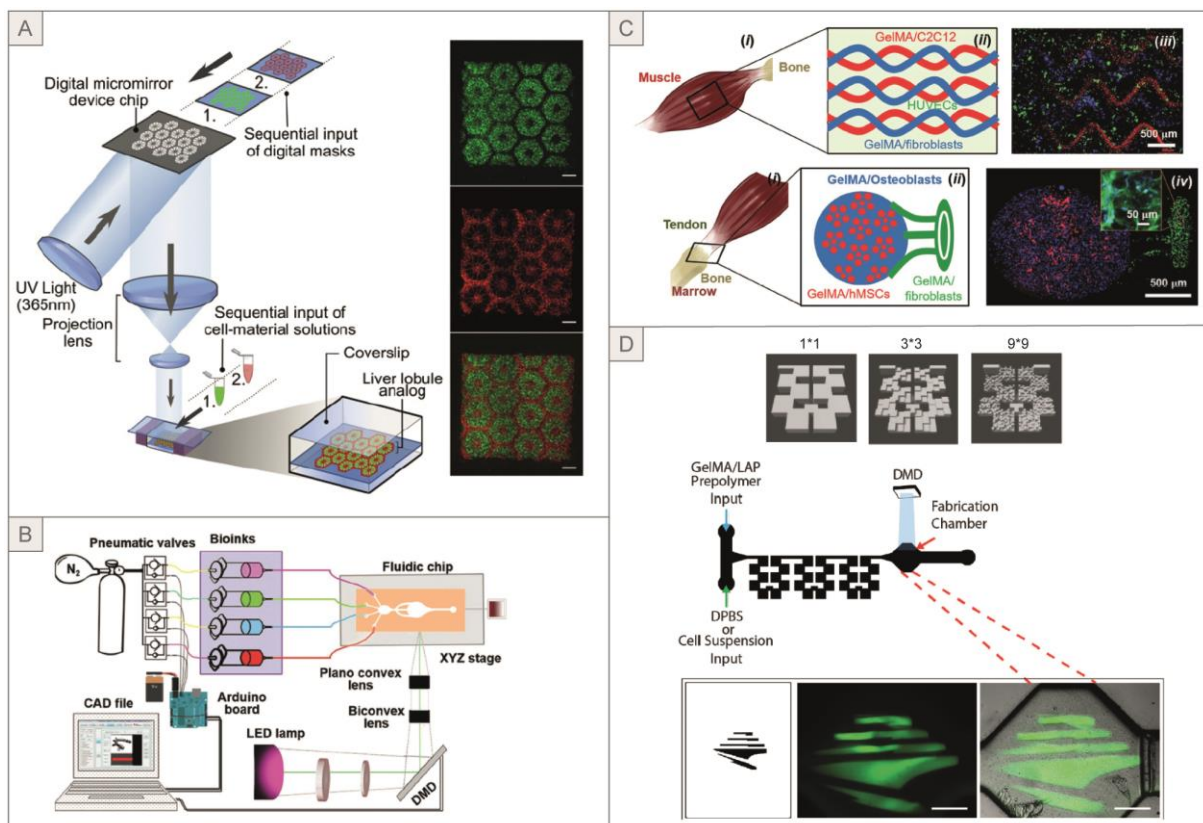


Figure 2.40 | Various approaches for multimaterial printing based on projection VP. (A) Bioprinting using two types of bioresins with sequential recoating of each layer, and fluorescence images of bioprinted constructs (green, hepatic progenitors in Gel-MA; red, supporting cells in Gel-MA/HA-MA) (scale bars: $500 \mu\text{m}$). (B) Schematic of a microfluidic device with four inlets combined with a DLP device. (C) Bioprinted, biomimetic hydrogels containing multiple cell types. Muscle: a bioprinted multicellular pattern comprised

of C2C12 cells (red), fibroblasts (blue), and HUVECs (green) after 48 h of in vitro culture. Tendon: a bioprinted structure composed of osteoblasts (blue), MSCs (red), and fibroblasts (green), and the inset shows the region of fibroblasts at high magnification where cells were stained with green (F-actin) and blue (nuclei) dyes (scale bars: 500 μm). (D) Digital models for variable height micromixers (VHMs) with different numbers of repeating units and schematic of a VHM device combined with a DLP printer. (A) Adapted with permission from ref ⁵⁹¹. Copyright 2016 U.S. National Academy of Sciences. (B,C) Adapted with permission from ref ²⁰⁸. Copyright 2018 Wiley-VCH. (D) Adapted with permission from ref ⁵⁹³. Copyright 2016 The Royal Society of Chemistry.

2.4.1.2. Applications

Recent progress in the biofabrication of cell-laden constructs using projection VP opens up possibilities for the generation of functional tissue analogues closely mimicking microscale biological and physical features of native tissue. Several studies have tried to bioprint specific types of tissue and assess biological aspects of them in depth, where bioprinting was used to (1) biofabricate macroscale cell-laden 3D hydrogels according to 3D models, (2) recapitulate microscale biological, mechanical and/or geometrical features of native tissue to form tissue analogues, or (3) generate ECM-mimicking micropatterns, providing cells with biophysical cues.

To date, several bioresins have been developed for bioprinting 3D-tissue analogues of cartilage or bone based on PEG derivatives, ⁵⁹⁵ Gel-MA, ^{571, 596-597} HA-MA, ⁵⁹⁶ and PVA-MA, ⁴¹² which showed good printability as well as biocompatibility. In particular, volumetric printing showed great promise of printing large-scale structures within a reasonable time. ⁵⁷¹ A trabecular bone model was biofabricated using a bioresin composed of Gel-MA and MSCs based on a μCT -scanned 3D model. A 3D trabecular architecture (8.5 mm \times 9.3 mm) retaining interconnected porous structures was generated in 12.5 s with resolution of $144.69 \pm 13.55 \mu\text{m}$ (the smallest resolved feature size) (Figure 2.41A). The bioprinted MSCs were homogeneously distributed throughout the construct and successfully cultured in osteogenic medium for 7 days (Figure 2.41B, left). The porous structure of the printed model allowed the construct to be seeded with endothelial colony-forming cells and MSCs, generating a multicellular structure. After three days of coculture of three different types of cells in the construct, the formation of early angiogenic sprouts by the endothelial colony-forming cells was observed, and the postseeded MSCs were aligned along with the nascent sprouts (Figure 2.41B, right). The observations imply that the bioprinted MSCs were able to promote the angiogenic process of the neighboring cells by generating paracrine signals. In addition to the bone model, a centimeter scale chondrogenitor-laden meniscus was printed in 28 s using a Gel-MA bioresin (Figure 2.41C). After 7 days of in vitro culture, the bioprinted cells showed increased metabolic activity compared to day 1, glycosaminoglycan (GAG) and collagen deposition as well as mechanical maturation. The compressive modulus of the bioprinted tissue was ca. 25 kPa at day 1 and reached ca. 267 kPa after 28 days of in vitro culture.

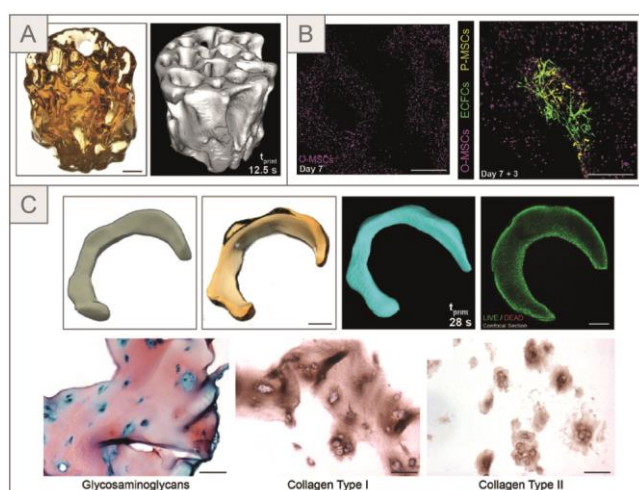


Figure 2.41 | Bone and cartilage analogues bioprinted by volumetric printing. (A) A bioprinted MSC-laden trabecular bone model (left) and a μ CT scan of the model (right) (scale bar: 2 mm). (B) Left: The bioprinted MSCs (pink) cultured in osteogenic medium for seven days (scale bar: 1 mm). Right: The bioprinted bone model containing MSCs (O-MSCs, pink) was seeded with endothelial colony-forming cells (ECFCs, green) and MSCs (P-MSCs, yellow) and cultured in vitro for three days. ECFCs were interconnected with each other and filled the pore space of the bioprinted construct (scale bar = 500 μ m). (C) A bioprinted meniscus analogue (top). In vitro matrix deposition in the analogue cultured for 28 days (bottom) (scale bars = 2 mm). Adapted with permission from ref ⁵⁷¹. Copyright 2019 Wiley-VCH.

Some studies have taken advantage of the high resolution of projection VP printing to mimic microarchitecture and mechanical heterogeneity of tissue. Ma et al. biofabricated a liver disease model where regionally varying mechanical properties and biomimetic hexagonal microarchitectures are found.⁵⁹⁸ Liver dECM and Gel-MA-based bioresins were used to bioprint hydrogels with three different stiffnesses (0.5, 5, and 15 kPa corresponding to softer than normal tissue, healthy tissue, and cirrhotic tissue, respectively) by varying irradiation time. They confirmed that HepG2 cells in the stiff gel showed reduced in vitro growth over 7 days (Figure 2.42A), as well as higher expression of an apoptosis marker gene (CASP8) and lower expression of hepatic function marker genes (ALB, AFP) compared to the soft or medium gel. In addition, expression of marker genes related to metastasis or ECM degradation (MMP2, MMP9, TWIST1) was upregulated in the stiff gel compared to the other two gels, which resembles characteristics of cells in cirrhotic liver tissue. Using a DLP bioprinter and three bioresins, they printed lobule-like structures with varying local stiffness, where higher outgrowth of cells was observed in the stiff region compared to the other two regions (Figure 2.42B,C). The printed liver model showed good promise as a biomimetic platform to study the invasion of hepatic cancer cells from cirrhotic tissue into adjacent healthy tissue. In the follow-up study, they printed heart analogues using a bioresin based on heart dECM and Gel-MA.⁵⁸⁹ The bioresin containing hiPSC-derived cardiomyocytes was printed to form parallel lines with 60 μ m of width and spacing. Compared to the 2D control, bioprinted cells showed a significantly increased expression of myosin regulatory light chain 2 ventricular isoform (MLC-2v), a marker of force generation caused by the movement of actin

filaments, which was attributed to biophysical cues provided by printed lines. In addition, significant upregulation of troponin T, a mature cardiac marker regulating contraction of the heart muscle, was observed for the bioprinted tissue compared to the 2D control and the bioprinted tissue without dECM but with collagen I.

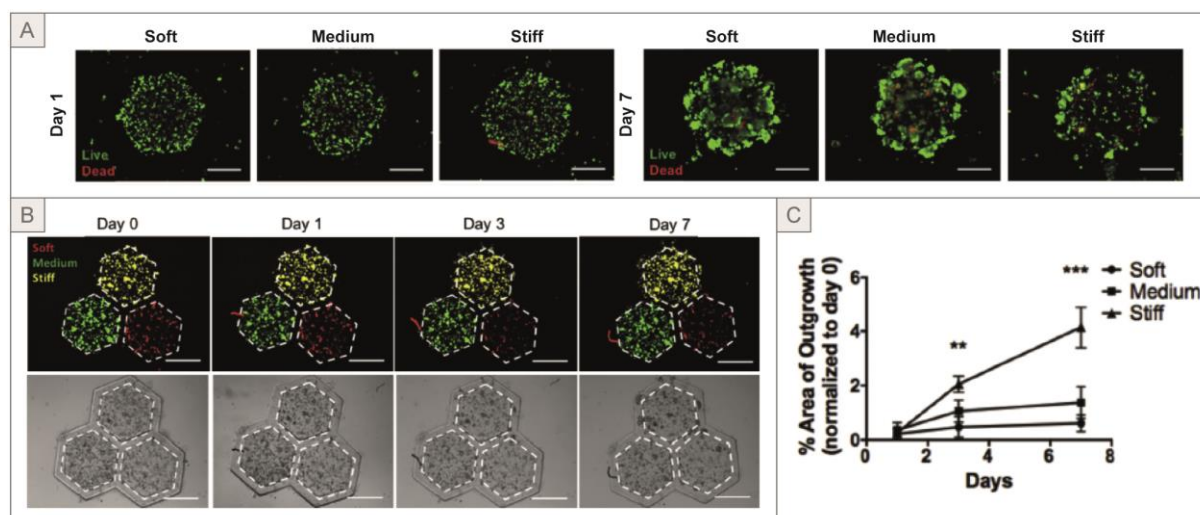


Figure 2.42 | Bioprinted liver analogue with mechanical heterogeneity. (A) Live/dead staining of HepG2 cells cultured in gels with different stiffness (soft, medium, stiff) for 1 (left) or 7 days (right). (B) Fluorescence (top, cell trackers: red, green, and yellow for soft, medium and stiff gel, respectively) and bright-field (bottom) images of the printed liver analogue. (C) Percent area of cell outgrowth originating from three different regions (soft, medium, stiff) over time (scale bars: 500 μm). Adapted with permission from ref ⁵⁹⁸. Copyright 2018 Elsevier Ltd.

Biofabrication of vascularized constructs has also been of interest in the field of projection VP. Zhu et al. biofabricated vascularized tissue constructs using Gel-MA and glycidyl methacrylate-HA (GM-HA).⁵⁹² A sheet-like first layer was printed using a resin composed of Gel-MA (5 w/v %), on top of which a cell-laden vascular pattern (Figure 2.43A, left) was bioprinted with a bioresin comprised of Gel-MA (2.5 w/v %), GM-HA (1 w/v %) and cells (HUVECs and 10T1/2 cells at the ratio of 50:1). The vascular pattern was then enclosed by printing a third layer of Gel-MA (5 w/v %). Considering the much lower elastic modulus of the crosslinked bioresin (Gel-MA + GM-HA) (ca.3 kPa at 0.1 Hz) than that (ca. 5 kPa at 0.1 Hz) of the crosslinked resin (Gel-MA) and presence of hyaluronidase in the in vivo environment, the authors hypothesized that the printed cells would preferably line along the edge of the vascular pattern, inducing the formation of channel-like structures. Indeed, the vascular pattern was eventually endothelialized by the printed cells, leading to the formation of lumen-like structures with a range of diameters (50–250 μm) after 1 week of in vitro culture (Figure 2.43A). They also confirmed endothelial network formation of the bioprinted construct after two weeks of subcutaneous implantation. More recently, generation of a complex multivascular network within a monolithic hydrogel with high resolution (voxel resolution of 50 μm) was

demonstrated using food dyes as photoabsorbers.⁵⁷⁴ Hepatic aggregates encapsulated in a fibrin gel with 3D printed hydrogel anchors were combined with a 3D printed vascular construct (Figure 2.43B). In a rodent chronic liver injury model, the hepatocytes in the implanted vascularized hydrogel expressed albumin, indicating the presence of functional hepatocytes. Furthermore, the microchannels in the hydrogel were perfused with host blood, which was confirmed by H&E staining (Figure 2.43B) and immunostaining of Ter-119, which detects red blood cells and those of erythroid lineage.

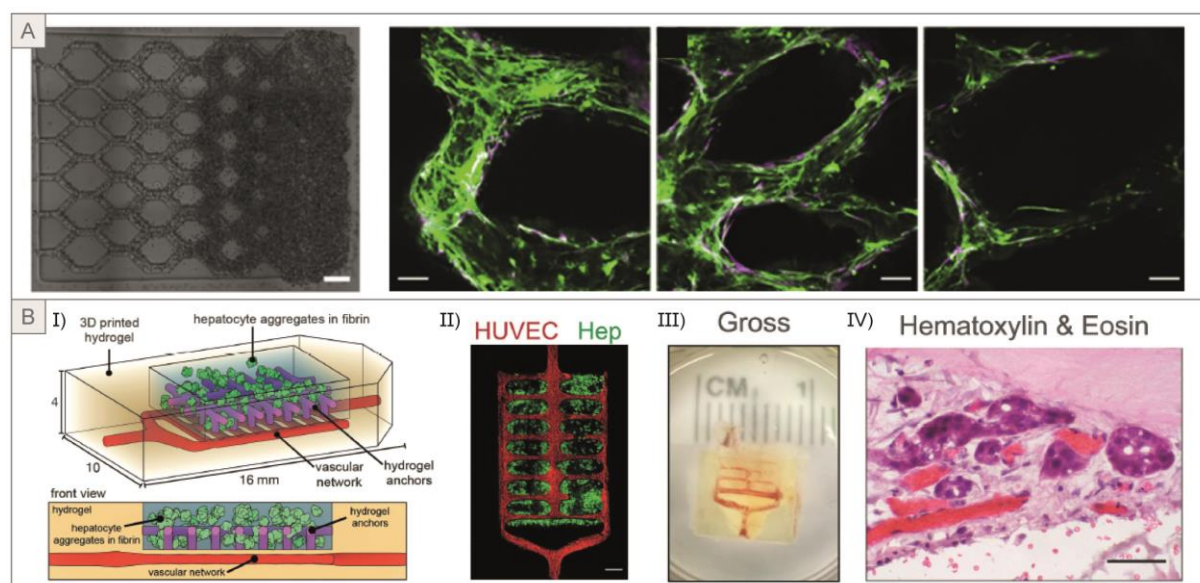


Figure 2.43 | Biofabrication of vascularized tissue based on projection VP. (A) Left: Bioprinted vascular structures with varying vessel diameters ranged from 50 to 250 μm (scale bar: 250 μm). Right: Three fluorescent images of cells (HUVECs and supportive MSCs stained as green and purple, respectively) aligned within the channels with different diameters (scale bars: 100 μm). (B) (I) Schematic and (II) fluorescence staining image of bioprinted hepatic aggregates on prevascularized networks (scale bar: 1 mm). (III) A macrograph and (IV) H&E staining image of bioprinted constructs infiltrated with host blood after 14 days in mice (scale bar: 40 μm). (A) Adapted with permission from ref⁵⁹². Copyright 2017 Elsevier Ltd. (B) Adapted with permission from ref⁵⁷⁴. Copyright 2019 by the authors, some rights reserved; exclusive licensee American Association for the Advancement of Science.

2.4.1.3. Limitations and Outlook

Projection VP provides high resolution as well as a high degree of freedom of printable structures, which enables the biofabrication of tissue analogues recapitulating microarchitecture, multicellularity, and mechanical heterogeneity of native tissue. Still, several issues should be addressed before the method can be broadly applied to bioprint functional cell-laden constructs.

So far, most of the bioprinted cell-laden structures are limited to thin constructs composed of a few layers, which is partly due to the slow layer-by-layer multistep printing procedure which causes possible cell death and/or sedimentation when printing a tall structure. Layerless volumetric printing shows great promise by

bioprinting centimeter-scale structures within a minute. However, for all types of VP printing methods, bioprinting tissues with high cell density, such as epithelial tissue, is challenging due to cell sedimentation, possible light scattering by cells, and the very high number of cells required to fill the vat, not all of which are used in the product. More importantly, for bioprinting, a vat should be filled with a bioresin, and uncrosslinked bioresin volume is discarded. Considering the cost and effort of securing clinical grade cells, this aspect could greatly impede the practical use of the technique in the clinic. Furthermore, the process for printing multimaterials using projection VP is extremely slow due to the necessity of repeated washing steps after printing each layer. Therefore, strategies for printing multimaterials with high speed should be developed to achieve the biofabrication of biomimetic tissue analogues within a reasonable time frame.

Another challenge is to bioprint a tissue analogue with mechanical properties matched to native tissue. The bioresins developed for projection VP are mostly based on Gel-MA and/or PEG-DA, which limits the range of attainable mechanical properties. Therefore, diversification of resin materials and crosslinking chemistry will widen possible applications of projection VP. As mentioned in section 2.4.1.1, a silk-based DLP bioresin was successfully printed into various structures with high mechanical strength.⁵⁸⁴ Recently, a nanocellulose-reinforced PEG-based resin was reported by Li et al.⁵⁹⁹ To increase the dispersibility of nanocellulose in PEG, 1,3-diglycerolate DA (diGlyDA)-modified PEG (PEG-diGlyDA) was mixed with PEG-DA and used as a polymeric matrix. The nanocomposite resin composed of nanocellulose PEG-DA/PEG-diGlyDA exhibited high printing fidelity as well as enhanced mechanical strength, which was attributed to the controlled swelling and mechanical reinforcement given by nanocellulose. Incorporation of nanoparticles can provide not only mechanical enhancement but also anisotropic architecture in a hydrogel. In the study by Yang et al., an electrically assisted DLP printing method was developed to print 3D nanocomposite constructs retaining anisotropic fiber alignment.⁶⁰⁰ They used a resin composed of surface-modified multiwalled carbon nanotubes (S-MWCNTs) embedded in a commercially available polymer resin (Polymer Resin A, 3D Systems). Alignment of the S-MWCNTs was induced by an electric field generated by electrodes installed in the printing vat. At the same time, the direction of alignment was precisely controlled by rotating the printing platform. As a result, they printed a meniscus with biomimetic radial and circumferential alignment of S-MWCNTs, which retained tensile and compressive moduli comparable to a native meniscus.

A construct with large x - y dimension can easily be printed with projection VP methods. However, in terms of resolution, for a given DMD size, a larger x - y dimension will lead to decreased x - y resolution due to the principle of light projection by a mirror (i.e., pixel size). Therefore, printing, for example, an HT array of microtissue of several tens of μm would be challenging given that the largest available DMD size is $2560\text{p} \times 1600\text{p}$.⁶⁰¹

Still, projection VP bioprinting has recently shown remarkable progress and achieved technical innovations toward rapid, layerless biofabrication of cell-laden constructs. The layerless printing also provides high structural integrity without delamination between layers. In addition, microfluidics-assisted approaches showed great promise for printing multimaterials with projection VP. Together with recent advances in biocompatible photochemistry and photoactivated materials, the generation of biomimetic organ or tissue structures with desired resolution within a reasonable time frame is within reach.

2.4.2. Two-Photon SL

During the last 15 years, another light-mediated 3D fabrication technique named two-photon stereolithography (2P-SL) (also named two-photon lithography or direct laser writing DLW) has seen impressive growth in interest from the research community. Among the current additive manufacturing technologies, 2P-SL is the only one able to offer 3D control over complex structures with submicrometer precision. These unique features are based on a nonlinear photophysical phenomenon known as two-photon absorption (2PA). In the following section, the principles of 2PA and its exploitation for biofabrication are presented, with special emphasis on relevant concepts for biological applications.

2.4.2.1. Principles of 2P-SL

2.4.2.1.1. 2P Absorption. 2PA process was first predicted by Maria Göppert-Mayer in her doctoral dissertation in 1931.⁶⁰² It was, however, only experimentally proven 30 years later, once the laser had been invented. It was Werner Kaiser who finally demonstrated 2P-excited fluorescence using an europium-doped crystal.⁶⁰³ 2PA is a third-order nonlinear process whose probability “ p ” scales quadratically with the light intensity “ I ” ($p \propto I^2$), and therefore a high intensity light source such as a laser is needed to trigger it. In the linear one-photon absorption process, a molecule can be excited from the ground state (S_0) to an excited electronic state (S_n) if the photon energy matches the energy gap between the two states. However, this molecular electronic transition can also occur when two photons having half the energy (twice the wavelength) of the corresponding one-photon transition are simultaneously absorbed⁶⁰²⁻⁶⁰⁴ (Figure 2.44). It follows that 2PA takes place with red-shifted wavelengths, more commonly in the near-infrared (NIR) and infrared (IR) region.

In short, when a first photon interacts with the molecule, an intermediate and extremely short-lived virtual state ($\sim 10^{-15}$ – 10^{-16} s) is formed above the ground state. The electronic transition to the real excited state takes place only if a second photon interacts with the molecule within this short time frame (Figure 2.44). Exploiting 2PA allows the use of NIR light sources instead of UV–vis ones, which brings two relevant advantages to biofabrication in the presence of cells, namely less cytotoxicity due to photodamage and higher penetration depth into the sample thanks to lower absorption and scattering. Biological tissues have indeed

a low absorption window around 800–950 nm with water starting to act as a light filter above it.¹⁹⁵ This optical “transparency window” strongly reduces the risk related to photodamage and therefore represents an intrinsic biocompatible feature of 2P-SL when compared to one-photon absorption-driven biofabrication approaches (e.g., SLA and DLP).⁶⁰⁵ Moreover, the biocompatibility of noninvasive *in vivo* 2P imaging^{195, 606-609} indicates that *in vivo* remote physicochemical control of photoactivated material might also represent a future direction of 2P-SL.

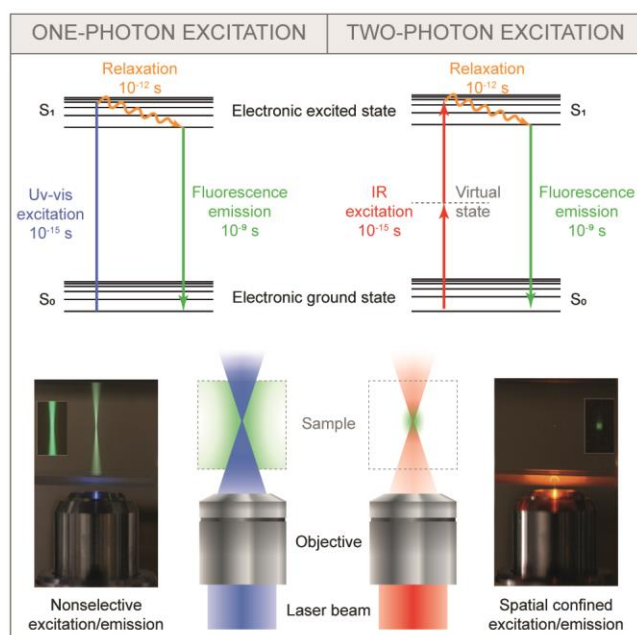


Figure 2.44 One-photon and two-photon excitation. On the left side, one-photon absorption and subsequent fluorescence emission take place in the whole UV–vis excitation light cone that encounters the sample. However, in two-photon infrared (IR) excitation (right side), the nonlinear nature of the absorption process defines a very confined excitation and subsequent fluorescence limited by the focal volume of the laser beam. One-photon vs two-photon fluorescence images adapted with permission by Steven Ruzin and Holly Aaron, UC Berkeley.

2P microscopy setups generally make use of tightly focused NIR femtosecond (fs, 10⁻¹⁵ s) pulsed lasers. The alternation of high peak intensity pulses with duration of ~100 fs with breaks (zero laser intensity) in the nanoseconds range (MHz frequency) gives mild average power, thus reducing the possible damage of sensitive biological specimens. Its nonlinear behavior makes 2PA several orders of magnitude weaker (less probable) than linear one-photon absorption. Therefore, the probability of 2PA rapidly decreases away from the intensity maximum and the excitation remains localized within the 2P focal volume generated by a tightly focused laser beam (Figure 2.44). This intrinsic confocality basically eliminates out-of-focus photodamage to cells and undesired photochemical reactions. Upon 2PA, the excited PIs can decay through an ISC transition to a long-lived triplet state (T₁), from which active species (ions, radicals) are generated. Therefore, photochemical reactions such as radical chain growth polymerization, step-growth polymerization, or

photocleavage can be triggered in the confined ellipsoidal focal volume (Figure 2.47). Thus, 3D structures/patterns can be obtained within the photoactivated material by precisely scanning the focal spot in x , y , and z . It follows that 2P-SL is not limited by the layer-by-layer constraints typical of most of the 3D fabrication techniques, but in principle it enables a purely 3D freeform processing. A system suitable for 2P-microfabrication typically includes photosensitive monomers/polymers (e.g., acrylate, epoxy, or vinyl derivatives) transparent to the excitation wavelength and a molecule, a 2PI, which is efficiently excited by 2PA and produces active species. In other strategies, such as 2P-patterning, which will be discussed later, a photocage that can be cleaved from the substrate upon 2PA is present.

2.4.2.1.2. Instrument Setup and Fabrication Parameters. The instrument setup for 2P-SL generally comprises a laser source, beam control elements, focusing optics, sample motion systems, and control software. Other optional components such as spatial light modulators (SLMs)⁶¹⁰ or microlens arrays⁶¹¹ can also be implemented. All together, these elements contribute to define key processing parameters.

Figure 2.45A describes the main components and parameters of 2P-SL, further explained in the following section. It does not claim to be an exhaustive explanation of the technical and physical concepts underlying 2P-SL, but rather a short overview of the main concepts to give the nonexpert readers a general background and a state-of-the-art perspective of this technique prior to discussion of its biofabrication-related applications. More comprehensive and detailed technical dissertations can be found elsewhere.^{319, 612-614}

Laser Source. As previously discussed, high-intensity light sources such as fs-pulsed lasers are necessary to drive the 2P excitation. In this context, Ti:sapphire fs-pulsed lasers represent the standard for most of the instrument setups. Other light sources such as second harmonic fiber lasers and amplified ultrafast yttrium–aluminum-garnet (YAG) lasers have been used but represent a substantial minority for the topic covered in this review. Titanium sapphire doped lasing medium (Ti_2O_3 into a melt of Al_2O_3) is used to construct highly tunable lasers that can operate in a wavelength range that spans from about 660–1100 nm.⁶¹⁵ Therefore, this solid-state laser emerged as an ideal light source for biomedically oriented applications, for its ability to conveniently operate around the biological “transparency window” (~800 nm), where it exhibits its maximum gain and efficiency (Figure 2.46B). The generation of ultrashort fs pulses (10^{-15} s) relies on the so-called mode-locking.⁶¹⁶⁻⁶¹⁷ In short, when a fixed-phase relationship between the stationary waves (modes) that oscillate in the laser optical cavity is established, constructive interferences can occur periodically, giving rise to laser pulses. In this context, the laser is defined as phase- or mode-locked. The mode-locking can be either passive, where nonlinear phenomena are introduced in the cavity with elements such as natural or artificial saturable absorbers, or active, when externally driven modulators are used.

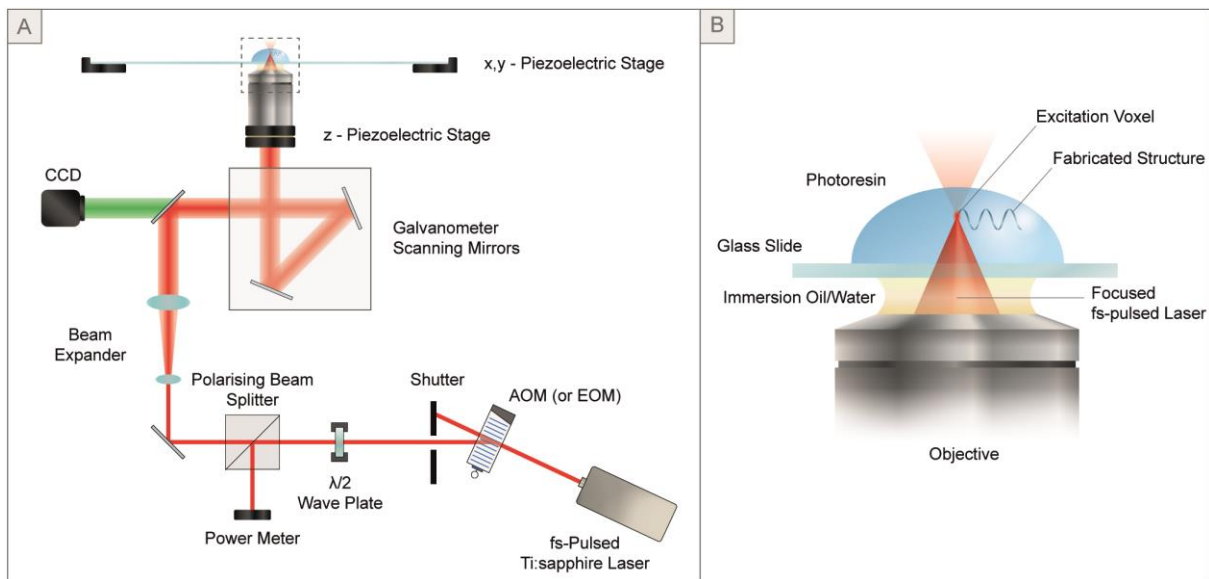


Figure 2.45 | 2P-SL setup. (A) Common setup of 2P-SL apparatus showing the beam path from the fs-pulsed laser source to the sample. (B) Detail of the sample and fabrication process in which a solid spiral structure (blue) is formed in a drop of liquid photoresin (light blue).

Laser Parameters. The pulsed laser is mainly defined by means of repetition rate, pulse width, wavelength, and laser power (peak P and average P_{av}), which are all crucial parameters for an optimal 2P-SL platform.

The repetition rate (frequency f_{rep}) of the train of laser pulses depends on the cavity round trip time (τ) of the laser (time taken for the light to make a round trip of the optical cavity), which is determined by resonator size (L) and light speed (c) (Figure 2.46A). The most common repetition rate of the lasers employed for 2P-SL is ~ 80 MHz, which corresponds to 12.5 ns separation ($\tau = 1/f_{rep}$) between consecutive pulses. The laser pulse duration or pulse width (t_p) is instead determined by the number of phase-locked modes and, for Ti:sapphire lasers operating in a mode-locking regime, it normally spans from 20 to 150 fs. The power output of the peaks (P) increases with the cavity length (L) because more and closer oscillating modes are generated. However, because pulse separation depends on the resonator size (L), an increase of the latter also determines an increase of the repetition rate (f_{rep}).

The pulsed nature of the laser enables a concentration of the excitation in the time domain, with the energy per voxel (E) easily calculable as product of power (P) and pulse duration (t_p) (Figure 2.46A), while tightly focusing high numerical aperture (NA) objectives concentrate the excitation in space. Additionally, the concentration in time of high-intensity peaks (I_{peak}) determines an overall lower average intensity resulting in lower risks of thermal- and photodamage. For fabrication or patterning applications, one pulse per pixel is necessary to trigger a photochemistry reaction. Therefore, scanning speed, dwell time (time that the laser spends on every pixel), f_{rep} , and t_p should always be chosen so that at least one peak per pixel is assured. With

writing speeds varying from a few $\mu\text{m/s}$ to 1 m/s, common values ranges for Ti:sapphire laser-driven 2P-SL are 0.5–200 mW (P_{av}), 50–150 fs (t_p) and ~ 80 –100 MHz (f_{rep}).

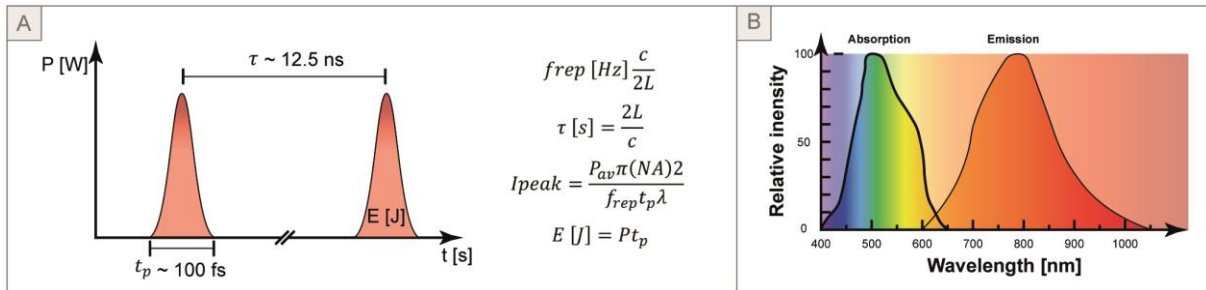


Figure 2.46 | Laser parameters and spectra. (A) Characteristics of the laser pulse train and respective equations. The time scale is not realistic but meant to illustrate the main concepts of temporal focusing of peak intensity. (B) Absorption and emission spectra of Ti:sapphire lasing medium. Ti:sapphire is normally pumped with argon or frequency-doubled Nd:YVO₄ lasers which emit in its absorption range. Then, the emission spectrum shows a peak at around 800 nm, where the laser has its maximum output intensity.

Regarding the wavelength, the broad tuning range of Ti:sapphire lasers generally enables the user to choose the 2PI maximum absorption. However, the user should be aware that this modulation affects the laser beam output power. The maximum power output is indeed different at the center (~ 800 nm) or at the edges of the tuning curve (Figure 2.46B). Because this value can strongly influence the whole fabrication process, an optimal 2P-SL setup requires the implementation of a power meter in the beam path to control the power fluctuations and thus improve the process reproducibility and comparability with the work of other groups.

Laser Beam Path. Shutter System. The rapid blanking of the beam during the scanning process is guaranteed by optical modulators. Because the maximum frequency modulation of optical choppers (rotating mechanical shutters) is limited to the kHz range, fast acousto-optic modulators (AOM), or electro-optic modulators (EOM) with responses in the MHz range are commonly preferred. When the modulators are switched on (acoustic wave generation for AOM and electric field for EOM), the first-order diffracted laser pulses selectively pass through the shutter aperture and continue toward the beam path, while the undiffracted ones (zero-order) are dissipated onto the shutter (Figure 2.45A). When the modulators are switched off, the laser is not diffracted (blanked) and therefore is not directed toward the sample.

Laser Power. A combination of half-waveplate ($\lambda/2$ waveplate) and a polarizing beam splitter is typically included in the beam path to control the laser power. Neutral-density filters or variable attenuators have also been used to reduce the light intensity with no wavelength selectivity. The average energy that is directed to the focal spot and encounters the photosensitive material can be easily estimated (Figure 2.46A). With the most common 2P-SL setups (80 MHz, 1–200 mW), energy from about 10 to 200 pJ can be applied at the focal volume. Other factors, such as energy loss along the beam path and the addition of other optical

components such as SLM affect the final output power and need to be evaluated with the implementation of laser power meters.

Focusing and Scanning. The laser beam is manipulated in shape, size, and direction through a system of lenses and mirrors. It commonly includes a beam expander system, scanning mirrors, and objective lens. To minimize power loss and distortions, NIR-corrected and optimized optics need to be used. Beam expander lenses are used to adjust the laser beam size to fill the back aperture of the objective. This enables the user to maximize the power transmission and reduce the focal volume.⁶⁰⁹ Several types of objective have been used, from 10× water immersion to 100× oil immersion with numerical apertures (NA) ranging from 0.3 to 1.4. The focus spot generated from these objectives is moved within the sample to create 3D structures. As explained in more detail in the next paragraph, higher NA leads to a smaller focus spot and therefore better resolution. Conversely, higher magnification power leads to a reduction of the objective field of view (FOV). Galvanometer mirrors are commonly implemented to increase the laser scanning speed within the objective FOV. However, to fabricate structures with dimensions that exceed the FOV a motion system is necessary.

Stage/Objective Movement. Commonly, the objective (or the stage) moves in the z direction thanks to piezoelectric actuators, while the movement in the x,y plane of the sample stage is produced either by piezoelectric actuators or linear motors. Depending on the requirements, linear motors that guarantee high speed and long travel range but low precision, or piezoelectric actuators that reach nanometer precision but are limited to short travel range (hundreds of μm) and low speed (hundreds of μm per second) are chosen. To fully profit from 2P-SL resolution, piezoelectric-controlled movements are necessary. This aspect also hinders potential in vivo applications. With an objective moving in the three dimensions by piezoelectric actuators, even small movements/vibrations of the patients will result in a substantial error in the biofabrication or patterning process. In in vitro systems, however, coordinated combinations of the aforementioned technologies allow, thanks also to an efficient photocurable system, writing speed up to 1 m/s to be achieved.^{329, 618-619}

Resolution. Characteristics of the laser, optics, photoresin, PI, and motion system together determine the minimum feature size, the overall dimension of the biofabricated structure, and the processing writing speed. To describe the accuracy of the biofabrication process, attention should be paid to the terms used to describe the resolution:⁶²⁰

Line width resolution: defines the minimum size feature that can be generated.

Writing resolution: defines the minimum distance at which two adjacent features can be biofabricated without overlap.

Both types of resolution can be specified in the axial (z) and lateral (x - y) directions. The line width mainly depends on light diffraction, thus on objective NA and laser wavelength. In the x - y plane the diffraction limit, d , (distance at which two distinct elements can be resolved) is generally defined by the Abbe's equation:

$$d = 0.61 \frac{\lambda}{NA} \text{ (Rayleigh criterion coefficient)} \quad (2.4)$$

Therefore, higher NA objectives decrease the feature size and are preferred. Considering a NA value of 1.4 and a λ of 800 nm, the value of d_{xy} would be approximately 350 nm. In the z axis, the d_z value is roughly three times bigger, giving an ellipsoidal excitation volume (voxel). However, the dependence of 2PA on the square of light intensity determines a narrower dose response profile by a factor of $\sqrt{2}$ (Figure 2.47).⁶²⁰ For Gaussian like pulses, the voxel dimension intended as full width at half-maximum (fwhm) can be calculated as follows:⁶⁰⁶

$$FWHM_{xy} = \frac{32\lambda}{\sqrt{2}NA} 2\sqrt{\ln 2} \quad (2.5)$$

$$FWHM_z = \frac{0.53\lambda}{\sqrt{2}} \left[\frac{1}{n - \sqrt{n^2 - NA^2}} \right] 2\sqrt{\ln 2} \quad (2.6)$$

For example, as shown by Dobos et al. at 720 nm, a $10\times/0.3NA$ objective results in a $31.1 \mu\text{m}^3$ voxel while a $2.5\times/0.085NA$ objective results in a 2.67mm^3 voxel.⁶¹⁹ Also, an increase in laser intensity (Figure 2.47) and exposure time results in a larger voxel size.⁶²¹

The subdiffraction limit line width is also a result of a threshold response of the photoactivated material. Taking the radical polymerization process as an example, its threshold is overcome only when the active species (radicals) generated by PI excitation are enough to drive the polymerization of the liquid resin. The radicals can be quenched by oxygen or other additional quenchers.⁶²² Therefore, the actual volume where the threshold is exceeded (polymerization voxel) can be made smaller or larger by varying the inhibiting species type and concentration. It follows that a common rule to minimize the feature size is to set the laser intensity slightly above the threshold (Figure 2.47). To date, it has been possible to obtain feature sizes down to few tens of nanometers.⁶²³ Beside "conventional" 2P-SL setups, the implementation of a doughnut-shaped inhibition beam inspired by stimulated emission depletion (STED)⁶²⁴ has already shown the possibility of going down to 9 nm line width resolution, thus achieving a scale that was previously only obtained with electron beam lithography.⁶²⁵

The writing resolution in the axial or lateral direction is instead generally much larger than the line width (Figure 2.47). The active species generated in the peripheral volume in which the intensity is below the threshold do not contribute to the fabrication process. However, these peripheral active species can accumulate with the ones generated during the polymerization of an adjacent feature and thus, by activating

the chemical reaction in undesired regions, lower the resolution. It follows that active species half-life, diffusivity, and writing speed influence the system resolution.⁶²⁶

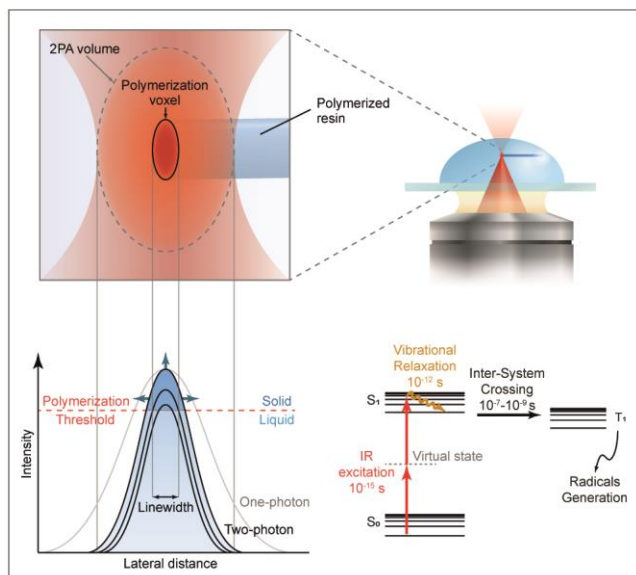


Figure 2.47 | Relationship between laser intensity, polymerization voxel dimension, and line width. (top left) Detail of the focal volume in which 2PA takes place and inner polymerization voxel where the polymerization threshold is exceeded and the photochemical reaction occurs. (bottom left) Narrowing dose–response profile for the 2PA process compared to one-photon absorption (light gray). The arrows and the three black curves indicate the increase in polymerization voxel dimension (and therefore also line width) with an increase of laser intensity. Thus, the minimum intensity that exceeds the threshold leads to the minimum line width resolution. (bottom-right) Jablonski diagram showing the intersystem-crossing transition to the triplet state T_1 and subsequent radical generation that takes place in the 2PA volume and triggers the polymerization in the inner polymerization voxel where the radical concentration exceeds the threshold.

It is noteworthy that, for a number of years, several companies have provided commercially available, desktop-sized and user-friendly 2P-SL systems: Photonic Professional GT2 (Nanoscribe), μ FAB-3D (Microlight3D), NanoOne (UpNano), and Holograph X (Cellink). The possibility of having access to ready-to-use instruments without the need for customized microscopes led to a notable increase in publications, in particular on microfabrication with commercially available resins.⁶²⁷⁻⁶³²

2P-SL can be used by means of bond formation and bond cleavage. For clarity, the use of these two strategies for both 2P-microfabrication and 2P-patterning is presented in separate respective sections. From this point forward, the term 2P-microfabrication will be used to refer both to polymerization/crosslinking of liquid resins (negative photoresists) and to degradation of solid structure (positive photoresists), which gives spatiotemporal control over hydrogel stiffness and degradation kinetics.⁶³³ Both of these approaches of spatiotemporal control of phase transition can indeed be used to microfabricate 3D structures. On the other hand, for 2P-patterning, we refer to the spatially and temporally controlled immobilization of bioactive signals

within hydrogels. This can take place in different ways, generalizable into direct photo-crosslinking (bond formation) or indirect uncaging mediated (bond cleavage) selective immobilization (Figure 2.48).

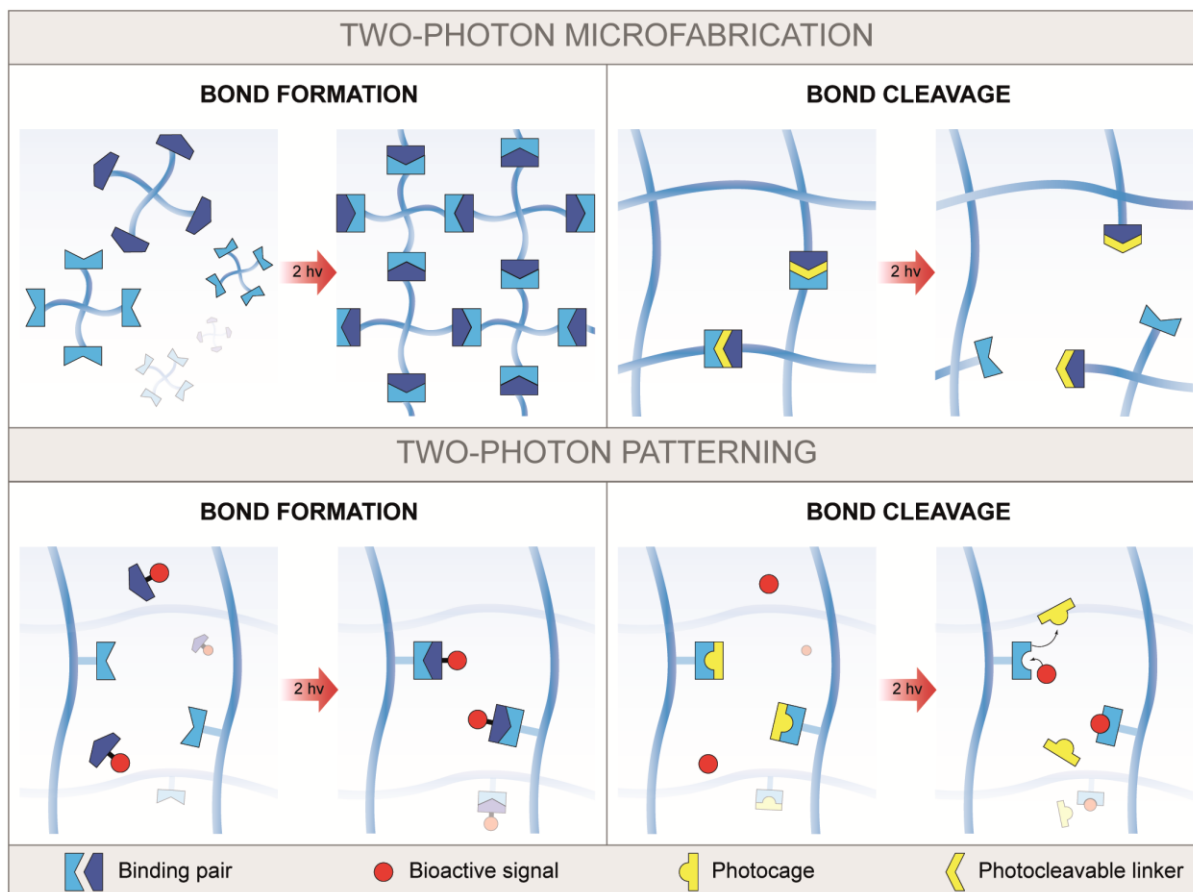


Figure 2.48 | 2P-microfabrication and 2P-patterning. General illustration of the fabrication and patterning approaches that have been exploited and are covered in this review. 2P-microfabrication can be either obtained by bond formation through radical mediated polymerization/crosslinking (top left) or by bond degradation when a photocleavable linker is used (top right). 2P-patterning can be either obtained by direct immobilization of a bioactive signal through radical mediated conjugation (bottom left) or indirect immobilization following the removal of a photocage from a functional group that can then bind the bioactive signal (bottom right).

2.4.2.2. 2P-Microfabrication Applications

The main achievements of 2P biofabrication by means of bond formation and bond cleavage are herein presented with particular interest paid to biocompatible and cell-laden photosensitive systems.

2.4.2.2.1. Bond Formation in Microfabrication. The first example of 3D 2P-microfabrication dates back to 1997, when Maruo et al. used a commercially available acrylate-based resin (SCR500) to polymerize a spiral structure with micrometer size line width (Figure 2.49A).⁶³⁴ A subdiffraction line width was achieved just a few years later, with the manufacturing of a ~ 10 μm bull model showing outstandingly small, detailed features down to 120 nm⁶³⁵ (Figure 2.49B), which inspired the advent of a new and exciting research field based on

this technique. The fabrication of cellular/subcellular-sized structures represents an ability that is still unmatched by any other biofabrication technique and whose potential has probably not yet been fully exploited.

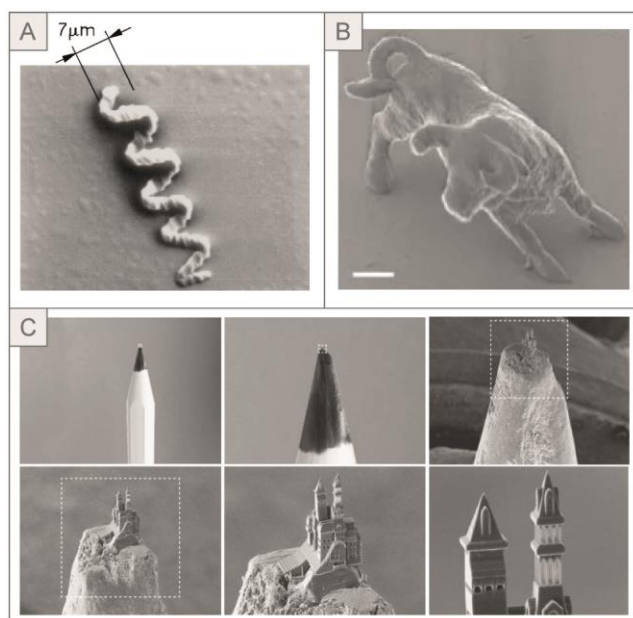


Figure 2.49 | 2P-microfabrication of micro-/nanoscale features. (A) First example of 3D 2P-microfabrication with urethane acrylate photoresin SCR500. (B) Submicrometer printing of a bull model (scale bar: 2 μm) with urethane acrylate photoresin SCR500. (C) Castle model fabricated on the tip of a pencil. (A) Adapted with permission from ref ⁶³⁴. Copyright 1997 The Optical Society. (B) Adapted with permission from ref ⁶³⁵. Copyright 2001 Springer Nature. (C) Adapted with permission from ref ³¹⁹. Copyright 2016 John Wiley and Sons.

Acrylate Based Materials. *Synthetic Polymers.* Acrylic (e.g., SR9008, SR368, IP-L 780) and hybrid organic–inorganic resins (e.g., ORMOCER) have been extensively used in 2P-microfabrication. ⁶²² The high reactivity of acrylate groups and the use of highly efficient PIs enable fast fabrication of 3D CAD models with impressive accuracy ^{636–637} (Figure 2.49C), extending line width down to 65 nm. ⁶²³ In most of these cases, the reaction is performed in organic solvents and extensive washing steps to eliminate uncrosslinked resin are necessary. Clearly, these harsh conditions hinder the possibility of a direct encapsulation of cells and limit the use of these systems to a postfabrication cell seeding approach. However, the faithful replication of almost any CAD shape and the high printing reproducibility obtainable with synthetic resins are a significant advantage for systematic *in vitro* cell studies. ^{638–639} Moreover, the thermal, chemical, and mechanical stability of the final structures make synthetic resins suitable for various biomedical applications. ⁶⁴⁰

Ovsianikov et al. first introduced the use of 2P-microfabrication for 3D tissue scaffolds. ⁶⁴¹ Since then, several materials, architectures, and cell types have been exploited for the generation of 3D scaffolds with negligible cytotoxicity. ^{627, 642–644} Nevertheless, the absent or reduced cytotoxicity was achieved by extensive washing of

generally toxic unreacted monomers/oligomers and PIs. Because these washing steps are undertaken with noncytocompatible solvents such as ethanol, 2-propanol, acetone, or even more nonpolar mixtures, one then needs to be sure that all the toxic components are washed away before seeding cells. Biomimetic structures such as bone trabeculae⁶²⁷ (Figure 2.50A), cardiac tissue model⁶⁴² (Figure 2.50B), and retina model⁶⁴⁴ have been manufactured by means of 2P-microfabrication with organic–inorganic hybrid resins (ORMOCERs). The precise reproduction of trabeculae-like structures from human bone μ -CT scans with a cell adhesive ORMOCER resin named OrmoComp seemed to positively affect the osteogenic differentiation of SaOS-2 bone-like cells compared to flat control surfaces. This biomimicry at the nanoscale has also been recently exploited by Marino et al. to reproduce an *in vitro* real-scale human model of the blood–brain barrier with the epoxy-based photoresin SU-8 (Figure 2.50C).⁶⁴³ Postfabrication coculture of endothelial-like and glioblastoma cells rendered this system suitable for biological studies or HT drug screening on disease models.

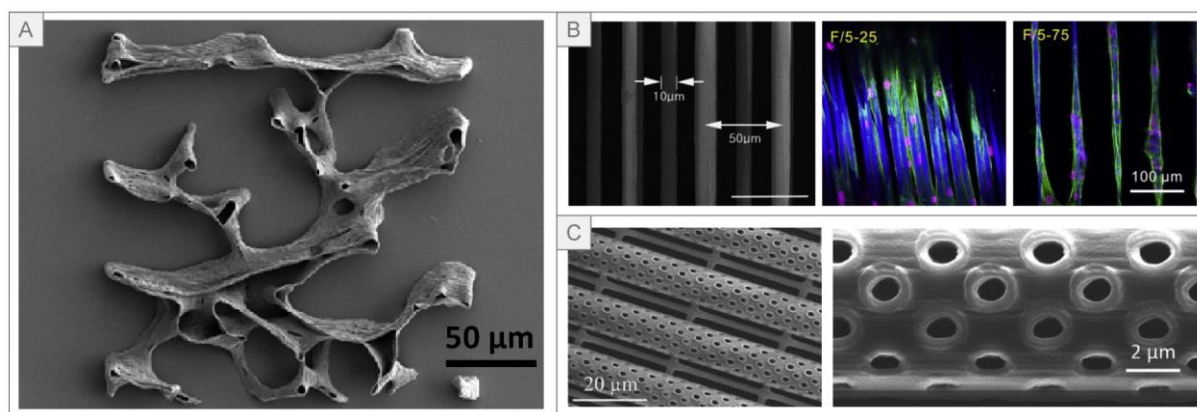


Figure 2.50 | 2P-microfabrication of biomimetic structures with synthetic polymers. (A) Bone trabeculae fabricated with organic–inorganic hybrid photoresin OrmoComp (scale bar: 50 μ m). (B) Cardiomyocyte alignment on ORMOCER fabricated fibers with different diameters and spacing (scale bar: 50 and 100 μ m). (C) SU-8 biomimetic blood–brain barrier with dimension comparable to those that can be found *in vivo* and 1 μ m pores to mimic mass transport (scale bar: 20 and 2 μ m). (A) Adapted with permission from ref⁶²⁷. Copyright 2014 Elsevier Ltd. (B) Adapted with permission from ref⁶⁴². Copyright 2013 Elsevier Ltd. (C) Adapted with permission from ref⁶⁴³. Copyright 2017 John Wiley and Sons.

During the last 10 years, many acrylate derivatives of synthetic polymers such as biodegradable methacrylated polylactide (PLA),^{645–646} acrylamide,^{315, 647} organometallic polymers,⁶⁴⁸ poly(2-ethyl-2-oxazoline) diacrylates,⁶⁴⁹ and stimulus-responsive poly(ionic liquid)s⁶⁵⁰ have been investigated as potential materials for tissue-engineered scaffolds made by 2P-SL. To get specific features that resemble natural systems, one could also rely on the preparation of nanocomposites. Carbon nanotubes,⁴⁶³ zinc oxide nanowires,⁶⁵¹ and nanoparticles^{315, 647, 652–654} are just a few examples of composite materials that have been used for 2P-microfabrication.

Nevertheless, acrylate-based and hybrid resins have also been widely exploited to generate scaffolds for single-cell force measurements and cell migration studies. With the spread of user-friendly 2P-SL systems and photopolymerizable resins, this field has become increasingly important. Excellent reviews on this topic have recently been published.⁶⁵⁵⁻⁶⁵⁶ Furthermore, it is noteworthy that 2P-microfabrication with synthetic acrylates and hybrid resins has been used to develop a new generation of biomedical devices such as stents,⁶³⁰ needles,⁶⁵⁷⁻⁶⁵⁸ and valves⁶⁵⁹ with outstanding precision. To give an example, recently Lölsberg et al. developed a microfluidic 2P vertical flow lithography to fabricate free-standing thin ($<1\ \mu\text{m}$) microtubes with tunable diameter (1–400 μm), wall porosity (pore size 1–20 μm), and length (hundreds of micrometers) with potential uses including stents or nerve guides.⁶³⁰ Another relevant potential biomedical application of 2P-SL that is not discussed here is the manufacturing of nano/microrobots. In recent years, micromotors,⁶⁶⁰ mobile magnetic,^{628, 653, 661-663} and biodegradable microrobotic swimmers⁶⁶⁴⁻⁶⁶⁶ have been fabricated, opening up new perspectives for diagnostics and targeted drug and cell delivery.

Among the various synthetic polymers used for 2P-microfabrication of cell scaffolds, PEG-DA certainly has been one of the most promising and most investigated.^{390-391, 667-668} Ovsianikov and colleagues combined the accuracy of 2P-microfabrication of PEG-DA with cell seeding by laser-induced forward transfer (LIFT) in what is, to our knowledge, the first hybrid biofabrication technique that includes 2P-SL.⁶⁶⁹ A highly porous periodic scaffold was obtained by 2P-SL, and thanks to precise LIFT cell deposition, a multicellular construct was obtained (Figure 2.51A). Precise deposition of vascular smooth muscle-like cells (vSMCs) in the outer part of the PEG-DA scaffold and ECs in the inner part resembled the arrangement of natural blood vessels. LIFT was used to achieve higher cell density and a better homogeneous distribution over the whole structure height (300 μm). However, this concept is limited to thin and highly porous constructs and therefore cannot replace biofabrication in the presence of cells, which has the advantage of reaching high density and homogeneous cell distribution within the hydrogel.

As the focus of this review is on biocompatible systems for cell-laden approaches, the use of this technique to fabricate acellular tissue scaffolds,^{629, 645-646, 667, 670-675} cell and drug delivery carriers,^{653, 676-677} and other 2P-microfabrication applications are not addressed in depth. Therefore, the interested reader is invited to read the previously cited reviews and papers.

Successful cell encapsulation within a photoactivated material (bioresin) depends on many factors. Undoubtedly, the first requirement is to be able to perform the biofabrication process in an aqueous environment. The first example of 2P-microfabrication in an aqueous medium in which a 2P specific PI was used comes from Jhaveri et al.⁶⁷⁸ In this case, the hydrophobic PI AF240, which has a large 2P cross section ($\sigma^{2PA} \sim 100\ \text{GM}$ at 800 nm), was dissolved in aqueous media by using the nonionic surfactant Pluronic F127 (PF127). 2P-SL was then performed in a water-soluble monomer solution composed of 2-hydroxyethyl

methacrylate (HEMA) and PEG-DA. A few years later, Torgersen et al. successfully performed 2P-microfabrication in the presence of a whole living organism (*C. elegans*) (Figure 2.51B).³²⁸

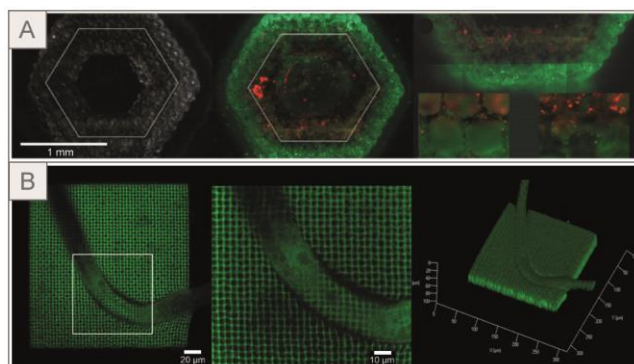


Figure 2.51 | 2P-microfabrication of 3D scaffolds with PEG-DA. (A) 2P-microfabricated PEG-DA scaffold seeded by means of LIFT with two cell types: ovine vascular smooth muscle (vSMCs, green) and endothelial cells (EC, red) (scale bar: 1 mm). (B) *C. elegans* trapped in 2P-microfabricated woodpile hydrogel structures made of PEG-DA (scale bar: 20 and 10 μm). (A): Adapted with permission from ref⁶⁶⁹. Copyright 2010 IOP Publishing Ltd. (B) Adapted with permission from ref³²⁸. Copyright 2012 SPIE. Distributed under a Creative Commons Attribution NonCommercial License 4.0 (CC BY-NC) <http://creativecommons.org/licenses/by-nc/4.0/>.

The PEG-DA solution in combination with the highly efficient water-soluble 2PI, WSPI ($\sigma^{2PA} = 120 \text{ GM}$ at 780 nm) enabled fast processing speed (10 mm/s), comparable to organic-based systems. This study again showed the importance of high water content systems to reach good biocompatibility. The above-mentioned work, together with the 2P-microfabrication of waveguides for selective single yeast cells' immobilization and illumination⁶⁷⁹ in PEG-DA hydrogel, is, to our knowledge, the only study in which cell-laden synthetic polymers have been used. Importantly, the writing process exhibited high cytotoxicity that can be attributed to the Irgacure 819 which, being an inefficient 2PI, requires higher laser doses. It is therefore clear that efficient water-soluble 2PIs play a crucial role for biocompatibility. In the past decade, different strategies for their development have been employed, ranging from host–guest interactions^{322, 668} or tailoring hydrophobic cores with hydrophilic moieties^{213, 321} to the use of semiconductor–metal hybrid nanorods.⁶⁰¹ For a detailed discussion of PIs, the reader is referred to section 2.2.2: Water-Soluble Photoinitiators (PIs).

The substantial absence of 2P-driven biofabrication with synthetic polymers can be attributed to the fact that a majority of synthetic photoresins are better or only soluble in organic solvents. Even if they can be easily used for acellular scaffold manufacturing because of their conveniently tunable mechanical and chemical properties, they do not accurately resemble the composition in native ECM, and they generally need to be loaded or conjugated with bioactive molecules. Given the above, most of the 2P biofabrication studies employed natural polymers, such as polysaccharides or peptides that have been made photoactive by

functionalization with various vinyl moieties (e.g., acrylates, methacrylates, vinyl esters) as discussed in the next paragraph.

Naturally Derived Polymers. To date, as also seen for other photomediated biofabrication techniques, Gel-MA is the predominantly used photoactive naturally derived polymer. It was first used in the presence of I2959 and at an excitation wavelength of 515 nm to fabricate a woodpile microstructure-mimicking cellular microenvironment.⁶⁸⁰ These constructs successfully supported adhesion and proliferation of porcine bone marrow-derived MSCs seeded on top of them. This study, like all others employing postfabrication cell seeding, avoids the potential toxicity of radical mediated crosslinking that was shown in a following study.⁶⁸¹

The first cell-laden hydrogel microfabrication revealed significant cytotoxicity on human osteosarcoma cells (MG63) resulting from reactive oxygen species (ROS)-induced cell damage (Figure 2.52A). Notably, IR laser radiation (800 nm) alone showed no impact on cell viability. The use of highly efficient water-soluble 2PIs (G2CK, P2CK) enabled a writing speed of up to 7 mm/s to be reached with a formulation consisting of 80% cell culture medium content. Later, the source of the cell damage was partially reduced by suppressing the diffusion of PI into cell cytoplasm with a hyaluronan–PI (HAPI) conjugate.³²⁶ Limiting ROS generation within the cells led to a considerable improvement in cytocompatibility. Successful direct encapsulation of mouse calvaria-derived preosteoblasts cells (MC3T3) into Gel-MA 3D microstructures was obtained at a printing speed of 100 mm/s (Figure 2.52B). Another approach used to limit the main source of cytotoxicity, 2PI-generated radicals, relied on the development of a cleavable diazosulfonate (DAS) initiator.³²⁹ By using the latter in combination with Gel-MA bioresin, ADSCs maintained normal metabolic activity and good viability within a microstructure biofabricated at the record speed of 1 m/s (Figure 2.52C).³²⁹ This demonstrates the promising potential of this biofabrication technique as a powerful tool in tissue engineering, namely to construct stem cell/organoids niches with subcellular features or tissue models for drug discovery.

To date, 2P biofabrication based on photoactivated natural polymers has mainly been done with Gel-MA formulations and simple constructs. However, other methacrylated polysaccharides, such as dextran,⁶⁸² HA,⁶⁷⁰ chitosan,⁶⁸³⁻⁶⁸⁴ cellulose,⁶⁸⁵ and pullulan,⁶⁸⁶ or those with other types of functionalization, like tyramine conjugation,²⁹⁷ have been successfully used for 2P-SL. The choice of natural polymers over synthetic ones is driven by their biocompatibility, biodegradability, potential bioactivity, and in general by their ability to better resemble the native ECM. However, the modification of such polymers does not come without costs. The functionalization with photosensitive moieties inevitably increases their toxicity³⁸⁰ and changes the properties of these materials to a certain degree. As an example, a high degree of methacrylation of primary amines (97%) and carboxylic acids (56%) of gelatin results in a better processability but also in the loss of thermal gelation.³⁶⁷ In general, increasing the DF can help to get a faster processing speed and, indeed, most of the papers cited presented a DF > 60% and up to 95%.³²⁹ Another approach,

again on the material side, to increase printing speed and tunability of mechanical properties without a dramatic loss of native polymer properties relies on the addition of a crosslinker. Photosensitive crosslinkers such as PEG-DA^{670, 687} have been widely used to tune the crosslinking of naturally derived polymers. Different stiffnesses can be obtained by varying their content in the initial formulation of naturally derived polymers and result in a tunable ability of cells to invade the hydrogel and migrate into it.⁶⁸⁷

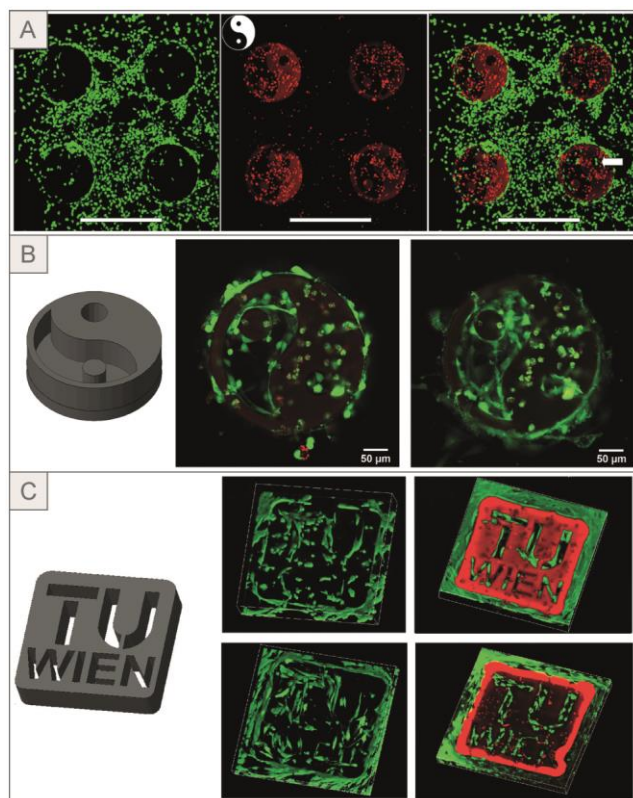


Figure 2.52 | 2P-microfabrication in the presence of cells with Gel-MA bioresins. (A) Live/dead staining. Low viability (red-stained cells) in the region exposed to the laser in Gel-MA matrices (scale bar: 500 μm). (B) Viable (green-stained) MC3T3 cells after 2P-microfabrication of yin–yang CAD model with Gel-MA bioresin (scale bar: 50 μm). (C) Live/dead staining. 2P-microfabrication of a CAD model (left) done with 2PI DAS shows higher cell viability after 1 and 5 days (left top and bottom) when compared to 2P-microfabrication done with P2CK (right top and bottom) in Gel-MA bioresin. Viable cells in green and dead cells in red. (TU Wien logo dimension: 500 \times 500 \times 125 μm^3). (A) Adapted with permission from ref⁶⁸¹. Copyright 2013 American Chemical Society. (B) Adapted with permission from ref³²⁶. Copyright 2017 Royal Society of Chemistry. (C) Adapted with permission from ref³²⁹. Copyright 2018 Royal Society of Chemistry.

To date, the formation of cell scaffolds with synthetic and naturally derived acrylated/methacrylated polymers have represented, in many cases, an acceptable trade-off between processability and biocompatibility. However, although these polymers still represent the standard for light-induced microfabrication, their use for biological applications is limited because of their irritancy and cytotoxicity, in particular for highly reactive acrylates.⁶⁸⁸ Attention should be also paid to the fact that a certain degree of unreacted potentially toxic

monomers/oligomers will be generally present in the biofabricated structures in the absence of long and extensive washing steps and can therefore hamper cell viability. Alternative approaches based on click chemistry or on native unmodified polymers have been investigated and will be discussed in the following sections.

Step-Growth Thiol–ene Chemistry. Photoinitiated thiol–ene click chemistry for hydrogel formation was first introduced by Anseth group.^{272, 689} It was shown that the fast kinetics and the mild reaction conditions, together with the orthogonality toward other reactive groups, make them excellent candidates for cell-laden hydrogels. In addition to the possibility of being performed in an aqueous environment without being inhibited by oxygen, another clear advantage for cell-laden systems made by the step-growth mechanisms is the low amount of generated radicals, which leads to higher cell viability.^{390, 690} The advantages of thiol–ene chemistry over the commonly adopted radical-chain polymerization of acrylates and methacrylates have become increasingly evident.^{633, 691} However, despite the fact that thiol–ene reaction for light-driven additive manufacturing and 2P-patterning (see section 2.4.2.4) is increasingly explored, its use in 2P-microfabrication is so far limited to the work of Liska and Ovsianikov.^{365, 380, 618}

Gel-VE in the presence of reduced bovine serum albumin (BSA) acting as a macrothiol donor was first used and showed notable processability.³⁶⁵ Highly efficient water-soluble 2PI (WSPI) at 0.5 wt % enabled writing speeds as high as 50 mm/s at relatively low laser power (20 mW) to be obtained. As expected, a direct correlation between hydrogel stiffness and higher thiol to alkene ratio was observed, as well as low cytotoxicity and good retention of gelatin cell adhesion properties. Another naturally derived photoclickable polymer, HA vinyl ester (HA-VE), was obtained by lipase-catalyzed transesterification.³⁸⁰ A comparison with HA acrylate (HA-AC) and HA-MA in the presence of fibroblasts revealed significantly lower cytotoxicity of the HA-VE system and a comparable or higher crosslinking efficiency. The use of another water-soluble efficient 2PI (P2CK) in the presence of dithiothreitol (DTT) as thiol donor enabled fast 2P-microfabrication with a large processing window (20–100 mW average laser power, 1–56 mm/s writing speed) and relatively small feature size (4 μm). In both cases, the fabrication of complex 3D microstructures was demonstrated but only in the absence of cells (Figure 2.53A,B). Combination of PVA-ene and PVA-thiol also enabled 2P-microfabrication (Figure 2.53C) at relatively low laser power and high writing speed (1–100 mW, 1–178 mm/s) in the presence of water-soluble 2PI E2CK-THEMA.⁶⁹²

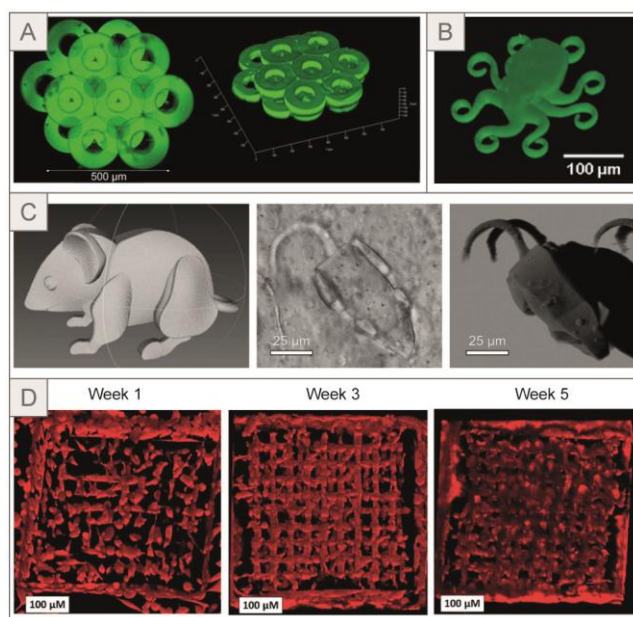


Figure 2.53 | Microfabrication of 3D structures by photoclick thiol-ene chemistry. (A) Construct made of Gel-VE/BSA (scale bar: 500 μm). (B) Octopus structure made of HA-VE/DTT (scale bar: 100 μm). (C) Reproduction of CAD mouse model (left) with PVA-ene/PVA-thiol resin visualized with light microscopy (middle) and SEM (right) (scale bar: 25 μm). (D) Z-Stack of Gel-NB grids biofabricated in the presence of mCherry labeled L929 fibroblasts after 1, 3, and 5 weeks showing cell spreading (week 3) and starting of hydrogel degradation and cell migration (week 5). (A) Adapted with permission from ref ³⁶⁵. Copyright 2013 John Wiley and Sons. (B) Adapted with permission from ref ³⁸⁰. Copyright 2014 Royal Society of Chemistry. (C) Adapted with permission from ref ⁶⁹². Copyright 2016 John Wiley and Sons. (D) Adapted with permission from ref ⁶¹⁸. Copyright 2019 John Wiley and Sons.

However, to date, Gel-NB appears as the most promising material for photo click-based 2P-microfabrication. First, Van Hoorick et al. showed the advantages of using highly reactive norbornene functionalities. Highly substituted Gel-NB (DF up to 90%) showed better processing capabilities when compared to commonly used Gel-MA. ⁶⁹¹ In particular, this led not only to faster processing and wider processable concentration range but also to lower laser power needed to exceed the fabrication threshold. Only recently, Dobos et al. exploited the high reactivity of such systems to perform the first photoclick-based 2P-microfabrication in the presence of cells. ⁶¹⁸ By using high DF (53%) Gel-NB, low molecular weight dithiol donor DTT, and thanks to the efficient water-soluble 2PI DAS, a record speed of 1 m/s was reached. Cell-embedded (L929 mouse fibroblasts) hydrogel constructs showed high cell viability when laser power below 100 mW was used. However, it is important to mention that in the regions exposed to the laser (from 50 to 90 mW), a strong decrease in proliferating cells was observed. ⁶¹⁸ Despite this, after 3–5 weeks, fibroblasts partially degraded the gelatin structure and migrated into it (Figure 2.53D). Clearly, as this technique is paving its way to biofabrication, there is an urgent need to better understand at a molecular level what determines such cell response to the biofabrication process.

In general, the better processability of thiol–ene-based systems and the more homogeneous network formation compared to chain-growth photochemical processes (see Section 2.2.1) represent key advantages for 2P-microfabrication of cell-laden hydrogels. Even though this photo click chemistry based approach has not been widely adopted so far for 2P-microfabrication, there is an expectation that the pioneering work in this direction will guide future efforts on the use of thiol–ene bioresins in 2P-SL as a high-resolution biofabrication technique.

Native Proteins. A small number of studies have demonstrated that 2P-induced biofabrication is also possible with native (unmodified) proteins, in the presence of photosensitizers such as Rose Bengal⁶⁹³⁻⁶⁹⁶ or flavin adenine dinucleotide.⁶⁹⁷⁻⁶⁹⁹ Following the excitation of the PI to the T1 state, two photo-oxidation mechanisms are believed to be responsible for the crosslinking process: generation of singlet molecular oxygen and hydrogen abstraction from amino acid residues. In the first case, crosslinking takes place when the singlet oxygen oxidizes a photo-oxidizable amino acid residue (e.g., histidine, cysteine, tryptophan, and tyrosine) that then forms a covalent bond with a second electron-deficient amino acid.⁷⁰⁰ In the absence of quenchers, because the cell-containing aqueous environment is not oxygen-free, the singlet oxygen formation is the most plausible mechanism.

2P-SL with collagen type I, II, and IV^{694,700} was performed in the presence of Rose Bengal diisopropyl amine or benzophenone dimers (BPDs). Unlike xanthene dyes, BPD can be used in acidic conditions, which facilitates the solubilization of collagen. Simple 1.5 μm collagen lines were biofabricated under physiological conditions and showed bioactivity retention (cell adhesion) and enzymatic degradation. Other native proteins such as BSA,^{693-694, 697-699, 701} fibrinogen,^{693, 701} avidin,⁶⁹⁷⁻⁶⁹⁸ and laminin⁶⁹⁷⁻⁶⁹⁸ have been used for 2P-microfabrication in biologically compatible aqueous environments and have shown good bioactivity retention. Notably, functional protein microstructures were biofabricated in the presence of cells by Kaehr et al. to guide neurite outgrowth of rat brain cortical neurons.⁶⁹⁷ The guidance structures were obtained without cytotoxic effects on the neurons. However, the potential harmful effect of FAD photoexcitation was not fully explored because no direct irradiation on the cells was required. Later, Kaehr et al. exploited 2P-mediated BSA crosslinking to realize cell chamber⁶⁹⁹ and dynamic hydrogel microactuators,⁶⁹⁸ proving effective *Escherichia coli* trapping, incubation, and release (Figure 2.54A). Similarly, gelatin and BSA were used in the presence of Rose Bengal to arrange polymicrobial communities within entrapping containers (Figure 2.54B).⁶⁹⁶

As a type II PI, Rose Bengal needs a co-initiator and TEA is commonly used. However, it was demonstrated that the proteins themselves can act as co-initiators.^{684, 693} Following a microinjection of Rose Bengal only, Basu et al. were able to fabricate simple structures within the cytoplasm of live starfish oocytes, demonstrating potential compartmentalization of cellular processes.⁶⁹⁵ PI-free 2P structuring of unmodified proteins

(collagen and fibrinogen) and liquids (fetal calf serum and human blood) was also investigated, and grids with micrometer width lines were obtained. However, the underlying structuring mechanism remains unclear.⁷⁰²

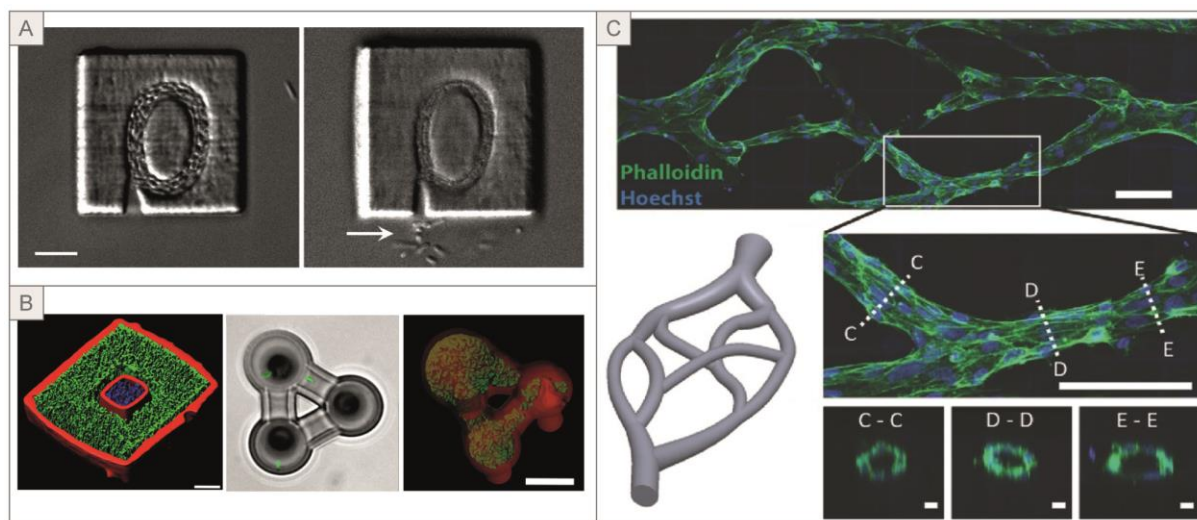


Figure 2.54 | 2P-microfabrication with unmodified proteins. (A) Dynamic trapping, incubation and release (arrow) of *E. coli* in crosslinked BSA (scale bar: 5 μm). (B) In situ encapsulation of *S. aureus* (blue) and *P. aeruginosa* (green) by microfabrication with gelatin/BSA (scale bar: 10 μm (left), 20 μm (right)). (C) Postfabrication seeded HUVECs in 3D microvasculature channels generated in collagen hydrogel (scale bar: 100 μm (top,middle), 10 μm (bottom)). (A) Adapted with permission from ref⁶⁹⁸. Copyright 2008 U.S. National Academy of Sciences. (B) Adapted with permission from ref⁶⁹⁶. Copyright 2013 U.S. National Academy of Sciences. (C) Adapted with permission from ref²⁰⁶. Copyright 2016 John Wiley and Sons.

To date, the 3D structural complexity and accuracy generally obtained with unmodified proteins does not yet achieve the standard reached with acrylate polymers and other modified materials, mainly because of the lower density of reactive groups (e.g., oxidizable amino acids such as tyrosine) and lower reactivity. In addition, the crosslinking of oxidizable residues in an aqueous environment with water-soluble dyes and amine co-initiators is heavily limited by the need for high laser intensities and low writing speeds, generally $\sim 5 \mu\text{m/s}$. To the best of our knowledge, the only exception is represented by the fast (400 mm/s) 3D microfabrication of biomimetic collagen microvasculature structures produced by fluorescein photobleaching by Skylar-Scott et al.²⁰⁶ High laser power (up to 2.5 nJ/pulse) was adopted to trigger the crosslinking process upon fluorescein photobleaching in a bulk collagen gel and form the channels wall. Upon postfabrication seeding of HUVECs via hydrostatic pressure-driven flow, the microvasculature network was readily covered by a confluent monolayer of VE cadherin positive cells (Figure 2.54C). This demonstrated the retention of cell adhesion properties of collagen after crosslinking. This simple setup, consisting of off-the-shelf polymers and fluorescein, holds great potential for 2P-microfabrication because it is readily accessible and does not involve complex synthesis or functionalization steps. However, it must be

emphasized that biofabricated collagen structures were in this case limited to a cell-seeding approach, because they need to be postprocessed in acetic acid or Tris buffer.

Commercially available hydrophilic dyes (e.g., eosin Y, Rose Bengal, fluorescein) are mainly used as UV-visible fluorophores and therefore show low σ^{2PA} and high fluorescent quantum yields. The use of efficient 2PIs also represents in this case the need to avoid compensating these suboptimal properties with high laser power, low writing speed, or high number of scans. Given the above, it is expected that the recent synthesis of highly efficient water-soluble 2PIs (e.g., WSPI, P2CK, E2CK, DAS) will renew interest in unmodified protein 2P-microfabrication.

2.4.2.2.2. Bond Cleavage in Microfabrication. The cell's extracellular environment is extremely complex and dynamic, undergoing continual remodeling. It is well established that mechanical signals of the extracellular milieu are as crucial in determining cell fate⁷⁰³ as GFs and other signaling molecules. Therefore, 3D microfabrication often does not sufficiently mimic the diverse and mutable properties of the native ECM. Real-time manipulation of light-induced degradation has proven to be a useful tool for addressing this limitation.⁷⁰⁴ Important advances in the design of dynamic hydrogels have been made in the past decade thanks to 2P-SL. Using photolabile crosslinkers, a 3D spatiotemporal control over hydrogel mechanical properties can be achieved. Pioneering work on locally induced changes in the network stiffness has been made by DeForest and Anseth.^{124, 337, 705} A major part of the studies on multiphoton-assisted photoscission rely on oNB derivatives as photolabile moieties. However, photocleavage strategies employing more efficient photolabile moieties such as coumarins³⁵³ and ruthenium complexes⁷⁰⁶ have also been investigated.

oNB Photodegradation. An oNB-based 2P-degradable hydrogel was first reported in the pioneering work by Kloxin et al.³³⁷ Site-specific degradation of a PEG hydrogel in the presence of cells allowed remote control over properties such as stiffness, water content, and diffusivity. The erosion of interconnected 3D channels was used to study cell migration of encapsulated fibrosarcoma cells. The possibility of studying cell migration and connectivity was further demonstrated in the presence of MSCs.²¹⁴ The precise control of cell adhesion sites by photolysis showed the utility of this material for 3D dynamic cell studies.

A similar system based on oNB-containing crosslinker was made more biocompatible by replacing acrylate-based crosslinking with cytocompatible SPAAC click-chemistry.¹²⁴ SPAAC reactions proceed rapidly, without a catalyst, in physiological conditions. Together with being remarkably bio-orthogonal and nontoxic, click-based hydrogel formation represents an advantageous approach for biological applications. The irreversible 2P cleavage of oNB (740 nm) was used to direct in situ growth of fibroblasts (3T3) contained within a fibrin clot. The authors reported a strong preference of 3D-directed cell outgrowth when channel erosion and subsequent functionalization with fibronectin adhesion peptides (RGDs) were used in combination (Figure 2.55A). In contrast, human MSCs encapsulated in the hydrogel without erosion and

RGD maintained a round morphology. Notably, the patterning of the short peptides was achieved with photoclick thiol–ene chemistry in the presence of Eosin Y showing wavelength orthogonality with oNB cleavage. Therefore, remote postgelation control of both chemical and physical properties was achieved with orthogonal light-based chemistry.

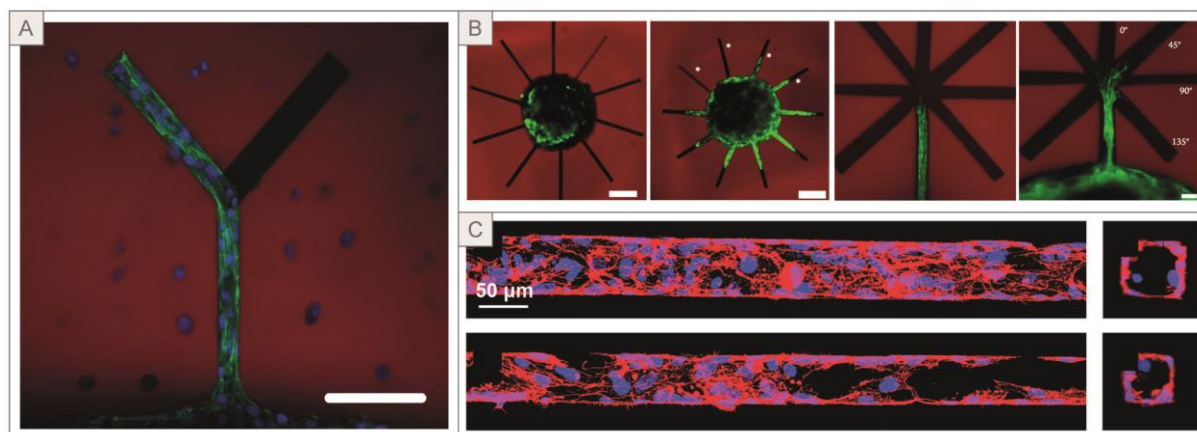


Figure 2.55 | *ortho*-Nitrobenzyl (oNB) mediated degradation. (A) 3T3 fibroblasts (green) confined outgrowth within oNB mediated photodegraded channels patterned with RGD adhesion peptide (left branch) via thiol–ene photoclick coupling. Rounded shaped human mesenchymal stem cells in blue in the outer region. Click-based PEG hydrogel in red (scale bar: 100 μm). (B) Motor axon extension (green) in oNB mediated eroded channels in PEG hydrogel (red) (Scale bar: 100 μm , 10 μm). (C) HUVECs endothelialized $60 \times 60 \mu\text{m}^2$ and $45 \times 45 \mu\text{m}^2$ channels generated by oNB photodegradation in MMP-sensitive PEG-based hydrogel (scale bar: 50 μm). (A) Adapted with permission from ref ¹²⁴. Copyright 2011 Springer Nature. (B) Adapted with permission from ref ²⁰⁷. Copyright 2014 American Chemical Society. (C) Adapted with permission from ref ²⁰⁵. Copyright 2017 John Wiley and Sons.

The possibility of forming channels within a 3D hydrogel and the observation that cell growth can be directed toward the eroded regions inspired the use of this approach for the biofabrication of perfusable vasculature networks ²⁰⁵ and neural networks ²⁰⁷ in cell-laden hydrogels. Embryonic stem cell-derived motor neurons axonal extensions were directed upon 740 nm fs-pulsed laser-induced hydrogel degradation. The system was exploited to investigate the dependence of neuron migration on channel dimension, erosion degree, and angle (Figure 2.55B). Besides the ability to study the influence of biophysical cues with 3D control, this biocompatible strategy was employed to direct the formation of neuromuscular junction in the presence of two cell types. C2C12 myotubes were coencapsulated with ESMN embryoid bodies. Thanks to the photocleavage of oNB-based linkers, channels connecting the two cell types were generated, allowing the neuron extension toward the muscle cells to then show evidence of neuromuscular junction formation. Another application of such systems to produce microchannels was presented by Arakawa et al. ²⁰⁵ Endothelialized vasculature networks with different channel diameters ranging from hundreds of micrometers down to 10 μm were generated. Successful attachment of HUVECs on the channel wall was then obtained by postfabrication seeding (Figure 2.55C). To date, possibly in combination with other

techniques such as one-photon SL to improve the scalability and reduce the processing time, the generation of multiscale vascular networks appears to be one of the most appealing applications of 2P-SL for tissue engineering purposes.

Recently, the DeForest group combined the established oNB photocleavage strategy in copper-free SPAAC crosslinked PEG hydrogels with other stimuli-degradable moieties to generate a complex “boolean logic”-responsive biomaterial.⁷⁰⁵ Diazide crosslinkers were engineered to respond to redox, enzyme, and light stimuli by the inclusion of disulfide bonds, MMPs-sensitive sequences, and oNB, respectively. The linker architecture was designed to achieve material degradation only in response to a specific combination of the environmental stimuli (reducing agent, proteolytic activity, and light exposure). The system showed a high degradation specificity, which has been tested by means of doxorubicin release in a cancer in vitro model and release of live cells. This platform offers unique opportunities for targeted drug delivery, tissue engineering, and in vitro spatiotemporal control over stem cells’ or organoids’ differentiation and development. The potential for the cells to modify the surrounding environment with the production of certain stimuli is a crucial aspect for an advanced 3D cell culture system. In addition, the inclusion of a photolabile group allows the operator to maintain the ability to remotely control the engineered matrix, moving her/his role on the cell fate from “passive” to “active”.

Even if largely employed for photodegradable systems, oNB linkers exhibit low σ^{2PA} , which significantly reduces their efficiency in 2P degradation. Recently, Lunzer et al. proposed a strategy to enhance the two-photon triggered cleavage of oNB.³⁴¹ The addition of a 2P active cyclic benzylidene ketone-based (P2CK) photosensitizer significantly improved the oNB ester cleavage upon NIR (800 nm) laser exposure and enabled cell-laden hydrogel degradation under moderate laser power. Microloop channels were photoeroded from a thiol-ene click-based HA hydrogel at a notable writing speed (200 mm/s) in the presence of hTERT-immortalized ADSCs. The system showed high cell viability after one and two weeks and therefore represents a good solution for oNB-based photocleavable hydrogels in which fast processing is needed. Another approach to improving the efficiency of two-photon degradation relies on the use of photolabile molecules with higher σ^{2PA} such as *ortho*-nitrobiphenyl⁷⁰⁷ or coumarin derivatives.

Coumarin Photoscission. Coumarin-based photodegradation has two main advantages compared to the oNB-based systems. First, as previously mentioned, coumarin’s optical properties are more suitable for 2P lithography and generally represent a better choice for cytocompatible platforms (red-shifted absorption). Second, coumarin byproducts are less reactive than the aldehyde or ketones generated by nitrobenzyl systems.³³⁶ However, unlike oNB, only a few examples of photolabile coumarin linkers for 2P hydrogel degradation can be found.³⁵³ Coumarin was exploited by Zhu et al. as a hydrophobic photolabile block for constructing a linear triblock copolymer in combination with PEG hydrophilic blocks.⁷⁰⁸ 2P-induced

uncaging of the coumarin changes the properties of the block copolymer, leading to disintegration of the physical crosslinking. A similar approach was used by Yoshii et al., who presented the first two-photon responsive supramolecular hydrogel.²¹⁵ By conjugating a coumarin derivative to a phenylalanine dipeptide, the authors were able to self-assemble a fibrous gel and subsequently induce a transition to solution through site-specific 2P uncaging. Notably, the entangled fiber network rapidly disassembled upon 2P-uncaging, leaving a highly fluid void space. In fact, the small molecule (dipeptide) composition of the fibers leads to a drastic change in viscosity upon light-mediated degradation. The self-assembly of supramolecular fiber hydrogels and their fast, complete, and precise degradation differ from most of the studies in this field, which make commonly use of crosslinked polymer networks, and therefore represents another interesting approach for spatiotemporal-controlled tissue engineering.

Coumarin uncaging was also employed to control the hydrogel crosslinking. The protection of a reactive site with a 2P sensitive photocage is a widely used approach for 2P-patterning (see section 2.4.2.4). However, it can also be used to trigger fast and cytocompatible gelation through thiol–ene Michael addition reaction.⁷⁰⁹ This approach enabled the build up of cell-laden hydrogels with negligible cytotoxicity. It combines the 3D control given by 2P-microfabrication at 800 nm with rapid thiol–ene click chemistry in a physiological environment (PBS, pH 7.4) and overcomes the radical-induced damage typically observed in photoinitiator-based microfabrication. Thiol–ene microfabrication obtained upon thiol photouncaging can be applied to almost any hydrogel system. Thiol functionalization of the polymer chain and use of maleimide, or even better norbornene-terminated linkers (or vice versa), render this approach a powerful tool for 2P-microfabrication in the presence of cells.

In addition to oNB and coumarin derivatives, photolysis by 2PA was also shown in ruthenium complex containing polyurea gel.⁷⁰⁶ Other mechanisms such as photoablation, upconverting nanoparticle (UCNP)-assisted photochemistry or one-photon processes³⁴³ have also been investigated. However, these approaches lie outside the scope of this review. Another strategy for achieving photodegradation is via radical addition–fragmentation chain transfer (AFCT) as proposed by Brown et al.⁷¹⁰ In this study, radical initiated thiol–ene exchange reaction was employed to tune the mechanical properties of a SPAAC-based PEG hydrogel in the presence of hMSCs. Even though this approach leads to faster bulk hydrogel degradation compared to oNB or coumarin-containing hydrogels, the presence of a soluble photoinitiator and the generation of potentially harmful radicals remain major concerns.

Spatiotemporal control over local network crosslinking by 2P-SL holds great promises in dynamic 3D cell culture systems, single cell studies, drug or cell delivery, and tissue engineering. Nevertheless, as comprehensively discussed by Brown and Anseth,⁶³³ the design of a photodegradable material should take into consideration different aspects such the chemistry of chain-growth or step-growth networks, σ^{2PA} of the

photolabile moiety and possible toxic or reactive byproducts that together define the material processability and biocompatibility.

2.4.2.3. 2P-Microfabrication Limitations and Outlook

Besides the recent notable results achieved with 2P-microfabrication, several limitations still need to be overcome. The most pressing of these is the low scalability of the technique when relevant size constructs are considered. Even at the max speed reported to date (1 m/s),³²⁹ the production of a 1 cm³ (100% infill) structure with 1 μm line width would require almost 12 days. On the material side, the writing speed depends on the PI efficiency in generating radicals and the density and reactivity of photo-crosslinkable cues. Therefore, the synthesis of novel, water-soluble, and highly efficient 2PI would further improve the 2P-microfabrication processability. On the other hand, because the use of highly substituted polymers generally presents a relevant source of cytotoxicity (see section 2.2.5), increasing the DF may not be a viable route for cell-laden constructs dependent on the biological properties of the polymer. Among the various chemical strategies, step-growth thiol–ene click chemistry appears in general to be a good trade-off between reactivity and biocompatibility. However, because thiols or disulfides are also normally present in proteins, such systems are not fully bioorthogonal.

On the instrumentation side, the maximum processing speed is obtainable with nonstop single-line, single-pass laser scanning.⁶⁷¹ To do so, the laser intensity needs to be high enough to trigger the photochemical reaction during each single pixel dwell time.

Technical solutions have also been investigated to enable the manufacturing of tall (mm to cm) 3D structures, which is normally limited by the use of short working distance for high NA objectives. Obata et al. proposed a setup in which the objective and the coverglass can be moved together in the liquid photoresin, therefore resulting in a wider objective working range.⁷¹¹ Structures with height (7 mm) beyond the objective working distance have been fabricated with micrometer resolution (Figure 2.56A). More recently, Chu et al. generated a centimeter-height 3D structure with 10–40 μm resolution (Figure 2.56B)⁷¹² in 15 h utilizing simultaneous spatiotemporal focusing of the fs-pulsed laser.⁷¹³ The resolution and the writing speed (400 μm/s) were limited by the low laser power (5 mW) and repetition rate (1 kHz) employed, but overall were enough to demonstrate that relatively tall constructs can also be generated by 2P-SL. The intrinsic drawback of being a serial (voxel-by-voxel) technique can be in part overcome by the use of a microlens array. The array of small lenses converts the collimated beam into multispots enabling parallel processing.⁶²⁶ Splitting the laser beam reduces the maximum energy in the excitation voxel, and therefore also in this case, highly efficient 2PIs are desired to lower the fabrication threshold. While this technique represents a powerful tool for speeding up the microfabrication of microscopic devices (e.g., MEMS) and periodic structures, to the best of our knowledge, it has not been applied for the development of cell-containing hydrogel constructs. Recently,

Saha et al. introduced a promising projection-based parallelization approach to speed up the printing process and overcome the point-by-point scanning.⁷¹⁴ Spatial and temporal focusing of ultrashort laser pulses was used to generate femtosecond light sheets at the desired focal plane. With the use of DMD, 2D arbitrary patterns can be projected in a layer-by-layer fashion, enabling 3D printing process similar to projection VP while maintaining 2P derived submicrometer resolution. Another innovative strategy to speed up the printing process, which is also now available on the market (Holograph X by Cellink), is instead based on the generation of holograms by using SLMs. The (bio)fabrication time of this holographic 2P-SL is proportionally reduced with the number of generated focal points.⁷¹⁵⁻⁷¹⁷

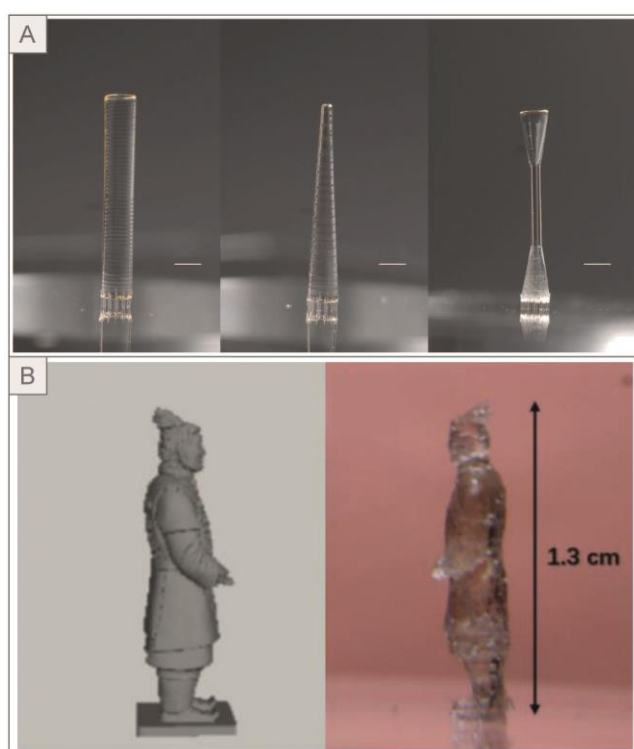


Figure 2.56 | 2P-microfabrication of centimeter size structures. (A) PEG-DA tube structures fabricated by wider objective working range 2P-microfabrication show the possibility to go beyond the limited objective working distance (scale bar: 1 mm). (B) Terra Cotta Warrior CAD model (left) and SU-8 2P-microfabricated cm tall structure (right). The laser scan along the contour 3D profile was performed at $400 \mu\text{m/s}$ and took 15 h. (A) Adapted with permission from ref⁷¹¹. Copyright 2013 Springer Nature. (B) Adapted with permission from ref⁷¹². Copyright 2018 John Wiley and Sons.

Another aspect that might limit the achievement of high resolution and structure fidelity, in particular with relatively soft materials such as hydrogels, are the time-dependent swelling and shrinkage that take place upon crosslinking or degradation. As these geometrical changes are often not predictable, an optimized CAD design that takes this aspect into consideration remains an open challenge.³⁶⁷

Moreover, 2P-SL is normally limited to the use of a single material throughout the whole manufacturing process. Multimaterial constructs can be made by postprinting single or multiple functionalization⁷¹⁸ or, as recently shown by Mayer et al., with microfluidic-based systems.⁷¹⁹ After a first microfabrication step with a resin, instead of manually repeating washing, application of a second resin and realignment steps, microfluidic based multimaterial printing can be used to automatize this cycle.

Although *in vivo* 2P-microfabrication has not yet been demonstrated, a few papers already showed good *in vivo* biocompatibility of 2P-microfabricated scaffolds upon implantation for cartilage⁷²⁰ and myocardial⁷²¹ tissue engineering applications and as cochlear drug release implants.⁷²² If it were possible to obtain relevant size constructs (cm³) in a reasonable amount of time, this technique would clearly emerge as an attractive approach for patient-specific scaffold manufacturing. Even if clinical use of 2P-SL may not be ready in the near future, we envision that the unrivaled ability to mimic native ECM in submicrometer-resolved grafts will lead to significant improvements in this field.

In conclusion, 2P-driven bond formation and bond degradation are powerful tools for the design of micrometer-/submicrometer-scale bioengineered matrices. However, because of the above-mentioned limitations, the advantages of this manufacturing technique in tissue engineering have not yet been fully explored. We envision that the exponential increase of research seen in recent years on this topic will hopefully bring forward novel efficient, water-soluble and wavelength-orthogonal PIs and photocages together with technical solutions to address the current limitations. We are also confident that this will shift the attention from the material and processing side to the biological side and contribute to advances in real-world biomedical applications.

2.4.2.4. 2P-Patterning Applications

Cell behavior in 3D culture systems does not only depend on matrix composition, architecture, and mechanical properties. The ECM is a highly mutable biochemical environment. During tissue development or regeneration, or in disease, the pattern of bioactive signals changes dramatically. *In vitro*, a fine control in time and space of bioactive cues can be obtained by 2P-patterning. In the last two decades, several photochemical approaches have been developed to immobilize biologically relevant molecules, ranging from small molecules and short peptides to whole enzymes, in a broad range of hydrogel substrates. Tailoring biochemical properties at the microscale has opened up unique opportunities for developing complex dynamic cell niches and studying fundamental cell behaviors such as migration, differentiation, and cell-matrix interactions. The 2P-patterning approaches are divided on the basis of their use of photocages or not. As seen for microfabrication, the excitation of a PI can lead to radical generation and therefore trigger radical mediated bond formation. In the first section (Bond Formation in Patterning) the “direct patterning” approach by radical mediated immobilization is discussed. In the second section (Bond Cleavage in

Patterning), we guide the reader toward the recent achievements of the indirect strategies that include uncaging steps. 2P labile molecules are exploited to cage (render inactive) functional reactive sites that are, upon light-mediated uncaging, used to immobilize a bioactive cue.

2.4.2.4.1. Bond Formation in Patterning. 3D immobilization of biomolecules was first reported by Hahn et al.⁷²³ In a series of studies, the authors demonstrated the ability to recapitulate complex gradients of adhesion peptides (e.g., RGD, CS-1, and IKVAV) within PEG hydrogels. In the presence of 2,2-dimethoxy-2-phenylacetophenone acting as PI, acrylated peptide derivatives were conjugated to PEG-DA gels by means of 2P (720 nm) radical-mediated conjugation. Using PEG-DA as a “blank slate”, the peptide adhesion properties were isolated and studied with different cell types. Notably, pre-encapsulated cells followed the guiding RGD pattern, while they failed to migrate toward the nonadhesive PEG-DA (Figure 2.57A).⁷²⁴ The same principle was adopted to control the formation of microvasculature network architectures derived from native tissues such as the retina, cerebral cortex, and subependymal neural stem cell (NSC) niche. 3D images of endogenous vasculature beds were converted to regions of interest (ROI) to define the laser scanning path and intensity (Figure 2.57B). Excellent peptide patterning fidelity and successfully guided formation of tubule-like network within specified “biomimetic” areas were obtained.⁷²⁵

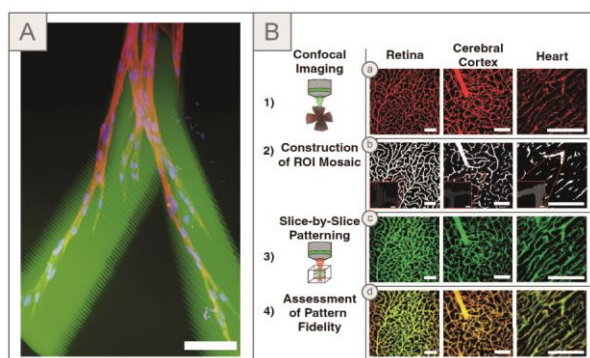


Figure 2.57 | 2P-patterning by bond formation in PEG-DA hydrogels. (A) Human dermal fibroblasts (red) migration within acrylate-RGD patterned region (green) in collagenase-sensitive PEG-DA hydrogel (scale bar: 100 μm). (B) Patterning of acrylate-RGD peptide (c) in regions of interest (ROI) reconstructed (b) from different tissue vasculature projections (a). Patterning fidelity was assessed by merging (a) and (c), with the yellow color indicating good overlapping (d) (scale bar: 5 μm). (A) Adapted with permission from ref⁷²⁴. Copyright 2008 Elsevier Ltd. (B) Adapted with permission from ref⁷²⁵. Copyright 2012 John Wiley and Sons.

In addition, it was shown that pattern resolution range can be tuned, utilizing objectives with different magnification and numerical aperture (Figure 2.58A).⁷²⁶ Furthermore, the concentration of the immobilized molecule depends on the energy applied and therefore can be controlled by varying laser intensity, scanning speed (Figure 2.58B), and number of scans.⁷²⁶⁻⁷²⁷ By controlling the light dose and the step size, smooth gradients can be obtained in the three dimensions (Figure 2.58C).

The Anseth group has explored another “direct patterning” approach based on radical mediated thiol–ene addition. A copper-free click chemistry reaction was adopted to form PEG hydrogels in the presence of cells under physiological conditions and combined with the orthogonal thiol–ene photocoupling click chemistry. Enzymatically degradable crosslinkers with pendant vinyl functionalities enabled photoimmobilization of cysteine-containing RGD peptides upon light irradiation with high cell viability.⁷²⁸ The system was further optimized with the addition of oNB photodegradable linkers, therefore providing the possibility of controlling the arrangement of biochemical (patterning) and physical (photodegradation) signals with “optical orthogonality”.¹²⁴ 2P-patterning of fluorescent cysteine-containing RGD peptides was achieved with subcellular resolution, which represents a relevant aspect for precise tuning of individual cells microenvironment.

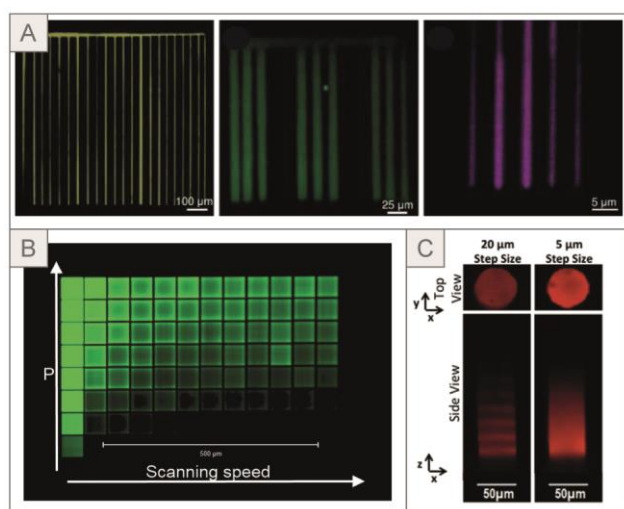


Figure 2.58 | Influence of laser processing parameters on 2P-patterning. (A) Higher line width resolution of fluorescent RGD patterning with higher magnification objective, from left to right: 10× (NA = 0.45) (scale bar: 100 μm) and 20× (NA = 0.75) (scale bar: 25 μm) resulted in a resolution in the order of 5–10 μm, while 63× (NA = 1.4) showed 1–2 μm patterned features (scale bar: 5 μm). (B) Controlled concentration of immobilized fluorescent cue (green) by varying scanning speed and laser power. Increasing the scanning speed leads to a diminished light dose per pixel and therefore to a decrease in patterning efficiency. On the other hand, increasing the laser power (P) is associated with an increased immobilization of the fluorescent moiety (scale bar: 500 μm). (C) Importance of step size for the formation of smooth gradients. Diminishing the scanning intervals ensures the formation of continuous gradients in the z axis. (A) Adapted with permission from ref⁷²⁶. Copyright 2010 Royal Society of Chemistry. (B) Adapted with permission from ref⁷²⁷. Copyright 2012 John Wiley and Sons. (C) Adapted with permission from ref²¹¹. Copyright 2018 Elsevier Ltd.

A similar principle was used to independently control the immobilization of a bioactive motif and its release. By synthesizing the bioactive cue with both a thiol (for thiol–ene reaction) and oNB moiety (for photorelease), the authors achieved a “reversible patterning” controllable with λ -orthogonal photochemistries: 860 nm (patterning) and 740 nm (release) (Figure 2.59A).¹²⁵ Recently, Qin et al. further

demonstrated the potential of thiol–ene photoclick chemistry with fast photopatterning of adhesive peptides in preformed PVA hydrogels by using the efficient 2PI P2CK.²¹⁹ The resulting exquisite control of multicellular invasion from spheroids of human dermal fibroblasts (HDF) (Figure 2.59B) suggests that this technology has sufficiently improved its speed, biocompatibility, and versatility to become a standard tool for biologists in the near future. Lately, the concept of “reversible patterning” was better captured by the elegant introduction of the addition–fragmentation chain transfer agent (AFCT) allyl sulfide.^{729–730} Allyl sulfide crosslinkers enable reversible addition and release of thiol-containing biological epitopes (Figure 2.59C). Dynamic changes of cell biochemical surroundings, meaning, i.e., exposure to bioactive signals such as growth factors, were proved to be possible with whole signaling proteins and a high degree of control. Unlike commonly used short adhesion peptides such as RGD, IKVAV, and PHSRN, the activity and effect of transient presentation of thiolated TGF- β 1 was assessed.⁷²⁹ Certainly, this first study on fully reversible whole protein patterning points toward new applications such as complex in vitro dynamic disease models.

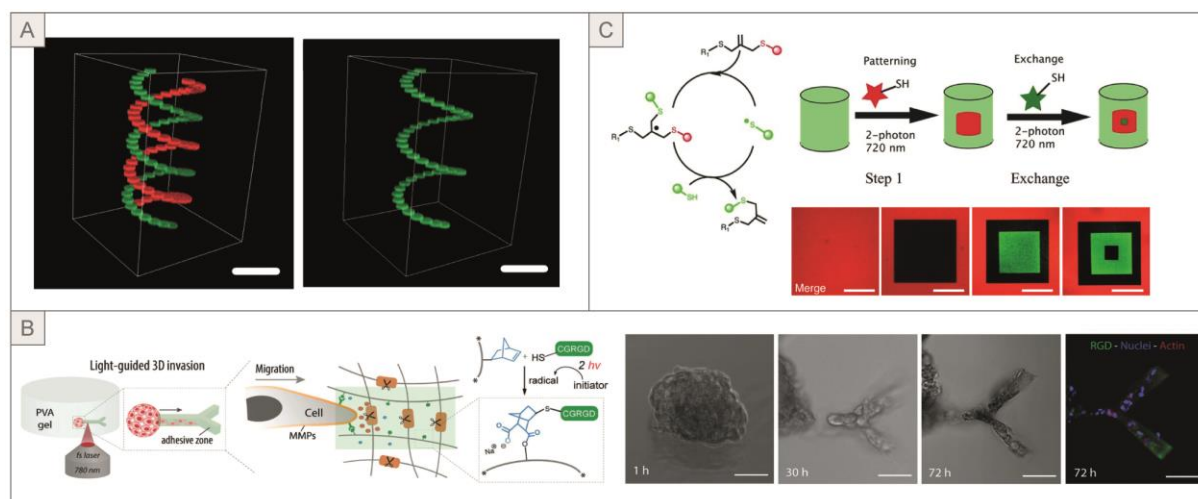


Figure 2.59 | 2P-patterning by thiol–ene conjugation. (A) 3D orthogonal thiol–ene 2P-patterning and subsequent oNB-based removal of prepatterned cues in PEG-based hydrogel (scale bars: 200 μ m). (B) Schematic of 2P-patterning guided cell invasion showing thiol–ene mediated RGD immobilization (left). Confined human fibroblasts invasion within cysteine-containing RGD patterned Y shape in PVA hydrogel (right, scale bars: 100 μ m). (C) Sequential allyl sulfide based patterning and release (scale bars: 100 μ m). (A) Adapted with permission from ref¹²⁵. Copyright 2011 John Wiley and Sons. (B) Adapted with permission from ref²¹⁹. Copyright 2018 John Wiley and Sons. (C) Adapted with permission from ref⁷²⁹. Copyright 2018 American Chemical Society. Adapted with permission from ref⁷³⁰. Copyright 2014 John Wiley and Sons.

Another direct 2P grafting strategy relies on photolysis of aromatic azides with high multiphoton absorption cross section.^{727, 731} In this case, a single-molecule insertion mechanism is obtained through the decomposition of azide groups to reactive nitrene species upon two- or three-photon irradiation. A second azide group or a terminal alkyne was then exploited as CuAAC sites to immobilize a desired clickable molecule in a localized fashion. With the use of organic solvents to form and pattern the PEG-DA gels, a

remarkable writing speed of ~ 550 mm/s was reported. Similar approaches, based on the photografting of a universal reaction substrate followed by immobilization of bioactive cues, were presented by Seidlits et al.⁷³² and Skylar-Scott et al.²⁰⁶ Following the photopatterning of a biotinylated molecule (BSA or fluorescein), NeutrAvidin or streptavidin was diffused into the gel to then enable the physical binding of a second biotinylated active motif. Notably, Skylar-Scott successfully combined 2P-patterning and 2P-microfabrication within the same system. Demonstration of P-selectin-mediated HL-60 human leukemia cells homing and capturing in 50 μm collagen microchannels was reported.

In general, the use of potentially toxic acrylate moieties and PIs, long incubation times, and radical generation give rise to concerns about deleterious effects of this patterning strategy on encapsulated cells. In this context, the use of photocages is a “milder” alternative to obtain localized patterns of bioactive epitopes. Nevertheless, as with any other strategy, advantages and disadvantages exist that will be discussed in more detail in the following section.

2.4.2.4.2. Bond Cleavage (Uncaging) in Patterning. Bond degradation upon light exposure offers remote and bioorthogonal control over photosensitive systems. This type of photochemistry has been widely explored for controlled release of neurotransmitters and signaling molecules and, as discussed in section 2.4.2.2, to control the stiffness of matrices for 3D cell culture. Photolabile molecules have also been used to protect functional reactive groups. Upon light exposure, the photocage is removed and functional groups such as thiols or amines are rendered available for site-specific reactions. It follows that photouncaging can be exploited for 2P-patterning. In this review, the literature regarding this application is divided into three categories called *covalent*, *physical binding*, and *preloaded latent patterning*. While patterning with covalent bonds used direct immobilization through covalent bond formation between the bioactive molecule and the uncaged reactive site, patterning with physical binding uses an indirect approach based on affinity binding pairs. With preloaded latent patterning, on the other hand, photocaged bioactive molecules are conjugated to the polymer backbone and activated in situ without further reactions.

Covalent Patterning. Light-mediated localized uncaging in a 3D hydrogel system was first introduced by Luo et al.⁷³³ Upon UV laser exposure, an oNB photocage was cleaved, leaving free thiol groups to react with maleimido-modified adhesion peptides. Thiol deprotection and subsequent Michael-addition coupling were extensively adopted and optimized by the Shoichet group in agarose^{333, 734-737} and HA^{213, 738-739} based matrices. To achieve a 2P-sensitive system, coumarin- and dibenzofuran-based protecting groups were used instead of oNB because of their higher efficiency for 2P cleavage. Agarose was covalently modified with 6-bromo-7-hydroxycoumarin (Bhc) sulfide derivatives, and these were used to immobilize maleimide-activated vascular endothelial growth factor (VEGF) in concentration gradients and to study their effect on cell activity.^{735, 737, 740} These works demonstrated the usefulness of chemically defined 3D culture systems in

investigating the role of GFs in processes such as migration and development. Immobilized VEGF-A was found to be more efficient than soluble VEGF-A in the induction of embryonic stem cells toward blood progenitor cells.⁷³⁵ Moreover, it was found that ECs follow the GF gradients forming tubular-like structures.⁷⁴⁰ Later, the coculture of ECs, retinal stem, and progenitor cells (RSPCs) on VEGF-A gradients revealed an unexpected EC inhibitory role on RSPC fate.⁷³⁷ 2P-patterning upon thiol deprotection was also studied with furan-modified HA.⁷³⁸

As previously explained in section 2.2.3.2, it is important to mention that even if Bhc has been the one of the most frequently adopted photocages for thiol groups, it is not the most efficient. In recent years, it has been shown that Bhc can undergo photoisomerization to a dead-end product (4-methylcoumarin-3-yl thioether)³⁵⁰ that limits its cleavage yield. 6-Bromo-7-hydroxy-3-methyl-coumarin (mBhc)⁷³⁹ and NDBF^{211, 350} were then found to lead to a more efficient thiol photodeprotection.^{211, 350}

The same principle presented above for thiol caging can be translated to other functional groups, such as amines,⁷⁴¹ and conjugation chemistries. As an example, DeForest and Tirrell exploited an oxime-ligation chemistry to immobilize full-length proteins (BSA, collagenase, mouse anti-6xHis monoclonal antibody, and GF Delta) in a synthetic PEG matrix.³⁵¹ Upon cleavage of low 2P efficient NPPOC photocage, alkoxyamines were rendered available for oxime-ligation with aromatic aldehyde-modified proteins. Interestingly, the aldehyde was introduced at the terminus of a photocleavable linker (oNB), thus making it possible to release the patterned protein upon a second light exposure (Figure 2.60A).

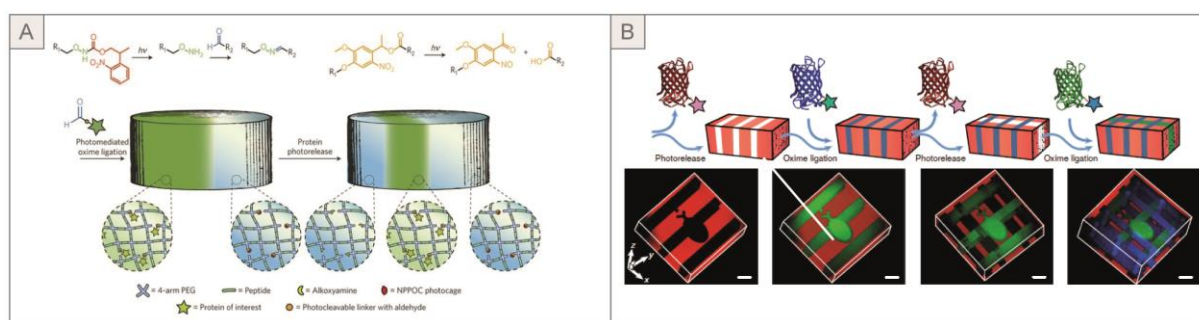


Figure 2.60 | Strategies for 2P-patterning based on photocleavage followed by covalent bond formation. (A) Schematic of 2P-patterning based on photomediated oxime-ligation and subsequent release based on oNB photolabile linker. (B) Cycles of 3D patterning of singly functionalized proteins and release based on oxime ligation and oNB cleavage. (A) Adapted with permission from ref³⁵¹. Copyright 2015 Springer Nature. (B) Adapted with permission from ref²¹². Copyright 2019 Springer Nature.

Mimicking the dynamic nature of native matrices is crucial to capturing the *in vivo* complexity and studying biological phenomena *in vitro*. Notably, the authors used the mentioned strategy to obtain a spatially defined reversible differentiation of human MSCs by the photoreversible immobilization of vitronectin. However, it is important to highlight that the native proteins need to be modified with an aldehyde linker in the latter

example³⁵¹ or with a maleimide-terminated linker for the Michael-type addition patterning described previously.^{735, 737, 740} Therefore, attention should be paid to the bioactivity retention of the derived protein. To this end, Shadish et al. recently used a chemoenzymatic sortase-mediated transpeptidation strategy to install single functional handles on fluorescent proteins, enzymes, and GFs.²¹² With this elegant one-step single functionalization and purification strategy named sortase-tag enhanced protein ligation (STEPL), proteins showed a near-native activity. Moreover, by exploiting the NPPOC photodeprotection-oxime-lygation and oNB-based photorelease strategy presented above, the authors achieved 2P-induced reversible patterning of entire functional proteins (Figure 2.60B). Mild and specific enzyme crosslinking can also be used to directly immobilize the desired molecule if the latter is previously tagged with the appropriate substrate.^{213, 244} By photoliberating a first substrate immobilized into an MMP-sensitive PEG matrix, Mosiewicz and colleagues were able to pattern recombinant proteins through photouncaging and subsequent enzymatic tethering of proteins by FXIIIa.²⁴⁴

Another interesting strategy for obtaining a bioorthogonal chemical patterning was developed by McNitt et al.²⁸⁴ Cyclopropenone-masked dibenzocyclooxynes were found to be decarbonylated and therefore available to a mild and specific click-chemistry conjugation with azide-terminated species upon two- and three-photon absorption. With a maximum efficiency at 690 nm, 3D photoclick patterning was reported into PAAm hydrogels.²⁸⁴

Physical Binding Patterning. Physical patterning is referred to here as the use of high affinity binding pairs for spatiotemporally defined immobilization of bioactive signals. A first covalent immobilization is still needed to pattern the first member of the binding pair. Then the introduction of the bioactive signal linked to the second binding partner enables the achievement of a site-specific patterning. Because the immobilization of these binding pairs is based on physical interactions, many chemical side reactions can be avoided. Moreover, the fact that it is performed in purely physiological conditions with no need of catalysts, pH changes, or potentially cytotoxic chemicals makes this step fully cytocompatible. In addition, the orthogonality of different binding partners guarantees higher specificity than most of the organic chemistry approaches and can contribute to a final lower background due to unwanted side reactions. The application of this concept to 2P-patterning was introduced for the first time by Wosnick et al.⁷³³ Upon localized thiol deprotection, the authors immobilized maleimide-derivatized biotin and then added a fluorescent streptavidin derivative that selectively bound the immobilized biotin.

Recently, Fisher et al. took advantage of the highly efficient thiol cage NDBF and immobilized maleimide-streptavidin in a concentration gradient fashion within a HA hydrogel (Figure 2.61A).²¹¹ Adding biotinylated epithelial growth factor (EGF) resulted in a bioactive GF pattern that was used to elucidate its influence on breast cancer cell invasion. Notably, the authors showed that EGF gradients can differentially influence the

cellular response to a drug, therefore highlighting the need for and usefulness of such complex drug screening platforms. By the same principle, Wylie et al. developed a system based on barnase–barstar and streptavidin–biotin, two orthogonal physical binding pairs.⁷³⁶ The maleimide modified binding peptides (barnase and streptavidin) were first patterned sequentially in different regions of an agarose hydrogel. Afterward, fusion proteins barstar–SHH (sonic hedgehog) and biotin–CNTF (ciliary neurotrophic factor) were added together and left to interact with their respective partners. The orthogonality of the binding partners enabled a “one-step” final process which leads to a precise “multi-color” patterning (Figure 2.61B). Similarly, fibroblast growth factor (FGF2) expressed as an albumin binding domain fusion protein was physically immobilized into an agarose hydrogel previously patterned with human serum albumin (HSA) (Figure 2.61C).³³³

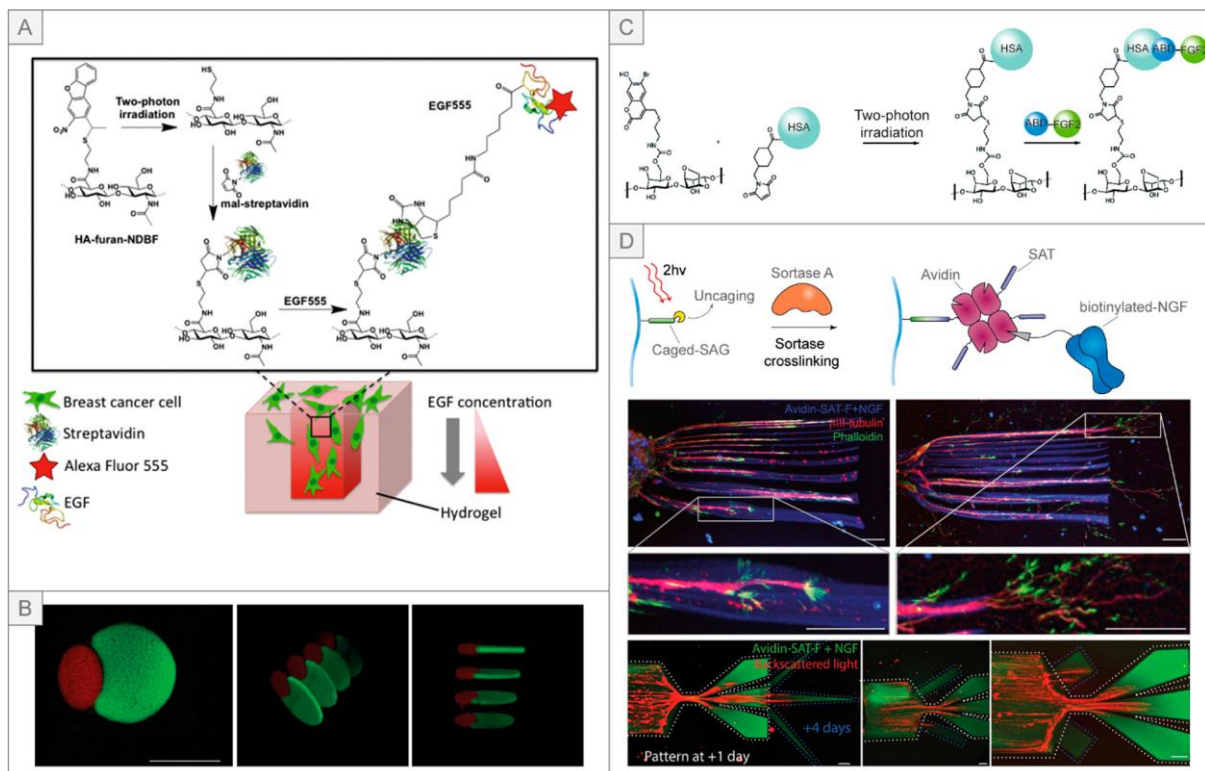


Figure 2.61 | 2P-patterning based on physical binding. (A) Schematic of nitro-dibenzofuran (NDBF) uncaging of thiol reactive groups and subsequent streptavidin–biotin based patterning of EGF. The ability to generate EGF gradients in a 3D matrix was exploited to study cancer cell invasion and cetuximab (EGF receptor inhibitor) response. (B) Patterning of multiple bioactive signals: CNTF (red) and SHH (green) (scale bar: 400 μm). (C) Schematic of coumarin uncaging of thiol reactive groups and subsequent albumin–albumin binding domain-based 3D patterning. (D) Schematic of sortase A mediated avidin–biotin patterning strategy (top) and fluorescence imaging showing axon (red) guidance into patterned (blue) regions (middle). The two sortase A substrates threonine donor peptide (SAT) and glycine donor peptide (SAG) can be ligated upon 2P uncaging of the latter. Biotinylated nerve growth factor (NGF) is immobilized through the binding with avidin bearing SAT. Bottom row shows delayed patterning, with neurons (red) following a first pattern (white dashed line) introduced after one day of culture and then a second one (blue dashed line) introduced after four days (Scale bars: 50 μm). (A) Adapted with permission from ref²¹¹. Copyright 2018 Elsevier Ltd. (B) Adapted with permission from ref⁷³⁶.

Copyright 2011 Springer Nature. (C) Adapted with permission from ref ³³³. Copyright 2011 American Chemical Society. (D) Adapted with permission from ref ²¹³. Copyright 2020 John Wiley and Sons.

Avidin–biotin affinity pair was also recently exploited to direct the neurite outgrowth of encapsulated dorsal root ganglia (DRG) from chicken embryo in transglutaminase crosslinked hyaluronan matrix ²¹³ (Figure 2.61D). 2P-uncaging of a sortase A substrate was followed by enzyme-mediated patterning of avidin bearing the second substrate. This, also with biotinylated-NGF binding, were performed as a one-step procedure, therefore circumventing the multiple incubation and washing steps needed in traditional 2P-patterning methods. The use of bacterial transpeptidase sortase A gives full orthogonality to mammalian matrices and enabled free-shape 3D patterning of NGF in the presence of cells with no cytotoxicity and negligible background. Broguiere et al. also demonstrated a time-controlled patterning, potentially applicable to any amine-containing matrices, with multiple rounds of growth factor immobilization at different time points following a preculture time in nonfunctionalized matrix. ²¹³ As it is probably the best-known example of physical high affinity binding in biological systems, DNA hybridization represents another elegant tool for 2P-patterning. To date, there are only a few examples of work in this direction. ⁷⁴²⁻⁷⁴⁵ Notably, Becker et al. achieved 3D patterning upon photorelease of NDBF protected oligonucleotides. ⁷⁴⁵ Uncaging of immobilized DNA strands allowed the hybridization with a second, complementary fluorescent DNA strand. However, this study did not explore the potential biological implications, such as the possibility to load the second DNA strand with bioactive signals. In addition to this, it is envisioned that the high compatibility and flexibility of DNA/RNA in terms of synthesis, modification, multiple dynamic interactions (e.g., toehold displacement), and capabilities (e.g., DNAzymes, ribozymes, aptamers, miRNA, siRNA) may bring new unexplored solutions into this field.

Preloaded Latent Patterning. Although many different materials have been developed to obtain spatiotemporal control over the presentation of bioactive ligands, none of them was tested in vivo. In addition to the complexity and generally high cost synthesis of small amounts of these materials, the major limitation lies in the unavoidably lengthy (30 min to days) incubation and washing steps. Notably, to overcome these limitations, Lee et al. “pre-loaded” caged-RGD adhesion peptides in PEG hydrogels with protease-degradable crosslinks. ⁷⁴⁶ Transdermal injection of this material allowed researchers to temporally and spatially control the presentation of the bioactive signals in vivo upon light exposure. Thus, in combination with the controlled release of incorporated VEGF, transdermal upregulation of adhesion, inflammation, and vascularization was shown. Using 3-(4,5-dimethoxy-2-nitrophenyl)-2-butyl ester (DMNPB) as a photolabile cage limited the study to the use of UV light (351 nm), which, as expected, showed a strong attenuation due to tissue absorption and scattering and may raise concerns about photodamage.

Recently, Farrukh et al. optimized the system by incorporating the efficient 2P cleavable group *p*-methoxynitrophenyl (PMNB). ⁷⁴⁷ Hence, the release of the photocage with NIR light (740 nm) having high

penetration depth and low damage potential was performed in the presence of cells (HUVECs and fibroblasts aggregate) and showed again the potential to direct adhesion, invasion (Figure 2.62), and angiogenic morphogenesis with spatiotemporal control. To date, the incorporation of caged bioactive ligands represents the closest strategy to *in vivo* 2P-patterning applications. However, it is worth mentioning that this approach appears to be limited to small molecules because immobilization and photocaging of whole proteins and enzymes without impairing their structure and activity represents a difficult task.

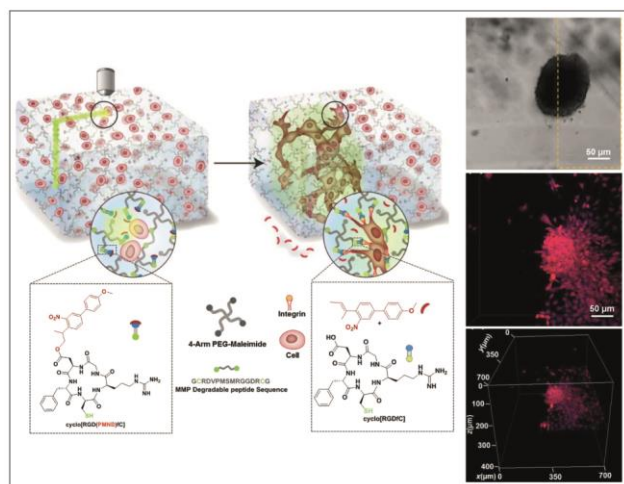


Figure 2.62 | Preloaded latent 2P-patterning. 2P uncaging of cyclic RGD adhesion peptide in MMP degradable PEG hydrogel (left). Light-guided cell migration from fibroblasts-laden fibrin clot (red) confined in the laser exposed region (yellow dashed box) after three days of culture (right) (scale bar: 50 μm). Adapted with permission from ref ⁷⁴⁷. Copyright 2018 John Wiley and Sons.

2.4.2.5. 2P-Patterning Limitations and Outlook

The precise positioning of bioactive cues by 2P-patterning offers a unique opportunity for *in vitro* micrometer control of the cells' extracellular environment. Technical developments and increasingly advanced chemical solutions are pushing this approach toward novel applications, both *in vitro* and *in vivo*. However, limitations remain, leaving room for improvement. The main issues of this technique are related to the long incubation and washing steps that normally require hours or days. Hydrogel dimension and porosity, diffusing signal dimension, and static or shaking conditions contribute to define the length of these steps. Therefore, the use of relatively large hydrogels and high molecular weight bioactive signals such as proteins leads to an exponential increase in the incubation time. To give an example, for a reaction-diffusion model of BSA into a 1 mm PEG hydrogel, 6.5 h are needed to ensure diffusion into the top 80% of the gel. ³⁵¹ Recently, the mixing of patternable signals directly with cells and gel precursor showed that a one-step patterning approach without incubation steps is also possible. ²¹³

In general, being a diffusion-limited process restricts the possibility of patterning multiple cues with multiple cages at orthogonal excitation wavelengths. In this case, by caging different reactive sites with selective cages

of different wavelength, one could immobilize multiple bioactive signals without the need for lengthy sequential incubation steps. We expect that the development of such a “multicolor” patterning strategy will strongly enhance the potential use of this technique.

Another aspect that needs to be considered is that immobilizing bioactive signals in a cell-laden matrix necessarily means that an excess of the soluble signal needs to be added in the first place. As a consequence, during this incubation step, the encapsulated cells are exposed to an uncontrolled burst of the bioactive signal. Only after several washing steps the pattern is revealed, and the cells can sense its different distribution in their surroundings. In this respect, the “pre-loaded” approach appears to be a valuable solution.

Another problem that may arise from the diffusion of the signal in the matrix is the undesired background as a result of off-target nonspecific binding to the matrix which might interfere with the patterned guidance cues. The use of antifouling inert polymers such as PEG and alginate helps, as well as the choice of more hydrophilic cages.²¹³ However, choosing the chemical strategy that better fits with these requirements does not necessarily lead to the desired processability. Therefore, it is important to first test and determine the processing window. For each system, the material response is different and needs to be evaluated in terms of scanning speed, laser power, and number of scans (Figure 2.58). In addition, identifying the processing window is necessary in understanding how to tune the parameters to generate chemical gradients.

In general, the ability to incorporate multiple biochemical signals in relative bioinert hydrogels will enable elucidation of many crucial biological processes such as chemotaxis, vasculogenesis, and neurite outgrowth in a biomimetic 3D environment. We envision that *in vitro* spatiotemporal manipulation of the cell/organoid environment will contribute to answering fundamental biological questions. The versatility of 2P-patterning also relies on the possibility of forming gradients of bioactive motifs at a scale (micrometers) that potentially enables single cell manipulation. Mimicking the true complexity of healthy and diseased tissues also holds great promise for several other applications, including drug discovery and regenerative medicine. Moreover, while *in vivo* applications remain unexplored, the state-of-the-art material/chemistry/instrument palette makes it a fascinating path to follow in the near future.

2.5. Outlook

In the previous sections, we have shared our honest perspectives on the strengths and limitations of photochemistries, bioinks/bioresins, and their use in photoactivated biofabrication. The progress in this field has been extensive, and for the first time in science, it is possible to print models of complex and challenging cellular interactions such as those found in the air–blood barrier,⁷⁴⁸ blood–brain barrier,⁶⁴³ epithelial–mesenchymal transition,⁷⁴⁹ models of thrombosis,⁷⁵⁰ and cancer metastasis⁷⁵¹ and to achieve continuous

mechanical and signaling gradients.⁵⁰⁰ Photoactivated materials have played an important role in this progress, and the benefits (and disadvantages) of this approach are summarized in Table 2.5.

Table 2.5 | Advantages and Disadvantages of Photoactivated Materials in Bioprinting.

Advantages	Disadvantages
<ul style="list-style-type: none"> • Spatiotemporal control • Applicable to wide ranges of materials • Mild crosslinking conditions • Applicable to all bioprinting techniques • Commercial availability of photo-activated printing materials • Enables physical/chemical gradients by tuning light intensity 	<ul style="list-style-type: none"> • Potential cytotoxicity of PIs, radicals and photo-reactive groups • Need for modification of polymers with photo-reactive moieties • Limited penetration depth • Dependency on optical transparency of materials

Although light-induced approaches have led to substantial advances in the biofabrication of tissue and ECM mimics, key challenges remain. As an example, radical chain-growth photo-crosslinking has dominated the field of light-responsive bioprinting, even though the toxicity of radicals, ROS, and PIs might be an issue in biological applications. Nevertheless, novel photoclick chemistry has emerged as a promising, more cell-friendly alternative. Despite its attractive features, the use of photoclick chemistry for bioprinting has been limited to date. Perhaps the most demanding challenge in the development of nonradical-based photo-crosslinking in bioprinting is the need to expand useful ligation reactions further into red-shifted regions. Visible and NIR light with upconverting nanoparticles will be a useful alternative to chromophore-based red-shifting. Besides using biologically benign light, longer wavelengths allow for greater penetration depths for novel volumetric printing. Moreover, wavelength selective λ -orthogonal photoactivation systems will allow for immobilization of multiple spatiotemporally controlled signals and for investigation of combinatorial effects, which may occur in diverse ECM. In addition, photoswitchable reactions have been widely explored in the past decade and could be used to add an additional level of spatiotemporal control for photoactivated materials. Beside the systems based on small molecules, such as azobenzene and ruthenium complexes, the exploitation of optogenetics proteins such as LOV2-J α (light-oxygen-voltage-sensing domain 2) and PhoCl showed promising results.⁷⁵²⁻⁷⁵³ An excellent review on this topic, with a focus on visible and NIR light activatable systems, has recently been published by Rapp and DeForest.⁷⁵⁴

Another important consensus from the current field is that highly substituted and highly concentrated photoresins are required for optimal processing parameters (faster processing speed, need of lower energy light source), yet the resulting hydrogels are highly crosslinked and dense with suboptimal biological properties. It is now well accepted that cells need relatively soft and porous permissive matrices to spread better and invade the material and to facilitate diffusion of nutrients and catabolic waste,⁷⁵⁵⁻⁷⁵⁶ as also shown by highly porous granular bioinks.^{474-477, 479-480} Functionalization can negatively influence the bioactivity of a

polymer⁷⁵⁷ or even determine the emergence of cytotoxicity/irritancy.⁷⁵⁸ The particular photoresins used in the publications of the review have been optimized for fabrication but not as ad hoc cell matrices. An important future direction of the field is to generate bioprinting materials which preserve more of the key biological properties of the unmodified polymers. It is interesting to note that the most significant results with deposition bioprinting have been achieved with nonmodified biological polymers (collagen, fibrin, PRP, matrigel). The major advantages and disadvantages of each of the biofabrication techniques described in this review are listed in Table 2.6. An important potential downside of orifice-dependent deposition bioprinting is the possible effects of biofabrication-associated stress on phenotypic expression of the cells, with broad changes in gene expression reported.^{175-176, 507, 509} More in vivo evidence is required to judge the impact of processing and chemical modifications of cells on their immunogenicity. Still, deposition printing is technically more compatible with printing multimaterials compared to VP printing, which is critical for fabrication of native tissue analogues with multimaterials and multiple cell types. Despite the difficulty in printing multimaterials at reasonable speed, the VP techniques allow biofabrication of more complex structures at higher resolution compared to deposition techniques, and thus, the VP techniques have high potential for mimicking the highly resolved nature of the ECM.

Table 2.6 | Summary of Advantages and Limitations of Each Bioprinting Technique.

		Advantages	Limitations
Deposition	Extrusion	<ul style="list-style-type: none"> • Printing anisotropy • Excellent multimaterial printing • Enable printing clinical-sized grafts 	<ul style="list-style-type: none"> • Shear stress to cells causes potential phenotypic changes • Low resolution • Clogging of nozzles • Layer-layer and line-line defects
	Droplet (voxelated printing)	<ul style="list-style-type: none"> • Facile generation of HT arrays • Excellent multimaterial printing • Control over the deposition pattern • Low cost of printers 	<ul style="list-style-type: none"> • Restricted to low viscosity inks • Clogging of nozzles • Mechanical stress to cells • Not suitable for printing tall structures • Stress to cells causes potential phenotypic changes
VP	Projection VP	<ul style="list-style-type: none"> • Fast printing speed in x-y plane • High resolution • High degree of freedom of printable structures (no need for supports) 	<ul style="list-style-type: none"> • Waste of cells and resins • Slow speed for multimaterial printing • Need to remove unreacted materials
	2P-SL	<ul style="list-style-type: none"> • Sub-cellular resolution • Use of cell-friendly IR light • High resolution patterning of biomolecules 	<ul style="list-style-type: none"> • High instrument cost • Small size of printable objects • Need to remove unreacted materials

Hybrid Bioprinting/Convergence of Biofabrication Techniques. One noticeable trend in the field is the emergence of contactless bioprinting modalities (i.e., acoustic,⁷⁵⁹ ultrasound,⁷⁶⁰ magnetic levitation,⁷⁶¹) and convergence of existing modalities to span length scales and achieve more accurate tissue models. For example, Liu et al. demonstrated that extrusion printing combined with droplet-based printing could provide multiscale control of cells in a gel, allowing for generation of in vitro tumor models with controlled relative positions of peripheral cells to cancer cell spheroids within a gel.⁷⁶² A bioink containing the spheroids was first printed by an extrusion printer, followed by deposition of single cells next to the spheroids with a resolution of 100 μm . Such constructs could not have been achieved either by an extrusion printer or a droplet-based printer, considering the limitations of each technique (Table 6). In addition, DLP,⁷⁶³ extrusion,⁷⁶⁴ or inkjet⁷⁶⁵ bioprinting combined with FDM printing have shown good promise in fabrication of mechanically reinforced tissue constructs.

Another hybrid approach that has emerged in recent years is the combination of different laser printing technologies,⁷⁶⁶ such as 2P-SL together with LIFT⁶⁶⁹ or multiphoton ablation.⁵⁹⁴ Laser ablation makes use of high laser power (10–100 times the P_{av} commonly used in 2P-SL) to induce optical breakdown in the material which results in permanent structural changes such as the formation of void spaces (subtractive method). Both single-photon ablation⁷⁶⁷ and 2P-ablation⁷⁶⁸ have been used to generate vasculature networks in biological matrices. However, 2P-ablation⁷⁶⁹ appears as a more powerful tool because of the intrinsic 3D confinement given by the nonlinear 2PA phenomenon. Recently, Kunwar et al. interestingly reported the use of UV–vis CLIP in combination with multiphoton ablation and 2P-microfabrication to achieve multiscale and multimaterial structures with construct size ranging from millimeters to centimeters and resolution from ~ 25 μm (CLIP) down to ~ 3 μm (multiphoton ablation and 2P-microfabrication).⁵⁹⁴ Nevertheless, it is noteworthy to mention that the 2P-SL key limitation of slow point-by-point laser scanning was not overcome by this work, because the 2P processing of a 600 μm^3 cube in a ~ 72 mm^3 pyramid construct made by CLIP required 62 min out of 66 min of the total fabrication.

The expanding palette of photoactivated materials shared between various biofabrication techniques represents a relevant strength of this field because it gives multiple possibilities for hybrid strategies that, to date, have only barely been explored. We envisage that well-designed hybrid bioprinting would allow generation of tissue/organ analogues with highly biomimetic multiscale architecture.

Acknowledgments. We are grateful to Dr. Killian Flegeau, Dr. Michael Müller, Dr. Xiao-Hua Qin, Dominic Rüttsche, Enrico Tosoratti, Lucca Trachsel, and Philipp Fisch for critically reading parts of the manuscript. Support from the Swiss National Science Foundation is acknowledged (CRSII5_173868 to M.Z.W.).

Contributions. M.L., R.R., F.S., and M.Z.W. listed as first authors contributed equally to this work.

CHAPTER 3

Volumetric (Bio)Printing

Introducing Photoclick Bioresins

In this chapter, a photoclick crosslinking mechanism based on thiol-norbornene chemistry is exploited for the first time in volumetric bioprinting. This novel printing technique enables printing of complex, low-defect 3D objects within seconds, overcoming major drawbacks of layer-by-layer additive manufacturing. Based on volumetric printing requirements, an optimized biocompatible photoresin based on gelatin-norbornene is developed showing excellent printing performances and biocompatibility. Simple, large-scale synthesis of gelatin-norbornene, printing time reduction and use of low polymer content are amongst the most relevant innovative aspects of this project.

MANUSCRIPT

Optimized Photoclick (Bio)Resins for Fast Volumetric Bioprinting

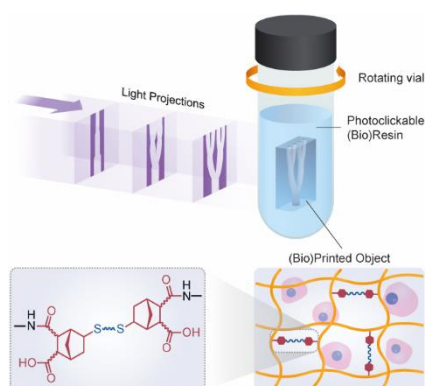
Riccardo Rizzo, Dominic Ruetsche, Hao Liu, Marcy Zenobi-Wong

Advanced Materials **2021** 33, 2102900

DOI: 10.1002/adma.202102900

Reprinted with permission from Adv. Mater. 2021, 33, 2102900, CC BY-NC 4.0, Wiley-VCH GmbH

Abstract



Volumetric printing (VP) is a light-mediated technique enabling printing of complex, low-defect 3D objects within seconds, overcoming major drawbacks of layer-by-layer additive manufacturing. An optimized photoresin is presented for VP in the presence of cells (volumetric bioprinting) based on fast thiol–ene step-growth photoclick crosslinking. Gelatin-norbornene (Gel-NB) photoresin shows superior performance, both in physicochemical and biocompatibility aspects, compared to (meth-)acryloyl resins. The extremely efficient thiol–norbornene reaction produces the fastest VP reported to date (≈ 10 s), with significantly lower polymer content, degree of substitution (DS), and radical species, making it more suitable for cell encapsulation. This approach enables the generation of cellular free-form constructs with excellent cell viability ($\approx 100\%$) and tissue maturation potential, demonstrated by development of contractile myotubes. Varying the DS, polymer content, thiol–ene ratio, and thiolated crosslinker allows fine-tuning of mechanical properties over a broad stiffness range (≈ 40 Pa to ≈ 15 kPa). These properties are achieved through fast and scalable methods for producing Gel-NB with inexpensive, off-the-shelf reagents that can help establish it as the gold standard for light-mediated biofabrication techniques. With potential applications from high-throughput bioprinting of tissue models to soft robotics and regenerative medicine, this work paves the way for exploitation of VPs unprecedented capabilities.

3.1. Introduction

In the last two decades, photochemical reactions have become increasingly used in the field of tissue engineering and biofabrication.¹³² Light as a remote trigger has enabled fine spatiotemporal control over biophysical^{214, 633} and biochemical properties^{212-213, 410} of photoactivated materials. Several 3D bioprinting techniques ranging from deposition-based (i.e., extrusion and droplet) to vat-polymerization-based (i.e., Digital Light Processing (DLP) and stereolithography (SL)) have exploited the versatile power of light to develop complex biomimetic cellular constructs within a broad range of size and resolution.^{132, 181, 578} Despite the great advances made with these techniques, however, there are still major limitations associated with the lengthy layer-by-layer manufacturing. First, the long printing process required to generate centimeter-scale constructs can impair scalability and clinical translation. The extended biofabrication time potentially compromises cell viability in addition to the intrinsic stress and cell death caused by the printing method itself (i.e., shear-stress during extrusion printing).^{175-176, 509, 536, 770} Also, printing in a layer-by-layer fashion is accompanied by structural limitations, such as the difficulties in generating unsupported overhangs and the presence of layer-layer and line-line defects.

Recently, there has been growing interest in a novel approach: volumetric printing (VP, also known as tomographic volumetric additive manufacturing or computed axial lithography), which promises to overcome current limitations of printing with cell-laden materials (bioprinting) and generate low-defect, free-form, complex large grafts within seconds.^{563, 570-571, 771} This powerful tool is based on the projection of dynamically evolving light patterns onto a rotating photosensitive resin (photoresin) container. When the resulting 3D light-dose accumulation locally exceeds the photo-crosslinking threshold, the desired solid object is generated. Recent reports have defined some of the key physicochemical features that theoretically define an optimal VP photoresin.^{563, 570} Viscosity emerged as a critical parameter affecting the printing resolution. Viscosity values >10 Pa s are necessary to effectively counterbalance the sedimentation of the solidified features during the printing process as demonstrated with the use of synthetic acrylate resins (i.e., SR399, polyethylene glycol diacrylate (PEG-DA)).^{563, 570} In addition, such high viscosity limits radicals and molecular diffusion-induced blurring.⁵⁶³ It follows that an ideal VP photoresin will benefit from reversible gelation properties. The first few reports on this method have indeed profited from the thermal gelation of photosensitive gelatin.⁵⁶³ In contrast to other vat-based techniques such as DLP and SLA, photoresin transparency is another essential feature, since light patterns need to pass through the entire depth of the rotating build volume. Because the vast majority of synthetic and naturally derived polymers do not absorb at the wavelength commonly associated with light-based printing (365–405 nm), photoresin transparency is determined by the photoinitiator (PI) concentration. However, when designing an ideal volumetric bioprinting (VBP) photoresin, physical and optical properties cannot be separated from its photochemical

performances. Photochemical reaction kinetics and mechanisms play a pivotal role in determining printing time, resolution, PI and polymer concentration. In addition, for biological applications, the interplay between physical and chemical properties should also guarantee high cell viability and the generation of a cell-permissive and cell-interactive matrix.

To date, these requirements have been only partially fulfilled with the chain-growth based crosslinking of highly concentrated (10%) gelatin methacryloyl (Gel-MA).⁵⁷¹ More efficient chemical strategies, such as thiol-ene photoclick reactions, have gained interest in recent years,^{132, 265-266, 268, 272, 381, 618, 772-774} and represent a viable way to overcome current limitations and satisfy VBP photoresin requirements. Thiol-ene step-growth crosslinking has a number of advantages compared to Gel-MA chain-growth polymerization.^{132, 268, 633, 774} Due to their exceptionally rapid reaction kinetic, thiol-ene photoresins require a significant lower generation of potentially harmful radicals compared to chain-growth mechanisms (i.e., Gel-MA) (Figure S3.1, Supporting Information).^{691, 773} This benefit is accompanied by the possibility to use a significantly lower polymer content, which results in a more permissive cellular matrix.^{755-756, 775} Furthermore, step-growth crosslinking efficiency makes it possible to significantly reduce the degree of substitution (DS), therefore largely retaining native biopolymer bioactive and physical properties.^{757, 776} In addition, oxygen insensitivity and selective reaction between the two complementary groups (thiol and -ene functionalities) pose a superior control over crosslinking reactions and lead to a homogeneous network formation with reduced shrinkage and mechanical stress, thereby overcoming another Gel-MA drawback that results from the generation of non-biodegradable kinetic chains and network defects.^{96, 776-777} Finally, Gel-MA has been the gold-standard for the past two decades in light-based biofabrication and its success, besides the desirable biophysical properties of gelatin, can be attributed to its ease of production and cost-effectiveness.⁹⁶ The straightforward synthesis and material handling made it possible for any lab to synthesize their own Gel-MA and resulted also in its commercialization. Therefore, for the field to adopt an alternative to Gel-MA, the photoresin should have the listed properties, but also be simple to produce at a large scale.

In this work we report on a gelatin-norbornene (Gel-NB)-based photoresin that fulfills all requirements as an ideal VBP photoresin. Starting from the establishment of a simple and scalable synthesis method, we demonstrate high tunability over rheological properties of Gel-NB step-growth based photo-crosslinkable resin and excellent biocompatibility, to serve as an ideal material for VBP, reporting the fastest centimeter-scale bioprinting process to date (≈ 10 – 11 s).

Among the various synthetic and naturally derived polymers that have been used in light-mediated biofabrication, we chose gelatin, by far the most widely studied material platform.^{96, 588, 778} Obtained via acidic or basic denaturation of collagen, the main component of human extracellular matrix, various gelatin derivatives have been successfully employed as a biocompatible matrix for virtually any cell type, ranging

from various primary cells^{588, 779} to cancer and stem cells.^{359, 591, 780} In addition to the retention of desirable collagen properties such as biocompatibility, enzyme-mediated biodegradability, and integrin binding sites (RGD), gelatin offers another key feature for VBP, represented by its reversible thermal gelation. By printing within a physically gelled bioresin, the printing resolution is maximized and cell sedimentation eliminated. In this study, gelatin has been functionalized with NB groups to obtain a resin crosslinkable via step-growth mechanism with optimal performance. In contrast to other –ene functionalities (i.e., vinyl sulfones and (meth)acryloyl), NB does not undergo Michael-type addition with free thiols, therefore limiting undesired side reactions.¹²⁹ Moreover, NB ring-strain conformation leads to an extremely fast relief upon thiyl radical addition, which outperforms other reported –ene photoreactive moieties and makes it an ideal candidate for our purposes.

3.2. Results and Discussion

The synthesis of Gel-NB is performed using carbic anhydride (CA) which, similar to the widely adopted synthesis method of Gel-MA with methacrylic anhydride,⁷⁸¹ reacts with free amino groups of the polypeptide chain. Compared to other previously reported Gel-NB synthesis strategies,^{691, 782-783} the use of CA offers several benefits. Among these, and of major importance for a widespread use of the resulting resin, CA is commercially available, inexpensive, and its reaction can be performed in aqueous solutions, thus avoiding the need for toxic organic solvents and complex multistep synthesis.⁶⁹¹ The use of an alkaline buffer (carbonate–bicarbonate 0.1 m, pH 9) limits gelatin free amino groups protonation, which inhibits the reaction with CA, and counterbalances the solution acidification that takes place during the formation of NB–dicarboxylic acid upon opening of the cyclic anhydride. Furthermore, the use of sequential pH adjustments and CA loading enables a better control over the reaction conditions and resulted in a 20-fold reduction of required reagent in addition to a major reduction in reaction time compared to previous reports (from 2–3 days to 1 h) (Figure 3.1).⁷⁸²⁻⁷⁸³ In short, to evaluate the most efficient synthesis strategy, we screened three different methods that differed in interval times between sequential CA loading and pH adjustment (Figure 3.1B). For each method, we also tested different Gel:CA w/w ratios (100:1, 50:1, 10:1) in order to target different DS. We showed that an interval time increase between CA additions, from 30 min (Method 1, M1) to 1 h (Method 2, M2), does not lead to a higher grafting yield (% of NB that has been successfully bounded to gelatin), thus suggesting a fast reagent consumption. In line with this observation, comparable DS and grafting yield can be obtained with an interval time reduced to just 10 min (Method 3, M3) (Figure 3.1C; Table S3.1, Supporting Information). To fulfill another desirable requirement, the production of large-scale batches, we adopted the fast M3 procedure to produce Gel-NB in synthesis scale up to 50 g. Thus, with a total reaction time of just 1 h, we show that a broad range of DS can be obtained, ranging from $\approx 0.01 \text{ mmol g}^{-1}$ ($\approx 3\%$) to $\approx 0.16 \text{ mmol g}^{-1}$ ($\approx 50\%$), and in reaction scales up to 50 g (Figure 3.1D;

Table S3.1, Figure S3.2, Supporting Information). The high photochemical performances of SH:NB photoclick reactions make it possible to use medium DS ($\approx 50\%$) for most light-assisted bioprinting techniques, including high definition two-photon stereolithography as recently demonstrated by Dobos et al.⁶¹⁸ Such DS enables the better preservation of gelatin bioactive and mechanical properties by largely leaving RGD motifs unmodified and by limiting the influence that functionalization can have on physical gelation.^{367, 776, 784-785} The reported inexpensive, accessible to nonexperts and scalable method for synthesizing Gel-NB with off-the-shelf reagents can contribute to its establishment as a gold-standard in light-mediated biofabrication techniques and its commercialization. On the other hand, in contrast to Gel-MA, Gel-NB based resins require the use of thiolated crosslinkers which can be, for example, represented by thiol-functionalized biopolymers (i.e., HA-SH, Gel-SH) or by the chemically defined and widely adopted bi- or multifunctional PEG thiol derivatives. High tunability, well-established safety profile, and commercial availability in gram scale^{111, 786} make PEG-based crosslinkers an attractive solution for standardized and relatively inexpensive Gel-NB based photoresins. As a rough estimation, by using the example of the VBP process demonstrated later in this work, a Gel-NB 50 g batch synthesis targeting a DS $\approx 50\%$ allows for about 250 to 500 prints (≈ 4 mL per print) using a Gel-NB concentration of 5% or 2.5%, respectively.

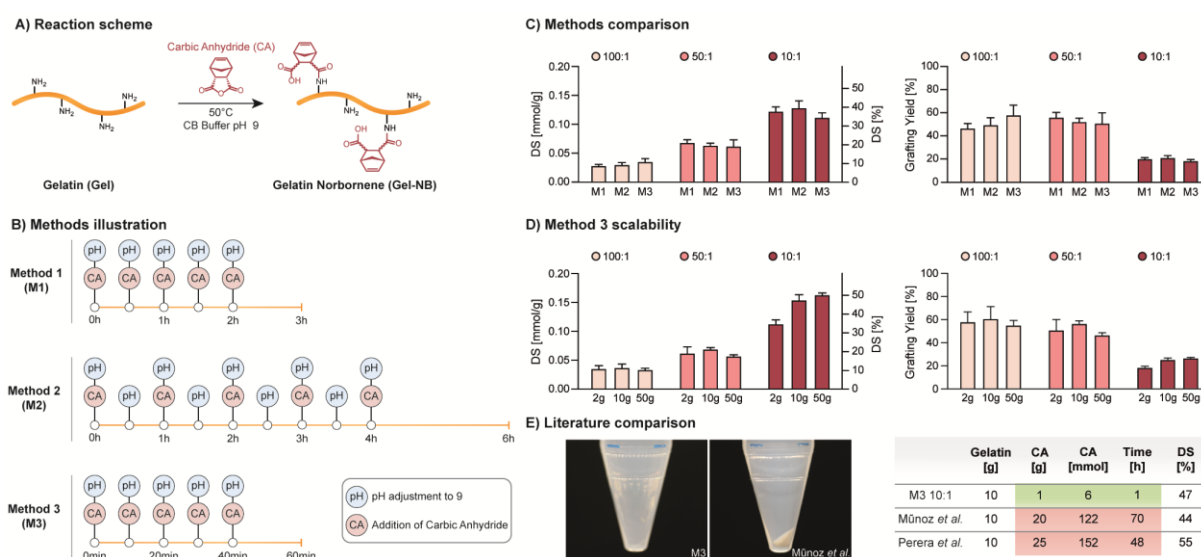


Figure 3.1 | Overview of gelatin-norbornene (Gel-NB) synthesis. A) Schematic of the reaction: carbic anhydride (CA) grafting on nonprotonated gelatin-free amines in pH 9 carbonate–bicarbonate (CB) buffer. B) Illustration of Gel-NB synthesis methods investigated in this study with varying interval time between sequential addition of CA and pH adjustment. C) Comparison of degree of substitution (DS, left) and norbornene grafting yield (right) obtained with the three different methods in 2 g scale synthesis. The synthesis was performed in 100:1, 50:1, and 10:1 Gel:CA w/w ratio. For DS comparison the right *y* axis (%) refers only to average values, standard deviations refer to left *y* axis (mmol g^{-1}). D) Comparison of DS and grafting yield resulting from Gel-NB synthesis at different reaction scales (2 g, 10 g, 50 g) using the fastest method (M3). The synthesis was performed with different Gel:CA ratio in order to target different DS. For DS comparison the right *y* axis (%) refers only to average values, standard deviations refer to left *y* axis (mmol g^{-1}). E) Comparison of Gel-NB synthesis ($\approx 50\%$ DS) with previous reports using CA.⁷⁸²⁻⁷⁸³ Compared to the

commonly used protocol developed by Muñoz et al.,⁷⁸² no visible excess of unreacted reagent is obtained upon centrifugation step at pH 7.4 using M3-based synthesis with 10:1 Gel:CA ratio (left). On the right, main improvements resulting from the use of M3 are highlighted.

We then showed strong control over the reaction's kinetic and mechanical properties obtainable by varying DS, Gel-NB concentration, SH:NB ratio, and thiolated crosslinker type (Figure 3.2). Photoreology was performed with 0.05% w/v LAP (Figure 3.2A), which has become the state-of-the-art PI for biofabrication purposes, thanks to its excellent water solubility, molar absorptivity, and better cytocompatibility compared to previous commonly used PIs such as I2959.³⁰³ Importantly, LAP-based photoresins are compatible with most light-mediated bioprinting techniques using 405 nm LED or laser diode light sources. Unless otherwise indicated, photoreology and VP have been performed with a formulation of Gel-NB and 4-arm-PEG-thiol (PEG4SH) in SH:NB equimolar amount containing 0.05% w/v LAP. As an example, a photoresin with a 1:1 SH:NB molar ratio formulation composed of 2.5% Gel-NB (DS \approx 50%) contains around 1.1% PEG4SH, for a total polymer content \approx 3.6%. First, Gel-NB DS showed excellent correlation with hydrogel stiffness (Figure 3.2B). Absence of hydrogel formation for DS \approx 3% suggests that a lower DS limit for a successful photo-crosslinking stands between 3% and 10%. In addition to tuning the mechanical properties based on DS, we tested the influence of Gel-NB concentration (DS \approx 50%), showing that a broad range of storage moduli (\approx 40 Pa to \approx 15 kPa) can be attained by changing the Gel-NB concentration from 1% to 10% (Figure 3.2C). In addition, the mechanical properties of the homogeneous step-growth photo-crosslinked network can be influenced by the SH:NB ratio (Figure 3.2D). In this respect, while keeping constant the Gel-NB concentration at 5% (DS \approx 50%), the use of 5 \times SH or 5 \times NB excess led to a less densely crosslinked network and therefore to a final lower storage modulus compared to a resin with 1:1 SH:NB ratio (Figure 3.2D). Notably, the alteration of the SH:NB ratio resulted in hydrogels with an excess of SH or NB moieties, which are therefore available for further functionalization steps (i.e., via photoclick chemistry or Michael-type addition).

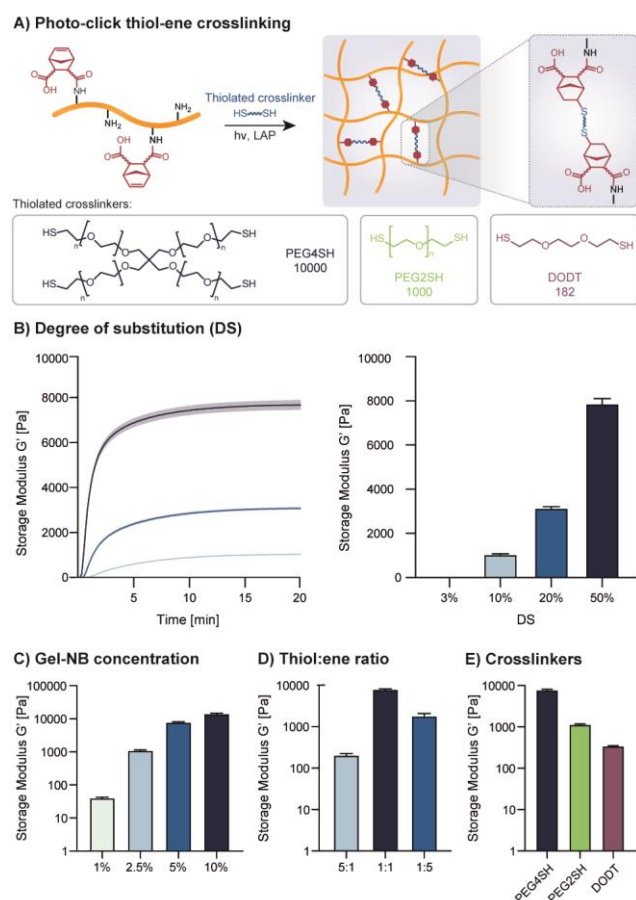


Figure 3.2| Photorheology characterization of Gel-NB-based resin using 0.05% w/v LAP as photoinitiator. Unless otherwise specified, photoresins are composed of 5% Gel-NB (DS \approx 50%) and PEG4SH at 1:1 SH:NB molar ratio A) Thiol-ene crosslinking scheme illustration of photoresin composed of Gel-NB and a thiolated crosslinker. Upon 405 nm excitation of LAP, the generation of radical initiation species leads to step-growth crosslinking (top). Structures and MW of thiolated crosslinkers used in this study (bottom). B) Investigation of DS influence on final hydrogel mechanical properties. The wide DS range results in tunable hydrogel stiffness. DS of \approx 3%, obtained with a Gel:CA ratio of 500:1, is also shown to be not enough to guarantee hydrogel formation. C) Investigation of Gel-NB concentration influence on final hydrogel mechanical properties. Highest storage modulus is observed for Gel-NB 10%. A reduction of polymer content is associated with a reduction of the final mechanical properties due to a less densely crosslinked network. D) Influence of SH:NB ratio on final hydrogel mechanical properties. The use of 5 \times norbornene or 5 \times thiols results in much weaker gels. E) Influence of different thiolated crosslinker on final hydrogel mechanical properties. The highest storage modulus is observed with PEG4SH, while a drastic reduction is shown with the use of bifunctional crosslinkers. A direct comparison between bifunctional crosslinker with different MW shows that also chain length plays an important role in determining hydrogel stiffness.

Furthermore, the use of different thiolated crosslinkers can influence the hydrogel properties (Figure 3.2E). In accordance with what has been recently shown by Van Hoorick et al.,⁷⁷² the use of multifunctional crosslinkers such as PEG4SH resulted in a higher storage modulus due to the grafting of multiple NB moieties in one junction knot. Less densely packed networks are instead formed with bifunctional linkers

such as PEG2SH or 3,6-dioxa-1,8-octanedithiol (DODT). Also, differences in the thiolated crosslinker chain length can have an impact on the final hydrogel properties, as has been shown here with the much lower storage modulus of Gel-NB/DODT formulation compared to Gel-NB/PEG2SH (Figure 3.2E). The extremely fast and highly tunable photo-crosslinking of Gel-NB represents an attractive advance for several 3D biofabrication techniques. In particular, in this work we report, for the first time, on its application in VP using a high-performance commercially available stand-alone tomographic 3D printer (Tomolite, Readily3D SA)⁷⁸⁷ (Figure 3.3A). To assess the VP performance of the photoresins, we used a built-in software function called “Dose Test” (see Supplementary Methods, Figures S3.3-3.5, Supporting Information). This function permits the study of photoresin behavior directly with the printer's light source, light path, and settings, therefore overcoming the problem of determining VP printability with measurement systems like photorheology. By projecting light into a nonrotating cuvette filled with resin, a matrix of dots with varying time exposure and light intensity is generated, allowing one to estimate the critical gelation threshold (CGT) for each photoresin formulation. CGT is the critical parameter for VP and can be defined as the minimum required light dose to form a stable gel. Below this threshold, the light absorbed by the photoresin is not sufficient to generate a stable crosslinked network, while above it overexposure occurs. The estimated CGT found with the parametric gelation map of the Dose Test facilitates the subsequent optimization of VP parameters which can slightly differ due to the lensing effect, rotating-mode, and volumetric absorption. During the printing process, the light-mediated gelation induces a change in refractive index of the crosslinked object which can be seen with a built-in camera (Video S3.1, Supporting Information). This change helps to identify the point in the printing process at which the object is formed and determines, after some reiteration, the optimal light dose. For sake of completeness, the CGTs found in this work are reported as light doses delivered from the printer in areal units (aCGT, mJ cm^{-2}) and, more accurately for such VP, in terms of volumetric absorbed energy (vCGT, mJ cm^{-3}) which takes into account build volume diameter and photoresin composition (PI absorption at excitation wavelength and concentration).

We show that, due to optimal physical and photochemical properties, Gel-NB/PEG4SH photoresins can be used to print perfusable branch models at relatively low light doses ($80\text{--}90 \text{ mJ cm}^{-2}$, volumetric absorbed energy: $8.59\text{--}9.69 \text{ mJ cm}^{-3}$), which corresponds to a printing time of only $\approx 10\text{--}11 \text{ s}$, the fastest reported to date, with a writing resolution of $\approx 200 \mu\text{m}$ (Figure S3.6, Supporting Information). Higher light-doses, and therefore longer printing time, led to overexposure and undesired photo-crosslinking (Figure 3.3B).

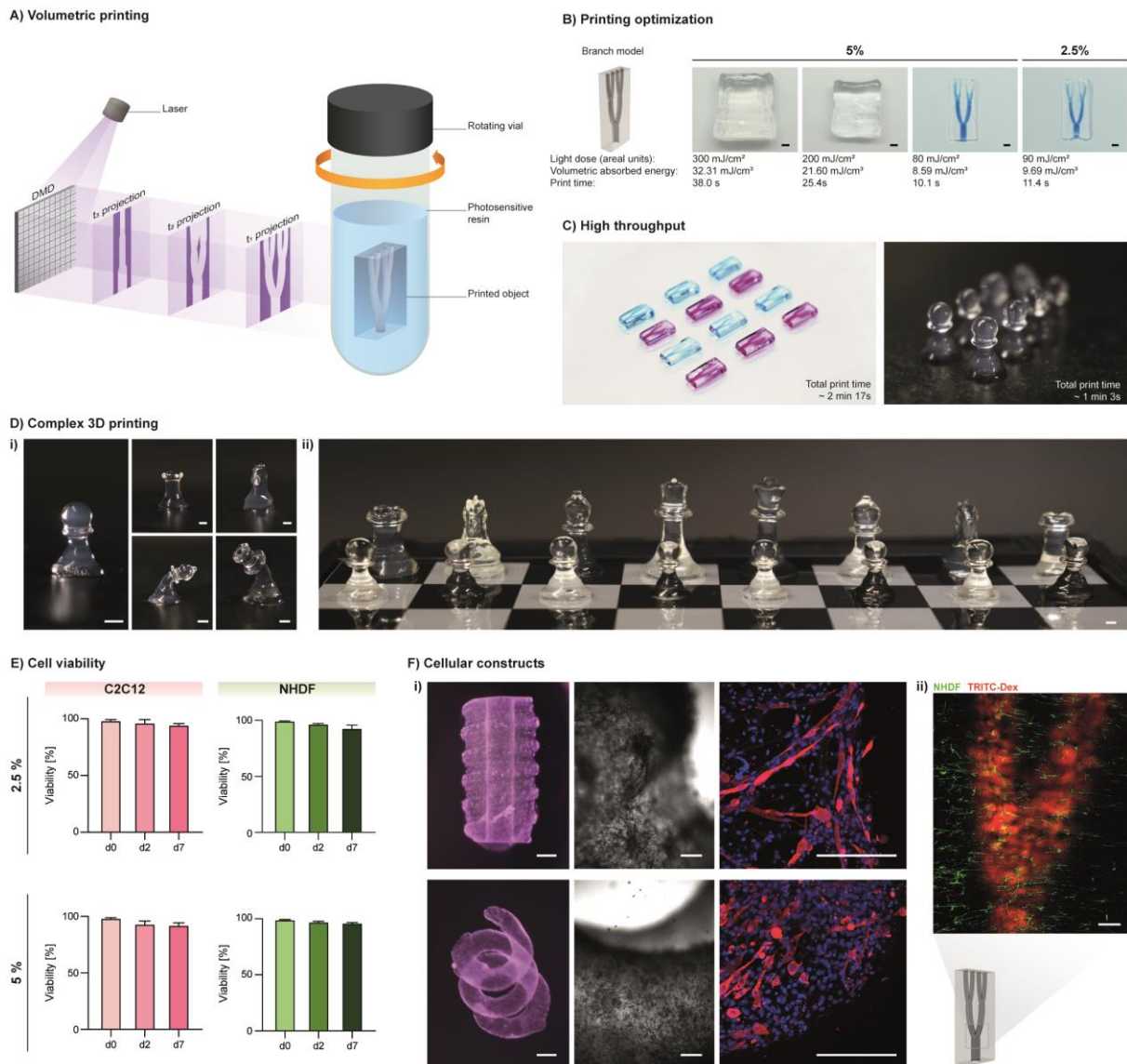


Figure 3.3 | Volumetric printing with Gel-NB. A) Illustration of volumetric printing principle of operation. A 405 nm laser beam (light purple) is directed toward a digital-micromirror-device (DMD), which generates dynamically evolving projection images (dark purple) in synchrony with the rotation of the glass vial containing the photosensitive resin. The desired object is solidified where the local light dose accumulation exceeds the gelation threshold. B) Printing parameter optimization using 5% and 2.5% Gel-NB/PEG4SH resin ($DS \approx 50\%$). A branch model perfusable with a high-MW blue-dextran solution is obtained with a low light dose, corresponding to extremely fast (≈ 10 – 11 s) printing (scale bar: 2 mm). C) Print upscaling with 2.5% Gel-NB/PEG4SH. The potential of fast printing is shown with the generation of replicas of twelve perfusable branch models (left, alternating perfusion with blue-dextran and TRITC-dextran) and eight pawn models (right). D) Printing of various 3D complex objects. i) VP with 2.5% Gel-NB/PEG4SH. From left to right: pawn, rook (top-left), knight (top-right), bishop (bottom-left), and queen (bottom-right). Due to the hydrogel softness, tall structures such as the bishop and queen models tend to bend when not submerged in liquid. ii) Printing at higher concentration (5% Gel-NB/PEG4SH) results in stiffer objects that can easily stand (scale bars: 2 mm). E) High cell viability ($>90\%$) after bioprinting is shown for mouse myoblasts (C2C12) and normal human dermal fibroblasts (NHDF) over 1 week of culture in both 5% and 2.5% Gel-NB/PEG4SH resin. F) Cellular constructs. i) Bioprinting of C2C12-laden complex free-form

objects with 2.5% Gel-NB/PEG4SH resin (left, scale bars: 2 mm). Bright-field close up on cellular construct after 1 week of culture showing cell spreading and proliferation on the soft matrix (right, scale bars: 200 μm). Immunofluorescence evidence of myotubes differentiation after 3 weeks of culture (Myosin Heavy Chain: red, Nuclei: blue, scale bars: 200 μm). ii) Confocal imaging of branch model bioprinted with NHDF-laden 2.5% Gel-NB/PEG4SH photoresin and perfused with TRITC-dextran (red) after 1 week of culture (scale bar: 500 μm).

Notably, the excellent NB photochemical properties allowed the developed resin to be printed at much lower Gel-NB concentrations (2.5%) compared to previous studies operating with 10% Gel-MA. Generation of low polymer content constructs is of paramount importance for biological applications, in order to enhance nutrient and catabolic waste diffusion, cell potency, proliferation, and migration.^{755-756, 775, 788} Furthermore, the combination of fast printing and lower polymer concentration significantly improves VP throughput. Taking into account that the printing time for VP is defined by the resin properties and not by the construct size, as with most of the other additive printing strategies, SH-NB photoclick reaction represents an unprecedented opportunity for upscaling printing of centimeter-sized complex geometries (Figure 3.3C). Moreover, in contrast to Gel-MA,⁵⁷¹ fast step-growth crosslinking of Gel-NB/PEG4SH makes a further postprinting curing step unnecessary, thereby limiting the total photo-crosslinking time to the few seconds of the printing process. In fact, when printed at the optimal CGT, the SH-NB based resin reaches $\approx 35\text{--}40\%$ of the fully crosslinked plateau stiffness (Figure S3.7, Supporting Information) upon a 8–14.5% conversion of NB groups (Figure S3.8, Supporting Information), which makes the generated object stable enough to be washed from uncrosslinked resin with warm solutions and to be stable under cell culture conditions for at least 3 weeks as shown later in this work. In this way, a wide variety of complex and stable 3D objects can be obtained with 2.5% Gel-NB/PEG4SH (Figure 3.3D i; Figure S3.9, Supporting Information) or 5% Gel-NB/PEG4SH photoresin (Figure 3.3D ii).

Low polymer content, low DS, low light exposure, and radical production are among the numerous desirable properties for a cell-containing photoresin (bioresin). Taking the retention of gelatin's biophysical properties together with its step-growth processability, Gel-NB emerges as an ideal material platform for VBP. Interestingly, we also observed that, in contrast to a recent work by Cook et al.,^[4] Gel-NB/PEG4SH does not require the addition of TEMPO as a radical scavenger, which in turn can have cytotoxic and genotoxic effects.⁷⁸⁹⁻⁷⁹⁰

In fact, the addition of a radical scavenger can be adopted to tune the gelation threshold by prolonging the initial induction period (exposure time without gelation). The resulting nonlinear gelation kinetics can help to improve the contrast between crosslinked and uncrosslinked parts during printing, but it does not represent a fundamental requirement for VP which is based on a pure threshold effect. For the generation of cell-encapsulated constructs, Gel-NB/PEG4SH photoresin was warmed to 37 $^{\circ}\text{C}$ and mixed with cells. The resulting bioresin was then transferred to the glass vial followed by thermal gelation upon cooling to 4

°C, to ensure high resolution printing and maintenance of homogeneous cell distribution. We showed excellent cell viability (>95%) upon printing and across 7 days of culture (>90%) (Figure 3.3E; Figure S3.10, Supporting Information) of encapsulated mouse myoblasts (C2C12) and normal human dermal fibroblasts (NHDF) for both the 2.5% and 5% Gel-NB conditions tested.

Although it has been observed that, due to the material's softness, some high-aspect-ratio designs printed with 2.5% Gel-NB/PEG4SH are not self-supporting in air (Figure 3.3D i, Bishop and Queen models), we show that complex free-form cell-laden structures can be bioprinted and easily cultured with good stability in cell culture media (Figure 3.3F). C2C12 muscle cells proliferated, spread, and differentiated into multinucleated contractile myotubes in the soft crosslinked matrix (Figure 3.3F i; Video S3.2, Supporting Information), opening new possibilities for rapid bioprinting of complex models and “living” biohybrid soft robotics.⁷⁹¹ Also, as a first tissue-on-a-chip proof-of-concept, we demonstrated the ability to bioprint a cell-laden (NHDF) perfusable branch model with mesoscale vasculature lumen size (Figure 3.3F ii).⁷⁹² Thanks to the high scalability given by the combination of simple Gel-NB synthesis and fast printing process, VBP holds great promise for high-throughput generation of complex tissue models such as skeletal muscle.

3.3. Conclusion

We have developed an optimized material platform (Gel-NB) for the novel VBP method and a simple and scalable synthesis strategy for its production. We anticipate that these findings will help overcome the limitations of Gel-MA and open new avenues for a more widespread use of high-performance Gel-NB resins in the field of tissue engineering and regenerative medicine. In addition, while pure gelatin-based resins have been shown to provide a good material platform for VBP, their limited bioactivity can be further tailored by relatively simple biofunctionalization with adhesion sites,⁷⁹³ drugs,⁷⁹⁴⁻⁷⁹⁶ and growth factors⁷⁹⁷ to target tissue-specific applications. We foresee that this VBP proof-of-concept will stimulate the development of other photoreins based on thermosensitive materials or non-thermosensitive, but highly viscous polymers modified for thiol–norbornene photoclick chemistry. For example, while maintaining Gel-NB as starting material, bringing in alternative biodegradable, cell-interactive thiol donors (i.e., HA-SH, Gel-SH, cysteines containing MMP cleavable peptides) will further broaden the VBP resin palette and improve the biological outcome.

3.4. Experimental Section

All chemicals were purchased from Merck and cell culture reagents from Gibco unless indicated otherwise.

Synthesis of Gel-NB. Gelatin type A from porcine skin was dissolved at 10% in 0.1 M pH 9 carbonate–bicarbonate buffer at 50 °C. Then, 1/5 of the total *cis*-5-norbornene-endo-2,3-dicarboxylic anhydride (carbic

anhydride, CA) necessary to get the desired Gel:CA ratio was added to the solution. Depending on the method used, the reaction was left to proceed for 30 min (Method 1 and 2) or 10 min (Method 3) prior to pH adjustment to 9 with NaOH 0.5 m solution. Under continuous stirring, pH adjustment and sequential addition of CA were repeated five times following the interval time defining each method (see Figure 3.1B). The solution was then diluted twofold with mQ H₂O prewarmed to 40 °C and the pH adjusted to 7.4 with a solution of HCl 0.5 m. Upon centrifugation for 15 min at 3000 rcf, unbound CA was deposited as white precipitate. The supernatant was then dialyzed at 40 °C against mQ H₂O with frequent water changes for 3–4 days and then freeze-dried. Gel-NB degree of substitution (DS) was determined by ¹H-NMR (Bruker Ultrashield 400 MHz, 1024 scans). In short, Gel-NB was solubilized at 40 mg mL⁻¹ in a solution of 0.5 mg mL⁻¹ 3-(trimethylsilyl)-1-propanesulfonic acid (DSS) in D₂O (Apollo Scientific). DSS was used as an internal standard to calculate NB millimoles per gram of gelatin by comparing integrals of the DSS nine methyl protons (≈0.5 to -0.5 ppm) with the two NB-ene protons (≈6.21–6.00 ppm) ($n = 3$, see Table S3.1, Figure S3.2, Supporting Information). DS given as a percentage was calculated based on the lysine + hydroxylysine content of porcine skin gelatin type A (0.325 mmol g⁻¹) estimated by Claaßen et al.³⁶¹

Synthesis of Gel-MA. Gel-MA was synthesized as previously described.⁴⁸⁹ DS was estimated with ¹H-NMR (Bruker Ultrashield 400 MHz, 1024 scans) in D₂O (Apollo Scientific). Gel-MA lysine integration signal (2.95–3.05 ppm) was compared to unmodified gelatin lysine integration signal (2.95–3.05 ppm). Phenylalanine signal (7.2–7.5 ppm) was used as internal reference. DS was found to be ≈55%.

Photoresin Preparation and Photoreology. Gel-NB photoresins were prepared by first dissolving the freeze-dried polymer in PBS at 37 °C. Either thiolated crosslinker, 10 kDa PEG4SH (JenKem Technology), 1 kDa PEG2SH or 3,6-dioxa-1,8-octanedithiol (DODT) was then added from a freshly prepared stock solution in PBS to get the desired SH:NB ratio. Similarly, the photoinitiator (PI) lithium phenyl-2,4,6-trimethylbenzoylphosphinate (LAP), was diluted in the photoresin mixture at 0.05% w/v from a freshly prepared 2% w/v stock solution in PBS. Gel-MA was prepared following the same procedure, without the addition of thiolated crosslinker.

Photoreology analyses were carried out on an Anton Paar MCR 301 equipped with a 20 mm parallel plate geometry, 6 mm glass floor, and Omnicure Series1000 lamp (Lumen Dynamics) used at 20% output power with 400–500 nm filter. All tests were performed at 37 °C to avoid physical gelation. A wet tissue paper was used in the chamber to prevent the sample from drying during the measurement. Samples were left to equilibrate for 5 min prior to starting the analysis. Oscillatory measurements were performed in triplicates ($n = 3$) at 5% shear rate and 2 Hz frequency with 200 μm gap and 10 s measuring point duration.

Volumetric Printing. 2.5% Gel-NB/PEG4SH and 5% Gel-NB/PEG4SH photoresins were prepared as indicated above, filtered through a 0.45 μm filter to remove potentially scattering particles and 3–4 mL were

transferred into the glass vial container. The photoresin was left to physically gel at 4 °C for 10–15 min. Printing was then performed on a commercially available volumetric printer (Tomolite, Readily3D SA)⁷⁸⁷ followed by heating in a warm bath to 37 °C to dissolve the uncrosslinked photoresin. Printed objects were washed in PBS prewarmed to 37 °C, while uncrosslinked photoresin was recovered for further use. For in-vial pictures, the printed objects were washed with PBS in the glass vial and imaged with printer built-in camera system. For in-air pictures, the printed objects were imaged with a Fujifilm XT-3 camera equipped with a macroextension tube. Branch models were perfused with high MW 2 MDa blue-dextran or 40 kDa tetramethylrhodamine isothiocyanate-dextran (TRITC-dextran).

Volumetric Bioprinting Procedure and Cell Viability. Gel-NB/PEG4SH photoresins were prepared as indicated above and filtered sterilized through a 0.20 µm filter. NHDFs were isolated from juvenile foreskin skin biopsies. Biopsies were taken under parental informed consent and their use for research purposes was approved by the Ethical Committee of Canton Zurich (BASEC-Request-Nr. 2018-00269). C2C12 and NHDF were added to Gel-NB/PEG4SH photoresin at 1 million cells mL⁻¹ and the resulting bioresin was transferred to glass vials sterilized via sequential EtOH 70% washing and UV-sterilization. After printing, the vials containing the printed objects were warmed up to 37 °C in a water bath. The cell-laden hydrogel was then washed under sterile conditions twice in warm PBS and then submerged in 6 mL cell culture media composed of DMEM + GlutaMAX-I + 2% horse serum + 1% ITS (Cornig) + 10 µg mL⁻¹ gentamicin for C2C12 and DMEM + GlutaMAX-I + 10% fetal bovine serum + 10 µg mL⁻¹ gentamicin for NHDF in a 6-well suspension culture plate (Greiner CELLSTAR). Media were changed every 4 days.

For the cell viability assay, samples after 0, 2, and 7 days of culture were incubated for 45 min in FluoroBrite DMEM supplemented with 1:2000 CalceinAM (Invitrogen), 1:500 Propidium Iodide (PI, Fluka), and 1:1000 Hoechst 33342 (Invitrogen). Imaging was performed on a Leica SP8 microscope (Leica) and Olympus Fluoview 3000 (Olympus) equipped with a 10× objective. Z-stacks were acquired from the samples surface at 5 µm steps and 300 µm into the sample. The presented pictures resulted from maximum intensity \bar{z} -projection. Cell viability after printing was assessed by counting viable (CalceinAM) and dead (PI) cells throughout the entire \bar{z} -range with the ImageJ Analyze particle function. Starting from day 2, due to the spread cell morphology, the total number of cells was more reliably calculated based on Hoechst 33342 stained nuclei.

Volumetric Bioprinting of Cellular Constructs. Cellular constructs were bioprinted following the described volumetric bioprinting procedure at 1 million cells mL⁻¹ for C2C12-laden spiral models and 10 000 cells mL⁻¹ for NHDF-laden branch models. Bright-field images of spiral-shaped cellular constructs and myotubes contraction videos were taken on a Axio Observer.Z1 (Zeiss) with a 5× and 10× objective, respectively. For immunofluorescence, after 3 weeks of culture, C2C12 constructs were washed 3× in PBS

and fixed in 4% paraformaldehyde for 2 h at 4 °C and washed again 3× in PBS + 0.02% BSA prior to permeabilization with 1% Triton-X100 in PBS for 15 min at room temperature. After washing three times in PBS + 0.02% BSA, the constructs were blocked for a further 15 min in a solution of 1% BSA, 1% Tween-20 in PBS, and then incubated with primary antihuman myosin heavy chain antibody (MF-20, DSHB, 1:20 in PBS + 0.02% BSA) for 2 h at room temperature. They were then washed three times with PBS, incubated with secondary antibody (Invitrogen, goat anti-mouse Alexa488, 1:1000 in PBS + 0.02% BSA), and Hoechst 33342 (Invitrogen, 1:1000 in PBS + 0.02% BSA) for 4 h at 4 °C. Samples were washed in PBS and imaged on Leica SP8 microscope (Leica) equipped with a 25× water immersion objective.

NHDF-laden branch models were stained by incubating them for 45 min in FluoroBrite DMEM supplemented with 1:2000 CalceinAM (Invitrogen). Prior to imaging on Leica SP8 microscope (Leica) equipped with a 10× objective, the samples were transferred to a glass coverslip and perfused with 40 kDa TRITC-dextran.

Acknowledgements. D.R. and H.L. contributed equally to this work. M.Z.-W. acknowledges ETH Grant application ETH-38 19-1 for their support. The authors further acknowledge Philipp Fisch for the help with compression testing, Dr. René Verel for the help with magic angle spinning NMR, and the assistance from ETH (ScopeM) imaging facility. Source .stl files for chess pieces were obtained from www.thingiverse.com/thing:585218 (under CC BY-SA 3.0 license). Source .stl files for glass, Klein bottle and ok-hand models were obtained from www.thingiverse.com/thing:460 (under GPLv2 license), www.thingiverse.com/thing:5217 (under Public Domain Certification) and www.thingiverse.com/thing:2216106 (under CC BY 4.0 license), respectively. [Correction added on 19 May 2022, after first online publication: CSAL funding statement has been added.]

Open Access Funding provided by Eidgenössische Technische Hochschule Zurich.

Contributions. R.R. conceived the project and designed the experiments. M.Z.-W. supervised the project. R.R. performed chemical synthesis, dose tests, volumetric printing, mechanical testing, confocal imaging and data analysis. D.C. and H.L. helped with cell culture, volumetric bioprinting and Live/Dead assays. The manuscript was written with the contributions of all authors.

3.5. Supporting Information

3.5.1. Supplementary Methods

Dose Test and VP optimization. Photorexin formulations prepared as indicated above were poured (~ 500-700 µL) into quartz cuvettes (CV10Q1400FS, Thorlabs) and left to physically gel at 4°C for 10-15

minutes. Cuvettes were then placed in a cuvette holder and then transferred onto a commercially available volumetric printer (Tomolite, Readily3D SA).^[1]

The Dose Test built-in function was used to project a matrix of dots (0.5 mm diameter, 0.5 mm spacing) within a variable broad dose range (see Figure S3.3, Supporting Information). After a first broad-range screening, a second, more refined Dose Test was performed within a smaller dose range to better estimate the critical gelation threshold (CGT). For VP optimization, photoresins were filtered through a 0.45 μm filter to remove potentially scattering particles and 3-4 mL were transferred into the glass vial container. The photoresin was left to physically gel at 4 $^{\circ}\text{C}$ for 10-15 minutes. Printing was performed with light dose around the CGT estimated by Dose Test. The crosslinking of the desired object was monitored with a built-in camera and printing process was stopped when the generated structure became visible due to change in refractive index (Video S3.1, Supporting Information). Printed objects were washed in PBS prewarmed to 37 $^{\circ}\text{C}$ to remove uncrosslinked photoresin. 4-5 additional prints were performed to fine tune the optimal light dose to be delivered to the resin container in order to get the desired structure. Calculation of $v\text{CGT}$ was done as previously reported,⁷⁷¹ using the following equation:

$$v\text{CGT} = I_{405} \alpha(\lambda_{405}) e^{-\alpha(\lambda_{405})z} t_e \quad (3.1)$$

where I_{405} corresponds to the light intensity delivered by the printer at 405 nm, $\alpha(\lambda_{405})$ is the absorption coefficient of the photoinitiator LAP at the same wavelength, z is the depth at the center of the photoresin volume and t_e is the exposure time. LAP absorption coefficient is calculated using the equation:

$$\alpha(\lambda_{405}) = 2.3\varepsilon(\lambda_{405})c \quad (3.2)$$

where $\varepsilon(\lambda_{405})$ is the molar extinction coefficient of LAP at the VP excitation wavelength (30 $\text{M}^{-1} \text{cm}^{-1}$ at 405 nm)¹⁵² and c is its molar concentration in the photoresin solution.

Compression test. Unconfined uniaxial compression tests were performed on a TA.XTplus Texture Analyzer (Stable Micro Systems) equipped with a 500 g load cell. Cylinder models of 2 mm height and 4 mm in diameter were generated by volumetric printing following the printing procedure described above. Fully-crosslinked control samples were prepared by filling PDMS ring molds (2 mm height and 4 mm inner diameter) with photoresin. The crosslinking was left to proceed in the photorheometer chamber for 20 minutes under the same light and temperature conditions used for photorheology. The samples were then placed between the compression plates and 0.1 g pre-load was applied to ensure full contact with the plates. Samples were left to relax for 2 minutes and then compress to 15% strain at a speed of 0.01 mm s⁻¹. Elastic compressive modulus was extrapolated by linear fitting of the initial linear region (0.5-5%) of the stress-strain curve.

Degree of conversion. Gel-NB (DS~50%) was analysed by $^1\text{H-NMR}$ (Bruker Ultrashield 400MHz, 1024 scans) in D_2O . Following the procedure indicated above, cylindrical objects (25 mm height, 4 mm diameter) were printed by volumetric printing at their optimized critical gelation threshold (CGT) with 5% Gel-NB/PEG4SH and 2.5% Gel-NB/PEG4SH photoresins containing 0.05% w/v LAP. After extensive washing with distilled H_2O prewarmed to 37°C , the cylindrical gels were freeze and lyophilized. Dried samples were then cut into small pieces, left to swell in D_2O , centrifuged to remove air bubbles and placed into 4 mm magic angle spinning (MAS) rotor. $^1\text{H-MAS-NMR}$ spectra were then taken on a Bruker Ascend DNP (400 MHz) with a spinning rate of 3.2 kHz. Norbornene alkene peaks ($\sim 6.21\text{-}6.00$ ppm) were normalized using phenylalanine protons ($7.5\text{-}7.15$ ppm) as internal standard.

Table S3.1 | Table summarizing the results obtained for Gel-NB synthesis with different methods, Gel:CA ratio and scale.

Method	Gel:CA ratio	Synthesis		DS [mmol/g]	DS [%]	Grafting yield [%]
		scale [g]				
M1	100:1	2		0.028 ± 0.002	8.7 ± 0.2	46.6 ± 3.5
	50:1	2		0.068 ± 0.004	20.9 ± 0.4	55.9 ± 3.7
	10:1	2		0.122 ± 0.006	37.6 ± 0.6	20.1 ± 1.0
M2	100:1	2		0.030 ± 0.003	9.2 ± 0.3	49.4 ± 5.3
	50:1	2		0.064 ± 0.003	19.6 ± 0.3	52.2 ± 2.6
	10:1	2		0.128 ± 0.010	39.5 ± 1.0	21.1 ± 1.6
M3	500:1	10		0.009 ± 0.001	2.9 ± 0.1	77.6 ± 10.0
		2		0.035 ± 0.004	10.8 ± 0.4	57.8 ± 7.2
	100:1	10		0.037 ± 0.005	11.4 ± 0.5	60.7 ± 8.7
		50		0.033 ± 0.002	10.3 ± 0.2	55.0 ± 3.5
	50:1	2		0.062 ± 0.009	19.0 ± 0.9	50.8 ± 7.5
		10		0.069 ± 0.002	21.1 ± 0.2	56.4 ± 2.0
		50		0.057 ± 0.002	17.4 ± 0.2	46.6 ± 1.7
		2		0.113 ± 0.006	34.6 ± 0.6	18.5 ± 1.0
		10		0.154 ± 0.008	47.3 ± 0.8	25.3 ± 1.3
10:1	10		0.154 ± 0.008	47.3 ± 0.8	25.3 ± 1.3	
	50		0.163 ± 0.003	50.1 ± 0.3	26.7 ± 0.5	

Table S3.2 | Volumetric printing parameters for 5% Gel-NB/PEG4SH (0.05% w/v LAP) and 2.5% Gel-NB/PEG4SH (0.05% w/v LAP).

	Photoresin	
	5%	2.5%
Printing Parameters	Gel-NB/PEG4SH (0.05% w/v LAP)	Gel-NB/PEG4SH (0.05% w/v LAP)
Light Dose	80 mJ cm ⁻²	90 mJ cm ⁻²
Volumetric Absorbed Energy	8.59 mJ cm ³ ⁻¹	9.69 mJ cm ³ ⁻¹
Average Intensity	7.89 mW cm ² ⁻¹	7.89 mW cm ² ⁻¹
Vial Turns	1	1
Rotation Speed	35.5° s ⁻¹	31.6° s ⁻¹
Projection Rate	123 Hz	110 Hz
Angle Step	0.288 °	0.288 °
Print Time	10.1 s	11.4 s

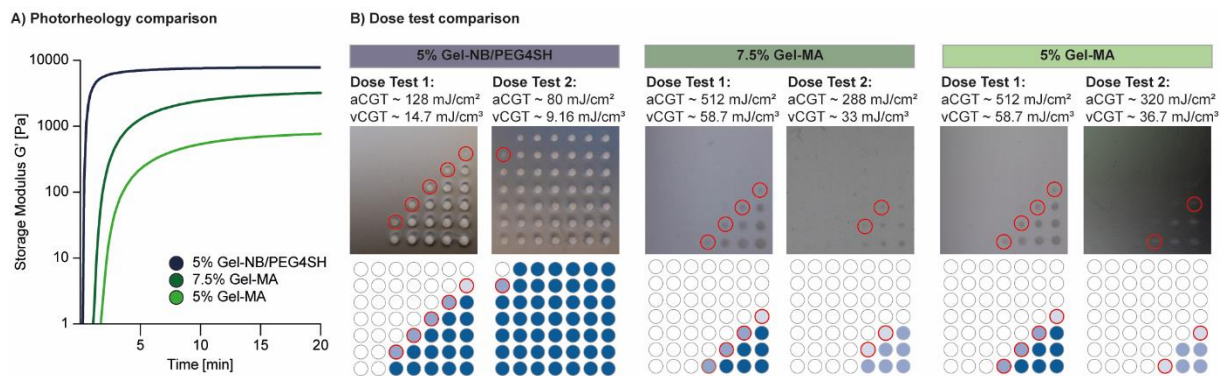


Figure S3.1 | Gel-NB vs Gel-MA. A) Photorheology comparison (average trace, $n=3$) of Gel-NB/PEG4SH and Gel-MA photoresins. Photoresin composed of 5% Gel-NB (DS~50%) and PEG4SH at 1:1 SH:NB molar ratio (total polymer content ~7.5%, 0.05% w/v LAP) shows a much faster photocrosslinking kinetic compared to Gel-MA (DS~55%) at 5% and 7.5% (0.05% w/v LAP), therefore generating fewer potentially harmful radicals to reach storage modulus plateau value. B) Dose test comparison showed a significantly lower critical gelation threshold (CGT) for Gel-NB/PEG4SH resin (aCGT: 80 mJ/cm^2 , vCGT: 9.16 mJ/cm^3) compared to Gel-MA (aCGT: 288-320 mJ/cm^2 , vCGT: 33-36.7 mJ/cm^3), confirming better performance of the photo-click thiol-norbornene-based resin.

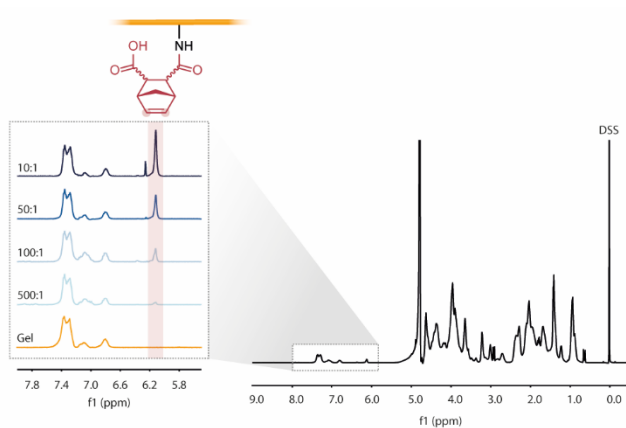


Figure S3.2 | NMR spectrum of Gel-NB. Norbornene alkene protons peak can be observed at ~6.21-6.00 ppm (red highlight), while it is absent in unmodified gelatin (Gel). Its integral is used to determine the DS in comparison with methyl protons of 3-(Trimethylsilyl)-1-propanesulfonic acid (DSS) internal standard (~0.5 to -0.5 ppm).

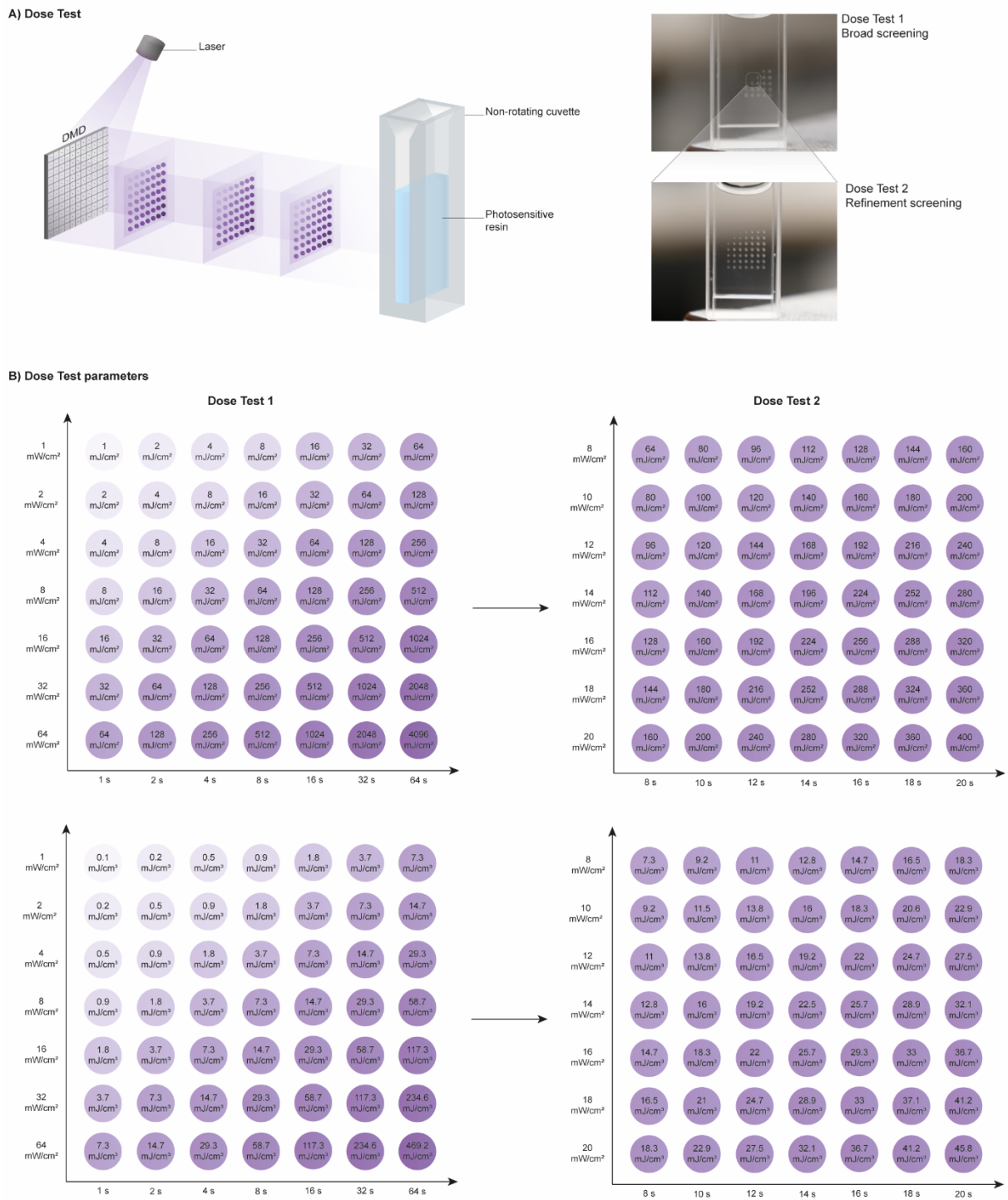


Figure S3.3| Dose Test. A) Illustration of Dose Test principle of operation (left). A 405 nm laser beam (light purple) is directed towards a digital-micromirror-device (DMD) which generates a grid of dots with varying light dose reported as purple shades (light purple = low light dose, dark purple = high light dose). The matrix of dots is projected towards a quartz cuvette containing the photoresin in static, non-rotating mode. When the light dose exceeds the critical gelation threshold (CGT), the crosslinked material becomes visible (right). After a first test performed in a broad light dose range (1 - 4096 mJ cm⁻²), a second Dose Test is performed in a narrower range around the estimated CGT which is identified by the visible dot crosslinked with the minimal light dose. This

refinement screening helps to better estimate the CGT for the following use of the photoresin in volumetric printing. B) Dose Test parameters used in this work reported as light dose per unit area (top row) and volumetric absorbed energy (bottom row) for Dose Test 1 and Dose Test 2.

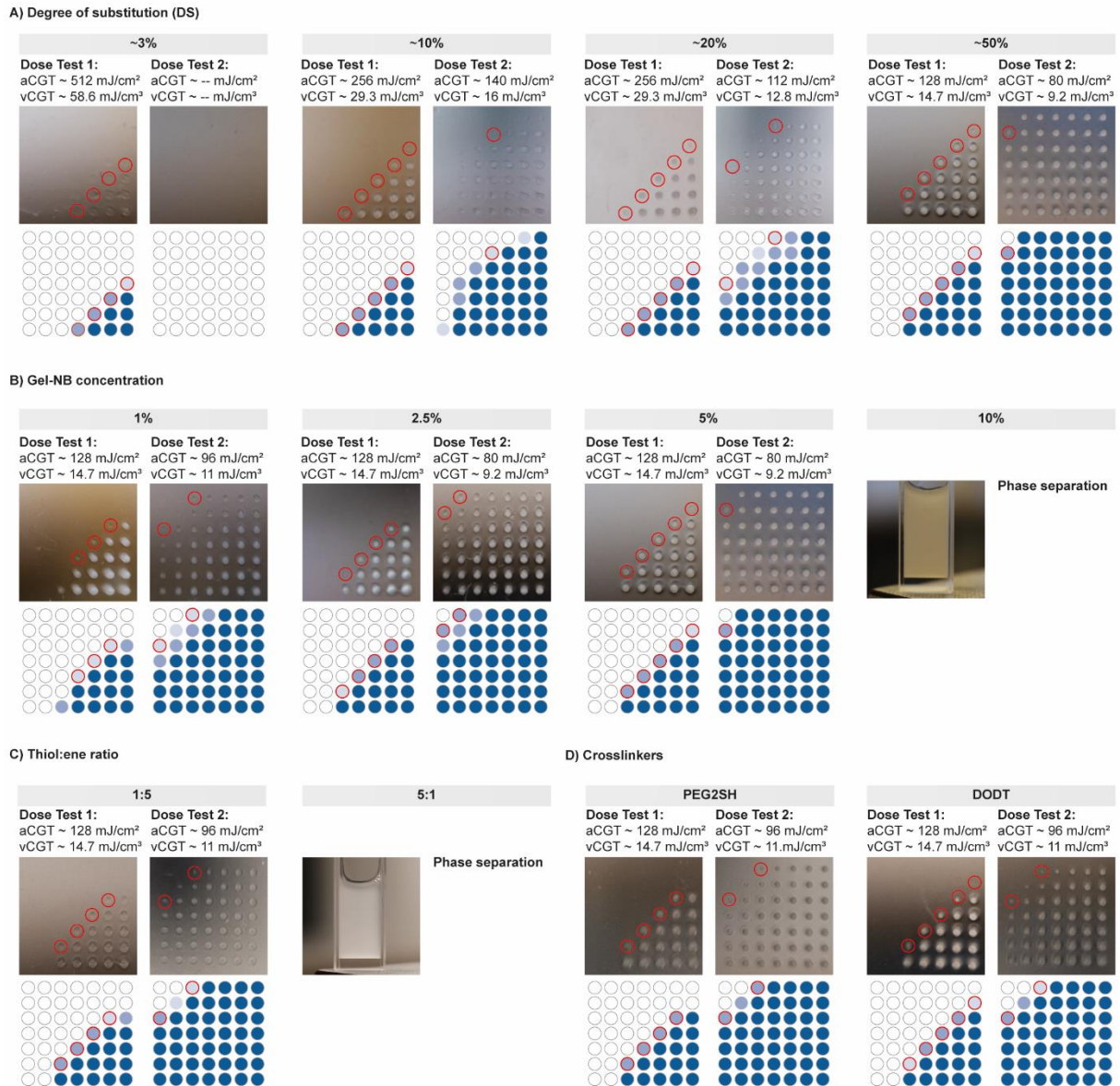


Figure S3.4 | Dose Test results for different photoresin formulations. Images of the cuvettes (top rows) are displayed as colored dots (bottom rows) with shades of blue from dark to pale blue referring to clearly visible to less visible crosslinked dot formation, respectively. Red circles highlight the dots obtained with the minimum light dose which identifies the critical gelation threshold (CGT). CGT values for each Dose Test are reported in areal unit (aCGT) referring to the light dose delivered from the printer and in volumetric unit (vCGT) referring to the volumetric energy absorbed by the photoresin. A) Results for photoresin composed of 5% Gel-NB with varying degree or substitution (DS), PEG4SH in 1:1 SH:NB molar ratio and 0.05% w/v LAP. B) Results for photoresin composed of Gel-NB (DS~50%) at varying concentrations, PEG4SH in 1:1 SH:NB molar ratio and 0.05% w/v LAP. For 10% Gel-NB formulation we observed phase separation when cooled down to 4°C. C) Results for photoresin composed of 5% Gel-NB

(DS~50%) and PEG4SH at varying SH:NB ratio, and 0.05% w/v LAP. For 5:1 thiol excess we observed phase separation when cooled down to 4°C. D) Results for photoresin composed of 5% Gel-NB (DS~50%) and varying thiolated crosslinker in 1:1 SH:NB ratio, and 0.05% w/v LAP.

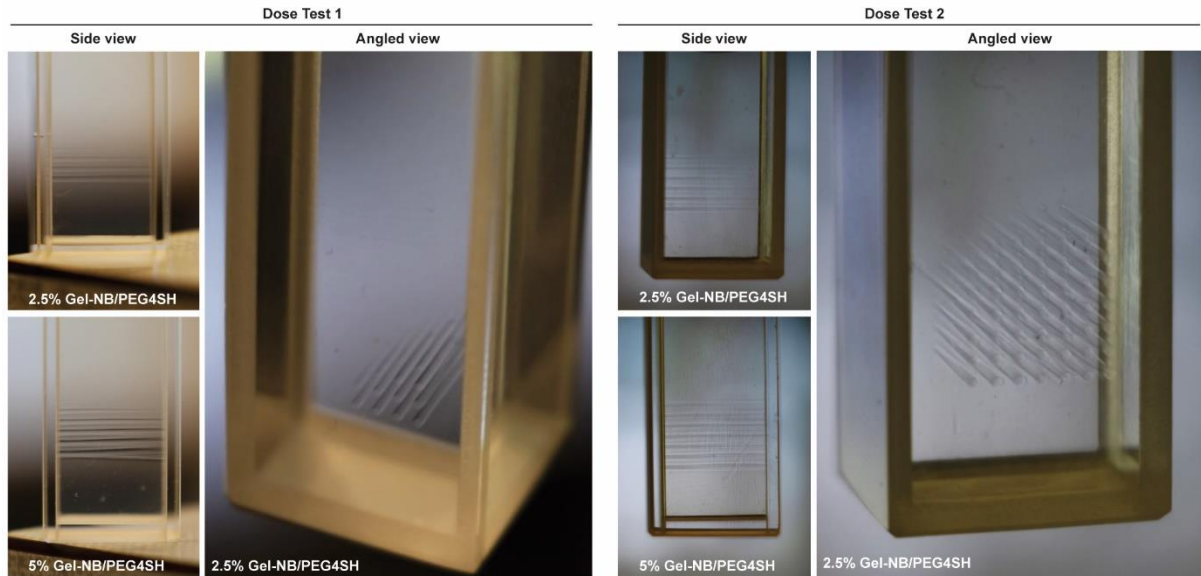


Figure S3.5 | Light penetration. Dose Test performed on 10 mm cuvettes showed light penetration and subsequent gelation throughout the entire path length (~89% of VP build volume diameter) for both 2.5% and 5% Gel-NB/PEG4SH photoresin formulations with 0.05% w/v LAP.

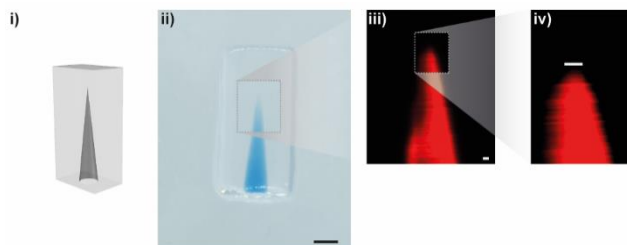


Figure S3.6 | Writing resolution, defined as the minimum distance at which two proximal features can be bioprinted without overlap, is estimated with the printing of an hollow cone structure. Image of the printed object perfused with high MW blue-dextran (Scale bar: 2 mm) and fluorescence imaging close upon TRITC-dextran perfusion (Scale bar: 200 μm).

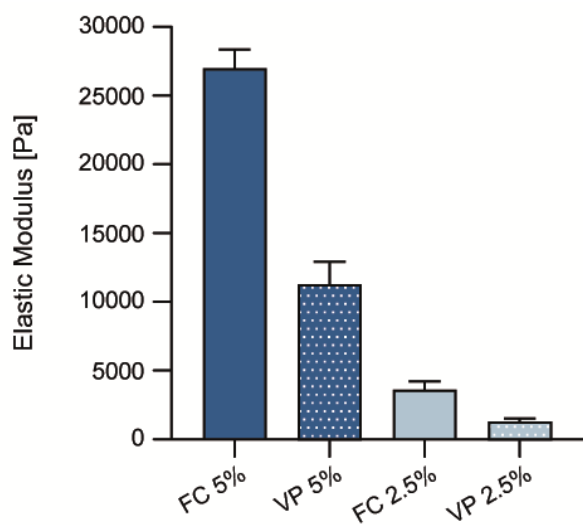


Figure S3.7 | Compression test on fully crosslinked (FC) and volumetric printed (VP) cylinders with 5% and 2.5% Gel-NB/PEG4SH photoresins with 0.05% w/v LAP. The resulting elastic modulus showed that the hydrogels obtained with volumetric printing at the critical gelation threshold have a lower stiffness (~35-40%) compared to their fully crosslinked counterparts.

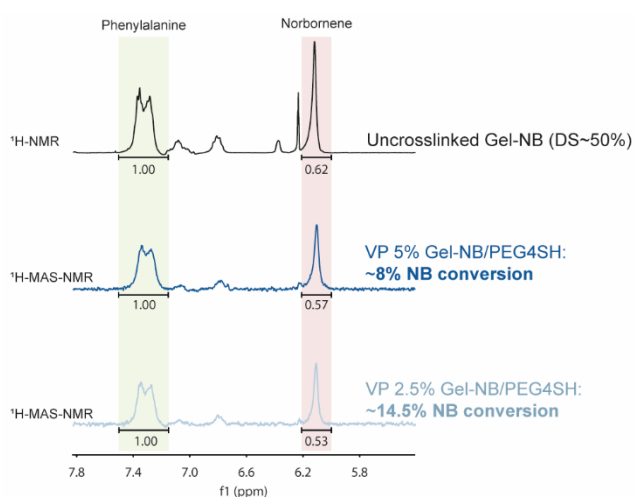


Figure S3.8 | Norbornene conversion. Comparison of norbornene alkene protons peak at ~6.21-6.00 ppm (red highlight) between Gel-NB (DS~50%) and hydrogels generated by volumetric printing with 5% Gel-NB(DS~50%)/PEG4SH and 2.5% Gel-NB(DS~50%)/PEG4SH photoresins. Phenylalanine protons (7.5-7.15 ppm, green highlight) were used as internal standard. The degree of conversion for the two photoresins was estimated to be around 8-14.5%.

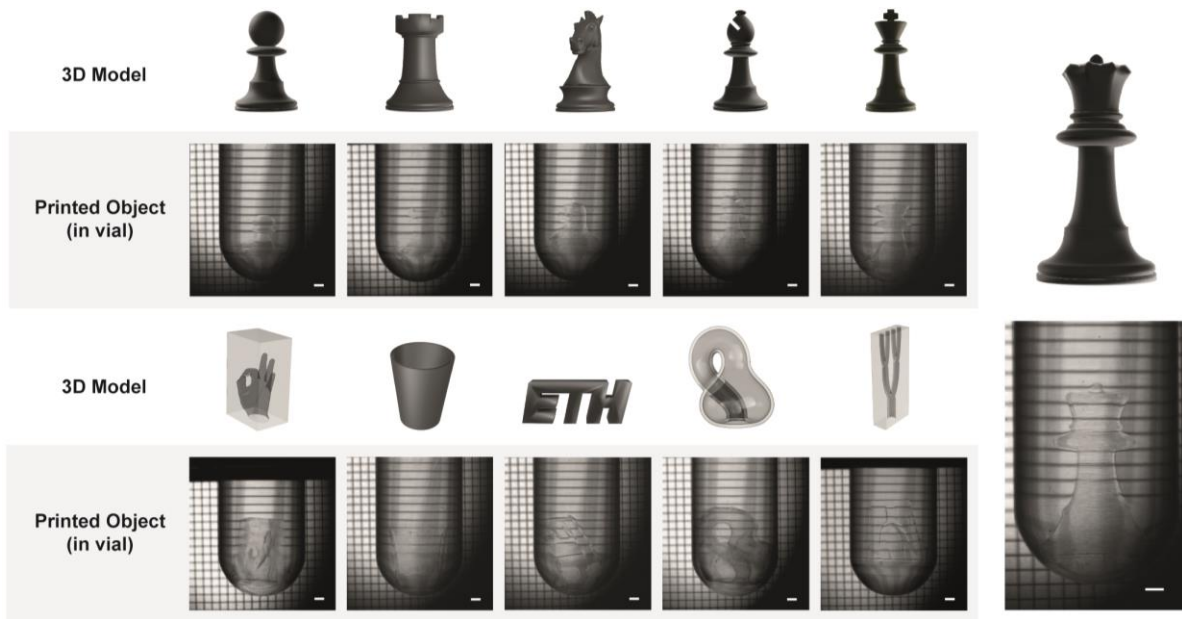


Figure S3.9 | 3D .stl models (top row) and respective volumetric printed object imaged in the glass vial photoresin container. From top left to bottom right: Pawn, Rook, Knight, Bishop, King, Queen, hollow ok-hand, glass, ETH logo, Klein bottle, Branch model. (Scale bar: 2 mm)

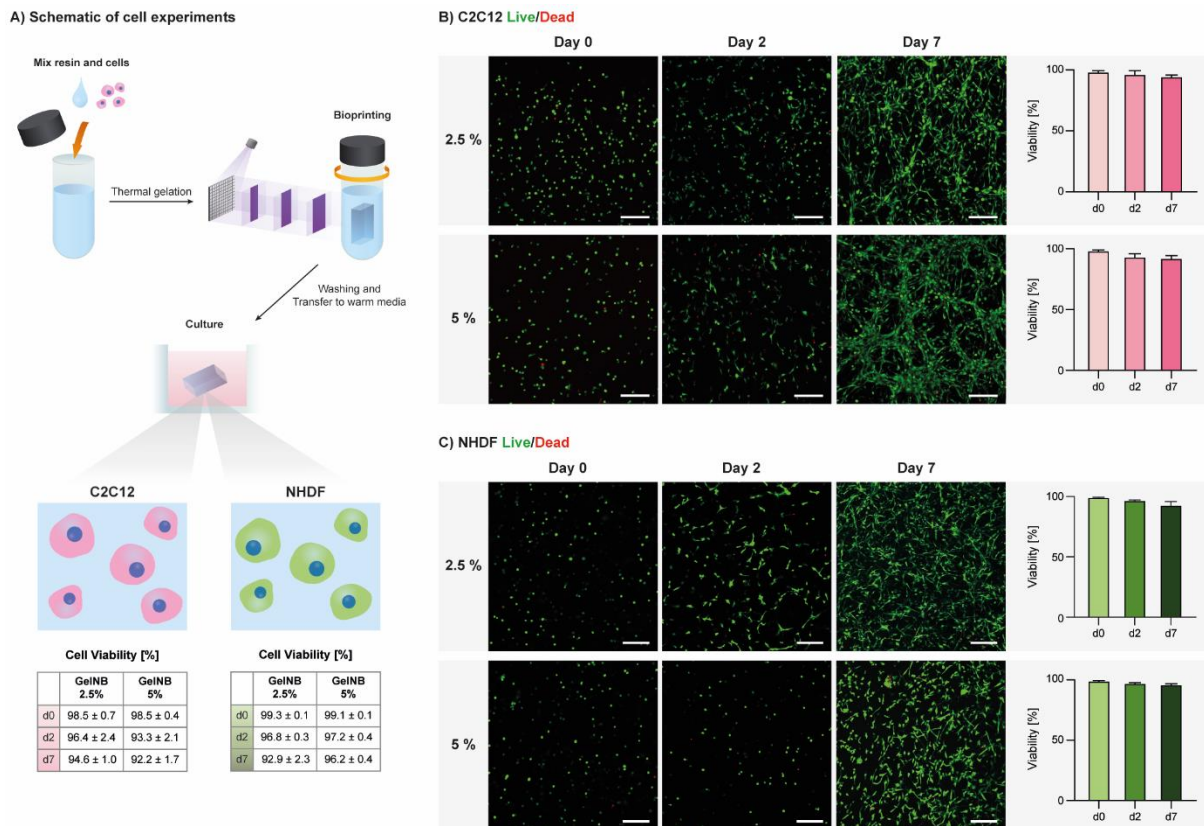


Figure S3.10 | A) Schematic of cell experiments procedure and summary of resulting viability. B) C2C12 Live/Dead viability assay with representative images C) NHDF Live/Dead viability assay with representative images (Scale bar: 200 μ m).

CHAPTER 4

Multiscale Hybrid Printing

As discussed in Chapter 3, volumetric printing can be used to generate perfusable hollow constructs opening to potential applications for organ/tissue-on-a-chip technologies. However, its current negative resolution is limited to few hundred micrometers. To generate perfusable geometries with higher definition, targeting microcapillary calipers, volumetric printing is herein combined for the first time with high resolution two-photon ablation. Defect-free volumetric printing, convergence of printing methods and the generation of organotypic multiscale perfusable constructs represent the key innovations of this project.

MANUSCRIPT IN REVISION

Multiscale Hybrid Fabrication: Volumetric Printing Meets Two-Photon Ablation

Riccardo Rizzo, † Dominic Ruetsche, † Hao Liu, Parth Chansoria, Anny Wang, Amelia Hasenauer, Marcy Zenobi-Wong

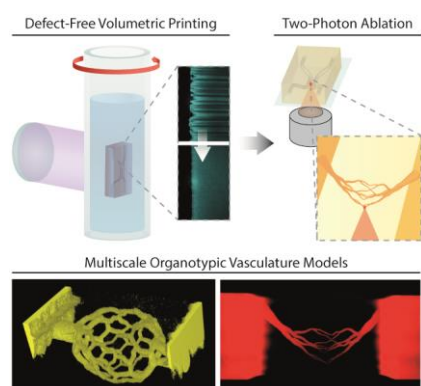
bioRxiv 2022

DOI: 10.1101/2022.10.28.513651

†Equal contributions.

Reprinted with permission from authors.

Abstract



The vascular tree spans length scales from centimeter to micrometer. Engineering multiscale vasculature, in particular from millimeter vessels to micrometer-size capillaries, represents an unmet challenge and may require the convergence of two or more printing modalities. Leveraging the great advances in light-based biofabrication, we herein introduce a hybrid strategy to tackle this challenge. By combining volumetric printing (VP) and high-resolution two-photon ablation (2PA), we demonstrate the possibility to create complex multiscale organotypic perfusable models with features ranging from mesoscale (VP) to microscale (2PA). To successfully combine these two methods, we first eliminated micrometer-size defects generated during VP process. Due to optical modulation instability of the laser source and self-focusing phenomenon that occurs when the light triggers the photoresin crosslinking, VP printed constructs feature micrometer-size filaments and channels. By optical tuning the refractive index of the photoresin, we demonstrate defect-free VP that can then be combined with 2PA. To facilitate the 2PA process and meet VP requirements, we introduce a purely protein-based photoclick photoresin combining gelatin-norbornene and gelatin-thiol. By optimizing defect-free VP and 2PA processes, we finally demonstrate the possibility to generate complex 3D vasculature-like constructs with features ranging from $\sim 400\ \mu\text{m}$ of VP to $\sim 2\ \mu\text{m}$ of 2PA. This hybrid strategy opens new possibilities to better recapitulate microtissues vasculature and complex architectures, with particular potential for microfluidics and organ/tissue-on-a-chip technologies.

4.1. Introduction

The engineering of organs and tissues on-a-chip holds great promise for biomedical applications such as drug testing and disease modeling.^{191, 798-800} Despite technological advances, current microtissues are much simpler than their native counterparts. In particular, engineering the complex perfusable architectures of the vasculature tree still represents a major challenge in this field. In the past decades, great effort has been made to individually recapitulate the various components of the vasculature tree, from centimeter-scale aorta to micrometer-scale capillaries.^{792, 801} However, the field lacks strategies that enable the engineering of multiscale constructs featuring meso- (hundreds of μm) and micro-vasculature (few – tens of μm).

Light-based printing offers a broadening and increasingly sophisticated range of techniques for precise fabrication of perfusable tissue architectures.¹³² Volumetric printing (VP) is a novel light-based biofabrication method emerging as a promising technology for such applications, enabling the printing of complex centimeter-size models within seconds. Recent studies have demonstrated the possibility to create hollow, perfusable structures, possibly targeting mesoscale vasculature.^{187, 802-803} However, to fully replicate a multiscale vasculature-like model, VP fall short of reaching microcapillaries size. Another light-based method named two-photon ablation (2PA) offers instead complementary capabilities, being limited in printing time and construct size, but reaching the highest resolution of any biofabrication method ($\leq 1 \mu\text{m}$). 2PA is based on multiphoton ionization induced by high-intensity pulsed lasers,⁸⁰⁴⁻⁸⁰⁵ and has been explored to form cell-instructive microchannels.⁸⁰⁶⁻⁸¹¹

Seeking to reproduce a multiscale vasculature-like construct, we show for the first time a hybrid VP and 2PA printing technology. In order to successfully combine these two techniques, we first developed a strategy to remove the VP-generated microdefects. As recently shown by Liu et al.,⁸¹² optical modulation instability (OMI) results in the formation of hydrogel microfilaments and microchannels (void spaces between microfilaments) in the range of 2 -30 μm propagating via self-focusing waveguides (Figure 4.1A). Therefore, although commonly described as defect-free due to the layer-less printing modality, VP printed constructs have in microfilaments and microchannels a major source of defects which can limit their applications. In fact, while on one hand microchannels can improve diffusion of nutrients into the printed construct, they can also act as physical guidance cues for cells to spread, migrate, align and deposit extracellular matrix (ECM).⁸¹² Although optimal for anisotropic tissues such as muscle and tendon, this unidirectional microarchitecture is not desirable for all applications requiring an isotropic cell spreading without preferential outgrowth direction or cell confinement in a defined region (i.e., channel wall). In particular for the combination with 2PA, the presence of microchannels hinders high-resolution printing which requires a homogeneous, defect-free material substrate to fully guarantee precise control over hollow architectures.

Recently, Rackson et al. proposed a strategy to reduce the filamentation effect by reducing the light exposure of the printing process, followed by LED-based uniform exposure (flood illumination) to develop the 3D constructs.⁸¹³ Although theoretically simple and inexpensive, this method requires significant fine-tuning of the exposure time that yields both high resolution and construct stability. In our experience, elimination of microchannels and microfilaments with hydrogel forming photoresins could not be successfully and consistently achieved using this method. In this study, we therefore first introduce an alternative strategy to remove the microdefects by optical tuning of the photoresins, eventually allowing the formation of homogeneous constructs suitable for complex VP / 2PA hybrid printing targeting multiscale organotypic perfusable models.

4.2. Results and Discussion

4.2.1. Refractive Index: How to Limit Self-Focusing Effect

In VP, a laser beam is directed towards a digital micromirror device (DMD) which projects a series of light patterns onto a rotating vial containing the photocrosslinkable material (photoresin) (Figure 4.1Ai). The projections result in a 3D light-dose accumulation in the photoresin. When the light-dose exceeds the material's critical gelation threshold, the desired 3D model is formed and can be retrieved with the removal of the uncrosslinked photoresin. However, when reaching the photoresin, the laser beam featuring a speckle-pattern intensity noise causes the formation of microfilaments and microchannels,⁸¹² herein also generally described as microdefects. This phenomenon originates from the non-linear nature of the photosensitive material which shows a change in refractive index (RI) between its uncrosslinked to crosslinked state. When the local intensity noise maxima crosslink the photoresin, the increase in RI of the crosslinked part results in a self-focusing effect which eventually acts as an optical trap reinforcing the generation of the microfilaments (Figure 4.1Aii).⁸¹⁴⁻⁸¹⁶ As the laser noise pattern features low intensity regions between local maxima, uncrosslinked volumes (microchannels) are also formed. Aiming to obtain homogenous, defect-free VP prints suitable for further processing by high-resolution 2PA, we investigated the impact of photoresin RI in limiting the self-focusing effect.

First, to match the requirements of both VP and 2PA, we chose to use a photoresin based on gelatin-norbornene (Gel-NB) and gelatin-thiol (Gel-SH) (Figure 4.1Aii). As previously shown, thiol-norbornene click-chemistry and gelatin thermal gelation make such photoresin an ideal candidate for VP.¹⁸⁷ Moreover, as 2PA is known to be more efficient with protein-based systems,⁸⁰⁴ here we introduce for the first time in VP a purely photoclick gelatin-based formulation featuring Gel-SH (Figure 4.1Aii). For all the experiments, a photoresin composed of 2.5% Gel-NB/SH (with 1:1 NB:SH molar ratio) and 0.05% lithium phenyl-2,4,6-trimethylbenzoylphosphinate (LAP) as photoinitiator (PI) was used.

This initial formulation (RI: 1.3390) was then optically tuned with the addition of iodixanol (Iod) at 10%, 25% or 50%. Iod is a non-toxic, water soluble, non-ionic radiocontrast agent that had also been recently used as RI-matching compound in VP (Figure 4.1B).⁸⁰³ The Iod stock solution (60%) has a significantly higher RI (1.4310) compared to the photoresin and its addition resulted in a linear increase in the photoresins RI up to 1.4195 for Iod 50% (Figure 4.1B). As described by Kip et al.,⁸¹⁷ the self-focusing effect due to OMI appears, for a given laser coherence length and intensity, only if the non-linearity (change in RI due to crosslinking) exceeds a certain threshold. We therefore hypothesized that, by adding a compound that increases the overall RI without participating to the crosslinking reaction, we could reduce the change in RI, thus reaching such threshold and eventually hindering microdefects formation (Figure S4.1, Supporting Information).

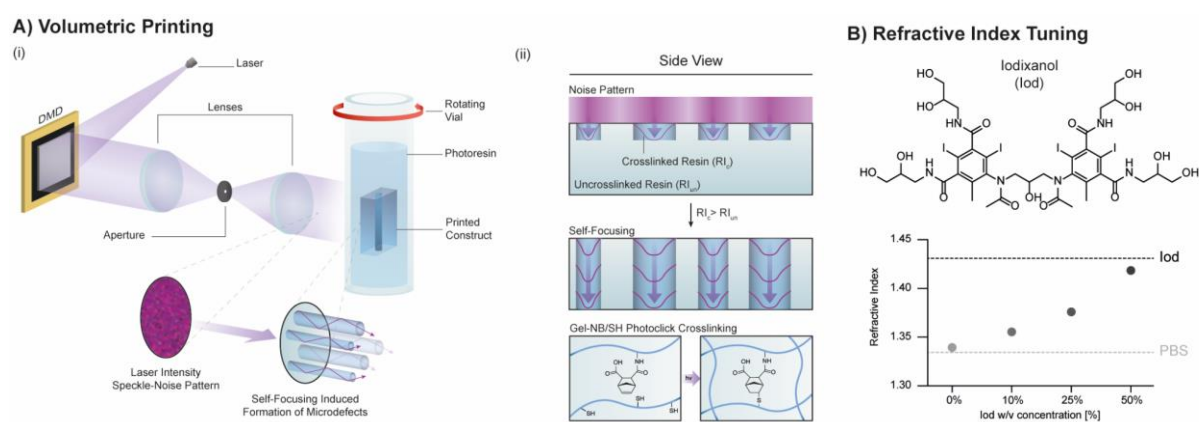


Figure 4.1 | A) (i) Illustration of volumetric printing (VP) method with close-up showing microfilament and microchannel (microdefect) formation due to self-focusing process. (ii) Side view of microdefects formation with details of refractive indices (RI) and photoclick crosslinking mechanism of the gelatin-norbornene (Gel-NB) / gelatin-thiol (Gel-SH) based photoresin. B) Chemical structure of Iodixanol (Iod, top) and linear increase of RI for 2.5% Gel-NB/Gel-SH photoresin containing various Iod %.

4.2.2. Towards Defect-Free Volumetric Printing (VP)

Using the same printing parameters (see Materials and Methods), photoresins containing 0%, 10%, 25% and 50% Iod were used to print a perfusable model (Figure 4.2Ai). The constructs could be successfully printed and perfused in all photoresin conditions and showed a clear difference in their surface roughness as seen with phase-contrast imaging (Figure 4.2Ai, close-ups). The microdefects appeared to be reduced with increasing Iod concentration. At 50% Iod, the gel appears macroscopically smooth and homogenous as corroborated by magnified phase-contrast images. To characterize these microdefects in the various formulations, we used confocal reflection imaging (Figure 4.2Aii). By collecting the light back-scattered from the sample, we could clearly distinguish between void spaces (microchannels, black areas) and gel (microfilaments, cyan areas). Images of the bulk gel and gel-to-PBS solution interface showed a noticeable decrease in the size of the microdefects ultimately resulting in homogeneous, defect-free gel for the

photoresin containing 50% Iod. As initially hypothesized, by introducing a high-enough RI homogenous ground level, the system non-linearity (difference in RI between crosslinked and uncrosslinked state) was insufficient to reach the threshold required to induce the self-focusing effect. Quantification of the microdefects size also showed significant reduction with Iod addition from the $\sim 20\ \mu\text{m}$ and $\sim 10\ \mu\text{m}$ for 0% Iod to the $10\ \mu\text{m}$ and $\sim 6\ \mu\text{m}$ for 25% Iod microfilaments and microchannels, respectively (Figure 4.2B). The reduction in microdefects size for intermediate conditions (10% and 25% Iod) could be explained by a distinct phenomenon. The self-focusing effect needs, to occur, an intensity higher than a critical value which is inversely proportional to the RI of the material (Figure S4.1, Supplementary Information). An increase in the photoresin RI could be therefore expected to induce a denser filamentation as also lower intensity peaks of the laser projection speckle noise pattern could induce self-focusing. To further illustrate the nature of channels and filaments, an infiltration test was conducted using a solution of fluorescently labeled dextran (TRITC-Dex, red). Without Iod, TRITC-Dex solution could easily percolate into the construct via the aligned microchannels (Figure 4.2C). In contrast, the absence of such void spaces limits solution infiltration to simple diffusion through the hydrogel mesh.

To obtain the desired defect-free printing, the addition of a significant amount of Iod (50%) was proven to be necessary. However, as anticipated, this did not seem to impact the gelation point, thus keeping the printing parameters constant between various formulations. Photorheology measurements conducted at 37°C , showed an essentially identical gelation onset for 0% Iod and 50% Iod formulations (Figure 4.2Di). This observation was further confirmed with a Dose Test (light dose screening) where the same critical gelation threshold was identified for two photoresins (Figure 4.2Dii, Figure S4.2, Supplementary Information). Notably, for the 0% Iod, the crosslinked dots appeared clearly visible before washing out the uncrosslinked resin due to the difference in RI between crosslinked (RI: 1.3445) and uncrosslinked (RI: 1.3390) resin (cause of self-focusing effect and microdefects). In contrast, for the 50% Iod formulation the crosslinked dots were substantially indistinguishable from the uncrosslinked material (unvaried RI: 1.4195) and could be revealed only with washing steps using PBS solution (RI: 1.3345).

Although Iod did not affect the gelation point, the photorheology measurement highlighted a drastic decrease in mechanical properties. It is likely that the large solvation volume of highly concentrated Iod hindered crosslinking completion for 50% Iod photoresin, hence resulting in a lower storage modulus (lower crosslinking density) and increased loss modulus (higher fraction of low crosslinked polymer chains). The mechanical properties of the constructs printed with VP were examined with uniaxial compression testing, confirming a substantial decrease in elastic (compression) modulus with Iod addition (Figure 4.2E).

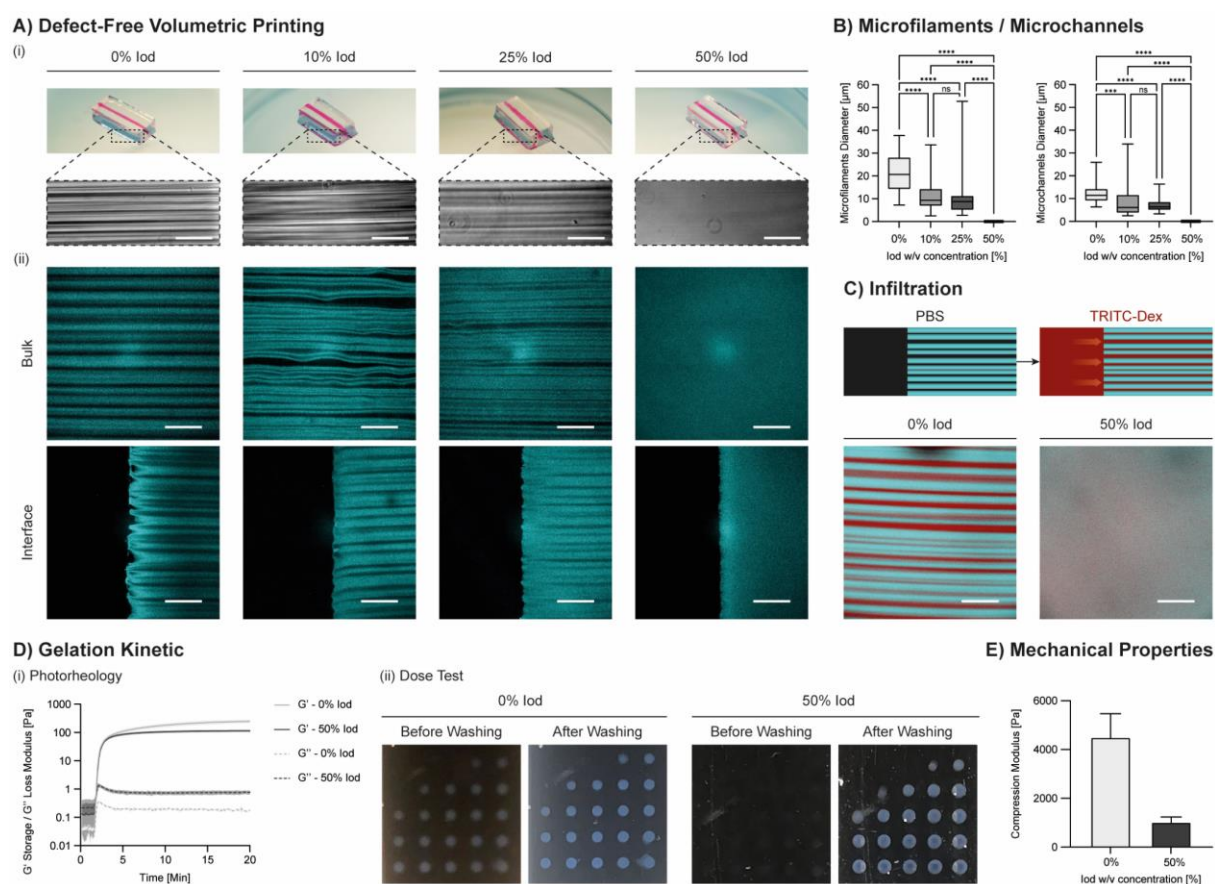


Figure 4.2 | Removal of VP-associated microdefects. A) (i) Volumetric printing of models using different Iod concentrations. Channels were perfused with TRITC-Dex (red). Close up showing phase contrast images of the microfilaments/microchannels. Scale bars: 150 μm (ii) Reflection imaging of the printed constructs taken at the center of the gels (bulk) and at their borders (interfaces) showing a reduction in microfilaments (cyan) and microchannels (black) size with increasing Iod concentration. At 50% Iod, microdefects appeared to be removed. B) Quantitative analysis of microfilaments and microchannels diameters with various Iod concentrations showing size reduction with increased Iod concentration. For 50% Iod, both defects were given a zero value as filamentous structures were discernable. C) Infiltration test with fluorescently labeled TRITC-Dex (40 kDa, red) confirming the presence of perfusable microchannels in 0% Iod condition, and their absence in 50% Iod condition. D) Impact of 50% Iod in gelation kinetic. (i) Photorheological comparison of 50% vs 0% Iod photoresin formulations showed that the presence of Iod determined a reduction in final storage modulus (247 ± 26 Pa for 0% Iod vs 114 ± 7 Pa for 50% Iod) and an increase in loss modulus (0.180 ± 0.008 Pa for 0% Iod vs 0.765 ± 0.085 Pa for 50% Iod), suggesting the formation of a less densely crosslinked network. However, gelation onset appeared to be comparable. (ii) Dose Test confirming comparable critical gelation thresholds (~ 28.4 mJ cm^{-3-1}) for the two conditions. Notably, due to negligible difference in RI, crosslinked dots in 50% Iod photoresin could not be visualized without washing out Iod excess. E) Uniaxial compression test on VP printed gels confirmed relevant impact in the mechanical properties of the printed constructs with Iod addition (4494 ± 800 Pa for 0% Iod vs 1014 ± 179 Pa for 50% Iod).

4.2.3. Optical Setup: Impact on Microdefects and Resolution

As a light-based method, VP can benefit from a number of optical technologies to further improve or tune the printing process, from lenses setups and DMD to different wavelengths and light sources. In the context of this work, where we aim to generate a multiscale perfusable hydrogel for on-a-chip technologies, VP printing resolution plays a key role. The manipulation of the lens setup is a simple method to improve the printing resolution at the expenses of construct size. In this study, we profited from an open-format VP printer (Readily 3D SA) with interchangeable optics to investigate the impact of an optical setup that doubles the resolution, and consequently decrease by a factor of 2 the projection size. For the sake of clarity, the optical setup used up to this point was termed '2x', whereas '1x' refers to the new optical setup with increased resolution and reduced projection size (Figure 4.3A). Photoresins with 0% and 50% Iod were tested and confirmed the presence of microdefects in the absence of Iod and homogeneous defect-free constructs with 50% Iod (Figure 4.3B). Interestingly, we also observed a reduction of the microdefects size by a factor of 2 when using the 1x setup (Figure 4.3C). This observation is in accordance with the 2-fold reduction in the projection size for the 1x setup.

The negative resolution attainable with these optical setups and photoresins were tested by printing hollow conical structures, which were then perfused with high-molecular weight fluorescently labeled dextran (0.5 MDa, FITC-Dex, green) (Figure 4.3D). The resolution improved from $\sim 420\ \mu\text{m}$ (2x) to $\sim 240\ \mu\text{m}$ (1x) for 0% Iod, and from $\sim 500\ \mu\text{m}$ (2x) to $\sim 380\ \mu\text{m}$ (1x) for 50% Iod. The difference between the two formulations, particularly evident for the 1x, can find a possible explanation in the softness of the matrix formed in the presence of Iod. While for 0% Iod the printed gel is sufficiently stiff to maintain the small diameter cone open, in the 50% Iod the structure tends to collapse as can also be inferred by the thin perfusable tip of the hollow cone.

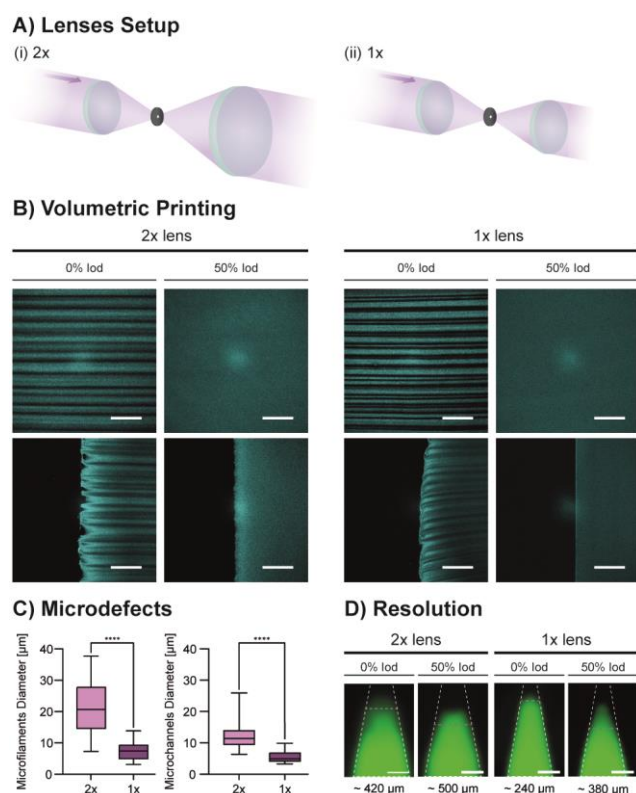


Figure 4.3 | Comparison of VP optical setups. A) Illustration of lenses setups with (i) 2x and (ii) 1x differing in the maximum resolution (double for 1x) and construct/projection size (double for 2x). B) Effect on microdefects of VP printed gels with different lenses setups. Scale bars: 100 μm. C) Quantification of microdefects showing 2-fold reduction in size when using 1x lenses setup compared to 2x. D) Negative resolution of 0% and 50% Iod photoresins performed with VP printing of hollow cones perfused with FITC-Dex (green) showing significant improvement with the use of 1x setup. The maximum resolution was identified with the last point at which the FITC-Dex signal matched the boundaries (grey dashed line) of the theoretical cone dimensions (white dashed line). For 50% Iod – 1x, the FITC-Dex signal was also observed closer to the cone tip, but as the resulting profile did not follow the one of the expected cone (grey dash line), the resolution value was not taken at that point. Scale bars: 300 μm.

4.2.4. Hybrid Printing: Combining Volumetric Printing (VP) with Two-Photon Ablation (2PA)

Having achieved defect-free VP with ~ 400 μm resolution, we then explored the possibility of combining it with 2PA (Figure 4.4A), a high-resolution method that can enable the fabrication of capillary-sized features. The capabilities of the 2PA setup (see Materials and Methods) were investigated on VP printed gels to identify the optimal parameter working space (printing time, maximum height and resolution). In order to define the areas to scan the laser, regions-of-interest (ROIs) of desired shape were drawn using built-in microscope software functions. As for the study of the microdefects, we used reflection imaging to identify void spaces (ablated areas, black) and printed construct (yellow).

First, we studied the ablation efficiency using different laser scans (number of times the laser scans the same line) and fluorescein concentration at 50 μm depth in the VP construct (Figure 4.4Bi). Due to its two-photon absorption at the laser peak intensity (205 mW cm^{-2} at 780 nm), fluorescein facilitates energy deposition in the matrix acting as a 2PA sensitizer.^{206, 818} In addition, fluorescein was chosen as it is a biocompatible, non-expensive and off-the-shelf compound. Fluorescein was found to be fundamental in making the 2PA process effective within the Gel-NB/SH volumetric printed gel. In particular, incubation of the gel in 200 μM fluorescein showed the best results, with efficient ablation even with single laser scanning.

Using a 25x water immersion objective we then used the optimal fluorescein concentration of 200 μM to identify the maximum depth at which we could perform 2PA. We reported successful ablation up to a depth of 500 μm with the use of 16 laser scans (Figure 4.4Bii). To further confirm proper ablation, we incubated the gel in a solution of TRITC-Dex (magenta) which was shown to infiltrate the void space created during the 2PA process.

Resolution of the 2PA process under optimized conditions was then tested using an ROI with decreasing size, from 50 μm to 1 μm (Figure 4.4C). The smallest ablated feature was found to be about $\sim 1.8 \mu\text{m}$. With the theoretical limit of the optical setup being $\sim 1 \mu\text{m}$, the maximum 2PA resolution was almost two times lower likely owed to heat transfer following the high number of scans.

Finally, we ablated an octopus model as a proof-of-concept of our capability to perform complex 3D 2PA (Figure 4.4D). For this purpose we started from the .stl model of the octopus and converted it into a sequence of layers designed as ROIs using a script previously developed in the lab.⁸¹⁹ Using the optimized 2PA conditions (200 μM fluorescein, 16 scans) the octopus model was shown to be successfully ablated in all its height and finer structures (Figure 4.4Di,ii,iii).

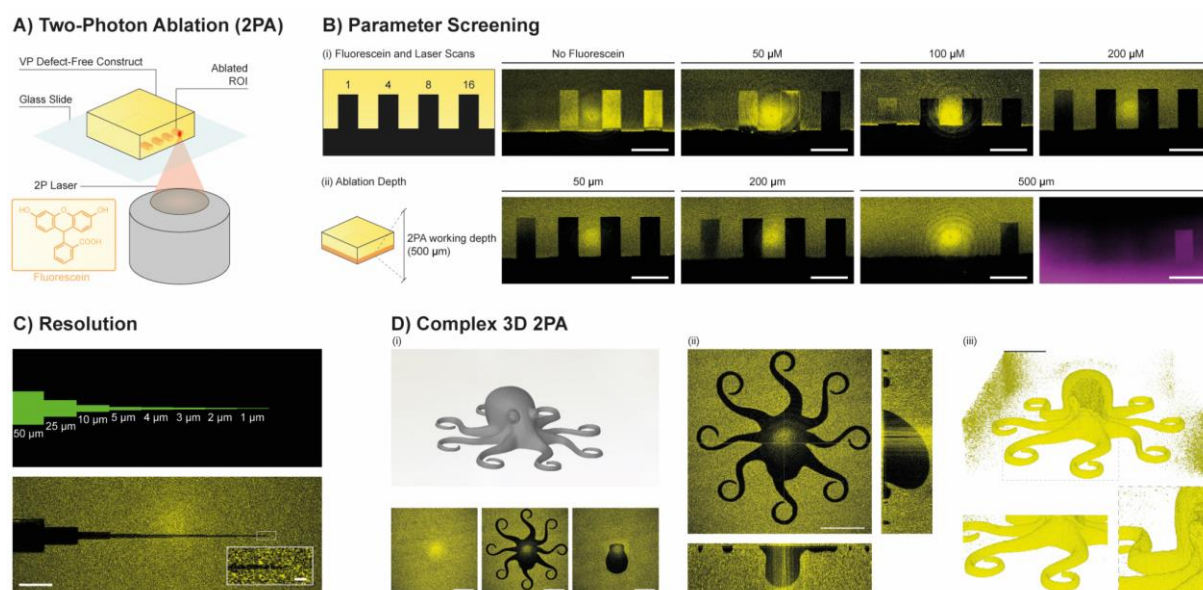


Figure 4.4 | Two-photon ablation (2PA). A) Illustration of 2PA procedure on VP printed gel (yellow). On the bottom-left, chemical structure of fluorescein, used in this work as 2PA-sensitizer. B) (i) Screening of 2PA performance on VP printed gel by varying fluorescein concentration (0, 50 μM , 100 μM and 200 μM) and laser scans (1, 4, 8, 16). Successful ablation of ROIs (in black) was verified using imaging reflection mode. (ii) The best condition (200 μM fluorescein, 16 scans) was used to investigate the maximum 2PA depth (50 μm , 200 μm and 500 μm). With optimized conditions, we found 2PA on VP printed gels to be efficient up to the 500 μm , as also confirmed by the infiltration of TRITC-Dextran (magenta) within the defined ROI. Scale bars: 100 μm . C) 2PA resolution was tested using optimized conditions and a ROI with step-wise decrease in size (green shape, top) and proved to be ~ 1.8 μm (bottom). Scale bar: 50 μm , close-up 5 μm . D) (i) Model of an octopus (grey, top-left) ablated to show the capability of processing complex 3D models. Images in reflection mode at various heights confirmed accurate spatial ablation. (ii) Orthogonal views of the ablated model showing successful ablation of small details (tentacles) and throughout the whole height. Scale bars: 100 μm . (iii) 3D reconstruction of the ablated octopus with close ups of tentacles and eye details. The artifact of laser reflection at the center of the field-of-view resulted in a distortion on the octopus head during 3D rendering, which is however clearly ablated as can be seen in (ii). Scale bar: 100 μm .

4.2.5. Printing of Complex Organotypic Multiscale Models

In the final set of experiments, defect-free VP and optimized high-resolution 2PA were used to generate complex multiscale perfusable models. As 2PA (with the optical setting used in this work) was limited to a maximum working depth of 500 μm , VP printed parts were designed with hollow channels running at this distance from the bottom of the gel (Figure 4.5A). Starting from the middle of the construct height to facilitate later connection to syringe needles, two parallel channels of 400 μm in diameter were designed to curve downwards reaching the 2PA working volume. The space between the channels was set to 400 μm , approximately corresponding to the field of view of the 2PA optical setup.

Figure 4.5B shows a first example of a complex multiscale perfusable model produced with the hybrid VP-2PA method. We exploited Hyperganic software platform to generate an organotypic 3D capillary network surrounding an alveolus model of physiological size ($\sim 100\ \mu\text{m}$ diameter) (Figure 4.5Bi). This 3D model was converted into a ROI sequence and ablated between the volumetrically printed parallel channels. Successful combination of defect-free VP and 2PA is shown using reflection imaging at various depths in the gel and 3D reconstruction (Figure 4.5Bii, Video S4.1 and S4.2, Supplementary Information).

To further exploit the potential of this hybrid technique, we ablated a complex organotypic capillary bed featuring branching microcapillaries (Figure 4.5C). Fluorescently labeled polymer (gelatin-rhodamine) was found to fully percolate into the channels obtained with the 2PA process, thus connecting mesoscale structures obtained with VP with microscale capillary-like structures (Figure 4.5Cii and iii, Video S4.3 and S4.4 Supplementary Information). Notably, the minimum capillary caliper was found to match the resolution limit of this method ($\sim 1.8\ \mu\text{m}$), thus making this example one of the finest capillary-like structure reported so far. The precise fabrication of such highly complex, multiscale models with physiologically relevant native-tissue dimensions opens up new avenues for on-a-chip biomedical applications, such as drug screening and disease modelling.

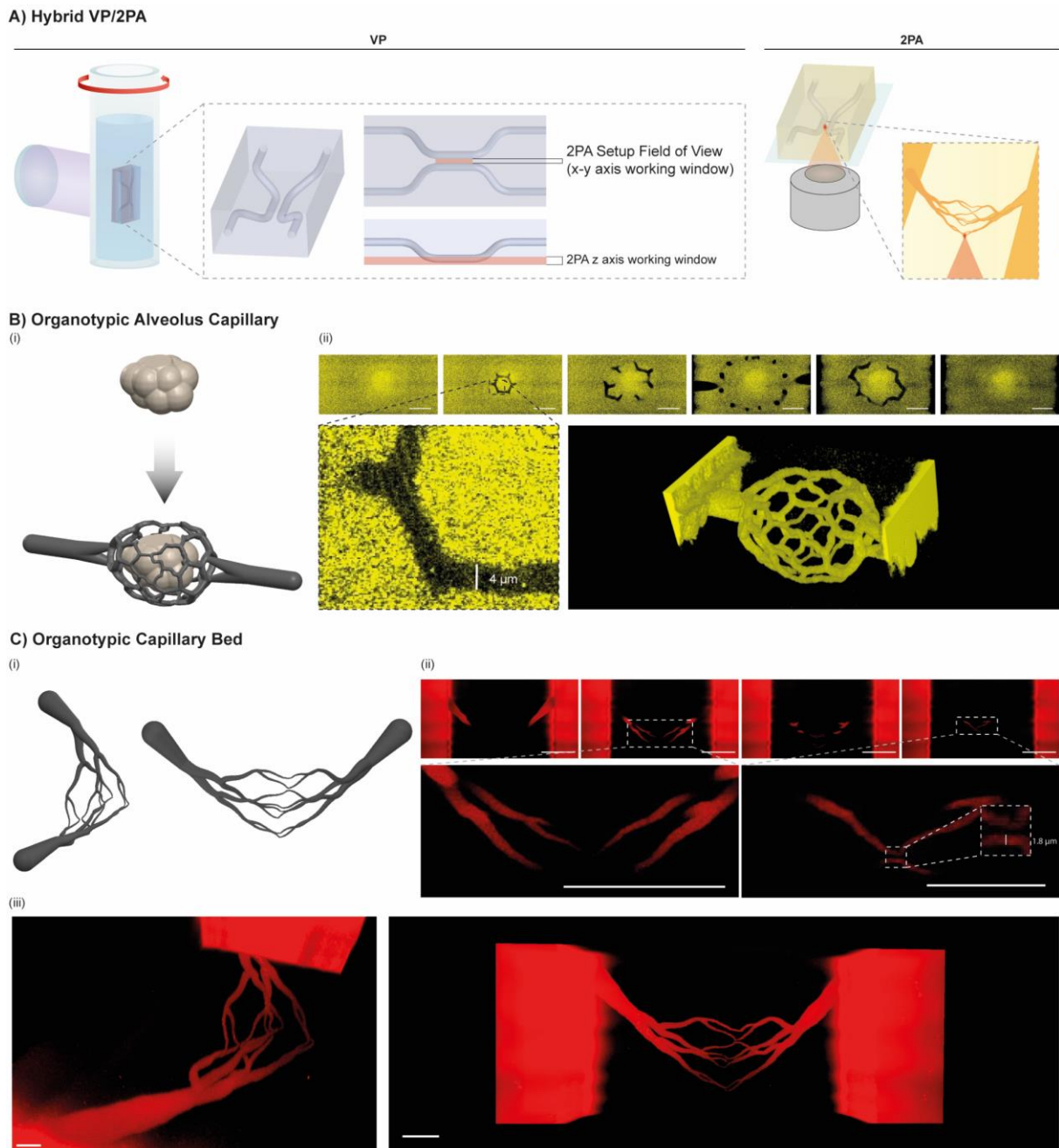


Figure 4.5 | A) Illustration of the hybrid VP/2PA method showing details of the perfusable model printed with VP (left) and following 2PA of capillary-like structures (right). B) Generation (i) and 2PA of complex organotypic capillary network modeled around an alveolus (ii). Successful ablation of the capillary network is shown with reflection images taken at increasing depth (from left to right, scale bar: 50 μm). Close-up showing minimum feature size of $\sim 4 \mu\text{m}$. On the bottom right a 3D rendering of the ablated model with inverted colors (in yellow the hollow ablated parts). Scale bars: 50 μm . C) (i) Organotypic capillary bed model. (ii) Confocal images at various depth in the gel showing perfusion of gelatin-rhodamine (Gel-Rho) solution. Close up showing details of the fine structures and minimum feature size ($\sim 1.8 \mu\text{m}$). Scale bars: 100 μm . (iii) 3D rendering of the perfused capillary bed model connecting mesoscale VP printed channels. Scale bars: 20 μm (left) and 40 μm (right).

4.3. Conclusion

In summary, we have introduced a strategy to obtain defect-free VP and leverage it to develop the first VP-based hybrid printing method featuring 2PA. We demonstrated that this method can target complex, multiscale organotypic models, thus opening new avenues for the next generation of on-a-chip technologies. We foresee that the findings of this work will stimulate further research into the optical tuning of the photoresins (i.e., use of various RI matching compounds) and optical setups (i.e., high-resolution VP, 2PA with larger working distance) as well as encourage biological studies in more physiologically relevant tissue models.

4.4. Experimental Section/Methods

Gelatin-Norbornene (Gel-NB) synthesis: The synthesis protocol was adapted from Rizzo et al.^{187, 820} In short, 25 g of gelatin type A from porcine skin was first dissolved in 0.5 M carbonate–bicarbonate pH 9 buffer at 10% at 40 °C. When completely dissolved, 0.5 g of cis-5-norbornene-endo-2,3-dicarboxylic anhydride (CA) was added to the reaction mixture under vigorous stirring. Every 10 min, 0.5 g of CA was added for a total amount of 2 g. Twenty minutes after the last addition, the solution was diluted 2-fold in prewarmed mQ H₂O, and the pH was adjusted to 7 with the addition of HCl 1 M. Then, 2.5 g of NaCl was added and the solution was filter-sterilized (0.2 μm) and dialyzed (12.4 kDa cutoff cellulose tubing) for 4–5 days against mQ H₂O at 30 °C with frequent water changes before freeze-drying. The degree of substitution (DS) was calculated using ¹H NMR (Bruker Ultrashield 400 MHz, 1024 scans), as previously reported,^{187, 820} and found to be ~ 0.091 mmol g⁻¹.

Gelatin-Thiol (Gel-SH) synthesis: The synthesis protocol was adapted from Rizzo et al.⁸²⁰ In short, 25 g of gelatin type A from porcine skin was first dissolved in 1.25 L of 150 mM MES pH 4 buffer warmed up to 40 °C for a final concentration of 2%. When completely dissolved, 2.38 g (10 mmol) of 3,3'-dithiobis(propionohydrazide) (DTPHY) was added to the reaction solution under stirring. When completely dissolved, 3.83 g (20 mmol) of 1-ethyl-3-(3'-dimethylaminopropyl)carbodiimide hydrochloride (EDC) was added, and the reaction was left to proceed overnight at 40 °C. Tris(2-carboxyethyl)phosphine (8.6 g, 30 mmol) was then added to the reaction mixture, and reduction left to proceed for 6 hours in a sealed flask under gentle stirring. Then, 2.5 g of NaCl was added and the solution was filter-sterilized (0.2 μm) and dialyzed (12.4 kDa cutoff cellulose tubing) for 4–5 days against mQ H₂O balanced to pH 4.5 with diluted HCl at 30 °C. After dialysis with frequent changes of acidified water, Gel-SH was finally freeze-dried. Gel-SH was stored under inert atmosphere at –20 °C prior to use. The degree of substitution (DS) was determined by ¹H NMR (Bruker Ultrashield 400 MHz, 1024 scans) as previously reported,⁸²⁰ and found to be ~ 0.276 mmol g⁻¹.

Gelatin-Rhodamine (Gel-Rho) synthesis: Gelatin-methacryloyl was synthesized as previously described.⁴⁸⁹ 1.0 g of GelMA was dissolved in 100 mL of 0.1 M sodium bicarbonate (pH 9.0) at 37 °C overnight. 10.0 mg of rhodamine B isothiocyanate was dissolved in 1.0 mL dimethyl sulfoxide (DMSO) and added to the GelMA solution. The reaction was left to proceed at room temperature overnight. The product was purified by dialysis (3.5 kDa cut-off) against mQ H₂O at 40 °C for 3 days with frequent water changes, protected from light, and then freeze dried.

Photoresin Preparation: Gel-NB and Gel-SH were dissolved in PBS at 37°C with 1:1 molar ratio of NB:SH. Iodixanol (OptiPrep™, STEMCELL Technologies) stock solution (60%) was added to the Gel-NB/SH mixture for a final concentration of 10%, 25% or 50%. Photoinitiator lithium phenyl-2,4,6-trimethylbenzoylphosphinate (LAP) was added from a stock solution of 2.5% in PBS to obtain a final concentration of 0.05%. Photoresins were prepared with a Gel-NB/SH total polymer concentration of 2.5%, 2.75 % or 3%. Before use, photoresins were filtered through 0.2 µm filters to remove debris and scattering particles.

Refractive Index: Refractive indices of the different Gel-NB/SH photoresins were measured using an Abbe refractometer (Kern ORT 1RS, KERN & SOHN GmbH). For measurements of hydrogel refractive indices, a thin film of photoresin was crosslinked on the measuring prism for 10 minutes in a UV-box (405 nm LEDs, 6.6 mW/cm² intensity).

Photoreology: Photoreology analyses were carried out on an Anton Paar MCR 302e equipped with a 20 mm parallel plate geometry and glass floor. Omnicure Series1000 lamp (Lumen Dynamics) was used in combination with sequential 400–500 nm and narrow 405 nm bandpass filters (Thorlabs). Gel-NB/SH photoresins were prepared as previously described. All procedures were performed in the dark. Oscillatory measurements were performed in triplicate ($n = 3$) at 37°C using 74 µL of photoresins at 2% shear rate and 1 Hz frequency with 200 µm gap and 10 s measuring point duration. Measurements were left to proceed in the dark for 1 minute before irradiating the sample with 405 nm light at (60%) 50 mW cm⁻² intensity. To prevent the sample from drying all tests were performed in the presence of a wet tissue paper in the chamber.

Dose Test: A Dose Test was conducted similarly to previously described protocol,¹⁸⁷ using an open-format printer (Readily3D). In short, photoresins were allowed to thermally gel in quartz cuvettes (CV10Q1400FS, Thorlabs) for 20 min at 4°C prior irradiation. A software built-in function was used to project a 5x5 matrix of dots (0.75 mm diameter, 0.75 mm gap) within a variable range of exposure time and intensity (see Figure S4.2, Supporting Information). After exposure, cuvettes were imaged before and after washing with PBS.

Volumetric Printing (VP): Volumetric printing was performed on an open-format machine, provided by Readily3D, equipped with swappable optics herein described as 2x (larger printing, lower resolution) and 1x (smaller printing, higher resolution). Photoresins were prepared as previously described and allowed to thermally gel in the glass vials for 20 min at 4°C prior printing. Printing was conducted with 7.52 mW cm⁻² laser intensity and 275 mJ cm⁻² light dose, 78.7 ° s⁻¹ rotational speed, 273 Hz projection rate. Right after the printing the vials were warmed up in a heating bath (37°C) and uncrosslinked resin was removed with extensive washing in prewarmed PBS with 0.05% LAP. Gels were post-cured in a UV-box (405 nm LEDs, 6.6 mW/cm² intensity) for 10 minutes.

Negative resolution was tested by printing a hollow cone, as previously reported,¹⁸⁷ perfused with high molecular weight FITC-dextran (0.5 MDa). Fluorescent images were taken on an EVOS M5000 (ThermoFisher). All 3D .stl models to be printed with VP were generated using SolidWorks (Dassault Systèmes).

Microfilaments/Microchannels Characterization: The microfilaments and microchannels generated during the volumetric printing procedure were imaged in reflection mode using 488 or 633 nm laser line and highly sensitive hybrid (Hyd) detector with HCX IRAPO 25X/0.95NA water immersion objective on Leica TCS SP8 (Leica) confocal microscope. Each condition was tested in triplicate and size of microfilaments and microchannels was measured manually using Fiji. Infiltration experiment was conducted by submerging printed constructs in a solution of 1% TRITC-Dextran (40 kDa) in PBS for 6 hours prior imaging.

Two-Photon Ablation (2PA): 2PA was performed on a Leica TCS SP8 (Leica) confocal microscope equipped with a Mai Tai two-photon laser (205 mW cm⁻² intensity, Spectra-Physics) tuned at 780 nm using HCX IRAPO 25X/0.95NA water immersion objective, 1 µm z-step, 600 Hz scanning, bi-directional scanning, 512x512 format and zoom factor of 1. To avoid drying during ablation procedure the gels were placed in 2 or 8-well glass chambers (Nunc™ Lab Tek™, ThermoScientific) and submerged in PBS with or without fluorescein. 2PA screening was conducted by submerging the VP printed gels for 6 hours in different PBS solutions containing 0, 50, 100 or 200 µM fluorescein. Rectangular-shaped regions-of-interest (ROIs) were designed using LAS X software functionalities and used to test different number of laser scans (1, 4, 8, and 16) and reachable depth in the gel (50, 200 and 500 µm). Resolution test was performed with optimized conditions (16 scans, 200 µM fluorescein) using a ROI designed to have a step-wise decrease in size, from 50 to 1 µm (see Figure 4.4C).

Ablation of the octopus 3D model was performed using a script previously developed in our lab (available at <https://github.com/nbroguiere/F2P2>),⁸¹⁹ which converts an .stl file into a stack of ROIs executable by the LAS X software in Live Data Mode. Ablated construct was imaged with 633 nm backscattered light (reflection mode), 0.5 µm z-step, and elaborated with Fiji.

Capillary bed and alveoli models were generated using Hyperganic (Hyperganic Group) and ablated using the same procedure described above. After ablation, samples were perfused with 0.5% Gel-Rho solution in PBS and imaged using Leica SP8 confocal microscope. 3D rendering and videos were generated with Fiji or Imaris.

Acknowledgements. M.Z.W. acknowledges ETH Grant application ETH-38 19-1 and Innosuisse funding application no. 55019.1 IP-ENG for their kind support. P.C. acknowledges a Marie Skłodowska Curie fellowship (grant number 101024341). D.R. acknowledges Swiss National Science Foundation project grant 205321_179012. The authors acknowledge ETH ScopeM imaging facility for their assistance.

Contributions. R.R. and D.C. listed as first authors contributed equally to this work, conceived the project, designed and performed the experiments. R.R. performed chemical synthesis, confocal imaging, mechanical testing and data analysis. R.R. and D.C. performed volumetric printing and 2PA processing. H.L. performed 3D rendering and aided in interpreting the results. P.C. and A.W. generated the 3D models and A.H. contributed to the 2PA processing. M.Z.W. supervised the project. The manuscript was written through the contributions of all authors.

4.5. Supporting Information

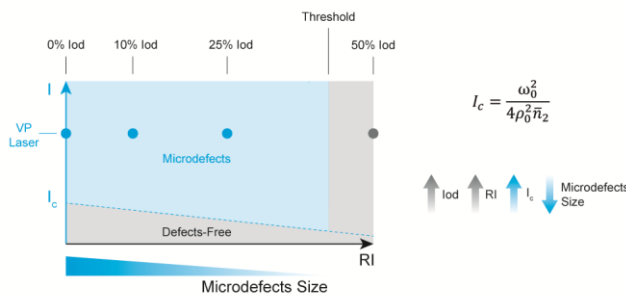
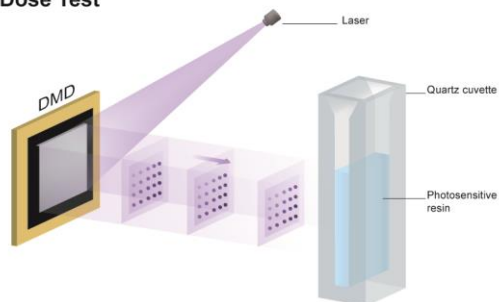


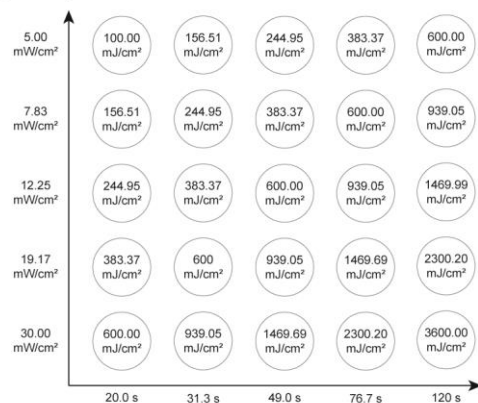
Figure S4.1| Illustration representing the two phenomena involved in the reduction and disappearance of microdefects. As displayed in the equation,⁸²¹ the critical light intensity (I_c) above which self-focusing effects occurs is inversely proportional to the refractive index (RI, n_2) of the material. Therefore, given the VP laser intensity, with an increase in iodixanol (Iod) concentration – and thus an increase in refractive index (RI) – the self-focusing effect occurs at lower intense speckles determining smaller microdefects. This phenomenon, observable with 10% and 25% Iod (see Figure 4.2A), occurs till a critical threshold at which the RI is so uniformly high that the RI change between crosslinked and uncrosslinked state is negligible and does not trigger microdefects formation via self-focusing effect. This defect-free region where a defects-free gel is formed was obtained using 50% Iod. The critical intensity I_c is also related to other parameters such as laser beam waist (ω) and Rayleigh length (q).

A) Dose Test



B) Dose Test Parameters

(i) Light dose per unit area



(ii) Light dose as volumetric absorbed energy

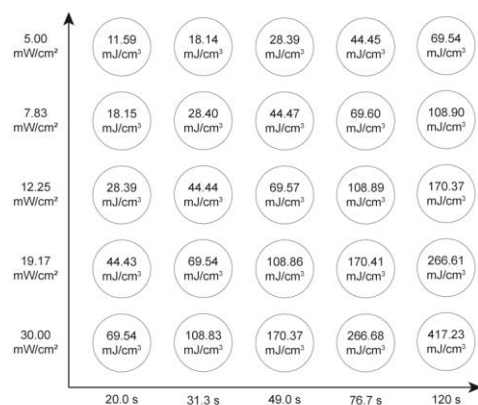


Figure S4.2 A) Illustration of Dose Test procedure with dots of various intensities projected, for different time, towards a static (non-rotating) quartz cuvette filled with photoresin. B) Parameters used for the matrix of dots with light dose in areal (i) and volumetric units (ii).

Video S4.1. Reflection imaging z-stack into VP printed gel (yellow) showing ablated regions (black) of the organotypic 3D capillary modeled around an alveolus-like shape.

Video S4.2. Animation of 3D rendered alveolus capillary network (yellow).

Video S4.3. Fluorescent imaging z-stack into VP printed gel (black) showing capillary-bed ablated regions perfused with gelatin-rhodamine solution (red).

Video S4.4. Animation of 3D rendered capillary-bed network (red).

CHAPTER 5

FLight Biofabrication

Aligned Cartilage Constructs with Zonal Architecture

In the previous chapter microdefects formed due to optical modulation instability and self-focusing were removed to generate homogeneous constructs. In this work instead, microfilaments and microchannels are exploited to obtain highly porous, cell instructive anisotropic constructs leading to directional deposition of cartilaginous ECM. This technique, termed FLight (Filamented Light) biofabrication and previously developed in our lab, showed to be promising for the maturation of cartilage tissue with zonal architecture, thus mimicking native-like structural and mechanical properties.

MANUSCRIPT IN PREPARATION

FLight Biofabrication of Anisotropic Articular Cartilage with Zonal Architecture

Riccardo Rizzo[†], Anna Puiggali-Jout, Angela Bonato, Marcy Zenobi-Wong

[†]Equal contributions.

Note: this work is based on FLight biofabrication, a technology developed in the lab and published as co-author:

Filamented Light (FLight) Biofabrication of Highly Aligned Tissue-Engineered Constructs

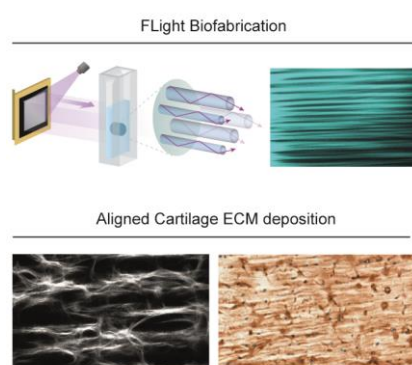
Hao Liu., Parth Chansoria, Paul Delrot, Emmanouil Angelidakis, Riccardo Rizzo, Dominic Rüttsche, Lee Ann Applegate, Damien Loterie, Marcy Zenobi-Wong

Adv. Mater. **2022**, 2204301

DOI: 10.1002/adma.202204301

Main contribution: synthesis of photoresins.

Abstract



Tissue engineering approaches that recapitulate cartilage biomechanical properties are emerging as promising solutions to restore the functions of the impaired tissue. However, despite significant progress in this research area, the generation of engineered cartilage constructs akin to native counterparts still represents an unmet challenge. In particular, the inability to accurately resemble cartilage zonal architecture with different collagen fibrils orientation represents a significant limitation. Cellular and extracellular matrix (ECM) arrangements play a fundamental role in determining the mechanical and biological function of the tissue. Here, we show that a novel light-based approach termed Filamented Light (FLight) biofabrication can be exploited to generate highly porous, cell instructive anisotropic constructs that eventually lead to directional deposition of collagen fibrils. Using a photoclick-based photoresin optimized for cartilage tissue engineering, we demonstrate the maturation of cartilaginous tissues with zonal architecture and native-like mechanical properties.

5.1. Introduction

Traumatic injuries, joint diseases, aging and obesity, are some of the factors which are increasing the need for cartilage repair technologies. Since cartilage lacks self-repair capabilities, tissue engineering approaches represent a great opportunity to fulfil this urgent need.⁸²²⁻⁸²⁶ Cartilage is an avascular, aneural, and alymphatic tissue composed of chondrocytes embedded in a dense extracellular matrix (ECM) mainly consisting of collagen type II and proteoglycans.⁸²⁷ Although a seemingly simple tissue, faithfully resembling articular cartilage with tissue engineering strategies remains an unmet challenge. Despite major advances in cell source, culture conditions and supporting biomaterials, cartilaginous anisotropic tissue architecture has still not been obtained.^{823-824, 827}

Articular cartilage has a distinctive zonal organization, with superficial, middle and deep zone varying in structure and function (Figure 5.1A).⁵⁵⁻⁵⁷ The superficial zone of the joint consists of flattened chondrocytes embedded in a thin layer of ECM mainly composed of collagen fibrils running parallel to the articular surface, thus conferring protection of deeper layers to shear-stress. The middle zone comprises sparsely distributed rounded chondrocytes in a proteoglycan-rich ECM. The deep zone is instead characterised by a columnar arrangement of chondrocytes and thick collagen fibrils running perpendicular to the articular surface. Due to its composition and structural organization, the deep zone provides high compressive resistance to the tissue. While the middle zone does not possess a peculiar fibrils orientation and can be more easily obtained with current tissue engineering methods, superficial and deep zones require technologies that can direct aligned ECM deposition on a cellular-scale. Liu et al. have recently introduced a method, named Filamented Light (FLight) biofabrication, that can meet such requirements (Figure 5.1B).⁸²⁸ FLight rapidly (few seconds) generates hydrogels composed of aligned microfilaments and microchannels with diameters in the range of 2-30 μm . Such unidirectional microstructure showed excellent cell instructive capabilities determining cell alignment and aligned ECM deposition with various cell types. In this work, we leverage FLight approach to generate anisotropic cartilage constructs featuring zonal architecture with cartilage-like ECM deposition and mechanical properties.

5.2. Results and Discussion

5.2.1. Design of FLight Photoresins for Cartilage Regeneration

FLight biofabrication is a light-based technique and, as such, requires the use of photoactivated materials. In recent years, step-growth photocrosslinking mechanisms (i.e., thiol-ene) have become the gold-standard choice over chain-growth mechanisms (i.e., methacryloyl or acrylate-based) for biofabrication methods.¹³² Among the various advantages, step-growth reactions are faster, thus requiring lower light exposure and

lower generation of harmful radicals, result in more homogeneous networks, are not sensitive to oxygen and do not form non-biodegradable, hydrophobic kinetic chains. In this work, we chose to use the highly efficient thiol-norbornene photoclick step-growth reaction to crosslink biomaterials optimized for cartilage applications. In the past decades, several synthetic and naturally-derived polymers have been studied to generate hydrogels for cartilage tissue engineering. Amongst these, hyaluronic acid (HA) and alginate (Alg) have arguably shown the most promising results.^{98-102, 509, 829} HA is a native polysaccharide present in human articular cartilage that offers chondrocyte binding sites (via CD44 adhesion receptor) and biodegradability/matrix remodelling potential (via hyaluronidase). Alg is instead a bioinert polysaccharide extracted from brown seaweed that offers attractive stress-relaxation properties via Ca²⁺ mediated ionic crosslinking.^{58, 155}

As previously shown by Broguiere et al. and Fisch et al.,^{98, 100} a hydrogel's initial stiffness plays a major role in determining proper tissue maturation. In particular, an initial stiffness < 1000 Pa was found to be optimal for cartilage maturation resulting in a tremendous increase in stiffness over the culturing period eventually reaching the range of native cartilage stiffness (reported to span from 0.1 to 6.2 MPa).⁸³⁰⁻⁸³³ These studies, reporting exceptional results for the biofabrication of cartilaginous constructs, were based on an enzymatic transglutaminase-crosslinkable HA (HA-TG). In this work we tried to build on the promising results showed with HA-TG hydrogels by synthesizing a photosensitive counterpart suitable for FLight biofabrication and by matching initial mechanical properties. High molecular weight HA (1.5 MDa) was modified with norbornene groups (HA-NB) and crosslinked with bioinert bifunctional thiolated PEG (PEG2SH) which played the role of the TG peptides (Figure 5.1C). Given the attractive stress-relaxation properties of Alg, we also screened for a second type of photoresin based on HA-NB/PEG2SH, which included an interpenetrating network of unmodified Alg.

Various formulations consisting of different concentrations of the polymeric components were tested (data not shown) so to fall in the desired range of stiffness. Optimized photoresins were found to be 0.75% HA-NB/ 0.84% PEG2SH and 0.75% HA-NB/ 0.70% PEG2SH/ 0.25% Alg and were used for the experiments reported in this work with 0.05% lithium phenyl-2,4,6-trimethylbenzoylphosphinate (LAP) as photoinitiator.

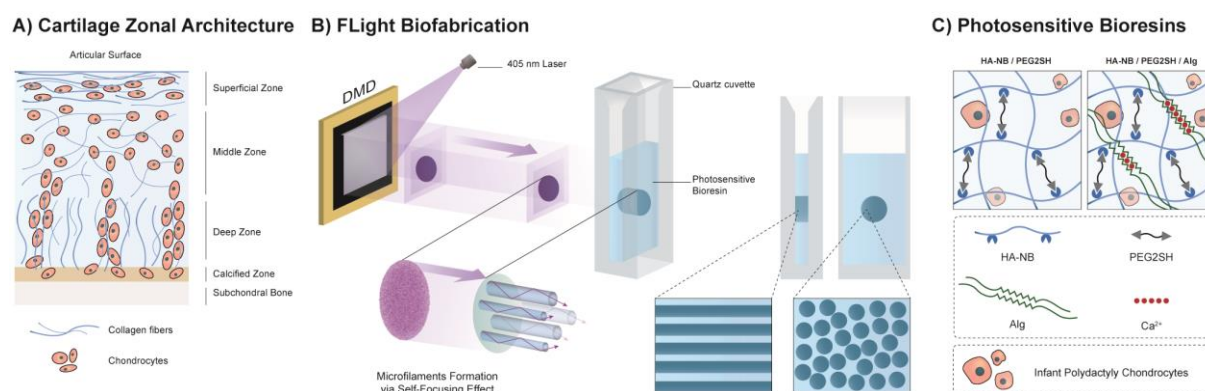


Figure 5.1 | A) Illustration of articular cartilage zonal architecture with relative cellular and fibrils arrangement. B) Illustration of FLIGHT biofabrication process. Light projections generated with a digital micromirror device (DMD) are directed towards a quartz cuvette containing the photosensitive bioresin. Due to a phenomenon known as optical modulation instability, projected light has an intrinsic intensity noise speckle-pattern that, together with the non-linearity of the photoresin, induces a self-focusing effect. This effect eventually results in the formation of microfilaments (blue) and microchannels (light blue, uncrosslinked regions). C) Illustration of hydrogels formed with the two bioresins formulations used in this study featuring hyaluronic acid-norbornene (HA-NB), thiolated PEG (PEG2SH), ionically crosslinked alginate (Alg) and infant polydactyly chondrocytes.

5.2.2. FLIGHT Hydrogels Characterization

Cylindrical hydrogels of 2 mm in height (within the human articular cartilage thickness range),⁸³⁴⁻⁸³⁵ and 4 mm in diameter were printed with FLIGHT and compared with ‘bulk’ hydrogels crosslinked with LED flood illumination. As LEDs are non-coherent light sources, thus do not show an optical modulation instability (OMI) effect, they do not induce the formation of microfeatures via self-focusing phenomenon, but rather a homogeneous gel. The printed samples were submerged for 15 minutes in a solution of fluorescently labelled dextran (FITC-Dex), and the presence of microchannels was analysed by confocal imaging (Figure 5.2A). As expected, infiltration of FITC-Dex was detected for FLIGHT constructs only, thus revealing the presence of microchannels that can enhance nutrient diffusion and guide the deposition of cell-secreted ECM. Interestingly, although both photoresin formulations reported a similar pore-to-gel proportion (70% channels, 30% filaments), for HA-NB/PEG2SH/Alg the microfeatures were significantly smaller (Figure 5.2Bi-ii). With the addition of Alg, the average size of microchannels and microfilaments showed a ~ 2 -fold reduction compared to HA/PEG2SH ($\sim 8 \pm 2 \mu\text{m}$ filaments and $\sim 14 \pm 5 \mu\text{m}$ channels). The difference in microfeatures size, due to the different thiolated crosslinker concentration and presence of the Alg secondary interpenetrating network, was expected to have an impact on cell behaviour and tissue maturation potential.

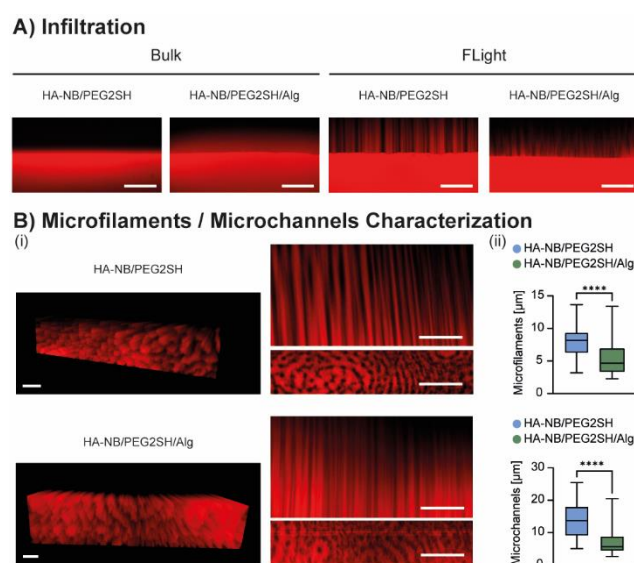


Figure 5.2 | A) Fluorescently labelled dextran (FITC-Dex, red) readily (15 minutes) infiltrated into the pores (microchannels) in between the microfilaments generated with FLight process. On the other hand, the bulk gels crosslinked with LED illumination as expected appeared to be homogeneous (no microfeatures), thus not allowing rapid infiltration of the FITC-Dex solution. Scale bars: 100 μm . B) (i) 3D reconstruction of microchannels (red) and microfilaments (black) for the FLight fabricated gels with HA-NB/PEG2SH and HA-NB/PEG2SH/Alg photoresins (left). On the right, images showing a top and side view from which microfeatures size and area distribution were analysed, respectively. (ii) Microfeatures were found to be significantly smaller for the photoresin including Alg ($\sim 5 \pm 2 \mu\text{m}$ filaments and $\sim 7 \pm 3 \mu\text{m}$ channels), while channel-to-filament ratio remained substantially unvaried (70% channels, 30% filaments).

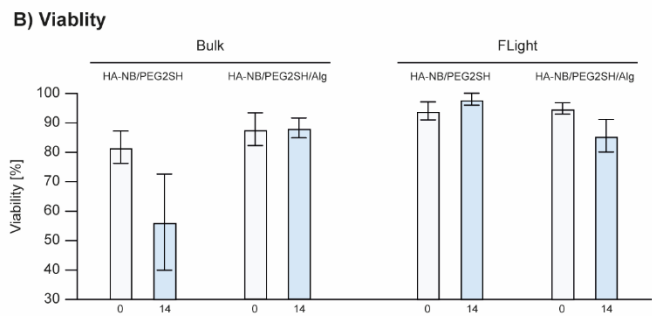
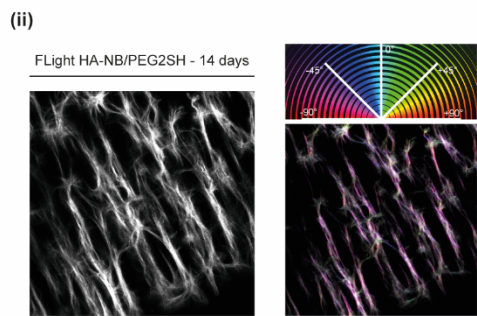
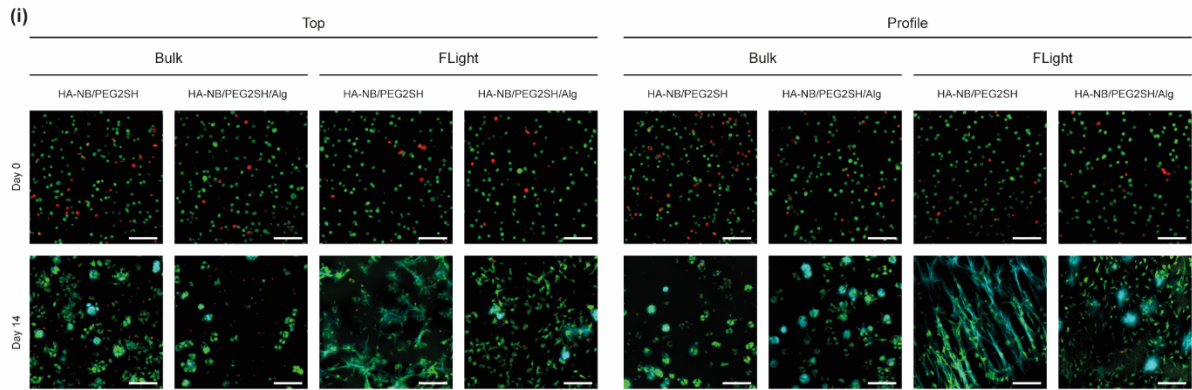
5.2.3. Tissue Maturation

To study the potential of FLight biofabricated construct to induce the development of aligned, matured articular cartilage, we embedded human infant polydactyly chondrocytes. Polydactyly chondrocytes have shown a steady proliferative rate, production of cartilage-like matrix and have been extensively investigated as non-immunogenic, off-the-shelf cell source for potential clinical applications.^{57, 836-839} Due to cell-induced light scattering, FLight was found to be limited in maximum cellular concentration. Above a certain threshold, found to be 5 million cells mL^{-1} for the photoresins used in this work, light scattering hinders the formation of microfilaments and microchannels. Dose Tests were first performed to identify the critical gelation threshold,^{187, 828} and thus the optimal printing time. Cylindrical FLight hydrogels (2 mm height, 4 mm diameter) containing 5 million cells mL^{-1} were printed with only 3.3 seconds exposure to 405 nm laser at $\sim 63 \text{ mW cm}^{-2}$ intensity ($\sim 208 \text{ mJ cm}^{-2}$ light dose). After removal of uncrosslinked photoresin, HA-NB/PEG2SH samples were readily placed in chondrogenic media, while HA-NB/PEG2SH/Alg samples were first incubated in buffer containing 100 mM CaCl_2 for 20 minutes to trigger Alg ionic crosslinking. As controls, the same photoresins were used to cast cylindrical gels of the same dimensions that were then crosslinked, using the same light-dose of the FLight process, but in a UV-box containing 405 nm LEDs.

Live/Dead assay was performed upon printing (day 0) and after 14 days of culture together with second harmonic generation (SHG) imaging which allows to identify the deposition of collagen fibrils (Figure 5.3Ai, 3B). FLight method showed excellent cell viability upon printing ($> 90\%$) and during culturing period ($98\% \pm 2$ for HA-NB/PEG2SH and 86 ± 6 for HA-NB/PEG2SH/Alg). Viability was found to be generally lower for bulk gels upon printing ($\sim 80\text{-}88\%$) and significantly reduced after two weeks of culture for HA-NB/PEG2SH samples ($56\% \pm 16$). By simply comparing the two bulk gels, the introduction of ionically crosslinked Alg network seemed to have a beneficial effect on embedded chondrocytes. This finding appeared to be in contrast with the FLights samples, for which the addition of Alg determined a reduction in viability. However, as evidenced in Figure 5.2B, in the FLight process Alg caused a reduction in microfilaments and microchannels, which is likely the causing the observed difference in viability. Remarkably, SHG signal revealed a clear difference between FLight HA-NB/PEG2SH and all the other samples in the deposition of aligned collagen fibrils (Figure 5.3Ai-ii). FLight HA-NB/PEG2SH/Alg hydrogels also did not show aligned matrix deposition, a result again likely caused by the microchannel size. As expected, after two weeks of culture the homogeneous bulk gels did not show aligned collagen deposition, but rather limited pericellularly. Calcein staining also provided a way to check cell morphology, revealing more spread and elongated morphologies for FLight gels (resembling superficial and deep zone chondrocytes) and more rounded for bulk ones (resembling middle zone chondrocytes).

We then further investigated the impact of hydrogel architecture (Flight vs bulk) and composition (with or without the Alg network) at the gene level with qPCR (Figure 5.3C). Gene expression analysis showed a general increase of Sox9, a key chondrogenesis transcription factor which induces the expression of cartilage-related genes such as collagen II. As expected, using infant chondrocytes and optimized materials, the upregulation of Sox9 confirmed chondrogenesis induction within the first two weeks of culture. Interestingly, the upregulation of Sox9 occurred earlier for hydrogels containing Alg (day 7) and independently of the hydrogel's architecture. Collagen II and collagen I expressions were also found to be upregulated after one week in culture, suggesting an onset in chondrocyte active matrix deposition. Notably, collagen II, the main structural component of articular cartilage, was found to be upregulated about 10 times more than the type I, indicating good chondrogenesis induction. After one week collagens were found to be significantly more upregulated (~ 3 times) in the samples containing the interpenetrating stress-relaxing alginate network, suggesting a positive effect of this component in chondrogenesis. Finally, the metalloproteinase ADAMTS5, which can serve as an indicator of ongoing matrix remodelling, was found to be upregulated in all samples and with a one-week delay compared to the collagen upregulation.

A) Live/Dead and SHG



C) Gene Expression

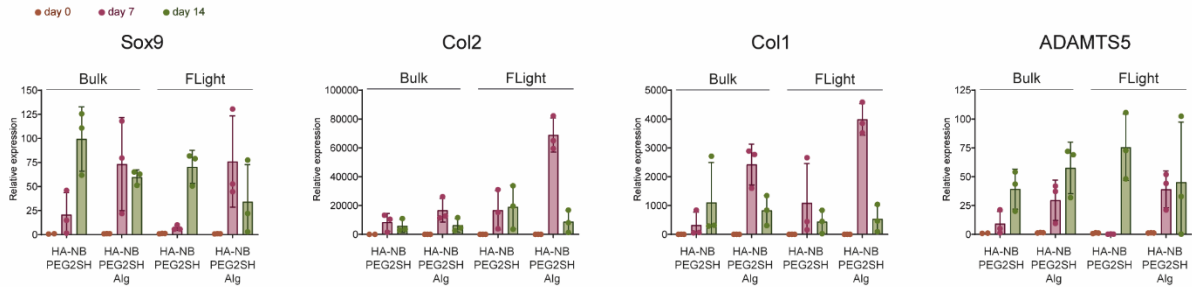


Figure 5.3 | A) (i) Viability (live cells in green, dead cells in red) and SHG (cyan) imaging upon biofabrication (day 0) and after 2 weeks of culture (day 14). (ii) Close up on SHG signal (white) of aligned collagen fibrils in FLight HA/PEG2SH construct (left) and colorized image showing directional fibrils deposition (right). B) Viability at day 0 and day 14 for the different photoresins and biofabrication methods. C) Gene expression at day 0, 7 and 14 for Sox9, collagen II (Col2), collagen I (Col1) and metalloprotease (ADMTS5).

Histological and immunohistological stainings were then used to further confirm tissue maturation after a culture period of 28 days (Figure 5.4A). Safranin O staining displayed a homogeneous glycosaminoglycans (GAGs) deposition in all samples, with slightly lower intensity for Alg-containing samples. As desired for articular cartilage tissue constructs, collagen I content was found to be less pronounced than collagen II and generally limited to pericellular deposition. Collagen II staining was also found to be mostly pericellular for FLight HA-NB/PEG2SH/Alg when compared to FLight HA-NB/PEG2SH. In the latter, the presence of larger microchannels successfully induced align collagen II fibrils deposition, confirming the observations of

SHG signals (Figure 5.3Ai-ii), and thus FLight biofabrication potential to generate anisotropic cartilage constructs. For FLight HA-NB/PEG2SH/Alg, although mainly deposited pericellularly, collagens were also observed to be starting to be deposited in an aligned fashion. We hypothesize that such behaviour could be due to the smaller microchannels and by the presence of a lower density Alg-only hydrogel in between the higher density HA-NB/PEG2SH/Alg microfilaments, thus hindering matrix deposition.

Successful maturation, evidenced with SHG and histology analysis, was also macroscopically appreciable by the change of samples appearance during the experiment towards cartilage-like (white and opaque) look at the end of the culture period (Figure 5.4B). Notably, FLight HA-NB/PEG2SH hydrogels deformed during the culture period while FLight HA/PEG2SH/Alg did not. This could be due to the heterogeneous nature of the HA-NB/PEG2SH constructs with void spaces filled with collagen II which led to a heterogeneous tissue maturation and/or also to the stress-relaxation properties of Alg enabling matrix deposition without significant displacement of the pre-existing polymeric network.

Maturation of the samples was also analysed with compression testing to capture changes in mechanical properties during the *in vitro* tissue development. In accordance with SHG and histology, compressive modulus increased over the course of 28 days, eventually reaching outstanding native cartilage-like values for FLight hydrogels (~ 1 MPa) after 56 days (Figure 5.4C). From histological and mechanical analysis, FLight biofabrication was proven to induce a significantly improved tissue maturation when compared to homogenous bulk gels. In particular, FLight HA-NB/PEG2SH appeared to be the best candidate for generating articular cartilage with zonal architecture as it resulted in constructs having both high stiffness and aligned deposition of collagen II fibrils.

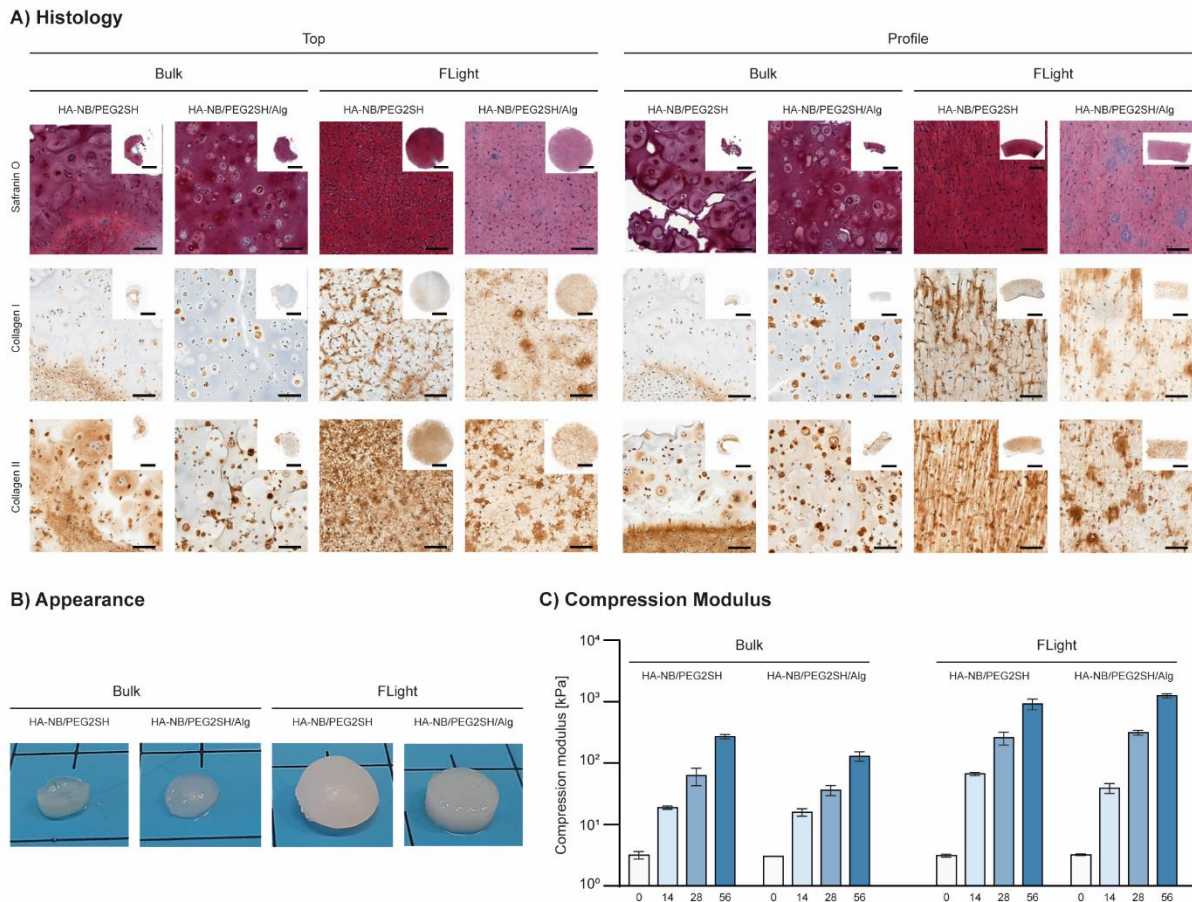


Figure 5.4 | A) Histological stainings of samples for GAGs (Safranin O), collagen I and collagen II. Sections from the “top” and the “profile” of the samples were generated showing remarkable tissue maturation for FLight printed constructs. Targeted aligned collagen II deposition was particularly evident for HA-NB/PEG2SH (profile panel). Scale bars: 2 mm, close ups: 100 μ m. B) Pictures showing white and opaque cartilage appearance of samples cultured for 56 days. FLight HA-NB/PEG2SH also showed deformation following tissue maturation, phenomenon not observed for HA-NB/PEG2SH/Alg double network. C) Uniaxial compression test showing mechanical stiffening of the samples resulting from tissue maturation, with FLight constructs reaching native cartilage stiffness (\sim 1 MPa).

5.3. Conclusions and Future Work

In summary, we proved that FLight biofabrication, when used with photoresins optimized for cartilage-specific applications, can be exploited to develop superficial/deep-zone-like constructs featuring unprecedented structural and mechanical properties. Ongoing and future experiments will explore the possibility to fully reconstruct articular cartilage featuring different zones by applying orthogonal projections in a multi-step procedure. Also, although we limited our samples to simple 4 mm gels, we foresee that the

flexibility given by using light projection could be exploited to generate large, centimeter-size constructs with patient-specific design (i.e., irregular shape matching patient cartilage defect).

5.4. Materials and Methods

All chemicals were purchased from Merck and cell culture reagents from Gibco unless indicated otherwise.

Synthesis of hyaluronic acid-norbornene (HA-NB). 2.5 g (6.25 mmol, 1 eq.) of high molecular weight HA (1.5 MDa, HTL Biotechnology) were left to dissolve overnight, under stirring, in 1 L of 150 mM MES buffer pH 4.5. 5.45 g of adipic acid dihydrazide (ADH, 31.25 mmol, 5 eq.) were then added to the solution. When completely dissolved, 300 mg of 1-Ethyl-3-(3-dimethylaminopropyl)carbodiimide (EDC, 1.56 mmol, 0.25 eq.) were solubilized in 2 mL of 150 mM MES buffer pH 4.5 and added dropwise to the reaction mixture. After 4h the pH was found to be 4.72 and the reaction was quenched by addition of NaOH 1M to reach pH 7. After addition of 2 g of NaCl the solution was dialyzed against mQ H₂O for 5 days with frequent water changes and freeze-dried. After lyophilization, 2.5g of HA-ADH were left to dissolve overnight, under stirring, in 1 L of PBS pH 7.4. Then, 2 g of carbic anhydride (12.5 mmol, 2 eq.) were dissolved in 10 mL of DMF and added dropwise to the solution. The reaction was left to proceed for 8 h with pH adjustments every 30 min using NaOH 2M to maintain pH 7.4. After addition of 2 g of NaCl the solution was dialyzed against mQ H₂O for 3 days using a tangential flow filtration system (ÄKTA Flux, Cytiva) and then freeze-dried. HA-NB degree of substitution (DS) was found to be 18% with ¹H-NMR (Bruker Ultrashield 400 MHz, 1024 scans) integrating norbornene double bond peak (~6.3 ppm, see Figure S7.13, Supporting Information). For NMR analysis the high viscous polymer was solubilized at 5 mg mL⁻¹ in 1 mL of 2 mM NaCl D₂O solution in the presence of a known amount of internal standard 3-(trimethylsilyl)-1-propanesulfonic acid (DSS). High ionic strength was found to be a powerful tool to improve the quality of the spectra. As reported by Ret et al., for long-chain, high viscous polymers in particular, the control of their conformation in solution can determine better proton mobility.⁸⁴⁰

Cell isolation and expansion. Human infant chondrocytes were isolated as previously described,⁸⁴¹ from the epiphyseal cartilage in joints removed during corrective surgery for polydactyly. Informed consent was obtained from the legal guardians of polydactyly patients, and experiments were approved by the Ethical Committee of Canton Zürich (Kantonale Ethikkommission, Kanton Zürich, license PB_2017-00510). Isolated cells were plated at a concentration of 10 000 cells cm⁻² and expanded in DMEM, 10% v/v FBS, 10 ng mL⁻¹ FGF-2 and 10 µg mL⁻¹ gentamicin until passage 3. At passage 3, cells were trypsinized, combined with DMEM, 10% v/v FBS, and 10 µg mL⁻¹ gentamicin and collected by centrifugation (5 min, 400 rcf). The cell pellet was finally carefully mixed with the different hydrogel precursors at a concentration of 5 million cells mL⁻¹.

FLight biofabrication. HA-NB and Alg (Pronova LVG, Novamatrix) were left to dissolve overnight under stirring in 150mM NaCl 50mM Tris buffer pH 7.4 at 1.2% and 1% respectively. Polymer solutions were then mixed with addition of PEG2SH (5 kDa, JenKem Technology, 5% in 150mM NaCl 50mM Tris buffer pH 7.4) and LAP solution (2.5% in 150mM NaCl 50mM Tris buffer pH 7.4) to obtain HA-NB/PEG2SH (0.75% HA-NB, 0.84% PEG2SH, 0.05% LAP) and HA-NB/PEG2SH/Alg (0.75% HA-NB, 0.7% PEG2SH, 0.25% Alg, 0.05% LAP) photoresin formulations. Photoresins were then filter-sterilized (0.2 μm filter) and mixed with infant polydactyl chondrocytes (passage 3) to a final concentration of 5 million cells mL^{-1} . Resulting bioresins were pipetted (0.6 mL) into quartz cuvettes (CV10Q7FA, Thorlabs). FLight projections were performed in a volumetric printer (Tomolite, Readily3D SA) in static mode (without sample rotation). Projected images (4 mm discs) were designed in Adobe Illustrator 2022 and projected for 3.3 seconds using a laser intensity of approximately 63 mW cm^{-2} . After printing, uncrosslinked resin was washed out using Tris buffer and samples were retrieved from the cuvettes using a spatula. HA-NB/PEG2SH samples were directly transferred to a 24-well plate with chondrogenic media (DMEM, $10 \mu\text{g mL}^{-1}$ gentamycin, 1% ITS+, $50 \mu\text{g mL}^{-1}$ L-ascorbate-2-phosphate, $40 \mu\text{g mL}^{-1}$ L-proline, and 10 ng mL^{-1} TGF- β 3), while HA-NB/PEG2SH/Alg samples were first incubated for 20 minutes in 100mM CaCl_2 50mM Tris buffer pH 7.4 to ensure ionic crosslinking of interpenetrating Alg network. Control (bulk) samples were instead casted in PDMS rings (4 mm diameter, 2 mm height) and crosslinked in a UV-box featuring 405 nm LED (light intensity $\sim 6.8 \text{ mW cm}^{-2}$) for 30 seconds, thus matching FLight procedure light dose ($\sim 208 \text{ mJ cm}^{-2}$). All samples were cultured in chondrogenic media in 24 well plates under gentle shaking with media change every 3 days.

Microchannels/Microfilaments infiltration test and characterization. Cell-free samples were fabricated as previously described as bulk or with FLight method. Samples were submerged in a solution of 1% FITC-Dextran (0.5 MDa) in PBS for 15 minutes prior imaging on Leica TCS SP8 (Leica) confocal microscope. For FLlight samples a z-stack of 100 μm (0.57 z-step) was taken to then obtain a 3D reconstruction (Imaris) (Figure 5.2Ai). Side and top sections (Fiji) were used to calculate the area distribution of channels and filaments using Fiji built-in functions and to measure manually the size of the microfeatures, respectively.

Uniaxial compression tests. Uniaxial unconfined compression tests were performed on a TA.XTplus Texture Analyzer (Stable Micro Systems) equipped with a 500 g load cell. Samples were placed between the compression plates and a pre-loaded (0.5 g at day 0, 2 g at day 14, 5 g at day 28 and 10 g at day 56) to ensure full contact with the plates. Samples were then allowed to relax for 2 minutes and then compressed to 15% strain at 0.01 mm s^{-1} . Compressive modulus was calculated by linear fitting the stress-strain curve from 0.5 to 5% strain.

Live/Dead and second harmonic generation (SHG) imaging. Samples were biofabricated as previously described and incubated in FluoroBrite DMEM supplemented with 1:2000 CalceinAM (Invitrogen) and 1:500 Propidium Iodide (PI, Fluka) for 40 minutes. Imaging was then performed on a Leica SP8 microscope (Leica) equipped with a 25× objective. SHG imaging was collected at ~450 nm with 800 nm two-photon excitation (Mai Tai laser, Spectra-Physics). Z-stacks were acquired from the sample surface at 2 μm steps and 100 μm into the sample. Gels were cut with a scalpel blade to then image their profiles. The pictures reported in the work resulted from maximum intensity z-projection. Cell viability was assessed by counting viable (CalceinAM) and dead (PI) cells with the ImageJ Analyze particle function.

Histology and immunohistochemistry. Samples were washed in Tris buffer, fixed in 4% paraformaldehyde for 4 h and dehydrated in graded ethanol solutions. After dehydration, samples were paraffin-embedded and 5 μm sections (from top and profile) cut on a microtome. Before staining, samples were deparaffinized and rehydrated. Imaging was performed on an automated slide scanner (Panoramic 250, 3D Histech).

For Safranin O staining the samples were first stained in Weigert's Iron Hematoxylin solution for 5 min, followed by washing in deionized water and in 1% acid-alcohol for 2 s. Sections were washed again in deionized water, stained in 0.02% Fast Green solution for 1 min and rinsed with 1% acetic acid for 30 s. Finally, sections were stained in 1% Safranin O for 30 min, dehydrated with xylene and mounted.

For immunohistochemistry (collagen I and collagen II stainings), antigen retrieval was performed with hyaluronidase (1200 U mL⁻¹) at 37 °C for 30 min. Sections were then blocked with 5% bovine serum albumin (BSA) in PBS for 1 h and then incubated overnight with the primary antibody, mouse anti collagen 1 (1:1000, Ab6308, abcam) or mouse anti collagen 2 (1:20, Hybridoma Product II-II6B3, DSHB) in 1% BSA in PBS at 4 °C. Sections were then incubated with the secondary antibody, goat anti-rabbit IgG-HRP (1:1000, ab6789, abcam), in 1% BSA in PBS for 1 h and developed with the DAB substrate kit (ab64238, abcam) according to manufacturer's protocol for 5 min. Sections were stained with Weigert's iron hematoxylin (Thermo Fisher Scientific) for 3 min, destained in 1% acid-alcohol, blued in 0.1% Na₂CO₃, and finally dehydrated with xylene and mounted.

Gene expression analysis. Gene expression levels were assessed through real-time PCR (qPCR) analysis. Samples were first washed with Tris buffer and then snap-frozen in liquid N₂. Frozen samples were mechanically disrupted with a pestle and then extraction of RNA was performed with NucleoZol (Macherey-Nagel) according to the manufacturer's instructions. Retrotranscription to cDNA was performed with GoScript Reverse Transcriptase (Promega) and cDNA was subsequently diluted 1:5 with RNase-free water for qPCR analysis. The analyzed genes were Col2A1 (Fw: GGA ATT CGG TGT GGA CAT AGG, Rv: ACT TGG GTC CTT TGG GTT TG), Col1A1 (Fw: CAG CCG CTT CAC CTA CAG C, Rv: TTT TGT

ATT CAA TCA CTG TCT TGC C), Runx2 (Fw: CGC ATT TCA GGT GCT TCA GA, Rv: GCA TTC GTG GGT TGG AGA A), Sox9 (Fw: TCT GGA GAC TTC TGA ACG AGA GC, Rv: TGT AAT CCG GGT GGT CCT TC), ADAMTS5 (Fw: CGA TGG CAC TGA ATG TAG GC; Rv: CTC CGC ACT TGT CAT ACT GC) and normalized to GAPDH expression (Fw: AGT CAG CCG CAT CTT CTT TT, Rv: CCA ATA CGA CCA AAT CCG TTG). Quantitative real-time PCR (qPCR) was performed with GoTaq qPCR Master Mix (Promega) on a QuantStudio 3 device (Applied Biosystems).

Acknowledgments. The authors thank Hao Liu for the help with 3D rendering and acknowledge the assistance from ETH (ScopeM) imaging facility.

Contributions. R.R. and A.P. listed as first authors contributed equally to this work, conceived the project, designed and performed the experiments. R.R. performed chemical synthesis, Live/Dead and SHG imaging. R.R. and A.P. performed biofabrication experiments. A.P. performed histology, immunohistochemistry and compression tests, A.B. performed gene expression analysis. M.Z-W. supervised the project. The chapter was written through the contributions of all authors.

CHAPTER 6

Microstrands for Tissue Alignment

In the previous Chapter, aligned tissue development was achieved by using FLight biofabrication. In this Chapter, another method to obtain aligned tissue constructs is explored. By simply sizing a photosensitive cell-laden hydrogel through a grid, tissue constructs composed of aligned microstrands and macropores can be generated, showing high potential in guiding oriented muscle tissue formation.

MANUSCRIPT

Macroporous Aligned Hydrogel Microstrands for 3D Cell Guidance

Riccardo Rizzo[†], Angela Bonato[†], Parth Chansoria, Marcy Zenobi-Wong

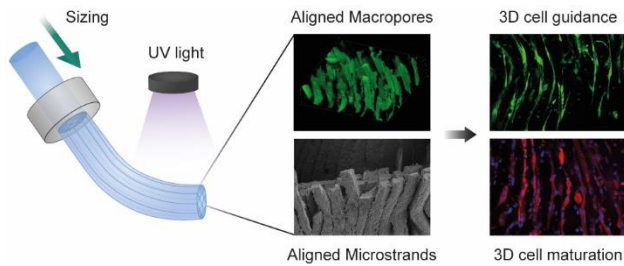
ACS Biomaterials Science & Engineering **2022**

DOI: 10.1021/acsbiomaterials.2c00370

[†]Equal contributions.

Reprinted with permission from ACS Biomater. Sci. Eng. 2022, 8, 9, 3871–3882, Copyright © 2022, American Chemical Society

Abstract



Tissue engineering strongly relies on the use of hydrogels as highly hydrated 3D matrices to support the maturation of laden cells. However, because of the lack of microarchitecture and sufficient porosity, common hydrogel systems do not provide physical cell-instructive guidance cues

and efficient transport of nutrients and oxygen to the inner part of the construct. A controlled, organized cellular alignment and resulting alignment of secreted ECM are hallmarks of muscle, tendons, and nerves and play an important role in determining their functional properties. Although several strategies to induce cellular alignment have been investigated in 2D systems, the generation of cell-instructive 3D hydrogels remains a challenge. Here, we report on the development of a simple and scalable method to efficiently generate highly macroporous constructs featuring aligned guidance cues. A precross-linked bulk hydrogel is pressed through a grid with variable opening sizes, thus deconstructing it into an array of aligned, high aspect ratio microgels (microstrands) with tunable diameter that are eventually stabilized by a second photoclick cross-linking step. This method has been investigated and optimized both *in silico* and *in vitro*, thereby leading to conditions with excellent viability and organized cellular alignment. Finally, as proof of concept, the method has been shown to direct aligned muscle tissue maturation. These findings demonstrate the 3D physical guidance potential of our system, which can be used for a variety of anisotropic tissues and applications.

6.1. Introduction

In the last decades, hydrogels have been extensively employed in the field of tissue engineering and bioprinting because of their high hydration, cell support in a 3D environment, and biomimetic properties.^{45, 108, 842-843} Although hydrogel-based bioprinting made it possible to generate complex macroscopic 3D shapes, the substantial homogeneity of common hydrogel formulations on a cellular scale lacks microstructure and porosity, both of which are pivotal elements to guide tissue formation.^{60, 844-845} The field has exploited two main approaches to direct tissue development and cell spatial arrangement within 3D matrices, namely, the introduction of either biochemical or physical cues.

Biochemical cues such as adhesion peptides, small molecules, and growth factors have been bound to hydrogel-forming polymers in various ways and used extensively to enhance the bioactivity and cell-interactive properties of hydrogel systems.⁸⁴⁶⁻⁸⁴⁸ They are reported to influence cell attachment, proliferation, and differentiation into the desired tissue type.⁸⁴⁹ In the past 20 years, the study of the effect of bioactive signals on cell fate and behavior in 3D matrices has also been made possible with fine spatiotemporal control using sophisticated light-based techniques such as two-photon patterning.^{132, 213, 724, 747, 850} Growth factors and small molecules have proved extremely valuable since they can recapitulate the biosignaling milieu of the developing tissue and act directly on cell migration, proliferation, and tissue maturation.^{109, 851-852} For example, adhesion peptides such as Arg-Gly-Asp (RGD) are widely used to mimic the presence of the extracellular matrix, thus favoring integrin-mediated cell adhesion.^{848, 853} Although some bioinert polymers need the incorporation of such small molecules to create anchor points for cells to better spread and migrate, other natural-derived polymers such as collagens or gelatin already possess such adhesion cues.⁸⁵⁴⁻⁸⁵⁶

Structural guidance of cells by physical cues is another powerful approach to directing tissue assembly and maturation.⁸⁵⁷⁻⁸⁵⁹ Unlike biochemical cues, biophysical ones persist for longer and are more versatile because their stiffness, porosity, pore size, and structural anisotropy can all be controlled.⁸⁴⁹ The polymer concentration and degree of substitution (DS) influence the resulting hydrogel stiffness, which has been shown to strongly influence stem cell fate toward differentiation into distinct tissues.⁸⁶⁰⁻⁸⁶² Porosity of the matrix is another important physical cue. It improves cell infiltration and migration, while also facilitating the diffusion of nutrients in the inner part of the construct in the absence of vascularization.⁶⁰ Several methods for producing porous hydrogel systems have been investigated, such as phase-transition,⁵⁹ freeze-drying,⁸⁶³ use of microribbons⁸⁶⁴⁻⁸⁶⁵ or sacrificial porogens,⁸⁶⁶⁻⁸⁶⁷ to name a few, and more recently the deconstruction of preformed hydrogels via sizing through a grid.⁴⁸⁹ Although some manufacturing techniques ensure size-controlled, macroporous, and biocompatible hydrogels, they often lack defined pore orientation and interconnection throughout the construct. The generation of complex, anisotropic cellular

organization, such as the one found in vasculature or musculoskeletal and connective tissues, plays a critical role in tissue microarchitecture and impacts both biological and mechanical properties of the tissue; it relies on geometrical constraints that can induce directional cell orientation.⁸⁶⁸⁻⁸⁶⁹

The abovementioned desired characteristics for an engineered construct for controlling cell behavior eventually need to also meet a size requirement for the intended application (i.e., *in vitro* model, *in vivo* implantation). Commonly, fabrication methods that are precise at a small scale also require lengthy processing times that pose a major limitation on cell viability. Conversely, quick and easy manufacturing techniques of large constructs may be less damaging to the cells but then lack the microstructure and macroporosity needed to instruct cell architecture at the microscopic level.

Here, we report on the development of a simple and scalable method to produce anisotropic macroporous constructs with high-aspect-ratio-aligned microgels (microstrands) acting as physical guidance cues. By pressing a gelatin-based bulk hydrogel through a grid with a tunable opening size, aligned microstrands are generated. The sized constructs are then stabilized for cell culture by a secondary cross-linking step based on a state-of-the-art photoclick thiol–norbornene reaction. Encapsulated cells benefit from oriented macroporosity that permits nutrient and oxygen supply within the construct and from the aligned microstrands that provide a preferred direction of growth. The sizing method is simple, fast, easily upscalable, and it can be carried out without special expertise, thus making it an attractive solution for the generation of various aligned tissue formations. In this work, we adopted myoblasts as a proof-of-concept model for aligned muscle tissue development.

6.2. Materials and Methods

Unless indicated otherwise, all chemicals are purchased from Merck, and cell culture reagents were purchased from Gibco.

Synthesis of Gelatin Norbornene (Gel-NB). The synthesis protocol was adapted from Rizzo et al. (Figure S6.1A).¹⁸⁷ In short, 50 g of gelatin type A from porcine skin was first dissolved in pH 9 0.1 M carbonate–bicarbonate buffer at 10% at 50 °C. When completely dissolved, 1 g of *cis*-5-norbornene-*endo*-2,3-dicarboxylic anhydride (CA) was added to the reaction mixture under vigorous stirring. After 10 min, the pH was checked and adjusted to 9 using NaOH 1 M before the addition of another gram of norbornene reactant. The same procedure was repeated up to the addition of a total of 5 g of CA. Twenty minutes after the last addition, the solution was diluted 2-fold in prewarmed mQ H₂O, and the pH was adjusted to 7 with the addition of HCl 1 M. The solution was then centrifuged for 15 min at 3000 rcf, and the supernatant was dialyzed for 3–4 days against mQ H₂O at 40 °C with frequent water changes before finally being freeze-dried. The Gel-NB degree

of substitution (DS) was calculated using ^1H NMR (Bruker Ultrashield 400 MHz, 1024 scans), as previously reported ($n = 3$, see Figure S6.2, Supporting Information).¹⁸⁷

Synthesis of Gelatin Thiol (Gel-SH). Gelatin type A from porcine skin (25 g) was dissolved in 1.25 L of pH 4 150 mM MES buffer warmed to 40 °C for a final concentration of 2%. When completely dissolved, 2.38 g (10 mmol) of 3,3'-dithiobis(propionohydrazide) (DTPHY) was added to the reaction mixture. Once completely dissolved, 3.83 g (20 mmol) of 1-ethyl-3-(3'-dimethylaminopropyl)carbodiimide hydrochloride (EDC) was added, and the reaction was left to proceed at 40 °C overnight. Then, tris(2-carboxyethyl)phosphine (8.6 g, 30 mmol) was added to the solution, and the reduction of the disulfide bonds was left to proceed for 6 h in a sealed flask (Figure S6.1B). Then, 1 g of NaCl was added to the solution before dialysis against mQ H₂O balanced it to pH 4.5 with diluted HCl. Finally, Gel-SH was freeze-dried and stored under inert atmosphere at -20 °C prior to use. The Gel-SH degree of substitution (DS) was determined by ^1H NMR (Bruker Ultrashield 400 MHz, 1024 scans). In short, Gel-SH was solubilized in a solution of 3-(trimethylsilyl)-1-propanesulfonic acid (DSS) in D₂O (Apollo Scientific). DSS methyl protons (0.1 to -0.1 ppm) were adopted as internal standards to calculate the SH millimoles per gram of gelatin by comparison with DTPHY methylene protons (2.85 to 2.75 ppm and 2.7 to 2.6 ppm) ($n = 3$, see Figure S6.3, Supporting Information).

Sizing Devices. The sizing devices used in this work were designed to fit inside a common 1 or 3 mL plastic syringe (Braun). These syringe holders were fabricated with a threaded end onto which a metal open cap was screwed to hold the desired grid in place (Figure 6.1A). The nylon grids had openings sizes of 20 μm , 40 μm , 100 μm (Merck Millipore) and 70 μm (cell strainer, Falcon). The grids were cut to a 9, 13, or 18 mm diameter to fit into 1, 3, or 10 mL sizing devices, respectively. As illustrated in Figure 6.1A, the assembly of the sizing device consisted of positioning the cut nylon mesh into the open cap, which was then tightly screwed onto the metal syringe holder to secure enough tension on the nylon fibers to cut the hydrogel. For cell experiments, all the components were sterilized using 70% EtOH and UV treatment.

Sizing Process: Generation of Aligned Microstrands. Gel-SH and Gel-NB were mixed at an SH:NB equimolar amount (1:1 ratio) in PBS at 37 °C with a total polymer concentration (Gel-SH + Gel-NB) of 2%, 5%, or 10%. In each formulation, the photoinitiator lithium phenyl-2,4,6-trimethylbenzoylphosphinate (LAP) was used at 0.05%. When completely solubilized, the photosensitive gelatin solution was filter-sterilized using 0.2 μm filters and then transferred to 1 mL or 3 mL sterile syringes, paying particular attention to avoid air bubbles. For the 10 mL sizing device, the solution was added directly into the stainless-steel tool previously sterilized with 70% EtOH and UV treatment. The syringes were then sealed with sterile plastic caps and parafilm, placed in ice, and protected from light. After 30 min on ice to allow for thermal cross-linking, the syringe tip was removed with a scalpel. The syringe filled with physically cross-linked

photosensitive gelatin was then inserted into the sizing device, previously assembled as described above. The hydrogel was sized onto a Petri dish by gently pushing on the syringe piston while moving it laterally (see Video S6.1, Supporting Information). Following a 2 min exposure in a UV box (405 nm) to covalently cross-link the aligned microstrands, the construct was cut into 1 cm pieces and transferred into cell culture media or PBS. The UV intensity was found to be 6.6 mW/cm² using a Thorlabs power meter (PM100D equipped with S120VC Standard Photodiode Power Sensor). The video of the sizing process (Video S6.1, Supporting Information) and the pictures showing the system scalability (Figure 6.1B) were taken with a Fujifilm X-T3 camera.

Rheological Analysis. Rheological measurements were carried out on an Anton Paar MCR 301 with 20 mm parallel plate geometry. A wet tissue paper was added to the chamber to prevent Gel-NB/Gel-SH photoresins from drying during analysis. The storage and loss modulus of the thermally cross-linked Gel-NB/Gel-SH formulations were obtained under oscillatory conditions (2% strain, 1 Hz frequency, 0.2 mm gap, 10 s measuring point duration). The samples were first allowed to equilibrate at 37 °C in the humidified chamber for 5 min prior to starting the measurements. Physical cross-linking was induced with a linear cooling ramp (2 °C/min) from 37 to 8 °C (minimum temperature attainable) followed by 45 min at 8 °C to reach plateau values. Following the oscillatory analysis, the samples were kept at 8 °C to determine the yield stress by performing a strain sweep analysis with strain values going from 10⁻¹ to 10³ (1 Hz frequency, 0.2 mm gap, 10 s measuring point duration). The yield stress was calculated as the peak value of the elastic stress (σ' , product of storage modulus G' and strain amplitude) plotted against strain, as previously reported.⁸⁷⁰⁻⁸⁷¹

Initial viscosity and shear thinning behavior were characterized on thermoreversibly cross-linked photoresins in rotational tests (0.2 mm gap). The shear rate was increased logarithmically from 0.01 to 300 s⁻¹, while the measurement point duration was decreased logarithmically from 300 s per point to 1 s per point.

Compression Test of Bulk Hydrogels. TA.XTplus Texture Analyzer (Stable Micro Systems) equipped with a 500 g load cell was used to perform unconfined uniaxial compression tests. Solutions composed of 0.05% LAP and different total Gel-NB/Gel-SH concentrations (2%, 5%, 10%) in PBS were warmed to 37 °C, filter-sterilized, and pipetted into PDMS molds of 4 mm in diameter and 2 mm in height. The samples were allowed to thermally cross-link in ice for 30 min, thus mimicking the temperature variation that occurs during the sizing procedure, and were then UV cross-linked for 2 min. After a washing in PBS, the cylinders were placed between the compression plates and a 0.1 g preload was applied to ensure full contact. The samples were left to relax for 2 min and then compressed with a speed of 0.01 mm/s to 15% strain. The elastic compressive modulus was determined by linear fitting of initial linear section of the stress–strain curve (0–5%). The measurements were performed in triplicate ($n = 3$).

SEM Imaging. Aligned microstrands were prepared as indicated above. After washing in PBS, the cross-linked, structured hydrogels were cut into 1–2 mm slices with a scalpel and fixed in 4% paraformaldehyde in PBS for 2 h at room temperature. Samples were then washed with Milli-Q H₂O and then dehydrated by stepwise treatment first with ethanol in mQ H₂O (30%, 50%, 70%, 90%, 100%) and then with hexamethyldisilazane (HMDS) in ethanol (30%, 50%, 70%, 90%, 100%) with a 20 min incubation for each step. After 1 h in 100% HMDS, the samples were left to dry in a fume hood. The dried samples were sputter coated (CCU-010 HV, Safematic) with platinum–palladium (Pt/Pd) and imaged with a Hitachi SU5000 field emission SEM. The nylon grids were simply sputter coated with Pt/Pd prior to imaging.

Macroporosity and Percolation. Aligned microstrands were generated as described above using a total gelatin concentration of 2%. The aligned constructs were then submerged in a solution of high molecular weight FITC-Dextran (500 kDa) in PBS for 15 min. The percolation (fluid movement through porous material) of the fluorescent polymer in the macroporous construct was then imaged using a Leica SP8 confocal microscope (Leica) equipped with a 25× objective. \times -Stacks of 100 μm were acquired from the sample surface with 1 μm \times -steps. The images were processed using Fiji.

Computational Modeling of the Shear Stress during Sizing. The computational model constituted a steady-state inelastic non-Newtonian fluid flow model in COMSOL Multiphysics (COMSOL Inc., SE). The shear-thinning characteristics of the photoresin at different concentrations (2, 5, and 10% w/v) were defined by the power law:⁸⁷²

$$\mu(\dot{\gamma}) = m\dot{\gamma}^{n-1} \quad (6.1)$$

where μ is the dynamic viscosity of the resin, $\dot{\gamma}$ is the shear rate, and m and n are the flow consistency and flow behavior indices, respectively. Through rheological measurements of thermoreversibly cross-linked photoresin samples at each concentration, the flow consistency indices were 22, 229, and 1750 Pa s for 2, 5, and 10% w/v resin concentrations, respectively. Furthermore, a constant flow behavior index of 0.2 was deemed to generate the best-fit model for the dynamic viscosity variation with shear rate. The models comprising the sizing meshes constituted a small 3×3 grid of the sizing grid with a bulk fluid domain above the mesh (Figure 6.4B). The grid dimensions were determined from SEM images of the nylon meshes. A normal inflow velocity of 5 mm/s was applied at the fluid domain to mimic the speed at which the sizing process was conducted, and a free flow constraint was applied at the output of the sizing grid. A no-slip condition was applied at the walls of the sizing grid. As for the meshing criteria, a free tetrahedral mesh with maximum element size of 2 μm (i.e., one-tenth the size of the minimum feature dimension of 20 μm), similar to in previous studies, was applied.^{873–874} The compilation time for a parametric sweep across the three flow consistency indices was 18 min. The resulting shear stress was plotted across the entire width of an opening

within the sizing grid. For the model without the sizing grid, a simple cylindrical ($\Phi = 5$ mm, $h = 10$ mm) shear thinning model was used, and the shear stress was determined throughout the entire width of the model.

Cell Culture and Encapsulation. C2C12 myoblasts were expanded in cell culture media composed of DMEM + 10% fetal bovine serum + 10 $\mu\text{g}/\text{mL}$ gentamicin in 5-layer flasks (Falcon). The C2C12 cells were trypsinized and mixed with warm (37 °C) and sterile Gel-NB/Gel-SH photosensitive solutions at 10 million cells/mL. Following the sizing procedure described above, the cell-encapsulated aligned microstrands were directly transferred into 24-well plates and cultured from day 0 in differentiation media composed of DMEM + 2% horse serum + 1% ITS (Corning) + 10 $\mu\text{g}/\text{mL}$ gentamicin for up to 3 weeks with a media change every other day. Videos of the myotubes twitching (Video S6.2, Supporting Information) were taken after 3 weeks of culture on an Axio Observer.Z1 (Zeiss) in bright-field mode with 5 \times or 10 \times magnification.

Cell Viability. A cell viability assay was performed as previously described.¹⁸⁷ In short, the samples at day 0, day 2, and day 7 of culture were incubated for 45 min in FluoroBrite DMEM supplemented with 5 $\mu\text{g}/\text{mL}$ of Hoechst 33342 (Invitrogen), 8 μM of calcein AM (Invitrogen), and 0.5 $\mu\text{g}/\text{mL}$ of propidium iodide (PI, Fluka). The samples were then imaged with a Leica SP8 confocal microscope (Leica) equipped with a 25 \times water immersion objective. z -Stacks of 50 μm were acquired from the sample surface with 5 μm z -steps. The images were processed using Fiji. The cell viability was determined by counting nuclei stained with Hoechst 33342 as the total cell number and those with the propidium iodide signal as dead cells. Because of the myoblasts spread and fusion into the myotubes, calcein AM could not be used as a reliable signal to count live cells.

Analysis of Nuclei Alignment. The samples were stained, as described above, with Hoechst 33342 (Invitrogen) and calcein AM (Invitrogen) after 7 days of culture. Images were taken with the microstrands aligned vertically. The software Fiji was used to identify the nuclei via the Hoechst 33342 channel by applying a Gaussian blur filter, followed by thresholding to create a binary image, and finally by using the watershed method to separate close nuclei. The segmented objects were then analyzed with the Extended Particle Analyzer function to evaluate the nuclei angle and circularity distributions. The data were plotted using Prism 8 (GraphPad).

Immunofluorescence. After 3 weeks in culture, the samples were washed 3 \times in PBS and fixed in 4% paraformaldehyde for 4 h at room temperature, followed by washing 3 \times in PBS supplemented with 0.02% BSA. The samples were then permeabilized using a solution of 1% Triton-X100 in PBS for 10 min, followed by washing 3 \times in PBS + 0.02% BSA. After a blocking step using 1% BSA and 1% Tween-20 solution in PBS for 30 min, the constructs were incubated with primary antihuman myosin heavy-chain antibody (MF-20, DHSB), diluted 1:20 in PBS overnight. After washing 3 \times in PBS, the constructs were incubated with

fluorescent secondary antibody (goat antimouse Alexa488, Invitrogen) and Hoechst 33342 (Invitrogen), diluted 1:1000 in PBS in the presence of 0.02% BSA for 2 h. Imaging was performed on a Leica SP8 confocal microscope (Leica) equipped with a 25× water immersion objective.

For ki-67 staining, the samples were treated as described above up to the blocking step and then incubated with anti ki-67 antibody (550609, BD), diluted 1:200 in PBS overnight. After 3× washes, the samples were incubated with the Alexa 488 secondary antibody antimouse and Hoechst, as described previously. Imaging was performed on a Leica SP8 confocal microscope (Leica), equipped with a 40× water immersion objective.

For actin staining, the samples were treated as described above, washed 3× in PBS, and incubated for 2 h at room temperature in a solution containing Hoechst 33342 (1:1000 dilution) and Phalloidin-TRITC (0.13 µg/mL in 1% PBS-BSA, P1951, Sigma). After washing 3× with PBS, the samples were imaged on a Leica SP8 equipped with a 40× water immersion objective.

Gene Expression Analysis. RNA was extracted from the samples with NucleoZol (Macherey-Nagel) according to the manufacturer's instructions. Retrotranscription to cDNA was performed with GoScript Reverse Transcriptase (Promega) and subsequently diluted 1:5 with RNase-free water for qPCR analysis. The analyzed genes were MyoD (Fw: AAGACGACTCTCACGGCTTG, Rv: CGGGGCCTGTCAAGTCTATG), MyoG (Fw: AGCCCAGCGAGGGAATTTAG, Rv: GGGACATTAACAAGGGGGCT), MyH1 (Fw: CATCCCTAAAGGCAGGCTCT, Rv: GACTTCCGGAGGTAAGGAGC), Pax7 (Fw: CCCATGGTTGTGTCTCCAAGAT, Rv: CGGAGTCGCCACCTGTCTG), and all were compared to GAPDH expression as the housekeeping gene (Fw: GGTGAAGGTCGGTGTGAACGGATTTGG, Rv: GGTC AATGAAGGGGTCGTTGATGGCAAC). Quantitative real-time PCR (qPCR) was performed with GoTaq PCR (Promega) on a QuantStudio 3 device (Applied Biosystems).

6.3. Results and Discussion

6.3.1. Sizing Process and Choice of the Material

The physical guidance of cells by means of oriented hydrogel microarchitecture represents an attractive solution for the tissue engineering of naturally aligned tissues, such as muscles and tendons. The presence of physical cues can provide preferential directionality for cell spreading and migration, eventually having an impact on cell differentiation and tissue functionality. Importantly, this organized cellular alignment should be induced not only on the surface of the scaffold, but also in its depth. In fact, although many successful studies on the effect of structural patterns were conducted on 2D systems,⁸⁷⁵⁻⁸⁷⁶ 3D structural guidance

remains a challenge. In this work, an easy method to generate macroporous hydrogel constructs with aligned microstructures for 3D cellular alignment is presented.

As illustrated in Figure 6.1A, this method is based on the deconstruction of a bulk hydrogel into long, aligned microstrands with tunable dimension by sizing it through a grid of variable opening sizes. The microstrand construct was then stabilized with a secondary UV cross-linking process. As a proof of concept, aligned microstrands were generated starting with 1, 3, or 10 mL of photosensitive material (photoresin) using sizing devices of various dimensions, thus showing the scalability of the method (Figure 6.1B). A material suitable for such a sizing process should be able to undergo a first cross-linking step in the syringe to form a bulk hydrogel and a second cross-linking step after the sizing procedure to stabilize the construct.

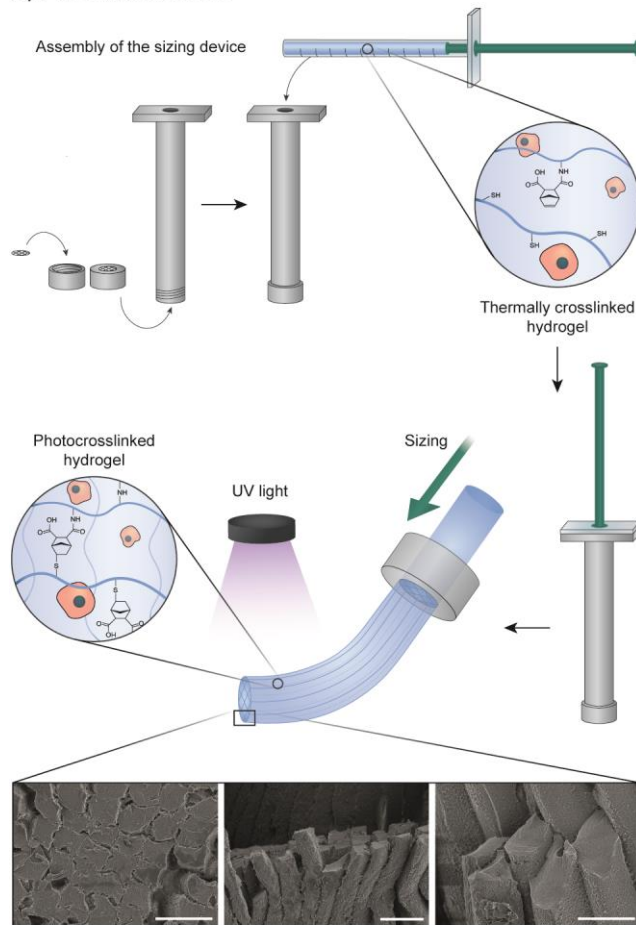
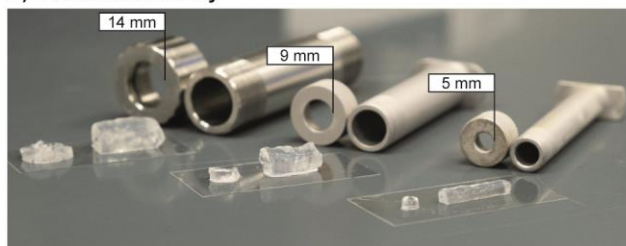
A) Procedure scheme**B) Method scalability**

Figure 6.1 | Sizing process. (A) Illustration of the procedure. On top, the assembly of the sizing device is shown with a nylon grid, syringe, and mesh metal holders, with the syringe filled with cell-laden photoresin based on Gel-NB/Gel-SH. Upon cooling to obtain a thermally reversible gel, the cell-laden hydrogel is pushed through the grid to obtain a hydrogel construct composed of aligned cellular microstrands. The latter is then stabilized via UV exposure to trigger photoclick thiol–norbornene reactions. At the bottom is a close-up with SEM images of the aligned microstrands forming the sized gel. Scale bar: 50 μm . (B) Sized gels of various dimensions (cross section and entire gel) on glass slides. On the side, devices are used to show the method scalability. From left to right: 10 mL, 3 mL, and 1 mL device. Labels refer to the aperture of the grid holder, which in turn reflects the final gel diameter.

This could be achieved with a variety of methods ranging from physical or ionic cross-linking^{113, 877-878} to enzymatic^{104, 879} or photo-cross-linking.¹³² We fulfilled this requirement by using a combination of gelatin-

norbornene (Gel-NB) and gelatin-thiol (Gel-SH) as a model system in this work (Figure 6.1A). Gelatin represents one of the most widely used biopolymers in the field of bioprinting and tissue engineering because of its biocompatibility, bioactivity (i.e., presence of RGD adhesion sites), biodegradability, and low cost.^{96, 588, 778, 880} It has intrinsic reversible thermal gelation properties and is relatively easy to functionalize with reactive moieties. We exploited the gelatin thermoreversible physical gelation induced by cooling as a first cross-linking strategy and introduced the highly efficient photoclick thiol–norbornene reaction as the secondary cross-linking strategy. In recent years, thiol–ene chemistry appeared to be a more attractive solution for biomedical applications when compared to traditional chain-growth polymerization (i.e., methacryloyl derivatives such as Gel-MA) because of its faster reaction kinetics, which reduces the need for long light exposures and free-radical formation.^{268, 689, 691, 774} Among the various advantages, the click-like reaction also leads to a more homogeneous network formation than the one formed with the growth of a hydrophobic kinetic chain of chain-growth systems. In this study, Gel-NB (DS: 0.163 ± 0.003 mmol/g) and Gel-SH (DS: 0.276 ± 0.016 mmol/g) (Figures S6.1–S6.3, see Supporting Information) were combined to have an equimolar amount of the reactive groups for a total polymer concentration of 2%, 5%, or 10%. For every formulation, the state-of-the-art water-soluble photoinitiator LAP was used at a final concentration of 0.05%, as was proven to be highly biocompatible in previous works.^{187, 881–882}

6.3.2. Macroporosity and Percolation

The effects of four different commercially available nylon grids with opening sizes of 20 μm , 40 μm , 70 μm , and 100 μm were investigated in comparison with common monolithic bulk hydrogel (Figure 6.2A). The sizing process was shown to lead to the formation of aligned high aspect ratio microstrands with tunable dimensions reflecting the opening size (Figure 6.2B). The presence of such anisotropic microarchitecture was observed also within the construct, which indicated a potential for 3D physical guidance.

Notably, it was observed that the sizing process generated macropores between the elongated microstrands, thus significantly enhancing the biological relevance of this system (Figure 6.3). In fact, the porosity of a scaffold is a pivotal aspect for the sufficient transport of nutrients and oxygen and the removal of catabolic waste. The presence of micrometer-sized void spaces can also facilitate cell infiltration and migration,^{59, 882–884} and this is commonly referred to as macroporosity for pore diameters in the range of ~ 0.1 – 10 μm and supermacroporosity for pore cross sections ranging from tens to hundreds of micrometers.⁸⁸⁵ The latter term is, however, almost exclusively found to describe cryogels.^{886–888} Bulk hydrogels' porosity is instead commonly referred to as nanoporosity because of the fact that the intricate cross-linked mesh of polymer chains leaves pores in the range of nanometers.^{889–892} Such a dense network strongly limits mass transport,

which is therefore restricted to a limited diffusion distance ($\sim 100\text{--}200\ \mu\text{m}$), and is a major obstacle in the tissue engineering field of millimeter- to centimeter-sized structures.⁸⁹³

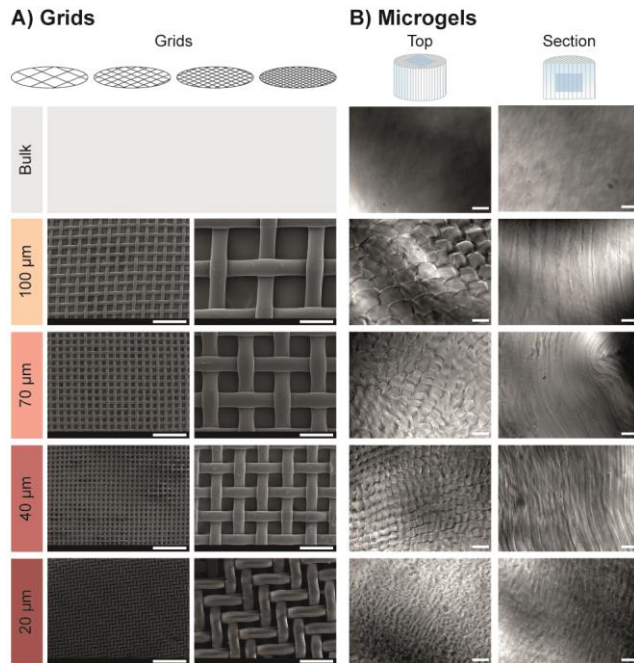


Figure 6.2 | Grids and sized gels. (A) SEM images of nylon grids of various openings size. For the bulk gel, no grid was used. Scale bar: left $500\ \mu\text{m}$, right $100\ \mu\text{m}$. (B) Brightfield images of sized gels showing aligned microstrand structures with variable size from the top (left) and from the side in an inner section (right). Scale bar: $100\ \mu\text{m}$.

The formation of the macroporous structures was assessed by submerging the sized gels into a solution of fluorescent, high molecular weight dextran (FITC-Dextran). Confocal imaging revealed the presence of elongated macropores running along the interfaces between proximal microstrands, while there was complete absence of percolation (fluid movement through porous material) in the bulk gel (Figure 6.3A). Because the use of smaller grids results in more numerous microstrands, the total porosity appeared to be inversely correlated to the grid size. The 20 and 40 μm grids showed a porosity of $\sim 25\%$, while the void fraction was $\sim 15\%$ and $\sim 8\%$ for the bigger 70 and 100 μm grids, respectively (Figure 6.3B). However, the pores' size seemed to have a less pronounced correlation to the grid openings' size, although larger pores are more likely to be found with the bigger grids. Pore size is, in fact, most probably dependent on the dimensions of nylon fibers, which are found to be larger ($45\ \mu\text{m}$ versus $30\ \mu\text{m}$) and thicker ($60\ \mu\text{m}$ versus $45\ \mu\text{m}$) for the 100 and 70 μm grids when compared with the 20 and 40 μm (Figure 6.2A). As a result, the sized constructs showed a pore size ranging from a minimum average of $\sim 190\ \mu\text{m}^2$ for the 20 μm grid to a maximum average of $\sim 526\ \mu\text{m}^2$ for the 70 μm grid (Figure 6.3C). Such void spaces create an ideal percolating system throughout the

whole construct, which facilitates mass transport, thereby overcoming the diffusion distance barrier and creating an excellent environment for cell infiltration.

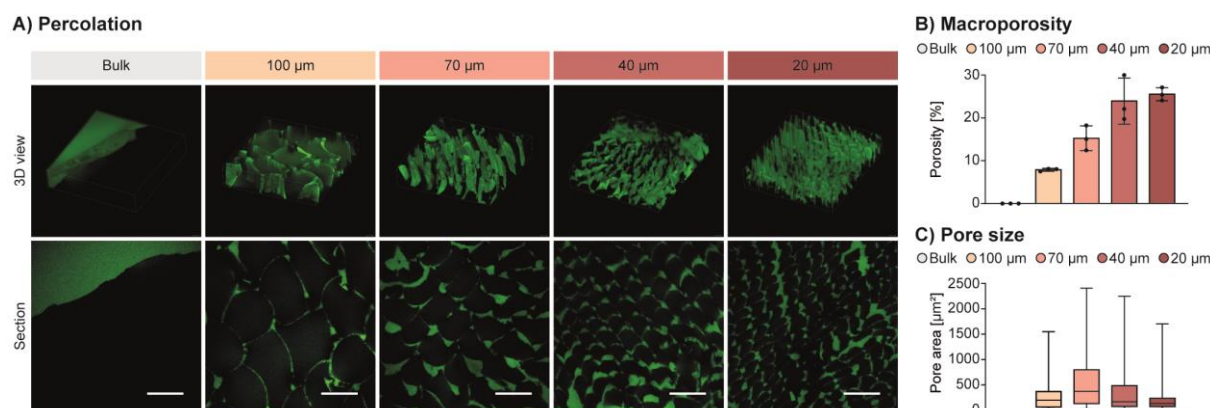


Figure 6.3 | Macroporosity. (A) Confocal images of fluorescent high molecular weight dextran (FITC-dextran) percolating into the aligned macropores found between proximal microstrands. For the bulk gel, no percolation was observed because of the absence of macroporosity. The fluorescent signal comes from the FITC-dextran solution around the gel itself. On top is a 3D volume reconstruction of a 100 μm z -stack. At the bottom is a 2D section of the porous constructs. Scale bar: 100 μm . (B) Sized gel macroporosity reported as a percentage of void fraction showing a tendency toward higher porosity for smaller grid size. (C) Average pore size for various sized constructs with a distribution ranging from $\sim 20 \mu\text{m}^2$ to over 2000 μm^2 . Macropores were instead not found in the bulk gel.

6.3.3. Computational Modeling and Cell Viability

We gained more insights into the effect of the sizing process on cell viability, which relies on the application of mechanical forces to sieve the bulk hydrogel through the grid, by running a finite element analysis (FEA) and comparing these results with an *in vitro* viability assay. First, rheological tests were performed to extrapolate the storage modulus, yield stress, and viscosity of the thermally cross-linked 2%, 5% and 10% photoresins to better model the sizing process for our Gel-NB/Gel-SH formulation (Figure 6.4A). The physically cross-linked gelatin-based hydrogel storage modulus ranged from $\sim 270 \text{ Pa}$ for the soft 2% condition to ~ 3.4 and $\sim 11.4 \text{ kPa}$ for the much stiffer 5% and 10% gels, respectively (Figure 6.4A, top). Yield stress, determined as the peak value of elastic stress obtained with a strain sweep, also followed the same trend, spanning from $\sim 588 \text{ Pa}$ for 2%, to ~ 11.5 and $\sim 28.7 \text{ kPa}$ for 5% and 10%, respectively (Figure 6.4A, middle). Shear thinning tests were used to determine the initial viscosity and flow behavior index of the different hydrogels (Figure 6.4A, bottom).

As expected, polymer concentration plays a central role in the induced shear stress. Because of the larger photoresin viscosity and stiffness, the computational modeling showed that the shear stress for the 10% condition (max $\sim 12 \text{ kPa}$) was an order of magnitude higher than 5% (max $\sim 1.6 \text{ kPa}$) and 2 orders of

magnitude higher than for 2% (max ~ 155 Pa). In addition, the simulations revealed a correlation between the grid openings' size and shear stress magnitude. Smaller grids were, in fact, found to induce the highest shear stress for each photoresin formulation.

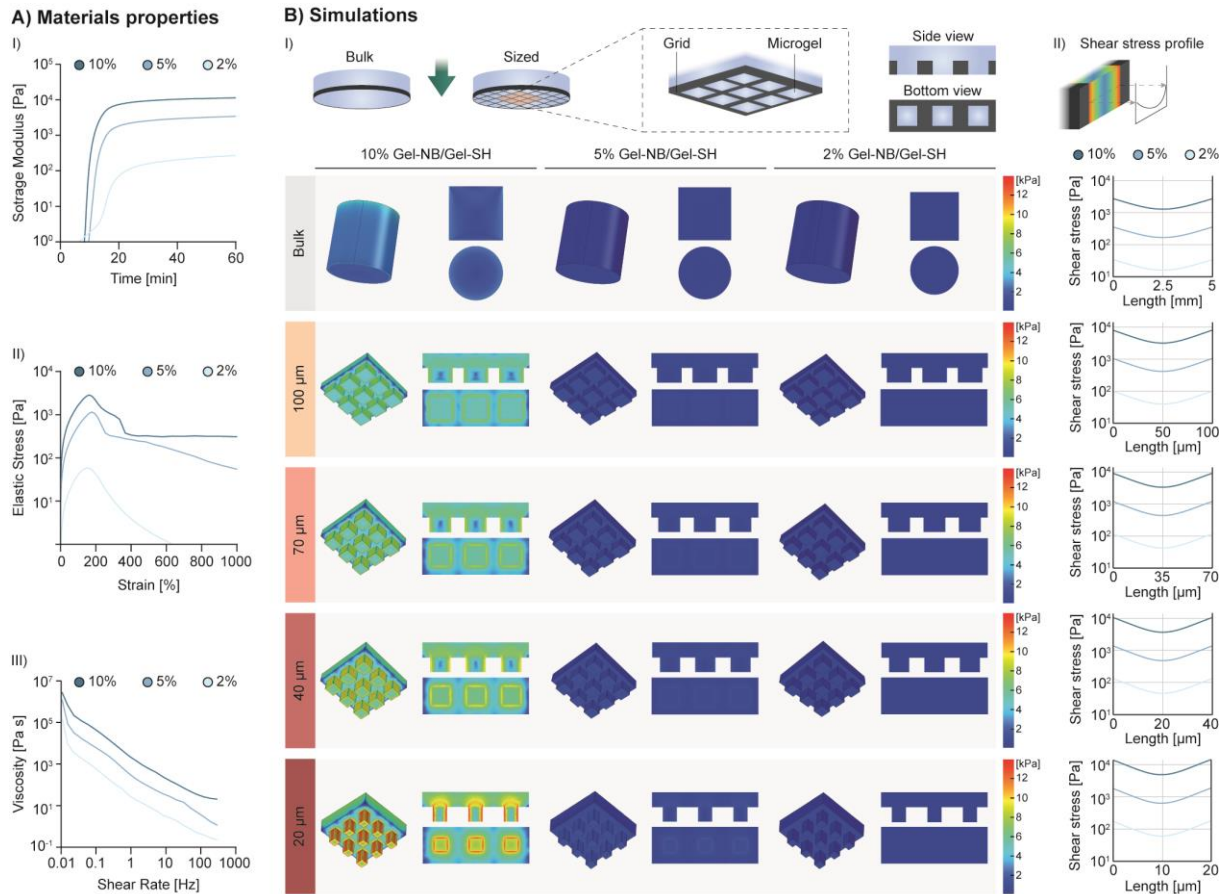


Figure 6.4 | Computational modeling of the sizing of Gel-NB/Gel-SH thermally cross-linked hydrogels. (A) Rheological measurements used to determine the storage modulus (top), yield stress (middle) and viscosity (bottom) of the material to be used for the computational models. All the photoresin concentrations tested demonstrated a shear thinning characteristic following the power law (equation 6.1, see Materials and Methods) with a flow behavior index of 0.2 and flow consistency indices of 22, 229, and 1750 Pa s for 2%, 5%, and 10% concentrations, respectively. (B) (I) Color-coded output of shear stress determined by an inelastic non-Newtonian flow model in COMSOL (see Materials and Methods section). The results are shown for the whole bulk gel (without sizing grid) and 3×3 mesh of the sizing grid for sized constructs, as illustrated on the top row. The simulation results are presented in a 3D view, side cross section, and bottom cross section, as illustrated on the top row. For clarity, the nylon grids are not shown in the simulations. (II) Shear stress distribution in a single-forming microstrand illustration (top) and results (bottom) plotted for the bulk condition and the different grid sizes. The profiles showed a clear increase in shear stress for stiffer hydrogels (higher polymer concentration) and smaller grid size. In all the conditions, the shear stress was found to be highest on the periphery of the microstrands.

For the bulk gel, where no grid was used, the shear stress was found to be significantly lower (max ~ 4 kPa for 10%, ~ 550 Pa for 5%, and ~ 50 Pa for 2%) and was confined only to the outer periphery of the tube where the no-slip boundary condition applies.⁸⁹⁴ For the sized gels, because of the same concept of the no-slip boundary, the highest shear stress values were reported at the periphery of the single opening of the sizing grid and showed to be more pronounced for smaller grid sizes. This phenomenon could be attributed to the increased fluid flow velocity in the smaller opening due to a constrained volume. A detailed distribution of the shear stress for a single microstrand within a single grid opening (or the whole bulk hydrogel in the syringe) is reported in Figure 6.4B,II. In short, from the *in silico* analysis it can be inferred that a combination of high polymer content and small sizing grid will lead to the worst conditions, in terms of shear stress, experienced by encapsulated cells, which would eventually affect the viability of the construct. Conversely, the sizing of soft, low-polymer-content hydrogels is expected to have no or negligible harmful effects. Extensive investigation on shear-stress-induced cell damage in the bioprinting field found a threshold around 5 kPa, above which cell survival tends to be significantly reduced.^{536, 895} Other studies set the bar of critical stress much lower (~ 250 – 500 Pa).⁸⁹⁶⁻⁸⁹⁷ Therefore, the 2% condition appears to be the most likely to result in a satisfying biocompatibility output.

The results of the simulations were compared with the cell viability of C2C12 myoblasts sized under the same conditions (Figure 6.5). Specifically, the sizing of cell-laden Gel-NB/Gel-SH thermally cross-linked hydrogels was conducted by varying the grid size (20 μm , 40 μm , 70 μm , 100 μm , and bulk) and polymer concentration (2%, 5%, and 10%). For every condition, the viability was determined in the outer part of the gel (surface) and the inner part of the gel. The latter was performed by cutting the gel in half prior to imaging, which allowed for the assessment of this method's potential to truly guide cellular alignment in 3D (Figure 6.5A).

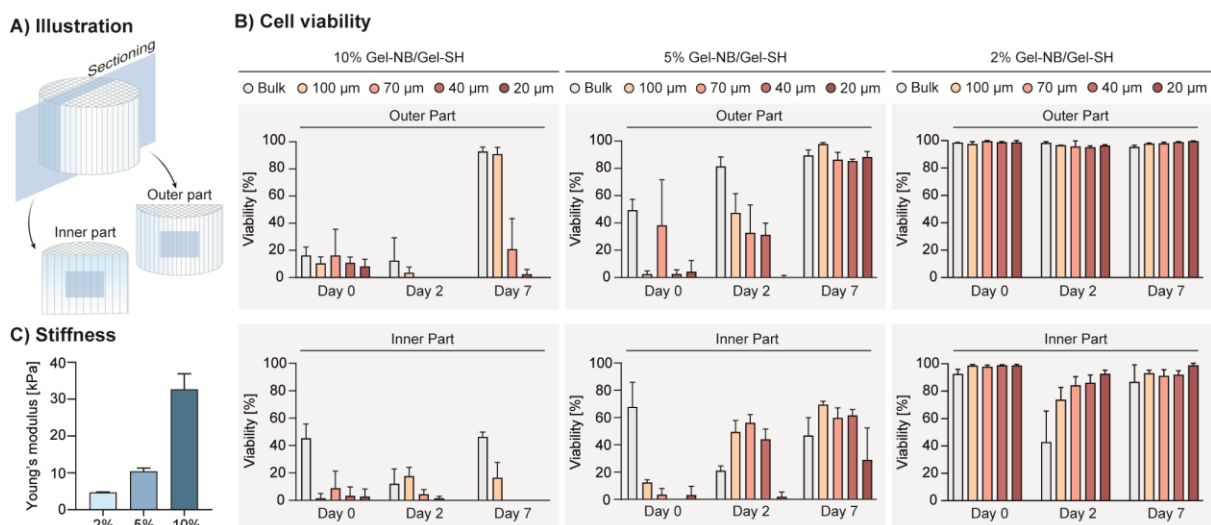


Figure 6.5 | Viability assay. (A) Schematic depicting the imaging procedure, taking into account both the surface of the hydrogels (outer part) and the core (inner part) to verify the impact of the aligned microstrands within the whole 3D construct. (B) Cell viability determined at day 0 (immediately after extrusion), day 2, and day 7 of 10%, 5%, and 2% Gel-NB/Gel-SH hydrogels sized with the various grids. (C) Compressive (Young's) modulus of the hydrogels after the stabilizing secondary cross-linking via UV exposure.

As predicted by the FEA simulation, higher polymer concentrations (5% and 10%), which are associated with higher shear stress, led to extensive cell death at day 0 immediately after the extrusion (Figure 6.5B). The viability only partially recovered in the following days, both in the inner and outer parts of the constructs. In particular, the conditions that were predicted to be the harshest (10% polymer concentration, 20–40 μm grids) showed an almost complete absence of viable cells after 1 week (Figure S6.4A, Supporting Information). However, for the 5% hydrogels, the cells that were not irreversibly damaged during the sizing procedure proliferated in both the inner and outer parts of the constructs (Figure S6.4B, Supporting Information), as was also confirmed by the presence of ki-67 positive cells (Figure S6.5, Supporting Information). Finally, as expected on the basis of simulations, a polymer concentration of 2% yielded the best result, with excellent cell viability (>90%) immediately after sizing and during the first week of culture. Although high viability at day 0 can be attributed to low shear stress, its retention during the 7 days of culture probably depends on the hydrogel mechanical properties and the generated microarchitecture. On one hand, after the stabilizing photo-cross-linking step, the compressive modulus for the Gel-NB/Gel-SH constructs was reported to be ~ 4.7 kPa for 2%, ~ 10 kPa for 5%, and ~ 32 kPa for 10% (Figure 6.5C). Matrix stiffness has, in fact, been shown to strongly influence C2C12 spreading and differentiation, with better output for softer gels.⁸⁹⁸ On the other hand, as evidenced in the previous paragraph, the sizing process facilitates mass transports within the construct because of the presence of aligned macropores in between the formed microstrands. This provides more nutrients and space for the cells to grow in the inner part of the gel compared with the bulk condition, as could be inferred by the drop in cell viability for such monolithic constructs after 2 days. Recovery in cell viability for the bulk gel (inner part) at day 7 appears instead artificially high. At this time point, because of the drastic decrease in cell number reported after day 2 (see Figure S6.6, Supporting Information), the percentage of the few remaining live cells becomes similar to the one of the other conditions.

6.3.4. 3D Physical Guidance of Oriented Cell Maturation

Using a Gel-NB/Gel-SH concentration of 2%, which was found to be the optimal condition both *in silico* and *in vitro*, the cell guidance potential of the microstrands was investigated. Importantly in this case, both the surface of the gel (outer part) and its core (inner part) were also analyzed in order to have a complete view on cell behavior in the 3D constructs. Muscle tissue is a good example of highly aligned tissue, with fiber alignment playing a crucial role in dictating its mechanical function (muscle contraction). Tissue-

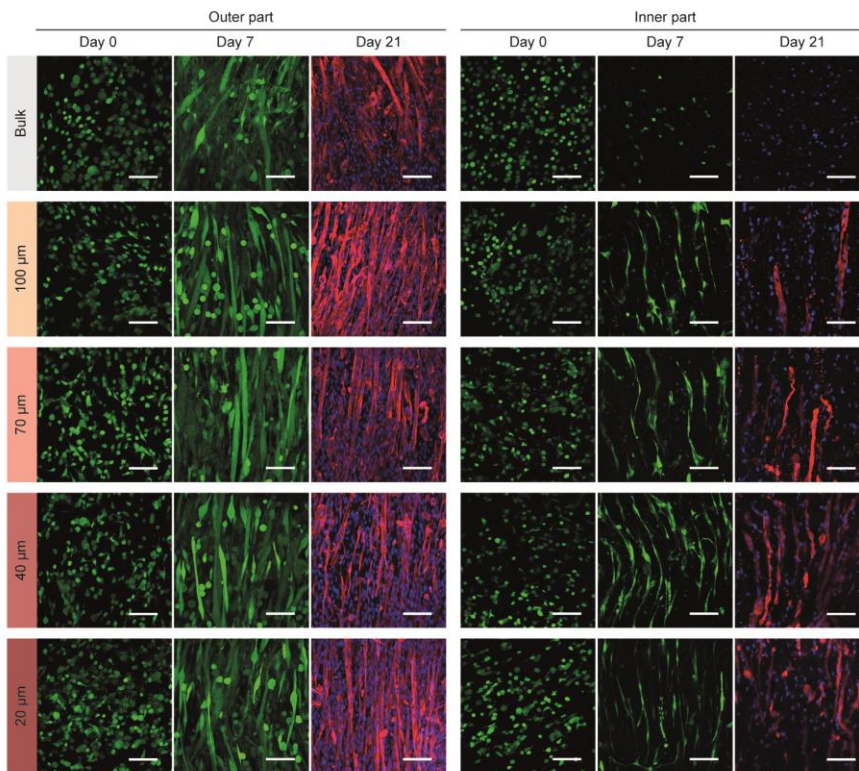
engineered muscle constructs that are able to mimic the native microarchitecture can be used as functional *in vitro* models,⁸⁹⁹⁻⁹⁰² and they are seen as a promising treatment for muscle traumas or disorders such as volumetric muscle loss (VML)⁹⁰³⁻⁹⁰⁴ and sarcopenia.⁹⁰⁵⁻⁹⁰⁶ In this study, mouse myoblasts (C2C12) were used as a proof-of-concept model to test the method's ability to generate aligned skeletal muscle tissues. C2C12 cells were found to be highly viable (Figure 6.5B) and homogeneously distributed upon seeding at day 0 (Figure 6.6A). After 1 week, a clear preferential orientation was observed along the direction of the microstrands. On the surface, myoblasts fused to form multinucleated myotubes, which were oriented parallel to the microstrands. As expected, this phenomenon was found to be less pronounced for the bulk gel, where a plain surface did not induce a favored orientation for cellular alignment.

Interestingly, a more pronounced difference was found when comparing the inner part of the constructs. In the bulk gel, a clear reduction in viable cells was shown, in accordance with the drastic cell death reported upon 2 days of culture (Figure 6.5B). Also for the bulk gel, the cells maintained a round shape, which suggests the absence of spreading and migration and, consequently, the absence of myotubes, whose formation depends on the ability of cells to come into close contact with each other (Figure 6.6B). For the sized constructs, however, the presence of the physical cues represented by the aligned microstrands and the aligned macropores induced marked cell alignment (Figure S6.7, Supporting Information). Myoblasts were mainly observed on the surface of the microstrands where macropores were found, which indicates that the cells had migrated from the hydrogel into the void spaces. These findings, together with the better cell viability of sized constructs compared with the bulk condition in the inner part of the gel, show that our method contributes to a drastic enhancement of oriented 3D cell guidance and viability. On one hand, the presence of macropores facilitates media percolation and creates a favorable niche for cell infiltration and migration to overcome the limit of the diffusion distance; on the other hand, high-aspect-ratio-aligned microstrands provide a preferred growth direction.

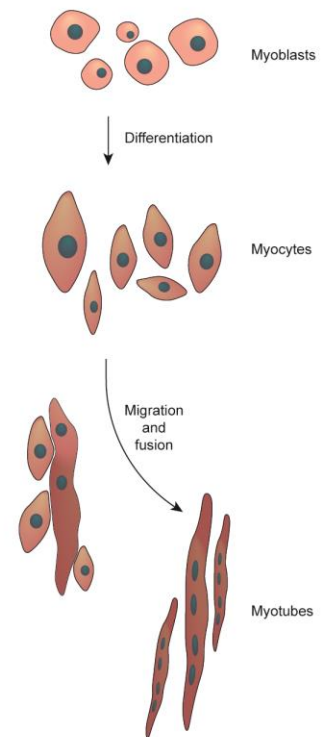
We further evaluated the possibility of creating physiologically relevant models by culturing the constructs for 3 weeks and staining them for myosin heavy chain (MHC). Immunofluorescence confirmed differentiation into multinucleated myotubes (Figure 6.6A), which were also found to be contractile (Video S6.2, Supporting Information), both in the outer part and in the inner part of the gels. Again, for the homogeneous bulk hydrogel, no formation of MHC-positive myotubes was observed in the inner part. The cells were also shown to differentiate by means of gene expression analysis (Figure S6.8, Supporting Information). Common markers for myoblast differentiation, MyoD, MyoG and MyoH1, were found to be increasingly expressed over time. Also, the expression of Pax7 after 3 weeks of culture indicates that a fraction of the cells possibly returned to a quiescent state, which is reminiscent of satellite cells responsible for homeostasis and the repair of the muscle tissue. We quantified cell alignment in our C2C12 model system by

evaluating the nucleus circularity and nucleus orientation. When elongated multinucleated myotubes are formed, the nuclei tend to assume an oval shape (circularity < 1) and align along the major axis of the myotube (Figure 6.6B).⁹⁰⁷⁻⁹¹² In accordance with the qualitative observation of Figure 6.6A, the nuclei were found to be more elongated in all the conditions, with the exception of the inner part of the bulk gel (Figure 6.6C). In this case, the nucleus circularity was found to be close to 1, as expected for nondifferentiated round cells. Nucleus orientation was also found to confirm the presence of aligned myotubes in all the conditions, with the exception of the inner part of the bulk gel (Figure 6.6D).

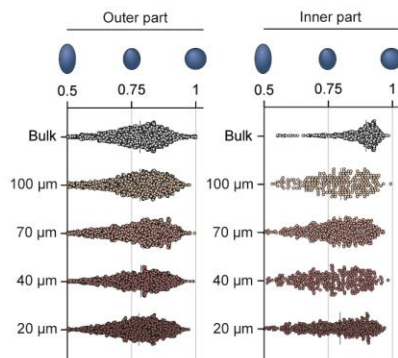
A) Physically oriented maturation



B) Myotube formation



C) Nuclei circularity



D) Nuclei orientation

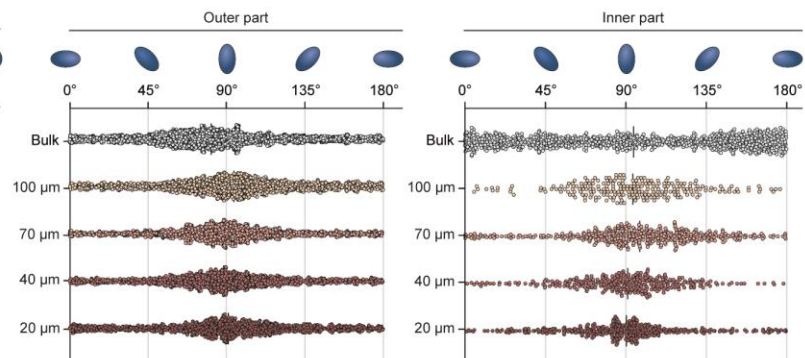


Figure 6.6 | 3D physical cell guidance. (A) Calcein AM staining (green) of the outer part (left) and inner part (right) of bulk and sized constructs at day 0 and day 7 showing oriented tissue development. In red, immunofluorescence myosin heavy chain staining after 21 days showing maturation into myotubes. The bulk gel did not provide a suitable 3D environment for myoblast maturation and alignment, especially on the inner part. Scale bar: 100 μm . (B) Illustration of myotube formation with an alignment of nuclei along cell orientation and a reduction in nuclei circularity. (C) Nuclei circularity in outer and inner part of bulk and sized constructs after 7 days of culture. A clear difference is shown for the internal bulk gel, where nuclei remain substantially round and suggest no cell maturation. (D) Nuclei orientation in outer and inner part of bulk and sized constructs after 7 days of culture. Within the bulk gel, where no macropores and physical cues were present, a random nuclei orientation reflects the absence of cell alignment and myotube formation.

6.4. Conclusions

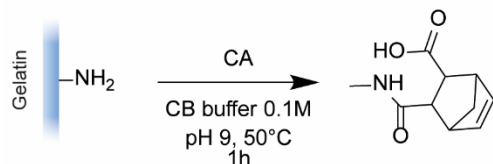
We have developed and optimized a simple method of generating large (mm to cm) macroporous anisotropic constructs with aligned physical cues to induce oriented cell alignment. Although we used myoblasts for proof of concept, we foresee that the promising results obtained with such cells will encourage the generation of more complex, multicellular constructs of aligned tissues. In addition, in this study we adopted the thermal cross-linking of gelatin as the primary cross-linking and the highly efficient photoclick thiol–norbornene reaction as the secondary cross-linking. However, other natural or synthetic polymers and different cross-linking strategies can be applied to tailor the materials' mechanical or bioactive properties to specific needs. Finally, the exploration of the effects of different grid geometries (i.e., circular or star-shaped openings) in tuning the shape, size, and proportion of microstrands and macropores can broaden the potential of the technique presented in this work.

Acknowledgments. The authors would like to thank Peter Schwilch for the help in the design and production of the sizing devices. The authors further acknowledge the assistance from the ETH imaging facilities (ScopeM).

Contributions. R.R. and A.B. contributed equally. R.R., A.B. and M.Z-W designed the study. R.R. synthesized the functionalized polymers, A.B. cultured the cells. A.B. and R.R. encapsulated the cells in the hydrogel and cultured the constructs. R.R. performed and analysed percolation studies. A. Bonato and R.R. performed and imaged live/dead staining and A.B. wrote the FIJI macro to analyse the data. A. Bonato performed immunofluorescence staining and qPCR analysis. R.R. performed phalloidin staining. R.R. analysed nuclei alignment and A.B. developed the plotting strategy. A.B. and R.R. performed confocal imaging. R.R. performed SEM imaging. R.R. plotted the data in graphs and created the figures. P.C. performed finite element analysis. R.R. and A.B. wrote the manuscript and M.Z-W revised it.

6.5. Supporting Information

A) Gelatin-Norbornene (Gel-NB)



B) Gelatin-Thiol (Gel-SH)

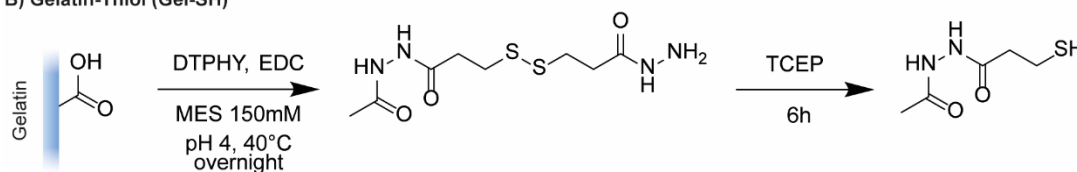


Figure S6.1 | Synthesis of A) Gel-NB and B) Gel-SH. Abbreviations: CA: cis-5-norbornene-endo-2,3-dicarboxylic anhydride, CB: carbonate-bicarbonate, DTPHY: 3,3'-dithiobis(propionohydrazide), EDC: 1-ethyl-3-(3'-dimethylaminopropyl)carbodiimide hydrochloride, MES: 2-(N-morpholino)ethanesulfonic acid, TCEP: Tris(2-carboxyethyl)phosphine.

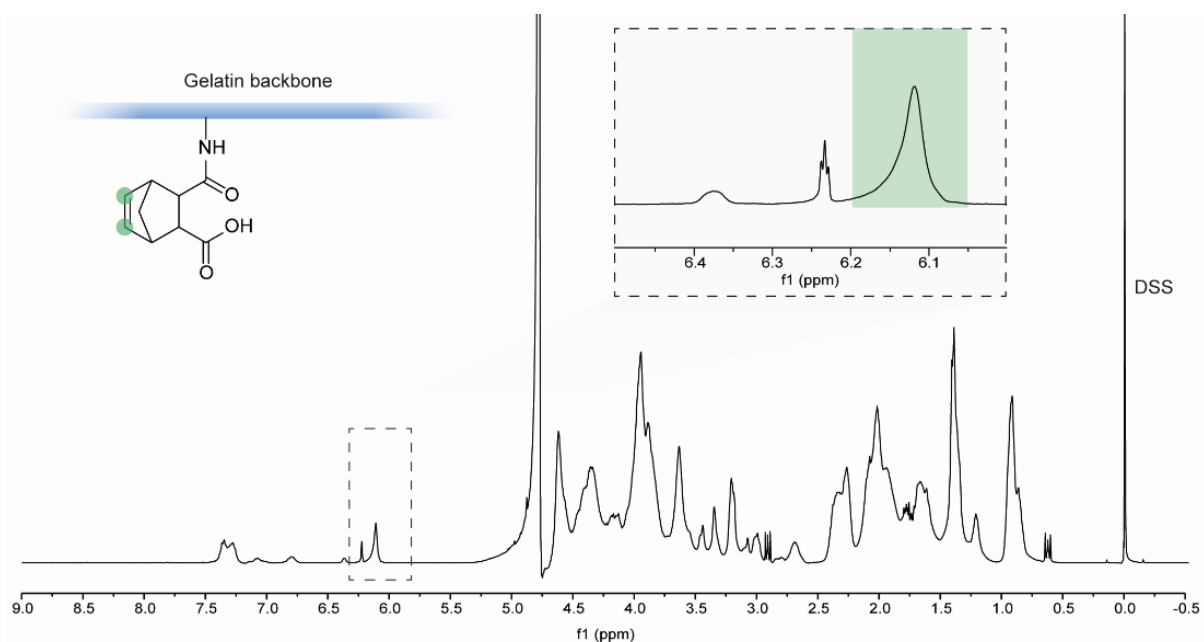


Figure S6.2 | NMR spectrum of Gel-NB. Alkene protons (6.2 to 6.05 ppm) used to determine the DS are highlighted in green in the norbornene bearing moiety illustration (left) and NMR spectrum close-up (right). The integrals of the -ene peaks are compared to the methyl protons of the DSS internal standard (0.05 to -0.05) on the right end side of the spectrum.

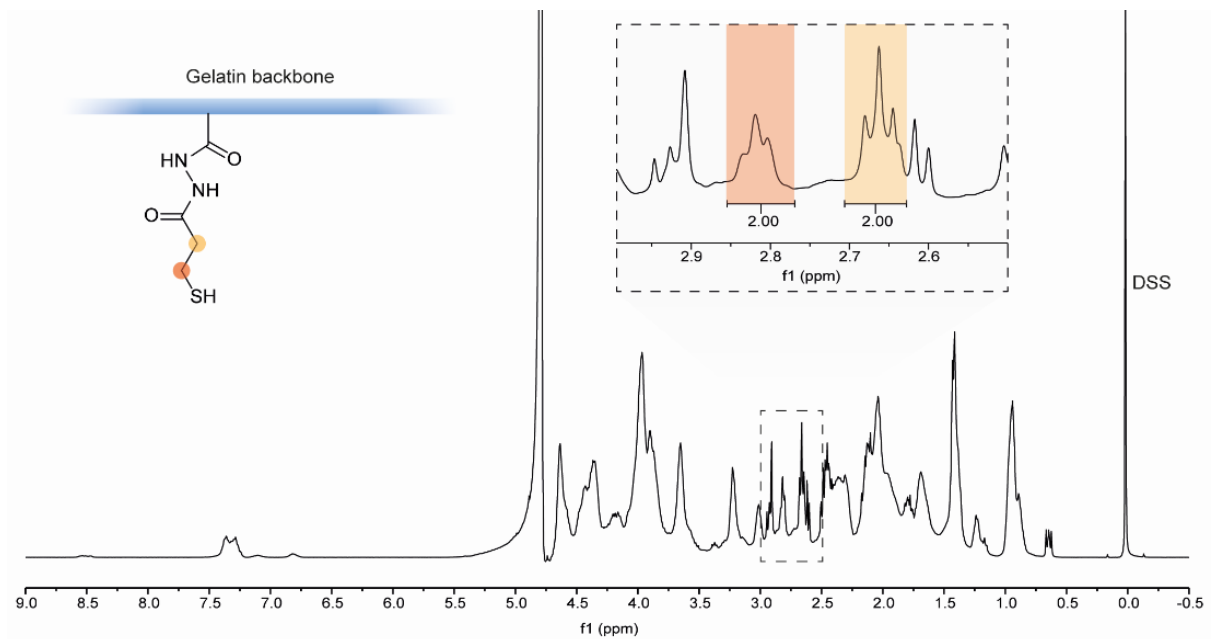
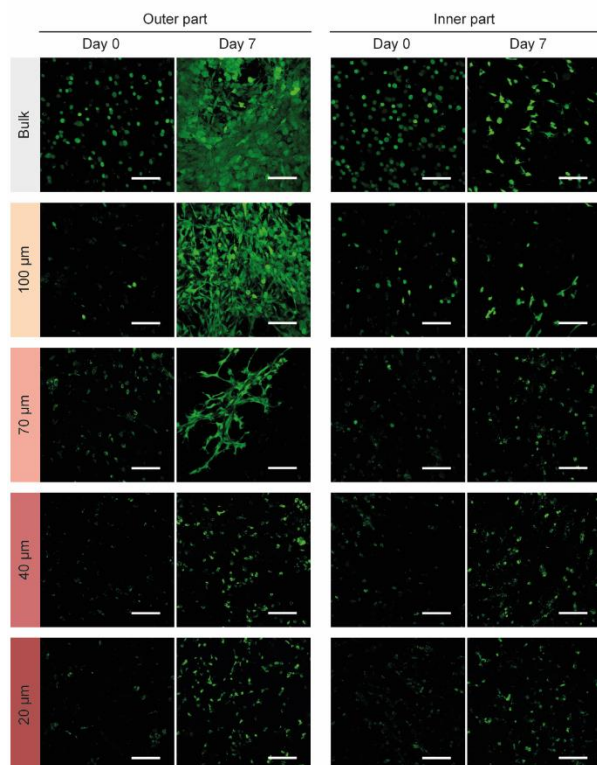


Figure S6.3 | NMR spectrum of Gel-SH. Triplets of methylene groups (2.82 and 2.66 ppm) used to determine the DS are highlighted in shades of orange in the thiol-bearing moiety illustration (left) and NMR spectrum close-up (right). The integrals of the methylene peaks are compared to the methyl protons of the DSS internal standard (0.05 to -0.05) on the right end side of the spectrum.

A) Physically oriented maturation: 10% Gel-NB/Gel-SH



B) Physically oriented maturation: 5% Gel-NB/Gel-SH

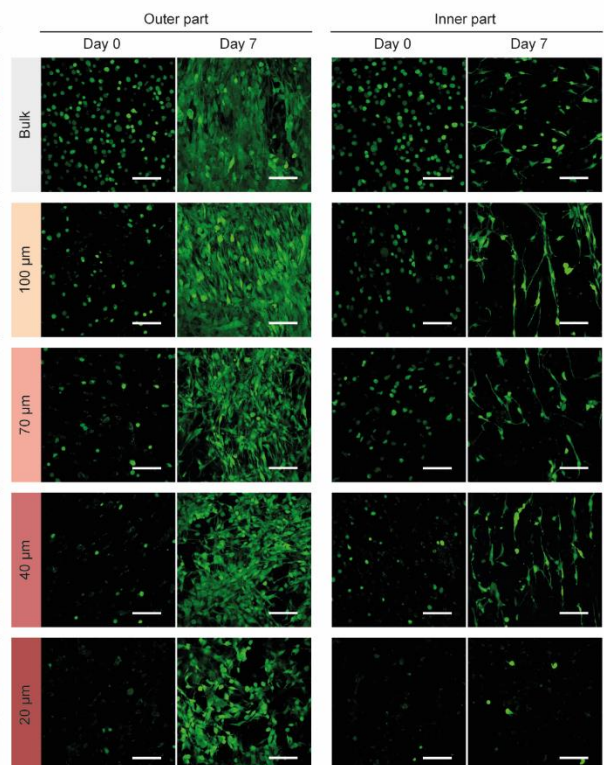


Figure S6.4 | Calcein AM staining (green) of the outer part (left) and inner part (right) of bulk and sized constructs at day 0 and day 7 for A) 10% Gel-NB/Gel-SH and B) 5% Gel-NB/Gel-SH formulations. Scale bars: 100 μ m.

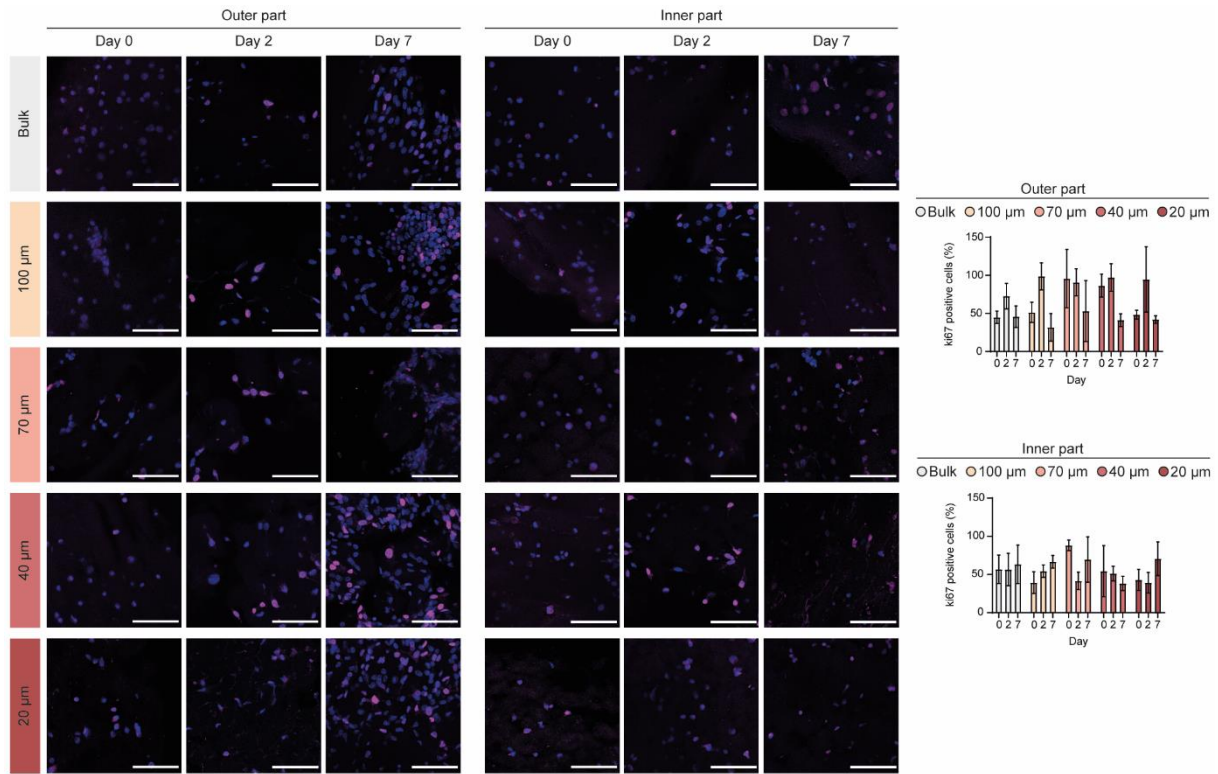


Figure S6.5 | Immunofluorescence images of ki67 (magenta) and HOECHST (blue) stained nuclei for 5% Gel-NB/Gel-SH sized gels in outer and inner parts at day 0, 2 and 7. Scale bar: 100 μ m. On the right, bar graphs evidencing the presence of proliferating cells (ki-67 positive) during the first week of culture.

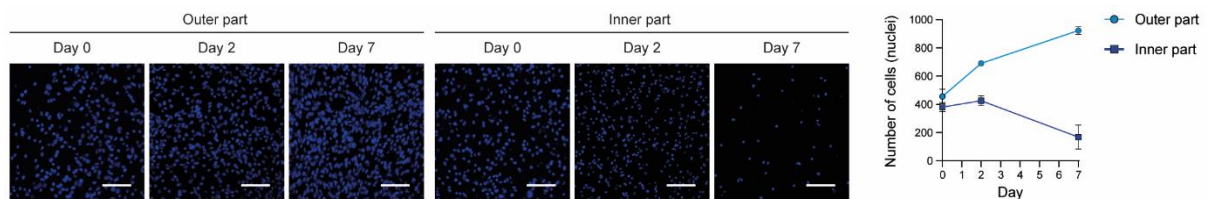


Figure S6.6 | Images showing the changes in number of cells (HOECHST-stained nuclei in blue) for bulk gel during the first week of culture in outer and inner parts (left). Scale bar: 100 μ m. On the right, trendline reporting the increase in cell number in the outer part of the bulk gel and decrease in cell number in the inner part due to cell death.

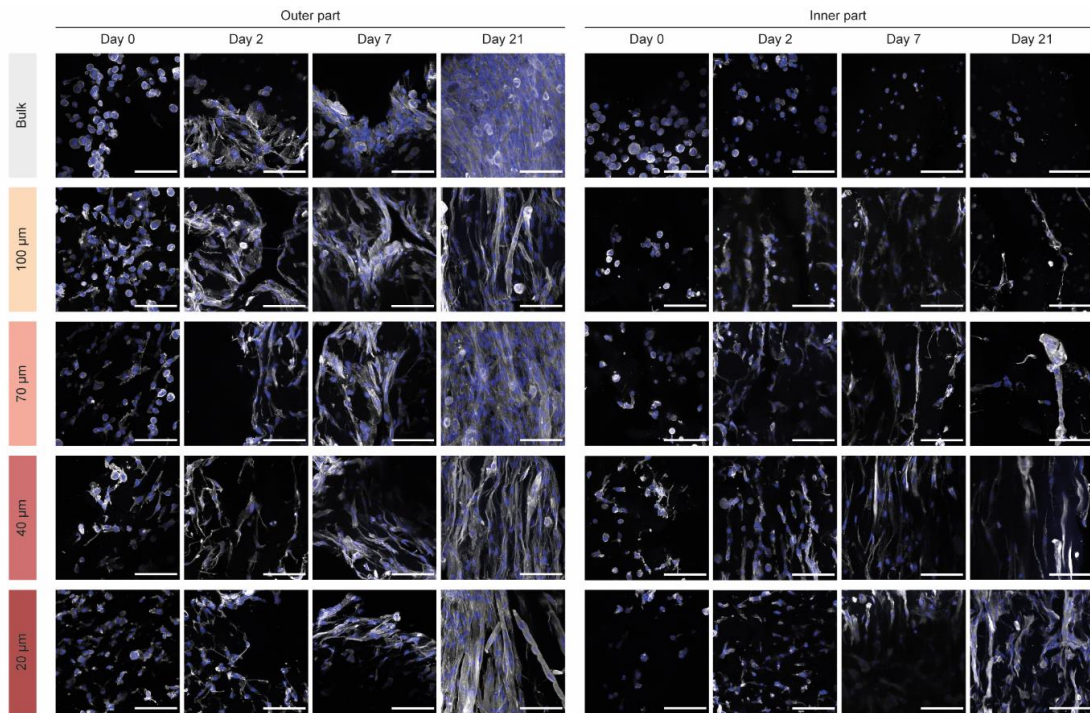


Figure S6.7 | Change in cell morphology over 21 days of culture for the outer part (left) and inner part (right) of bulk and sized constructs. In grey, immunofluorescence staining of cytoskeletal actin shows significant difference between the spread, elongated morphology of cells in the inner part of sized constructs and the round morphology observable in monolithic (bulk) gels. This panel re-enforces the finding that bulk gel did not provide a suitable 3D environment for myoblast maturation and alignment. Scale bar: 100 μm

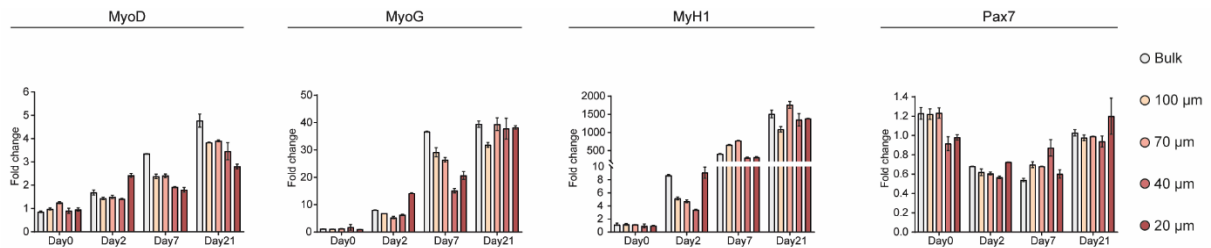


Figure S6.8 | Gene expression analysis of myoblast differentiation markers. Samples were collected at day 0, 2, 7 and 21 and expression of MyoD, MyoG, MyH1 and Pax7 genes was compared to day 0 of differentiation. In this case, gels were analysed as a whole, without separating inner and outer part. For bulk constructs, for which the inner part was shown to not induce formation of myotubes (Figure 6, Figure S7), high expression of differentiation markers can be referred to the myotubes formed in the outer part of the gel.

Video S6.1 | Sizing process, from assembly of sizing device to extrusion of the aligned construct.

Video S6.2 | Brightfield view of bulk and sized constructs after 3 weeks of culture. Muscle twitching is appreciable for the sized constructs, while it appears negligible or absent for the bulk gel (top row). The twitching contribution of the myotubes found in the inner part (bottom row) and the presence of the microarchitecture (aligned microstrands and macropores) enhance the displacement of the whole gel during the contractions. Scale bars: 100 μm

CHAPTER 7

Radical-Free Biofabrication

In previous chapters, photoinitiator producing radicals were used to trigger free-radical crosslinking for various biofabrication techniques. However, for biomedical applications radical species can raise concerns of potential cytotoxicity. This chapter reports on a universal, radical-free photocrosslinking strategy to be used for light-mediated biofabrication. Leveraging photouncaging process and Michael-addition reaction, cell-laden constructs are generated by means of one- and two-photon irradiation, paving the way for a shift towards radical-free light-based bioprinting.

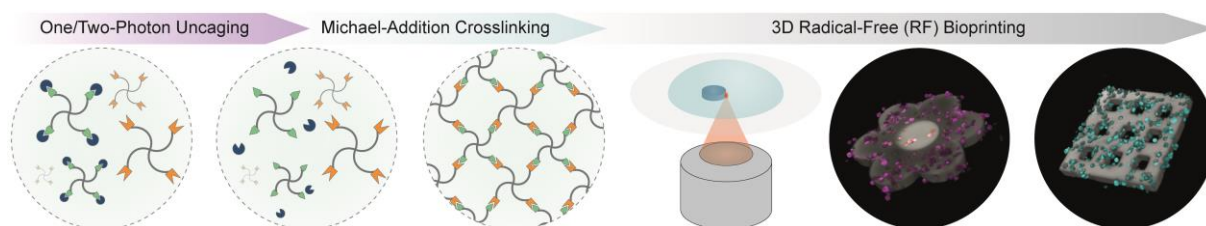
MANUSCRIPT IN REVISION

From Free-Radical to Radical-Free: A Paradigm Shift in Light-Mediated Biofabrication

Riccardo Rizzo, Nika Petelinšek, Angela Bonato, Marcy Zenobi-Wong

2022

Abstract



In recent years, the development of novel photocrosslinking strategies and photoactivatable materials has stimulated widespread use of light-mediated biofabrication techniques. However, despite great progress towards more efficient and biocompatible photochemical strategies, current photoresins still rely on photoinitiators (PIs) producing radical-initiating species to trigger the so-called free-radical crosslinking/polymerization. In the context of bioprinting, where cells are encapsulated in the bioink, the presence of radicals raises concerns of potential cytotoxicity. In this work, we present a universal, radical-free (RF) photocrosslinking strategy to be used for light-based technologies. Leveraging radical-free uncaging mechanisms and Michael addition, we photocrosslinked cell-laden constructs by means of one- and two-photon excitation with high biocompatibility. A hydrophilic coumarin-based group is used to cage a universal RF photocrosslinker based on 4-arm-PEG-thiol. Upon light exposure, thiols are uncaged and react with an alkene counterpart to form a hydrogel. RF photocrosslinker is shown to be highly stable, enabling potential for off-the-shelf products. While PI-based systems cause a strong upregulation of reactive oxygen species (ROS)-associated genes, ROS were not detected in RF photoresins. Finally, optimized RF photoresin is successfully exploited for high resolution two-photon stereolithography using remarkably low polymer concentration (< 1.5 %), paving the way for a shift towards radical-free light-based bioprinting.

7.1. Introduction

Light can serve as a remote, contactless trigger to drive a wide range of photochemical reactions. In tissue engineering, this powerful tool is used to form or break chemical bonds,^{330, 913} playing an increasingly important role in the field of three-dimensional (3D) bioprinting.^{132, 914} Photoactivated materials have been introduced in traditional bioprinting methods such as extrusion printing, or for technologies that have specifically been designed for light-triggered processes, such as one-photon stereolithography (DLP, SLA),^{132, 239, 915-916} two-photon stereolithography (2P-SL),^{132, 917-918} and more recently volumetric bioprinting.^{187, 802-803} Despite major advances in the design of highly reactive and biocompatible photoresins, light-based printing still relies on free radicals to trigger the crosslinking mechanism. When cells are embedded in photoactivated hydrogels, the presence of free-radicals and, consequently, reactive oxygen species (ROS), raises concerns of potential cytotoxicity.⁹¹⁹⁻⁹²³

Common photoresin formulations contain a photoinitiator (PI) species that absorbs light and then undergoes a photochemical reaction that generates unpaired valence electrons (radicals) (Figure 7.1A). PI radicals then initiate and propagate the crosslinking process that can occur via chain-growth (i.e., for acryloyl and methacryloyl groups) or step-growth (i.e., for thiol-norbornene photoclick chemistry) reactions. Although more efficient, water-soluble and biocompatible PIs such as lithium phenyl-2,4,6-trimethylbenzoylphosphinate (LAP) have been introduced in recent years, radical species remain an intrinsic disadvantage for biocompatibility.⁹¹⁹⁻⁹²³ Most light-based bioprinting studies lack in-depth analysis on the deleterious effect of light and radicals. However, some studies in this direction made clear that mild near-UV irradiation ($\sim 1\text{-}20\text{ mW cm}^{-2}$) itself does not lead to cell damage.⁹²² It is instead the generation of radicals that leads to negative downstream effects. For applications where, for example, delicate radical-sensitive cells are used, a simple and widely usable alternative approach is currently missing.

In this study, a universal radical-free (RF) strategy is presented, showing the possibility of shifting the deep-rooted paradigm of free-radical photocrosslinking to radical-free (RF) (Figure 7.1A). The RF method relies on a radical-free photouncaging mechanism,⁹²⁴ and base-catalysed click reaction between thiols and electron-deficient alkene groups (Michael addition).^{129, 925} Photocages (PC), also known as photoremovable protecting groups, are light-sensitive molecules that temporally inactivate/mask active compounds or functional groups by being bound to them.⁹²⁴ As they can be released on demand via photolysis, this approach has been adopted in biological studies to have spatiotemporal control over cellular processes.^{924, 926} PCs have also found a role in tissue engineering, to gain spatiotemporal control over mechanical properties by introducing them in photodegradable linkers^{353, 927-929} or to liberate bioactive molecules or functional groups for patterning purposes.^{819, 930} Here a hydrophilic coumarin-based PC was employed to mask a thiolated crosslinker, thus providing spatiotemporal control over thiol-Michael addition reaction. Upon light exposure, the PC is

removed in a radical-free fashion and thiols react with -ene modified polymers to form a hydrogel. Thiol-Michael addition reaction has been widely used for many tissue engineering applications, due to its ability to proceed in a robust, click-fashion under physiological conditions.¹²⁹⁻¹³⁰

Starting from the synthesis and characterization of a universal RF crosslinker based on 4-arm-PEG-thiol (PEG4SH), we demonstrated high stability of the product and wide tunability of reaction kinetics and mechanical properties by varying parameters such as -ene structure, light intensity, concentration, and polymer functionality. In contrast to PI-based photoresins, the absence of ROS in RF photocrosslinking did not affect the expression profile of the tested gene set and resulted in excellent cell viability. Finally, we showed bioprinting proof-of-principle with high resolution 2P-SL using remarkably low RF photoresin concentration (< 1.5%), a pivotal aspect in biological applications for enhanced nutrient diffusion and cell migration.^{102, 775, 788}

7.2. Results and Discussion

7.2.1. Design, Synthesis and Characterization of RF Crosslinker

To prove the feasibility of the proposed approach, we designed a RF photocrosslinker to be hydrophilic, biocompatible, suitable for one and two-photon applications, and applicable to any photoresin formulation with Michael acceptor (-ene) moieties. As a starting material we chose PEG4SH (10 kDa), a widely used biocompatible material in the field, commercially available, easy to chemically modify and with 4 reactive groups per molecule, which helps to accelerate the gelation kinetics.⁹⁶ As PC, we synthesized, as previously reported, the non-fouling hydrophilic 7-di-(carboxymethyl)amino 4-hydroxymethylcoumarin (PC).⁸¹⁹ Coumarins have been extensively used in the past decade and preferred over nitro-benzyl groups because of their higher one and two-photon cross section and nontoxic photolysis byproducts.¹³² The absorption spectrum of the PC extends in the UV-Vis range, allowing uncaging at 365-405 nm, wavelengths of choice for the vast majority of current light-based printers (see Figure S7.1, Supporting Information). On the other hand, its high two-photon absorption makes the PC suitable also for two-photon stereolithography (2P-SL).

In this study, the PC was coupled to the terminal thiols of PEG4SH via the formation of thiocarbonate bonds (see Figure S7.2, Supporting Information), resulting in the photocaged RF crosslinker PEG4SPC (Figure 7.1B). Upon light absorption, a heterolytic bond cleavage results in an intermediate coumarinylmethyl cation, which eventually re-forms the PC by reacting with H₂O, and a thiocarbonic acid that then undergoes decarboxylation to give free thiol (PEG4SH) (Figure S7.3, Supporting Information).⁹²⁴

When caged, thiol groups are not free to react with the -ene counterpart. In addition, the PC protects thiols from oxidation that would lead to formation of disulfide bonds and limit the storage potential. The storage

stability of PEG4SPC was evaluated with $^1\text{H-NMR}$ under two conditions: dry state (lyophilized) and wet state (solubilized in D_2O). The purified, lyophilized product was stored at -20°C and showed no detectable signs of hydrolysis for up to 6 months (Figure 7.1C). Such a shelf life supports the potential marketability of this product, which would make RF accessible to non-experts in organic synthesis. Hydrolytic stability was also proven to be ideal when PEG4SPC was kept in solution at room temperature for up to 1 month (Figure 7.1C). Good stability under wet conditions facilitates daily lab work, overcoming the need to continuously prepare fresh solutions.

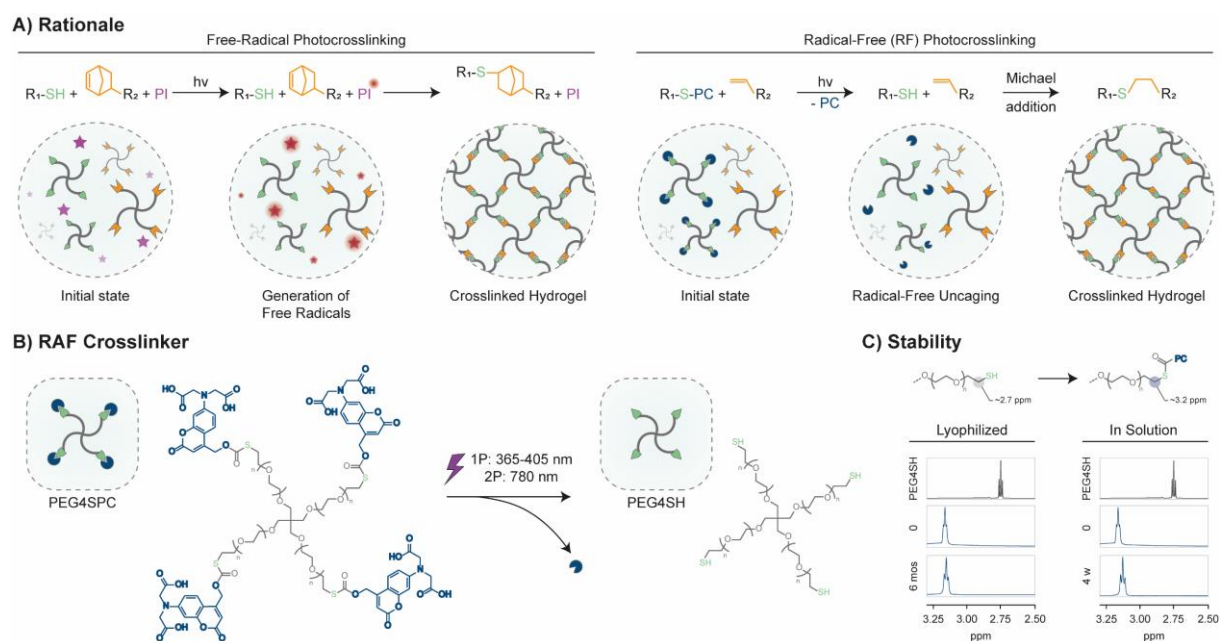


Figure 7.1 A) Rationale of the work. Thiol-norbornene step-growth chemistry is illustrated as an example of free-radical photocrosslinking (left). Upon light absorption, the photoinitiator (PI) radicals (red) drive the formation of a crosslinked network. In the case of free-radical (RF) approach (right), upon light absorption, the photocages (PC, blue) are removed in a radical-free fashion. This exposes thiols (green) to Michael addition with -ene (orange) functionalized polymers, resulting in the formation of a crosslinked hydrogel. B) Chemical structure of RF crosslinker PEG4SPC. PEG4SH is caged with PC via the formation of a thiocarbonate bond. Upon one- or two-photon excitation, PC is removed and PEG4SH is re-formed. C) Stability study of RF crosslinker with $^1\text{H-NMR}$. Shift of terminal methylene in uncaged (highlighted in grey) and caged form (highlighted in blue), from ~ 2.7 ppm to ~ 3.2 ppm, was used to identify uncaging degree. PEG4SPC was found to be perfectly stable (no detectable uncaging) when kept in the dark in lyophilized form (stored at -20°C) for up to 6 months and in solution (D_2O) for up to 1 month (stored at 25°C).

7.2.2 RF Photocrosslinking

The Michael addition is a robust click reaction that progresses under mild, aqueous conditions.¹²⁹ However, its kinetics can vary widely, depending on various parameters, such as nature of the -ene functionality and pH. To exclude a source of variability, and envisioning biological applications, all the experiments in this study were conducted at physiological pH of 7.4. To study the crosslinking behavior of the developed

PEG4SPC, three different 4-arm-PEG-ene counterparts were used: vinyl sulfone (PEG4VS), aryl-methyl sulfone (PEG4MS) and maleimide (PEG4Mal) (Figure 7.2A). While VS and Mal undergo traditional Michael addition, the reaction involving MS is instead a nucleophilic aromatic substitution that yields aryl-thioether adducts and release of a methylsulfonate anion.⁹³¹⁻⁹³² For both reaction mechanisms, the more electron-deficient the -ene is, the more susceptible it is to forming a thioether bond. The order of reactivity is therefore expected to be: PEG4Mal > PEG4MS > PEG4VS. However, on the one hand, vinyl sulfones have slow reaction kinetics, but the thioether adduct that is formed has strong stability. On the other hand, maleimides reacts fast, but the formed thioether is prone to hydrolysis.^{931, 933-934} The aryl-methyl sulfone selected for this study was only very recently introduced by Paez et al.⁹³² and represents an intermediate condition between maleimides and vinyl sulfones, showing a relatively fast reaction with thiols and good hydrolytic stability.

Photorheology analysis using 405 nm irradiation was performed with 1:1 SH:ene ratio to compare the reactivity of the various photoresin formulations (Figure 7.2). As expected, PEG4Mal showed the fastest kinetics. The use of PEG4MS resulted in a relevant delay (~10 min) in gelation, while the photoresin prepared with PEG4VS did not show any sign of gelation after 1 hour of light exposure (Figure 7.2Bi). By evaluating the uncaging profile of PEG4SPC under the same conditions used for photorheology, the gelation of PEG4Mal/PEG4SPC photoresin was shown to be the only one close to theoretical approximation of Flory-Stockmayer theory (see Figure S7.4, Supporting Information). Although our system cannot be considered ideal for various reasons (i.e., possible formation of loops and entanglements, unidirectional light exposure, two-step reaction process), Flory-Stockmayer theory approximates the gelation threshold at around 33% (of total bond formation) for an ideal system composed of two tetrafunctional polymers of the same molecular weight and mixed in 1:1 molar ratio. Under the conditions tested, 33% of uncaging was reached after ~8 min of light exposure, with PEG4Mal gelation starting within the following 2 min.

The significantly lower reactivity of the photoresin containing PEG4MS was first hypothesized to be due to photolysis of the tetrazole ring.⁹³⁵⁻⁹³⁶ This phenomenon has been commonly reported for irradiation with < 300 nm light. NMR analysis revealed perfect stability with 405 nm irradiation under the conditions used in this work (see Figure S7.5, Supporting Information). Slow crosslinking of PEG4MS formulation can therefore simply be attributed to the slower mechanism of reaction of MS aromatic substitution compared to Michael-addition using Mal. In addition to varying the -ene functionality, gelation tunability was demonstrated by exposing the photoresin to different light intensities (Figure 7.2Bii).

Although RF photocrosslinking was proven to be possible, light-based bioprinting methods require much faster gelation kinetics. Following again the Flory-Stockmayer theory of gelation process, an increase in polymer functionality (f) was expected to improve the kinetics of network formation. High molecular weight (~1.5 MDa) hyaluronic acid (HA) was modified with Mal and, for the first time, with MS (Figure 7.2Biii). VS

condition was discarded due to the slow kinetics shown with PEG-based formulations (Figure 7.2Bi). Compared to PEG4Mal/MS ($f = 4$), the functionality of the obtained HA-MS (DS: 22%) and HA-Mal (DS: 27.5%) was orders of magnitude higher ($f \sim 800$). By combining PEG4SPC with -ene functionalized high molecular weight HA, the gel point was estimated to be reached with only 2% of formed thioether bonds. Indeed, the use of HA-Mal and HA-MS resulted in a tremendous increase in the speed of RF photocrosslinking (Figure 7.2Biii). In particular, HA-Mal appeared to be the best candidate and was therefore explored for light-based biofabrication applications.

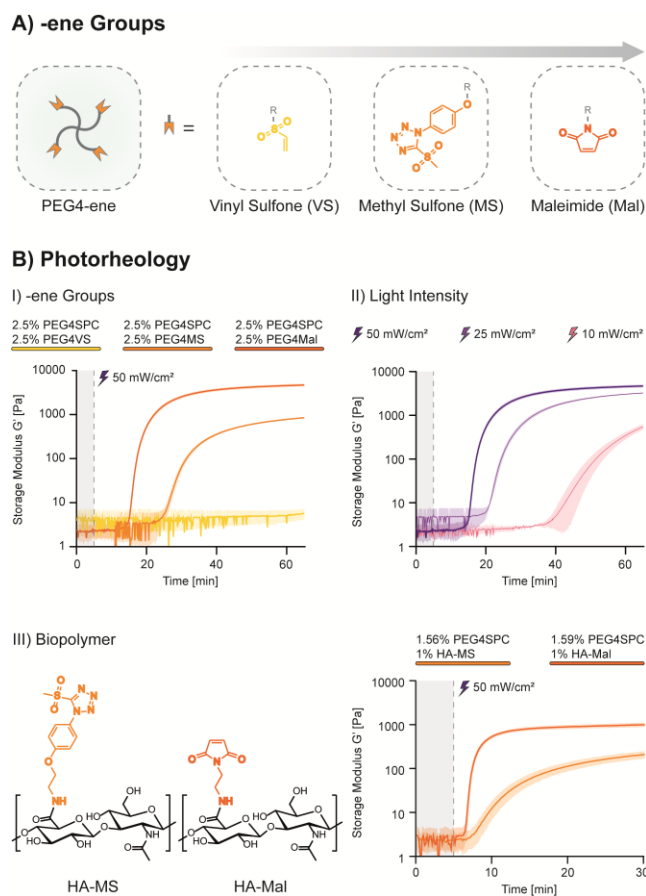


Figure 7.2 | Photoreology analysis of RF crosslinking. A) -ene functionalities adopted in this study in ascending order (from left to right) of reactivity. B) (i) Photoreology analysis of the various functionalized PEG4-ene derivatives with RF crosslinker PEG4SPC. After 5 minutes of measurement, the samples were continuously irradiated with 50 mW cm⁻² light at 405 nm. As expected, photoresin containing PEG4Mal showed the fastest gelation kinetics, followed by PEG4MS. PEG4VS did not show signs of gelation in the time of the experiment (60 minutes irradiation). (ii) Tunable gelation shown with varying light intensity using 2.5% PEG4SPC / 2.5% PEG4Mal. (iii) Chemical structure of HA-MS and HA-Mal (left) and photoreology (right) showing improved performances with the use of high molecular weight HA bearing -ene groups.

It is noteworthy to mention that, although photoreology gave an indication of crosslinking kinetics and allowed comparison and selection of photoresin formulations, the presence of a relevant amount of PC,

unidirectional irradiation and defined gap distance can lead to underestimation/overestimation of the photoresin performance. The PC used in this work has, at 405 nm, an extinction coefficient 100 times higher than LAP (Figure S7.1, Supporting Information). Therefore, the higher the concentration of PEG4SPC, the stronger the absorption of the photoresin. As an example, if a 2.5% PEG4SPC were to be used, Beer-Lambert law estimates a total light absorption with a path length of only $\sim 260 \mu\text{m}$. A simple variation in PEG4SPC concentration or gap distance could therefore significantly impact the rheological output (see Figure S7.6, Supporting Information). Due to the inherent high absorption of RF photoresins, this chemical strategy does not appear suitable for technologies in which light penetration is fundamental, like volumetric printing.^{187, 570, 802} On the other hand, RF appears suitable for layer-by-layer stereolithography where light absorption is a desirable property and commonly sought through the addition of photoabsorbers.^{582, 915, 937-939}

7.2.3 Cellular Response to Absence of Reactive Oxygen Species (ROS)

Design, synthesis and photochemical characterization of RF photoresins proved the core hypothesis of this work to be feasible. However, to translate such a chemical strategy to biological applications, it must prove to be biocompatible. First, the difference between free-radical (LAP-based) and RF (PC-based) systems in terms of radical generation and deleterious impact on cell viability was assessed with ROS and Live/Dead assays using cell-laden photoresins (Figure 7.3). As a free-radical comparison to the selected HA-Mal-based formulation, we chose HA-norbornene (HA-NB), which undergoes radical-initiated photoclick step-growth reactions with a thiolated crosslinker. To better compare the two formulations, HA-NB was synthesized to have a similar degree of substitution (DS: $\sim 18 \%$) to that of HA-Mal. Instead of PEG4SPC, HA-NB was mixed with non-caged PEG4SH and 0.05% LAP. The resulting hydrogels embedded with primary normal human dermal fibroblasts (NHDF) showed significant differences both in terms of ROS detection and cell viability. The intracellular ROS-triggered oxidation of the fluorogenic dye 2',7'-dichlorofluorescein diacetate (DCFDA) was clearly detectable (green fluorescence) for the cells in HA-NB/PEG4SH hydrogel. In contrast, no fluorescence was detected for the cells in RF photoresin HA-Mal/PEG4SPC (Figure 7.3A). Excellent cell viability ($\sim 100\%$) was reported for RF photoresin upon gelation (day 0), while the impact of ROS in free radical-based photoresin resulted in considerable cell death (Figure 7.3B).

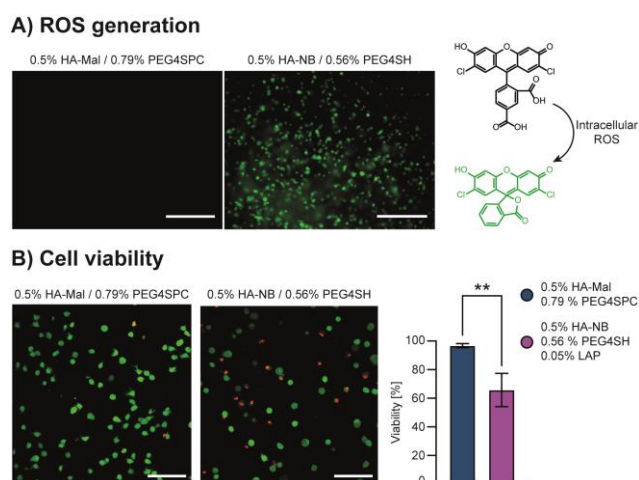


Figure 7.3 | A) ROS fluorescence assay of cell-laden HA-Mal/PEG4SPC and HA-NB/PEG4SH/LAP hydrogels formed under 405 nm irradiation (15 min, 50 mW cm^{-2}). On the right, illustration of intracellular ROS driven oxidation of non-fluorescent compound (black) to highly fluorescent 2',7'-dichlorofluorescein (green). While for LAP containing photoresin the cellular response to ROS was evidenced by green fluorescence, RF photoresin showed no detectable signal. Scale bar: $300 \mu\text{m}$. B) Live/Dead assay of cell-laden hydrogels (405 nm irradiation, 15 min, 50 mW cm^{-2}) showed excellent viability for RF system and significant cell death for free-radical based photoresin that can be attributed to ROS generation. Scale bar: $100 \mu\text{m}$.

The coumarin uncaging process is known to not generate harmful radicals, as also proved in Figure 7.4, but for the system to be fully biocompatible, the PC itself needs to show no signs of cytotoxicity. For example, the photolysis byproducts of nitrobenzyl derivatives (a commonly used class of photoremovable groups in tissue engineering) are reactive and potentially toxic aldehydes and ketones.^{132, 924} In the case of the PC used in this work, the uncaging reaction simply releases 7-di-(carboxymethyl)amino 4-hydroxymethylcoumarin (PC) and a CO_2 molecule (Figure S7.3, Supporting Information). To assess whether this molecule has a deleterious effect on human cells, we performed an MTS assay (Figure 7.4A). The impact of PC on NHDFs was compared to LAP, the state-of-the-art PI for light-based printing. Various incubation times (30 min, 5 hours and 1 day) and concentrations (0.1, 1 and 10 mM) were tested. The assay showed a significant reduction in metabolic activity only for LAP and when used at highest concentration. PC was shown to have no toxic effect on cells with incubations up to 1 day, suggesting high biocompatibility of the molecule even in cases of a long printing process.

A more in-depth analysis on the impact of PC vs LAP in the presence or absence of light was conducted with gene expression analysis, focusing on the cellular response to ROS. We have chosen, based on the literature, SOD1, Nrf2, NF- κ B, Txn, and TP53 genes to track the multifaceted response to ROS from different perspectives. Superoxide dismutase (SOD) overexpression is a consequence of ROS presence in the cellular environment.⁹⁴⁰⁻⁹⁴³ SOD catalyzes conversion of superoxide to oxygen and hydrogen peroxide, acting as a first-line defense against the potential toxicity of these molecules.⁹⁴⁴ Nrf2 and NF- κ B are transcription

factors whose activation by elevated ROS enables the expression of antioxidant pathways as thioredoxin (Txn),⁹⁴⁵ and detoxification enzymes as glutathione S-transferases (GST).⁹⁴⁶⁻⁹⁴⁷ Tumor suppressor protein 53 (TP53) is a transcription factor linked to DNA damage resulting from different stimuli, with the role of avoiding propagation of mutated genomes by inducing cell cycle arrest, senescence or apoptosis.⁹⁴⁸ Overall, an upregulation of these genes is a consequence of an ROS accumulation in the cellular environment which requires a fast response to avoid toxicity and mutagenesis.

Of particular interest for the bioprinting community, the alteration of the cellular redox state, was found to induce cell differentiation and impact cell proliferative capacity.⁹⁴⁹ A cell can thus remain viable thanks to the activation of the above-mentioned protective pathways, but might hide some significant changes. When printing is performed with delicate primary or stem cells, highly susceptible to alteration of intracellular and extracellular environment, the removal of a source of variability (ROS via RF strategy) is desirable.

When kept in the dark, primary NHDFs did not show signs of upregulation of the tested genes, in accordance with the hypothesis that ROS are not generated when the photosensitive molecules (LAP or PC) are not excited (Figure 7.4B). In contrast, light exposure triggered a significant upregulation of the investigated genes in the presence of LAP. Cells therefore sensed and responded to the increase of ROS generated with LAP excitation. Notably, no gene upregulation was detected for NHDF incubated with PC. The striking difference between the two conditions revealed substantially unexplored territory in this field, suggesting the need for a more in-depth understanding of the cellular response to light-based methods. The fast and outstanding progress in photochemistry and hardware development of light-based printers has not been accompanied by a comparable effort on the biological side. With the advent of commercially available products, light-based printing will no longer be limited to engineers and materials scientists but will reach a broader community including biologists, who can unveil unexplored future cellular effects (i.e., consequence of ROS accumulation) of various printing technologies.

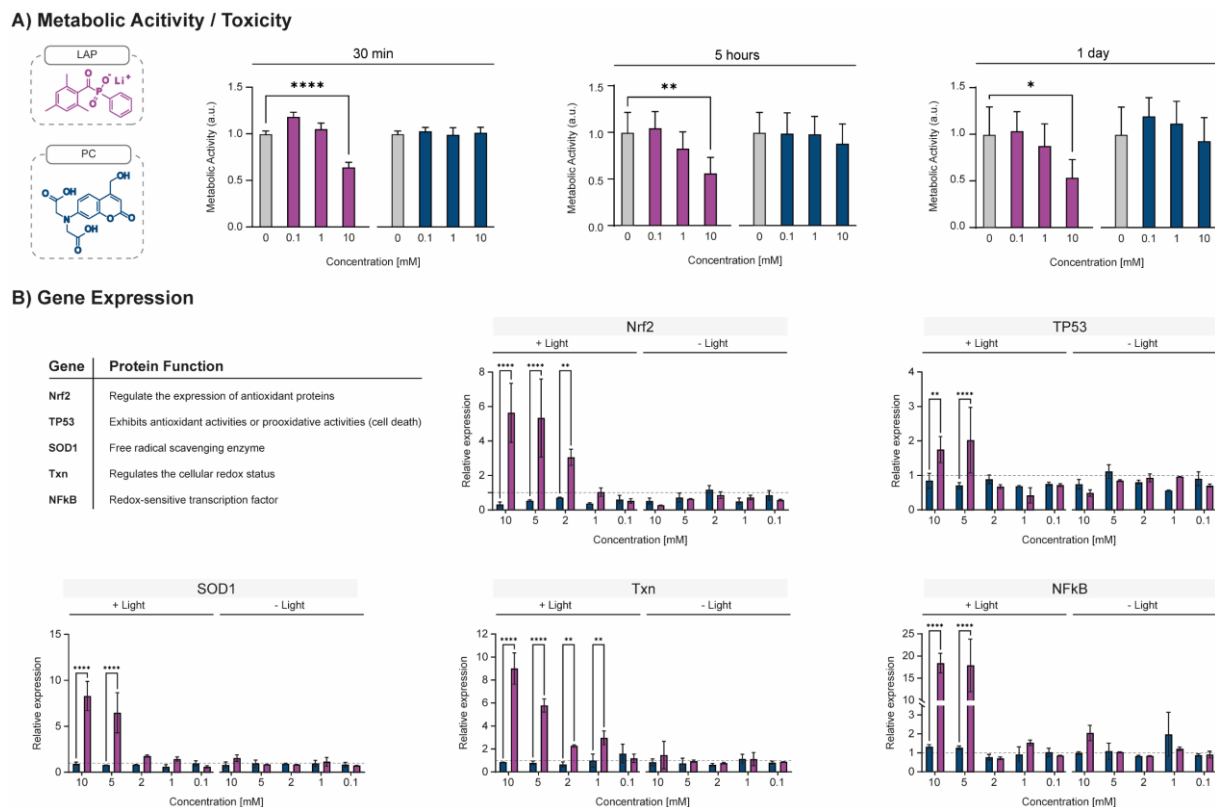


Figure 7.4 | Comparison of LAP and PC for biological applications. A) MTS assay on NHDF incubated with LAP (pink) or PC (blue) at different concentrations for 30 min, 5 hours and 1 day. Cells showed a significant decrease in metabolic activity only when LAP was used at 10 mM. The PC used in this study did not show any deleterious effect on NHDF under the conditions tested. B) Gene expression analysis targeting ROS responsive genes for NHDF exposed to various concentrations of LAP and PC. Samples were irradiated with 405 nm light (6.8 mW cm^{-2}) for 15 minutes and the results compared to non-irradiated samples. As expected, non-irradiated samples showed no up-regulation of target genes. In the absence of light, no radicals are, in fact, produced by the compounds under study. In the presence of light, samples exposed to LAP showed pronounced upregulation of genes involved in antioxidant and radical scavenging activities. A negligible effect was only reported for the lowest concentration (0.1 mM). Remarkably, for samples incubated with PC, upregulation was not reported under any condition.

7.2.4 2P-SL (Bio)Printing

Overall, RF photocrosslinking was proven to be effective, tunable and highly biocompatible. In this final section, proof-of-concept of RF applicability for light-based printing technologies is presented using 2P-SL (Figure 7.5A). This method is based on the scanning of a tightly focused femtosecond-pulsed infrared laser and offers the highest printing resolution in the field.^{132, 319, 917} It requires fast reaction kinetics and has been traditionally used with highly functionalized polymers and high photoresin concentrations (i.e., 10-15% Gel-MA or Gel-NB with DS: $\sim 90\%$).^{772, 777}

Thanks to the significant two-photon absorption cross section of coumarin derivatives, this class of photoremovable groups has been used for applications involving 2P uncaging processes.^{353, 950-951} The PC used in this work was therefore hypothesized to also be suitable for 2P-SL (bio)printing.

First, a parameter screening was performed (Figure 7.5B). The laser intensity and the number of scans were varied to identify the optimal printing conditions. Cylinders of 70 μm diameter and height were designed using the region-of-interest (ROI) function, which allows the user to demarcate the areas to be scanned. Upon washing of uncrosslinked resin, cylindrical objects were observable by phase-contrast imaging for PEG4Mal/PEGSPC and HA-Mal/PEG4SPC photoresins. Notably, the PEG4Mal-based formulation resulted in significant swelling. Again, HA-Mal-based formulation performed better, as no swelling was observed. This different degree of swelling can be attributed to the degree of crosslinking of the formed hydrogel. The higher the crosslinking density, the lower the water uptake; this is consistent with the reaction kinetics of the two formulations found with photorheology (Figure 7.2). The swelling behavior can strongly affect the final printing fidelity. As an example, ROI designs depicting a gorilla, alpaca, palm tree, and the ETH logo were printed using the optimal laser dose, which was identified using the screened values (Figure 7.5B). While structures printed with PEG4Mal/PEG4SPC swelled significantly, deviating from the original dimensions, HA-Mal/PEG4SPC printed objects replicated the desired shapes with high fidelity. To better evaluate the capabilities of this RF photoresin, maximum resolution was investigated. Writing resolution (or negative resolution) is defined as the minimum distance between two printed objects and was found to be $\sim 1 \mu\text{m}$ (Figure 7.5Bii). Line width resolution (or positive resolution), which refers to the minimum feature size that can be printed, was found to be $\sim 1 \mu\text{m}$. Considering the objective set-up (25x, 0.95 NA, water immersion), both negative and positive resolutions came close to matching the theoretical maximum, proving excellent performance of the optimized RF system. Optimal photoresin and laser parameters were used to print the 3D model of a “sleeping cat”. By using a script previously developed in our lab,⁸¹⁹ which converts an .stl model into a stack of ROIs, it was possible to use a commercial 2P-microscope (Leica SP8 equipped with Spectra Physics Mai Tai laser) as a 2P-SL printer. Upon washing of uncrosslinked resin and profiting from the fluorescence of residual PC molecules, 3D reconstruction of the printed model was possible via confocal imaging (Figure 7.5Biii).

Finally, building on the findings described above, RF 2P-SL bioprinting was explored (Figure 7.5C). First, a “Swiss flag”-shaped microwell was printed and post-seeded with NHDF (Figure 7.5Ci). Consistent to what has been reported for one-photon crosslinking (Figure 7.4), 2P-SL in the presence of cells was also shown to be highly biocompatible (Figure 7.5Cii). Excellent viability upon printing ($\sim 100\%$) also indicated that no photodamage due to the 2P laser scanning occurred under optimized conditions (7.2 mW cm^{-2} , 3 scans). A cell-laden grid was generated to highlight the possibility of bioprinting diverse shapes (Figure 7.5Cii, bottom). Finally, a multistep approach was adopted to bioprint a multicellular flower-shaped construct (Figure 7.5Ciii).

A first printing step used NHDFs pre-incubated with a first fluorescent cell tracker. After washing of uncrosslinked resin, a second printing step used photoresin with NHDFs incubated with a second photo-orthogonal cell tracker. As a result, a multicolor/multicellular flower-like print was obtained.

Notably, all the 2P-SL printing was performed with a remarkably low polymer concentration (0.5% HA-Mal) compared to the standards of this method. This highlights the excellent kinetics of the presented RF process and its potential suitability for a variety of printing methods relying on fast gelation. The use of low polymer concentration is of particular interest for tissue engineering applications, since the resulting hydrogels have generally better properties for cell migration, spreading and matrix deposition (i.e., larger mesh size, better diffusivity of nutrients, softness).^{102, 775, 788}

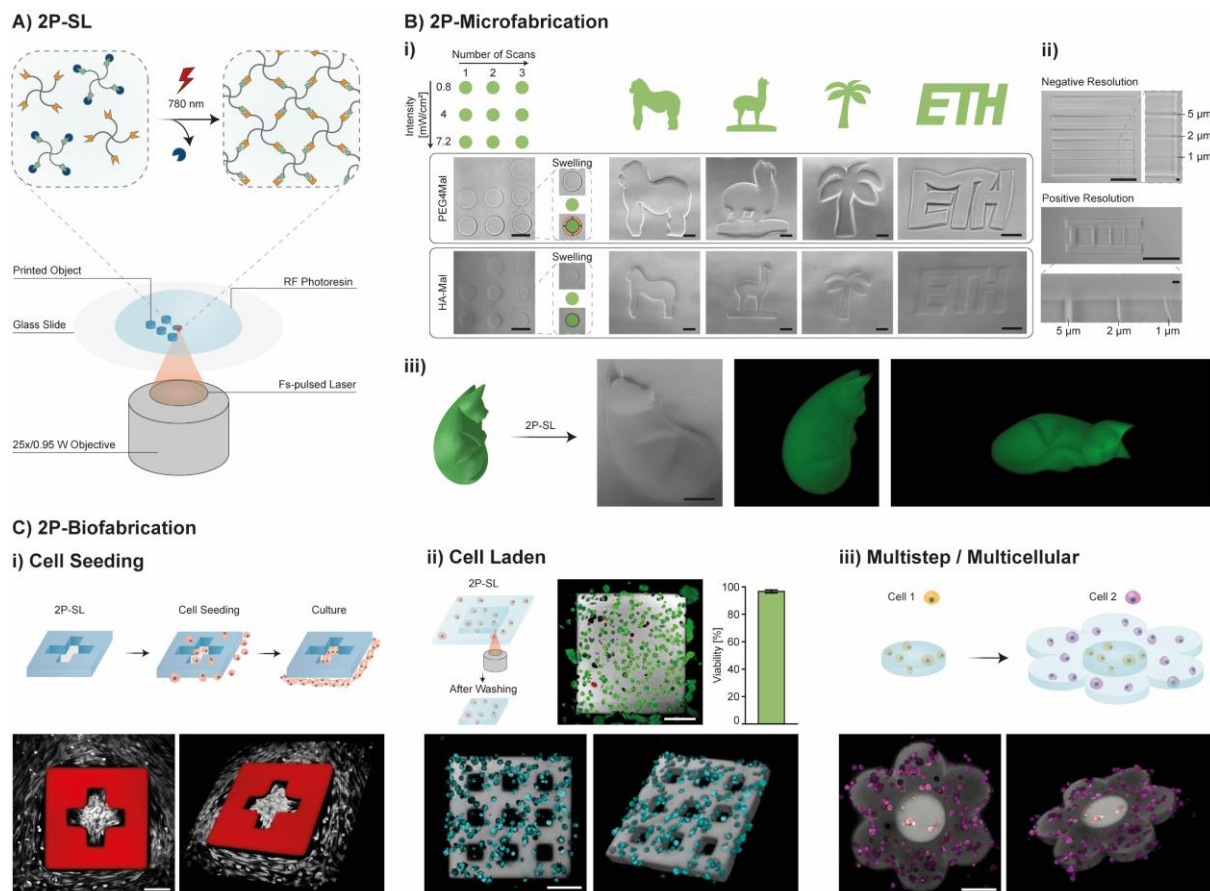


Figure 7.5 | 2P-SL RF (bio)printing. A) Illustration of 2P-SL with RF photoresin. B) (i) Printing parameter screening and examples of printed designs. The use of HA-Mal is shown to drastically reduce the swelling and therefore better reproduce the desired shapes. Scale bars: 100 μm . (ii) Negative (writing) and positive (line width) resolution for the optimized HA-Mal-based photoresin. Scale bars: 100 μm , and 5 μm in close ups. (iii) Example of 2P-SL of a 3D object. A .stl model of a “sleeping cat” was printed using HA-Mal/PEG4SPC photoresin and imaged exploiting residual PC fluorescence. Scale bar: 100 μm . C) Proof-of-concept of 2P-based biofabrication with optimized HA-Mal/PEG4SPC photoresin. (i) Illustration of fabrication and post-seeding procedure (top). 3D “Swiss flag”-like microwell (red) and post seeded NHDF (white) (bottom). (ii) 2P-SL in the presence of cells (NHDF) showed

excellent viability upon printing (day 0) (top). Example of bioprinting of user-defined shape (grey) in the presence of cells (blue) (bottom). (iii) Illustration of multistep/multicellular printing concept (top) and actual bioprinted multicellular object (bottom). Scale bars: 100 μm .

7.3. Conclusion

In summary, a radical-free (RF) photocrosslinking approach was demonstrated. It offers a valid alternative to common free-radical strategies that use potentially toxic PIs and radical-initiating species. RF photocrosslinking was demonstrated to be fast, tunable and suitable to one- and two-photon excitations. High biocompatibility and negligible ROS generation were also established, making this approach a potentially beneficial tool for bioprinting in the presence of radical-sensitive molecules and cells (i.e., cell/drug delivery with 3D printed microcarriers/microrobots). In addition, the possibility of synthesizing RF crosslinker in gram scale and storing it with high stability makes RF a potentially marketable off-the-shelf solution. We believe that this seminal work will also stimulate the generation of a variety of RF crosslinkers having different polymer backbones, functionality, and also different PCs, opening to potentially orthogonal uncaging wavelengths.

7.4. Experimental Section

All chemicals were purchased from Merck and cell culture reagents from Gibco unless indicated otherwise. All cell experiments were performed using normal human dermal fibroblasts (NHDFs) isolated from juvenile foreskin skin biopsies. Biopsies were taken under parental informed consent and their use for research purposes was approved by the Ethical Committee of Canton Zurich (BASEC-Request-Nr. 2018-00269).

Synthesis and characterization of photocage (DCMAC-OH and PC): 7-di((tert-butyl-carboxy)methyl)amino 4-hydroxymethylcoumarin (DCMAC-OH) was synthesized in gram scale as previously described.⁸¹⁹ The compound was purified by C18 preparative HPLC (Agilent) in a gradient from 10 to 100 % ACN in H₂O with 0.1% TFA. Identity of the compound was verified by ¹H-NMR (Bruker Ascend 500 MHz, 128 scans, see Figure S7.7, Supporting Information) and LC-MS (m/z: [M + H] calcd 419.19; found, 420). Tert-butyl deprotection was performed with acid treatment in 1:1 DCM:TFA for 15-30 min. After removal of DCM and TFA by evaporation under nitrogen stream, the product 7-(dicarboxymethylamino)-4-(hydroxymethyl)-coumarin (PC) was purified by C18 preparative HPLC (Agilent) in a gradient from 10 to 100 % ACN in H₂O with 0.1% TFA. Identity of the compound was verified by LC-MS (m/z: [M + H] calcd 307.07; found, 307). For analysis of absorption spectrum and extinction molar coefficient at 405 nm (ϵ_{405}), PC was dissolved in HEPES 25mM, 150 mM NaCl pH 7.4 at 10 mM final concentration. Micro-volume UV-Vis absorbance analysis were performed at 25°C, from 300 nm to 700 nm with 1 nm step (Synergy H1, BioTek). The same procedure was used for LAP.

Synthesis of 7-di-((tert-butyl-carboxy)methyl)amino coumarin 4-yl)methyl carbonate (DCMAC-NPC): DCMAC-NPC synthesis was adapted from a previously published protocol.⁸¹⁹ 100 mg (0.24 mmol) of DCMAC-OH were dissolved in 1 ml of dry DCM with 50 μ L N,N-diisopropylethylamine (DIPEA). 48 mg (0.24 mmol) of 4-nitrophenyl chloroformate (NPC) pre-dissolved in 1 ml of DCM were added dropwise to this solution while stirring. The reaction, monitored by HPLC (Hitachi), appeared to be completed in around 20 min. The reaction mixture was dried under reduced pressure and used for the synthesis of PEG4SPC without further purification.

Synthesis and stability tests of photocaged 4-arm-peg-thiol (PEG4SPC): 650 mg of 10 kDa PEG4SH (JenKem Technology USA) (0.26 mmol of SH, 1 eq.) were dissolved in 2 mL of dry DMF in the presence of 475 μ L DIPEA (2.7 mmol, 10 eq.). 227 mg of DCMAC-NPC (0.39 mmol, 1.5 eq.) were dissolved in 1 mL of dry DMF and added dropwise to the solution under stirring. Reaction was monitored with HPLC (Hitachi) and found to be completed after 30 min. Tert-butyl deprotection was performed with acid treatment in by adding TFA to a total 1:5 DMF:TFA ratio for 15-30 min. After deprotection, TFA was removed by evaporation under nitrogen stream. PEG4SPC was further diluted in 10 mL of ACN and purified by C18 preparative HPLC (Agilent) in a gradient from 10 to 90% ACN in H₂O with 0.1% TFA. Identity of the compound was verified by ¹H-NMR (see Figure S7.8, Supporting Information).

Stability of the RF crosslinker PEG4SPC was determined with ¹H-NMR (Bruker Ultrashield 400 MHz, 1024 scans) by evaluating the ratio of the chain-end methylene protons close to caged thiols (t, 2H, CH₂, 3.16 ppm) and close to uncaged thiols (t, 2H, CH₂, 2.75 ppm) (see Figure 7.1C and Figure S7.8, Supporting Information). Lyophilized product stored at -20°C was dissolved in D₂O and analyzed right after freeze-drying and after 6 months of storage. For the stability of PEG4SPC in solution, the product was dissolved in D₂O, kept at room temperature (protected from light) and analyzed after 4 weeks.

Synthesis of 2-(4-(5-(methylsulfonyl)-1H-tetrazol-1-yl)phenoxy)ethan-1-amine (MS): The synthesis was performed as recently reported by Paez et al.⁹³² The final product (MS) was purified by C18 preparative HPLC (Agilent) in a gradient from 10 to 90 % ACN in H₂O with 0.1% TFA. Identity of the compound was verified by ¹H-NMR in DMSO-d₆ (see Figure S7.9, Supporting Information) and LC-MS (m/z: [M + H] calcd 283.07; found, 284). Photostability of MS was investigated by irradiating a 2.5% solution of the product in D₂O under the conditions used for photorheology (405 nm, 200 μ m gap, 50 mW/cm²) for 30 min and then analyzed with ¹H-NMR (see Figure S7.5, Supporting Information)

Synthesis of 4-arm-PEG-methyl sulfone (PEG4MS): The synthesis was performed as recently reported by Paez et al.,⁹³² using 10k Da PEG4- Succinimidyl Carboxymethyl Ester (PEG4SCM, Creative PEGWorks). The product was purified by C18 preparative HPLC (Agilent) in a gradient from 10 to 90 % ACN in H₂O

with 0.1% TFA. Identity of the compound was verified by $^1\text{H-NMR}$ in D_2O (Bruker Ascend 500 MHz, 128 scans, see Figure S10, Supporting Information).

Synthesis of hyaluronic acid methyl sulfone (HA-MS): 125 mg (0.3 mmol, 1 eq.) of high molecular weight HA (1.5 MDa, HTL Biotechnology) were left to dissolve overnight, under stirring, in 50 mL 150 mM MES buffer pH 4.5. Then, 71.25 mg of 1-Ethyl-3-(3-dimethylaminopropyl)carbodiimide (EDC, 3.7 mmol, 1.2 eq) and 43.15 mg (1.2 eq) of N-hydroxysuccinimide (NHS) were dissolved in 5 mL of 150 mM MES buffer pH 4.5 and quickly transferred to the reaction mixture. Finally, 106 mg of MS (1.2 eq) previously dissolved in 1 mL H_2O were added dropwise. The reaction was left to proceed under stirring for 24 h, dialyzed against acidified mQ H_2O (pH 4 using HCl) for 5 days with frequent water changes and freeze-dried. The degree of substitution (DS) of the resulting HA-MS was estimated with $^1\text{H-NMR}$ in D_2O using internal standard 3-(trimethylsilyl)-1-propanesulfonic acid (DSS, 2H, ~ 0.75 ppm) and MS aromatic ring protons (~ 7.4 and 7.8 ppm, see Figure S7.11, Supporting Information).

Synthesis of hyaluronic acid maleimide (HA-Mal): 125 mg (0.3 mmol, 1 eq.) of high molecular weight HA (1.5 MDa, HTL Biotechnology) were left to dissolve overnight, under stirring, in 50 mL 150 mM MES buffer pH 4.5. Then, 71.25 mg of 1-Ethyl-3-(3-dimethylaminopropyl)carbodiimide (EDC, 3.7 mmol, 1.2 eq) and 43.15 mg (1.2 eq) of N-hydroxysuccinimide (NHS) were dissolved in 5 mL of 150 mM MES buffer pH 4.5 and quickly transferred to the reaction mixture. Finally, 91 mg of N-(2-aminoethyl)maleimide trifluoroacetate salt (1.2 eq) previously dissolved in 1 mL H_2O were added dropwise. The reaction was left to proceed under stirring for 24 h, dialyzed against acidified mQ H_2O (pH 4 using HCl) for 5 days with frequent water changes, and freeze-dried. The degree of substitution (DS) of the resulting HA-Mal was estimated with $^1\text{H-NMR}$ in D_2O using N-acetyl protons peak (~ 2 ppm) and maleimide double bond peak (~ 7 ppm, see Figure S7.12, Supporting Information).

Synthesis of hyaluronic acid norbornene (HA-NB): 2.5 g (6.25 mmol, 1 eq.) of high molecular weight HA (1.5 MDa, HTL Biotechnology) were left to dissolve overnight, under stirring, in 1 L of 150 mM MES buffer pH 4.5. Then 5.45 g of adipic acid dihydrazide (ADH, 31.25 mmol, 5 eq.) were added to the solution. When completely dissolved, 300 mg of 1-Ethyl-3-(3-dimethylaminopropyl)carbodiimide (EDC, 1.56 mmol, 0.25 eq.) were solubilized in 2 mL of 150 mM MES buffer pH 4.5 and added dropwise to the reaction mixture. After 4h the pH was found to be 4.72 and the reaction was quenched by addition of NaOH 1M to reach pH 7. After addition of 2 g of NaCl the solution was dialyzed against mQ H_2O for 5 days with frequent water changes and freeze-dried. After lyophilization, 2.5g of HA-ADH were left to dissolve overnight, under stirring, in 1 L of PBS pH 7.4. Then, 2 g of carbic anhydride (12.5 mmol, 2 eq.) were dissolved in 10 mL of DMF and added dropwise to the solution. The reaction was left to proceed for 8 h with pH adjustments every 30 min using NaOH 2M to maintain pH 7.4. After addition of 2 g of NaCl the solution was dialyzed

against mQ H₂O for 3 days using a tangential flow filtration system (ÄKTA Flux, Cytiva) and then freeze-dried. HA-NB degree of substitution (DS) was found to be 18% with ¹H-NMR (Bruker Ultrashield 400 MHz, 1024 scans) integrating norbornene double bond peak (~6.3 ppm, see Figure S7.13, Supporting Information). For NMR analysis the high viscous polymer was solubilized at 5 mg mL⁻¹ in 1 mL of 2 mM NaCl D₂O solution in the presence of a known amount of internal standard 3-(trimethylsilyl)-1-propanesulfonic acid (DSS). High ionic strength was found to be a powerful tool to improve the quality of the spectra. As reported by Ret et al., for long-chain, high viscous polymers in particular, the control of their conformation in solution can determine better proton mobility.⁸⁴⁰

MTS assay: NHDFs cultured in DMEM + GlutaMAX-I + 10% fetal bovine serum + 10 µg mL⁻¹ gentamicin were seeded at passage 7 in 96 well plate at 50'000 cells/well. Cells were left to adhere overnight, and then the medium was changed to serum-free 24 hours before treatment. Cells were then cultured in medium containing LAP (0.1, 1, 10 mM), PC (0.1, 1, 10 mM) or control medium (no LAP, no PC) for 30 minutes, 5 hours and 1 day. Each condition was tested in triplicate (n = 3). Following provider (abcam) protocol, media was changed with fresh serum-free media containing 20 µL of MTS reagent. Color was left to develop for 3.5 h under standard culture conditions prior to measuring absorbance at 490 nm with a microplate reader (Synergy H1, BioTek).

Gene expression analysis: Gene expression levels were assessed through real-time PCR (qPCR) analysis. NHDF (passage 8) were plated and grown to confluence. Medium was changed to serum-free for 24 hours before treatment. Cells were incubated with medium containing PC or LAP at different concentrations (0.1, 1, 2, 5, 10 mM) for 30 min and then exposed to 405 nm light (~6.8 mW cm⁻²) for 15 minutes. After light exposure, the media was changed for fresh, serum-free media without PC or LAP. RNA was extracted after 8 hours with NucleoZol (Macherey-Nagel) following manufacturer's instructions and retrotranscribed to cDNA with GoScript Reverse Transcriptase (Promega). After 1:5 dilution with RNase-free water, cDNA was used for qPCR analysis with GoTaq PCR mix (Promega) on a QuantStudio 3 device (Applied Biosystems). Analysed genes were SOD1 (Fw: CCTAGCGAGTTATGGCGACG, Rv: CCACACCTTCACTGGTCCAT), NF-κB (Fw: GC'TTAGGAGGGAGAGCCAC, Rv: AACATTTGTTCAAGCCCTTCCC), Txn (Fw: CT'TGGACGCTGCAGGTGATA, Rv: AGCAACATCATGAAAGAAAGGCT), Nrf2 (Fw: AGGTTGCCACATTCCCAA, Rv: AGTGA'CTGAAACGTAGCCGA), TP53 (Fw: CGCTTCGAGATGTTCCGAGA, Rv: CTTCA'GGTGGCTGGAGTGAG). Values were all normalized to GAPDH (Fw: AGTCAGCCGCATCTTCTTTT, Rv: CCAATACGACCAAATCCGTTG). Statistical analysis was performed with Prism using two-way ANOVA.

Photorheology: Photoreology analyses were carried out on an Anton Paar MCR 301 equipped with a 10 mm parallel plate geometry and 6 mm glass floor. An Omnicure Series1000 lamp (Lumen Dynamics) was used as a light source. Sequential 400–500 nm and narrow 405 nm bandpass filters (Thorlabs) were placed within the optical fiber path. Photoresin components (PEG4SPC, PEG4-VS/MS/Mal) were dissolved in NaCl 150 mM, 25 mM HEPES buffer pH 7.4 at 10%. pH was checked and adjusted if necessary to 7.4 using NaOH 1M. Photoresins with 1:1 SH:ene molar ratio, and various concentrations were then prepared from this starting stock solution by mixing (pipetting) and diluting in NaCl 150 mM, 25 mM HEPES buffer pH 7.4. All procedures were performed in the dark. All tests were performed at 25 °C in the presence of a wet tissue paper in the chamber to prevent the sample from drying. Oscillatory measurements were performed in triplicate ($n = 3$) using 18 μL photoresins at 2% shear rate and 1 Hz frequency with 200 μm gap and 10 s measuring point duration.

Uncaging test: A solution of 2.5% PEG4SPC in 150 mM NaCl, 25mM HEPES buffer pH 7.4 was prepared as described above. Using the same photorheology conditions described above (light intensity: 50 mW cm^{-2} , gap distance: 200 μm), but a larger parallel plate (20 mm), 74 μL of the solution were irradiated for 1 min, 2 min, 10 min, and 60 min. 50 μL of this solution were then diluted 1:1 with H_2O and used for HPLC analysis (Hitachi) in a gradient from 10 to 90% ACN in H_2O with 0.1% TFA. Uncaging was estimated by tracking the reduction of the PC peak on the 385 nm trace compared to the non-exposed PEG4SPC solution.

Cell laden photocrosslinking and Live/Dead assay: RF photoresins composed of 0.5% HA-Mal and 0.79% PEG4SPC were prepared as indicated above by solubilizing the polymers in 150 mM NaCl 25 mM MES buffer pH 7.4. Free-radical photoresin was prepared with 0.5% HA-NB, 0.56% PEG4SH and 0.05% LAP in the same buffer. Solutions were filtered sterilized through 0.20 μm filters. Then, NHDFs were resuspended in these photoresins at 1 million cells mL^{-1} and the resulting bioresin was pipetted (15 μL) into PDMS molds (rings with 4 mm internal diameter, 6 mm external diameter, 1 mm height) positioned onto 8-well glass chambers (Nunc™ Lab Tek™, ThermoScientific). Glass chambers and PDMS molds were previously sterilized via sequential EtOH 70% washing and UV-treatment. The samples were crosslinked for 15 min using the same photorheology setting described above, with 405 nm light, 50 mW cm^{-2} intensity. After crosslinking, FluoroBrite DMEM supplemented with 1:2000 CalceinAM (Invitrogen), 1:500 Propidium Iodide (PI, Fluka) was added. After 40 min, imaging was performed on a Leica SP8 microscope (Leica) equipped with a 25 \times objective. Z-stacks were acquired from the sample surface at 2 μm steps and 100 μm into the sample. The ensuing pictures resulted from maximum intensity z-projection. Cell viability was assessed by counting viable (CalceinAM) and dead (PI) cells with the ImageJ Analyze particle function.

ROS assay: Hydrogels were prepared as indicated above, using 2 million cells mL⁻¹. The resulting bioresins were pipetted (15 μ L) into PDMS molds positioned onto 8-well glass chambers (Nunc™ Lab Tek™, ThermoScientific). Glass chambers and PDMS molds were previously sterilized via sequential EtOH 70% washing and UV-treatment. The samples were crosslinked for 15 min using the same photorheology setting described above, with 405 nm light, 50 mW cm⁻² intensity. After crosslinking, the cellular ROS assay (ab113851, abcam) was performed following provider's instructions. Serum-free DMEM supplemented with 20 mM DCFDA was added to the wells. After 4 h, imaging was performed on EVOS M5000 imaging system (ThermoFisher) equipped with a 4 \times objective. Images were taken using the same parameters and elaborated using Fiji, subtracting the same background level.

Two-photon stereolithography (2P-SL): RF photoresin composed of 0.5% HA-Mal and 0.79% PEG4SPC was prepared as previously described and pipetted (15 μ L) into PDMS molds (ring with 4 mm internal diameter, 6 mm external diameter, 1 mm height) positioned onto 8-well glass chambers (Nunc™ Lab Tek™, ThermoScientific). 2P-SL was performed using a Leica TCS SP8 (Leica) confocal microscope equipped with a Mai Tai two-photon laser (Spectra-Physics) tuned at 780 nm. Regions-of-interest (ROIs) were designed in the desired shape (circle, gorilla, alpaca, palm, ETH logo) using LAS X software functionalities. For parameter screening, a thermal power sensor (S175C, Thorlabs) was used to determine the light intensity at various laser output power. 2P-SL was performed with HCX IRAPO 25X/0.95NA water immersion objective, 1 μ m z-step, 600 Hz scanning, bi-directional scanning, 1024x1024 format and zoom factor of 1. Imaging was performed on EVOS M5000 imaging system (ThermoFisher) equipped with 4 \times and 10 \times objectives.

3D model “Sleeping cat” was printed using a script previously developed in our lab (available at <https://github.com/nbroguiere/F2P2>). The script slices the .stl model into a sequence of ROIs which are then executed under the LAS X Live Data Mode. To ensure attachment to the glass slide, the printing was set to start \sim 5 μ m below the glass surface. After extensive washing of uncrosslinked photoresin, imaging of the 3D model was performed on Leica SP8 microscope (Leica) equipped with a 25 \times objective, taking advantage of two-photon triggered fluorescence of residual photocage.

Two-photon biofabrication and Live/Dead assay: RF photoresin composed of 0.5% HA-Mal and 0.79% PEG4SPC was prepared as previously indicated. The resulting bioresin was pipetted (15 μ L) into PDMS molds (ring with 4 mm internal diameter, 6 mm external diameter, 1 mm height) positioned onto 8-well glass chambers (Nunc™ Lab Tek™, ThermoScientific). Glass chambers and PDMS molds were previously sterilized via sequential EtOH 70% washing and UV-treatment. 2P-SL was performed as previously indicated using ROI functionality. For the “cells seeding” example of Figure 7.5Ci, after 2P-SL the uncrosslinked resin was washed out with 5x media changes. Then, a suspension of NHDF (1 million cells mL⁻¹) was added and

cells were left to adhere for 1 h. After washing 3x with media, cells were left to spread for 3 days. Then, FluoroBrite DMEM supplemented with 1:2000 CalceinAM (Invitrogen) was added and after 40 min, imaging was performed on a Leica SP8 microscope (Leica) equipped with a 25× objective.

For the cell-laden applications (Figure 7.5Cii and Figure 7.5Ciii), NHDFs were resuspended in the photoresins at 1 million cells mL⁻¹. After 2P-SL, the uncrosslinked bioresin was washed with 5x media changes prior to imaging. For the Live/Dead assay, FluoroBrite DMEM supplemented with 1:2000 CalceinAM (Invitrogen), 1:500 Propidium Iodide (PI, Fluka) was added. After 40 min, imaging was performed on a Leica SP8 microscope (Leica) equipped with a 25× objective. For “multistep/multicellular” of Figure 7.5Ciii, NHDFs were previously incubated with CellTracker Green dye CMFDA (Invitrogen) and Cell Tracker Red dye CMTPIX (Invitrogen) in serum-free media at a working concentration of 10 μM. After 1 h in the incubator, green-labeled and red-labeled NHDFs were washed 3x with PBS. The two labeled-NHDFs were resuspended at 1 million cells mL⁻¹ in two separate photoresins (0.5% HA-Mal and 0.79% PEG4SPC) and used for sequential 2P-SL. After the printing of the first cylinder-like structure with red-labeled NHDFs, uncrosslinked bioresin was washed out with 5x media changes prior to adding the second green-labeled NHDFs bioresin. After the printing of the external flower-shape, uncrosslinked bioresin was washed out with 5x media changes prior imaging.

Acknowledgements. The authors acknowledge ETH ScopeM imaging facility for their assistance. “Sleeping cat” .stl file was obtained from <https://www.thingiverse.com/thing:3050876> (under CC BY 4.0 license).

Contributions. R.R. conceived the project and designed the experiments. M.Z-W. supervised the project. R.R. and N.P. performed chemical synthesis and mechanical testing. R.R. performed uncaging tests, cellular assays and printing. A.B. performed gene expression analysis. The manuscript was written with the contribution of all authors.

7.5 Supporting Information

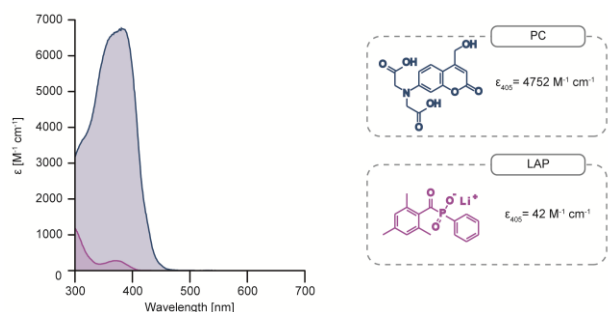


Figure S7.1| Absorption spectra of PC (blue) and LAP (magenta) with respective extinction coefficient (ϵ) values at 405 nm.

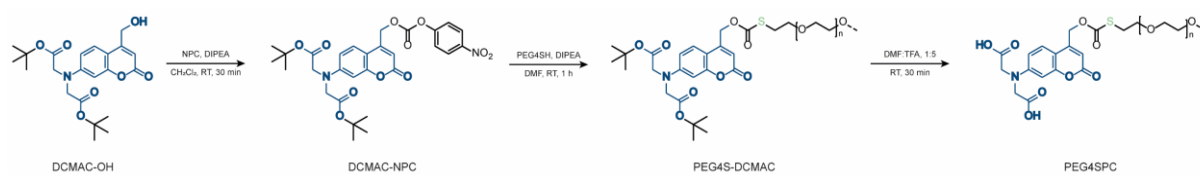


Figure S7.2 Final synthesis steps of PEG4SPC. The photocage 7-di-((tert-butyl-carboxy)methyl)amino 4-(hydroxymethyl)-coumarin (DCMAC-OH) was activated with 4-nitrophenyl chloroformate (NPC) and reacted with PEG4SH forming a thiocarbonate bond. Final product PEG4SPC was obtained with trifluoroacetic acid treatment (TFA).

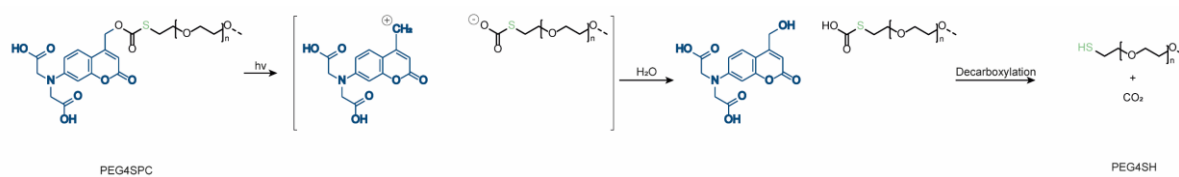


Figure S7.3 Uncaging process. Upon light absorption, PC (blue) is released from PEG4SPC with the formation of an intermediate coumarinylmethyl cation and thiocarbonate anion. PC cation reacts with solvent (H_2O) to generate the initial stable product (PC) while the unstable anion undergoes decarboxylation to give free thiol (PEG4SH).

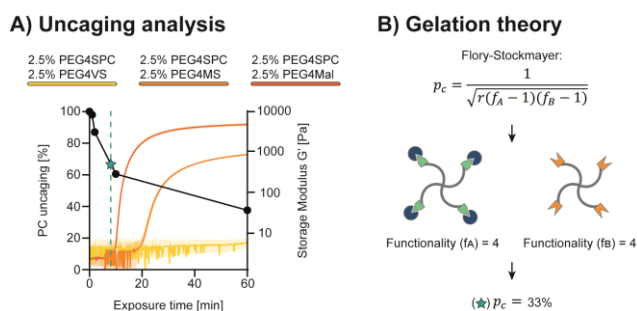


Figure S7.4 A) PC uncaging analysis (black trace, left y axis) performed under the same conditions used for photorheology (405 nm, gap: 200 μm , light intensity: 50 mW cm^{-2}). Photorheology curves shown in Figure 2Bii are overlapped (right y axis) to better visualize the relationship between uncaging and gelation kinetics of the various photoresin formulations. The theoretical gelation point is shown as a green star and dashed line. B) Flory-Stockmayer gelation theory reporting the critical gelation point (p_c) in relation to the molar ratio (r) of the two initial components and their functionalities (f_A and f_B). If considered as an ideal system, PEG4SPC and PEG4ene formulation has a p_c of 33%. Although far from being an ideal system, the formation of the gel based on PEG4SPC/PEG4Mal was the one that came closer to such theoretical estimate, suggesting a much faster reaction between uncaged PEG4SH and PEG4Mal when compared to PEG4MS and PEG4VS.

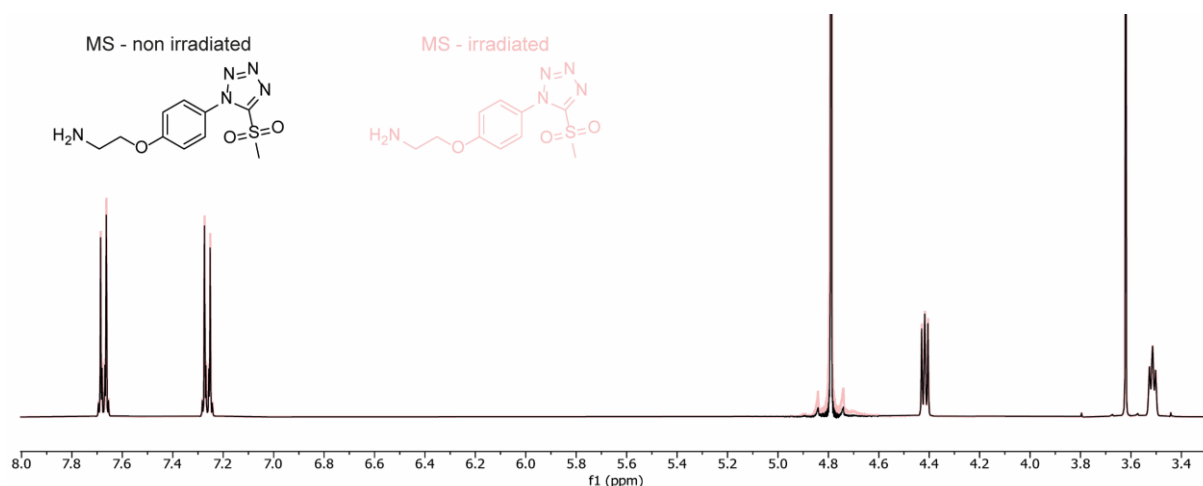


Figure S7.5 | Photostability of MS verified with $^1\text{H-NMR}$ in D_2O . When irradiated with 405 nm light at 50 mW cm^{-2} for 30 min (pink trace), MS did not show signs of photodegradation (equivalent NMR spectrum compared to non-irradiated MS, black).

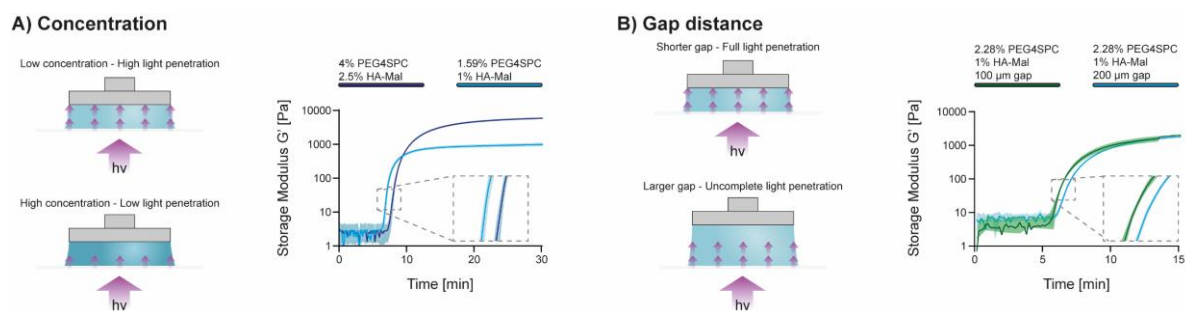


Figure S7.6 | Impact of change in RF crosslinker concentration (A) and gap distance (B) during photorheology measurements. A) Because of the high extinction molar coefficient of PC at 405 nm, light does not efficiently penetrate throughout the higher concentrated photoresin (illustration on the left), therefore resulting in a slower crosslinking kinetics (right). However, when the total polymer concentration was increased, higher plateau storage modulus was found. B) By changing the gap distance between the rheometer probes, a similar effect can be observed as light does not efficiently penetrate through larger gaps (illustration left). Photorheology measurements showed, in fact, that when using the same photoresin, a faster crosslinking occurs with a shorter gap distance (right). Overall, these observations suggest that photorheology could be used to compare various photoresins when using the same measuring conditions and RF crosslinker concentration, but light absorption played a crucial role in the resulting crosslinking kinetics.

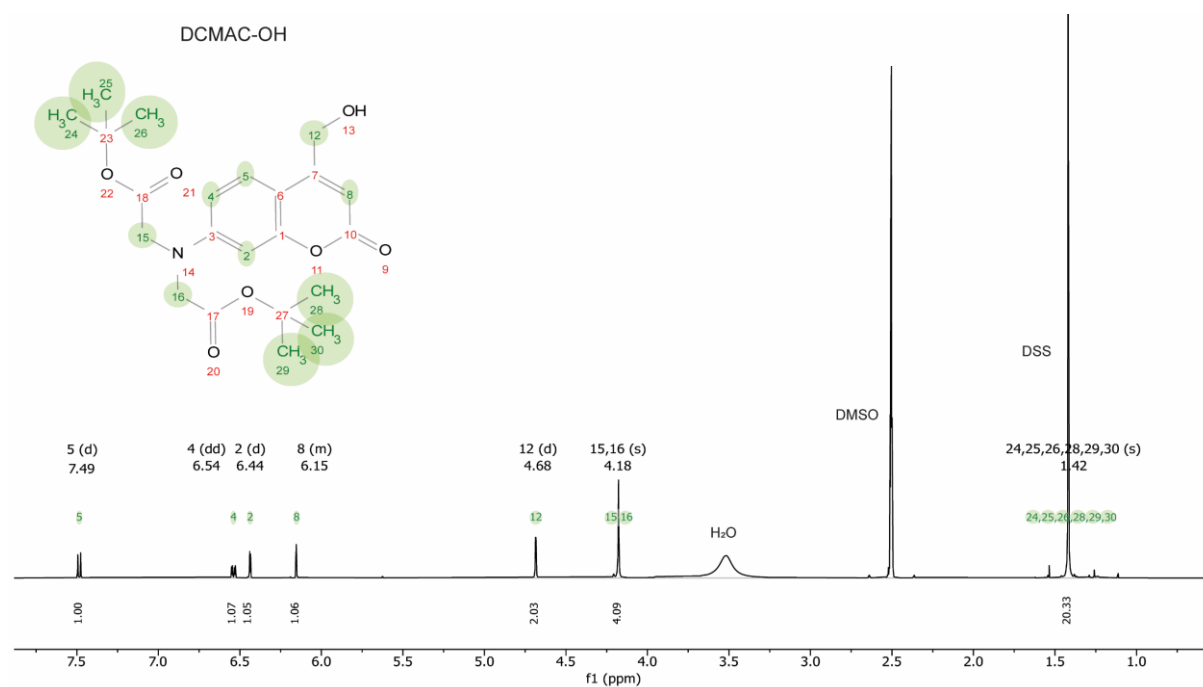


Figure S7.7 | ¹H-NMR of DCMAC-OH in DMSO-d₆. Assigned peaks are highlighted in green.

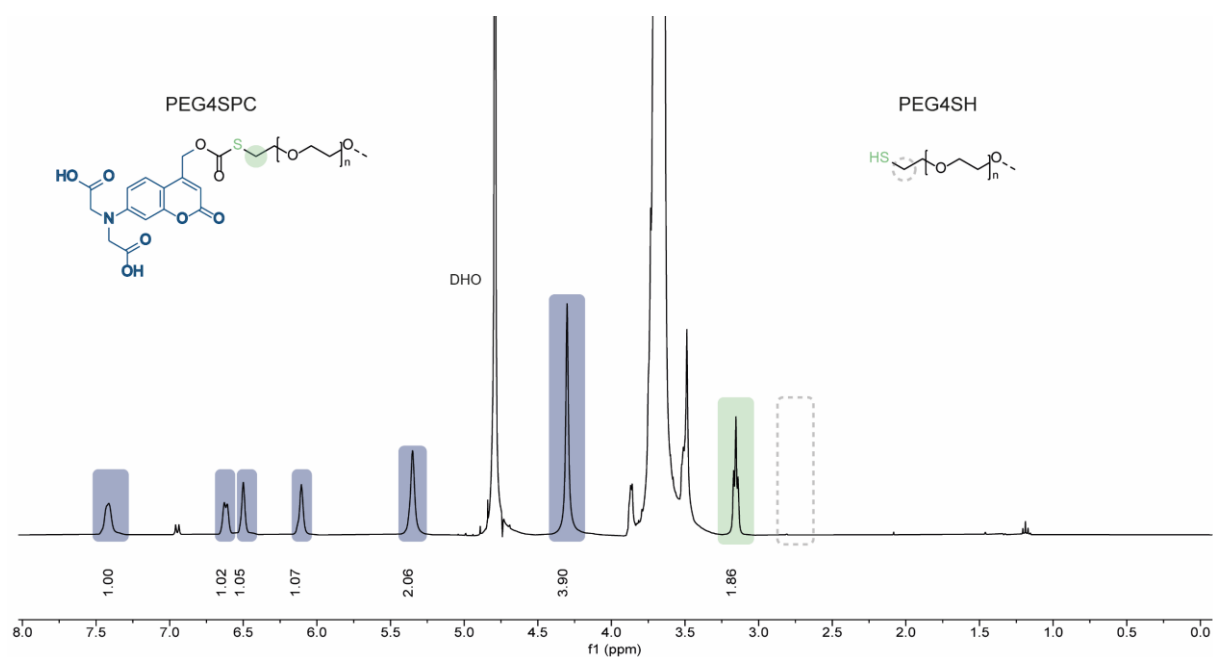


Figure S7.8 | ¹H-NMR of PEG4SPC in D₂O. PC peaks (see Figure S7) are highlighted in blue, while terminal methylene group (2H, ~3.2 ppm) of the 4-arm-PEG is highlighted in green. Absence of terminal methylene group of PEG4SH (dashed line) confirmed complete caging of the thiols. As indicated in Figure 1C, the presence of the photocage shifts the terminal methylene peak of the PEG from ~2.7 to 3.2 ppm.

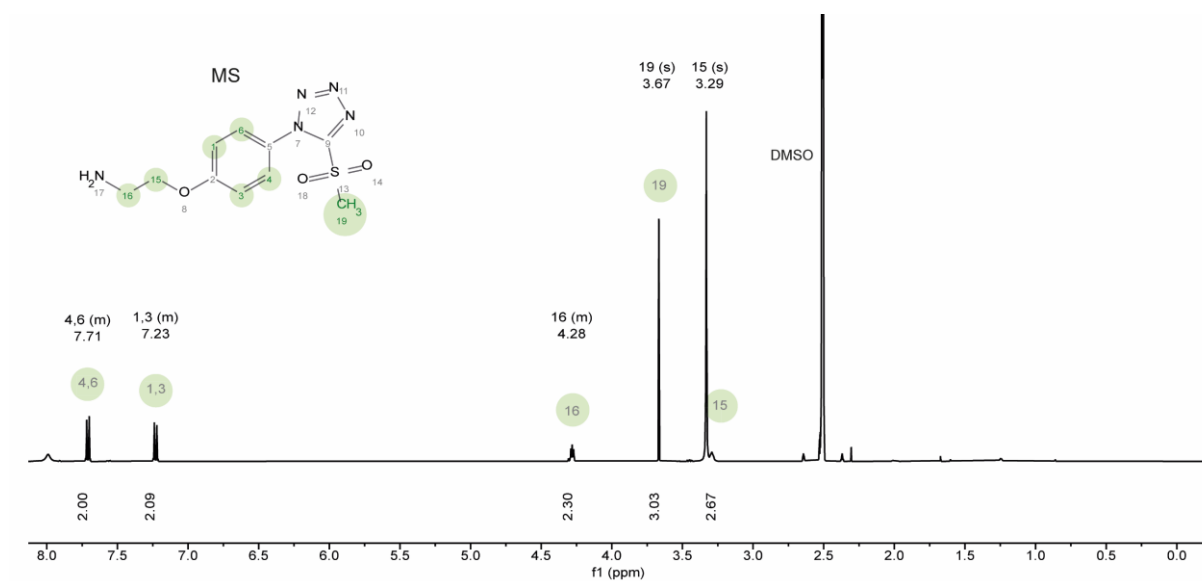


Figure S7.9 | $^1\text{H-NMR}$ of MS in DMSO-d_6 . Assigned peaks are highlighted in green.

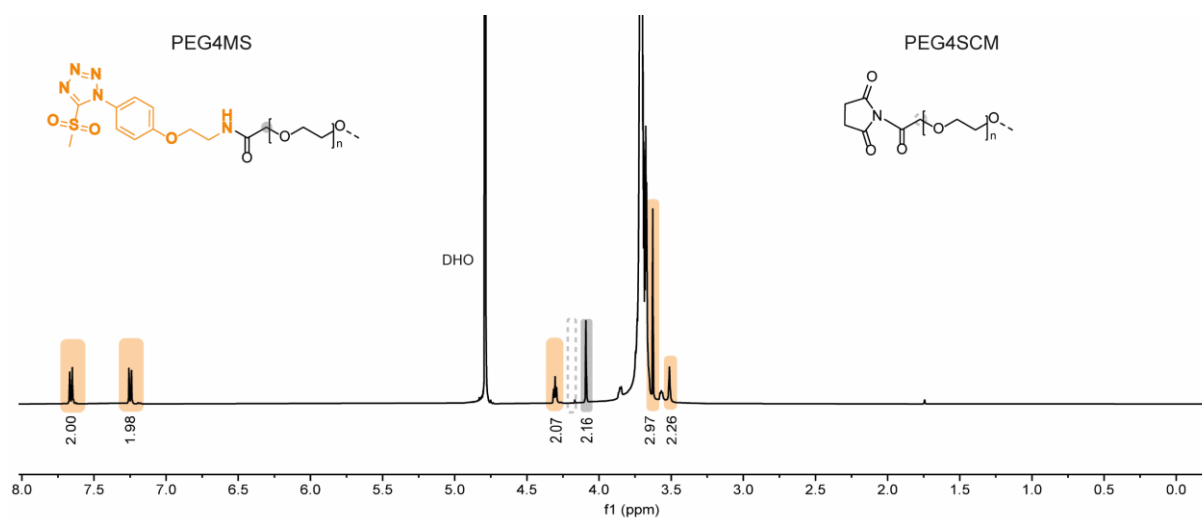


Figure S7.10 | $^1\text{H-NMR}$ of PEG4MS in D_2O . MS peaks are highlighted in orange, while terminal methylene peak (2H, ~ 4.09 ppm) of the PEG chain is highlighted in grey. Absence of terminal methylene group of PEG4SCM (dashed line) confirmed completion of reaction. The presence of the MS moiety shifts the terminal methylene peak of the PEG from ~ 4.21 to 4.09 ppm.

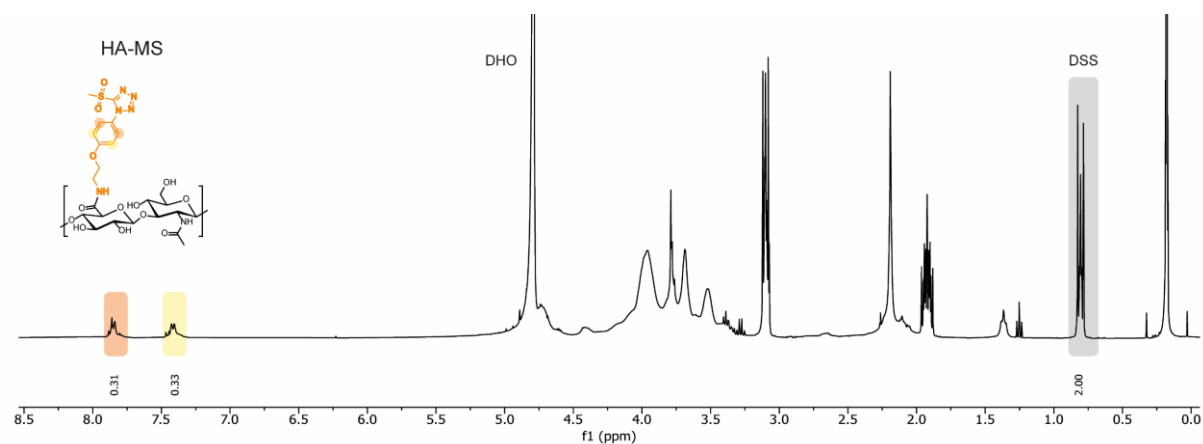


Figure S7.11 | $^1\text{H-NMR}$ of HA-MS in D_2O . Internal standard 3-(trimethylsilyl)-1-propanesulfonic acid (DSS) is highlighted in grey (2H, ~ 0.75 ppm), and MS aromatic ring protons (4H, ~ 7.4 and 7.8 ppm) are highlighted in orange and yellow. These integrals were used to determine the HA-MS degree of substitution (DS: 22%).

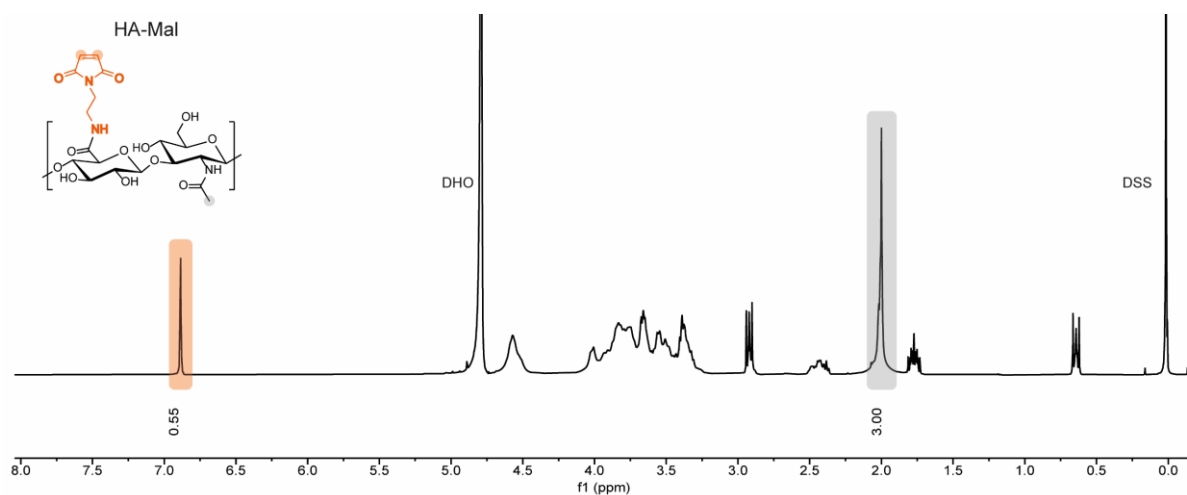


Figure S7.12 | $^1\text{H-NMR}$ of HA-Mal in D_2O . Maleimide -ene protons (2H) are highlighted in orange (~ 7 ppm) and methyl protons of N-acetyl group are highlighted in grey (3H, ~ 2 ppm). These integrals were used to determine the HA-Mal degree of substitution (DS: 27.5%).

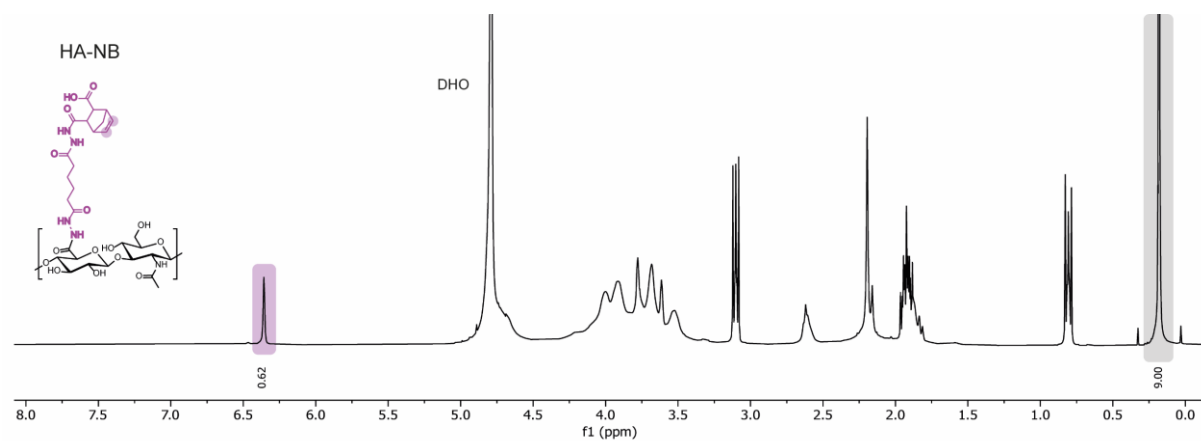


Figure S7.13 | $^1\text{H-NMR}$ of HA-NB in D_2O . Norbornene -ene protons (2H) are highlighted in purple (~ 6.3 ppm) and internal standard 3-(trimethylsilyl)-1-propanesulfonic acid (DSS) is highlighted in grey (9H, ~ 0.2 ppm). These integrals were used to determine the HA-NB degree of substitution (DS: 18%).

CHAPTER 8

Two-Photon Patterning

The two-photon uncaging mechanism presented in Chapter 7 is herein exploited to immobilize (pattern) growth factors in 3D matrices. Using non-fouling hydrophilic photocage and Sortase A enzymatic coupling, morphogenesis is guided by 3D-patterned growth factors in a one-step, low-background, time-controlled procedure.

MANUSCRIPT

Morphogenesis Guided by 3D Patterning of Growth Factors in Biological Matrices

Nicolas Broguiere, Ines Lüchtefeld†, Lucca Trachsel†, Dmitry Mazunin†, Riccardo Rizzo†, Jeffrey W. Bode, Matthias P. Lutolf, Marcy Zenobi-Wong

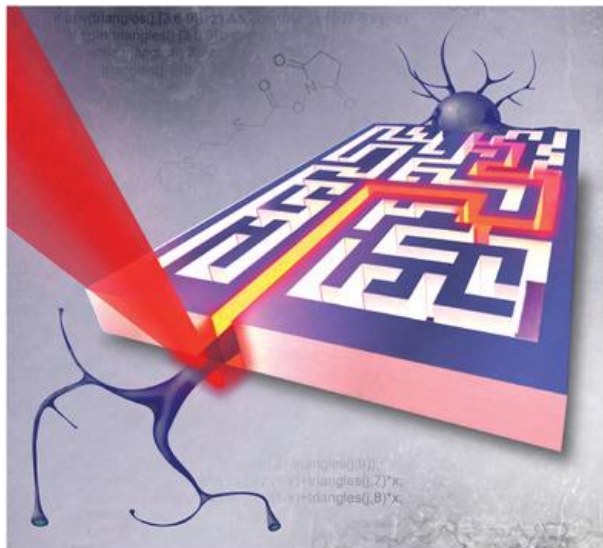
Advanced Materials **2020**, 32, 1908299

DOI: 10.1002/adma.201908299

†Equal contribution.

Reprinted with permission from Adv. Mater. 2020, 32, 1908299, Copyright © 2020, WILEY-VCH Verlag GmbH & Co. KGaA, Weinheim

Abstract



Three-dimensional (3D) control over the placement of bioactive cues is fundamental to understand cell guidance and develop engineered tissues. Two-photon patterning (2PP) provides such placement at micro- to millimeter scale, but nonspecific interactions between proteins and functionalized extracellular matrices (ECMs) restrict its use. Here, a 2PP system based on nonfouling hydrophilic photocages and Sortase A (SA)-based enzymatic coupling is presented, which offers unprecedented orthogonality and signal-to-noise ratio in both inert hydrogels and complex mammalian matrices.

Improved photocaged peptide synthesis and protein functionalization protocols with broad applicability are introduced. Importantly, the method enables 2PP in a single step in the presence of fragile biomolecules and cells, and is compatible with time-controlled growth factor presentation. As a corollary, the guidance of axons through 3D-patterned nerve growth factor (NGF) within brain-mimetic ECMs is demonstrated. The approach allows for the interrogation of the role of complex signaling molecules in 3D matrices, thus helping to better understand biological guidance in tissue development and regeneration.

8.1. Main Text

Fluorescent proteins heralded in a paradigm shift in the biosciences in the 1990s, enabling for the first time the visualization of biological processes in living specimens. The development of a wealth of light-based biosensors followed, notably calcium reporters,⁹⁵²⁻⁹⁵³ facilitating the observation of complex processes in vivo. A second revolution has been unfolding in the past 15 years, with light being used to control living systems rather than monitoring them.⁹⁵⁴⁻⁹⁶⁰ In the fields of biomaterials and tissue engineering, this concept has been adopted for controlling, in space and time, the display of extracellular signaling cues to living cells embedded in three-dimensional (3D) gels.³³³ This technique, called two-photon patterning (2PP), has opened up exciting perspectives for the in situ manipulation of mammalian cells and, in particular, the study of biological guidance.⁷⁰⁴ Indeed, 2PP and related methods, such as two-photon polymerization⁶⁰⁵ and two-photon ablation,^{207, 337, 961} have become increasingly useful as biofabrication tools, enabling a potentially unique control over cell and tissue organization at the micro- to millimeter scale.⁹⁶²

Because of their modularity and low nonspecific interactions, synthetic bioactive hydrogels have been a major focus of 2PP, culminating in the recent ability to reversibly pattern an active growth factor in the presence of living cells^{212, 244, 728, 731, 736} in polyethylene glycol (PEG) hydrogels. Nevertheless, despite increasingly sophisticated coupling strategies based on click chemistry and traditional photocages, it has not been possible to utilize 2PP for growth factor guided tissue morphogenesis, a much sought-after application of this approach. We hypothesized that achieving this milestone would require orthogonal 2PP protocols that are fully compatible with native ECMs, which are most commonly used in fundamental biology studies involving primary cultures or derivation of tissues from self-organizing stem cells. These matrices are however chemically complex, which makes them prone to high levels of signal background from nonspecific interactions. Complex biological guidance cues, such as growth factors, are also more prone than simple peptides to adsorption onto traditional photocages, due to their hydrophobicity. Improvements in 2PP patterning specificity, both in terms of physical interactions and of coupling specificity, are therefore crucial. This would ideally be achieved using one-step processes that avoid lengthy incubations and could thus maintain the phenotype and potency of fragile cell types that are currently not photomodulatable via 2PP.

We therefore devised a 2PP workflow geared toward improved specificity (Figure 8.1). First, we developed protocols to selectively cage selected amino groups on synthetic peptides with two-photon labile protecting groups. Those were used to cage substrate peptides for Sortase A (SA), a bacterial ligase that provides excellent cross-linking kinetics and outstanding orthogonality to eukaryotic systems.⁹⁶³⁻⁹⁶⁶ We then demonstrated 2PP in inert alginate hydrogels, as well as in an array of naturally derived matrices that are widely used in cell culture and representative of the various mammalian extracellular matrices (ECMs). Using a hydrophilic photocage was essential to avoid nonspecific fouling. Our scheme enables one-step processes,

which are not only highly advantageous for *in vitro* 2PP in the presence of cells, but also open future horizons for 2PP, such as the development of *in situ* patterning protocols directly in tissues *in vivo* or *ex vivo*. Furthermore, most labs use standard two-photon microscopes for their patterning and are limited to simple extruded 2D shapes, which we addressed with a new open-source library for advanced 2PP on standard commercial multiphoton microscopes. Finally, we succeeded in guiding axons along defined 3D patterns of nerve growth factor (NGF) in brain ECM-mimetic matrices. These results demonstrate the unprecedented potential of our approach for the 2PP-based induction of tissue morphogenesis.

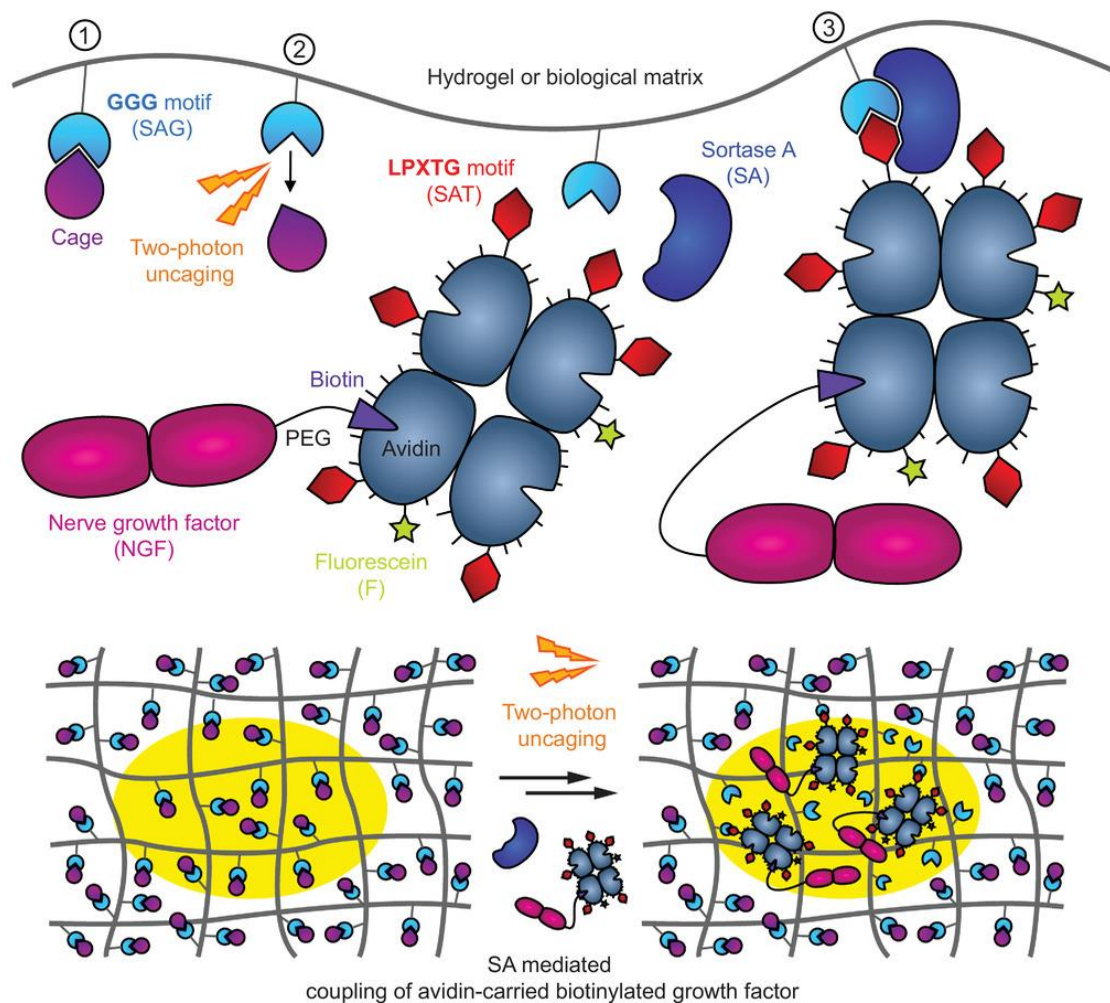


Figure 8.1 | Summary of the two-photon patterning (2PP) process. In the first step, a hydrogel which harbors caged Sortase A (SA) glycine donor peptides (SAG) (1) is formed in the presence of cells and other components needed for the patterning process (i.e., an avidin carrier modified with a SA threonine donor peptide and fluorescein (avidin-SAT-F), SA, and biotinylated biological cues). After gel formation (typically within minutes), two-photon uncaging is performed in user-defined positions (2). SA-mediated ligation then anchors the biotinylated biological cue (here, NGF) in the exposed areas (3) through avidin-SAT-F. Note that the growth factor is minimally modified and can be readily exchanged for other biotinylated bioactive cues, that two-photon excitation provides three-

dimensional (3D) patterning possibilities, and that the resulting patterns can be monitored using the fluorescent tag on the avidin. Bold letters indicate the motifs recognized by SA, in amino acid one-letter code.

We synthesized peptides inactivated by various photocages. We studied the traditional 2-(2-nitrophenyl) propoxycarbonyl (NPPOC),⁹⁶⁷ which is widely used in the synthesis of DNA arrays and has been used to cage amino acids,⁹⁶⁸ but is known to be relatively insensitive to two-photon uncaging in the absence of a sensitizer,⁹⁶⁹ as other cages derived from *o*-nitrophenyl. We then studied 6-bromo 7-hydroxycoumarin (BHC), the first described cage with high two-photon uncaging cross-section,^{734, 970} as well as a newer variant with improved stability, 7-diethylaminocoumarin (DEAC).⁹⁷¹⁻⁹⁷² Finally, as we were concerned with the hydrophobicity of these traditional cages, we studied a more recently described variant of DEAC, 7-dicarboxymethylaminocoumarin (DCMAC),⁹⁷³ which has extremely favorable water solubility and two-photon uncaging properties.⁹⁷⁴ DCMAC has only been sparingly used, despite of its interesting features, most likely due to the lack of a high yielding synthesis. This led us to develop a new procedure, performing the reaction solvent-free in the presence of a radical inhibitor, leading to 80–90% yield in the critical first step of the synthesis.

Photocages could be readily added on the N-terminus of solid phase supported peptides after 4-nitrophenyl chloroformate activation. Conveniently, the resulting carbamate linkages resisted standard peptide cleavage conditions, notably including concentrated aqueous trifluoroacetic acid and thiols. This method was used to cage SA glycine (SAG) donor peptides with DCMAC (Figure 8.2a) and other cages (Figure S8.1–S8.3, Supporting Information). Interestingly, the protocol can be combined with base-insensitive orthogonal protecting groups such as Ddiv, to enable the selective caging of any side chain amino group. As an example, we caged on its lysine side chain the peptidic substrate (FKGG-ERCG) of the human transglutaminase activated factor XIII (TG), which yielded functional two-photon activatable TG substrates (Figure S8.4a,b, Supporting Information). The procedure complements existing protocols for site-specific cysteine caging,⁹⁷⁵ and is a versatile route to generate two-photon activatable bioactive peptides.

Hydrophilic cages would be useful to incorporate into other 2PP strategies. As an example, we demonstrated the incorporation of DCMAC into a caged thiol–patterned maleimide 2PP workflow (Figure S4d, Supporting Information).

Developing new tagged proteins is a time-consuming and expensive process, especially when it involves cloning and recombinant expression. Biotinylated proteins on the other hand are already a standard, and most growth factors are readily available in a biotinylated format. We therefore devised a flexible 2PP strategy based on functionalized avidin, that could act as a carrier by binding biotinylated growth factors.

In order to decorate fluorescein-tagged avidin with thiol-bearing SA threonine (SAT) donor peptides, we investigated several classical amine-thiol heterodifunctional cross-linkers with limited success. A few

problems encountered were low substitution efficiency with maleimide–PEG–NHS 3.4 kDa (likely due to the large polymer chain crowding the NHS environment), lysis of linkages created by Traut's reagent in the presence of thiols at physiological pH, and retro-Michael addition from maleimide linkers, all known issues.⁹⁷⁶⁻⁹⁷⁷

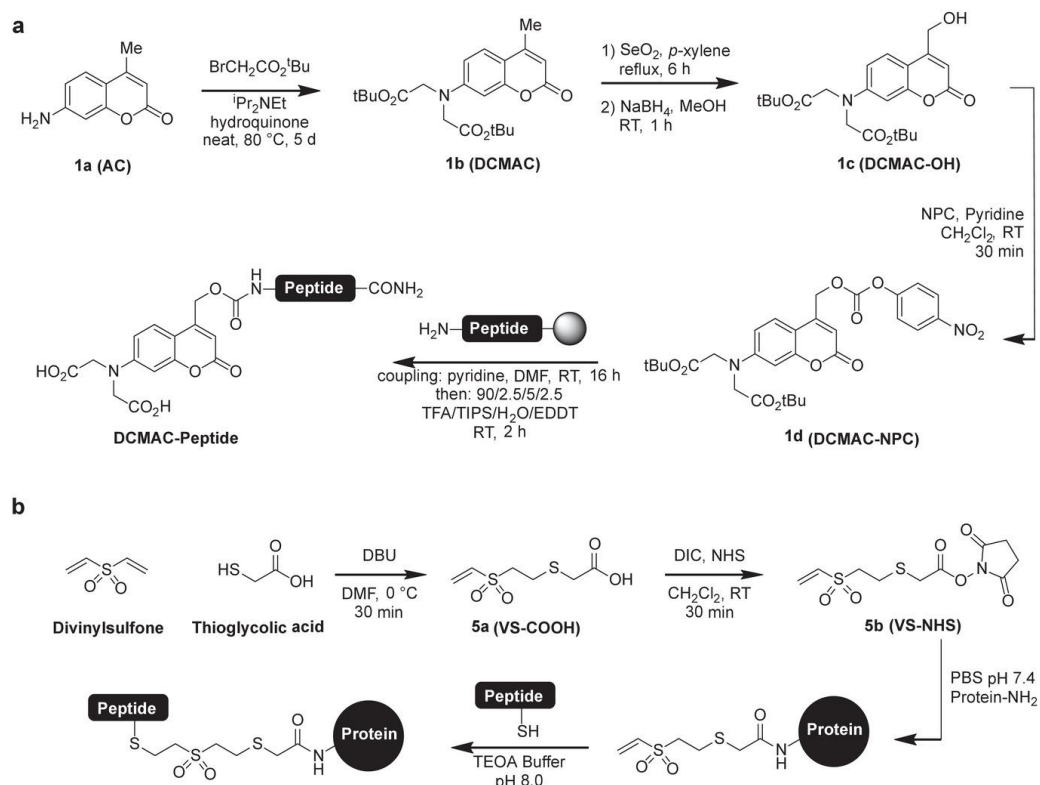


Figure 8.2 | a,b) Synthesis of: a) the hydrophilic cage DCMAC and caged peptides, and b) the heterobifunctional cross-linker VS-NHS and stable protein–peptide conjugates. Abbreviations: AC: 7-amino 4-methylcoumarin, DCMAC: 7-dicarboxymethylaminocoumarin (and by extension the 4-methyl and $t\text{Bu}$ protected derivatives), NPC: 4-nitrophenyl chloroformate and 4-nitrophenyl carbonate ester, TFA: trifluoroacetic acid, TIPS: triisopropylsilane, EDDT: 2,2'-(ethylenedioxy)diethanethiol, DBU: 1,8-Diazabicyclo[5.4.0]undec-7-ene, TEOA: triethanolamine, PBS: phosphate buffered saline, VS: vinylsulfone, NHS: N-hydroxysuccinimide, DIC: *N,N'*-diisopropylcarbodiimide.

This motivated the synthesis of a short and highly reactive heterodifunctional cross-linker, vinylsulfone-(S)-glycolic acid-(N)-hydroxysuccinimide ester (VS–NHS, **5b**), that is straightforward to synthesize (Figure 8.2b) and gives highly stable³⁹⁵ amide and thioether linkages (Figure 8.2b). Remarkably, based on these properties, VS–NHS would be an advantageous alternative to the commonly used cross-linker succinimidyl 4-(*N*-maleimidomethyl) cyclohexane-1-carboxylate (SMCC) for the construction of protein conjugates, avoiding altogether hydrophobic spacers and retro-Michael addition issues. This route was used to prepare highly substituted avidin, with 6 SAT peptides per avidin, as demonstrated by mass spectrometry (Figure S5a,b, Supporting Information). SAT peptides with the sequence Ac-GCRE-DDD-LPMTGG-NH₂ were chosen,

where the first block provides a reactive cysteine for conjugation,⁹⁷⁸ the LPXTG with X=M was chosen for its high reactivity,⁹⁷⁹ and DDD was acting as a spacer and as a protein stabilizer through supercharging.⁹⁸⁰ The binding of biotinylated NGF, used as a model growth factor, to the substituted avidin-SAT-F was confirmed by gel permeation chromatography (Figure S8.5c–f, Supporting Information). We successfully used NGF biotinylated with standard NHS-ester chemistry, but site-specific protein modification approaches have been developed²¹² that could help to retain more growth factor activity, in certain cases. Since our 2PP procedure is centered around the functionalized avidin, any biotinylation protocol would be equally compatible with our workflow.

Next, we performed a side-by-side comparison of photocages to see how the choice of the cage influences the brightness and specificity of 2PP using SA-mediated patterning of avidin-SAT-F as model system (Figure 8.3a–c). To minimize background signal, we used inert nonfouling alginate hydrogels as a blank canvas. Optimal laser intensities were determined for each cage. While low laser power failed to uncage, too high power was equally detrimental, causing photodamage to the ligands or hydrogels. It is indeed a well-known property of fs-lasers that high intensity irradiation results in plasma-mediated ablation,^{808, 981} which occurred on our SP8/Mai Tai MP system with 80% laser power, while 40% laser power caused a small amount of photodamage and 20% laser power was harmless (Figure S8.6, Supporting Information). The optimal laser power for one-scan uncaging was around 20–30% at a frame rate of 0.6 Hz, depending on the cage, similar to the power used for two-photon imaging. Patterns obtained with the hydrophilic two-photon active cage DCMAC were highly specific, whereas traditional cages only enabled faint patterns that were barely above background.

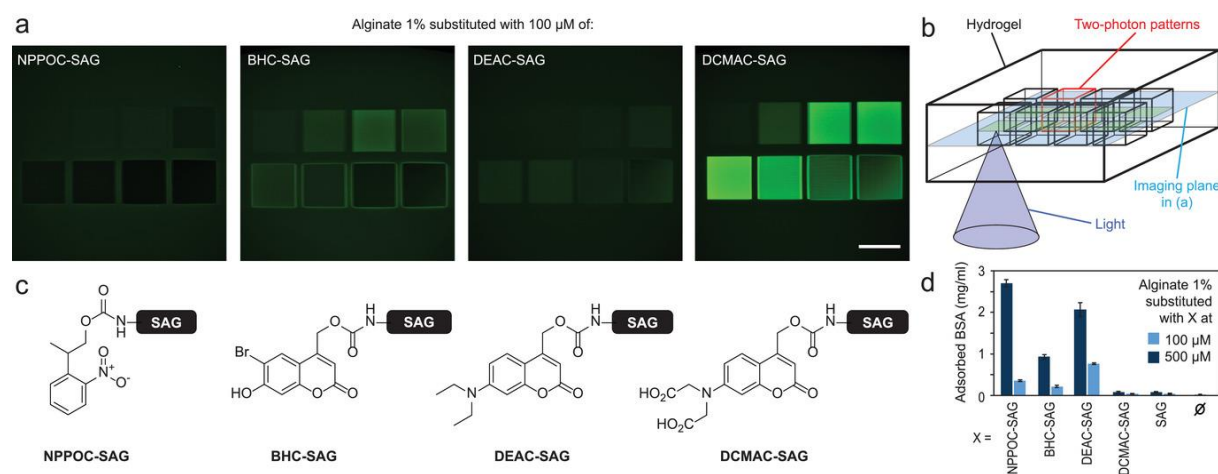


Figure 8.3 | Comparison of photocages. a) Two-photon patterns of avidin in alginate obtained with different cages. Scale bar: 100 μm . Coupling is done with Avidin-SAT-F 0.35 mg mL^{-1} , Sortase A (SA) 4×10^{-6} m , CaCl_2 10×10^{-3} m . Uncaging is done at 770 nm with a fs-pulsed Mai Tai laser at laser powers of 2.5, 5, 10, 20% (top row) and 30, 40, 60, 80% (bottom row). Confocal imaging of the fluorescein reporter mid-depth of the cubes was acquired with quantitative photon counting detectors and is displayed with

identical brightness and true background values. b) Schematic of the experimental setup: the hydrogel is functionalized with avidin on a three-dimensional (3D) array of 100 μm cubes. c) Chemical structures of the cages tested on SAG peptides. d) Quantification of the nonspecific adsorption of rhodamine-tagged bovine serum albumin (BSA) onto hydrogels substituted with caged peptides and controls. The BSA was incubated at 2 mg mL^{-1} for 100 min, and fluorescence readout was done after 48 h of washing. Error bars: SD, $n = 4$.

DEAC and DCMAC share an identical photoactive core and therefore nearly identical photoproperties: both molecules and their derivatives have absorption maxima at $\approx 390 \text{ nm}$,^{971, 975, 982} fluoresce at approximately 500 nm, and have molar extinction coefficients of 16–20 $\text{m}^{-1} \text{ cm}^{-1}$. Yet, DCMAC improves the specificity of 2PP by orders of magnitudes compared to DEAC. Additionally, BHC has lower two-photon uncaging cross-section than DEAC,⁹⁸³ but gave slightly better results. The photoproperties of the coumarin derivatives therefore do not explain the differences in pattern quality.

Hydrophobic surfaces are known to induce strong adsorption of proteins,⁹⁸⁴ and we therefore hypothesized that the poor outcomes with traditional cages, which are quite hydrophobic, might be primarily due to protein adsorption, increasing the background close to the surface and depleting the gel of free mobile proteins available for specific couplings in the core. We tested this hypothesis by quantifying the adsorption of bovine serum albumin (BSA), the serum protein most typically used for adsorption studies, to alginate hydrogels modified with various moieties (Figure 8.3d). A rhodamine reporter was conjugated to the BSA for sensitive fluorescent readout using red light that does not interfere with the photocages. We found that unmodified alginate retains little adsorbed protein ($25 \pm 5 \mu\text{g mL}^{-1}$, SD $n = 8$), and alginate substituted with unmodified SAG or DCMAC-SAG at a concentration of $100 \times 10^{-6} \text{ m}$, typical for 2PP, did not retain significantly more BSA ($p > 0.75$). Other cages at the same concentration retained from 5 to 20 times more protein ($p < 1 \times 10^{-7}$). Higher concentrations exacerbated the difference even further, with 10 to 40 times more adsorption on traditional cages than on DCMAC. Nonspecific adsorption is therefore an essential property that should be optimized for high quality 2PP.

After identifying the superior performance of DCMAC, we next generated an array of DCMAC-caged SAG peptides bearing a variety of handles for easy incorporation in all common synthetic and biological matrices (Figure 8.4a). Equipped with these tools, we demonstrated 2PP in a collection of mammalian matrices, representative of the ECM of connective (collagen), epithelial (Matrigel), central nervous system (hyaluronan¹⁰⁴), and regenerative (fibrin) tissue (Figure 8.4b). Remarkably, optimal uncaging could be achieved in a single scan. This enables relatively fast pattern formation in around 1.5 min for patterns of $500 \times 200 \times 200 \mu\text{m}$. Higher exposures resulted in damage to the hydrogel and peptide handles rather than increased uncaging, as evidenced by a reduction in the coupling efficiency (e.g., Figure 8.4b with 40% laser power and 4 scans in fibrin and hyaluronan).

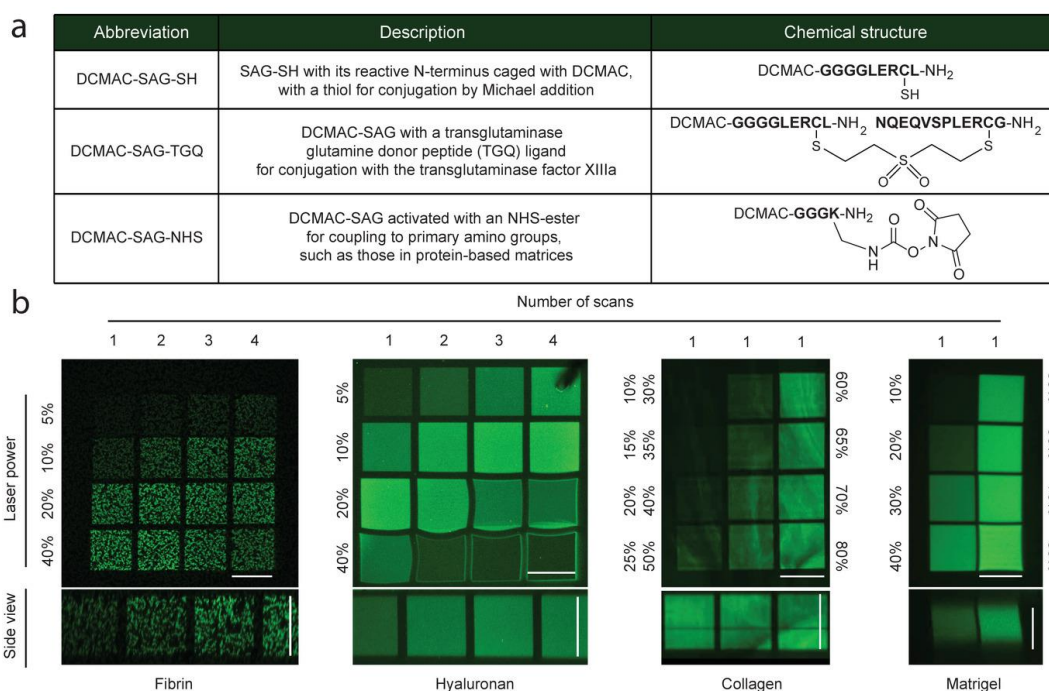


Figure 8.4 | Two-photon patterning (2PP) in biological matrices. a) Peptides used as substrates for enzymatic couplings, and caged derivatives used to functionalize various gel backbones. Characters in bold are amino acids in one-letter code. Critical functional groups on the side chains of amino acids used for couplings are highlighted in explicit chemical notations. $-NH_2$ indicates amidated C-terminus, and $Ac-$ indicates acetylated N-terminus. b) 2PP of avidin-SAT-F in the main mammalian extracellular matrices (ECMs), uncaging each test cube with a different laser power or scan number. Confocal fluorescence images of the fluorescein reporter were acquired with quantitative photon-counting detectors, with backgrounds not subtracted in order to display true nonspecific adsorption outside of the patterns. The images in collagen are average intensity projections over the whole cube thickness to mitigate the inhomogeneities due to collagen fibers, other images are single planes. Patterns in fibrin follow the natural microfibrillar structure of this ECM. Patterns in fibrin and hyaluronan were produced on a Leica SP8 inverted with a $25\times$ water immersion objective and MaiTai fs-laser, collagen, and Matrigel on an SP5 inverted with a $20\times$ water immersion objective and Chameleon fs-laser. Scale bars: $100\ \mu m$.

The enzymatic reactions used for hydrogel cross-linking (TG, thrombin) and 2PP couplings (SA) are fully orthogonal and compatible with physiological conditions, bypassing the need for serial incubations, which were necessary in previous photopatterning systems.^{124, 211-212, 244, 728, 734} This advance is key to reduce the handling time and the exposure of 3D encapsulated cells to soluble bioactive cues, and could also open the way to in situ patterning after delivery into a tissue defect in vivo, an application that is of utmost interest for aligned tissue reconstruction. For example, in vivo 2PP might be used to create guidance channels in damaged neural tissue that match the surrounding structures, or to alter guidance in developing embryos in order to study the mechanisms of morphogenesis. We tested the feasibility of this one-step process in vitro by including the modified avidin, growth factor, as well as gel cross-linking and 2PP-coupling enzymes in the same gelling mix as the biopolymer. Gelation occurred within minutes, which enables immediate

photopatterning and transfer to cell culture. This incubation-free one-step process worked equally well as a classical two-step procedure (Figure S8.4c, Supporting Information).

While two-photon polymerization instruments are common in microfabrication facilities, and advanced 2PP setups for biological applications have been built by a handful of bioengineering labs,^{206, 727} most biologists can only rely on standard two-photon microscopes for their two-photon uncaging. Scanning a region of interest (ROI) over a 3D stack or continuously changing the laser power enables the formation of extruded 2D shapes or simple gradients on such instruments, but more complex gradients or truly 3D shapes are out of reach. In an effort to make advanced 2PP available to biologists using existing infrastructure, we developed an open-source Matlab library that automatically generates instructions for standard commercial Leica two-photon microscopes (Figure 5).

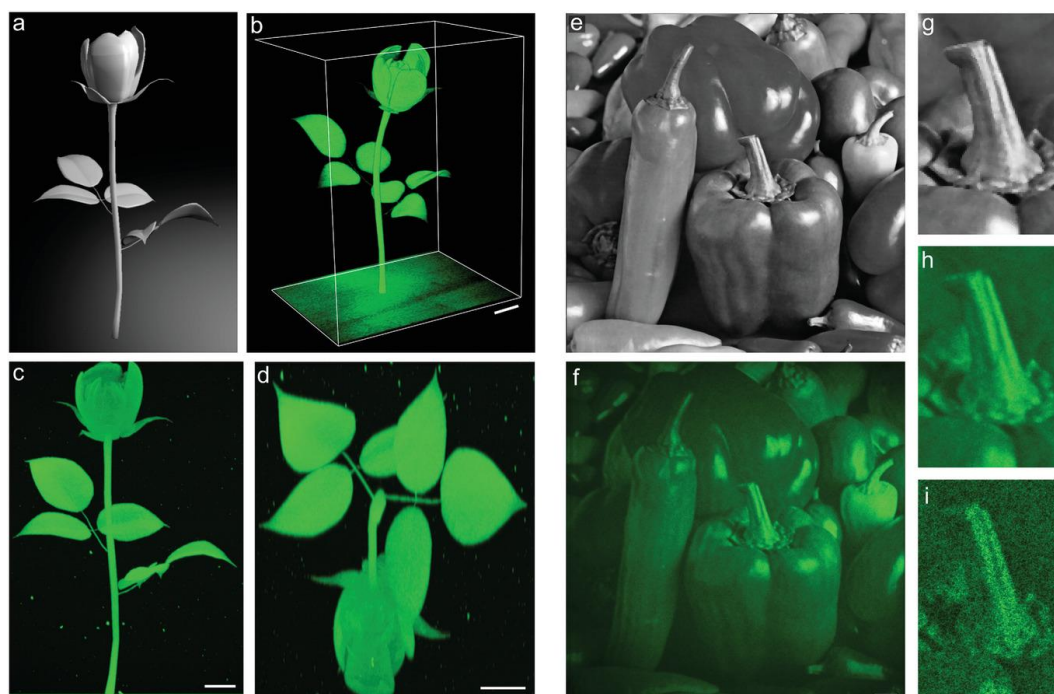


Figure 8.5 | Two-photon patterning (2PP) of complex gradients and three-dimensional (3D) shapes using a standard commercial two-photon microscope. a) 3D model and b) 2PP of avidin-SAT-F in a transglutaminase cross-linked hyaluronan hydrogel using a one-step process, as seen with two-photon imaging of the fluorescein tag (Fiji 3D viewer surface view). c,d) Maximum intensity projections in orthogonal planes. e) Gray-scale image exhibiting complex gradients, and f) reproduction as an avidin-SAT-F pattern in a collagen matrix (average intensity projection of a 200 μm thick pattern, invariant in the z direction). g,h) Close-ups of the reference and pattern. i) Single-plane view, with the collagen microstructure visible in the absence of averaging. Scale bars: 50 μm .

In order to provide some robustness to various machine setups and facilitate setting the parameters that are kept constant (e.g., scanning speed, objective, filter positions), our scripts use a template exported from the microscope. Complex instructions are generated based on this template, by adjusting the laser power, z -positions, and scan areas. The scripts were tested on different instruments, including a Leica SP8 inverted

with a Spectra Physics Mai Tai laser (Figure 8.5a-d) and an SP5 upright with a Chameleon laser (Figure 8.5e-i).

We then ensured the patterning instructions can be given in standard open formats: complex 3D shapes are input as triangular mesh data in the stereolithography (.stl) format, that can be exported/converted from most 3D modeling software, including open-source software such as Blender and Meshlab. The scripts slice the mesh to create a series of closed paths, which are then converted to a series of regions of interests (ROIs) associated with a z -position, selectively exposed during 3D scan using standard built-in electro-optical modulators (EOM) as a switch. Complex gradients are input as pixel data, typically tagged image format (.tif) files, together with calibration curves of pattern intensity versus uncaging conditions and laser power versus hardware filter position. Masks associated to different intensity levels in the reference image are then serially exposed to the appropriate laser powers, as defined by the reference curves, for accurate patterning.

Using this library, we could reproduce fine intricate 3D models (Figure 8.5a-d) as well as complex gradients (Figure 8.5e-i) as micropatterns of functionalized avidin. Of note, the fidelity of the patterning process depends on the optical system rather than on our chemical or software tools. In particular, the patterning resolution is defined by the size of the point spread function, which is linked to the choice of the objective and is well known from standard two-photon microscopy. We believe our algorithms will highly facilitate the use of two-photon fabrication–functionalization techniques in life science research, turning commonly available commercial microscopes into flexible two-photon fabrication instruments.

The development of the complex architecture of the nervous system arises from patterns of morphogens which guide axonal outgrowth. Models recapitulating this type of biological guidance would ideally use 3D rather than 2D cultures, for physiologically relevant growth cone cytoskeletal organization. They would also use biological or biomimetic background matrices providing a relevant microenvironment.

To implement this concept, we chose sensory neurons from dorsal root ganglia (DRG) explants of E9-10 chick embryos as a model system, well known for its response to NGF affecting neuron survival and axonal growth.⁹⁸⁵ Since biological matrices are likely to interfere with the response to the growth factor, we first compared the axonal growth from DRGs with or without soluble NGF in the medium, in an array of biological matrices (Figure S7, Supporting Information). Ideally, a good matrix for precise guidance would support axonal growth in the presence of the growth factor and inhibit it otherwise. Matrigel, collagen, and fibrin supported extensive glial and axonal outgrowth both in the presence and absence of NGF, consistently with previous findings,⁹⁸⁵⁻⁹⁸⁷ which limits their usefulness here. Hyaluronan gels, on the other hand, were almost entirely resistant to DRG axonal growth in the absence of NGF, but moderately supportive in the presence of soluble NGF, which is in agreement with previous reports that soluble hyaluronan is inhibitory for axonal growth from DRGs⁹⁸⁸ and notably different to the fast neurite outgrowth from central neurons in

these gels.¹⁰⁴ Axonal growth was found to be much enhanced in the presence of immobilized growth factor (Figure S8c, Supporting Information), a rather surprising finding even though there are prior reports of moderately increased axonal growth upon immobilization of NGF.⁹⁸⁹⁻⁹⁹⁰ Hyaluronan was therefore chosen as an ideal background.

Micropatterns of NGF were formed in apposition with freshly encapsulated DRGs. When NGF was immobilized in large regions ($200 \times 500 \times 500 \mu\text{m}^3$), axons extended at a fast rate of $\approx 100 \mu\text{m day}^{-1}$ and stayed confined in the area, which was particularly striking as axons collectively took sharp 90° turns when reaching pattern edges (Figure 8.6a-e). This demonstrates the robustness of the approach, and gives a bioengineered model of how anchored morphogens can strictly restrict cell processes to the tissues to which they belong.

Our method is also intrinsically compatible with time-controlled functionalization and growth factor display: matrix substitution with DCMAC-SAG-NHS could be done in the presence of DRGs after a preculture time, and could be followed by additional NGF patterning to dynamically control the guidance. Specifically, a first round of 2PP was made on Day 1 and axons grew into the patterns for 3 days. On Day 4, a second pattern of guidance was added which permitted further invasion over the following days (Figure 8.6l,m, Figure S8.9, Supporting Information). Guidance was confined to the patterned areas, but did not result in a complete filling of all of these regions.

In a classical understanding of NGF guidance, chemotaxis follows gradients of the soluble growth factor. Nevertheless, other mechanisms might have been missed due to the lack of experimental systems enabling 3D immobilization. We hypothesized that microchannels with dimensions comparable to the size of a growth cone could effectively orient axonal growth, similarly to lines of Schwann cells during nerve regeneration. We therefore patterned microchannels of 2–40 μm width in front of encapsulated DRGs (Figure 8.6f,h,j). Interestingly, axons grew as bundles strictly aligned with the microchannels, and upon reaching the end, de-bundled to form an arborization (Figure 8.6g,i,k). In order to ensure reproducibility, the DRG guidance results were repeated 3 times, using at least 2 different batches for the synthesis of each compound, with similar results. We also ensured that the guidance is specifically mediated by immobilized NGF by performing mock patterning, replacing biotinylated-NGF with nonbiotinylated NGF, which did not enable the growth (Figure S8.8a,b, Supporting Information). The bundles and trees are reminiscent of the behavior of axons that grow along a tract and spread upon reaching their target tissue, and this reproduction in a bioengineered system sheds new light on how the microenvironment can guide these morphogenetic events.

Our protocol for 2PP based on an orthogonal enzymatic coupling and nonfouling hydrophilic photocages enabled the patterning of avidin-linked biotinylated growth factors in mammalian ECMs. Patterns of NGF in hyaluronan gels successfully guided axonal growth from sensory neurons in 3D. The system therefore

introduces new opportunities for studying the mechanisms involved in axonal guidance by NGF signaling in 3D space. Importantly, it also lays the foundation for guidance studies based on other cues, cells, and matrices, as the methods are straightforward to translate to other biotinylated growth factors/morphogens due to the versatility of avidin as a carrier. The low off-target interactions of the optimized building blocks act as a safety net against toxicity, make intermediate washing or blocking steps unnecessary, and limit background from nonspecific protein binding.

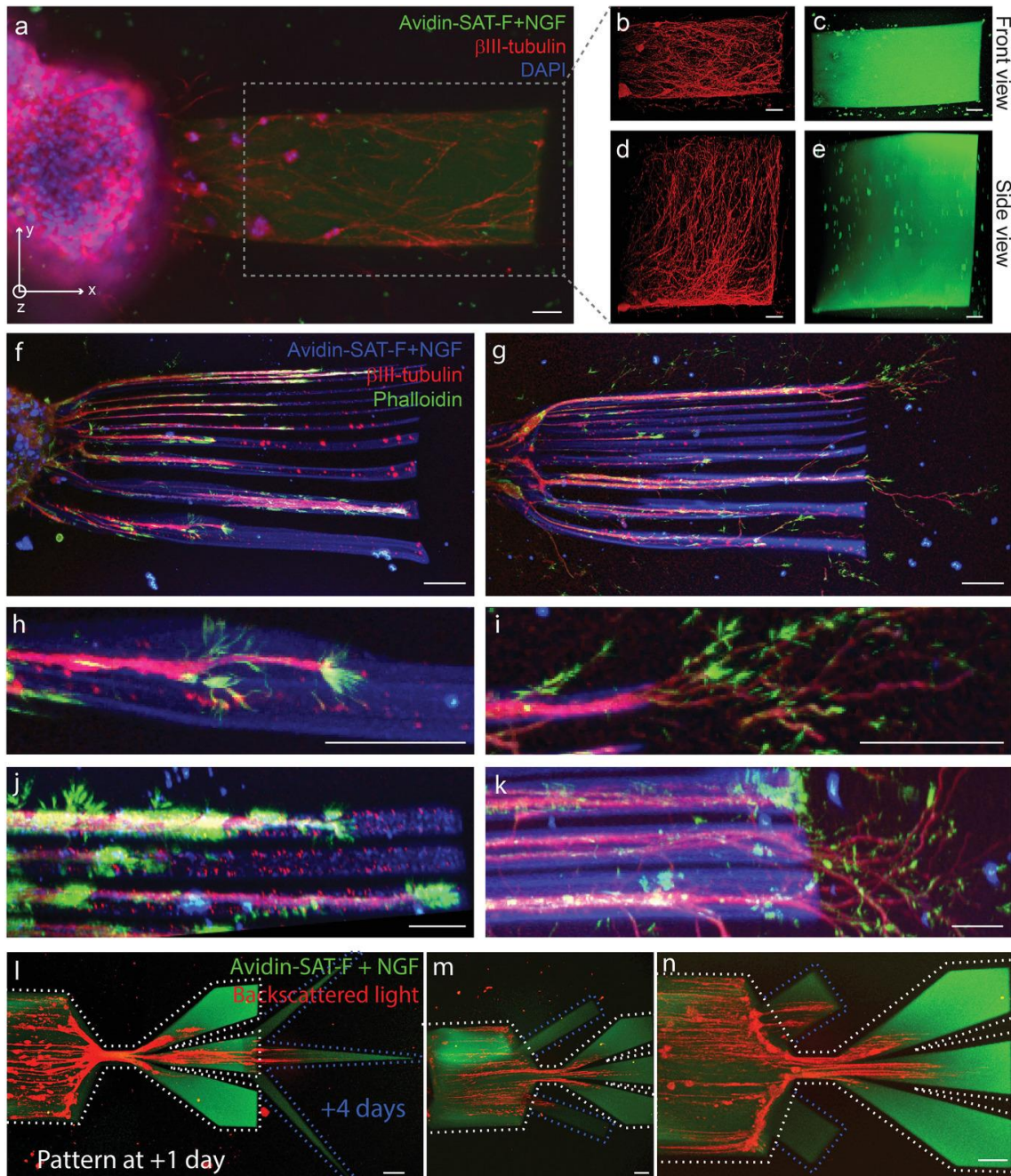


Figure 8.6 | Axonal guidance from chick dorsal root ganglia (DRG) into transglutaminase cross-linked hyaluronan matrix patterned with nerve growth factor (NGF). a–e) Representative images of axon confinement within a large rectangular NGF-positive region ($200 \times 400 \times 400 \mu\text{m}^3$) after 10 days in vitro. a) Widefield fluorescence showing the DRG as a DAPI⁺ structure on the left, the pattern as a fluorescein-tagged rectangle, and β III-tubulin⁺ axons confined to the patterned area. b–e) Maximal intensity projections (MIPs) from confocal imaging of the pattern area in (a), x -projected (b,c), and y -projected (d–e). f–k) Axon guidance with microchannels of NGF (2–40 μm wide from top to bottom), after 2 days of culture. f,g) MIP from confocal x -stacks, and h–k) close-ups from (f–g) in front (h,i) and side view (j,k), respectively. l–n) Time-controlled guidance, MIP from backscattered light and fluorescence confocal data at day 9. Images are adjusted for brightness/contrast/gamma for clarity. Scale bars: 50 μm .

2PP of sensitive biomolecules in complex matrices being particularly demanding, we were led to develop some chemical tools that might be of interest for use in much broader fields. First, our new heterodifunctional cross-linker, VS-NHS, could be an interesting alternative to the maleimide–NHS SMCC to form protein conjugates with improved linkage stability and reduced hydrophobicity. Our high yielding synthesis of a hydrophilic two-photon active cage could be incorporated in other 2PP strategies, in order to avoid nonspecific adsorption when patterning proteins. Our protocols to protect peptides with weakly interactive and highly water soluble two-photon active cages on any amino group could lead to improved substrates to study the signaling events generated by biologically active peptides with precise control over 3D position and time.

Further improvements in 2PP protocols could include multicolor extension of one-step high-specificity 2PP: the development of hydrophilic cages activated at orthogonal wavelengths together with the validation of additional orthogonal enzymes/ligands would be a natural path forward. Finally, this first demonstration of a one-step protocol to pattern growth factors in biological matrices and guide morphogenesis should motivate the development of in vivo 2PP, aiming toward in situ microaligned guidance of tissue regeneration.

Acknowledgements. I.L., L.T., D.M., and R. R. contributed equally to this work. The authors would like to thank David Fercher for technical assistance with peptide and protein production, and Prof. Esther Stoeckli and Dr. Beat Kunz for help with DRG isolation. The authors are grateful to Konstantin Schulz-Schönhagen, Michèle Dai, and Jasmin Feike for technical assistance during the preliminary exploration of cage synthesis options. The authors further acknowledge the assistance from the imaging facilities of the ETH (ScopeM) and EPFL (BIOP), with particular thanks to Dr. Justine Kusch and Thierry Laroche. Ethical approval for this work involving E9-10 chick embryos was not required. The 2PP library is available at: <https://github.com/nbroguiere/F2P2>.

Contributions. R.R. contributed in DRG isolation, chemical synthesis, 2PP and imaging for Figures 8.6l–n, S8.4d and S8.9.

8.2. Supporting Information

Experimental Section

General procedures. All chemicals are from Sigma-Aldrich-Merck, and cell culture reagents from ThermoFischer Scientific, unless indicated otherwise. NMR spectra were acquired on a Bruker AVIII400 or similar instruments and are provided in annex. High performance liquid chromatography (HPLC) was performed on C18 columns using Agilent instruments, using Poroshell 120 EC-C18 4.6 x 150 mm, 2.7 μm particle size columns for analytical HPLC, with a gradient from 10 to 90% acetonitrile (ACN) in water over 5 min in the presence of 0.1% trifluoroacetic acid (TFA) at 2 ml/min and 50°C, unless indicated otherwise. Preparative HPLC were on an Agilent Prep C18, 100 Å pore size, 10 μm particle size, 20 x 150 mm column at a flow rate of 20 ml/min and room temperature (RT), for up to 50 mg of peptide, or the equivalent 50 mm diameter column at a flow rate of 80 ml/min for up to 300 mg of peptide, using gradients of 10 to 90% ACN in water over 40 min in the presence of 0.1% TFA unless indicated otherwise. Gel permeation chromatography (GPC) were on an AdvanceBio SEC 300 Å pore size, 2.7 μm particle size, 7.8 x 300 mm column from Agilent. Liquid chromatography – mass spectroscopy (LCMS) were acquired on a Waters HPLC instrument equipped with electrospray ionization (ESI) and an SQ detector 2. Matrix-assisted laser desorption and ionization time-of-flight mass spectrometry (MALDI-TOF) on α -cyano-4-hydroxycinnamic acid (HCCA) matrix in the presence of TFA were acquired on a Bruker Autoflex instrument. Peptide sequences in amino-acid one-letter code are highlighted in bold throughout the methods.

Synthesis of 7-di-((tert-butyl-carboxy)methyl)amino 4-methylcoumarin (DCMAC, 1b). 1 g (5.7 mmol) of 7-aminocoumarin (AC, 1) was mixed with 3 ml (17.2 mmol) of *i*Pr₂NEt, 3 ml (20 mmol) of tertbutyl bromoacetate (BrAcOtBu), and 100 mg of hydroquinone in a Schlenk tube. The tube was sealed and the slurry was left to react at 80 °C for 5 days in the dark with magnetic stirring. At this point, the slurry was dissolved in dichloromethane (DCM), washed with water and brine, dried over MgSO₄, and purified by flash chromatography (EtOAc:Hexane 1:2) with dry loading. The compound (1.91 g, 83%) was recovered as a white crystalline solid after drying under reduced pressure. R_f=0.6 (EtOAc:Hexane 1:1).

Synthesis of 7-di-((tert-butyl-carboxy)methyl)amino 4-hydroxymethylcoumarin (DCMAC-OH, 1c). 2 g (5 mmol) of DCMAC 1b were refluxed under nitrogen for 6h with 1.1 g (10 mmol) of selenium dioxide in 25 ml of *p*-xylene. Insoluble tars were removed by hot filtration, and the solvent was removed on a rotovap. The compound was resuspended in 40 ml of MeOH, and 190 mg (5 mmol) of NaBH₄ were added during stirring. After 30 min at RT, the pH of the mixture was balanced to 2 by addition of aqueous HCl 1M, and further diluted with water before extracting 4 times with DCM. The combined organic phases were washed with brine, dried over MgSO₄, and evaporated onto silica gel for purification by flash chromatography with

dry loading (EtOAc:Hexane 1:1). Upon drying, a dense dark yellow solid was obtained, which was resuspended in 10 ml of dimethyl formamide (DMF) and further purified by C18 preparative HPLC in a gradient from 40 to 100 % ACN in water with 0.1% TFA. After lyophilization, 1 g (48%) of the compound was obtained as a light off-white powder. Rf=0.2 (EtOAc:Hexane 1:1).

Synthesis of (7-di-((tert-butyl-carboxy)methyl)amino coumarin 4-yl)methyl (4-nitrophenyl) carbonate (DCMAC-NPC, 1d). 335 mg (0.8 mmol) of DCMAC-OH 1c and 0.3 ml (3.72 mmol) of pyridine were dissolved in 4 ml of dry DCM, and 153 mg (0.8 mmol) of 4-nitrophenyl chloroformate (NPC) predissolved in 2 ml of DCM were added dropwise to this solution while stirring. The activation was monitored by analytical HPLC (40 to 100% ACN in water, with 0.1% TFA), and additional NPC was added if needed. The reaction was completed in around 30 min. The reaction mixture was then dried under reduced pressure, and used in the next step without further purification, since the 4-nitrophenol 2 and pyridinium chloride byproducts do not interfere with the following reaction. Rf=0.6 (EtOAc:Hexane 1:1).

Synthesis of 7-di-((tert-butyl-carboxy)methyl)amino 4-bromomethylcoumarin (DCMAC-Br, 1e). Mesyl chloride (MsCl, 28 μ L, 0.36 mmol, 1.5 eq.) was added under an argon atmosphere to a solution of DCMAC-OH (1c, 100 mg, 0.24 mmol, 1 eq.) in 2 mL of dry DCM containing triethylamine (66 μ L, 0.48 mmol, 2 eq.) at 0 °C. After 30 min of stirring, TLC showed complete consumption of DCMACOH Rf=0.2, and conversion to DCMAC-OMs Rf=0.39 (EtOAc:Hexane, 1:1). The reaction mixture was washed three times with ice-cold 5% aqueous NaHCO₃ and water and dried over MgSO₄. Evaporation of DCM gave DCMAC-OMs, which was directly converted to DCMAC-Br by reacting with anhydrous LiBr (83 mg, 0.95 mmol, 4 eq.) in 2 mL of dry THF for 1 h. After removal of THF, the residue was picked up in 5 mL DCM, washed twice with brine, and finally dried over MgSO₄. The organic phase was concentrated to 2 mL, and 10 mL of hexane were added followed by incubation at 4 °C overnight. The precipitate was recovered by filtration, washed with 5 mL of ice-cold hexane, and dried under vacuum to yield DCMAC-Br (104 mg, 0.22 mmol, 90%) as a yellow solid. Rf=0.83 (THF:Hex, 1:2). [M+H]⁺ expected/found: 482.

Synthesis of (7-di-(carboxymethyl)amino coumarin 4-ylmethyl)(2-mercaptoethyl)thioether (DCMAC-EDT, 1f). DCMAC-Br (1e, 40 mg, 1eq) was dissolved in 1 ml of dry and degassed DMF and added dropwise into a solution of 1,2-ethanedithiol (EDT, 100 μ L, 20eq) in 2 ml of dry and degassed DMF in the presence of iPrNEt₃ (290 μ L, 20eq). The reaction was left to proceed under argon, and monitoring by analytical HPLC showed the reaction was complete after 2h. The product (tert-butyl protected DCMAC-EDT) was isolated by preparative HPLC and its identity was confirmed by LC-MS. MW [M+H]⁺ expected/found: 496. Tert-butyl deprotection was left to proceed for 20 min in the presence of TFA:thioanisole:anisole:TIPS:EDDT in proportions 87:5:2:3:3. TFA was evaporated under a nitrogen stream, and the product was purified by preparative HPLC. [M+H]⁺ expected/found: 384.

General procedures for peptide synthesis. Peptides were synthesized with classical Fmoc-protected solid-phase supported synthesis on rink-amide resin, using (1-Cyano-2-ethoxy-2-oxoethylideneaminoxy)dimethylamino-morpholino-carbenium hexafluorophosphate (COMU) as a coupling reagent in the presence of iPr₂NEt, and 20% piperidine in DMF for Fmoc deprotection. Peptides were dried under nitrogen flow in the reaction vessel, cleaved and deprotected by incubation for 2 h in of TFA:TIPS:EDDT:H₂O 90:2.5:2.5:5 (trifluoroacetic acid : triisopropyl silane : 2,2'-(Ethylenedioxy)diethanethiol : water) and precipitated in 10 volumes of ice cold Et₂O, collected by centrifugation, and washed with the same volume of ice cold Et₂O, before purification by preparative HPLC. The peptides were then lyophilized, resuspended in ultrapure water, neutralized (to pH 6.0 to avoid cysteine oxidation) with dilute NaOH, sterilized by filtration at 0.2 μm, aliquoted and lyophilized. Dry aliquots were stored at -20 °C or below.

Synthesis of DCMAC-SAG-SH. 0.2 mmol of SAG-SH with the sequence GGGGLERCL-NH₂, still bound to rink-amide resin and bearing standard side chain protecting groups (OtBu on glutamate, Pbf on Arginine, Trt on cysteine) and with its N-terminal Fmoc removed, was caged by introducing 0.8 mmol DCMAC-NPC (1d) dissolved in 4 ml of DMF:Pyridine 10:1 in the reaction vessel. The reaction was left to proceed overnight in the dark with shaking. The substitution was found to be quantitative at this point with analytical HPLC monitoring on microcleavages. After extensive washing of the resin supported caged peptide with DMF and DCM and nitrogen-flow drying, the peptide was cleaved, deprotected, washed, purified, neutralized, sterilized and stored as described above. The identity of the caged peptide was confirmed by MALDI-TOF. [M+H]⁺ expected/found: 1195.

Synthesis of DEAC derivatives (2a, 2b, 2c, 2d, DEAC-SAG-SH). 7-diethylamino 4-methylcoumarin (DEAC, 2a) was purchased from TCI Deutschland GmbH. The following derivatizations followed the same procedures as described for DCMAC derivatives, with comparable yields.

Synthesis of 6-bromo 7-hydroxy 4-chloromethyl coumarin (BHC-Cl, 4a). 2 g (10.6 mmol) of 4-bromoresorcinol were dissolved in 25 ml of methanesulfonic acid. 2.2 mL of ethyl 4-chloroacetoacetate (16 mmol) was added dropwise and the reaction was stirred for 2 h at RT. The mixture was then precipitated by dropwise addition into 500 mL of ice-cold water with vigorous stirring, and left standing on ice for 30 min. The precipitate was recovered by vacuum filtration, washed 5 times with 50 mL of cold water, and dried overnight at 50 °C under high vacuum, to yield 2.9 g of the product (94% yield), as an off-white solid.

Synthesis of 6-bromo 7-hydroxy 4-hydroxymethyl coumarin (BHC-OH, 4b). 1 g (3.5 mmol) of BHC-Cl (4a) was dissolved in 30 ml of DMF, and 15 ml of 1 M HCl were added. The mixture was refluxed at 95 °C under nitrogen for 24 h, and concentrated on a rotary evaporator at 65 °C under reduced pressure. The

residue was resuspended in ≈ 20 ml of DMF and purified by preparative HPLC to yield 0.63 g of the product as a white solid (67% yield).

Synthesis of (6-bromo 7-hydroxy coumarin 4-yl)methyl (4-nitrophenyl) carbonate (BHC-NPC, 4c).

63 mg (0.23 mmol) of BHC-OH (4b) and 55 mg (0.28 mmol) of NPC were reacted in 500 μ l of pyridine on ice with vigorous stirring. The reaction was monitored by analytical HPLC. The resulting solution of BHC-NPC was used directly in the following step.

Synthesis of BHC-SAG-SH. Freshly activated BHC-NPC (4c), ≈ 0.2 mmol in pyridine solution, was reacted with 0.05 mmol of solid-phase supported SAG-SH (after N-terminal Fmoc removal, sidechains still protected). The reaction was left to proceed overnight at RT with vigorous shaking. The peptide was then cleaved and purified as described above.

Synthesis of NPPOC-SAG-SH. 0.05 mmol of solid-phase supported SAG-SH (after N-terminal Fmoc removal) was reacted with 50 μ l (0.13 mmol) of 2-(2-Nitrophenyl)propyl chloroformate (NPPOC-Cl, 3) in the presence of 34 μ l (0.2 mmol) *i*Pr₂NEt in 4 ml of DMF. After 15 minutes, the reaction was found to be complete and the cleavage and purification were done as described above.

Synthesis of DCMAC-SAG-NHS. A DCMAC-SAG peptide of sequence DCMAC-GGGK-NH₂ was cleaved from Rink-amide resin and deprotected as described above. The peptide identity was confirmed by LC-MS: [M+H]⁺ expected = 649.46 found = 649.6. Then, 100 mg (0.15 mmol) of peptide in 5 ml of dry DMSO were added dropwise to 200 mg (0.78 mmol) of disuccinimidyl carbonate (DSC) in 4 ml of dry DMSO. Monitoring on analytical HPLC monitoring showed around 10-15% peptide substitution. After dropwise addition of 27 μ l (0.15 mmol) of *i*Pr₂NEt, monitoring showed around 80% peptide substitution, and an additional 27 μ l of *i*Pr₂NEt showed complete conversion. The product was purified by preparative HPLC on a gradient from 5 to 50% ACN in water+0.1% TFA in 25 min, to yield 82.5 mg (68%) of DCMAC-GGGK(N-hydroxysuccinimide carbamate)-NH₂ (DCMAC-SAGNHS), as confirmed by LC-MS: [M+H]⁺ expected/found = 790.7. The peptide was then lyophilized, resuspended in water, sterilized by filtration, re-lyophilized in small aliquots (1.6 mg, 0.2 μ mol), and stored at -20 °C.

Synthesis of DCMAC-SAG-TGQ. 20 mg (15 μ mol) of TG glutamine donor peptide (TGQ) with sequence NQEQVSPLERCG-NH₂ were reacted with 4 μ l (40 μ mol) of divinyl sulfone in 1 ml of TEOA buffer (triethanolamine 300 mM, pH 8.0). After 30 s, test with Ellman's reagent showed all the thiols were reacted and the reaction was stopped by freezing in liquid nitrogen. The vinyl sulfone- 4 peptide conjugate was purified by preparative HPLC. The collected fractions were lyophilized, and resuspended in TEOA buffer for further reaction with 2.5 mg of DCMAC-SAG-SH (2 μ mol). The reaction appeared to be complete after 15 min with analytical HPLC monitoring, and the conjugate (as well as unreacted excess TGQ for recycling)

was HPLC-purified, lyophilized, resuspended in water, neutralized, sterilized by filtration, aliquoted, re-lyophilized, and stored at -20 °C. Conjugation of the DCMAC-SAG-TGQ peptides at 400 μ M to 0.83% hyaluronan bearing the other TG ligand (TGK, sequence Ac-FKGGGERCG-NH₂) in the presence of 20 U/ml TG (Fibrogammin, CSL Behring) was studied by GPC, and the conjugation was found to happen swiftly, with a time constant of 2.4 to 2.6 min but until a limit of approximately 50% coupling. Further attempts to form a gel from these pre-reacted DCMAC-SAG-TGQ and hyaluronan did not work, showing that the limit is due to quick loss of enzymatic activity of TG in the presence of its substrate peptides. As a result, DCMAC-SAG-TGQ peptides were not pre-reacted but rather added to the other gel precursors and coupled to the polymer backbone simultaneously with gelation.

Synthesis of DCMAC-TGK-SH. The peptide Ac-FK(DCMAC)GGGERCG-NH₂ (DCMAC-TGK-SH) was synthesized as a proof-of-concept of caging on arbitrary amino groups other than the N-terminus of the peptide. We synthesized with standard methods the peptide Ac-FKGGGERCG-NH₂ using a lysine with a hydrazine-sensitive orthogonally-protected side chain, Fmoc-Lys(Ddiv)-OH. The other protecting groups were standard acid-labile groups, i.e. fmoc-Glu(tBu)-OH, Fmoc-Cys(Trt)-OH, Fmoc-Arg(Tbf)-OH. The resin-supported protected-peptide, Ac-FK(Ddiv)GGE(tBu)R(Tbf)C(Trt)G- (Rink Amide), was then treated with 2% hydrazine in DMF until complete Ddiv removal, exposing the side chain amino group of the lysine residue. DCMAC-NPC coupling and peptide cleavage and deprotection were then performed as described above, and the identity of DCMAC-TGK-SH was confirmed by MALDI-TOF: [M+H⁺] expected/found = 1185. Of note, when acetylation of the Nterminus is unwanted, terminal fmoc should still be removed and replaced by a TFA-labile tertbutyloxycarbonyl (BOC) protecting group before Ddiv deprotection and cage conjugation, as carbamate linked two-photon active cages do not withstand piperidine:DMF treatment used for fmoc removal.

Synthesis of alginate-vinyl sulfone. 1.17 g (6 mmol) of MES were dissolved in 40 ml of water, followed by 400 mg (2 mmol of the repeat unit) of high molecular weight sodium alginate (Sigma A7128), dissolved overnight with gentle rocking. The pH of the resulting solution was 4.5. We then added 11.9 mg (0.05 mmol) of 3,3'-dithiobis(propanoic dihydrazide) (DTPHY, Frontier scientific), and 19.2 mg of (0.1 mmol) of EDC (Fluka) predissolved in 1 ml of water and added dropwise over vigorous stirring. Stirring was then stopped, and the reaction was left to proceed overnight. The disulfides were then reduced with 57.3 mg (0.2 mmol) of tricarboxyethyl phosphine hydrochloride (TCEP, Fluorochem), predissolved in 1 ml of water and added dropwise while swirling the flask. The reduction was left to proceed overnight in the sealed standing flask at RT. The resulting thiolated alginate solution was supplemented with 2 g of NaCl, and dialyzed against ultrapure water balanced to pH 4.5 by addition of HCl. After 24 h, the solution was recovered and added dropwise over stirring to 0.5 ml (10 mmol) of divinyl sulfone in 10 ml of TEOA. Special care was taken as divinyl sulfone is fatal in contact with skin. After 3 h of reaction at RT, the solution was supplemented with

4 g NaCl and dialyzed against ultrapure water. After completion, the alginate-vinyl sulfone sodium salt solution was sterilized by filtration, aliquoted, lyophilized, and stored at -20 °C. The structure of the vinyl sulfonated polymer was confirmed by NMR, and the substitution ratio was measured with a modified version of the Ellman's assay. A 10 mg/ml alginate resuspended stock in TEOA buffer was reacted in equal proportions with a 3 mM β -mercaptoethanol solution in the same buffer. A control without alginatevinyl sulfone was included in parallel. The Michael addition was left to proceed for 5 h at RT, and the remaining thiols were quantified with a classical Ellman's assay. We found 1.6 mM of thiols in this 10 mg/ml stock, which corresponds to 3.2% substitution.

Synthesis of TG cross-linkable hyaluronan. The synthesis was done as described previously.^{98,104}

Synthesis of 2-((2-(vinylsulfonyl)ethyl)thio)acetic acid (VS-COOH, 5a). 50 μ l (0.7 mmol) of thioglycolic acid, 140 μ l (1.4 mmol) of divinyl sulfone, and 7 μ l (0.05 mmol) of DBU were reacted in 1 ml DMF for 30 min on ice. The reaction mixture was then diluted to 10 ml with 30 mM aqueous HCl, and purified by HPLC (5% ACN for 10 min, 5 to 90 over 20 min), followed by lyophilization, to get the product in quantitative yield (114 mg) as a white crystalline solid.

Synthesis of 2,5-dioxopyrrolidin-1-yl 2-((2-(vinylsulfonyl)ethyl)thio)acetate (VS-NHS, 5b). 160 mg (0.76 mmol) of VS-COOH were dissolved in 8 ml of DCM, and reacted with 180 μ l (1.14 mmol) of DIC and 132 mg (1.14 mmol) of NHS for 10 min at RT. Monitoring on thin layer chromatography (TLC) in EtOAc with KMnO₄ staining showed the reaction was complete ($R_f = 0.64$). The product was purified by flash chromatography in EtOAc, and the solvent was removed under reduced pressure, to get 191 mg (82% yield) of product as a white crystalline solid.

Synthesis of DCMAC-SAG-fibrinogen. 40 mg of bovine fibrinogen powder (Sigma F86030), which include 30 mg (88.2 μ mol) of actual protein, were dissolved in 1 ml of PBS (Gibco, calcium and magnesium free, pH7.4). 154 μ g (500 nmol) of VS-NHS were then taken as 3.08 μ l of a 5% stock in DMSO, prediluted in 100 μ l of PBS, and the fibrinogen solution was added to the VS-NHS solution and mixed swiftly. The mixture was let to react for 20 min before adding 770 μ g (650 nmol) of DCMAC-SAG-SH, pre-dissolved in 200 μ l of TEOA buffer. As peptides typically contain some salts, the exact peptide molarity was measured by Ellman's assay rather than only on a microbalance. The reaction was left to proceed for 2h at 37°C, sterilized by filtration, and the modified fibrinogen was then precipitated by adding 2 volumes of sterile brine, and recovered by centrifugation at 2000 g for 2 min. After further washing with brine:water 1:1, the pellet was resuspended in 1.5 ml of sterile PBS (keeping the suspension at 37 °C until it clarifies), and the protein and cage concentrations were measured on a spectrophotometer, using calibration curves for the absorbance at 280 nm of fibrinogen solutions, and for the fluorescence at 400/470 nm of DCMAC-SAG-SH. The final

stocks were found to have 15 mg/ml of fibrinogen (75% recovery) with 187 μ M of DCMAC-SAG substitution (4.2 caged peptides/protein, 75% efficiency in the substitution reaction).

Synthesis of Avidin-SAT-F. 300 μ g (4.41 nmol) of Avidin (Thermo) stored frozen in 150 μ l of water were melted and reacted with 16.2 μ g (53 nmol) of VS-NHS (the 5% VS-NHS stock in DMSO was prediluted 100-fold in PBS, and 32.4 μ l of this solution were added) and 21 μ g (45 nmol) of fluorescein-NHS (Thermo, from a 1% fluorescein-NHS stock in DMSO stored frozen, prediluted 50 fold in PBS before addition of 105 μ l). The reaction was left to proceed for 30 min at RT, before adding 650 μ g (462 nmol) of a SA threonine-containing substrate peptide (SAT) with the sequence AcGCREDDDLPMTGG-NH₂, pre-dissolved in 100 μ l of TEOA buffer (300 mM, pH 8.0). The reaction was left to proceed further for 1 h at 37 °C, and the Avidin-SAT-F was purified by GPC using Tris 50 mM + NaCl 300 mM balanced to pH 7.5 as the running phase. The collected fractions were diluted two-fold with ultrapure water to balance the osmolarity, sterilized by filtration, and re-concentrated with vivaspin protein concentrators (GE Healthcare, 10 000 MWCO) to recover 500 μ l of stock at 0.4 μ g/ μ l of protein content (approx. 60% protein recovery), with 6 SAT peptides/avidin tetramer (as quantified on MALDI-TOF, Fig. S8.5). This stock was stored frozen in small aliquots until use.

Synthesis of NGF-PEG-Biotin. 80 μ g of NGF in water solution at 1 μ g/ μ l was reacted with 1.2 equivalents (over the dimer) of NHS-PEG12-Biotin (Thermo), pre-dissolved in 32 μ l of PBS. The reaction appeared complete after 2 h according to HPLC monitoring, and the stock was aliquoted and frozen without further purification. The substitution ratio (60% of the monomers, 1.2 Biotin per dimer) was measured on HPLC and confirmed by MALDI-TOF mass spectroscopy.

BSA-rhodamine. 10 mg of bovine serum albumin (BSA) in 500 μ l of carbonate buffer, 100 mM, pH 9.5 were reacted with 20 μ l of a DMSO stock of 10 mg/ml rhodamine-isothiocyanate (RITC). The protein was purified by GPC and re-concentrated with a Vivaspin protein concentrator, 10 000 MWCO. The 5 mg/ml resulting stock was stored at -20°C.

Alginate gels with caged peptides. Vinyl sulfonated alginate and unmodified alginate, 1% stocks in TEOA buffer (300 mM, pH 8.0), were combined in order to have a 1% alginate stock with 500 μ M vinyl sulfone handles. This stock was further reacted by Michael addition with NPPOC-SAG-SH, BHC-SAG-SH, DEAC-SAG-SH, and DCMAC-SAG-SH, with the peptides added at 1 mM from dry powder and reacted overnight. To form gels for bulk non-specific adsorption measurements, 10 μ l drops of these 1% functionalized alginate stocks (or non-functionalized control alginate, or mixtures of these to achieve lower molarities of functional groups) were deposited on top of 100 μ l of CaCl₂ solution in each well of a 96 well plate. The gels were further washed twice one hour with the CaCl₂ solution in order to remove unbound peptide. For two-photon patterning experiments, 1% alginate stocks with 100 μ M of caged peptides were cast into

polydimethylsiloxane (PDMS) cylindrical molds of 500 μm height and 3 mm inner diameter adhered to glass-bottom microscopy chambers, and precoated with poly-L-lysine (PLL, 1 mg/ml inserted in the PDMS mold for 10 min followed by washing with ultrapure water and drying). A cellulose filter membrane pre-wetted with 100 mM CaCl_2 was then deposited on the top surface, and an additional 100 μl of 100 mM CaCl_2 added on top. Gelation was left to proceed for 1 h, before covering the gels with a 1:1 mixture of 100 mM CaCl_2 and Tris buffered saline (TBS, Tris 50 mM, NaCl 150 mM, pH7.5) until photopatterning.

BSA adsorption study. Functionalized alginate gels were incubated for 1 h in 1 mg/ml BSA-rhodamine solution (mixing the protein stock and CaCl_2 solutions 1:4). They were then washed with a 1:1 mixture of TBS and CaCl_2 100 mM, for 48 h in total with frequent buffer changes. Finally, the fluorescence of the gels was measured on a plate reader (excitation 555 nm emission 590 nm). A calibration curve from serial dilutions of BSA-rhodamine in the same buffer was also constructed in order to convert the fluorescence values to adsorbed protein concentrations. Control gels with the various caged peptides or no functionalization were also measured, without incubation with the fluorescent rhodamine, and found to have no fluorescence at these wavelengths that would compromise the assay.

Photo-patternable collagen gels. An aliquot of DCMAC-SAG-NHS (1.6 mg, 0.2 μmol) was resuspended in 20 μl of dry DMSO to form a 1 mM stock. Patternable collagen was formed by mixing 50 μl of ice-cold collagen acidic stock (AteloCell, bovine dermis collagen, 5 mg/ml), 1 μl of DCMACSAG-NHS DMSO stock, and 20 μl of 5% w/v NaHCO_3 for neutralization and balancing of osmotic/ionic strength. The mixture was mixed vigorously while still standing on ice, and cast into PDMS molds. Gelation was left to proceed for 10-20 min at 37 $^\circ\text{C}$, 5% CO_2 . The gels were then covered with TBS to wash unbound peptides and avoid drying during the following photopatterning process. Fluorescence measurements on a plate reader against a calibration curve from serial dilutions of DCMAC-SAG were used to determine the substitution of collagen gels, and the final bound peptide concentration was found to be of $\approx 145 \mu\text{M}$.

Photo-patternable basement membrane extract (Matrigel). An aliquot of DCMAC-SAG-NHS (1.6 mg, 0.2 μmol) was resuspended in 1 ml of sterile water, neutralized with dilute NaOH using a small amount of phenol red as a pH indicator, and sub-aliquoted in portions of 0.16 mg (0.02 μmol), snap-frozen in liquid nitrogen, and re-lyophilized for storage at -20 $^\circ\text{C}$. 0.02 μmol aliquots were then individually resuspended in 80 μl of ice-cold Matrigel (Corning, 9 mg/ml in Dulbecco's modified Eagle's medium), and cast in PDMS molds. After 15 min of gelation at 37 $^\circ\text{C}$, the gels were washed with PBS (incl. calcium), and used for two-photon patterning as described below. Quantification of DCMAC-SAG 7 coupling was performed using full gel fluorescence readings on a plate reader (gels washed overnight were loaded between the windows of a 1 mm pathlength Take3 plate) against a calibration curve from serial dilutions of peptide as described above, and we found that the gels were substituted with 200 μM of caged peptides.

Photo-patternable Hyaluronan gels. The gelling mixture consisted of DCMAC-SAG-TGQ at 200 μ M, TG cross-linkable hyaluronan at 0.75% w/v and activated factor XIII (TG, Fibrogammin from CSL Behring) at 20 U/ml, in a buffer consisting of 100 mM glucose, 50 mM Tris, 50 mM CaCl₂, pH 7.5. Gelation followed within 1 minute, and the gels were then covered with TBS after 10-15 min and until patterning.

Photo-patternable fibrin gels. DCMAC-SAG-fibrinogen and thrombin (Tisseel, Baxter) stocks were combined in TBS + 1 mM CaCl₂ for final concentrations of fibrin 3 mg/ml and thrombin 0.5 U/ml. Gelation was left to proceed for 15 min at 37 °C, and the gels were then covered with TBS.

DRG isolation and embedding (for two-step patterning, Fig. 8.6a-e). Dorsal root ganglia (DRGs) were isolated from E9-10 chick embryo, and collected in PBS on ice. Immediately before preparing the gels, they were washed in a 0.75% solution functionalized TG-cross-linkable hyaluronan, to avoid the formation of a thin buffer layer between the DRGs and their matrix. Number 5 forceps (FST) were used to transport DRGs, coated with albumin (by dipping in a 5% solution in PBS) to avoid DRG attachment. Gels were casted as described above, and one DRG placed in the center of each gel before gelation occurs. The DRGs were then cultured at 37 °C, 5%CO₂, in neurobasal medium with B27, glutamax and penicilin/streptomycin. Medium was added immediately after gel formation and when applicable twophoton patterning, and changed twice during the first 24 h to remove uncoupled protein. Half of the medium was then renewed once a week.

Two-photon patterning (2PP, Fig. 8.3a, 4b, 5e-h). The glass-bottom chambers with gels formed with one of the five materials listed above were loaded on a Leica SP8 multiphoton microscope equipped with a spectra physics Mai Tai laser, 25x water immersion objective and LASX software, or a Leica SP5 multiphoton microscope equipped with a Coherent Chameleon laser, LAS-AF software and 20x water immersion objective. The laser intensity and scan number were varied as indicated in each figure legend. The step in the z direction was kept constant at 1 μ m, and the pixel size in the xy plane at 0.5 μ m. These dimensions approximately fit the size of the point spread function and ensure the formation of continuous patterns. The scanning speed was kept constant at 600 Hz. In order to pattern complex shapes or shades, we programmed custom Matlab scripts which take standard .tif pixel data or .stl 3D mesh data, and generate instructions matching the format of the Leica live data mode instructions. The 3D rose model used as a test file was created in Blender, exported as a binary .stl file, and re-exported as an ASCII .stl file using Meshlab. The scripts use a live data mode file exported from the microscope as a template for the formatting and an input for the microscope parameters (detector gains, lasers, filter positions etc). 3D structures (from .stl) are made layer by layer, using the region of interest (ROI) scanning possibility of the microscopes, which physically consists in fast light switching on and off by an electro-optical modulator (EOM). For shades of greyscale patterns, the EOM/ROIs are used as well, and we sequentially scan a series of ROIs (grey level masks) at increasing laser intensity. Calibration curves of pattern intensity vs uncaging power were taken into account

in order to produce a linear relation between the reference grey level and the final patterned avidin concentration. Of note, the Matlab library is separated into functions to import data, slice 3D shapes to generate layer by layer vectorial contours, or decompose greyscale images in intensity masks corresponding to a calibration curve of pattern intensity vs laser power, as well as visualize the shapes/gradients and their 8 processed decompositions, scale the forms to physical units, and generate a series of ready-to-pattern masks associated with z-coordinates and laser powers. These functions would be of general applicability. The last function is the only one that needs a Leica-specific template, to then reformat the mask data to fit the .xml nomenclature specific to Leica microscopes. This last function would need to be re-written specifically for each other currently non-compatible system. The main prerequisite to port the code to a new system is that the microscope should have a programmable EOM. Immediately after photopatterning, the buffer covering the gels was removed and the gels were covered with an incubation solution consisting of 0.7 $\mu\text{g}/\mu\text{l}$ avidin-SAT-F stock (80%), biotinylated NGF stock (5%), SA 80 μM stock (5%) and 100 mM CaCl_2 stock (10%). The coupling to the uncaged areas was left to proceed for 30-40 min, and the gels were then transferred to cell culture medium (with cells) or TBS.

One-step 2PP (Fig. S8.4c, 5a-d, 6f-k). One-step patterning was demonstrated in the hyaluronan and fibrin gels. The process is the same as for the two-step patterning, except that all the components normally added in the incubation solution are directly mixed with the gel precursors. The stocks combined for hyaluronan gels are: TG cross-linkable hyaluronan 3%, DCMAC-SAG-TGQ 4 mM, Avidin-SAT-F 0.4 $\mu\text{g}/\mu\text{l}$ + NGF-biotin 35 ng/ μl , SA 80 μM , and activated TG 200 U/ml. The percentage of these stocks in the mix are respectively: 25:10:50:5:10. The TG was added last to trigger the gelation. Freshly isolated DRGs were encapsulated within 30 s after gel casting when applicable. The stocks combined for fibrin gels were: DCMAC-SAG-fibrinogen 10 mg/ml, SA 80 μM , avidinSAT-F 0.4 $\mu\text{g}/\mu\text{l}$ + NGF-biotin 35 ng/ μl , thrombin 10 U/ml, and CaCl_2 100 mM, in proportions of 30:5:50:5:10. Thrombin was added last to trigger the gelation. Gelation occurred within minutes, and the gels were then immediately photo-patterned as described above, and then transferred to TBS (without cells) or cell culture medium (with cells).

Temporal control of functionalization and patterning (Fig. S8.9). E10 chick DRGs were isolated and encapsulated in non-functionalized TG cross-linked hyaluronan hydrogels as described above, and precultured for 24h in medium supplemented with soluble NGF 200 ng/ml. The culture chamber was then transferred on ice, washed for 20 min with ice-cold PBS (Gibco, pH7.4), and functionalized by incubating for 30 min in a 1 mM solution of DCMAC-SAG-NHS in PBS. The supernatant was then removed and the reaction stopped by addition of TBS + Glucose 10 mM, while the cultures were taken for 2PP of avidin-SAT-F + NGF with the two-step protocol described above. The growth into the patterns was monitored for 3 days, and a second round of 2PP was performed. The cultures were then monitored for an additional 6 days while they further invade the extended patterns.

Immunocytochemistry. Hydrogels were fixed for 1 h in ice-cold 4% formaldehyde solution in PBS, washed with PBS for at least 1 h, blocked with 5% bovine serum albumin (BSA) in PBS overnight, incubated with primary antibody for (Tuj1, Sigma T5076, 1:500 in PBS+3% BSA), washed with PBS 2 x 1h and 1x overnight, incubated with secondary antibody (goat anti-mouse Alexa 594, Thermo, 1:400 in PBS+3%BSA), washed with PBS 2x1h and 1x overnight, and stained with DAPI and phalloidin-tetramethylrhodamine (thermo) for 2 h, then washed with PBS and transferred on a coverslip for imaging with confocal/two-photon Leica SP8 microscopes with 20x or 25x water objectives.

Study of photodamage onto collagen gels (Fig. S8.6). Native rat tail collagen (Gibco, ~5 mg/ml) was neutralized by addition on ice of TEOA buffer pH8.0 in the presence of phenol red as a pH indicator, and quickly casted into 4 mm diameter PDMS molds adhered to glass-bottom chamber. The gelation was left to proceed for 15 min at 37 °C. The gels were then covered with 2 ml of PBS, and used to study photodamage with the various Mai Tai Ti:Sapphire fs-laser exposure conditions described in the figure legend.

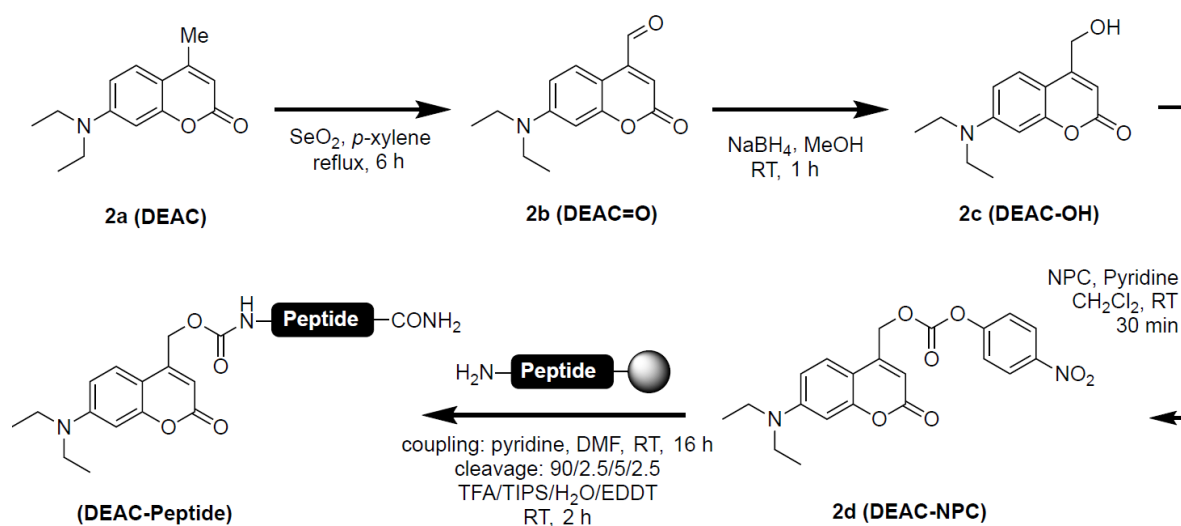


Figure S8.1 | Synthesis of 7-diethylaminocoumarin (DEAC) caged peptides.

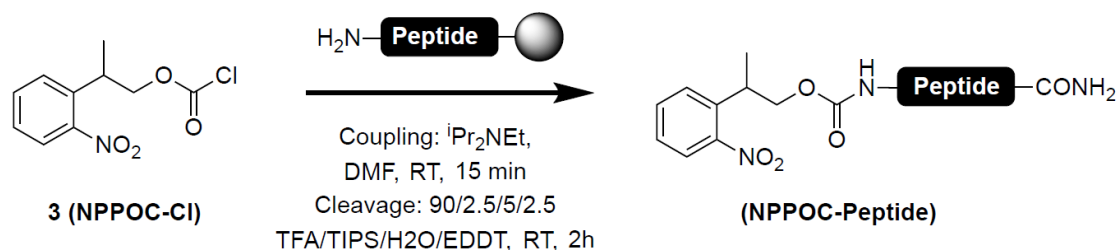


Figure S8.2 | Synthesis of 2-(2-Nitrophenyl)propyl carbamate (NPPOC) caged peptides.

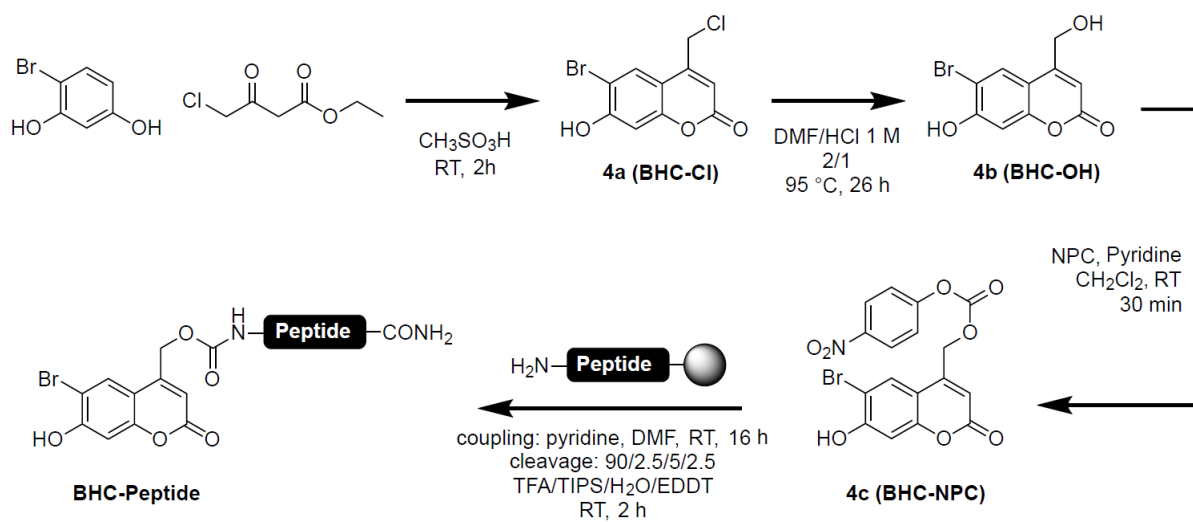
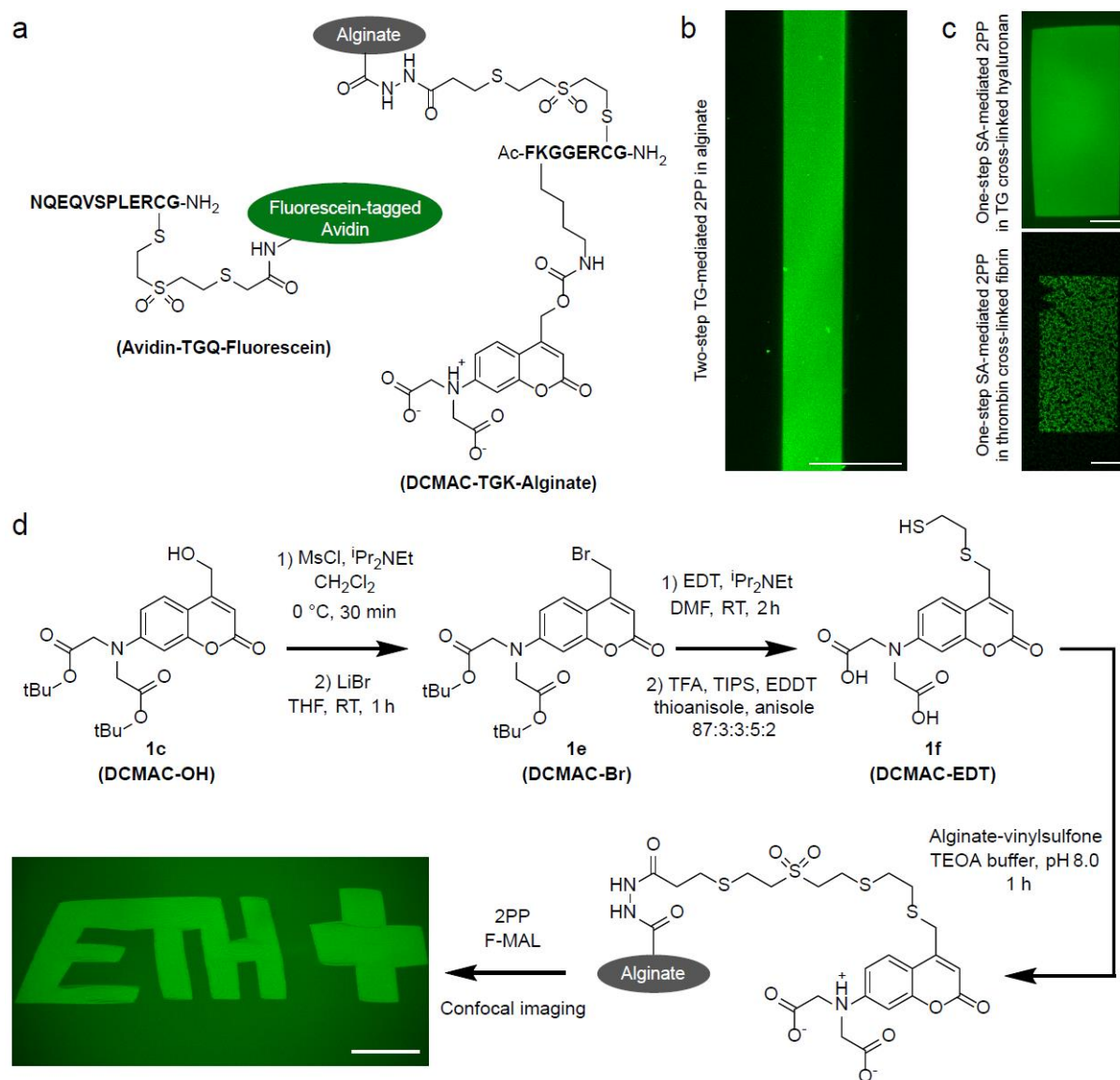


Figure S8.3 | Synthesis of 2-(2-Nitrophenyl)propyl carbamate (NPPOC) caged peptides.



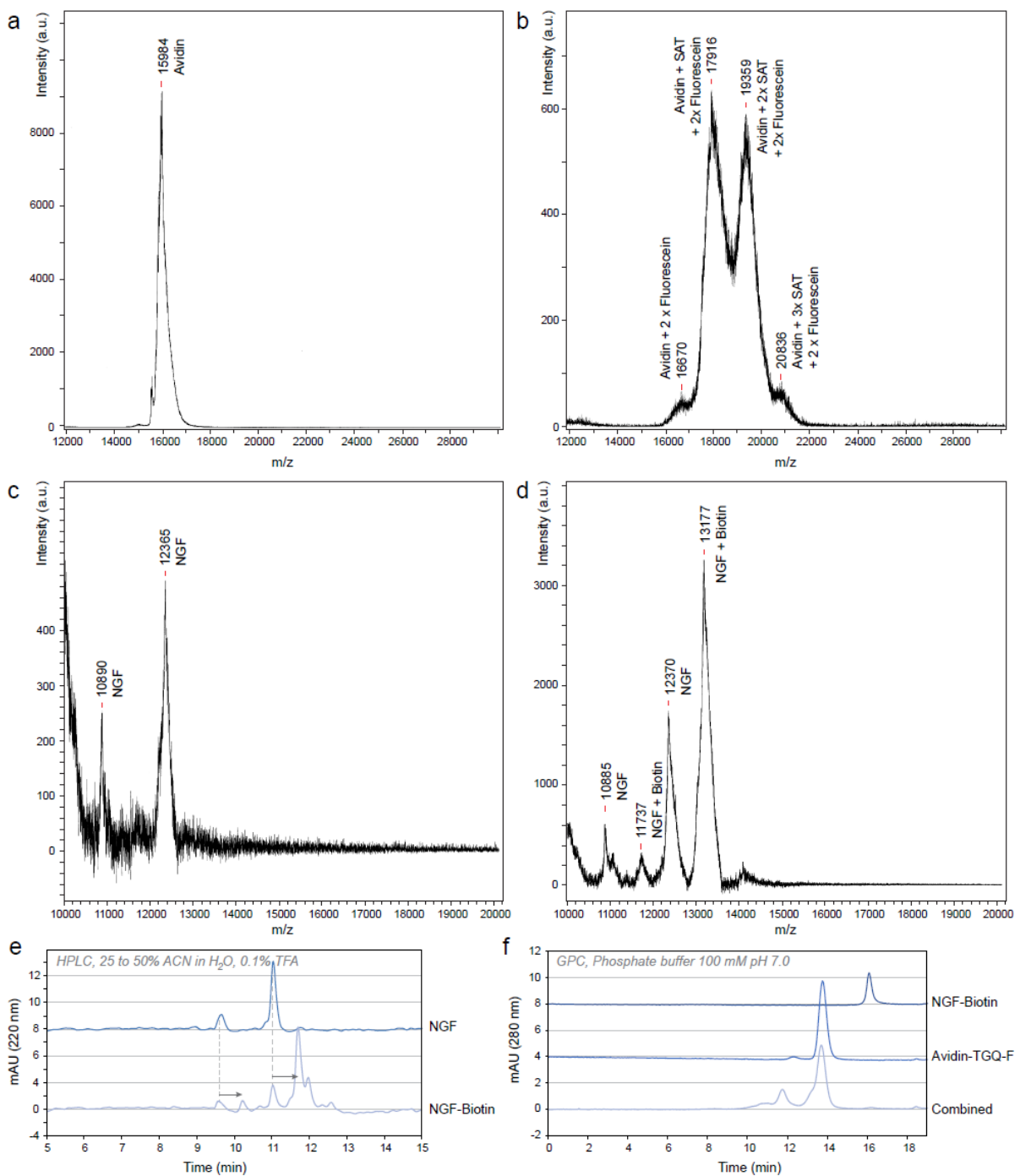


Figure S8.5 | Characterization of SAT and fluorescein-substituted avidin (Avidin-SAT-F) and biotinylated NGF (NGF-Biotin). (a,b) Matrix-assisted laser desorption and ionization time-of-flight mass spectroscopy (MALDI-TOF) of avidin and SAT-substituted avidin, showing approximately 1.5 substitutions on average per monomer, i.e. 6 substitutions per avidin tetramer. (c,d) MALDI-TOF of NGF-Biotin, showing approximately two thirds of the NGF monomer bear a biotin (with PEG spacer), i.e. ≈ 1.3 per NGF dimer. (e) Confirmation of the substitution of NGF with biotin on C18 analytical HPLC. (f) Confirmation of NGF-Biotin binding to modified avidin by gel permeation chromatography (GPC).

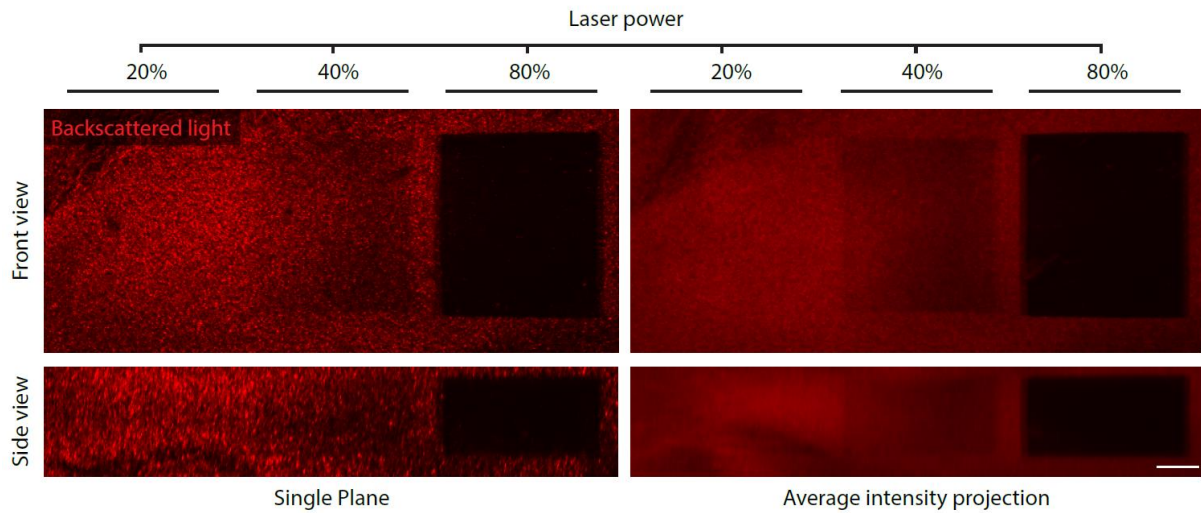


Figure S8.6 | Study of photodamage onto collagen gels. A laser power typically used for 2PP (20%) does not alter the hydrogel structure, whereas a power that would result in decreased pattern intensity (40%) does slight damage to the hydrogel, and higher power (80%) results in complete ablation. Backscattered light imaging on a Leica SP8 laser scanning confocal microscope after a single exposure to a Mai Tai fs-laser at 600 Hz line rate, 0.5 μm line/layer spacing, using a 25x water immersion objective and various laser powers as indicated. Scale bar: 25 μm .

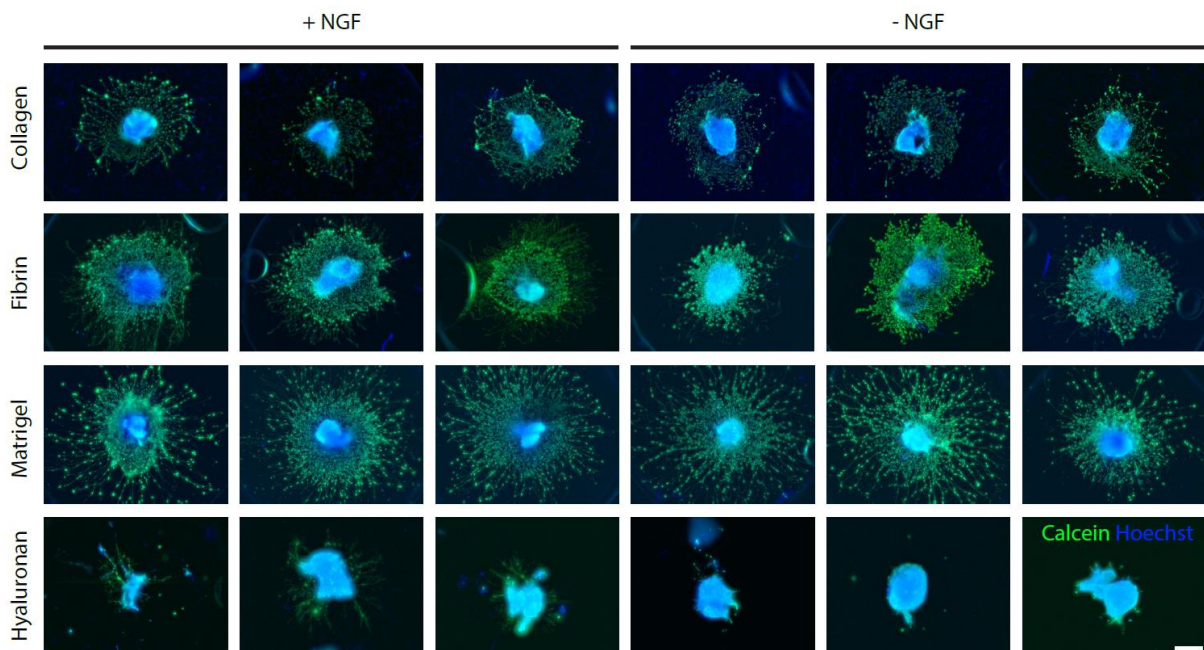


Figure S8.7 | Comparison of invasion by chick E9 DRGs axons and glia after 4 days in culture in various biological matrices, in the presence or absence of NGF at 200 ng/ml. Maximum intensity projection of widefield fluorescence images of calcein-AM (live cells and processes) and Hoechst (nuclei), with background subtracted and gamma adjusted to 0.3 to facilitate axon visualization. Scale bar: 500 μm .

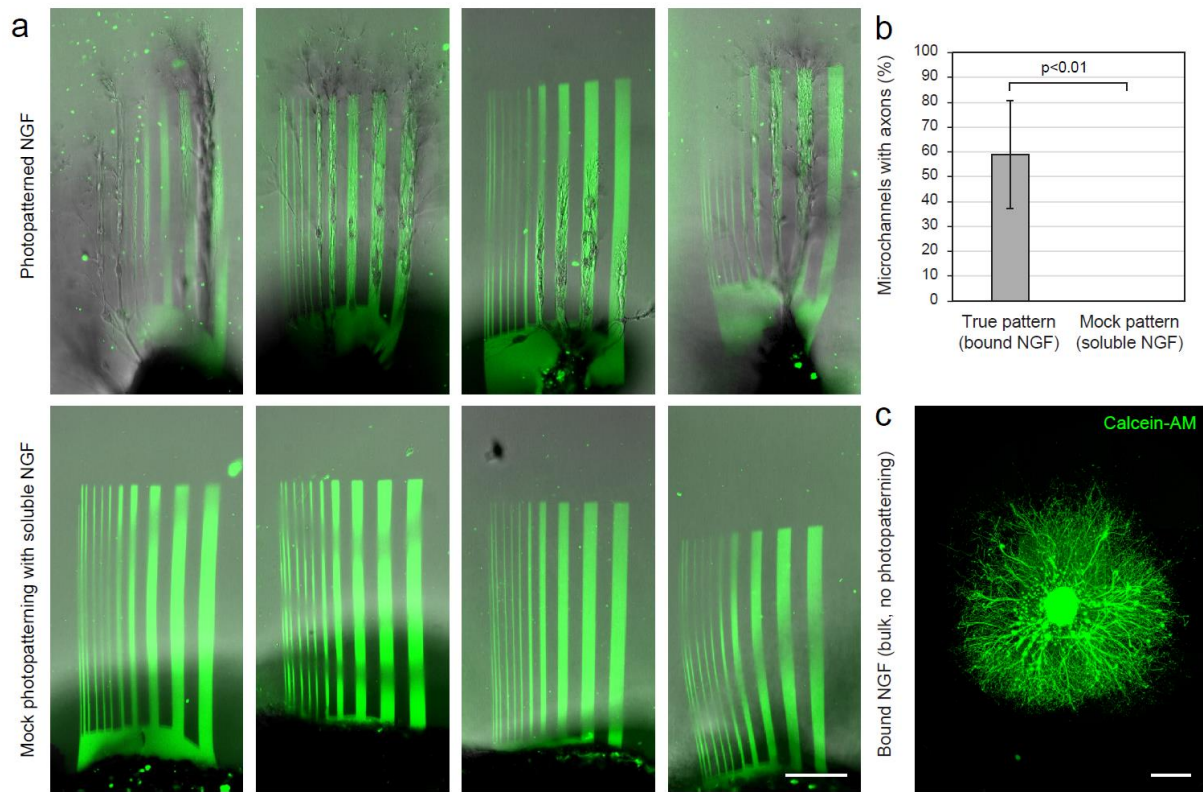


Figure S8.8 | The axonal growth and guidance in hyaluronan hydrogels are specifically mediated by immobilized NGF. (a-b) Comparison of the axon extension in standard 2PP experiments vs experiments replacing NGF-Biotin by soluble (non-biotinylated) NGF. Each image is from a replication on a different DRG, after 2 days in culture. Scale bar: 100 μm (c) Axonal growth from a chick E9 DRG in a hydrogel with NGF anchored in bulk (i.e. forming the hydrogel in the presence of avidin-TGQ, which is described in figure S8.1, and NGF-Biotin). Scale bar: 500 μm .

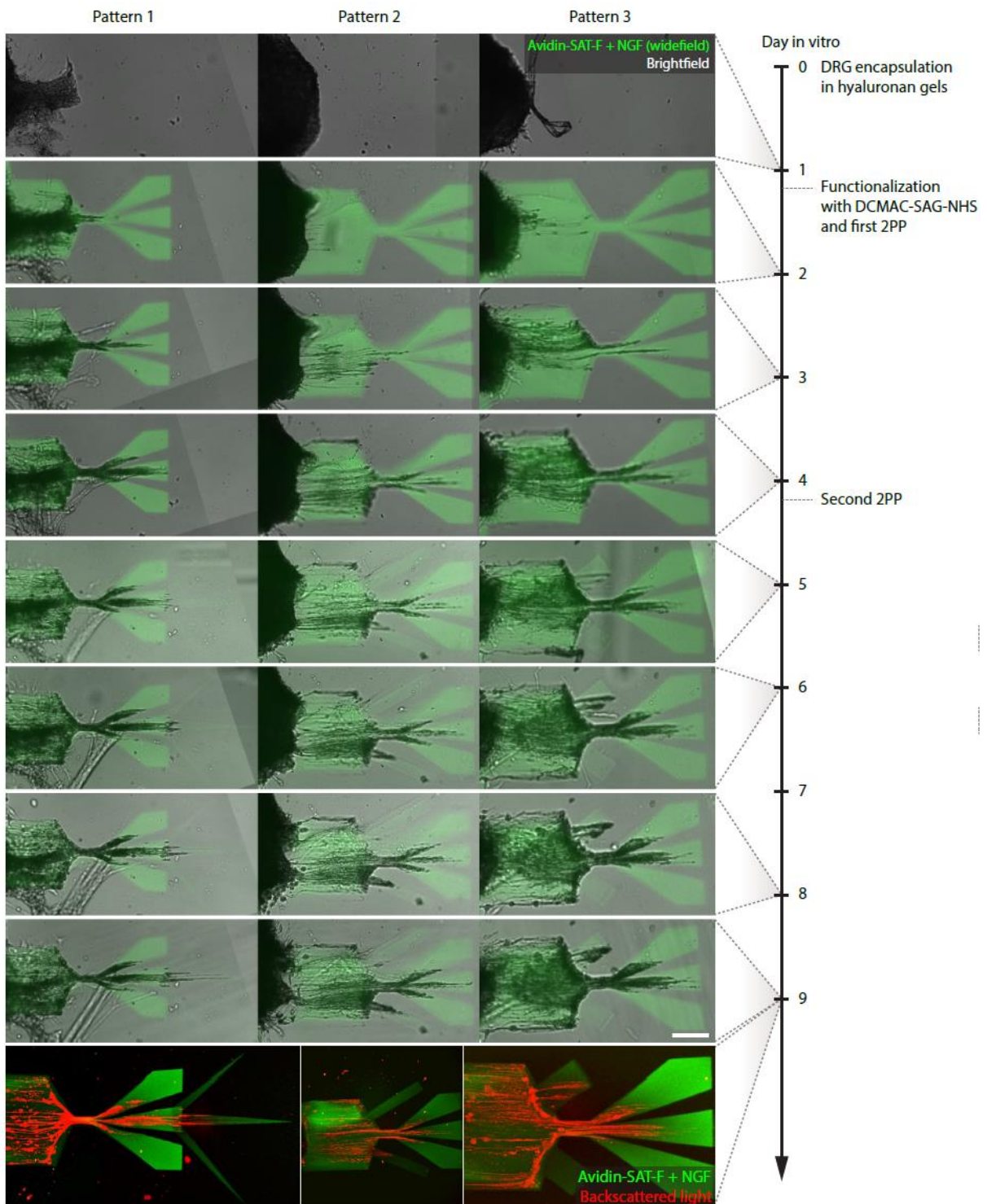


Figure S8.9 | Time control of the growth factor presentation and guidance. Live imaging was done on a Zeiss Observer with a 5x objective (widefield - brightfield, raw single focal plane pictures). Scale bar: 100 μm

For NMR spectra: <https://doi.org/10.1002/adma.201908299>

CHAPTER 9

Enzymatically Crosslinkable Chitosan Adhesive

In this Chapter a novel enzymatically crosslinkable chitosan derivative is presented. The biocompatible and clinically compliant enzymatic crosslinking of fibrin glue is herein applied for the first time to chitosan, thus generating an in situ crosslinkable cationic formulation with intrinsic antibacterial and electrostatic binding properties.

MANUSCRIPT

Factor XIII Cross-Linked Adhesive Chitosan Hydrogels

Ingrid Berg†, Riccardo Rizzo†, Mihyun Lee†, Qun Ren, Nicolas Brogiere, Marcy Zenobi-Wong

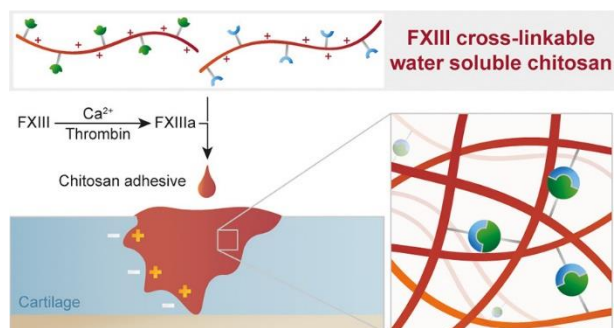
ACS Biomaterials Science & Engineering **2021**, 7, 6, 2198–2203

DOI: 10.1021/acsbiomaterials.1c00298

†Equal contribution.

Reprinted with permission from ACS Biomater. Sci. Eng. 2021, 7, 6, 2198–2203, Copyright © 2021, American Chemical Society

Abstract



Biomedical adhesives have been found to be an attractive alternative to suturing in several circumstances. However, to date most of the clinically approved formulations are based on synthetic and highly reactive toxic chemicals. In this work, we aimed to combine for the first time the bioactive properties of the cationic polysaccharide chitosan and its intrinsic electrostatic binding to negatively charged tissues with the biocompatible and clinically compliant enzymatic cross-linking scheme of fibrin glue. This synergistic activity led to the generation of a transglutaminase Factor XIII cross-linkable chitosan formulation with fast gelation kinetics, tunable mechanical properties, antibacterial activity, and strong adhesion to cartilage.

9.1. Main Text

In past decades tissue adhesives have increasingly gained attention as an alternative to suturing, in particular in those circumstances where suturing is impractical or ineffective.⁹⁹¹ Tissue adhesives mainly include synthetic or naturally derived liquid formulations that undergo cross-linking upon delivery to the damage site. Most biomedical adhesives are cyanoacrylate-, urethane-, formaldehyde-, and glutaraldehyde-based, which exhibit rapid cross-linking rates, as well as fast and strong adhesion to tissues. However, the nonspecific reactions of chemical glues, which can cause irritation, and the concerns about toxicity and carcinogenicity of the degradation products (*i.e.*, cyanoacetates and formaldehyde) represent major drawbacks.⁹⁹² This has motivated the development of safe and biocompatible bioadhesion strategies. Enzymatic reactions emerged as a promising solution because of their fast kinetics, high substrate selectivity, physiological reaction conditions (pH, temperature, and aqueous environment), and no need for toxic chemicals. Fibrin glue is a commercially available adhesive based on enzymatic cross-linking and one of the most widely used in clinics.⁹⁹³ Its cross-linking strategy is based on the activity of transglutaminase Factor XIII (FXIII) and thrombin, which in the presence of fibrinogen replicates the last stage of the blood coagulation cascade. Despite the several advantages of this formulation, concentrated human fibrinogen is pulled from donated blood, which makes it relatively expensive and subject to the risk of transferring blood-borne diseases.⁹⁹² In this context, polysaccharides have emerged as a highly attractive alternative because of their high abundance, safety, intrinsic bioactive effects, tunable mechanical and chemical properties, and ability to mimic the native extracellular matrix (ECM), thus promoting tissue regeneration.

Chitin, the most abundant natural biopolymer in the marine ecosystem and the second most abundant on Earth after cellulose, represents a valuable source of materials for various applications, including drug and gene delivery,⁹⁹⁴ tissue engineering,⁹⁹⁵⁻⁹⁹⁷ and modern biomimetics.⁹⁹⁸⁻⁹⁹⁹ Mainly found in fungi, diatoms, sponges, mollusks, and arthropods, chitin in its native form appears as a linear homopolymer of $\beta(1,4)$ -linked *N*-acetyl-d-glucosamine.¹⁰⁰⁰⁻¹⁰⁰¹ The tight parallel or antiparallel arrangement of the linear polysaccharide chains results in a crystalline form with poor water solubility. Its partially deacetylated derivative, chitosan, shows instead water solubility in acidic conditions (pH < 6) due to glucosamine amino group protonation, while retaining insolubility in aqueous solutions at neutral or basic pH. Despite this limited water solubility, chitosan has found use in many industries including food processing, cosmetics, and water treatment.⁹⁹⁷ To facilitate water solubility, several chitosan derivatives have been proposed in the most recent decades, for example, carboxymethyl-,¹⁰⁰² sulfated-,¹⁰⁰³ quaternarized-,¹⁰⁰⁴ and arginine-chitosan.¹⁰⁰⁵ As with other kinds of polysaccharides, chitosan offers key advantages for biomedical applications, such as biocompatibility, biodegradability, and nontoxic degradation products.¹⁰⁰⁶⁻¹⁰⁰⁸ Although factors such as purity, source, degree of deacetylation, and molecular weight may influence its *in vivo* therapeutic effects,

chitosan is considered nontoxic.¹⁰⁰⁹ In addition, mainly due to its polycationic nature, it offers a unique combination of biological properties such as antibacterial, antifungal, and antioxidant activity, as well as hemostatic potential and *in vivo* mucoadhesivity.^{1002, 1010} These versatile properties have made chitosan an excellent candidate as a biomedical adhesive.¹⁰¹¹

In this study we report for the first time the synthesis and characterization of a water-soluble transglutaminase (TG) cross-linkable chitosan to be used as an injectable adhesive. This formulation aims to combine the intrinsic bioactive and adhesive properties of chitosan with the clinically approved enzymatic cross-linking components of fibrin glue (FXIII and thrombin). First, to overcome a major disadvantage of chitosan that limits its biological applications, we have made it water-soluble at neutral pH by chemically grafting arginine through EDC/NHS activation of the amino acid α -carboxyl group (Figure 9.1A and Supporting Information (SI) Figure S9.1 and Table S10.1). Conjugation of arginine allows one to generate a protonated water-soluble derivative, while imparting significant antibacterial activity.¹⁰¹² The degree of arginine substitution was determined by ¹H NMR analysis to be ~13–18% (Supporting Information, NMR spectra). EDC activation was exploited also in a second step, during which a short hetero-difunctional linker (VS-COOH), previously developed in our group,⁸¹⁹ was grafted onto the arginine-chitosan (Arg-Chi) polymer, thereby providing a vinyl sulfone moiety to the polymer. In the final step, the vinyl sulfone reactive group was exploited to immobilize FXIII peptide substrates through click thiol-Michael addition (Figure 9.1A). The two peptides used in this study were previously reported by our group,^{104, 1013} with one containing a reactive glutamine (TG-Q) and the other a reactive lysine (TG-K). Arg-Chi derivatives with TG-Q and TG-K peptides (Arg-Chi-TG) were synthesized separately and then mixed in equal amounts. Their degree of substitution was calculated by ¹H NMR to be ~11–16%, based on the vinyl protons of the previous step, which are then found to be completely lost due to the formation of the thioether bond with the cysteine bearing peptides (Supporting Information, NMR spectra).

We first assessed the efficacy of our TG cross-linkable arginine-chitosan to form a hydrogel in the presence of thrombin and Ca²⁺, which activated FXIII (Figure 9.1B). The specific enzymatic activity of activated FXIII (FXIIIa) catalyzes the acyl-transfer reaction between the side-chain amide of glutamine and the ϵ -amino group of a lysine residue,¹⁰¹³ respectively in the TG-Q and TG-K Arg-Chi derivatives, which leads to the formation of a stable hydrogel (Figure 9.1C).

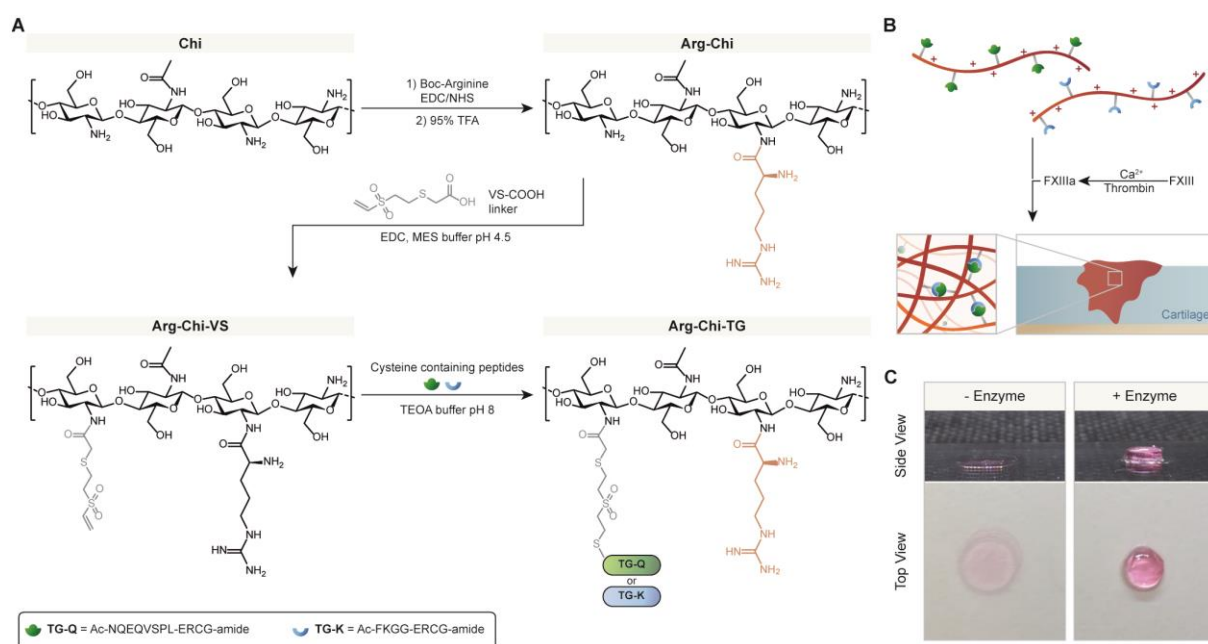


Figure 9.1 (A) Reaction scheme illustrating the consecutive grafting of arginine (orange), vinyl sulfone linker (gray), and transglutaminase substrate peptides TG-Q and TG-K. (B) Cross-linking strategy of the polycationic Arg-Chi-TG and illustration of *in situ* cross-linking in cartilage defect/damage with detail on hydrogel formation and cross-linking points. (C) Images showing that the formation of stable hydrogels (right) is due to the enzymatic activity. In the absence of thrombin and FXIII, Arg-Chi-TG does not form a gel (left).

The gelation behavior was studied by rheometry, which showed that the stiffness of the hydrogel can be tuned in a wide range that spans from ~ 10 to ~ 1000 Pa by varying the polymer concentration (Figure 9.2A,B). The gelation process starts within the first few minutes after adding the enzymes and reaches a plateau after around 10–15 min. The relatively fast kinetics of the enzymatic cross-linking satisfy a key requirement for an injectable biological adhesive. In addition, the gelation onset can be tuned according to the surgeon's need by varying the enzyme concentration.¹⁰⁴

We have also found our Arg-Chi-TG to be cohesive. When cut in half, the two resulting hydrogel pieces could be easily rejoined (Figure 9.2C). This “sticky” behavior, known as cohesiveness, is speculated to be dependent on the structural changes of chitosan helix, when the two surfaces are in contact, to a conformation which is more favorable for cohesive bonds (*i.e.*, hydrophobic, electrostatic, and van der Waals interactions).¹⁰¹⁴ This self-healing-like property was further assessed with a shear-recovery test (Figure 9.2D), confirming the ability to partially recover initial mechanical properties upon high shear rate. Overall, these findings suggest that the cohesive forces of our injectable hydrogel can provide stable adhesion, possibly over a longer time, by partially overcoming gel breaking and stress loads.

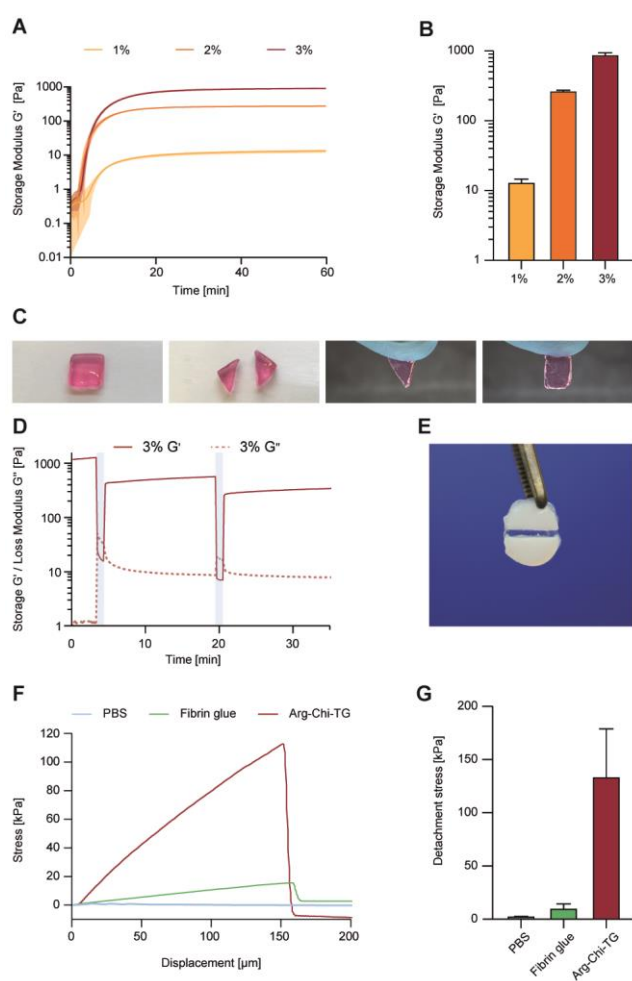


Figure 9.2 | Mechanical properties of Arg-Chi-TG hydrogels. (A) Average gelation curves (storage modulus, $n = 3$) monitored by oscillatory test at different polymer concentrations, showing fast gelation onset (2–3 min) with equilibrium reached after approximately 15 min. (B) Plateau storage modulus reached by hydrogels at different polymer concentrations, proving stiffness tunability. (C) Qualitative assessment of Arg-Chi-TG hydrogel cohesiveness. A hydrogel cube is cut in half with a scalpel, and the two resulting pieces are rejoined by simple juxtaposition showing cohesiveness and stability. (D) Shear-recovery test of 3% Arg-Chi-TG hydrogel showing recovery of hydrogel mechanical properties after high shear rate (light blue area, 500% strain, 1 Hz, 10 s). (E) Image showing Arg-Chi-TG hydrogel gluing together two bovine knee articular cartilage pieces. (F, G) Arg-Chi-TG hydrogel exhibits stronger adhesion to cartilage compared to fibrin glue and PBS during tensile test ($n = 3$).

Due to their polycationic nature, chitosan-based adhesives are especially attractive for mucin and tissues rich in negatively charged polymers, such as glycosaminoglycans (GAGs), for which electrostatic interactions can play a relevant role in strengthening the material-to-tissue adhesion. Cartilage would be an example of such a tissue, due to its high hyaluronan and aggrecan content, and was used as a model to test Arg-Chi-TG adhesion (Figure 9.2E). Adhesive properties have been investigated by means of tensile testing with bovine articular cartilage explants. Arg-Chi-TG hydrogels exhibited a much stronger adhesion compared to the clinically approved fibrin glue (Figure 9.2F,G). Since the two adhesives share the same enzymatic cross-

linking strategy, we hypothesized that the 1 order of magnitude detachment stress difference is due to electrostatic interactions between cartilage GAGs and positively charged chitosan chains (Figure 9.3A).

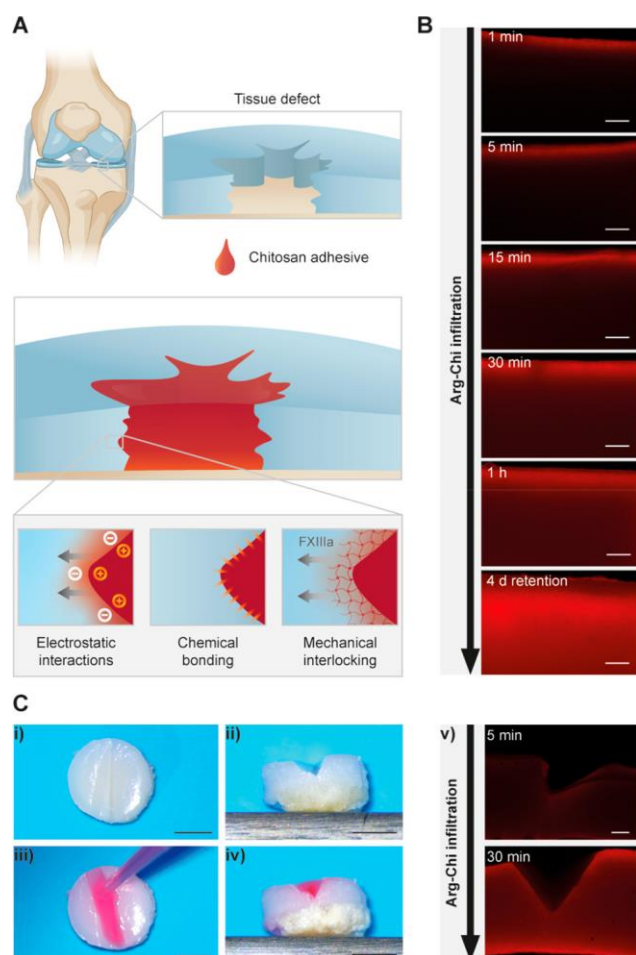


Figure 9.3 | (A) Schematic illustration of Arg-Chi-TG application on cartilage tissue defect and details on main adhesion mechanisms that take place in the material-to-tissue interface. (B) Infiltration and retention of fluorescently labeled Arg-Chi into cartilage explants over time (scale bar, 200 μm). (C) (i–iv) defect filling on osteochondral graft with Arg-Chi-TG 3% supplemented with TRITC-dextran (scale bar, 2 mm); (v) infiltration of fluorescently labeled Arg-Chi into cartilage defects (scale bar, 200 μm).

To further investigate this aspect, we evaluated Arg-Chi adsorption and infiltration into cartilage explants. A FITC-labeled derivative was synthesized and allowed to interact with and interpenetrate the cartilage matrix over a period of time spanning from 1 min to 1 h (Figure 9.3B and SI Figure S9.2). Fluorescence imaging of cartilage cross-sections showed a rapid adsorption of the chitosan derivative onto the cartilage–solution interface within the first minute as expected by Donnan partitioning mechanism.¹⁰¹⁵ This increased surface concentration of positively charged polymer generates a sharp gradient pointing inward which is expected to further promote tissue penetration. Over time, Arg-Chi is indeed shown to infiltrate the cartilage matrix, forming a mechanically interlocked network that we speculate is responsible for the improved adhesive

properties. Mechanical interlocking of polymer chains and electrostatic binding to negatively charged GAGs contribute to Arg-Chi retention in the host matrix after a few days in PBS washing solution (Figure 9.3B), in contrast with the behavior of a solution of the fluorescent dye only (SI Figure S9.2). While this suggests that its cationic nature facilitates fast penetration and retention into negatively charged matrices, the activity of FXIIIa could stabilize the integration within the tissue of the TG cross-linkable chitosan derivatives due to the natural presence of fibrinogens and other plasma proteins in articular cartilage.¹⁰¹⁶ Given the natural presence of fibrinogens and the higher permeability of osteoarthritic (OA) cartilage, which could facilitate the infiltration and integration into deeper layers, we speculate that our material might serve as a platform to further develop biological adhesives targeted for OA treatment. Figure 9.3C shows an example of cartilage defect filling (SI Video S9.1) and infiltration.

Overall, we have shown that Arg-Chi-TG, while sharing the same cross-linking mechanism as the clinically approved fibrin glue sealant, exhibits superior capabilities by substantially matching the main bioadhesion mechanisms: electrostatic interactions, chemical bonding, and mechanical interlocking (Figure 9.3A).⁹⁹²

Another desirable requirement for an injectable formulation that has led us to select chitosan as a starting material is its inherent antibacterial activity.^{1005, 1017} Although chitosan's antibacterial activity has been extensively investigated in past decades, we decided to confirm the retention of these properties for our newly synthesized Arg-Chi-TG formulation with an antibacterial test against *Staphylococcus aureus* (*S. aureus*), the most common pathogen causing septic arthritis and bacterial infections in orthopedic procedures.¹⁰¹⁸⁻¹⁰¹⁹ As expected, both the water-soluble Arg-Chi as well as the FXIIIa cross-linkable Arg-Chi-TG exhibited clear antimicrobial activity (Figure 9.4A). Then, the cytotoxicity of our cell-free injectable hydrogel was evaluated with an MTS assay using bovine articular chondrocytes. We tested the effect of non-cross-linked polymer solutions at different concentrations on cell metabolic activity and tested the effect of hydrogel supernatant containing potential degradation products (SI Figure S9.3). The colorimetric assay revealed an improved cell proliferation, compared to medium only, when cells were cultured in medium containing chitosan solutions or chitosan hydrogel supernatant (Figure 9.4B). Low-molecular-weight chitosan has been shown to scavenge active oxygen free radicals, thus behaving as an antioxidant.¹⁰²⁰⁻¹⁰²¹ We therefore hypothesize that short chains derived from biodegraded Arg-Chi-TG would have beneficial effects on cell viability by preventing DNA, protein, and lipid damage due to reactive radicals.

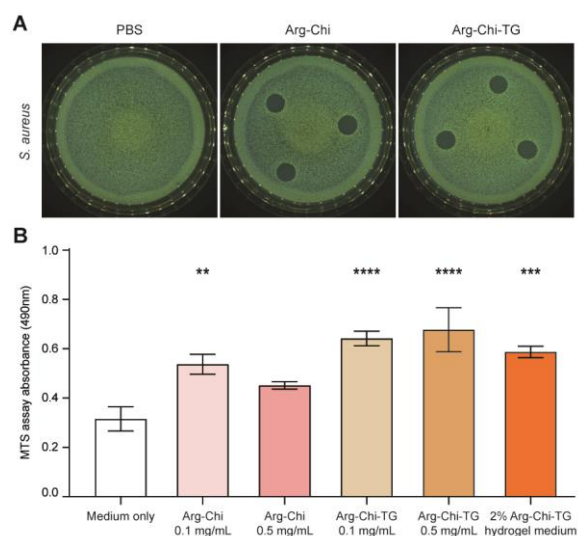


Figure 9.4 | Biological properties of Arg-Chi-TG. (A) Chitosan derivatives Arg-Chi and Arg-Chi-TG showed clear antibacterial activity against Gram-positive *S. aureus* compared to PBS control. (B) MTS assay with articular chondrocytes showed improved proliferation, compared to medium only, when cultured in the presence of chitosan derivatives Arg-Chi and Arg-Chi-TG at different concentrations, as well as with medium preincubated in the presence of Arg-Chi-TG hydrogel (one-way ANOVA; $n = 3$; *, $p < 0.05$).

In summary, we reported the development of the first FXIII cross-linked arginine-chitosan hydrogel and investigated its potential as an injectable bioadhesive. Its fast enzymatic gelation and tunable mechanical properties enable one to match the target tissue requirements and surgeons' needs for an effective procedure. From a clinical perspective, it represents a promising material due also to its hemostatic property. Arg-Chi-TG could actively stop blood loss due to injuries or during surgical procedures thanks to the combination of intrinsic hemostatic potential of chitosan,¹⁰²²⁻¹⁰²³ and interaction with patients' blood fibrinogen in the coagulation cascade, and also by acting as a mechanical barrier upon fast gelation. In this study, we chose cartilage as the target tissue for the proof-of-concept; however, we envision that, thanks to the TG cross-linking scheme and intrinsic cationic nature, our chitosan derivative could be applied to other tissues (*i.e.*, skin wound closure). In addition, inherent biocompatible, biodegradable, and antibacterial properties make our chitosan-based hydrogel a highly attractive material for future developments, not only as a bioadhesive but also more broadly in the fields of tissue engineering and regenerative medicine.

Acknowledgments. This work was financially supported by the Swiss National Science Foundation (CRSII5_173868 to M.Z.-W.); We thank Philipp Fisch for the help with mechanical testing, Dominic Rüttsche for the help with chemical synthesis, Flavia Zuber for the help with bacterial assay, and Dr. Anna Puiggali Jou and Maryam Asadi Korayem for providing the osteochondral grafts.

Contributions. I.B., M.L. and R.R. as first authors contributed equally to this work, conceived the project, designed and performed the experiments. I.B. and N.B. performed the chemical synthesis. I.B. and M.L.

performed mechanical testing. R.R. performed NMR and data analysis, infiltration and retention tests. Q.R. performed antibacterial assay. M.Z-W. supervised the project. The manuscript was written through the contributions of all authors.

9.2. Supporting Information

Materials and Methods

All chemicals are from Sigma-Aldrich-Merck, unless indicated otherwise.

Arg-Chi synthesis. The arginine-chitosan (Arg-Chi) synthesis protocol was adapted from Baker *et al.*¹⁰¹² 3 g chitosan (Heppe Medical Chitosan GmbH, 82.6 - 87.5% deacetylated, 80-200 kDa) were dissolved in 228 mL 0.1 M HCl. Separately, 5.437 g (47.24 mmol) N-hydroxysuccinimide (NHS) and 12.96 g (47.24 mmol) BOC-Arg-OH were dissolved in 240 mL mQ H₂O. Subsequently, 9.075 g (47.34 mmol) 1-Ethyl-3-(3-dimethylaminopropyl)carbodiimide hydrochloride (EDC, Fluorochem) were dissolved in 8.25 mL mQ H₂O and added to the NHS/BOC-Arg-OH mixture, stirred for 1 min and added dropwise to the chitosan solution. The mixture was gently stirred overnight. 22 g (0.38 mol) NaCl were added to the solution followed by dialysis against mQ H₂O for 3 days to yield a pure BOC-arginine-chitosan solution followed by lyophilization. The BOC protection group of arginine was removed from the Arg-Chi polymer by addition of 10 mL 95% Trifluoroacetic acid (TFA, Thermo Fisher Scientific) to 200 mg of lyophilized product and stirred for 3 h in a closed flask. TFA was subsequently evaporated by blowing nitrogen gas into the open flask while stirring. The dried sample was re-suspended in 20 mL mQ H₂O containing 0.5 g (8.56 mmol) NaCl and dialyzed against mQ H₂O containing 0.01 M NaCl for one day, followed by dialysis with pure mQ H₂O for another day. The sample was lyophilized for storage and the degree of arginine conjugation was estimated by ¹H-NMR analysis to be approximately 13-18%. In short, the degree of substitution (DS) was calculated based on the fact that for each successfully conjugated arginine, the 3 methyl protons of the acetyl group (peak around 2 ppm) correspond to 4 protons of two methylene groups of arginine (respectively around 1.65 and 1.85 ppm), using the equation below:

$$DS = \frac{\int ArgCH_2 \times 3}{\int GlcNAcCH_3 \times 4} \times (100 - DA)$$

Where DA is the degree of deacetylation.

VS-COOH synthesis. The synthesis of the heterodifunctional linker VS-COOH was adapted from Broguiere *et al.*⁸¹⁹ 28 μ l (0.19 mmol) 1,8-Diazabicyclo[5.4.0]undec-7-ene (DBU) and 560 μ l (5.58 mmol) divinyl sulfone (DVS) were added to 4 mL dimethylformamide (DMF, Thermo Fisher Scientific) and stirred on ice. 200 μ l (2.88 mmol) thioglycolic acid were added dropwise to the solution. The mixture was stirred on ice for 30 min before diluting with 5 mL of 30 mM aqueous HCl. The solution was immediately purified by preparative HPLC (Agilent Prep-C18, 100 Å pore size, 10 μ m particle size, 250x50 mm) using 5% ACN in H₂O in the presence of 0.1% TFA for 10 min followed by a gradient of 5 to 90% acetonitrile over 20 min

with an 80 mL/min flow rate. The residual acetonitrile in the collected VS-COOH solution was removed using a rotary evaporator and the resulting pure product was lyophilized. The successful synthesis of the desired product was confirmed by ¹H-NMR analysis.

Arg-Chi-VS synthesis. The Arg-Chi-VS synthesis protocol was adapted from Broguiere *et al.*¹⁰⁴ 610 mg of Arg-Chi were dissolved in 248.7 mL 2-morpholinoethanesulfonic acid solution (MES, pH 4.5, 150 mM). 684 mg (3.25 mmol) VS-COOH were dissolved separately in 31 mL MES solution and added to the Arg-Chi solution. The pH was adjusted back to 4.5 by addition of aqueous NaOH. 624 mg (3.26 mmol) EDC were dissolved in 23.3 mL mQ H₂O and added dropwise to the reaction mixture under vigorous stirring. The stirring was slowed down, and the reaction left to proceed for 2 h. Subsequently, 217 mg (1.13 mmol) EDC were dissolved in 8 mL mQ H₂O and added dropwise to the solution and the reaction was left to continue for another 2 h. Then, 5 g (85.56 mmol) NaCl were added and the solution was dialyzed against mQ H₂O containing 20 mM NaCl for 3 days. After dialysis, the sample containing 20 mM NaCl was immediately used for the next synthesis step due to limited solubility after the freeze-drying procedure. A small amount of Arg-Chi-VS was lyophilized only for ¹H-NMR analysis. The degree of VS-COOH conjugation was determined by ¹H-NMR to be approximately 11-16 %. In short, DS was calculated based on the fact that for each successfully conjugated vinyl sulfone (VS) moiety, the 3 vinyl sulfone protons (peaks around 6.4 and 6.9 ppm) correspond to the 3 methyl protons of the acetyl group (peak around 2 ppm), using the equation below:

$$DS = \frac{\int VS_{peaks} \times 3}{\int GlcNAcCH_3 \times 3} \times (100 - DA)$$

Where DA is the degree of deacetylation.

Peptide synthesis. TG-Q (Ac-NQEQVSPL-ERCG-NH₂) and TG-K (Ac-FKGG-ERCG-NH₂) peptide synthesis was performed on Prelude[®]X (Gyros Protein Technologies) by means of classical solid phase peptide synthesis (SPPS) with rink-amide resins and Fmoc-protected amino acids.

Arg-Chi-TG synthesis. The Arg-Chi-TG synthesis protocol was adapted from Broguiere *et al.*¹⁰⁴ One part of Arg-Chi-VS was conjugated to the glutamine-providing peptide TG-Q and the other to the lysine-providing peptide TG-K, serving as substrates for transglutaminase mediated crosslinking. 1 mL TEOA buffer (300 mM, pH 8) was added per 10 mL of Arg-Chi-VS solution. The solution was then split into two equal parts, sealed in a flask and deoxygenized by bubbling with nitrogen gas for 15 min. TG-Q (864 mg, 0.64 mmol) and TG-K (576 mg, 0.64 mmol) were each dissolved in 15 mL mQ H₂O and added to the sealed flasks which were then deoxygenized a second time. The reaction was left to proceed overnight at room temperature without stirring. 4 g (68.45 mmol) NaCl were added to each flask and the solutions were dialyzed against mQ H₂O for 3 days with frequent H₂O changes. The samples were subsequently lyophilized and

complete conjugation of TG peptides was confirmed by the disappearance of the vinyl peaks on $^1\text{H-NMR}$ spectra.

Zeta-potential analysis. Measurements were performed in triplicates at 25°C on ZetaSizer Nano ZS (Malvern Panalytical) with 5 mg/mL polymer solutions in 0.1 M HCl to ensure complete solubility of all tested materials.

General procedure for hydrogel preparation. Arg-Chi-TG-K and Arg-Chi-TG-Q were separately dissolved at 3% in Tris buffer (50 mM Tris, 50 mM CaCl_2 and 100 mM D-glucose) and pH was adjusted to 7. 1% and 2% polymer solutions were prepared by dilution of the 3% stock with Tris buffer (pH 7). Arg-Chi-TG-K and Arg-Chi-TG-Q solutions were mixed together in equal amounts shortly before use. After addition of 2.5 μL thrombin (500 U/mL, Baxter) and 5 μL FXIII (200 U/mL, Fibrogammin, CSL Behring) per 92.5 μL of Arg-Chi-TG solution, the mixture was quickly mixed by pipetting for a few seconds to ensure homogenous distribution of the enzymes before gelation onset.

Rheology. Gelation kinetics and shear-recovery hydrogel behavior were recorded on an Anton Paar MCR 301 rheometer equipped with a 20 mm parallel plate geometry. The gap was set to 0.2 mm and measurements were performed in a humidified chamber at 25°C . After preparation of the hydrogels as described above, 76 μL were immediately loaded onto the rheometer in order to start the measurement shortly after the addition of the enzymes. Both storage and loss modulus were measured in triplicates with oscillatory tests at a frequency of 1 Hz and 2% strain with 20 second measurement steps for a total of 1 hour. For the shear recovery test, hydrogels were prepared according to the same method and incubated for 30 min for completion of gelation. Storage and loss modulus were measured at 1 Hz for the hydrogels exposed to the following sequence of mechanical stress twice: 0.5% strain for 200 s, 500% strain for 10 s and 0.5% strain for 10 min.

Tensile test. Adhesion strength to cartilage tissue was measured through tensile testing using a texture analyzer (Stable Micro Systems, London, England). Bovine articular cartilage samples were obtained from a calf knee (3-6 months of age, Metzgerei Angst, Zürich). Cartilage samples of approximately 1-2 mm thickness were collected and cut into 4 mm diameter discs using biopsy punches (Kai Medical, Japan). A disc was attached to the lower sample holder with super glue. Arg-Chi-TG 3% solution was prepared as described above, quickly mixed using a pipette and placed onto the cartilage disc surface. Rapidly, a second cartilage disc was placed on top of the gelling solution and pressed together until complete gelation. Super glue was then used to attach the upper sample holder to the top surface of the second cartilage disc. After 15 min, the upper disc was pulled upward with a speed of 0.5 mm/s until the two discs detached from each other. As

controls, the same measurements were performed using 10 μL of PBS or commercially available fibrin glue (5 μL component A + 5 μL component B, Tisseel, Baxter, USA). Measurements were performed in triplicates.

Degradation test. 15 μL of 3% Arg-Chi-TG hydrogels were prepared according to the method described above. Each hydrogel was transferred to a pre-weighted Eppendorf tube filled with 0.2 mL PBS. After incubation of the hydrogels for 0, 3 and 9 days, the tubes' contents were freeze-dried. The weights of the empty tubes and the tubes filled with dried gels were compared to calculate relative dry weight of hydrogels at each time point.

Cartilage infiltration. Cartilage discs of approximately 1-2 mm in thickness and 4 mm in diameter were obtained as described above. Cartilage defects were manually made with a scalpel. To visualize infiltration of Arg-Chi in articular cartilage, the polymer was labeled with Fluorescein 5(6)-isothiocyanate (FITC). In short, Arg-Chi was dissolved at 10 mg/mL in mQ H_2O and subsequently an equal dimethyl sulfoxide (DMSO) volume was added to the solution while stirring. FITC was separately dissolved at 0.47 mg/mL in DMSO and slowly added to the Arg-Chi solution at a 1:2 volume ratio. The reaction was left to proceed in the dark for 3 h. Then, 0.1 g (1.71 mmol) NaCl were added and the solution was dialyzed against mQ H_2O for 24 h followed by lyophilization. Arg-Chi-FITC was dissolved in PBS (10 mg /mL) and the cartilage samples were incubated in this solution for 1, 5, 15, 30 and 60 min in the dark before washing with PBS 3 times for 3 min. Additionally, samples were incubated in the Arg-Chi-FITC solution for 60 min and subsequently incubated in PBS for 4 days to visualize retention within the cartilage tissue. After the washing steps, samples were cut in half to image their cross sections. Following the same incubation and washing steps, a solution of Fluorescein 77 μM in PBS was used to study the infiltration and retention behavior of the dye only. All images were acquired at 5x magnification (Zeiss Axio Observer Z1) and processed with Zeiss Zen Light Edition.

Cartilage defect filling. Osteochondral grafts were obtained from a calf knee. Cartilage defect was manually made with a scalpel. Arg-Chi-TG 3% solution was prepared as described above and quickly mixed with minimum amount of 40kDa TRITC-dextran to ensure better visualization of the polymer solution. The solution was pipetted into the defect. After 3 minutes, successful crosslinking was assessed by touching the hydrogel surface with a needle. Images and videos were acquired with Leica M80.

Assessment of antibacterial activity. *Staphylococcus aureus* ATCC 6538 were cultured in 5 mL of Tryptic Soy Broth (TSB) at 37°C and 160 rpm overnight. The cultures were then diluted to 10^6 colony-forming units (CFU)/mL, of which 200 μL were plated onto PC-Agar plates. Samples Arg-Chi and Arg-Chi-TG were dissolved in PBS to 2 mg/mL. 5 μL drops of the polymer solution were loaded on the prepared bacterial agar plates. The plates were incubated overnight at 37 °C prior to imaging. All samples were tested in at least triplicate for each condition.

MTS assay. Bovine articular chondrocytes (passage 3) were seeded into 96-well plates at 10^4 cells per well and incubated at 37°C in DMEM (Gibco) containing 10% fetal bovine serum (Gibco), gentamycin (10 $\mu\text{g}/\text{ml}$, Gibco) and FGF2 (50 ng/ml , Peprotech) for 24 h. Separately, 2% Arg-Chi-TG hydrogels were cast into polydimethylsiloxane (PDMS) rings (1 mm height, 4 mm inner diameter), incubated for 30 min for complete gelation, washed with cell medium, and followed by incubation for 24 h in the medium described above (1 mL per sample). After 24 h in culture, the cell medium of the chondrocytes was replaced by the medium incubated with the hydrogels as well as with solutions of non-crosslinked Arg-Chi and Arg-Chi-TGQ/K (1:1 mix) dissolved in the medium described above at 0.1 and 0.5 mg/mL . The cells were incubated for 72 h. 10 μl MTS reagent (Abcam) were added per well and incubated at 37°C for 40 min. Absorbance was measured at 490 nm (Synergy H1 Hybrid Reader, BioTek) and blank (sample medium only) values for each sample set were subtracted from the measured values of wells containing cells and samples. The assay was performed in triplicates (100 $\mu\text{l}/\text{well}$).

Supplementary Figures

Table S9.1 | Zeta-potential measurements of chitosan and chitosan derivatives showing retention of positive charges upon polymer functionalization ($n=3$).

	Zeta Potential [mV]	Conductivity [mS/cm]	Mobility [$\mu\text{m cm}/\text{V s}$]
Chitosan	38.4 ± 3.1	39.5 ± 0.3	3.007 ± 0.244
Arg-Chi	31.3 ± 1.6	45.3 ± 0.2	2.458 ± 0.125
Arg-Chi-TGQ	21.7 ± 0.3	44.8 ± 0.4	1.703 ± 0.027
Arg-Chi-TGK	25.0 ± 0.4	45.1 ± 0.1	1.958 ± 0.035



Figure S9.1 | Solubility of chitosan and arginine-chitosan. Unmodified chitosan (left) is not soluble in PBS at neutral pH and forms clear precipitates. In contrast, Arg-Chi (right) is nicely soluble at neutral pH, resulting in a clear solution with no precipitation.

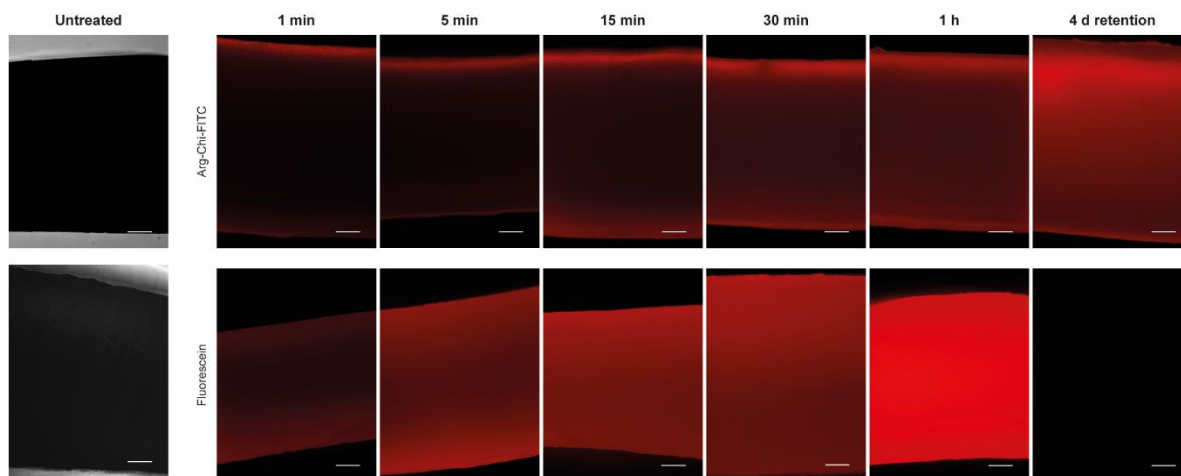


Figure S9.2 | Infiltration test. Comparison of Arg-Chi-FITC and Fluorescein infiltration and retention in bovine cartilage samples. Complete cross-section imaging (scale bar: 200 μm).

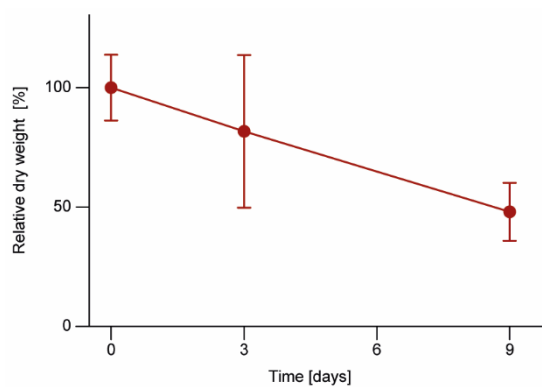
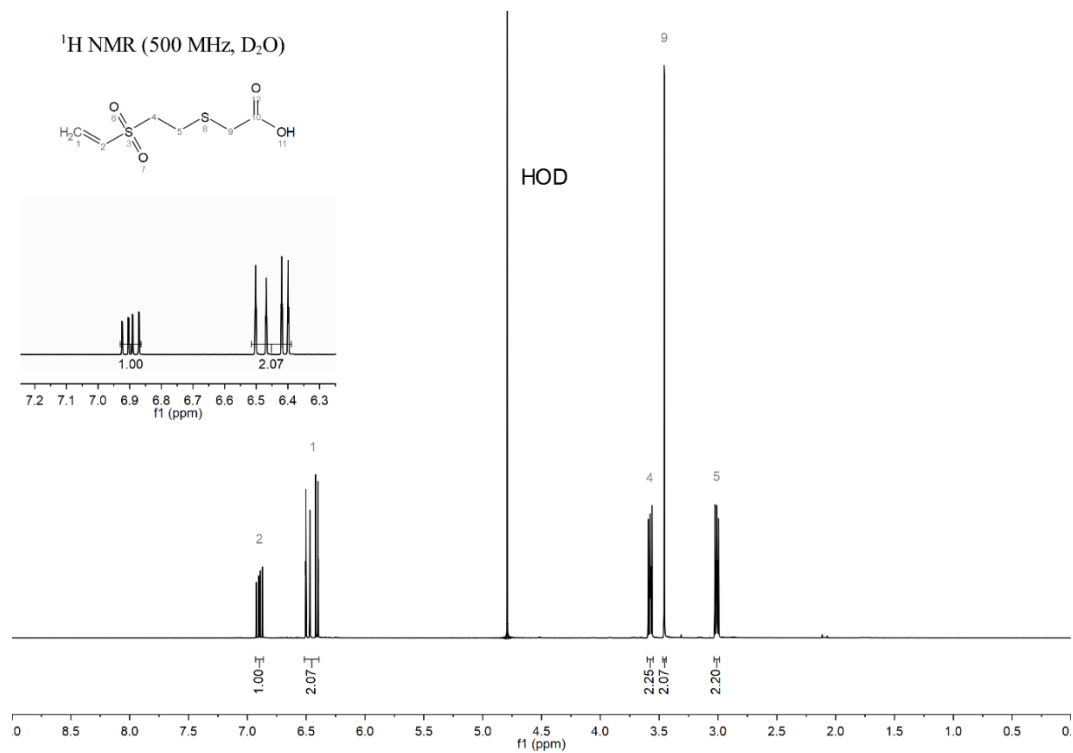


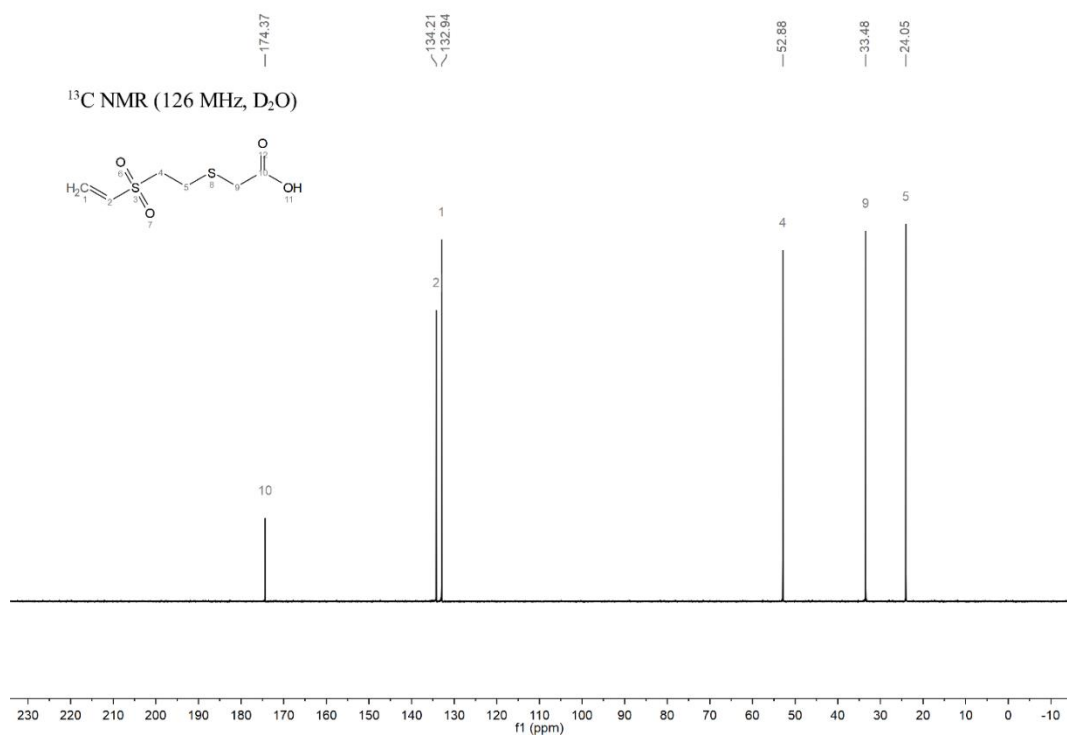
Figure S9.3 | Degradation of Arg-Chi-TG hydrogels. Relative dry weight of the hydrogels incubated at 37 $^{\circ}\text{C}$ for 0, 3 and 9 days in PBS solution.

NMR spectra

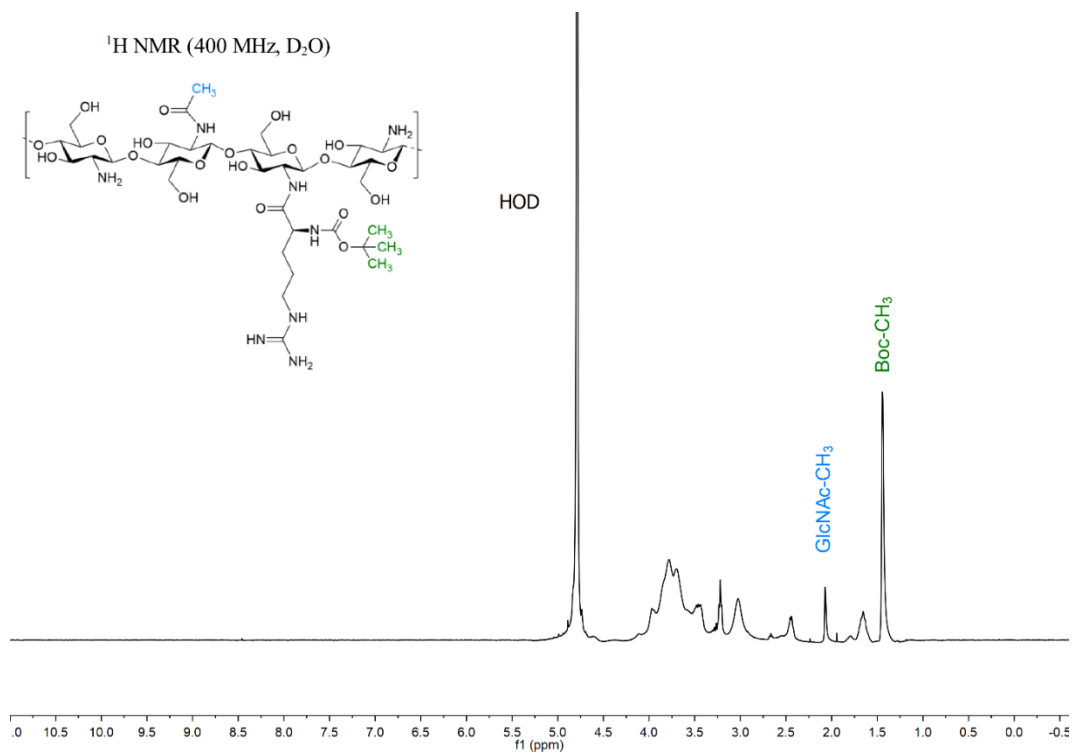
NMR spectra were acquired on Bruker Ultrashield 400MHz or Bruker Ascend 500MHz.

VS-COOH

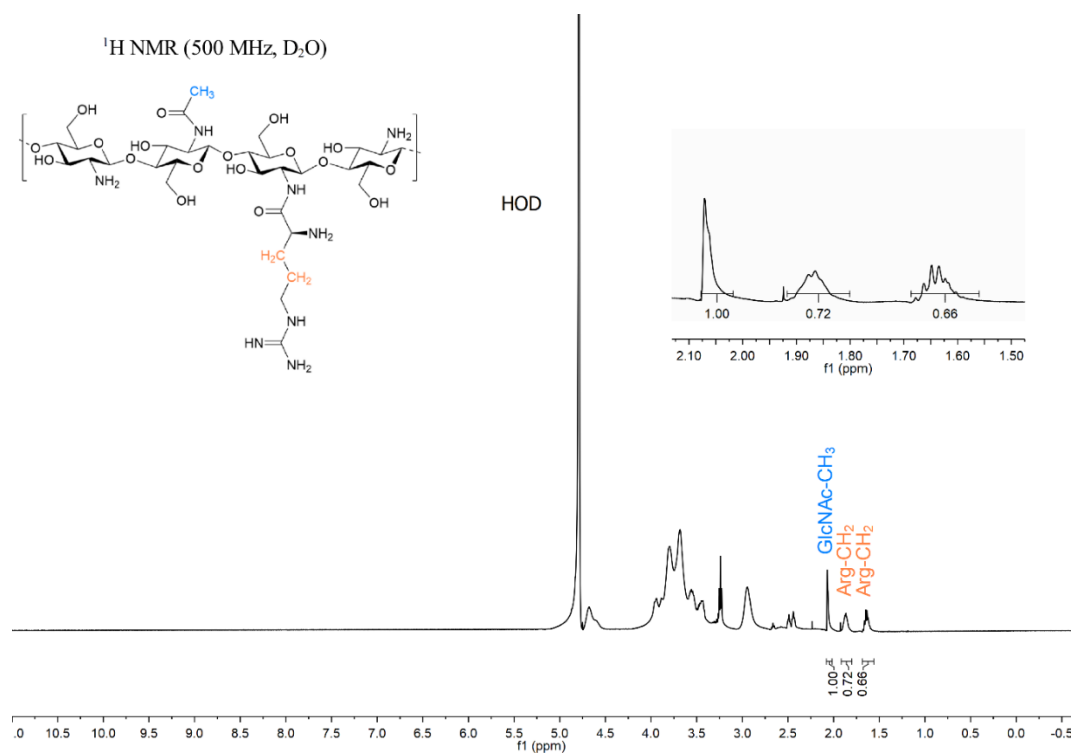




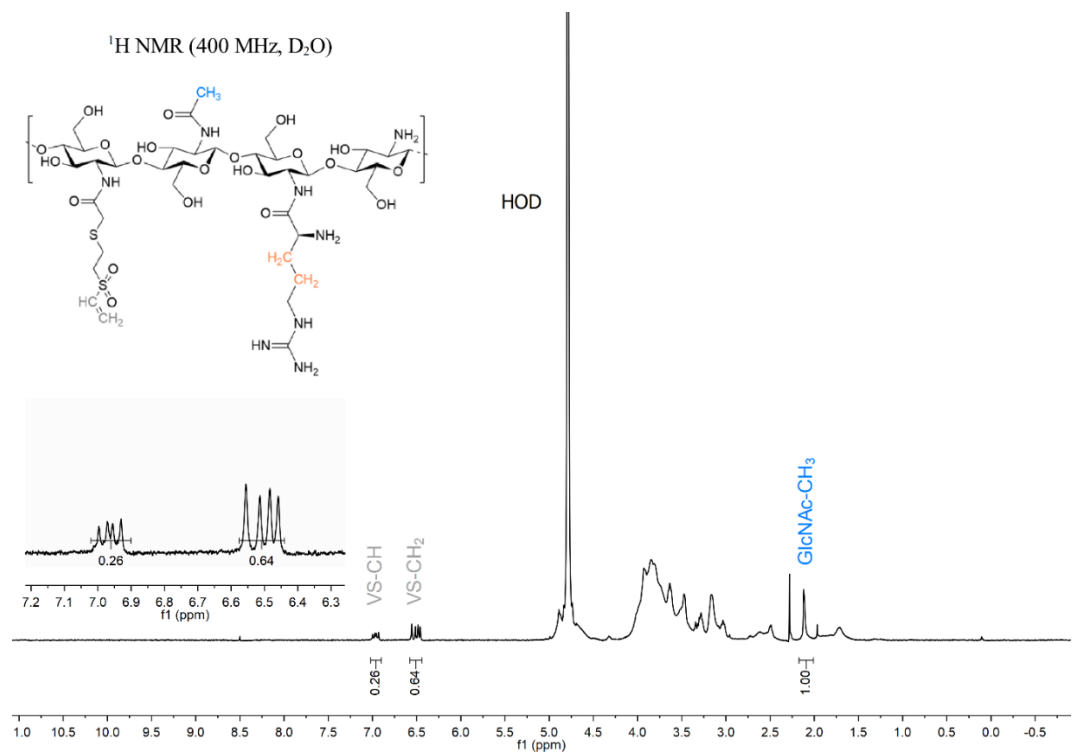
Arg-Boc-Chi



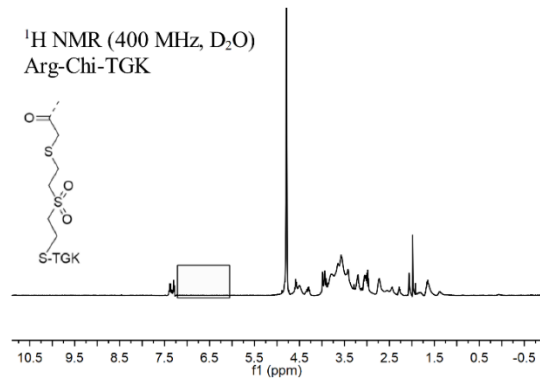
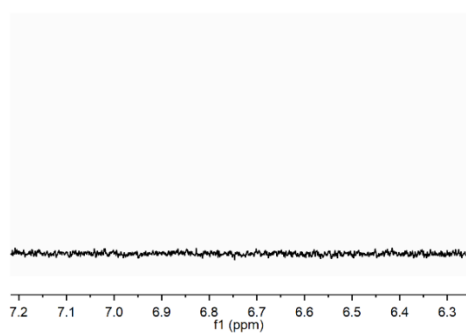
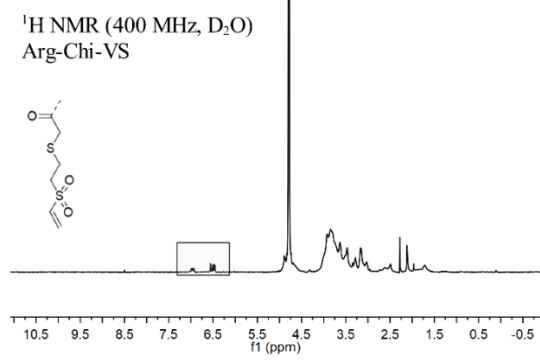
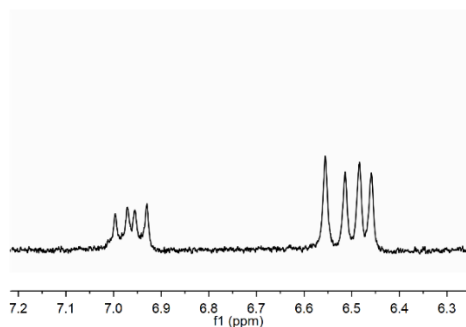
Arg-Chi



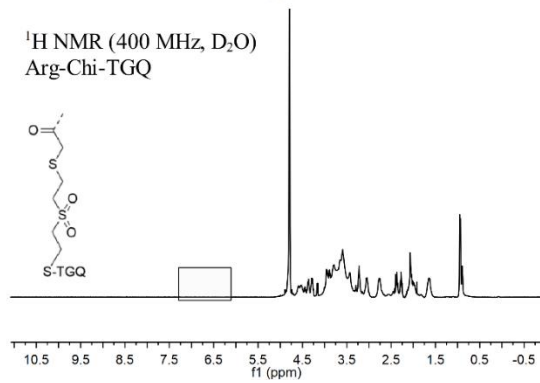
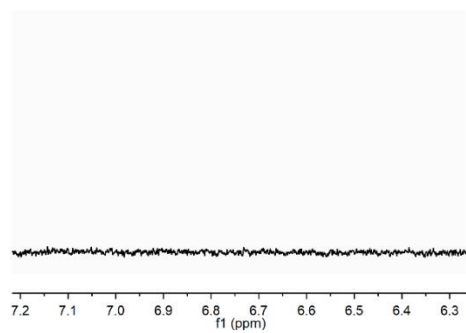
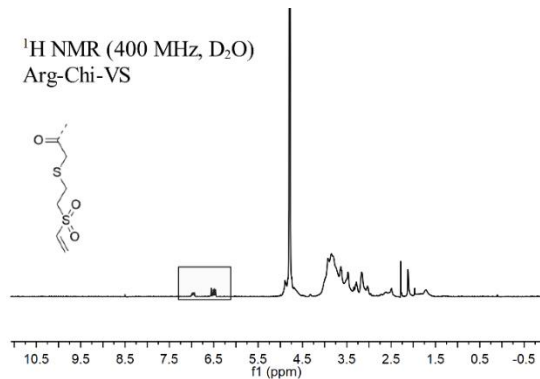
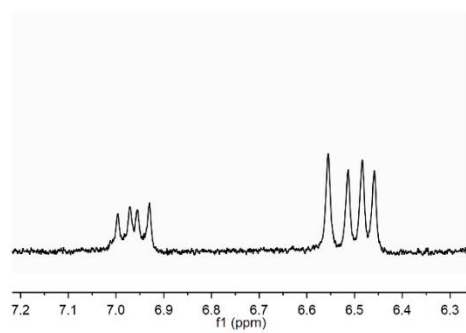
Arg-Chi-VS



Arg-Chi-VS and Arg-Chi-TGK



Arg-Chi-VS and Arg-Chi-TGQ



CHAPTER 10

Conclusions & Outlook

In this final Chapter, the major contributions of this dissertation are summarized and accompanied by future perspectives.

The work presented in this thesis on the development of optimized photosensitive bioresins for light-mediated biofabrication strategies offered significant contributions in the field that are expected to stimulate further exciting research. The major contributions and future outlook can be summarized as follows:

Chapter 2 presents a comprehensive literature review on light-mediated biofabrication including detailed discussion on photochemical reactions, photoactivated materials, as well as biological and engineering aspects. By including principles, applications and limitations of each light-based technique as well as the identification of emerging trends, this review offers one of the most exhaustive up-to-date documents covering this emerging field. This work is foreseen to play an important role in introducing non-experts to the field and ease the interested readers to identify the best suited approach for their purposes.

Chapter 3. An optimized photoclick (bio)resin based on thiol-norbornene chemistry was applied, for the first time, in volumetric printing (VP). This allowed to print at significantly faster speed and lower polymer content, making this photoresin an ideal candidate for cell encapsulation, as demonstrated then by excellent viability and tissue maturation potential. A fast, scalable and inexpensive synthesis method was also introduced to produce large quantities of gelatin-norbornene (Gel-NB), the main component of the optimized photoresin, thus facilitating its establishment as possible future gold-standard for light-based biofabrication technologies. Building on the excellent performance of Gel-NB based photoresin, future work will need to make a step forward towards possible applications. In particular, given the size limit (~ 2 cm) of the printed construct, on-a-chip technologies are envisaged as a promising direction. The printing of perfusable, hollow channels within a cell-laden hydrogel has been already demonstrated in this Chapter, thus making vascularized *in vitro* tissue models a realistic future outcome of VP. Moreover, thiol-norbornene chemistry could be applied to various photoresins specifically tailored for the targeted tissue. Following the example provided in Chapter 5 with the synthesis of HA-NB to promote cartilage maturation, other polymers or tissue-specific decellularized ECM can be modified to bear NB functionalities, thus easily expanding the palette of available VP photoresins. Lastly, there is an evident need to making VP a multimaterial printing method so to make it appealing for a much broader range of applications which require multiple cell types and materials.

Chapter 4. A new method to obtain defect-free VP was proposed, making it suitable for hybrid printing with high resolution two-photon ablation (2PA). To achieve this results, optical tuning of the photoresins refractive index (RI) was conducted to get rid of microdefects induced by self-focusing phenomenon. By combining defect-free VP and 2PA, highly complex, multiscale, organotypic vasculature-like models were generated opening new possibilities for precise microtissue on-a-chip technologies. A natural continuation of this work will be the addition of endothelial cells to cover the meso- and micro-vasculature channels. To achieve this goal, the printed models can be connected to a perfusion system.¹⁰²⁴ Based on previous

findings,⁸⁰⁶ endothelialization of the VP channels will need to be performed first. Then, 2PA process will generate preferential outgrowth roots for pre-formed microvessels. Given the capabilities of VP and 2PA, also more complex tissue models can be targeted by including cells within the photoresin and/or adding a third channel to form for example an epithelial duct surrounded by microcapillaries (i.e., lung or mammary alveoli).

Chapter 5. The novel Filamented Light (FLight) biofabrication method was exploited to generate cartilaginous constructs with remarkable zonal architecture and native-like mechanical properties. By introducing a photoresin optimized for cartilage applications based on highly reactive hyaluronic acid-norbornene (HA-NB), constructs were printed in only few seconds and induced excellent maturation with deposition of articular cartilage-like extracellular matrix (ECM) rich in glycosaminoglycans (GAGs) and aligned collagen type II fibrils. These promising results will stimulate further research on FLight potential in cartilage-tissue engineering, aiming to fully recapitulate the tissue architecture and eventually implant functional constructs to restore damaged/injured cartilage in patients. To achieve this goal, a multistep procedure combining two orthogonal light projection will be needed, thus creating zones with different architecture within the same construct. Moreover, building on the well-established procedures and high expertise of the group in cartilage tissue engineering, the optimized constructs could be tested *in vitro* for integration potential on human cartilage samples and then *in vivo* for pre-clinical evaluations. FLight is also expected to be successfully applicable to other tissues featuring anisotropic architecture such as muscle, tendon and nerves.

Chapter 6. A simple method to biofabricate macroporous aligned hydrogel with 3D cell guidance properties was introduced. This approach exploited high performance gelatin-norbornene (Gel-NB) / gelatin-thiol (Gel-SH) photo-click bioresin and showed successful maturation of aligned muscle tissue constructs. These results foster further research on more complex, multicellular constructs as well as on other anisotropic tissues such as tendons or nerves. Another future direction could involve the exploration of the effect of various grid geometries. This is expected to determine variations of porosity, pores size and microgel structure, thus eventually lead to different biological outcomes. Moreover, possible multicellular/multimaterial printing is envisioned with the design of compartmentalized cartridges. Different compartments could be filled with the desired bioresins and then jointly pressed through a grid, with potentially region-specific design, to create a complex multimaterial anisotropic construct.

Chapter 7. A novel radical-free (RF) photocrosslinking strategy was introduced to move beyond the deep-rooted paradigm of free-radical photocrosslinking in 3D light-mediated biofabrication. The proposed universal RF crosslinker was synthesized in gram scale and showed high storage stability, enabling potential for marketable off-the-shelf products. Cell-laden photoresins based on synthetic and naturally-derived

polymers were investigated and demonstrated absence of reactive oxygen species (ROS)-related gene upregulation when compared to photoinitiator (PI)-based systems. Optimized RF photoresins were used for high resolution two-photon stereolithography (2P-SL) with remarkably low polymer content. This work offers unprecedented possibilities for light-based tissue engineering and drug/cell delivery applications where radical-sensitive cells and molecules are used. Among the multiple possible research directions offered by the RF approach, its establishment in one-photon stereolithography (DLP, SLA) could have a relevant impact. Intrinsically rich in light-absorbing molecules (photocages), RF photoresins possess very little penetration depth, a desirable property for DLP generally obtained with the addition of photo-absorbing molecules. Moreover, there is a large space for introducing different material compositions by simply synthesizing maleimide derivatives, thus targeting tissue-specific bioresins. Lastly, given the great progress of recent years in the development of photocages sensitive to visible and near-infrared wavelengths, RF approach could be expanded to be applicable in the whole UV to near-IR spectrum.

Chapter 8. A novel, two-photon patterning (2PP) method was introduced to provide spatiotemporal controlled immobilization of bioactive signals in various 3D biological matrices. The use of non-fouling photocage and Sortase A (SA)-based enzymatic coupling resulted in unprecedented orthogonality and signal-to-noise ratio. Peripheral neuron axons were successfully guided by the patterning of nerve growth factor (NGF) in brain-mimetic ECM. This approach offers an elegant way to interrogate the tissue morphogenesis role of complex signalling cues, from small molecules to large growth factors, in 3D matrices. A possible attractive continuation of this work would be to investigate morphogenesis potential in other tissue models. For example, 2PP could be used to direct organoid polarization in a spatiotemporal, user-defined manner, by patterning morphogens such as sonic hedgehog or bone morphogenetic protein. Moreover, another possible direction could be the further optimization of the chemical strategy with the introduction of photodegradable linkers or hydrolysable bonds. With the current strategy, the bioactive signal is immobilized to the matrix via strong avidin-biotin binding pair, making it a substantially static system. However, many biological processes are driven by receptor-ligand binding followed by internalization.

Moreover, although not featuring photochemical reactions, a biomedical adhesive targeting negatively charged tissues was described in **Chapter 9**. Leveraging the clinically compliant transglutaminase-based enzymatic crosslinking, a formulation with fast gelation kinetics, tunable mechanical properties, antibacterial activity and strong adhesion to cartilage was presented. Such biomedical adhesive offers an attractive alternative to suturing and to fibrin glue, the commercially available gold-standard adhesive, thanks to its superior mechanical and biological properties. However, since cartilage lacks self-repair capabilities, an effective cartilage-adhesive applicable to large defects should also support tissue regeneration. Although preliminary data (not shown) showed that the chitosan formulation developed in this work can sustain cartilage maturation from embedded chondrocytes, further experiments will be needed to validate this system.

Overall, the advances introduced with this work offer novel tools, from high performance biocompatible photoresins to novel biofabrication methods, to overcome various current limitations of the field and foster new exciting research toward the end goal of tissue engineering: regenerate and repair human tissues and organs. Considering the pace of recent years progress in the multiple disciplines converging into tissue engineering, this long-sought goal could be expected to be reached, for some tissues, already within the next 20 years.

At the time of writing this outlook, we can print features with subcellular resolution and organ-size constructs, precisely analyse and edit genomes of single cells, simulate complex biomechanics, chemically synthesize and functionalize materials in a wide variety of fast and biocompatible ways, inspect mechanical properties, rationally design hydrogels with desired properties, isolate and culture a vast number of primary and stem cells, perform highly informative imaging using electromagnetic waves from X-rays to radio waves. What else do we need to regenerate a functional human tissue? Maybe not much. Without taking into account regulatory requirements for clinical translation, from a technical point of view what appears to be the main milestone to be reached is the biofabrication of constructs featuring high cellular density and spatial organization. Unprecedented spatial and temporal details given by genomics and transcriptomics uncovered a daunting level of complexity in human tissues and organs, with cells apparently uniform macroscopically, but instead significantly different in their function, gene expression and arrangement. Organs such as kidney, liver or brain are therefore composed of tens of different cell types embedded in a soft, complex 3D architecture. While from a purely manufacturing standpoint such complex architectures can already be replicated, researchers are far from being able to accompany the printing process with the precise positioning of multiple cell types at high density. A *de novo* biofabrication of a whole organ via cell-by-cell deposition remains sci-fi, but advances in stem cells and differentiation technologies can help to bridge the gap. Somehow replicating the *in vivo* formation of an organ, a guided differentiation of stem cells within 3D constructs appears nowadays as a promising strategy to mature functional tissues with the cell spatial heterogeneity necessary to resemble physiological functions.

On the other hand, if for engineering complex organs we still need significant technological advances, simpler tissues presenting lower cell density, lower architectural complexity and stiffer matrices such as cartilage, skin or bone, can probably be obtained with existing technologies. The growing number of companies already focusing on the clinical translation gives an indication of the advanced status of the field, substantially marking the transition into a new era for tissue engineering. The question is no longer if the core paradigm coined three decades ago will prove to be feasible or not, but which tissues and organs will make it, and when, from the bench to the bedside.

To conclude, light-based biofabrication is foreseen to play a fundamental role for the next generation of tissue engineered constructs. In particular, stereolithography represents the most versatile technology, offering high resolution and large construct size. Although technically demanding, with this technique one can theoretically explore the combination of multiple light-triggered processes, from uncaging and crosslinking to degradation, upconversion, ablation or filamentation, in a layer-by-layer fashion. Fast, biocompatible and orthogonal photochemical reactions could be fully exploited with the simultaneous use of multiple wavelengths. The further implementation of high-precision multimaterial and multicellular printing could then allow to generate virtually any organ featuring cellular spatial heterogeneity and matrix architecture. Finally, although light-based techniques are highly versatile, the combination of multiple printing methods is foreseen to play a key role in constructing engineered tissues that better match native biophysical and biochemical properties and functions. Considerable challenges remain and go beyond biofabrication hurdles (i.e., cell sourcing and expansion, regulation requirements), but the great advances of recent years hold great promises for a bright future.

Acknowledgements

This dissertation is the product of four years of work, that was made possible only with the contribution and support of many people. First and foremost, I would like to thank Professor Marcy Zenobi-Wong for giving me the chance to be part of the TEB group. Thank you, Marcy, for the endless support and expert guidance, for your openness to explore new projects and for providing me with the tools needed to support my research. I feel privileged to have done my doctoral studies at ETH and for have being part of the TEB family. From the daily lab work and common projects to retreats and barbeques, the group you assembled and kept together has been of invaluable importance during these four years.

Special thanks go to Professor DeForest and Professor Zhang to have accepted of being part of my examination committee and took the time to go through this document. Your pioneering work has inspired me in these years, and I have been therefore honoured to have had the possibility to discuss my results with you. I would also like to express my gratitude to Prof. Ralph Müller, I hold great respect for your contribution to the field and I truly appreciate your availability for being the chair of my defense session.

None of this would have been possible without the help of my colleagues, from postdocs to students. A bunch of good-hearted people before being great scientists. A big, warm hug to the past and present members of TEB group in which I found friends and great collaborative spirit. You have made it possible to work in a pleasant and joyful environment; I will keep a lot of great memories from these years.

I would also like to deeply thank my family, who despite the physical distance I have always felt here to support me.

And Lisa, you have been my guiding light during these rollercoaster years of up and downs. You have always been there to support and comfort me when things were falling apart, to take me out of the fog when I was losing the path. Your mentoring has been indispensable, pushing me when my lazy side kicked in, bluntly criticized me when I started too many projects, but always the first to cheer for my achievements. I am forever grateful for what you have done, for the joy and perspective you bring to my life and the example of strength and perseverance you are. This work is also yours. There wouldn't have been any Dr. Rizzo without a Dr. Nadal.

References

1. Langer, R.; Vacanti, J. P., Tissue Engineering. *Science* **1993**, *260* (5110), 920-926.
2. Khademhosseini, A.; Langer, R., A decade of progress in tissue engineering. *Nature Protocols* **2016**, *11* (10), 1775-1781.
3. Bianco, P.; Robey, P. G., Stem cells in tissue engineering. *Nature* **2001**, *414* (6859), 118-121.
4. O'Connor, C.; Brady, E.; Zheng, Y.; Moore, E.; Stevens, K. R., Engineering the multiscale complexity of vascular networks. *Nature Reviews Materials* **2022**, *7* (9), 702-716.
5. Cho, S.; Discher, D. E.; Leong, K. W.; Vunjak-Novakovic, G.; Wu, J. C., Challenges and opportunities for the next generation of cardiovascular tissue engineering. *Nature Methods* **2022**, *19* (9), 1064-1071.
6. Tullie, L.; Jones, B. C.; De Coppi, P.; Li, V. S. W., Building gut from scratch — progress and update of intestinal tissue engineering. *Nature Reviews Gastroenterology & Hepatology* **2022**, *19* (7), 417-431.
7. Koons, G. L.; Diba, M.; Mikos, A. G., Materials design for bone-tissue engineering. *Nature Reviews Materials* **2020**, *5* (8), 584-603.
8. Uygun, B. E.; Yarmush, M. L.; Uygun, K., Application of whole-organ tissue engineering in hepatology. *Nature Reviews Gastroenterology & Hepatology* **2012**, *9* (12), 738-744.
9. Camp, J. G.; Wollny, D.; Treutlein, B., Single-cell genomics to guide human stem cell and tissue engineering. *Nature Methods* **2018**, *15* (9), 661-667.
10. Ringe, J.; Burmester, G. R.; Sittinger, M., Regenerative medicine in rheumatic disease—progress in tissue engineering. *Nature Reviews Rheumatology* **2012**, *8* (8), 493-498.
11. Makris, E. A.; Gomoll, A. H.; Malizos, K. N.; Hu, J. C.; Athanasiou, K. A., Repair and tissue engineering techniques for articular cartilage. *Nature Reviews Rheumatology* **2015**, *11* (1), 21-34.
12. Bliley, J. M.; Shiwarski, D. J.; Feinberg, A. W., 3D-bioprinted human tissue and the path toward clinical translation. *Science Translational Medicine* *14* (666), eabo7047.
13. Celikkin, N.; Presutti, D.; Maiullari, F.; Fornetti, E.; Agarwal, T.; Paradiso, A.; Volpi, M.; Świączkowski, W.; Bearzi, C.; Barbetta, A.; Zhang, Y. S.; Gargioli, C.; Rizzi, R.; Costantini, M., Tackling Current Biomedical Challenges With Frontier Biofabrication and Organ-On-A-Chip Technologies. *Frontiers in Bioengineering and Biotechnology* **2021**, *9*.
14. Khademhosseini, A.; Ashammakhi, N.; Karp, J. M.; Gerecht, S.; Ferreira, L.; Annabi, N.; Darabi, M. A.; Sirabella, D.; Vunjak-Novakovic, G.; Langer, R., Chapter 27 - Embryonic stem cells as a cell source for tissue engineering. In *Principles of Tissue Engineering (Fifth Edition)*, Lanza, R.; Langer, R.; Vacanti, J. P.; Atala, A., Eds. Academic Press: 2020; pp 467-490.
15. Moysidou, C.-M.; Barberio, C.; Owens, R. M., Advances in Engineering Human Tissue Models. *Frontiers in Bioengineering and Biotechnology* **2021**, *8*.
16. Zakrzewski, W.; Dobrzyński, M.; Szymonowicz, M.; Rybak, Z., Stem cells: past, present, and future. *Stem Cell Research & Therapy* **2019**, *10* (1), 68.
17. Angelos, M. G.; Kaufman, D. S., Pluripotent stem cell applications for regenerative medicine. *Current Opinion in Organ Transplantation* **2015**, *20* (6).
18. Shi, X.; He, L.; Zhang, S.-M.; Luo, J., Human iPS Cell-derived Tissue Engineered Vascular Graft: Recent Advances and Future Directions. *Stem Cell Reviews and Reports* **2021**, *17* (3), 862-877.
19. Bayir, E.; Sahinler, M.; Celtikoglu, M. M.; Sendemir, A., 27 - Bioreactors in tissue engineering: mimicking the microenvironment. In *Biomaterials for Organ and Tissue Regeneration*, Vrana, N. E.; Knopf-Marques, H.; Barthes, J., Eds. Woodhead Publishing: 2020; pp 709-752.
20. Martin, I.; Wendt, D.; Heberer, M., The role of bioreactors in tissue engineering. *Trends in Biotechnology* **2004**, *22* (2), 80-86.
21. Chaudhuri, J.; Al-Rubeai, M., *Bioreactors for Tissue Engineering: Principles, Design and Operation*. Springer: 2005.

22. Castro, N.; Ribeiro, S.; Fernandes, M. M.; Ribeiro, C.; Cardoso, V.; Correia, V.; Minguez, R.; Lanceros-Mendez, S., Physically Active Bioreactors for Tissue Engineering Applications. *Advanced Biosystems* **2020**, *4* (10), 2000125.
23. Ho, D. L. L.; Lee, S.; Du, J.; Weiss, J. D.; Tam, T.; Sinha, S.; Klinger, D.; Devine, S.; Hamfeldt, A.; Leng, H. T.; Herrmann, J. E.; He, M.; Fradkin, L. G.; Tan, T. K.; Traul, D.; Vicard, Q.; Katikireddy, K.; Skylar-Scott, M. A., Large-Scale Production of Wholly-Cellular Bioinks via the Optimization of Human Induced Pluripotent Stem Cell Aggregate Culture in Automated Bioreactors. *Advanced Healthcare Materials* **2022**, *n/a* (n/a), 2201138.
24. Grzesik, P.; Warth, S. C., One-Time Optimization of Advanced T Cell Culture Media Using a Machine Learning Pipeline. *Frontiers in Bioengineering and Biotechnology* **2021**, *9*.
25. Xiao, Z.; Sabourin, M.; Piras, G.; Gorfien, S. F., Screening and Optimization of Chemically Defined Media and Feeds with Integrated and Statistical Approaches. In *Animal Cell Biotechnology: Methods and Protocols*, Pörtner, R., Ed. Humana Press: Totowa, NJ, 2014; pp 117-135.
26. Wright Muelas, M.; Ortega, F.; Breitling, R.; Bendtsen, C.; Westerhoff, H. V., Rational cell culture optimization enhances experimental reproducibility in cancer cells. *Scientific Reports* **2018**, *8* (1), 3029.
27. Yao, T.; Asayama, Y., Animal-cell culture media: History, characteristics, and current issues. *Reproductive Medicine and Biology* **2017**, *16* (2), 99-117.
28. van der Valk, J.; Brunner, D.; De Smet, K.; Fex Svenningsen, Å.; Honegger, P.; Knudsen, L. E.; Lindl, T.; Noraberg, J.; Price, A.; Scarino, M. L.; Gstraunthaler, G., Optimization of chemically defined cell culture media – Replacing fetal bovine serum in mammalian in vitro methods. *Toxicology in Vitro* **2010**, *24* (4), 1053-1063.
29. Bajic, A.; Tarantino, R.; Chiu, L. L. Y.; Duever, T.; Waldman, S. D., Optimization of culture media to enhance the growth of tissue engineered cartilage. *Biotechnology Progress* **2020**, *36* (5), e3017.
30. Ventura, M.; Boerman, O. C.; de Korte, C.; Rijpkema, M.; Heerschap, A.; Oosterwijk, E.; Jansen, J. A.; Walboomers, X. F., Preclinical Imaging in Bone Tissue Engineering. *Tissue Engineering Part B: Reviews* **2014**, *20* (6), 578-595.
31. Wu, M.; Junker, D.; Branca, R. T.; Karampinos, D. C., Magnetic Resonance Imaging Techniques for Brown Adipose Tissue Detection. *Frontiers in Endocrinology* **2020**, *11*.
32. Garra, B. S., Imaging and Estimation of Tissue Elasticity by Ultrasound. *Ultrasound Quarterly* **2007**, *23* (4).
33. Mostaço-Guidolin, L.; Rosin, N. L.; Hackett, T.-L. Imaging Collagen in Scar Tissue: Developments in Second Harmonic Generation Microscopy for Biomedical Applications *International Journal of Molecular Sciences* [Online], 2017.
34. Hofer, M.; Lutolf, M. P., Engineering organoids. *Nature Reviews Materials* **2021**, *6* (5), 402-420.
35. Skylar-Scott, M. A.; Uzel, S. G. M.; Nam, L. L.; Ahrens, J. H.; Truby, R. L.; Damaraju, S.; Lewis, J. A., Biomufacturing of Organ-Specific Tissues with High Cellular Density and Embedded Vascular Channels. *Sci. Adv.* **2019**, *5*, eaaw2459.
36. Gupta, A.; Lutolf, M. P.; Hughes, A. J.; Sonnen, K. F., Bioengineering in vitro models of embryonic development. *Stem Cell Reports* **2021**, *16* (5), 1104-1116.
37. Rossi, G.; Manfrin, A.; Lutolf, M. P., Progress and potential in organoid research. *Nature Reviews Genetics* **2018**, *19* (11), 671-687.
38. Tang, X.-Y.; Wu, S.; Wang, D.; Chu, C.; Hong, Y.; Tao, M.; Hu, H.; Xu, M.; Guo, X.; Liu, Y., Human organoids in basic research and clinical applications. *Signal Transduction and Targeted Therapy* **2022**, *7* (1), 168.
39. Kim, J.; Koo, B.-K.; Knoblich, J. A., Human organoids: model systems for human biology and medicine. *Nature Reviews Molecular Cell Biology* **2020**, *21* (10), 571-584.
40. Unagolla, J. M.; Jayasuriya, A. C., Recent advances in organoid engineering: A comprehensive review. *Applied Materials Today* **2022**, *29*, 101582.
41. Revah, O.; Gore, F.; Kelley, K. W.; Andersen, J.; Sakai, N.; Chen, X.; Li, M.-Y.; Birey, F.; Yang, X.; Saw, N. L.; Baker, S. W.; Amin, N. D.; Kulkarni, S.; Mudipalli, R.; Cui, B.; Nishino, S.; Grant, G. A.;

- Knowles, J. K.; Shamloo, M.; Huguenard, J. R.; Deisseroth, K.; Paşca, S. P., Maturation and circuit integration of transplanted human cortical organoids. *Nature* **2022**, *610* (7931), 319-326.
42. Zhang, Y.; Huang, Y., Rational Design of Smart Hydrogels for Biomedical Applications. *Frontiers in Chemistry* **2021**, *8*.
43. Lou, J.; Mooney, D. J., Chemical strategies to engineer hydrogels for cell culture. *Nature Reviews Chemistry* **2022**.
44. Zhu, J.; Marchant, R. E., Design properties of hydrogel tissue-engineering scaffolds. *Expert Review of Medical Devices* **2011**, *8* (5), 607-626.
45. Mota, C.; Camarero-Espinosa, S.; Baker, M. B.; Wieringa, P.; Moroni, L., Bioprinting: From Tissue and Organ Development to in Vitro Models. *Chemical Reviews* **2020**, *120* (19), 10547-10607.
46. Wichterle, O.; LÍM, D., Hydrophilic Gels for Biological Use. *Nature* **1960**, *185* (4706), 117-118.
47. Thakur, S.; Thakur, V. K.; Arotiba, O. A., History, Classification, Properties and Application of Hydrogels: An Overview. In *Hydrogels: Recent Advances*, Thakur, V. K.; Thakur, M. K., Eds. Springer Singapore: Singapore, 2018; pp 29-50.
48. Mouw, J. K.; Ou, G.; Weaver, V. M., Extracellular Matrix Assembly: A Multiscale Deconstruction. *Nat. Rev. Mol. Cell Biol.* **2014**, *15*, 771-785.
49. Hynes, R. O., The Extracellular Matrix: Not Just Pretty Fibrils. *Science* **2009**, *326* (5957), 1216-1219.
50. Frantz, C.; Stewart, K. M.; Weaver, V. M., The extracellular matrix at a glance. *Journal of Cell Science* **2010**, *123* (24), 4195-4200.
51. Zhang, W.; Liu, Y.; Zhang, H., Extracellular matrix: an important regulator of cell functions and skeletal muscle development. *Cell & Bioscience* **2021**, *11* (1), 65.
52. Hu, M.; Ling, Z.; Ren, X., Extracellular matrix dynamics: tracking in biological systems and their implications. *Journal of Biological Engineering* **2022**, *16* (1), 13.
53. Watt, F. M.; Huck, W. T. S., Role of the extracellular matrix in regulating stem cell fate. *Nature Reviews Molecular Cell Biology* **2013**, *14* (8), 467-473.
54. Tonti, O. R.; Larson, H.; Lipp, S. N.; Luetkemeyer, C. M.; Makam, M.; Vargas, D.; Wilcox, S. M.; Calve, S., Tissue-specific parameters for the design of ECM-mimetic biomaterials. *Acta Biomaterialia* **2021**, *132*, 83-102.
55. Antons, J.; Marascio, M. G. M.; Nohava, J.; Martin, R.; Applegate, L. A.; Bourban, P. E.; Pioletti, D. P., Zone-dependent mechanical properties of human articular cartilage obtained by indentation measurements. *Journal of Materials Science: Materials in Medicine* **2018**, *29* (5), 57.
56. Poole, A. R.; Kojima, T.; Yasuda, T.; Mwale, F.; Kobayashi, M.; Laverty, S., Composition and Structure of Articular Cartilage: A Template for Tissue Repair. *Clinical Orthopaedics and Related Research*® **2001**, *391*.
57. Baumann, C. A.; Hinckel, B. B.; Bozynski, C. C.; Farr, J., Articular Cartilage: Structure and Restoration. In *Joint Preservation of the Knee: A Clinical Casebook*, Yanke, A. B.; Cole, B. J., Eds. Springer International Publishing: Cham, 2019; pp 3-24.
58. Chaudhuri, O.; Gu, L.; Klumpers, D.; Darnell, M.; Bencherif, S. A.; Weaver, J. C.; Huebsch, N.; Lee, H.-p.; Lippens, E.; Duda, G. N.; Mooney, D. J., Hydrogels with tunable stress relaxation regulate stem cell fate and activity. *Nature Materials* **2016**, *15* (3), 326-334.
59. Broguiere, N.; Husch, A.; Palazzolo, G.; Bradke, F.; Madduri, S.; Zenobi-Wong, M., Macroporous hydrogels derived from aqueous dynamic phase separation. *Biomaterials* **2019**, *200*, 56-65.
60. Annabi, N.; Nichol, J. W.; Zhong, X.; Ji, C.; Koshy, S.; Khademhosseini, A.; Dehghani, F., Controlling the Porosity and Microarchitecture of Hydrogels for Tissue Engineering. *Tissue Engineering Part B: Reviews* **2010**, *16* (4), 371-383.
61. Birch, H. L., Extracellular Matrix and Ageing. In *Biochemistry and Cell Biology of Ageing: Part I Biomedical Science*, Harris, J. R.; Korolchuk, V. I., Eds. Springer Singapore: Singapore, 2018; pp 169-190.
62. Bonnans, C.; Chou, J.; Werb, Z., Remodelling the extracellular matrix in development and disease. *Nature Reviews Molecular Cell Biology* **2014**, *15* (12), 786-801.
63. Theocharis, A. D.; Manou, D.; Karamanos, N. K., The extracellular matrix as a multitasking player in disease. *The FEBS Journal* **2019**, *286* (15), 2830-2869.

64. Cox, T. R.; Erler, J. T., Remodeling and homeostasis of the extracellular matrix: implications for fibrotic diseases and cancer. *Disease Models & Mechanisms* **2011**, *4* (2), 165-178.
65. Benton, G.; Arnaoutova, I.; George, J.; Kleinman, H. K.; Koblinski, J., Matrigel: From discovery and ECM mimicry to assays and models for cancer research. *Advanced Drug Delivery Reviews* **2014**, *79-80*, 3-18.
66. Kim, Y. S.; Majid, M.; Melchiorri, A. J.; Mikos, A. G., Applications of decellularized extracellular matrix in bone and cartilage tissue engineering. *Bioengineering & Translational Medicine* **2019**, *4* (1), 83-95.
67. Zhang, X.; Chen, X.; Hong, H.; Hu, R.; Liu, J.; Liu, C., Decellularized extracellular matrix scaffolds: Recent trends and emerging strategies in tissue engineering. *Bioactive Materials* **2022**, *10*, 15-31.
68. Hussey, G. S.; Dziki, J. L.; Badylak, S. F., Extracellular matrix-based materials for regenerative medicine. *Nature Reviews Materials* **2018**, *3* (7), 159-173.
69. Aisenbrey, E. A.; Murphy, W. L., Synthetic alternatives to Matrigel. *Nature Reviews Materials* **2020**, *5* (7), 539-551.
70. Correa, S.; Grosskopf, A. K.; Lopez Hernandez, H.; Chan, D.; Yu, A. C.; Stapleton, L. M.; Appel, E. A., Translational Applications of Hydrogels. *Chemical Reviews* **2021**, *121* (18), 11385-11457.
71. Kim, B.-S.; Cho, C.-S., Injectable Hydrogels for Regenerative Medicine. *Tissue Engineering and Regenerative Medicine* **2018**, *15* (5), 511-512.
72. Yang, J.-A.; Yeom, J.; Hwang, B. W.; Hoffman, A. S.; Hahn, S. K., In situ-forming injectable hydrogels for regenerative medicine. *Progress in Polymer Science* **2014**, *39* (12), 1973-1986.
73. Yang, J.; Yu, H.; Wang, L.; Liu, J.; Liu, X.; Hong, Y.; Huang, Y.; Ren, S., Advances in adhesive hydrogels for tissue engineering. *European Polymer Journal* **2022**, *172*, 111241.
74. Chen, S.; Gil, C. J.; Ning, L.; Jin, L.; Perez, L.; Kabboul, G.; Tomov, M. L.; Serpooshan, V., Adhesive Tissue Engineered Scaffolds: Mechanisms and Applications. *Frontiers in Bioengineering and Biotechnology* **2021**, *9*.
75. Mooney, D. J.; Vandenburgh, H., Cell Delivery Mechanisms for Tissue Repair. *Cell Stem Cell* **2008**, *2* (3), 205-213.
76. Sivaraj, D.; Chen, K.; Chattopadhyay, A.; Henn, D.; Wu, W.; Noishiki, C.; Magbual, N. J.; Mittal, S.; Mermin-Bunnell, A. M.; Bonham, C. A.; Trotsyuk, A. A.; Barrera, J. A.; Padmanabhan, J.; Januszyk, M.; Gurtner, G. C., Hydrogel Scaffolds to Deliver Cell Therapies for Wound Healing. *Frontiers in Bioengineering and Biotechnology* **2021**, *9*.
77. Rubinstein, M.; Colby, R. H., *Polymer Physics*. OUP Oxford: 2003.
78. Jones, R. A. L., *Soft Condensed Matter*. OUP Oxford: 2002.
79. Sakai, T., *Physics of Polymer Gels*. Wiley: 2020.
80. Ma, Y.; Han, T.; Yang, Q.; Wang, J.; Feng, B.; Jia, Y.; Wei, Z.; Xu, F., Viscoelastic Cell Microenvironment: Hydrogel-Based Strategy for Recapitulating Dynamic ECM Mechanics. *Advanced Functional Materials* **2021**, *31* (24), 2100848.
81. Creton, C., 50th Anniversary Perspective: Networks and Gels: Soft but Dynamic and Tough. *Macromolecules* **2017**, *50* (21), 8297-8316.
82. Zhong, M.; Wang, R.; Kawamoto, K.; Olsen, B. D.; Johnson, J. A., Quantifying the impact of molecular defects on polymer network elasticity. *Science* **2016**, *353* (6305), 1264-1268.
83. Hild, G., Model networks based on 'endlinking' processes: synthesis, structure and properties. *Progress in Polymer Science* **1998**, *23* (6), 1019-1149.
84. Buwalda, S. J.; Boere, K. W. M.; Dijkstra, P. J.; Feijen, J.; Vermonden, T.; Hennink, W. E., Hydrogels in a historical perspective: From simple networks to smart materials. *Journal of Controlled Release* **2014**, *190*, 254-273.
85. Caliaro, S. R.; Burdick, J. A., A practical guide to hydrogels for cell culture. *Nature Methods* **2016**, *13* (5), 405-414.
86. Peppas, N. A.; Hilt, J. Z.; Khademhosseini, A.; Langer, R., Hydrogels in Biology and Medicine: From Molecular Principles to Bionanotechnology. *Advanced Materials* **2006**, *18* (11), 1345-1360.
87. Rosales, A. M.; Anseth, K. S., The design of reversible hydrogels to capture extracellular matrix dynamics. *Nature Reviews Materials* **2016**, *1* (2), 15012.

88. Varghese, S. A.; Rangappa, S. M.; Siengchin, S.; Parameswaranpillai, J., Chapter 2 - Natural polymers and the hydrogels prepared from them. In *Hydrogels Based on Natural Polymers*, Chen, Y., Ed. Elsevier: 2020; pp 17-47.
89. Chen, Y., *Hydrogels Based on Natural Polymers*. Elsevier Science: 2019.
90. Gelse, K.; Pöschl, E.; Aigner, T., Collagens—structure, function, and biosynthesis. *Advanced Drug Delivery Reviews* **2003**, *55* (12), 1531-1546.
91. Shoulders, M. D.; Raines, R. T., Collagen Structure and Stability. *Annual Review of Biochemistry* **2009**, *78* (1), 929-958.
92. Doyle, A. D.; Carvajal, N.; Jin, A.; Matsumoto, K.; Yamada, K. M., Local 3D matrix microenvironment regulates cell migration through spatiotemporal dynamics of contractility-dependent adhesions. *Nature Communications* **2015**, *6* (1), 8720.
93. Dinescu, S.; Albu Kaya, M.; Chitoiu, L.; Ignat, S.; Kaya, D. A.; Costache, M., Collagen-Based Hydrogels and Their Applications for Tissue Engineering and Regenerative Medicine. In *Cellulose-Based Superabsorbent Hydrogels*, Mondal, M. I. H., Ed. Springer International Publishing: Cham, 2019; pp 1643-1664.
94. Sarrigiannidis, S. O.; Rey, J. M.; Dobre, O.; González-García, C.; Dalby, M. J.; Salmeron-Sanchez, M., A tough act to follow: collagen hydrogel modifications to improve mechanical and growth factor loading capabilities. *Materials Today Bio* **2021**, *10*, 100098.
95. Jaipan, P.; Nguyen, A.; Narayan, R. J., Gelatin-based hydrogels for biomedical applications. *MRS Communications* **2017**, *7* (3), 416-426.
96. Van Hoorick, J.; Tytgat, L.; Dobos, A.; Ottevaere, H.; Van Erps, J.; Thienpont, H.; Ovsianikov, A.; Dubruel, P.; Van Vlierberghe, S., (Photo-)crosslinkable gelatin derivatives for biofabrication applications. *Acta Biomaterialia* **2019**, *97*, 46-73.
97. Tsanaktidou, E.; Kammona, O.; Kiparissides, C. Recent Developments in Hyaluronic Acid-Based Hydrogels for Cartilage Tissue Engineering Applications *Polymers* [Online], 2022.
98. Broguiere, N.; Cavalli, E.; Salzmann, G. M.; Applegate, L. A.; Zenobi-Wong, M., Factor XIII Cross-Linked Hyaluronan Hydrogels for Cartilage Tissue Engineering. *ACS Biomater. Sci. Eng.* **2016**, *2*, 2176-2184.
99. Öztürk, E.; Arlov, Ø.; Aksel, S.; Li, L.; Ornitz, D. M.; Skjåk-Bræk, G.; Zenobi-Wong, M., Sulfated Hydrogel Matrices Direct Mitogenicity and Maintenance of Chondrocyte Phenotype through Activation of FGF Signaling. *Advanced Functional Materials* **2016**, *26* (21), 3649-3662.
100. Fisch, P.; Broguiere, N.; Finkielstein, S.; Linder, T.; Zenobi-Wong, M., Bioprinting of Cartilaginous Auricular Constructs Utilizing an Enzymatically Crosslinkable Bioink. *Advanced Functional Materials* **2021**, *31* (16), 2008261.
101. Galarraga, J. H.; Locke, R. C.; Witherel, C. E.; Stoeckl, B. D.; Castilho, M.; Mauck, R. L.; Malda, J.; Levato, R.; Burdick, J. A., Fabrication of MSC-laden composites of hyaluronic acid hydrogels reinforced with MEW scaffolds for cartilage repair. *Biofabrication* **2021**, *14* (1), 014106.
102. Bian, L.; Hou, C.; Tous, E.; Rai, R.; Mauck, R. L.; Burdick, J. A., The influence of hyaluronic acid hydrogel crosslinking density and macromolecular diffusivity on human MSC chondrogenesis and hypertrophy. *Biomaterials* **2013**, *34* (2), 413-421.
103. Palazzolo, G.; Broguiere, N.; Cenciarelli, O.; Dermutz, H.; Zenobi-Wong, M., Ultrasoft Alginate Hydrogels Support Long-Term Three-Dimensional Functional Neuronal Networks. *Tissue Engineering Part A* **2015**, *21* (15-16), 2177-2185.
104. Broguiere, N.; Isenmann, L.; Zenobi-Wong, M., Novel Enzymatically Cross-Linked Hyaluronan Hydrogels Support the Formation of 3D Neuronal Networks. *Biomaterials* **2016**, *99*, 47-55.
105. Kim, C.-H.; Park, S. J.; Yang, D. H.; Chun, H. J., Chitosan for Tissue Engineering. In *Novel Biomaterials for Regenerative Medicine*, Chun, H. J.; Park, K.; Kim, C.-H.; Khang, G., Eds. Springer Singapore: Singapore, 2018; pp 475-485.
106. Croisier, F.; Jérôme, C., Chitosan-based biomaterials for tissue engineering. *European Polymer Journal* **2013**, *49* (4), 780-792.
107. Magnusson, J. P.; Saeed, A. O.; Fernández-Trillo, F.; Alexander, C., Synthetic polymers for biopharmaceutical delivery. *Polymer Chemistry* **2011**, *2* (1), 48-59.

108. Bedell, M. L.; Navara, A. M.; Du, Y.; Zhang, S.; Mikos, A. G., Polymeric Systems for Bioprinting. *Chemical Reviews* **2020**, *120* (19), 10744-10792.
109. Lutolf, M. P.; Hubbell, J. A., Synthetic biomaterials as instructive extracellular microenvironments for morphogenesis in tissue engineering. *Nature Biotechnology* **2005**, *23* (1), 47-55.
110. Georgia, P.; Sonja, S.; Michael, T., Synthetic PEG Hydrogels as Extracellular Matrix Mimics for Tissue Engineering Applications. In *Biotechnology*, Reda Helmy, S., Ed. IntechOpen: Rijeka, 2012; p Ch. 8.
111. Lin, C.-C.; Anseth, K. S., PEG Hydrogels for the Controlled Release of Biomolecules in Regenerative Medicine. *Pharmaceutical Research* **2009**, *26* (3), 631-643.
112. Zhu, J., Bioactive modification of poly(ethylene glycol) hydrogels for tissue engineering. *Biomaterials* **2010**, *31* (17), 4639-4656.
113. GhavamiNejad, A.; Ashammakhi, N.; Wu, X. Y.; Khademhosseini, A., Crosslinking Strategies for 3D Bioprinting of Polymeric Hydrogels. *Small* **2020**, *16* (35), 2002931.
114. Hu, W.; Wang, Z.; Xiao, Y.; Zhang, S.; Wang, J., Advances in crosslinking strategies of biomedical hydrogels. *Biomaterials Science* **2019**, *7* (3), 843-855.
115. Augustine, R.; Alhussain, H.; Zahid, A. A.; Raza Ur Rehman, S.; Ahmed, R.; Hasan, A., Crosslinking Strategies to Develop Hydrogels for Biomedical Applications. In *Nano Hydrogels: Physico-Chemical Properties and Recent Advances in Structural Designing*, Jose, J.; Thomas, S.; Thakur, V. K., Eds. Springer Singapore: Singapore, 2021; pp 21-57.
116. Kolb, H. C.; Finn, M. G.; Sharpless, K. B., Click Chemistry: Diverse Chemical Function from a Few Good Reactions. *Angewandte Chemie International Edition* **2001**, *40* (11), 2004-2021.
117. Jiang, Y.; Chen, J.; Deng, C.; Suuronen, E. J.; Zhong, Z., Click hydrogels, microgels and nanogels: Emerging platforms for drug delivery and tissue engineering. *Biomaterials* **2014**, *35* (18), 4969-4985.
118. Madl, C. M.; Heilshorn, S. C., Bioorthogonal Strategies for Engineering Extracellular Matrices. *Adv. Funct. Mater.* **2018**, *28*.
119. Scinto, S. L.; Bilodeau, D. A.; Hincapie, R.; Lee, W.; Nguyen, S. S.; Xu, M.; am Ende, C. W.; Finn, M. G.; Lang, K.; Lin, Q.; Pezacki, J. P.; Prescher, J. A.; Robillard, M. S.; Fox, J. M., Bioorthogonal chemistry. *Nature Reviews Methods Primers* **2021**, *1* (1), 30.
120. Cadamuro, F.; Russo, L.; Nicotra, F., Biomedical Hydrogels Fabricated Using Diels–Alder Crosslinking. *European Journal of Organic Chemistry* **2021**, *2021* (3), 374-382.
121. Kirchhof, S.; Brandl, F. P.; Hammer, N.; Goepferich, A. M., Investigation of the Diels–Alder reaction as a cross-linking mechanism for degradable poly(ethylene glycol) based hydrogels. *Journal of Materials Chemistry B* **2013**, *1* (37), 4855-4864.
122. Madl, C. M.; Heilshorn, S. C., Rapid Diels–Alder Cross-linking of Cell Encapsulating Hydrogels. *Chemistry of Materials* **2019**, *31* (19), 8035-8043.
123. Smith, L. J.; Taimoory, S. M.; Tam, R. Y.; Baker, A. E. G.; Binth Mohammad, N.; Trant, J. F.; Shoichet, M. S., Diels–Alder Click-Cross-Linked Hydrogels with Increased Reactivity Enable 3D Cell Encapsulation. *Biomacromolecules* **2018**, *19* (3), 926-935.
124. DeForest, C. A.; Anseth, K. S., Cytocompatible Click-Based Hydrogels with Dynamically Tunable Properties Through Orthogonal Photoconjugation and Photocleavage Reactions. *Nat. Chem.* **2011**, *3*, 925-931.
125. DeForest, C. A.; Anseth, K. S., Photoreversible Patterning of Biomolecules within Click-Based Hydrogels. *Angew. Chem. Int. Ed.* **2012**, *51*, 1816-1819.
126. Ulrich, S.; Boturyn, D.; Marra, A.; Renaudet, O.; Dumy, P., Oxime Ligation: A Chemoselective Click-Type Reaction for Accessing Multifunctional Biomolecular Constructs. *Chemistry – A European Journal* **2014**, *20* (1), 34-41.
127. Farahani, P. E.; Adelmund, S. M.; Shadish, J. A.; DeForest, C. A., Photomediated Oxime Ligation as a Bioorthogonal Tool for Spatiotemporally-Controlled Hydrogel Formation and Modification. *J. Mater. Chem. B* **2017**, *5*, 4435-4442.
128. Rezakhani, S.; Gjorevski, N.; Lutolf, M. P., Low-Defect Thiol-Michael Addition Hydrogels as Matrigel Substitutes for Epithelial Organoid Derivation. *Advanced Functional Materials* **2020**, *30* (48), 2000761.

129. Nair, D. P.; Podgórski, M.; Chatani, S.; Gong, T.; Xi, W.; Fenoli, C. R.; Bowman, C. N., The Thiol-Michael Addition Click Reaction: A Powerful and Widely Used Tool in Materials Chemistry. *Chemistry of Materials* **2014**, *26* (1), 724-744.
130. Lutolf, M. P.; Hubbell, J. A., Synthesis and Physicochemical Characterization of End-Linked Poly(ethylene glycol)-co-peptide Hydrogels Formed by Michael-Type Addition. *Biomacromolecules* **2003**, *4* (3), 713-722.
131. Mueller, E.; Poulin, I.; Bodnaryk, W. J.; Hoare, T., Click Chemistry Hydrogels for Extrusion Bioprinting: Progress, Challenges, and Opportunities. *Biomacromolecules* **2022**, *23* (3), 619-640.
132. Lee, M.; Rizzo, R.; Surman, F.; Zenobi-Wong, M., Guiding Lights: Tissue Bioprinting Using Photoactivated Materials. *Chemical Reviews* **2020**, *120* (19), 10950-11027.
133. Elham, B.; Hosseini, M.; Mohajer, M.; Hassanzadeh, S.; Saghati, S.; Hilborn, J.; Khanmohammadi, M., Enzymatic Crosslinked Hydrogels for Biomedical Application. *Polymer Science, Series A* **2021**, *63* (1), S1-S22.
134. Moreira Teixeira, L. S.; Feijen, J.; van Blitterswijk, C. A.; Dijkstra, P. J.; Karperien, M., Enzyme-catalyzed crosslinkable hydrogels: Emerging strategies for tissue engineering. *Biomaterials* **2012**, *33* (5), 1281-1290.
135. Song, W.; Ko, J.; Choi, Y. H.; Hwang, N. S., Recent advancements in enzyme-mediated crosslinkable hydrogels: In vivo-mimicking strategies. *APL Bioengineering* **2021**, *5* (2), 021502.
136. Chen, C.; Wang, J.; Hao, R.; Wang, Z.; Hou, Z.; Zhao, Y.; Zong, C.; Xu, H., Transglutaminase-Triggered Gelation and Functionalization of Designed Self-Assembling Peptides for Guiding Cell Migration. *ACS Applied Bio Materials* **2018**, *1* (6), 2110-2119.
137. Hu, B.-H.; Messersmith, P. B., Rational Design of Transglutaminase Substrate Peptides for Rapid Enzymatic Formation of Hydrogels. *Journal of the American Chemical Society* **2003**, *125* (47), 14298-14299.
138. Chen, C.; Zhang, Y.; Fei, R.; Cao, C.; Wang, M.; Wang, J.; Bai, J.; Cox, H.; Waigh, T.; Lu, J. R.; Xu, H., Hydrogelation of the Short Self-Assembling Peptide I3QGK Regulated by Transglutaminase and Use for Rapid Hemostasis. *ACS Applied Materials & Interfaces* **2016**, *8* (28), 17833-17841.
139. Choi, S.; Ahn, H.; Kim, S.-H., Tyrosinase-mediated hydrogel crosslinking for tissue engineering. *Journal of Applied Polymer Science* **2022**, *139* (14), 51887.
140. Broguiere, N.; Formica, F. A.; Barreto, G.; Zenobi-Wong, M., Sortase A as a cross-linking enzyme in tissue engineering. *Acta Biomaterialia* **2018**, *77*, 182-190.
141. Khanmohammadi, M.; Dastjerdi, M. B.; Ai, A.; Ahmadi, A.; Godarzi, A.; Rahimi, A.; Ai, J., Horseradish peroxidase-catalyzed hydrogelation for biomedical applications. *Biomaterials Science* **2018**, *6* (6), 1286-1298.
142. Griffin, M.; Casadio, R.; Bergamini, C. M., Transglutaminases: Nature's biological glues. *Biochemical Journal* **2002**, *368* (2), 377-396.
143. Hennink, W. E.; van Nostrum, C. F., Novel crosslinking methods to design hydrogels. *Advanced Drug Delivery Reviews* **2012**, *64*, 223-236.
144. Li, X.; Sun, Q.; Li, Q.; Kawazoe, N.; Chen, G., Functional Hydrogels With Tunable Structures and Properties for Tissue Engineering Applications. *Frontiers in Chemistry* **2018**, *6*.
145. Appel, E. A.; del Barrio, J.; Loh, X. J.; Scherman, O. A., Supramolecular polymeric hydrogels. *Chemical Society Reviews* **2012**, *41* (18), 6195-6214.
146. Webber, M. J.; Appel, E. A.; Meijer, E. W.; Langer, R., Supramolecular biomaterials. *Nature Materials* **2016**, *15* (1), 13-26.
147. Sinawang, G.; Osaki, M.; Takashima, Y.; Yamaguchi, H.; Harada, A., Biofunctional hydrogels based on host-guest interactions. *Polymer Journal* **2020**, *52* (8), 839-859.
148. Klouda, L.; Mikos, A. G., Thermoresponsive hydrogels in biomedical applications. *European Journal of Pharmaceutics and Biopharmaceutics* **2008**, *68* (1), 34-45.
149. Liu, Y.; Hsu, S.-h., Synthesis and Biomedical Applications of Self-healing Hydrogels. *Frontiers in Chemistry* **2018**, *6*.
150. Ikura, R.; Park, J.; Osaki, M.; Yamaguchi, H.; Harada, A.; Takashima, Y., Design of self-healing and self-restoring materials utilizing reversible and movable crosslinks. *NPG Asia Materials* **2022**, *14* (1), 10.

151. Sahoo, D. R.; Biswal, T., Alginate and its application to tissue engineering. *SN Applied Sciences* **2021**, *3* (1), 30.
152. Sun, J.; Tan, H. Alginate-Based Biomaterials for Regenerative Medicine Applications *Materials* [Online], 2013, p. 1285-1309.
153. Lee, K. Y.; Mooney, D. J., Alginate: Properties and biomedical applications. *Progress in Polymer Science* **2012**, *37* (1), 106-126.
154. Gacesa, P., Alginates. *Carbohydrate Polymers* **1988**, *8* (3), 161-182.
155. Chaudhuri, O.; Gu, L.; Darnell, M.; Klumpers, D.; Bencherif, S. A.; Weaver, J. C.; Huebsch, N.; Mooney, D. J., Substrate stress relaxation regulates cell spreading. *Nature Communications* **2015**, *6* (1), 6365.
156. Huebsch, N.; Arany, P. R.; Mao, A. S.; Shvartsman, D.; Ali, O. A.; Bencherif, S. A.; Rivera-Feliciano, J.; Mooney, D. J., Harnessing traction-mediated manipulation of the cell/matrix interface to control stem-cell fate. *Nature Materials* **2010**, *9* (6), 518-526.
157. Morgan, F. L. C.; Moroni, L.; Baker, M. B., Dynamic Bioinks to Advance Bioprinting. *Adv. Healthcare Mater.* **2020**, 1901798.
158. Wang, H.; Heilshorn, S. C., Adaptable Hydrogel Networks with Reversible Linkages for Tissue Engineering. *Advanced Materials* **2015**, *27* (25), 3717-3736.
159. Han, Y.; Cao, Y.; Lei, H. Dynamic Covalent Hydrogels: Strong yet Dynamic *Gels* [Online], 2022.
160. Zhang, K.; Feng, Q.; Fang, Z.; Gu, L.; Bian, L., Structurally Dynamic Hydrogels for Biomedical Applications: Pursuing a Fine Balance between Macroscopic Stability and Microscopic Dynamics. *Chemical Reviews* **2021**, *121* (18), 11149-11193.
161. Rizwan, M.; Baker, A. E. G.; Shoichet, M. S., Designing Hydrogels for 3D Cell Culture Using Dynamic Covalent Crosslinking. *Advanced Healthcare Materials* **2021**, *10* (12), 2100234.
162. Sun, J.-Y.; Zhao, X.; Illeperuma, W. R. K.; Chaudhuri, O.; Oh, K. H.; Mooney, D. J.; Vlassak, J. J.; Suo, Z., Highly stretchable and tough hydrogels. *Nature* **2012**, *489* (7414), 133-136.
163. Chen, Q.; Chen, H.; Zhu, L.; Zheng, J., Fundamentals of double network hydrogels. *Journal of Materials Chemistry B* **2015**, *3* (18), 3654-3676.
164. Huang, X.; Li, J.; Luo, J.; Gao, Q.; Mao, A.; Li, J., Research progress on double-network hydrogels. *Materials Today Communications* **2021**, *29*, 102757.
165. Lorenzo Moroni, T. B., Jason A. Burdick, Carmelo De Maria, Brian Derby, Gabor Forgacs, Jürgen Groll, Qing Li, Jos Malda, Vladimir A. Mironov, Carlos Mota, Makoto Nakamura, Wenmiao Shu, Shoji Takeuchi, Tim B.F. Woodfield, Tao Xu, James J. Yoo, Giovanni Vozzi, Biofabrication: A Guide to Technology and Terminology. *Trend Biotechnol* **2017**, *36*, 384.
166. Lorenzo Moroni, J. A. B., Christopher Highley, Sang Jin Lee, Yuya Morimoto, Shoji Takeuchi, James J. Yoo, Biofabrication strategies for 3D in vitro models and regenerative medicine. *Nat. Rev. Mater.* **2018**, *3*, 21.
167. Guvendiren, M., *3D Bioprinting in Medicine: Technologies, Bioinks, and Applications*. Springer International Publishing: 2019.
168. Levato, R.; Jungst, T.; Scheuring, R. G.; Blunk, T.; Groll, J.; Malda, J., From Shape to Function: The Next Step in Bioprinting. *Adv. Mater.* **2020**, *32*, 1906423.
169. Truby, R. L.; Lewis, J. A., Printing soft matter in three dimensions. *Nature* **2016**, *540* (7633), 371-378.
170. Ruskowitz, E. R.; DeForest, C. A., Proteome-Wide Analysis of Cellular Response to Ultraviolet Light for Biomaterial Synthesis and Modification. *ACS Biomater. Sci. Eng.* **2019**, *5*, 2111-2116.
171. Wong, D. Y.; Ranganath, T.; Kasko, A. M., Low-Dose, Long-Wave UV Light Does Not Affect Gene Expression of Human Mesenchymal Stem Cells. *PLoS One* **2015**, *10*, e0139307.
172. Yoshii, E., Cytotoxic effects of acrylates and methacrylates: Relationships of monomer structures and cytotoxicity. *Journal of Biomedical Materials Research* **1997**, *37* (4), 517-524.
173. Bryant, S. J.; Nuttelman, C. R.; Anseth, K. S., Cytocompatibility of UV and Visible Light Photoinitiating Systems on Cultured NIH/3T3 Fibroblasts in Vitro. *J. Biomater. Sci. Polymer Edn.* **2000**, *11*, 439-457.

174. Williams, C. G.; Malik, A. N.; Kim, T. K.; Manson, P. N.; Elisseeff, J. H., Variable Cytocompatibility of Six Cell Lines with Photoinitiators Used for Polymerizing Hydrogels and Cell Encapsulation. *Biomaterials* **2005**, *26*, 1211-1218.
175. Solis, L. H.; Ayala, Y.; Portillo, S.; Varela-Ramirez, A.; Aguilera, R.; Boland, T., Thermal Inkjet Bioprinting Triggers the Activation of the VEGF Pathway in Human Microvascular Endothelial Cells in Vitro. *Biofabrication* **2019**, *11*, 045005.
176. Campbell, A.; Mohl, J. E.; Gutierrez, D. A.; Varela-Ramirez, A.; Boland, T., Thermal Bioprinting Causes Ample Alterations of Expression of LUCAT1, IL6, CCL26, and NRN1L Genes and Massive Phosphorylation of Critical Oncogenic Drug Resistance Pathways in Breast Cancer Cells. *Front. Bioeng. Biotechnol.* **2020**, *8*, 82.
177. Murphy, S. V.; Atala, A., 3D bioprinting of tissues and organs. *Nature Biotechnology* **2014**, *32* (8), 773-785.
178. Zhang, Y. S.; Haghiashtiani, G.; Hübscher, T.; Kelly, D. J.; Lee, J. M.; Lutolf, M.; McAlpine, M. C.; Yeong, W. Y.; Zenobi-Wong, M.; Malda, J., 3D extrusion bioprinting. *Nature Reviews Methods Primers* **2021**, *1* (1), 75.
179. Gudapati, H.; Dey, M.; Ozbolat, I., A Comprehensive Review on Droplet-Based Bioprinting: Past, Present and Future. *Biomaterials* **2016**, *102*, 20-42.
180. Angelopoulos, I.; Allenby, M. C.; Lim, M.; Zamorano, M., Engineering inkjet bioprinting processes toward translational therapies. *Biotechnology and Bioengineering* **2020**, *117* (1), 272-284.
181. Schwab, A.; Levato, R.; D'Este, M.; Piluso, S.; Eglin, D.; Malda, J., Printability and Shape Fidelity of Bioinks in 3D Bioprinting. *Chemical Reviews* **2020**, *120* (19), 11028-11055.
182. Wohlers, T.; Gornet, T., *History of additive manufacturing*. Wohlers Associates, Inc.: 2014; p 1-34.
183. Zhao, J.; He, N., A mini-review of embedded 3D printing: supporting media and strategies. *Journal of Materials Chemistry B* **2020**, *8* (46), 10474-10486.
184. Highley, C. B.; Rodell, C. B.; Burdick, J. A., Direct 3D Printing of Shear-Thinning Hydrogels into Self-Healing Hydrogels. *Advanced Materials* **2015**, *27* (34), 5075-5079.
185. Bhattacharjee, T.; Zehnder, S. M.; Rowe, K. G.; Jain, S.; Nixon, R. M.; Sawyer, W. G.; Angelini, T. E., Writing in the Granular Gel Medium. *Sci. Adv.* **2015**, *1*, e1500655.
186. Lee, A.; Hudson, A. R.; Shiwariski, D. J.; Tashman, J. W.; Hinton, T. J.; Yerneni, S.; Bliley, J. M.; Campbell, P. G.; Feinberg, A. W., 3D Bioprinting of Collagen to Rebuild Components of the Human Heart. *Science* **2019**, *365*, 482-487.
187. Rizzo, R.; Ruetsche, D.; Liu, H.; Zenobi-Wong, M., Optimized Photoclick (Bio)Resins for Fast Volumetric Bioprinting. *Advanced Materials* **2021**, *33* (49), 2102900.
188. Bliley, J. M.; Shiwariski, D. J.; Feinberg, A. W., 3D-bioprinted human tissue and the path toward clinical translation. *Science Translational Medicine* **2022**, *14* (666), eabo7047.
189. Webber, M. J.; Khan, O. F.; Sydlik, S. A.; Tang, B. C.; Langer, R., A Perspective on the Clinical Translation of Scaffolds for Tissue Engineering. *Annals of Biomedical Engineering* **2015**, *43* (3), 641-656.
190. Shafiee, A.; Atala, A., Tissue Engineering: Toward a New Era of Medicine. *Annual Review of Medicine* **2017**, *68* (1), 29-40.
191. Bhatia, S. N.; Ingber, D. E., Microfluidic organs-on-chips. *Nature Biotechnology* **2014**, *32* (8), 760-772.
192. Yu, Y. A.; Shabahang, S.; Timiryasova, T. M.; Zhang, Q.; Beltz, R.; Gentschev, I.; Goebel, W.; Szalay, A. A., Visualization of Tumors and Metastases in Live Animals with Bacteria and Vaccinia Virus Encoding Light-Emitting Proteins. *Nat. Biotechnol.* **2004**, *22*, 313-320.
193. Rice, B. W.; Cable, M. D.; Nelson, M. B., In Vivo Imaging of Light-Emitting Probes. *J. Biomed. Opt.* **2001**, *6*, 432-440.
194. Widder, E. A., Bioluminescence in the Ocean: Origins of Biological, Chemical, and Ecological Diversity. *Science* **2010**, *328*, 704-708.
195. König, K., Multiphoton Microscopy in Life Sciences. *J. of Microscopy* **2000**, *200*, 83-104.
196. Dolmans, D.; Fukumura, D.; Jain, R. K., Photodynamic Therapy for Cancer. *Nat. Rev. Cancer* **2003**, *3*, 380-387.

197. Dougherty, T. J.; Gomer, C. J.; Henderson, B. W.; Jori, G.; Kessel, D.; Korbek, M.; Moan, J.; Peng, Q., Photodynamic Therapy. *J. Natl. Cancer Inst.* **1998**, *90*, 889-905.
198. Agostinis, P.; Berg, K.; Cengel, K. A.; Foster, T. H.; Girotti, A. W.; Gollnick, S. O.; Hahn, S. M.; Hamblin, M. R.; Juzeniene, A.; Kessel, D.; al., e., Photodynamic Therapy of Cancer: An Update. *Cancer J. Clin.* **2011**, *61*, 250-281.
199. Yizhar, O.; Fenno, L. E.; Davidson, T. J.; Mogri, M.; Deisseroth, K., Optogenetics in Neural Systems. *Neuron* **2011**, *71*, 9-34.
200. Deisseroth, K., Optogenetics. *Nat. Methods* **2011**, *8*, 26-29.
201. Deisseroth, K., Optogenetics: 10 Years of Microbial Opsins in Neuroscience. *Nat. Neurosci.* **2015**, *18*, 1213-1225.
202. Polesskaya, O.; Baranova, A.; Bui, S.; Kondratev, N.; Kananykhina, E.; Nazarenko, O.; Shapiro, T.; Nardia, F. B.; Kornienko, V.; Chandhoke, V.; al., e., Optogenetic Regulation of Transcription. *BMC Neurosci* **2018**, *19*, 12.
203. Meshik, X.; O'Neill, P. R.; Gautam, N., Optogenetic Control of Cell Migration. In *Cell Migration: Methods and Protocols*, Gautreau, A., Ed. Springer New York: New York, NY, 2018; pp 313-324.
204. Zhou, X. X.; Zou, X.; Chung, H. K.; Gao, Y.; Liu, Y.; Qi, L. S.; Lin, M. Z., A Single-Chain Photoswitchable CRISPR-Cas9 Architecture for Light-Inducible Gene Editing and Transcription. *ACS Chem. Biol.* **2018**, *13*, 443-448.
205. Arakawa, C. K.; Badeau, B. A.; Zheng, Y.; DeForest, C. A., Multicellular Vascularized Engineered Tissues through User-Programmable Biomaterial Photodegradation. *Adv. Mater.* **2017**, *29*, 1703156.
206. Skylar-Scott, M. A.; Liu, M.-C.; Wu, Y.; Dixit, A.; Yanik, M. F., Guided Homing of Cells in Multi-Photon Microfabricated Bioscaffolds. *Advanced Healthcare Materials* **2016**, *5* (10), 1233-1243.
207. McKinnon, D. D.; Brown, T. E.; Kyburz, K. A.; Kiyotake, E.; Anseth, K. S., Design and Characterization of a Synthetically Accessible, Photodegradable Hydrogel for User-Directed Formation of Neural Networks. *Biomacromolecules* **2014**, *15*, 2808-2816.
208. Miri, A. K.; Nieto, D.; Iglesias, L.; Goodarzi Hosseinabadi, H.; Maharjan, S.; Ruiz-Esparza, G. U.; Khoshakhlagh, P.; Manbachi, A.; Dokmeci, M. R.; Chen, S.; al., e., Microfluidics-Enabled Multimaterial Maskless Stereolithographic Bioprinting. *Adv. Mater.* **2018**, *30*, e1800242.
209. Gao, G.; Kim, H.; Kim, B. S.; Kong, J. S.; Lee, J. Y.; Park, B. W.; Chae, S.; Kim, J.; Ban, K.; Jang, J.; al., e., Tissue-Engineering of Vascular Grafts Containing Endothelium and Smooth-Muscle Using Triple-Coaxial Cell Printing. *Appl. Phys. Rev.* **2019**, *6*, 041402.
210. Zhang, Y. S.; Arneri, A.; Bersini, S.; Shin, S.-R.; Zhu, K.; Goli-Malekabadi, Z.; Aleman, J.; Colosi, C.; Busignani, F.; Dell'Erba, V.; al., e., Bioprinting 3D Microfibrous Scaffolds for Engineering Endothelialized Myocardium and Heart-on-a-Chip. *Biomaterials* **2016**, *110*, 45-59.
211. Fisher, S. A.; Tam, R. Y.; Fokina, A.; Mahmoodi, M. M.; Distefano, M. D.; Shoichet, M. S., Photo-immobilized EGF Chemical Gradients Differentially Impact Breast Cancer Cell Invasion and Drug Response in Defined 3D Hydrogels. *Biomaterials* **2018**, *178*, 751-766.
212. Shadish, J. A.; Benuska, G. M.; DeForest, C. A., Bioactive Site-Specifically Modified Proteins for 4D Patterning of Gel Biomaterials. *Nat. Mater.* **2019**, *18*, 1005-1014.
213. Broguiere, N.; Luchtefeld, I.; Trachsel, L.; Mazunin, D.; Rizzo, R.; Bode, J. W.; Lutolf, M. P.; Zenobi-Wong, M., Morphogenesis Guided by 3D Patterning of Growth Factors in Biological Matrices. *Adv. Mater.* **2020**, 1908299.
214. Tibbitt, M. W.; Kloxin, A. M.; Dyamenahalli, K. U.; Anseth, K. S., Controlled Two-Photon Photodegradation of PEG Hydrogels to Study and Manipulate Subcellular Interactions on Soft Materials. *Soft Matter* **2010**, *6*, 5100-5108.
215. Yoshii, T.; Ikeda, M.; Hamachi, I., Two-Photon-Responsive Supramolecular Hydrogel for Controlling Materials Motion in Micrometer Space. *Angew. Chem.* **2014**, *126*, 7392-7395.
216. Costantini, M.; Testa, S.; Mozetic, P.; Barbetta, A.; Fuoco, C.; Fornetti, E.; Tamiro, F.; Bernardini, S.; Jaroszewicz, J.; Swieszkowski, W.; al., e., Microfluidic-Enhanced 3D Bioprinting of Aligned Myoblast-Laden Hydrogels Leads to Functionally Organized Myofibers in Vitro and in Vivo. *Biomaterials* **2017**, *131*, 98-110.

217. Guven, S.; Chen, P.; Inci, F.; Tasoglu, S.; Erkmén, B.; Demirci, U., Multiscale Assembly for Tissue Engineering and Regenerative Medicine. *Trends Biotechnol* **2015**, *33*, 269-279.
218. Pi, Q.; Maharjan, S.; Yan, X.; Liu, X.; Singh, B.; van Genderen, A. M.; Robledo-Padilla, F.; Parra-Saldivar, R.; Hu, N.; Jia, W.; al., e., Digitally Tunable Microfluidic Bioprinting of Multilayered Cannular Tissues. *Adv. Mater.* **2018**, *30*, e1706913.
219. Qin, X.-H.; Wang, X.; Rottmar, M.; Nelson, B. J.; Maniura-Weber, K., Near-Infrared Light-Sensitive Polyvinyl Alcohol Hydrogel Photoresist for Spatiotemporal Control of Cell-Instructive 3D Microenvironments. *Advanced Materials* **2018**, *30* (10), 1705564.
220. OpenStax, *Anatomy & Physiology*. OpenStax CNX: 2013.
221. Gillies, A. R.; Lieber, R. L., Structure and Function of the Skeletal Muscle Extracellular Matrix. *Muscle Nerve* **2011**, *44*, 318-331.
222. Pappano, A. J.; Wier, W. G., *Cardiovascular Physiology: Mosby Physiology Monograph Series*. Elsevier Health Sciences: 2012.
223. Hunziker, E. B.; Quinn, T. M.; Hauselmann, H. J., Quantitative Structural Organization of Normal Adult Human Articular Cartilage. *Osteoarthr. Cartil.* **2002**, *10*, 564-572.
224. Junatas, K. L.; Tonar, Z.; Kubíková, T.; Liška, V.; Pálek, R.; Mik, P.; Králíčková, M.; Witter, K., Stereological Analysis of Size and Density of Hepatocytes in the Porcine Liver. *J. Anat.* **2017**, *230*, 575-588.
225. Atala, A.; Kasper, F. K.; Mikos, A. G., Engineering Complex Tissues. *Science Translational Medicine* **2012**, *4* (160), 160rv12-160rv12.
226. Meek, K. M., Corneal Collagen-Its Role in Maintaining Corneal Shape and Transparency. *Biophys Rev* **2009**, *1*, 83-93.
227. Wong, R.; Geyer, S.; Weninger, W.; Guimberteau, J.-C.; Wong, J. K., The Dynamic Anatomy and Patterning of Skin. *Exp. Dermatol.* **2016**, *25*, 92-98.
228. Kocgozlu, L.; Saw, Thuan B.; Le, Anh P.; Yow, I.; Shagirov, M.; Wong, E.; Mège, R.-M.; Lim, Chwee T.; Toyama, Y.; al., e., Epithelial Cell Packing Induces Distinct Modes of Cell Extrusions. *Curr. Biol.* **2016**, *26*, 2942-2950.
229. Pourchet, L. J.; Thepot, A.; Albouy, M.; Courtial, E. J.; Boher, A.; Blum, L. J.; Marquette, C. A., Human Skin 3D Bioprinting Using Scaffold-Free Approach. *Advanced Healthcare Materials* **2017**, *6* (4), 1601101.
230. Abaci, H. E.; Coffman, A.; Doucet, Y.; Chen, J.; Jacków, J.; Wang, E.; Guo, Z.; Shin, J. U.; Jahoda, C. A.; al., e., Tissue Engineering of Human Hair Follicles Using a Biomimetic Developmental Approach. *Nat. Commun.* **2018**, *9*, 5301.
231. Wegst, U. G. K.; Bai, H.; Saiz, E.; Tomsia, A. P.; Ritchie, R. O., Bioinspired Structural Materials. *Nat. Mater.* **2015**, *14*, 23-36.
232. Muiznieks, L. D.; Keeley, F. W., Molecular Assembly and Mechanical Properties of the Extracellular Matrix: A Fibrous Protein Perspective. *Biochim. Biophys. Acta.* **2013**, *1832*, 866-875.
233. Byron, A.; Humphries, J. D.; Humphries, M. J., Defining the extracellular matrix using proteomics. *International Journal of Experimental Pathology* **2013**, *94* (2), 75-92.
234. Ascenzi, M. G.; Roe, A. K., The Osteon: The Micromechanical Unit of Compact Bone. *Front. Biosci.* **2012**, *17*, 1551-1581.
235. Eriksen, E. F., Cellular Mechanisms of Bone Remodeling. *Rev Endocr Metab Disord* **2010**, *11*, 219-227.
236. Li, M.; Fu, X.; Gao, H.; Ji, Y.; Li, J.; Wang, Y., Regulation of an Osteon-Like Concentric Microgrooved Surface on Osteogenesis and Osteoclastogenesis. *Biomaterials* **2019**, *216*, 119269.
237. Malarkey, D. E.; Johnson, K.; Ryan, L.; Boorman, G.; Maronpot, R. R., New Insights into Functional Aspects of Liver Morphology. *Toxicol. Pathol.* **2005**, *33*, 27-34.
238. Halpern, K. B.; Shenhav, R.; Matcovitch-Natan, O.; Tóth, B.; Lemze, D.; Golan, M.; Massasa, E. E.; Baydatch, S.; Landen, S.; Moor, A. E.; al., e., Single-Cell Spatial Reconstruction Reveals Global Division of Labour in the Mammalian Liver. *Nature* **2017**, *542*, 352-356.

239. Ma, X.; Qu, X.; Zhu, W.; Li, Y.-S.; Yuan, S.; Zhang, H.; Liu, J.; Wang, P.; Lai, C. S. E.; Zanella, F.; Feng, G.-S.; Sheikh, F.; Chien, S.; Chen, S., Deterministically patterned biomimetic human iPSC-derived hepatic model via rapid 3D bioprinting. *Proceedings of the National Academy of Sciences* **2016**, *113* (8), 2206-2211.
240. Naik, J.; Knight, M.; Drew, N.; Johnsen, N.; Grosberg, A., Cardiac Tissue Organization and Contractility. *Biophys J* **2017**, *112*, 237a.
241. Carmeliet, P.; Jain, R. K., Angiogenesis in Cancer and Other Diseases. *Nature* **2000**, *407*, 249-257.
242. Lemma, E. D.; Spagnolo, B.; Rizzi, F.; Corvaglia, S.; Pisanello, M.; De Vittorio, M.; Pisanello, F., Microenvironmental Stiffness of 3D Polymeric Structures to Study Invasive Rates of Cancer Cells. *Adv. Healthcare Mater.* **2017**, *6*, 1700888.
243. Song, K. H.; Highley, C. B.; Rouff, A.; Burdick, J. A., Complex 3D-Printed Microchannels within Cell-Degradable Hydrogels. *Adv. Funct. Mater.* **2018**, *28*, 1801331.
244. Mosiewicz, K. A.; Kolb, L.; van der Vlies, A. J.; Martino, M. M.; Lienemann, P. S.; Hubbell, J. A.; Ehrbar, M.; Lutolf, M. P., In Situ Cell Manipulation Through Enzymatic Hydrogel Photopatterning. *Nat. Mater.* **2013**, *12*, 1072-1078.
245. Blasco, E.; Wegener, M.; Barner-Kowollik, C., Photochemically Driven Polymeric Network Formation: Synthesis and Applications. *Adv. Mater.* **2017**, *29*, 1604005.
246. Nguyen, K. T.; West, J. L., Photopolymerizable Hydrogels for Tissue Engineering Applications. *Biomaterials* **2002**, *23*, 4307-4314.
247. Shirai, M., Photoinitiated Polymerization. In *Encyclopedia of Polymeric Nanomaterials*, Kobayashi, S.; Müllen, K., Eds. Springer Berlin Heidelberg: Berlin, Heidelberg, 2015; pp 1579-1585.
248. Moad, G.; Solomon, D. H., *The Chemistry of Radical Polymerization*. 2nd ed.; Elsevier Science: 2005.
249. O'Brien, A. K.; Bowman, C. N., Modeling the Effect of Oxygen on Photopolymerization Kinetics. *Macromol. Theory Simul.* **2006**, *15*, 176-182.
250. O'Brien, A. K.; Cramer, N. B.; Bowman, C. N., Oxygen Inhibition in Thiol-Acrylate Photopolymerizations. *J. Polym. Sci. A Polym. Chem.* **2006**, *44*, 2007-2014.
251. O'Brien, A. K.; Bowman, C. N., Impact of Oxygen on Photopolymerization Kinetics and Polymer Structure. *Macromolecules* **2006**, *39*, 2501-2506.
252. de Kock, J. B. L.; Van Herk, A. M.; German, A. L., Bimolecular Free-Radical Termination at Low Conversion. *J. Macromol. Sci. Part C* **2001**, *41*, 199-252.
253. Andrzejewska, E., Photopolymerization Kinetics of Multifunctional Monomers. *Prog. Polym. Sci.* **2001**, *26*, 605-665.
254. Gou, L.; Coretsopoulos, C. N.; Scranton, A. B., Measurement of the Dissolved Oxygen Concentration in Acrylate Monomers with a Novel Photochemical Method. *J. Polym. Sci. A Polym. Chem.* **2004**, *42*, 1285-1292.
255. Aguirre-Soto, A.; Kim, S.; Kaastrup, K.; Sikes, H. D., On the Role of N-Vinylpyrrolidone in the Aqueous Radical-Initiated Copolymerization with PEGDA Mediated by Eosin Y in the Presence of O₂. *Polym. Chem.* **2019**, *10*, 926-937.
256. White, T. J.; Liechty, W. B.; Guymon, C. A., The Influence of N-Vinyl Pyrrolidone on Polymerization Kinetics and Thermo-Mechanical Properties of Crosslinked Acrylate Polymers. *J. Polym. Sci. A Polym. Chem.* **2007**, *45*, 4062-4073.
257. Kloosterboer, J. G. In *Network Formation by Chain Crosslinking Photopolymerization and Its Applications in Electronics*, Electronic Applications, Berlin, Heidelberg, Springer Berlin Heidelberg: Berlin, Heidelberg, 1988; pp 1-61.
258. Decker, C.; Jenkins, A. D., Kinetic Approach of Oxygen Inhibition in Ultraviolet- and Laser-Induced Polymerizations. *Macromolecules* **1985**, *18*, 1241-1244.
259. Salinas, C. N.; Anseth, K. S., Mixed Mode Thiol-Acrylate Photopolymerizations for the Synthesis of PEG-Peptide Hydrogels. *Macromolecules* **2008**, *41*, 6019-6026.
260. Fouassier, J. P.; Rabek, J. F., *Radiation Curing in Polymer Science and Technology*. Springer Netherlands: 1993.

261. Anandkumar R. Kannurpatti, J. W. A., Christopher N. Bowman, A Study of the Evolution of Mechanical Properties and Structural Heterogeneity of Polymer Networks Formed by Photopolymerizations of Multifunctional (Meth)Acrylates. *Polymer* **1998**, *39*, 2507-2513.
262. Bowman, C. N.; Peppas, N. A., Coupling of Kinetics and Volume Relaxation during Polymerizations of Multiacrylates and Multimethacrylates. *Macromolecules* **1991**, *24*, 1914-1920.
263. Lee, T. Y.; Roper, T. M.; Jönsson, E. S.; Guymon, C. A.; Hoyle, C. E., Influence of Hydrogen Bonding on Photopolymerization Rate of Hydroxyalkyl Acrylates. *Macromolecules* **2004**, *37*, 3659-3665.
264. Lu, H.; Stansbury, J. W.; Bowman, C. N., Towards the Elucidation of Shrinkage Stress Development and Relaxation in Dental Composites. *Dental Materials* **2004**, *20*, 979-986.
265. Sawicki, L. A.; Kloxin, A. M., Design of Thiol–Ene Photoclick Hydrogels Using Facile Techniques for Cell Culture Applications. *Biomater. Sci.* **2014**, *2*, 1612-1626.
266. Kharkar, P. M.; Rehmann, M. S.; Skeens, K. M.; Maverakis, E.; Kloxin, A. M., Thiol–Ene Click Hydrogels for Therapeutic Delivery. *ACS Biomater. Sci. Eng.* **2016**, *2*, 165-179.
267. Hoyle, C. E.; Lee, T. Y.; Roper, T., Thiol–Enes: Chemistry of the Past with Promise for the Future. *J. Polym. Sci. A Polym. Chem.* **2004**, *42*, 5301-5338.
268. Hoyle, C. E.; Bowman, C. N., Thiol–Ene Click Chemistry. *Angew. Chem. Int. Ed.* **2010**, *49*, 1540-1573.
269. Deng, J.-R.; Chung, S.-F.; Leung, A. S.-L.; Yip, W.-M.; Yang, B.; Choi, M.-C.; Cui, J.-F.; Kung, K. K.-Y.; Zhang, Z.; Lo, K.-W.; al., e., Chemoselective and Photocleavable Cysteine Modification of Peptides and Proteins Using Isoxazoliniums. *Comm. Chem.* **2019**, *2*, 93.
270. Anderson, S. B.; Lin, C.-C.; Kuntzler, D. V.; Anseth, K. S., The Performance of Human Mesenchymal Stem Cells Encapsulated in Cell-Degradable Polymer-Peptide Hydrogels. *Biomaterials* **2011**, *32*, 3564-3574.
271. Schwartz, M. P.; Fairbanks, B. D.; Rogers, R. E.; Rangarajan, R.; Zaman, M. H.; Anseth, K. S., A Synthetic Strategy for Mimicking the Extracellular Matrix Provides New Insight about Tumor Cell Migration. *Integr. Biol.* **2009**, *2*, 32-40.
272. Fairbanks, B. D.; Schwartz, M. P.; Halevi, A. E.; Nuttelman, C. R.; Bowman, C. N.; Anseth, K. S., A Versatile Synthetic Extracellular Matrix Mimic via Thiol-Norbornene Photopolymerization. *Adv. Mater.* **2009**, *21*, 5005-5010.
273. Lin, C.-C.; Raza, A.; Shih, H., PEG Hydrogels Formed by Thiol-Ene Photo-Click Chemistry and Their Effect on the Formation and Recovery of Insulin-Secreting Cell Spheroids. *Biomaterials* **2011**, *32*, 9685-9695.
274. Wiley, K. L.; Ovadia, E. M.; Calo, C. J.; Huber, R. E.; Kloxin, A. M., Rate-Based Approach for Controlling the Mechanical Properties of ‘Thiol–Ene’ Hydrogels Formed with Visible Light. *Polym. Chem.* **2019**, *10*, 4428-4440.
275. Reddy, K. S.; Okay, O.; Bowman, C. N., Network Development in Mixed Step-Chain Growth Thiol-Vinyl Photopolymerizations. *Macromolecules* **2006**, *39*, 8832-8843.
276. Rydholm, A. E.; Reddy, S. K.; Anseth, K. S.; Bowman, C. N., Controlling Network Structure in Degradable Thiol–Acrylate Biomaterials to Tune Mass Loss Behavior. *Biomacromolecules* **2006**, *7*, 2827-2836.
277. Chu, S.; Maples, M. M.; Bryant, S. J., Cell Encapsulation Spatially Alters Crosslink Density of Poly(Ethylene Glycol) Hydrogels Formed from Free-radical Polymerizations. *Acta Biomater.* **2020**, *109*, 37-50.
278. Fairbanks, B. D.; Scott, T. F.; Kloxin, C. J.; Anseth, K. S.; Bowman, C. N., Thiol–Yne Photopolymerizations: Novel Mechanism, Kinetics, and Step-Growth Formation of Highly Cross-Linked Networks. *Macromolecules* **2009**, *42*, 211-217.
279. Xi, W.; Krieger, M.; Kloxin, C. J.; Bowman, C. N., A New Photoclick Reaction Strategy: Photo-Induced Catalysis of the Thiol-Michael Addition Via a Caged Primary Amine. *Chem Comm.* **2013**, *49*, 4504-4506.
280. Vrabel, M.; Carell, T., *Cycloadditions in Bioorthogonal Chemistry*. Springer International Publishing: 2016.

281. Madl, C. M.; Katz, L. M.; Heilshorn, S. C., Bio-Orthogonally Crosslinked, Engineered Protein Hydrogels with Tunable Mechanics and Biochemistry for Cell Encapsulation. *Adv. Funct. Mater.* **2016**, *26*, 3612-3620.
282. Bjercknes, M.; Cheng, H.; McNitt, C. D.; Popik, V. V., Facile Quenching and Spatial Patterning of Cylooctynes via Strain-Promoted Alkyne–Azide Cycloaddition of Inorganic Azides. *Bioconjug. Chem.* **2017**, *28*, 1560-1565.
283. Sutton, D. A.; Yu, S.-H.; Steet, R.; Popik, V. V., Cyclopropanone-caged Sondheimer diyne (dibenzo[a,e]cyclooctadiyne): a photoactivatable linchpin for efficient SPAAC crosslinking. *Chemical Communications* **2016**, *52* (3), 553-556.
284. McNitt, C. D.; Cheng, H.; Ullrich, S.; Popik, V. V.; Bjercknes, M., Multiphoton Activation of Photo-Strain-Promoted Azide Alkyne Cycloaddition “Click” Reagents Enables in Situ Labeling with Submicrometer Resolution. *J. Am. Chem. Soc.* **2017**, *139*, 14029-14032.
285. Clovis, J. S.; Eckell, A.; Huisgen, R.; Sustmann, R., 1.3-Dipolare Cycloadditionen, XXV. Der Nachweis des freien Diphenylnitrilimins als Zwischenstufe bei Cycloadditionen. *Chem. Berichte* **1967**, *100*, 60-70.
286. Song, W.; Wang, Y.; Qu, J.; Lin, Q., Selective Functionalization of a Genetically Encoded Alkene-Containing Protein via “Photoclick Chemistry” in Bacterial Cells. *J. Am. Chem. Soc.* **2008**, *130*, 9654-9655.
287. Wang, J.; Zhang, W.; Song, W.; Wang, Y.; Yu, Z.; Li, J.; Wu, M.; Wang, L.; Zang, J.; Lin, Q., A Biosynthetic Route to Photoclick Chemistry on Proteins. *J. Am. Chem. Soc.* **2010**, *132*, 14812-14818.
288. Wang, Y.; Song, W.; Hu, W. J.; Lin, Q., Fast Alkene Functionalization In Vivo by Photoclick Chemistry: HOMO Lifting of Nitrile Imine Dipoles. *Angew. Chem. Int. Ed.* **2009**, *48*, 5330-5333.
289. Lim, R. K. V.; Lin, Q., Photoinducible Bioorthogonal Chemistry: A Spatiotemporally Controllable Tool to Visualize and Perturb Proteins in Live Cells. *Acc. Chem. Res.* **2011**, *44*, 828-839.
290. Fan, Y.; Deng, C.; Cheng, R.; Meng, F.; Zhong, Z., In Situ Forming Hydrogels via Catalyst-Free and Bioorthogonal “Tetrazole–Alkene” Photo-Click Chemistry. *Biomacromolecules* **2013**, *14*, 2814-2821.
291. Yu, Z.; Ohulchanskyy, T. Y.; An, P.; Prasad, P. N.; Lin, Q., Fluorogenic, Two-Photon-Triggered Photoclick Chemistry in Live Mammalian Cells. *J. Am. Chem. Soc.* **2013**, *135*, 16766-16769.
292. Devaraj, N. K.; Weissleder, R.; Hilderbrand, S. A., Tetrazine-Based Cycloadditions: Application to Pretargeted Live Cell Imaging. *Bioconjug. Chem.* **2008**, *19*, 2297-2299.
293. Blackman, M. L.; Royzen, M.; Fox, J. M., Tetrazine Ligation: Fast Bioconjugation Based on Inverse-Electron-Demand Diels–Alder Reactivity. *J. Am. Chem. Soc.* **2008**, *130*, 13518-13519.
294. Truong, V. X.; Tsang, K. M.; Ercole, F.; Forsythe, J. S., Red Light Activation of Tetrazine–Norbornene Conjugation for Bioorthogonal Polymer Cross-Linking across Tissue. *Chem. Mater.* **2017**, *29*, 3678-3685.
295. Truong, V. X.; Li, F.; Forsythe, J. S., Versatile Bioorthogonal Hydrogel Platform by Catalyst-Free Visible Light Initiated Photodimerization of Anthracene. *ACS Macro Lett.* **2017**, *6*, 657-662.
296. Adzima, B. J.; Tao, Y.; Kloxin, C. J.; DeForest, C. A.; Anseth, K. S.; Bowman, C. N., Spatial and Temporal Control of the Alkyne–Azide Cycloaddition by Photoinitiated Cu(II) Reduction. *Nat. Chem.* **2011**, *3*, 256-259.
297. Loebel, C.; Broguiere, N.; Alini, M.; Zenobi-Wong, M.; Eglin, D., Microfabrication of Photo-Cross-Linked Hyaluronan Hydrogels by Single- and Two-Photon Tyramine Oxidation. *Biomacromolecules* **2015**, *16* (9), 2624-2630.
298. Wang, J.; Stanic, S.; Altun, A. A.; Schwentenwein, M.; Dietliker, K.; Jin, L.; Stampfl, J.; Baudis, S.; Liska, R.; Grützmacher, H., A Highly Efficient Waterborne Photoinitiator for Visible-Light-Induced Three-Dimensional Printing of Hydrogels. *Chem. Comm.* **2018**, *54*, 920-923.
299. Decker, C.; Masson, F.; Schwalm, R., How to Speed up the UV Curing of Water-Based Acrylic Coatings. *JCT Res.* **2004**, *1*, 127-136.
300. Avens, H. J.; Bowman, C. N., Mechanism of Cyclic Dye Regeneration During Eosin-Sensitized Photoinitiation in the Presence of Polymerization Inhibitors. *J. Polym. Sci. A Polym. Chem.* **2009**, *47*, 6083-6094.

301. Chesneau, E.; Fouassier, J. P., Polymérisation Induite Sous Irradiation Laser Visible. 2. Sensibilisation Par Les Colorants. *Angew. Makromol. Chem.* **1985**, *135*.
302. Lu, Y.; Hasegawa, F.; Goto, T.; Ohkuma, S.; Fukuhara, S.; Kawazu, Y.; Totani, K.; Yamashita, T.; Watanabe, T., Highly Sensitive Measurement in Two-Photon Absorption Cross Section and Investigation of the Mechanism of Two-Photon-Induced Polymerization. *J. Lumin.* **2004**, *110*, 1-10.
303. Benedikt, S.; Wang, J.; Markovic, M.; Moszner, N.; Dietliker, K.; Ovsianikov, A.; Grützmacher, H.; Liska, R., Highly Efficient Water-Soluble Visible Light Photoinitiators. *J. Polym. Sci. Part A: Polym. Chem.* **2016**, *54*, 473-479.
304. Azo Polymerization Initiators Comprehensive Catalog. Wako Pure Chemicals Industries, L., Ed.
305. Lim, K. S.; Klotz, B. J.; Lindberg, G. C. J.; Melchels, F. P. W.; Hooper, G. J.; Malda, J.; Gawlitta, D.; Woodfield, T. B. F., Visible Light Cross-Linking of Gelatin Hydrogels Offers an Enhanced Cell Microenvironment with Improved Light Penetration Depth. *Macromol. Biosci.* **2019**, *19*, e1900098.
306. Balzani, V.; Ceroni, P.; Gestermann, S.; Gorka, M.; Kauffmann, C.; Vögtle, F., Fluorescent Guests Hosted in Fluorescent Dendrimers. *Tetrahedron* **2002**, *58*, 629-637.
307. Chen, Y.; Shen, Z.; Pastor-Pérez, L.; Frey, H.; Stiriba, S.-E., Role of Topology and Amphiphilicity for Guest Encapsulation in Functionalized Hyperbranched Poly(Ethylenimine)s. *Macromolecules* **2005**, *38*, 227-229.
308. Krowczynski, L., [Technological methods for improving the solubility and increasing the dissolution rate of slightly soluble drugs (author's transl)]. *Die Pharmazie* **1982**, *37* (1), 79-83.
309. Koziol, J., Studies on Flavins in Organic Solvents-I*. Spectral Characteristics of Riboflavin, Riboflavin Tetrabutryate and Lumichrome. *Photochem. Photobiol.* **1966**, *5*, 41-54.
310. Benedikt, S.; Wang, J.; Markovic, M.; Moszner, N.; Dietliker, K.; Ovsianikov, A.; Grützmacher, H.; Liska, R., Highly efficient water-soluble visible light photoinitiators. *Journal of Polymer Science Part A: Polymer Chemistry* **2016**, *54* (4), 473-479.
311. Billiet, T.; Gevaert, E.; De Schryver, T.; Cornelissen, M.; Dubruel, P., The 3D Printing of Gelatin Methacrylamide Cell-Laden Tissue-Engineered Constructs with High Cell Viability. *Biomaterials* **2014**, *35*, 49-62.
312. Fancy, D. A.; Denison, C.; Kim, K.; Xie, Y.; Holdeman, T.; Amini, F.; Kodadek, T., Scope, Limitations and Mechanistic Aspects of the Photo-Induced Cross-Linking of Proteins by Water-Soluble Metal Complexes. *Chem. Biol.* **2000**, *7*, 697-708.
313. Wang, Z.; Abdulla, R.; Parker, B.; Samanipour, R.; Ghosh, S.; Kim, K., A Simple and High-Resolution Stereolithography-Based 3D Bioprinting System Using Visible Light Crosslinkable Bioinks. *Biofabrication* **2015**, *7*, 045009.
314. Nguyen, A. K.; Gittard, S. D.; Koroleva, A.; Schlie, S.; Gaidukeviciute, A.; Chichkov, B. N.; Narayan, R. J., Two-photon polymerization of polyethylene glycol diacrylate scaffolds with riboflavin and triethanolamine used as a water-soluble photoinitiator. *Regenerative Medicine* **2013**, *8* (6), 725-738.
315. Pawar, A. A.; Halivni, S.; Waiskopf, N.; Ben-Shahar, Y.; Soreni-Harari, M.; Bergbreiter, S.; Banin, U.; Magdassi, S., Rapid Three-Dimensional Printing in Water Using Semiconductor-Metal Hybrid Nanoparticles as Photoinitiators. *Nano Lett.* **2017**, *17*, 4497-4501.
316. Shpichka, A.; Koroleva, A.; Kuznetsova, D.; Burdukovskii, V.; Chichkov, B.; Bagratashvili, V.; Timashev, P., Two-Photon Polymerization in Tissue Engineering. In *Polymer and Photonic Materials Towards Biomedical Breakthroughs*, Van Hoorick, J.; Ottevaere, H.; Thienpont, H.; Dubruel, P.; Van Vlierberghe, S., Eds. Springer, Cham: 2018; pp 71-98.
317. Ash, C.; Dubec, M.; Donne, K.; Bashford, T., Effect of Wavelength and Beam Width on Penetration in Light-Tissue Interaction Using Computational Methods. *Lasers Med. Sci.* **2017**, *32*, 1909-1918.
318. Ovsianikov, A.; Mironov, V.; Stampfl, J.; Liska, R., Engineering 3D Cell-Culture Matrices: Multiphoton Processing Technologies for Biological and Tissue Engineering Applications. *Expert Rev. Med. Devices* **2012**, *9*, 613-633.
319. Stampfl, J.; Liska, R.; Ovsianikov, A., *Multiphoton Lithography: Techniques, Materials, and Applications*. Wiley-VCH: 2016.

320. Steiger, W.; Gruber, P.; Theiner, D.; Dobos, A.; Lunzer, M.; Van Hoorick, J.; Van Vlierberghe, S.; Liska, R.; Ovsianikov, A., Fully Automated Z-Scan Setup Based on a Tunable Fs-Oscillator. *Opt. Mater. Express* **2019**, *9*, 3567-3581.
321. Li, Z.; Torgersen, J.; Ajami, A.; Mühleder, S.; Qin, X.; Husinsky, W.; Holnthoner, W.; Ovsianikov, A.; Stampfl, J.; Liska, R., Initiation Efficiency and Cytotoxicity of Novel Water-Soluble Two-Photon Photoinitiators for Direct 3D Microfabrication of Hydrogels. *RSC Adv.* **2013**, *3*, 15939-15946.
322. Xing, J.; Liu, J.; Zhang, T.; Zhang, L.; Zheng, M.; Duan, X., A Water Soluble Initiator Prepared Through Host–Guest Chemical Interaction for Microfabrication of 3D Hydrogels Via Two-Photon Polymerization. *J. Mater. Chem. B* **2014**, *2*, 4318-4323.
323. Ajami, A.; Husinsky, W.; Tromayer, M.; Gruber, P.; Liska, R.; Ovsianikov, A., Measurement of degenerate two-photon absorption spectra of a series of developed two-photon initiators using a dispersive white light continuum Z-scan. *Applied Physics Letters* **2017**, *111* (7), 071901.
324. Huang, X.; Wang, X.; Zhao, Y., Study on a Series of Water-Soluble Photoinitiators for Fabrication of 3D Hydrogels by Two-Photon Polymerization. *Dyes Pig.* **2017**, *141*, 413-419.
325. Wan, X.; Zhao, Y.; Xue, J.; Wu, F.; Fang, X., Water-Soluble Benzylidene Cyclopentanone Dye for Two-Photon Photopolymerization. *J. Photochem. Photobiol. A: Chem* **2009**, *202*, 74-79.
326. Tromayer, M.; Gruber, P.; Markovic, M.; Rosspeintner, A.; Vauthey, E.; Redl, H.; Ovsianikov, A.; Liska, R., A Biocompatible Macromolecular Two-Photon Initiator Based on Hyaluronan. *Polym. Chem.* **2017**, *8*, 451-460.
327. Woo, H. Y.; Liu, B.; Kohler, B.; Korystov, D.; Mikhailovsky, A.; Bazan, G. C., Solvent Effects on the Two-Photon Absorption of Distyrylbenzene Chromophores. *Journal of the American Chemical Society* **2005**, *127* (42), 14721-14729.
328. Jan, T.; Aleksandr, O.; Vladimir, M.; Niklas, P.; Xiaohua, Q.; Zhiquan, L.; Klaus, C.; Thomas, M.; Robert, L.; Verena, J.; Jürgen, S., Photo-sensitive hydrogels for three-dimensional laser microfabrication in the presence of whole organisms. *Journal of Biomedical Optics* **2012**, *17* (10), 105008.
329. Tromayer, M.; Dobos, A.; Gruber, P.; Ajami, A.; Dedic, R.; Ovsianikov, A.; Liska, R., A Biocompatible Diazosulfonate Initiator for Direct Encapsulation of Human Stem Cells Via Two-Photon Polymerization. *Polym. Chem.* **2018**, *9*, 3108-3117.
330. Brown, T. E.; Anseth, K. S., Spatiotemporal hydrogel biomaterials for regenerative medicine. *Chemical Society Reviews* **2017**, *46* (21), 6532-6552.
331. Cai, Z.; Huang, K.; Bao, C.; Wang, X.; Sun, X.; Xia, H.; Lin, Q.; Yang, Y.; Zhu, L., Precise Construction of Cell-Instructive 3D Microenvironments by Photopatterning a Biodegradable Hydrogel. *Chem. Mater.* **2019**, *31*, 4710-4719.
332. Lee, T. T.; García, J. R.; Paez, J. I.; Singh, A.; Phelps, E. A.; Weis, S.; Shafiq, Z.; Shekaran, A.; del Campo, A.; García, A. J., Light-triggered in vivo activation of adhesive peptides regulates cell adhesion, inflammation and vascularization of biomaterials. *Nature Materials* **2015**, *14* (3), 352-360.
333. Wylie, R. G.; Shoichet, M. S., Three-Dimensional Spatial Patterning of Proteins in Hydrogels. *Biomacromolecules* **2011**, *12*, 3789-3796.
334. Horn-Ranney, E. L.; Khoshakhlagh, P.; Kaiga, J. W.; Moore, M. J., Light-Reactive Dextran Gels with Immobilized Guidance Cues for Directed Neurite Growth in 3D Models. *Biomat. Sci.* **2014**, *2*, 1450-1459.
335. Mosiewicz, K. A.; Kolb, L.; van der Vlies, A. J.; Lutolf, M. P., Microscale Patterning of Hydrogel Stiffness Through Light-Triggered Uncaging of Thiols. *Biomat. Sci.* **2014**, *2*, 1640-1651.
336. Klán, P.; Šolomek, T.; Bochet, C. G.; Blanc, A.; Givens, R.; Rubina, M.; Popik, V.; Kostikov, A.; Wirz, J., Photoremovable Protecting Groups in Chemistry and Biology: Reaction Mechanisms and Efficacy. *Chem. Rev.* **2013**, *113*, 119-191.
337. Kloxin, A. M.; Kasko, A. M.; Salinas, C. N.; Anseth, K. S., Photodegradable Hydrogels for Dynamic Tuning of Physical and Chemical Properties. *Science* **2009**, *324*, 59-63.
338. Zhu, C.; Ninh, C.; Bettinger, C. J., Photoreconfigurable Polymers for Biomedical Applications: Chemistry and Macromolecular Engineering. *Biomacromolecules* **2014**, *15*, 3474-3494.

339. Kharkar, P. M.; Kiick, K. L.; Kloxin, A. M., Designing Degradable Hydrogels for Orthogonal Control of Cell Microenvironments. *Chem. Soc. Rev.* **2013**, *42*, 7335-7372.
340. Tsang, K. M. C.; Annabi, N.; Ercole, F.; Zhou, K.; Karst, D. J.; Li, F.; Haynes, J. M.; Evans, R. A.; Thissen, H.; Khademhosseini, A.; Forsythe, J. S., Facile One-Step Micropatterning Using Photodegradable Gelatin Hydrogels for Improved Cardiomyocyte Organization and Alignment. *Advanced Functional Materials* **2015**, *25* (6), 977-986.
341. Lunzer, M.; Shi, L.; Andriotis, O. G.; Gruber, P.; Markovic, M.; Thurner, P. J.; Ossipov, D.; Liska, R.; Ovsianikov, A., A Modular Approach to Sensitized Two-Photon Patterning of Photodegradable Hydrogels. *Angew. Chem. Int. Ed.* **2018**, *57*, 15122-15127.
342. Cheng, Y.; He, C.; Ren, K.; Rong, Y.; Xiao, C.; Ding, J.; Zhuang, X.; Chen, X., Injectable Enzymatically Cross-Linked Hydrogels with Light-Controlled Degradation Profile. *Macromol. Rapid. Comm.* **2018**, *39*, 1800272.
343. Zeng, X.; Zhou, X.; Wu, S., Red and Near-Infrared Light-Cleavable Polymers. *Macromol. Rapid. Comm.* **2018**, *39*, 1800034.
344. Takezaki, M.; Hirota, N.; Terazima, M., Nonradiative Relaxation Processes and Electronically Excited States of Nitrobenzene Studied by Picosecond Time-Resolved Transient Grating Method. *J. Phys. Chem. A* **1997**, *101*, 3443-3448.
345. Schwörer, M.; Wirz, J., Photochemical Reaction Mechanisms of 2-Nitrobenzyl Compounds in Solution, I. 2-Nitrotoluene: Thermodynamic and Kinetic Parameters of the aci-Nitro Tautomer. *Helv. Chim. Acta* **2001**, *84*, 1441-1458.
346. Hansen, M. J.; Velema, W. A.; Lerch, M. M.; Szymanski, W.; Feringa, B. L., Wavelength-Selective Cleavage of Photoprotecting Groups: Strategies and Applications in Dynamic Systems. *Chem. Soc. Rev.* **2015**, *44*, 3358-3377.
347. Bao, C.; Zhu, L.; Lin, Q.; Tian, H., Building Biomedical Materials using Photochemical Bond Cleavage. *Adv. Mater.* **2015**, *27*, 1647-1662.
348. Aujard, I.; Benbrahim, C.; Gouget, M.; Ruel, O.; Baudin, J.-B.; Neveu, P.; Jullien, L., o-Nitrobenzyl Photolabile Protecting Groups with Red-Shifted Absorption: Syntheses and Uncaging Cross-Sections for One- and Two-Photon Excitation. *Chem. Eur. J.* **2006**, *12*, 6865-6879.
349. Shin, D.-S.; You, J.; Rahimian, A.; Vu, T.; Siltanen, C.; Ehsanipour, A.; Stybayeva, G.; Sutcliffe, J.; Revzin, A., Photodegradable Hydrogels for Capture, Detection, and Release of Live Cells. *Angew. Chem. Int. Ed.* **2014**, *53*, 8221-8224.
350. Mahmoodi, M. M.; Abate-Pella, D.; Pundsack, T. J.; Palsuledesai, C. C.; Goff, P. C.; Blank, D. A.; Distefano, M. D., Nitrodibenzofuran: A One- and Two-Photon Sensitive Protecting Group That Is Superior to Brominated Hydroxycoumarin for Thiol Caging in Peptides. *J. Am. Chem. Soc.* **2016**, *138*, 5848-5859.
351. DeForest, C. A.; Tirrell, D. A., A Photoreversible Protein-Patterning Approach for Guiding Stem Cell Fate in Three-Dimensional Gels. *Nat. Mater.* **2015**, *14*, 523-531.
352. Zhao, Y.; Zheng, Q.; Dakin, K.; Xu, K.; Martinez, M. L.; Li, W.-H., New Caged Coumarin Fluorophores with Extraordinary Uncaging Cross Sections Suitable for Biological Imaging Applications. *J. Am. Chem. Soc.* **2004**, *126*, 4653-4663.
353. Azagarsamy, M. A.; McKinnon, D. D.; Alge, D. L.; Anseth, K. S., Coumarin-Based Photodegradable Hydrogel: Design, Synthesis, Gelation, and Degradation Kinetics. *ACS Macro Letters* **2014**, *3* (6), 515-519.
354. Olson, J. P.; Kwon, H.-B.; Takasaki, K. T.; Chiu, C. Q.; Higley, M. J.; Sabatini, B. L.; Ellis-Davies, G. C. R., Optically Selective Two-Photon Uncaging of Glutamate at 900 nm. *J. Am. Chem. Soc.* **2013**, *135*, 5954-5957.
355. Fournier, L.; Aujard, I.; Le Saux, T.; Maurin, S.; Beaupierre, S.; Baudin, J.-B.; Jullien, L., Coumarinylmethyl Caging Groups with Redshifted Absorption. *Chem. Eur. J.* **2013**, *19*, 17494-17507.
356. Truong, V. X.; Li, F.; Ercole, F.; Forsythe, J. S., Visible-Light-Mediated Cleavage of Polymer Chains Under Physiological Conditions via Quinone Photoreduction and Trimethyl Lock. *Chem. Comm.* **2017**, *53*, 12076-12079.

357. Groll, J.; Boland, T.; Blunk, T.; Burdick, J. A.; Cho, D. W.; Dalton, P. D.; Derby, B.; Forgacs, G.; Li, Q.; Mironov, V. A.; al., e., Biofabrication: Reappraising the Definition of an Evolving Field. *Biofabrication* **2016**, *8*, 013001.
358. Michon, C.; Cuvelier, G.; Launay, B., Concentration Dependence of the Critical Viscoelastic Properties of Gelatin at the Gel Point. *Rheol. Acta* **1993**, *32*, 94-103.
359. Loessner, D.; Meinert, C.; Kaemmerer, E.; Martine, L. C.; Yue, K.; Levett, P. A.; Klein, T. J.; Melchels, F. P. W.; Khademhosseini, A.; Hutmacher, D. W., Functionalization, Preparation and Use of Cell-Laden Gelatin Methacryloyl-Based Hydrogels as Modular Tissue Culture Platforms. *Nat. Prot.* **2016**, *11*, 727-746.
360. Shirahama, H.; Lee, B. H.; Tan, L. P.; Cho, N.-J., Precise Tuning of Facile One-Pot Gelatin Methacryloyl (GelMA) Synthesis. *Sci. Rep.* **2016**, *6*, 31036.
361. Claßen, C.; Claßen, M. H.; Truffault, V.; Sewald, L.; Tovar, G. E. M.; Borchers, K.; Southan, A., Quantification of Substitution of Gelatin Methacryloyl: Best Practice and Current Pitfalls. *Biomacromolecules* **2018**, *19*, 42-52.
362. Yue, K.; Li, X.; Schrobback, K.; Sheikhi, A.; Annabi, N.; Leijten, J.; Zhang, W.; Zhang, Y. S.; Hutmacher, D. W.; Klein, T. J.; al., e., Structural Analysis of Photocrosslinkable Methacryloyl-Modified Protein Derivatives. *Biomaterials* **2017**, *139*, 163-171.
363. Zheng, J.; Zhu, M.; Ferracci, G.; Cho, N.-J.; Lee, B. H., Hydrolytic Stability of Methacrylamide and Methacrylate in Gelatin Methacryloyl and Decoupling of Gelatin Methacrylamide from Gelatin Methacryloyl through Hydrolysis. *Macromol. Chem. Phys.* **2018**, *219*, 1800266.
364. Dobos, A.; Van Hoorick, J.; Steiger, W.; Gruber, P.; Markovic, M.; Andriotis, O. G.; Rohatschek, A.; Dubruel, P.; Thurner, P. J.; Van Vlierberghe, S.; Baudis, S.; Ovsianikov, A., Thiol-Gelatin-Norbornene Bioink for Laser-Based High-Definition Bioprinting. *Advanced Healthcare Materials* **2020**, *9* (15), 1900752.
365. Qin, X.-H.; Torgersen, J.; Saf, R.; Mühleder, S.; Pucher, N.; Ligon, S. C.; Holthöner, W.; Redl, H.; Ovsianikov, A.; Stampfl, J.; al., e., Three-Dimensional Microfabrication of Protein Hydrogels via Two-Photon-Excited Thiol-Vinyl Ester Photopolymerization. *J. Polym. Sci. A Polym. Chem.* **2013**, *51*, 4799-4810.
366. Bertlein, S.; Brown, G.; Lim, K. S.; Jungst, T.; Boeck, T.; Blunk, T.; Tessmar, J.; Hooper, G. J.; Woodfield, T. B. F.; Groll, J., Thiol-Ene Clickable Gelatin: A Platform Bioink for Multiple 3D Biofabrication Technologies. *Adv. Mater.* **2017**, *29*, 1703404.
367. Van Hoorick, J.; Gruber, P.; Markovic, M.; Tromayer, M.; Van Erps, J.; Thienpont, H.; Liska, R.; Ovsianikov, A.; Dubruel, P.; Van Vlierberghe, S., Cross-Linkable Gelatins with Superior Mechanical Properties Through Carboxylic Acid Modification: Increasing the Two-Photon Polymerization Potential. *Biomacromolecules* **2017**, *18*, 3260-3272.
368. Zhou, X.; Cui, H.; Nowicki, M.; Miao, S.; Lee, S. J.; Masood, F.; Harris, B. T.; Zhang, L. G., Three-Dimensional-Bioprinted Dopamine-Based Matrix for Promoting Neural Regeneration. *ACS Appl. Mater. Interfaces* **2018**, *10*, 8993-9001.
369. Fu, Y.; Xu, K.; Zheng, X.; Giacomini, A. J.; Mix, A. W.; Kao, W. J., 3D Cell Entrapment in Crosslinked Thiolated Gelatin-Poly(Ethylene Glycol) Diacrylate Hydrogels. *Biomaterials* **2012**, *33*, 48-58.
370. Gaffney, J.; Matou-Nasri, S.; Grau-Olivares, M.; Slevin, M., Therapeutic Applications of Hyaluronan. *Mol. Biosyst.* **2010**, *6*, 437-443.
371. Fraser, J. R. E.; Laurent, T. C.; Laurent, U. B. G., Hyaluronan: Its Nature, Distribution, Functions and Turnover. *J. Int. Med.* **1997**, *242*, 27-33.
372. Aruffo, A.; Stamenkovic, I.; Melnick, M.; Underhill, C. B.; Seed, B., CD44 Is the Principal Cell Surface Receptor for Hyaluronate. *Cell* **1990**, *61*, 1303-1313.
373. Allison, D. D.; Grande-Allen, K. J., Review. Hyaluronan: A Powerful Tissue Engineering Tool. *Tissue Eng.* **2006**, *12*, 2131-2140.
374. Jiang, D.; Liang, J.; Noble, P. W., Hyaluronan in Tissue Injury and Repair. *Annu. Rev. Cell. Dev. Biol.* **2007**, *23*, 435-461.
375. Zheng Shu, X.; Liu, Y.; Palumbo, F. S.; Luo, Y.; Prestwich, G. D., In Situ Crosslinkable Hyaluronan Hydrogels for Tissue Engineering. *Biomaterials* **2004**, *25*, 1339-1348.

376. Smeds, K. A.; Pfister-Serres, A.; Hatchell, D. L.; Grinstaff, M. W., Synthesis of a Novel Polysaccharide Hydrogel. *J. Macromol. Sci. Part A* **1999**, *36*, 981-989.
377. Smeds, K. A.; Grinstaff, M. W., Photocrosslinkable Polysaccharides for in Situ Hydrogel Formation. *J. Biomed. Mater. Res.* **2001**, *54*, 115-121.
378. Baier Leach, J.; Bivens, K. A.; Patrick Jr, C. W.; Schmidt, C. E., Photocrosslinked Hyaluronic Acid Hydrogels: Natural, Biodegradable Tissue Engineering Scaffolds. *Biotechnol. Bioeng.* **2003**, *82*, 578-589.
379. Debnath, S. K.; Saisivam, S.; Debanth, M.; Omri, A., Development and evaluation of Chitosan nanoparticles based dry powder inhalation formulations of Prothionamide. *PLOS ONE* **2018**, *13* (1), e0190976.
380. Qin, X.-H.; Gruber, P.; Markovic, M.; Plochberger, B.; Klotzsch, E.; Stampfl, J.; Ovsianikov, A.; Liska, R., Enzymatic Synthesis of Hyaluronic Acid Vinyl Esters for Two-Photon Microfabrication of Biocompatible and Biodegradable Hydrogel Constructs. *Polym. Chem.* **2014**, *5*, 6523-6533.
381. Lin, C.-C.; Ki, C. S.; Shih, H., Thiol-Norbornene Photoclick Hydrogels for Tissue Engineering Applications. *J. Appl. Polym. Sci.* **2015**, *132*, 41563.
382. Galarraga, J. H.; Kwon, M. Y.; Burdick, J. A., 3D Bioprinting via an in Situ Crosslinking Technique Towards Engineering Cartilage Tissue. *Sci. Rep.* **2019**, *9*, 19987.
383. Burdick, J. A.; Prestwich, G. D., Hyaluronic Acid Hydrogels for Biomedical Applications. *Adv. Mater.* **2011**, *23*, H41-H56.
384. Bencherif, S. A.; Srinivasan, A.; Horkay, F.; Hollinger, J. O.; Matyjaszewski, K.; Washburn, N. R., Influence of the Degree of Methacrylation on Hyaluronic Acid Hydrogels Properties. *Biomaterials* **2008**, *29*, 1739-1749.
385. Niidome, T.; Yamagata, M.; Okamoto, Y.; Akiyama, Y.; Takahashi, H.; Kawano, T.; Katayama, Y.; Niidome, Y., PEG-modified gold nanorods with a stealth character for in vivo applications. *Journal of Controlled Release* **2006**, *114* (3), 343-347.
386. Nishiyama, N.; Kataoka, K., Current state, achievements, and future prospects of polymeric micelles as nanocarriers for drug and gene delivery. *Pharmacology & Therapeutics* **2006**, *112* (3), 630-648.
387. Cruise, G. M.; Scharp, D. S.; Hubbell, J. A., Characterization of Permeability and Network Structure of Interfacially Photopolymerized Poly(Ethylene Glycol) Diacrylate Hydrogels. *Biomaterials* **1998**, *19*, 1287-1294.
388. Gao, G.; Schilling, A. F.; Hubbell, K.; Yonezawa, T.; Truong, D.; Hong, Y.; Dai, G.; Cui, X., Improved Properties of Bone and Cartilage Tissue from 3D Inkjet-Bioprinted Human Mesenchymal Stem Cells by Simultaneous Deposition and Photocrosslinking in PEG-GelMA. *Biotechnol. Lett.* **2015**, *37*, 2349-2355.
389. Mazzocchi, A.; Devarasetty, M.; Huntwork, R.; Soker, S.; Skardal, A., Optimization of Collagen Type I-Hyaluronan Hybrid Bioink for 3D Bioprinted Liver Microenvironments. *Biofabrication* **2018**, *11*, 015003.
390. Ovsianikov, A.; Malinauskas, M.; Schlie, S.; Chichkov, B.; Gittard, S.; Narayan, R.; Löbler, M.; Sternberg, K.; Schmitz, K. P.; Haverich, A., Three-Dimensional Laser Micro- and Nano-Structuring of Acrylated Poly(Ethylene Glycol) Materials and Evaluation of Their Cytotoxicity for Tissue Engineering Applications. *Acta Biomater.* **2011**, *7*, 967-974.
391. Weiß, T.; Schade, R.; Laube, T.; Berg, A.; Hildebrand, G.; Wyrwa, R.; Schnabelrauch, M.; Liefelth, K., Two-Photon Polymerization of Biocompatible Photopolymers for Microstructured 3D Bointerfaces. *Advanced Engineering Materials* **2011**, *13* (9), B264-B273.
392. Xin, S. J.; Chimene, D.; Garza, J. E.; Gaharwar, A. K.; Alge, D. L., Clickable PEG Hydrogel Microspheres as Building Blocks for 3D Bioprinting. *Biomater. Sci.* **2019**, *7*, 1179-11878.
393. Mautner, A.; Qin, X.; Wutzel, H.; Ligon, S. C.; Kapeller, B.; Moser, D.; Russmueller, G.; Stampfl, J.; Liska, R., Thiol-Ene Photopolymerization for Efficient Curing of Vinyl Esters. *J. Polym. Sci. A Polym. Chem.* **2013**, *51*, 203-212.
394. Yu, Y.; Chau, Y., One-Step "Click" Method for Generating Vinyl Sulfone Groups on Hydroxyl-Containing Water-Soluble Polymers. *Biomacromolecules* **2012**, *13*, 937-942.

395. Morpurgo, M.; Veronese, F. M.; Kachensky, D.; Harris, J. M., Preparation and Characterization of Poly(Ethylene Glycol) Vinyl Sulfone. *Bioconjug. Chem.* **1996**, *7*, 363-368.
396. Banerjee, I.; Pangule, R. C.; Kane, R. S., Antifouling Coatings: Recent Developments in the Design of Surfaces That Prevent Fouling by Proteins, Bacteria, and Marine Organisms. *Advanced Materials* **2011**, *23* (6), 690-718.
397. Yu, J.; Chen, F.; Wang, X.; Dong, N.; Lu, C.; Yang, G.; Chen, Z., Synthesis and Characterization of MMP Degradable and Maleimide Cross-Linked PEG Hydrogels for Tissue Engineering Scaffolds. *Polym. Degrad. Stab.* **2016**, *133*, 312-320.
398. Chou, A. I.; Akintoye, S. O.; Nicoll, S. B., Photo-crosslinked alginate hydrogels support enhanced matrix accumulation by nucleus pulposus cells in vivo. *Osteoarthritis and Cartilage* **2009**, *17* (10), 1377-1384.
399. Ooi, H. W.; Mota, C.; ten Cate, A. T.; Calore, A.; Moroni, L.; Baker, M. B., Thiol-Ene Alginate Hydrogels as Versatile Bioinks for Bioprinting. *Biomacromolecules* **2018**, *19*, 3390-3400.
400. Sakai, S.; Mochizuki, K.; Qu, Y.; Mail, M.; Nakahata, M.; Taya, M., Peroxidase-Catalyzed Microextrusion Bioprinting of Cell-Laden Hydrogel Constructs in Vaporized Ppm-Level Hydrogen Peroxide. *Biofabrication* **2018**, *10*, 045007.
401. Sakai, S.; Komatani, K.; Taya, M., Glucose-triggered Co-enzymatic Hydrogelation of Aqueous Polymer Solutions. *RSC Adv.* **2012**, *2*, 1502-1507.
402. Jeon, O.; Alt, D. S.; Ahmed, S. M.; Alsberg, E., The Effect of Oxidation on the Degradation of Photocrosslinkable Alginate Hydrogels. *Biomaterials* **2012**, *33*, 3503-3514.
403. Lee, B. H.; Lum, N.; Seow, L. Y.; Lim, P. Q.; Tan, L. P., Synthesis and Characterization of Types A and B Gelatin Methacryloyl for Bioink Applications. *Materials (Basel)* **2016**, *9*, 797.
404. Kim, W.; Kim, G., A Functional Bioink and Its Application in Myoblast Alignment and Differentiation. *Chem. Eng. J.* **2019**, *366*, 150-162.
405. Brinkman, W. T.; Nagapudi, K.; Thomas, B. S.; Chaikof, E. L., Photo-Cross-Linking of Type I Collagen Gels in the Presence of Smooth Muscle Cells: Mechanical Properties, Cell Viability, and Function. *Biomacromolecules* **2003**, *4*, 890-895.
406. Gaudet, I. D.; Shreiber, D. I., Characterization of Methacrylated Type-I Collagen as a Dynamic, Photoactive Hydrogel. *Biointerphases* **2012**, *7*, 25.
407. Poshusta, A. K.; Anseth, K. S., Photopolymerized Biomaterials for Application in the Temporomandibular Joint. *Cells Tissues Organs* **2001**, *169*, 272-278.
408. Tronci, G.; Russell, S. J.; Wood, D. J., Photo-Active Collagen Systems with Controlled Triple Helix Architecture. *J. Mater. Chem. B* **2013**, *1*, 3705-3715.
409. Lotz, C.; Schmid, F. F.; Oechsle, E.; Monaghan, M. G.; Walles, H.; Groeber-Becker, F., Cross-linked Collagen Hydrogel Matrix Resisting Contraction To Facilitate Full-Thickness Skin Equivalents. *ACS Appl. Mater. Int.* **2017**, *9*, 20417-20425.
410. Qin, X. H.; Wang, X.; Rottmar, M.; Nelson, B. J.; Maniura-Weber, K., Near-Infrared Light-Sensitive Polyvinyl Alcohol Hydrogel Photoresist for Spatiotemporal Control of Cell-Instructive 3D Microenvironments. *Adv. Mater.* **2018**, *30*, 1705564.
411. Martens, P.; Holland, T.; Anseth, K. S., Synthesis and Characterization of Degradable Hydrogels Formed from Acrylate Modified Poly(Vinyl Alcohol) Macromers. *Polymer* **2002**, *43*, 6093-6100.
412. Lim, K. S.; Levato, R.; Costa, P. F.; Castilho, M. D.; Alcalá-Orozco, C. R.; van Dorenmalen, K. M. A.; Melchels, F. P. W.; Gawlitta, D.; Hooper, G. J.; Malda, J.; al, e., Bio-Resin for High Resolution Lithography-Based Biofabrication of Complex Cell-Laden Constructs. *Biofabrication* **2018**, *10*, 034101.
413. Peng, Q.; Juzeniene, A.; Chen, J.; Svaasand, L. O.; Warloe, T.; Giercksky, K.-E.; Moan, J., Lasers in Medicine. *Rep. Prog. Phys.* **2008**, *71*, 056701.
414. Hensman, C.; Hanna, G. B.; Drew, T.; Moseley, H.; Cuschieri, A., Total radiated power, infrared output, and heat generation by cold light sources at the distal end of endoscopes and fiber optic bundle of light cables. *Surgical Endoscopy* **1998**, *12* (4), 335-337.
415. Sinha, R. P.; Häder, D.-P., UV-Induced DNA Damage and Repair: A Review. *Photochem. Photobiol. Sci.* **2002**, *1*, 225-236.

416. Burhans, W. C.; Weinberger, M., DNA Replication Stress, Genome Instability and Aging. *Nucleic Acids Res* **2007**, *35*, 7545-7556.
417. Fairbanks, B. D.; Schwartz, M. P.; Bowman, C. N.; Anseth, K. S., Photoinitiated polymerization of PEG-diacrylate with lithium phenyl-2,4,6-trimethylbenzoylphosphinate: polymerization rate and cytocompatibility. *Biomaterials* **2009**, *30* (35), 6702-6707.
418. Lowe, A. B.; Bowman, C. N.; Shipp, D.; Theato, P.; Haddleton, D. M.; Davis, T. P.; Son, D.; Anseth, K.; du Prez, F.; Boutevin, B., *Thiol-X Chemistries in Polymer and Materials Science*. Royal Society of Chemistry: 2013.
419. Wilts, E. M.; Pekkanen, A. M.; White, B. T.; Meenakshisundaram, V.; Aduba, D. C.; Williams, C. B.; Long, T. E., Vat Photopolymerization of Charged Monomers: 3D Printing with Supramolecular Interactions. *Polym. Chem.* **2019**, *10*, 1442-1451.
420. Viljanen, E. K.; Skrifvars, M.; Vallittu, P. K., Dendrimer/Methyl Methacrylate Co-Polymers: Residual Methyl Methacrylate and Degree of Conversion. *J. Biomater. Sci. Polymer Ed.* **2005**, *16*, 1219-1231.
421. Heller, C.; Schwentenwein, M.; Russmueller, G.; Varga, F.; Stampfl, J.; Liska, R., Vinyl Esters: Low Cytotoxicity Monomers for the Fabrication of Biocompatible 3D Scaffolds by Lithography Based Additive Manufacturing. *J. Polym. Sci. A Polym. Chem.* **2009**, *47*, 6941-6954.
422. Godar, D. E.; Gurunathan, C.; Ilev, I., 3D Bioprinting with UVA1 Radiation and Photoinitiator Irgacure 2959: Can the ASTM Standard L929 Cells Predict Human Stem Cell Cytotoxicity? *Photochem. Photobiol.* **2019**, *95*, 581-586.
423. Chimene, D.; Kaunas, R.; Gaharwar, A. K., Hydrogel Bioink Reinforcement for Additive Manufacturing: A Focused Review of Emerging Strategies. *Adv. Mater.* **2020**, *32*, 1902026.
424. McCormack, A.; Highley, C. B.; Leslie, N. R.; Melchels, F. P. W., 3D Printing in Suspension Baths: Keeping the Promises of Bioprinting Afloat. *Trends Biotechnol* **2020**, *38*, 584-593.
425. Fisch, P.; Holub, M.; Zenobi-Wong, M., Improved Accuracy and Precision of Bioprinting Through Progressive Cavity Pump-Controlled Extrusion. *bioRxiv* **2020**, 2020.01.23.915868.
426. McIlroy, C.; Olmsted, P. D., Disentanglement Effects on Welding Behaviour of Polymer Melts During the Fused-Filament-Fabrication Method for Additive Manufacturing. *Polymer* **2017**, *123*, 376-391.
427. Paxton, N.; Smolan, W.; Bock, T.; Melchels, F.; Groll, J.; Jungst, T., Proposal to Assess Printability of Bioinks for Extrusion-Based Bioprinting and Evaluation of Rheological Properties Governing Bioprintability. *Biofabrication* **2017**, *9*, 044107.
428. Habib, A.; Sathish, V.; Mallik, S.; Khoda, B., 3D Printability of Alginate-Carboxymethyl Cellulose Hydrogel. *Materials (Basel)* **2018**, *11*, 454.
429. Mouser, V. H.; Melchels, F. P.; Visser, J.; Dhert, W. J.; Gawlitta, D.; Malda, J., Yield Stress Determines Bioprintability of Hydrogels Based on Gelatin-Methacryloyl and Gellan Gum for Cartilage Bioprinting. *Biofabrication* **2016**, *8*, 035003.
430. Ashammakhi, N.; Ahadian, S.; Xu, C.; Montazerian, H.; Ko, H.; Nasiri, R.; Barros, N.; Khademhosseini, A., Bioinks and Bioprinting Technologies to Make Heterogeneous and Biomimetic Tissue Constructs. *Materials Today Bio* **2019**, *1*, 100008.
431. Drzewiecki, K. E.; Malavade, J. N.; Ahmed, I.; Lowe, C. J.; Shreiber, D. I., A Thermoreversible, Photocrosslinkable Collagen Bio-Ink for Free-Form Fabrication of Scaffolds for Regenerative Medicine. *Technology (Singap. World Sci.)* **2017**, *5*, 185-195.
432. Annabi, N.; Mithieux, S. M.; Zorlutuna, P.; Camci-Unal, G.; Weiss, A. S.; Khademhosseini, A., Engineered Cell-Laden Human Protein-Based Elastomer. *Biomaterials* **2013**, *34*, 5496-5505.
433. Cebe, T.; Ahuja, N.; Monte, F.; Awad, K.; Vyavhare, K.; Aswath, P.; Huang, J.; Brotto, M.; Varanasi, V., Novel 3D-Printed Methacrylated Chitosan-Laponite Nanosilicate Composite Scaffolds Enhance Cell Growth and Biomineral Formation in MC3T3 Pre-Osteoblasts. *J. Mater. Res.* **2018**, *35*, 58-75.
434. Costantini, M.; Idaszek, J.; Szoke, K.; Jaroszewicz, J.; Dentini, M.; Barbetta, A.; Brinchmann, J. E.; Swieszkowski, W., 3D Bioprinting of BM-MSCs-Loaded ECM Biomimetic Hydrogels for in Vitro Neocartilage Formation. *Biofabrication* **2016**, *8*, 035002.
435. Ali, M.; Pr, A. K.; Yoo, J. J.; Zahran, F.; Atala, A.; Lee, S. J., A Photo-Crosslinkable Kidney ECM-Derived Bioink Accelerates Renal Tissue Formation. *Adv. Healthcare Mater.* **2019**, *8*, e1800992.

436. Stichler, S.; Jungst, T.; Schamel, M.; Zilkowski, I.; Kuhlmann, M.; Bock, T.; Blunk, T.; Tessmar, J.; Groll, J., Thiol-Ene Clickable Poly(glycidol) Hydrogels for Biofabrication. *Ann. Biomed. Eng.* **2017**, *45*, 273-285.
437. Yeh, Y.-C.; Ouyang, L.; Highley, C. B.; Burdick, J. A., Norbornene-Modified Poly(Glycerol Sebacate) as a Photocurable and Biodegradable Elastomer. *Polym. Chem.* **2017**, *8*, 5091-5099.
438. Tytgat, L.; Van Damme, L.; Van Hoorick, J.; Declercq, H.; Thienpont, H.; Ottevaere, H.; Blondeel, P.; Dubruel, P.; Van Vlierberghe, S., Additive Manufacturing of Photo-Crosslinked Gelatin Scaffolds for Adipose Tissue Engineering. *Acta Biomater.* **2019**, *94*, 340-350.
439. Tigner, T. J.; Rajput, S.; Gaharwar, A. K.; Alge, D. L., Comparison of Photo Cross Linkable Gelatin Derivatives and Initiators for Three-Dimensional Extrusion Bioprinting. *Biomacromolecules* **2019**, *21*, 454-463.
440. Melchels, F. P. W.; Dhert, W. J. A.; Hutmacher, D. W.; Malda, J., Development and Characterisation of a New Bioink for Additive Tissue Manufacturing. *J. Mat. Chem. B* **2014**, *2*, 2282-2289.
441. Kesti, M.; Müller, M.; Becher, J.; Schnabelrauch, M.; D'Este, M.; Eglin, D.; Zenobi-Wong, M., A Versatile Bioink for Three-Dimensional Printing of Cellular Scaffolds Based on Thermally and Photo-Triggered Tandem Gelation. *Acta Biomater.* **2015**, *11*, 162-172.
442. Levato, R.; Webb, W. R.; Otto, I. A.; Mensinga, A.; Zhang, Y.; van Rijen, M.; van Weeren, R.; Khan, I. M.; Malda, J., The Bio in the Ink: Cartilage Regeneration with Bioprintable Hydrogels and Articular Cartilage-Derived Progenitor Cells. *Acta Biomater.* **2017**, *61*, 41-53.
443. Lee, A.; Hudson, A. R.; Shiwardski, D. J.; Tashman, J. W.; Hinton, T. J.; Yerneni, S.; Biley, J. M.; Campbell, P. G.; Feinberg, A. W., 3D bioprinting of collagen to rebuild components of the human heart. *Science* **2019**, *365* (6452), 482-487.
444. Jeon, O.; Lee, Y. B.; Jeong, H.; Lee, S. J.; Wells, D.; Alsberg, E., Individual Cell-Only Bioink and Photocurable Supporting Medium for 3D Printing and Generation of Engineered Tissues with Complex Geometries. *Mater. Horiz.* **2019**, *6*, 1625-1631.
445. Hinton, T. J.; Jallerat, Q.; Palchesko, R. N.; Park, J. H.; Grodzicki, M. S.; Shue, H. J.; Ramadan, M. H.; Hudson, A. R.; Feinberg, A. W., Three-Dimensional Printing of Complex Biological Structures by Freeform Reversible Embedding of Suspended Hydrogels. *Sci. Adv.* **2015**, *1*, e1500758.
446. Jeon, O.; Lee, Y. B.; Hinton, T. J.; Feinberg, A. W.; Alsberg, E., Cryopreserved Cell-Laden Alginate Microgel Bioink for 3D Bioprinting of Living Tissues. *Mater. Today Chem.* **2019**, *12*, 61-70.
447. Mirdamadi, E.; Muselmyan, N.; Koti, P.; Asfour, H.; Sarvazyan, N., Agarose Slurry as a Support Medium for Bioprinting and Culturing Freestanding Cell-Laden Hydrogel Constructs. *3D Print. Addit. Manuf.* **2019**, *6*, 158-164.
448. Compaan, A. M.; Song, K.; Huang, Y., Gellan Fluid Gel as a Versatile Support Bath Material for Fluid Extrusion Bioprinting. *ACS Appl. Mater. Int.* **2019**, *11*, 5714-5726.
449. Raddatz, L.; Lavrentieva, A.; Pepelanova, I.; Bahnemann, J.; Geier, D.; Becker, T.; Scheper, T.; Beutel, S., Development and Application of an Additively Manufactured Calcium Chloride Nebulizer for Alginate 3D-Bioprinting Purposes. *J. Funct. Biomater.* **2018**, *9*, 63.
450. Skardal, A.; Zhang, J.; McCoard, L.; Xu, X.; Oottamasathien, S.; Prestwich, G. D., Photocrosslinkable Hyaluronan-Gelatin Hydrogels for Two-Step Bioprinting. *Tissue Eng. Part A* **2010**, *16*, 2675-2685.
451. Ouyang, L.; Highley, C. B.; Sun, W.; Burdick, J. A., A Generalizable Strategy for the 3D Bioprinting of Hydrogels from Nonviscous Photo-crosslinkable Inks. *Advanced Materials* **2017**, *29* (8), 1604983.
452. Hiller, A.; Borchers, K.; Tovar, G. E. M.; Southan, A., Impact of Intermediate UV Curing and Yield Stress of 3D Printed Poly(Ethylene Glycol) Diacrylate Hydrogels on Interlayer Connectivity and Maximum Build Height. *Add. Manuf.* **2017**, *18*, 136-144.
453. Colosi, C.; Shin, S. R.; Manoharan, V.; Massa, S.; Costantini, M.; Barbetta, A.; Dokmeci, M. R.; Dentini, M.; Khademhosseini, A., Microfluidic Bioprinting of Heterogeneous 3D Tissue Constructs Using Low-Viscosity Bioink. *Adv. Mater.* **2016**, *28*, 677-684.
454. Van Belleghem, S.; Torres Jr, L.; Santoro, M.; Mahadik, B.; Wolfand, A.; Kofinas, P.; Fisher, J. P., Hybrid 3D Printing of Synthetic and Cell-Laden Bioinks for Shape Retaining Soft Tissue Grafts. *Adv. Funct. Mater.* **2020**, *30*, 1907145.

455. Pati, F.; Jang, J.; Ha, D. H.; Won Kim, S.; Rhie, J. W.; Shim, J. H.; Kim, D. H.; Cho, D. W., Printing Three-Dimensional Tissue Analogues with Decellularized Extracellular Matrix Bioink. *Nat. Commun.* **2014**, *5*, 3935.
456. de Ruijter, M.; Ribeiro, A.; Dokter, I.; Castilho, M.; Malda, J., Simultaneous Micropatterning of Fibrous Meshes and Bioinks for the Fabrication of Living Tissue Constructs. *Adv. Healthcare Mater.* **2019**, *8*, e1800418.
457. Lee, J. W.; Choi, Y.-J.; Yong, W.-J.; Pati, F.; Shim, J.-H.; Kang, K. S.; Kang, I.-H.; Park, J.; Cho, D.-W., Development of a 3D Cell Printed Construct Considering Angiogenesis for Liver Tissue Engineering. *Biofabrication* **2016**, *8*, 015007.
458. Castilho, M.; Mouser, V.; Chen, M.; Malda, J.; Ito, K., Bi-Layered Micro-Fibre Reinforced Hydrogels for Articular Cartilage Regeneration. *Acta Biomater.* **2019**, *95*, 297-306.
459. Castilho, M.; van Mil, A.; Maher, M.; Metz, C. H. G.; Hochleitner, G.; Groll, J.; Doevendans, P. A.; Ito, K.; Sluijter, J. P. G.; Malda, J., Melt Electrowriting Allows Tailored Microstructural and Mechanical Design of Scaffolds to Advance Functional Human Myocardial Tissue Formation. *Adv. Funct. Mater.* **2018**, *28*, 1803151.
460. Xu, W. Y.; Molino, B. Z.; Cheng, F.; Molino, P. J.; Yue, Z. L.; Su, D. D.; Wang, X. J.; Willfor, S.; Xu, C. L.; Wallace, G. G., On Low-Concentration Inks Formulated by Nanocellulose Assisted with Gelatin Methacrylate (GelMA) for 3D Printing toward Wound Healing Application. *ACS Appl. Mater. Int.* **2019**, *11*, 8838-8848.
461. Cidonio, G.; Alcala-Orozco, C. R.; Lim, K. S.; Glinka, M.; Mutreja, I.; Kim, Y.-H.; Dawson, J. I.; Woodfield, T. B. F.; Oreffo, R. O. C., Osteogenic and Angiogenic Tissue Formation in High Fidelity Nanocomposite Laponite-Gelatin Bioinks. *Biofabrication* **2019**, *11*, 035027.
462. Zhou, X.; Nowicki, M.; Cui, H.; Zhu, W.; Fang, X.; Miao, S.; Lee, S.-J.; Keidar, M.; Zhang, L. G., 3D Bioprinted Graphene Oxide-Incorporated Matrix for Promoting Chondrogenic Differentiation of Human Bone Marrow Mesenchymal Stem Cells. *Carbon* **2017**, *116*, 615-624.
463. Ushiba, S.; Shoji, S.; Masui, K.; Kono, J.; Kawata, S., Direct Laser Writing of 3D Architectures of Aligned Carbon Nanotubes. *Advanced Materials* **2014**, *26* (32), 5653-5657.
464. Izadifar, M.; Chapman, D.; Babyn, P.; Chen, X.; Kelly, M. E., UV-Assisted 3D Bioprinting of Nanoreinforced Hybrid Cardiac Patch for Myocardial Tissue Engineering. *Tissue Eng. Part C Methods* **2018**, *24*, 74-88.
465. Ramón-Azcón, J.; Ahadian, S.; Estili, M.; Liang, X.; Ostrovidov, S.; Kaji, H.; Shiku, H.; Ramalingam, M.; Nakajima, K.; Sakka, Y.; Khademhosseini, A.; Matsue, T., Dielectrophoretically Aligned Carbon Nanotubes to Control Electrical and Mechanical Properties of Hydrogels to Fabricate Contractile Muscle Myofibers. *Advanced Materials* **2013**, *25* (29), 4028-4034.
466. Ahadian, S.; Banan Sadeghian, R.; Yaginuma, S.; Ramon-Azcon, J.; Nashimoto, Y.; Liang, X.; Bae, H.; Nakajima, K.; Shiku, H.; Matsue, T.; Nakayama, K. S.; Khademhosseini, A., Hydrogels containing metallic glass sub-micron wires for regulating skeletal muscle cell behaviour. *Biomater Sci* **2015**, *3* (11), 1449-58.
467. Cross, L. M.; Carrow, J. K.; Ding, X.; Singh, K. A.; Gaharwar, A. K., Sustained and Prolonged Delivery of Protein Therapeutics from Two-Dimensional Nanosilicates. *ACS Appl. Mater. Int.* **2019**, *11*, 6741-6750.
468. Lee, M.; Bae, K.; Levinson, C.; Zenobi-Wong, M., Nanocomposite Bioink Exploits Dynamic Covalent Bonds Between Nanoparticles and Polysaccharides for Precision Bioprinting. *Biofabrication* **2019**, *12*, 025025.
469. Lee, M.; Bae, K.; Guillon, P.; Chang, J.; Arlov, O.; Zenobi-Wong, M., Exploitation of Cationic Silica Nanoparticles for Bioprinting of Large-Scale Constructs with High Printing Fidelity. *ACS Appl. Mater. Int.* **2018**, *10*, 37820-37828.
470. Marco-Dufort, B.; Tibbitt, M. W., Design of Moldable Hydrogels for Biomedical Applications Using Dynamic Covalent Boronic Esters. *Mater. Today Chem.* **2019**, *12*, 16-33.

471. Kim, S. W.; Kim, D. Y.; Roh, H. H.; Kim, H. S.; Lee, J. W.; Lee, K. Y., Three-Dimensional Bioprinting of Cell-Laden Constructs Using Polysaccharide-Based Self-Healing Hydrogels. *Biomacromolecules* **2019**, *20*, 1860-1866.
472. Wang, L. L.; Highley, C. B.; Yeh, Y.-C.; Galarraga, J. H.; Uman, S.; Burdick, J. A., Three-Dimensional Extrusion Bioprinting of Single- and Double-Network Hydrogels Containing Dynamic Covalent Crosslinks. *J. Biomed. Mater. Res. A* **2018**, *106*, 865-875.
473. Shin, M.; Galarraga, J. H.; Kwon, M. Y.; Lee, H.; Burdick, J. A., Gallol-Derived ECM-Mimetic Adhesive Bioinks Exhibiting Temporal Shear-Thinning and Stabilization Behavior. *Acta Biomater.* **2018**, *95*, 165-175.
474. Griffin, D. R.; Weaver, W. M.; Scumpia, P. O.; Di Carlo, D.; Segura, T., Accelerated wound healing by injectable microporous gel scaffolds assembled from annealed building blocks. *Nature Materials* **2015**, *14* (7), 737-744.
475. Dumont, C. M.; Carlson, M. A.; Munsell, M. K.; Ciciriello, A. J.; Strnadova, K.; Park, J.; Cummings, B. J.; Anderson, A. J.; Shea, L. D., Aligned Hydrogel Tubes Guide Regeneration Following Spinal Cord Injury. *Acta Biomater.* **2019**, *86*, 312-322.
476. Nair, S. K.; Basu, S.; Sen, B.; Lin, M. H.; Kumar, A. N.; Yuan, Y.; Cullen, P. J.; Sarkar, D., Colloidal Gels with Tunable Mechanomorphology Regulate Endothelial Morphogenesis. *Sci. Rep.* **2019**, *9*, 1072.
477. Riley, L.; Schirmer, L.; Segura, T., Granular Hydrogels: Emergent Properties of Jammed Hydrogel Microparticles and Their Applications in Tissue Repair and Regeneration. *Curr. Opin. Biotechnol.* **2019**, *60*, 1-8.
478. Ying, G.-L.; Jiang, N.; Maharjan, S.; Yin, Y.-X.; Chai, R.-R.; Cao, X.; Yang, J.; Miri, A. K.; Hassan, S.; Zhang, Y., Aqueous Two-Phase Emulsion Bioink-Enabled 3D Bioprinting of Porous Hydrogels. *Adv. Mater.* **2018**, *30*, 1805460.
479. Highley, C. B.; Song, K. H.; Daly, A. C.; Burdick, J. A., Jammed Microgel Inks for 3D Printing Applications. *Adv. Sci.* **2019**, *6*, 1801076.
480. Caldwell, A. S.; Aguado, B. A.; Anseth, K. S., Designing Microgels for Cell Culture and Controlled Assembly of Tissue Microenvironments. *Adv. Funct. Mater.* **2019**, 1907670.
481. Sheikhi, A.; de Rutte, J.; Haghniaz, R.; Akouissi, O.; Sohrabi, A.; Di Carlo, D.; Khademhosseini, A., Microfluidic-Enabled Bottom-Up Hydrogels from Annealable Naturally-Derived Protein Microbeads. *Biomaterials* **2019**, *192*, 560-568.
482. Sideris, E.; Griffin, D. R.; Ding, Y.; Li, S.; Weaver, W. M.; Di Carlo, D.; Hsiai, T.; Segura, T., Particle Hydrogels Based on Hyaluronic Acid Building Blocks. *ACS Biomater. Sci. Eng.* **2016**, *2*, 2034-2041.
483. Darling, N. J.; Xi, W.; Sideris, E.; Anderson, A. R.; Pong, C.; Carmichael, S. T.; Segura, T., Click by Click Microporous Annealed Particle (MAP) Scaffolds. *Adv. Healthcare Mater.* **2020**, *9*, 1901391.
484. Caldwell, A. S.; Rao, V. V.; Golden, A. C.; Anseth, K. S., Porous Bio-Click Microgel Scaffolds Control hMSC Interactions and Promote Their Secretory Properties. *Biomaterials* **2019**, 2322, 119725.
485. Song, K.; Compaan, A. M.; Chai, W.; Huang, Y., Injectable Gelatin Microgel-Based Composite Ink for 3D Bioprinting in Air. *ACS Appl. Mater. Int.* **2020**, *12*, 22453-22466.
486. Visser, C. W.; Kamperman, T.; Karbaat, L. P.; Lohse, D.; Karperien, M., In-Air Microfluidics Enables Rapid Fabrication of Emulsions, Suspensions, and 3D Modular (Bio)Materials. *Sci. Adv.* **2018**, *4*, eaao1175.
487. Guerzoni, L. P. B.; Rose, J. C.; Gehlen, D. B.; Jans, A.; Haraszti, T.; Wessling, M.; Kuehne, A. J. C.; De Laporte, L., Cell Encapsulation in Soft, Anisometric Poly(Ethylene) Glycol Microgels Using a Novel Radical-Free Microfluidic System. *Small* **2019**, *15*, 1900692.
488. Chen, P.-Y.; Yang, K.-C.; Wu, C.-C.; Yu, J.-H.; Lin, F.-H.; Sun, J.-S., Fabrication of Large Perfusible Macroporous Cell-laden Hydrogel Scaffolds Using Microbial Transglutaminase. *Acta Biomater.* **2014**, *10*, 912-920.
489. Kessel, B.; Lee, M.; Bonato, A.; Tinguely, Y.; Tosoratti, E.; Zenobi-Wong, M., 3D Bioprinting of Macroporous Materials Based on Entangled Hydrogel Microstrands. *Advanced Science* **2020**, *7* (18), 2001419.
490. Wu, W.; DeConinck, A.; Lewis, J. A., Omnidirectional Printing of 3D Microvascular Networks. *Adv. Mater.* **2011**, *23*, H178-H183.

491. Miller, J. S.; Stevens, K. R.; Yang, M. T.; Baker, B. M.; Nguyen, D.-H. T.; Cohen, D. M.; Toro, E.; Chen, A. A.; Galie, P. A.; Yu, X.; al., e., Rapid Casting of Patterned Vascular Networks for Perfusable Engineered Three-Dimensional Tissues. *Nat. Mater.* **2012**, *11*, 768-774.
492. Mirabella, T.; MacArthur, J. W.; Cheng, D.; Ozaki, C. K.; Woo, Y. J.; Yang, M. T.; Chen, C. S., 3D-printed vascular networks direct therapeutic angiogenesis in ischaemia. *Nature Biomedical Engineering* **2017**, *1* (6), 0083.
493. Ouyang, L.; Armstrong, J. P. K.; Chen, Q.; Lin, Y.; Stevens, M. M., Void-Free 3D Bioprinting for In Situ Endothelialization and Microfluidic Perfusion. *Adv. Funct. Mater.* **2020**, *30*, 1908349.
494. Liu, W.; Zhong, Z.; Hu, N.; Zhou, Y.; Maggio, L.; Miri, A. K.; Fragasso, A.; Jin, X.; Khademhosseini, A.; Zhang, Y. S., Coaxial Extrusion Bioprinting of 3D Microfibrous Constructs with Cell-Favorable Gelatin Methacryloyl Microenvironments. *Biofabrication* **2018**, *10*, 024102.
495. Jia, W.; Gungor-Ozkerim, P. S.; Zhang, Y. S.; Yue, K.; Zhu, K.; Liu, W.; Pi, Q.; Byambaa, B.; Dokmeci, M. R.; Shin, S. R.; al., e., Direct 3D Bioprinting of Perfusable Vascular Constructs Using a Blend Bioink. *Biomaterials* **2016**, *106*, 58-68.
496. Singh, N. K.; Han, W.; Nam, S. A.; Kim, J. W.; Kim, J. Y.; Kim, Y. K.; Cho, D.-W., Three-Dimensional Cell-Printing of Advanced Renal Tubular Tissue Analogue. *Biomaterials* **2019**, *232*, 119734.
497. Carolina, C.-M.; Maria Diaz de, L.-D.; Mohamadmahdi, S.; Carlos Fernando, C.-G.; Edna Johana, B.-M.; Christian Carlos, M.-B.; Sunshine, H.; Norma Alicia, G.-F.; Mohammad Ali, A.; Ivonne, G.-G.; al., e., Using Chaotic Advection for Facile High-Throughput Fabrication of Ordered Multilayer Micro- and Nanostructures: Continuous Chaotic Printing. *Biofabrication* **2020**.
498. Serex, L.; Bertsch, A.; Renaud, P., Microfluidics: A New Layer of Control for Extrusion-Based 3D Printing. *Micromachines (Basel)* **2018**, *9*, 86.
499. Liu, W.; Zhang, Y. S.; Heinrich, M. A.; De Ferrari, F.; Jang, H. L.; Bakht, S. M.; Alvarez, M. M.; Yang, J.; Li, Y.-C.; Trujillo-de Santiago, G.; al., e., Rapid Continuous Multimaterial Extrusion Bioprinting. *Adv. Mater.* **2017**, *29*, 1604630.
500. Idaszek, J.; Costantini, M.; Karlsen, T. A.; Jaroszewicz, J.; Colosi, C.; Testa, S.; Fornetti, E.; Bernardini, S.; Seta, M.; Kasarello, K.; al., E., 3D Bioprinting of Hydrogel Constructs with Cell and Material Gradients for the Regeneration of Full-Thickness Chondral Defect Using a Microfluidic Printing Head. *Biofabrication* **2019**, *11*, 044101.
501. Rocca, M.; Fragasso, A.; Liu, W.; Heinrich, M. A.; Zhang, Y. S., Embedded Multimaterial Extrusion Bioprinting. *SLAS Technol.* **2018**, *23*, 154-163.
502. Skylar-Scott, M. A.; Mueller, J.; Visser, C. W.; Lewis, J. A., Voxelated Soft Matter via Multimaterial Multinozzle 3D Printing. *Nature* **2019**, *575*, 330-335.
503. Lin, N. Y. C.; Homan, K. A.; Robinson, S. S.; Kolesky, D. B.; Duarte, N.; Moisan, A.; Lewis, J. A., Renal Reabsorption in 3D Vascularized Proximal Tubule Models. *Proc. Natl. Acad. Sci. U. S. A.* **2019**, *116*, 5399-5404.
504. Skylar-Scott, M. A.; Mueller, J.; Visser, C. W.; Lewis, J. A., Voxelated soft matter via multimaterial multinozzle 3D printing. *Nature* **2019**, *575* (7782), 330-335.
505. Maiullari, F.; Costantini, M.; Milan, M.; Pace, V.; Chirivi, M.; Maiullari, S.; Rainer, A.; Baci, D.; Marei, H. E.; Seliktar, D.; al., e., A Multi-Cellular 3D Bioprinting Approach for Vascularized Heart Tissue Engineering Based on HUVECs and iPSC-Derived Cardiomyocytes. *Sci. Rep.* **2018**, *8*, 13532.
506. Derr, K.; Zou, J. Y.; Luo, K.; Song, M. J.; Sittampalam, G. S.; Zhou, C.; Michael, S.; Ferrer, M.; Derr, P., Fully Three-Dimensional Bioprinted Skin Equivalent Constructs with Validated Morphology and Barrier Function. *Tissue Eng. Part C Methods* **2019**, *25*, 334-343.
507. Kim, H.; Jang, J.; Park, J.; Lee, K.-P.; Lee, S.; Lee, D.-M.; Kim, K. H.; Kim, H. K.; Cho, D.-W., Shear-Induced Alignment of Collagen Fibrils Using 3D Cell Printing for Corneal Stroma Tissue Engineering. *Biofabrication* **2019**, *11*, 035017.
508. England, S.; Rajaram, A.; Schreyer, D. J.; Chen, X., Bioprinted Fibrin-Factor XIII-Hyaluronate Hydrogel Scaffolds with Encapsulated Schwann Cells and Their in Vitro Characterization for Use in Nerve Regeneration. *Bioprinting* **2017**, *5*, 1-9.

509. Müller, M.; Öztürk, E.; Arlov, Ø.; Gatenholm, P.; Zenobi-Wong, M., Alginate Sulfate–Nanocellulose Bioinks for Cartilage Bioprinting Applications. *Annals of Biomedical Engineering* **2017**, *45* (1), 210-223.
510. Müller, M.; Fisch, P.; Molnar, M.; Eggert, S.; Binelli, M.; Maniura-Weber, K.; Zenobi-Wong, M., Development and Thorough Characterization of the Processing Steps of an Ink for 3D Printing for Bone Tissue Engineering. *Mater. Sci. Eng. C. Mater. Biol. Appl.* **2020**, *108*, 110510.
511. Hourd, P.; Medcalf, N.; Segal, J.; Williams, D. J., A 3D Bioprinting Exemplar of the Consequences of the Regulatory Requirements on Customized Processes. *Regen. Med.* **2015**, *10*, 863-883.
512. Ahlers, D. 3D Printing of Nonplanar Layers for Smooth Surface Generation. University of Hamburg, 2019.
513. Armstrong, A. A.; Norato, J.; Alleyne, A. G.; Wagoner Johnson, A. J., Direct Process Feedback in Extrusion-Based 3D Bioprinting. *Biofabrication* **2019**, *12*, 015017.
514. Bhattacharjee, N.; Urrios, A.; Kang, S.; Folch, A., The Upcoming 3D-Printing Revolution in Microfluidics. *Lab Chip* **2016**, *16*, 1720-1742.
515. Derby, B., Bioprinting: Inkjet Printing Proteins and Hybrid Cell-Containing Materials and Structures. *J. Mater. Chem.* **2008**, *18*, 5717-5721.
516. Hutchings, I. M.; Martin, G. D.; Hoath, S. D., 1.2 Drop Formation: Continuous Inkjet and Drop-on-Demand. In *Fundamentals of Inkjet Printing: The Science of Inkjet and Droplets*, John Wiley & Sons, Ed. 2015.
517. Saunders, R. E.; Derby, B., Inkjet Printing Biomaterials for Tissue Engineering: Bioprinting. *Intl. Mater. Rev.* **2014**, *59*, 430-448.
518. Li, X.; Chen, J.; Liu, B.; Wang, X.; Ren, D.; Xu, T., Inkjet Printing for Biofabrication. In *3D Printing and Biofabrication*, Ovsianikov, A.; Yoo, J. J.; Mironov, V., Eds. Springer International Publishing: 2018; pp 283-301.
519. Ng, W. L.; Lee, J. M.; Yeong, W. Y.; Naing, M. W., Microvalve-Based Bioprinting – Process, Bio-Inks and Applications. *Biomater. Sci.* **2017**, *5*, 632-647.
520. Jang, D.; Kim, D.; Moon, J., Influence of Fluid Physical Properties on Ink-Jet Printability. *Langmuir* **2009**, *25*, 2629-2635.
521. Reis, N.; Ainsley, C.; Derby, B., Ink-Jet Delivery of Particle Suspensions by Piezoelectric Droplet Ejectors. *J. Appl. Phys.* **2005**, *97*, 094903.
522. Derby, B., Inkjet Printing Ceramics: From Drops to Solid. *J. Eur. Ceram. Soc.* **2011**, *31*, 2543-2550.
523. Choi, I. H.; Kim, Y. K.; Lee, S.; Lee, S. H.; Kim, J., A Pneumatic Drop-on-Demand Printing System With an Extended Printable Liquid Range. *J. Microelectromech. Syst.* **2015**, *24*, 768-770.
524. Schulkes, R. M. S. M., The Contraction of Liquid Filaments. *J. Fluid. Mech.* **1996**, *309*, 277-300.
525. Derby, B., Inkjet Printing of Functional and Structural Materials: Fluid Property Requirements, Feature Stability, and Resolution. *Annu. Rev. Mater. Res.* **2010**, *40*, 395-414.
526. Soltman, D.; Subramanian, V., Inkjet-Printed Line Morphologies and Temperature Control of the Coffee Ring Effect. *Langmuir* **2008**, *24*, 2224-2231.
527. Gans, B. J.; Schubert, U. S., Inkjet Printing of Well-Defined Polymer Dots and Arrays. *Langmuir* **2004**, *20*, 7789-7793.
528. Smith, P. J.; Shin, D. Y.; Stringer, J. E.; Derby, B., Direct Ink-Jet Printing and Low Temperature Conversion of Conductive Silver Patterns. *J. Mater. Sci.* **2006**, *41*, 4153-4158.
529. Stringer, J.; Derby, B., Formation and Stability of Lines Produced by Inkjet Printing. *Langmuir* **2010**, *26*, 10365-10372.
530. Xu, T.; Zhao, W.; Zhu, J. M.; Albanna, M. Z.; Yoo, J. J.; Atala, A., Complex Heterogeneous Tissue Constructs Containing Multiple Cell Types Prepared by Inkjet Printing Technology. *Biomaterials* **2013**, *34*, 130-139.
531. Faulkner-Jones, A.; Fyfe, C.; Cornelissen, D. J.; Gardner, J.; King, J.; Courtney, A.; Shu, W., Bioprinting of Human Pluripotent Stem Cells and Their Directed Differentiation into Hepatocyte-Like Cells for the Generation of Mini-Livers in 3D. *Biofabrication* **2015**, *7*, 044102.
532. Yoon, S.; Park, J. A.; Lee, H.-R.; Yoon, W. H.; Hwang, D. S.; Jung, S., Inkjet–Spray Hybrid Printing for 3D Freeform Fabrication of Multilayered Hydrogel Structures. *Adv. Healthcare Mater.* **2018**, *7*, 1800050.

533. Sakai, S.; Ueda, K.; Gantumur, E.; Taya, M.; Nakamura, M., Drop-On-Drop Multimaterial 3D Bioprinting Realized by Peroxidase-Mediated Cross-Linking. *Macromol. Rapid Commun.* **2018**, *39*, 1700534.
534. Skardal, A.; Mack, D.; Kapetanovic, E.; Atala, A.; Jackson, J. D.; Yoo, J.; Soker, S., Bioprinted Amniotic Fluid-Derived Stem Cells Accelerate Healing of Large Skin Wounds. *Stem Cell Transl. Med.* **2012**, *1*, 792-802.
535. Lee, V.; Singh, G.; Trasatti, J. P.; Bjornsson, C.; Xu, X.; Tran, T. N.; Yoo, S. S.; Dai, G.; Karande, P., Design and Fabrication of Human Skin by Three-Dimensional Bioprinting. *Tissue Eng. Part C* **2014**, *20*, 473-484.
536. Blaeser, A.; Campos, D. F. D.; Puster, U.; Richtering, W.; Stevens, M. M.; Fischer, H., Controlling Shear Stress in 3D Bioprinting is a Key Factor to Balance Printing Resolution and Stem Cell Integrity. *Advanced Healthcare Materials* **2016**, *5* (3), 326-333.
537. Christensen, K.; Xu, C.; Chai, W.; Zhang, Z.; Fu, J.; Huang, Y., Freeform Inkjet Printing of Cellular Structures with Bifurcations. *Biotechnol. Bioeng.* **2014**, *112*, 1047-1055.
538. Cui, X.; Boland, T., Human Microvasculature Fabrication Using Thermal Inkjet Printing Technology. *Biomaterials* **2009**, *30*, 6221-6227.
539. Villar, G.; Graham, A. D.; Bayley, H., A Tissue-Like Printed Material. *Science* **2013**, *340*, 48-52.
540. Graham, A. D.; Olof, S. N.; Burke, M. J.; Armstrong, J. P. K.; Mikhailova, E. A.; Nicholson, J. G.; Box, S. J.; Szele, F. G.; Perriman, A. W.; Bayley, H., High-Resolution Patterned Cellular Constructs by Droplet-Based 3D Printing. *Sci. Rep.* **2017**, *7*, 7004.
541. Boland, T.; Mironov, V.; Gutowska, A.; Roth, E. A.; Markwald, R. R., Cell and Organ Printing 2: Fusion of Cell Aggregates in Three-Dimensional Gels. *Anat. Rec. A Discov. Mol. Cell. Evol. Biol.* **2003**, *272*, 497-502.
542. Biase, M. D.; Saunders, R. E.; Tirelliab, N.; Derby, B., Inkjet Printing and Cell Seeding Thermoreversible Photocurable Gel Structures. *Soft Matter* **2011**, *7*, 2639-2646.
543. Cui, X.; Breitenkamp, K.; Finn, M. G.; Lotz, M.; D'Lima, D. D., Direct Human Cartilage Repair Using Three-Dimensional Bioprinting Technology. *Tissue Engineering Part A* **2012**, *18* (11-12), 1304-1312.
544. Gao, G.; Yonezawa, T.; Hubbell, K.; Dai, G.; Cui, X., Inkjet-Bioprinted Acrylated Peptides and PEG Hydrogel with Human Mesenchymal Stem Cells Promote Robust Bone and Cartilage Formation with Minimal Printhead Clogging. *Biotechnol. J.* **2015**, *10*, 1568-1577.
545. Gao, G.; Schilling, A. F.; Yonezawa, T.; Wang, J.; Dai, G.; Cui, X., Bioactive Nanoparticles Stimulate Bone Tissue Formation in Bioprinted Three-Dimensional Scaffold and Human Mesenchymal Stem Cells. *Biotechnol. J.* **2014**, *9*, 1304-1311.
546. Gurkan, U. A.; El Assal, R.; Yildiz, S. E.; Sung, Y.; Trachtenberg, A. J.; Kuo, W. P.; Demirci, U., Engineering Anisotropic Biomimetic Fibrocartilage Microenvironment by Bioprinting Mesenchymal Stem Cells in Nanoliter Gel Droplets. *Mol. Pharm.* **2014**, *11*, 2151-2159.
547. Ji, Y.; Yang, Q.; Huang, G.; Shen, M.; Jian, Z.; Thoraval, M. J.; Lian, Q.; Zhang, X.; Xu, F., Improved Resolution and Fidelity of Droplet-Based Bioprinting by Upward Ejection. *ACS Biomater. Sci. Eng.* **2019**, *5*, 4112-4121.
548. Hoch, E.; Hirth, T.; Tovar, G. E. M.; Borchers, K., Chemical Tailoring of Gelatin to Adjust Its Chemical and Physical Properties for Functional Bioprinting. *J. Mater. Chem. B* **2013**, *1*, 5675-5685.
549. Ma, Y.; Ji, Y.; Huang, G.; Ling, K.; Zhang, X.; Xu, F., Bioprinting 3D Cell-Laden Hydrogel Microarray for Screening Human Periodontal Ligament Stem Cell Response to Extracellular Matrix. *Biofabrication* **2015**, *7*, 044105.
550. Ma, Y.; Ji, Y.; Zhong, T.; Wan, W.; Yang, Q.; Li, A.; Zhang, X.; Lin, M., Bioprinting-Based PDLSC-ECM Screening for in Vivo Repair of Alveolar Bone Defect Using Cell-Laden, Injectable and Photocrosslinkable Hydrogels. *ACS Biomater. Sci. Eng.* **2017**, *3*, 3534-3545.
551. Fujita, S.; Onuki-Nagasaki, R.; Fukuda, J.; Enomoto, J.; Yamaguchi, S.; Miyake, M., Development of Super-Dense Transfected Cell Microarrays Generated by Piezoelectric Inkjet Printing. *Lab Chip* **2013**, *13*, 77-80.

552. Jia, C.; Luo, B.; Wang, H.; Bian, Y.; Li, X.; Li, S.; Wang, H., Precise and Arbitrary Deposition of Biomolecules onto Biomimetic Fibrous Matrices for Spatially Controlled Cell Distribution and Functions. *Adv. Mater.* **2017**, *29*, 1701154.
553. Benning, L.; Gutzweiler, L.; Trondle, K.; Riba, J.; Zengerle, R.; Koltay, P.; Zimmermann, S.; Stark, G. B.; Finkenzeller, G., Assessment of Hydrogels for Bioprinting of Endothelial Cells. *J. Biomed. Mater. Res. A* **2018**, *106*, 935-947.
554. Onses, M. S.; Sutanto, E.; Ferreira, P. M.; Alleyne, A. G.; Rogers, J. A., Mechanisms, Capabilities, and Applications of High-Resolution Electrohydrodynamic Jet Printing. *Small* **2015**, *11* (34), 4237-4266.
555. Xu, C.; Zhang, M.; Huang, Y.; Ogale, A.; Fu, J.; Markwald, R. R., Study of Droplet Formation Process During Drop-on-Demand Inkjetting of Living Cell-Laden Bioink. *Langmuir* **2014**, *30*, 9130-9138.
556. Xu, T.; Jin, J.; Gregory, C.; Hickman, J. J.; Boland, T., Inkjet Printing of Viable Mammalian Cells. *Biomaterials* **2005**, *26*, 93-99.
557. Miller, D. J.; Fort, P. E., Heat Shock Proteins Regulatory Role in Neurodevelopment. *Front. Neurosci.* **2018**, *12*, 821.
558. Lanneau, D.; Brunet, M.; Frisan, E.; Solary, E.; Fontenay, M.; Garrido, C., Heat Shock Proteins: Essential Proteins for Apoptosis Regulation. *J. Cell. Mol. Med.* **2008**, *12*, 743-761.
559. Van Eden, W.; Van der Zee, R.; Prakken, B., Heat-Shock Proteins Induce T-Cell Regulation of Chronic Inflammation. *Nat. Rev. Immunol.* **2005**, *5*, 318-330.
560. Saunders, R. E.; Gough, J. E.; Derby, B., Delivery of Human Fibroblast Cells by Piezoelectric Drop-on-Demand Inkjet Printing. *Biomaterials* **2008**, *29*, 193-203.
561. Nishioka, G. M.; Markey, A. A.; Holloway, C. K., Protein Damage in Drop-on-Demand Printers. *J. Am. Chem. Soc.* **2004**, *126*, 16320-16321.
562. Nair, K.; Gandhi, M.; Khalil, S.; Yan, K. C.; Marcolongo, M.; Barbee, K.; Sun, W., Characterization of cell viability during bioprinting processes. *Biotechnol J* **2009**, *4* (8), 1168-77.
563. Kelly, B. E.; Bhattacharya, I.; Heidari, H.; Shusteff, M.; Spadaccini, C. M.; Taylor, H. K., Volumetric Additive Manufacturing via Tomographic Reconstruction. *Science* **2019**, *363*, 1075-1079.
564. Lee, B., Introduction to ± 12 Degree Orthogonal Digital Micromirror Devices (DMDs). *Copyright © 2008–2018, Texas Instruments Incorporated* **2018**.
565. Sun, C.; Fang, N.; Wu, D. M.; Zhang, X., Projection Micro-stereolithography Using Digital Micro-mirror Dynamic Mask. *Sens. Act. A Physical* **2005**, *121*, 113-120.
566. Januszewicz, R.; Tumbleston, J. R.; Quintanilla, A. L.; Mecham, S. J.; DeSimone, J. M., Layerless Fabrication with Continuous Liquid Interface Production. *Proc. Natl Acad. Sci. U. S. A.* **2016**, *113*, 11703-11708.
567. Tumbleston, J. R.; Shirvanyants, D.; Ermoshkin, N.; Januszewicz, R.; Johnson, A. R.; Kelly, D.; Chen, K.; Pinschmidt, R.; Rolland, J. P.; Ermoshkin, A.; Samulski, E. T.; DeSimone, J. M., Continuous Liquid Interface Production of 3D Objects. *Science* **2015**, *347*, 1349-1352.
568. Beer, M. P.; Laan, H. L.; Cole, M. A.; Whelan, R. J.; Burns, M. A.; Scott, T. F., Rapid, Continuous Additive Manufacturing by Volumetric Polymerization Inhibition Patterning. *Sci. Adv.* **2019**, *5*, eaau8723.
569. Kak, A. C.; Slaney, M., *Principles of Computerized Tomographic Imaging*. 1988.
570. Loterie, D.; Delrot, P.; Moser, C., High-resolution tomographic volumetric additive manufacturing. *Nature Communications* **2020**, *11* (1), 852.
571. Bernal, P. N.; Delrot, P.; Loterie, D.; Li, Y.; Malda, J.; Moser, C.; Levato, R., Volumetric Bioprinting of Complex Living-Tissue Constructs within Seconds. *Adv. Mater.* **2019**, *31*, 1904209.
572. Baldacchini, T., *Three-Dimensional Microfabrication Using Two-Photon Polymerization*. Elsevier Science: 2019.
573. Sakai, S.; Kamei, H.; Mori, T.; Hotta, T.; Ohi, H.; Nakahata, M.; Taya, M., Visible Light-Induced Hydrogelation of an Alginate Derivative and Application to Stereolithographic Bioprinting Using a Visible Light Projector and Acid Red. *Biomacromolecules* **2018**, *19*, 672-679.
574. Grigoryan, B.; Paulsen, S. J.; Corbett, D. C.; Sazer, D. W.; Fortin, C. L.; Zaita, A. J.; Greenfield, P. T.; Calafat, N. J.; Gounley, J. P.; Ta, A. H.; al., e., Multivascular Networks and Functional Intravascular Topologies Within Biocompatible Hydrogels. *Science* **2019**, *364*, 458-464.

575. Provin, C.; Monneret, S., Complex Ceramic-Polymer Composite Microparts Made by Microstereolithography. *IEEE Trans. Elect. Pack. Manuf.* **2002**, *25*, 59-63.
576. Chartier, T.; Badev, A.; Abouliatim, Y.; Lebaudy, P.; Lecamp, L., Stereolithography Process: Influence of the Rheology of Silica Suspensions and of the Medium on Polymerization Kinetics – Cured Depth and Width. *J. Eur. Ceram. Soc* **2012**, *32*, 1625-1634.
577. Sun, C.; Zhang, X., The Influences of the Material Properties on Ceramic Microstereolithography. *Sens. Act. A* **2002**, *101*, 364-370.
578. Lim, K. S.; Galarraga, J. H.; Cui, X.; Lindberg, G. C. J.; Burdick, J. A.; Woodfield, T. B. F., Fundamentals and Applications of Photo-Cross-Linking in Bioprinting. *Chem. Rev.* **2020**.
579. Chan, V.; Zorlutuna, P.; Jeong, J. H.; Kong, H.; Bashir, R., Three-Dimensional Photopatterning of Hydrogels Using Stereolithography for Long-Term Cell Encapsulation. *Lab Chip* **2010**, *10*, 2062–2070.
580. Lin, H.; Zhang, D.; Alexander, P. G.; Yang, G.; Tan, J.; Cheng, A. W. M.; Tuan, R. S., Application of Visible Light-Based Projection Stereolithography for Live Cell-Scaffold Fabrication with Designed Architecture. *Biomaterials* **2013**, *34*, 331-339.
581. Sun, A. X.; Lin, H.; Beck, A. M.; Kilroy, E. J.; Tuan, R. S., Projection Stereolithographic Fabrication of Human Adipose Stem Cell-Incorporated Biodegradable Scaffolds for Cartilage Tissue Engineering. *Front. Bioeng. Biotechnol.* **2015**, *3*, 115.
582. Lim, K. S.; Levato, R.; Costa, P. F.; Castilho, M. D.; Alcala-Orozco, C. R.; van Dorenmalen, K. M. A.; Melchels, F. P. W.; Gawlitta, D.; Hooper, G. J.; Malda, J.; Woodfield, T. B. F., Bio-resin for high resolution lithography-based biofabrication of complex cell-laden constructs. *Biofabrication* **2018**, *10* (3), 034101.
583. Hinczewski, C.; Corbel, S.; Chartier, T., Ceramic Suspensions Suitable for Stereolithography. *J. Eur. Ceram. Soc.* **1998**, *18*, 583-590.
584. Kim, S. H.; Yeon, Y. K.; Lee, J. M.; Chao, J. R.; Lee, Y. J.; Seo, Y. B.; Sultan, M. T.; Lee, O. J.; Lee, J. S.; Yoon, S.; Hong, I. N.; al., e., Precisely Printable and Biocompatible Silk Fibroin Bioink for Digital Light Processing 3D Printing. *Nat Comm* **2018**, *9*, 1620.
585. Wang, Z.; Kumar, H.; Tian, Z.; Jin, X.; Holzman, J. F.; Menard, F.; Kim, K., Visible Light Photoinitiation of Cell-Adhesive Gelatin Methacryloyl Hydrogels for Stereolithography 3D Bioprinting. *ACS Appl Mater Interfaces* **2018**, *10* (32), 26859-26869.
586. Wang, Z.; Jin, X.; Dai, R.; Holzmana, J. F.; Kim, K., An Ultrafast Hydrogel Photocrosslinking Method for Direct Laser Bioprinting. *RSC Adv.* **2016**, *6*, 21099-21104.
587. Raman, R.; Bhaduri, B.; Mir, M.; Shkumatov, A.; Lee, M. K.; Popescu, G.; Kong, H.; Bashir, R., High-Resolution Projection Microstereolithography for Patterning of Neovasculature. *Adv. Healthcare Mater.* **2016**, *5*, 610–619.
588. Klotz, B. J.; Gawlitta, D.; Rosenberg, A. J. W. P.; Malda, J.; Melchels, F. P. W., Gelatin-Methacryloyl Hydrogels: Towards Biofabrication-Based Tissue Repair. *Trends in Biotechnology* **2016**, *34* (5), 394-407.
589. Yu, C.; Ma, X.; Zhu, W.; Wang, P.; Miller, K. L.; Stupin, J.; Koroleva-Maharajh, A.; Hairabedian, A.; Chen, S., Scanningless and Continuous 3D Bioprinting of Human Tissues with Decellularized Extracellular Matrix. *Biomaterials* **2019**, *194*, 1-13.
590. Hong, J.; Shin, Y.; Kim, S.; Lee, J.; Cha, C., Complex Tuning of Physical Properties of Hyperbranched Polyglycerol-Based Bioink for Microfabrication of Cell-Laden Hydrogels. *Adv. Funct. Mater.* **2019**, *29*, 1808750.
591. Ma, X.; Qu, X.; Zhu, W.; Li, Y.; Yuan, S.; Zhang, H.; Liu, J.; Wang, P.; Lai, C. S. E.; Zanella, F.; al, e., Deterministically Patterned Biomimetic Human iPSC-Derived Hepatic Model via Rapid 3D Bioprinting. *Proc. Natl. Acad. Sci. U. S. A.* **2016**, *113*, 2206-2211.
592. Zhu, W.; Qu, X.; Zhu, J.; Ma, X.; Patel, S.; Liu, J.; Wang, P.; Lai, C. S. E.; Gou, M.; Xu, Y.; Zhang, K.; Chen, S., Direct 3D bioprinting of prevascularized tissue constructs with complex microarchitecture. *Biomaterials* **2017**, *124*, 106-115.
593. Liu, J.; Hwang, H. H.; Wang, P.; Whang, G.; Chen, S., Direct 3D-Printing of Cell-Laden Constructs in Microfluidic Architectures. *Lab Chip* **2016**, *16*, 1430-1438.

594. Kunwar, P.; Xiong, Z.; Zhu, Y.; Li, H.; Filip, A.; Soman, P., Hybrid Laser Printing of 3D, Multiscale, Multimaterial Hydrogel Structures. *Adv. Opt. Mater.* **2019**, *7*, 1900656.
595. Sun, A. X.; Lin, H.; Fritch, M. R.; Shen, H.; Alexander, P. G.; DeHart, M.; Tuan, R. S., Chondrogenesis of Human Bone Marrow Mesenchymal Stem Cells in 3-Dimensional, Photocrosslinked Hydrogel Constructs: Effect of Cell Seeding Density and Material Stiffness. *Acta Biomater.* **2017**, *58*, 302-311.
596. Lam, T.; Dehne, T.; Krüger, J. P.; Hondke, S.; Endres, M.; Thomas, A.; Lauster, R.; Sittinger, M.; Kloke, L., Photopolymerizable Gelatin and Hyaluronic Acid for Stereolithographic 3D Bioprinting of Tissue-Engineered Cartilage. *J. Biomed. Mater. Res. Part B* **2019**, *107B*, 2649-2657.
597. Lin, H.; Tang, Y.; Lozito, T. P.; Oyster, N.; Kang, R. B.; Fritch, M. R.; Wang, B.; Tuan, R. S., Projection Stereolithographic Fabrication of BMP-2 Geneactivated Matrix for Bone Tissue Engineering. *Sci. Rep.* **2017**, *7*, 11327.
598. Ma, X.; Yu, C.; Wang, P.; Xu, W.; Wan, X.; Lai, C. S. E.; Liu, J.; Koroleva-Maharajh, A.; Chen, S., Rapid 3D Bioprinting of Decellularized Extracellular Matrix with Regionally Varied Mechanical Properties and Biomimetic Microarchitecture. *Biomaterials* **2018**, *185*, 310-321.
599. Li, V. C.-F.; Kuang, X.; Mulyadi, A.; Hamel, C. M.; Deng, Y.; Qi, H. J., 3D Printed Cellulose Nanocrystal Composites Through Digital Light Processing. *Cellulose* **2019**, *26*, 3973-3985.
600. Yang, Y.; Chen, Z.; Song, X.; Zhang, Z.; Zhang, J.; Shung, K. K.; Zhou, Q.; Chen, Y., Biomimetic Anisotropic Reinforcement Architectures by Electrically Assisted Nanocomposite 3D Printing. *Adv. Mater.* **2017**, *29*, 1605750.
601. Chartrain, N. A.; Williams, C. B.; Whittington, A. R., A Review on Fabricating Tissue Scaffolds Using Vat Photopolymerization. *Acta Biomater.* **2018**, *74*, 90-111.
602. Göppert-Mayer, M., Über Elementarakte mit zwei Quantensprüngen. *Annalen der Physik* **1931**, *401*, 273-294.
603. Kaiser, W.; Garrett, C. G. B., Two-Photon Excitation in CaF₂:Eu²⁺. *Phys. Rev. Lett.* **1961**, *7*, 229-231.
604. Pawlicki, M.; Collins, H. A.; Denning, R. G.; Anderson, H. L., Two-Photon Absorption and the Design of Two-Photon Dyes. *Angew. Chem. Int. Ed.* **2009**, *48*, 3244-3266.
605. Torgersen, J.; Qin, X.-H.; Li, Z.; Ovsianikov, A.; Liska, R.; Stampfl, J., Hydrogels for Two-Photon Polymerization: A Toolbox for Mimicking the Extracellular Matrix. *Adv. Funct. Mater.* **2013**, *23*, 4542-4554.
606. Zipfel, W. R.; Williams, R. M.; Webb, W. W., Nonlinear Magic: Multiphoton Microscopy in the Biosciences. *Nat. Biotechnol.* **2003**, *21*, 1369-1377.
607. Squirrell, J. M.; Wokosin, D. L.; White, J. G.; Bavister, B. D., Long-Term Two-Photon Fluorescence Imaging of Mammalian Embryos Without Compromising Viability. *Nat. Biotechnol.* **1999**, *17*, 763-767.
608. Li, M.; Liu, F.; Jiang, H.; Lee, T. S.; Tang, S., Long-Term Two-Photon Imaging in Awake Macaque Monkey. *Neuron* **2017**, *93*, 1049-1057.
609. Helmchen, F.; Denk, W., Deep Tissue Two-photon Microscopy. *Nat. Methods* **2005**, *2*, 932-940.
610. Geng, Q.; Wang, D.; Chen, P.; Chen, S.-C., Ultrafast Multi-Focus 3-D Nano-Fabrication Based on Two-Photon Polymerization. *Nat. Commun.* **2019**, *10*, 2179.
611. Kato, J.-I.; Takeyasu, N.; Adachi, Y.; Sun, H.-B.; Kawata, S., Multiple-Spot Parallel Processing for Laser Micronanofabrication. *Appl. Phys. Lett.* **2005**, *86*, 044102.
612. Malinauskas, M.; Farsari, M.; Piskarskas, A.; Juodkazis, S., Ultrafast Laser Nanostructuring of Photopolymers: A Decade of Advances. *Phys. Rep.* **2013**, *533*, 1-31.
613. Van Hoorick, J.; Ottevaere, H.; Thienpont, H.; Dubruel, P.; Van Vlierberghe, S., *Polymer and Photonic Materials Towards Biomedical Breakthroughs*. Springer International Publishing: 2018.
614. Paschotta, R., *Encyclopedia of Laser Physics and Technology*. Wiley-VCH: 2008.
615. Yao, J.; Wang, Y., *Nonlinear Optics and Solid-State Lasers: Advanced Concepts, Tuning-Fundamentals and Applications*. Springer Berlin Heidelberg: 2012.
616. Haus, H. A., Mode-Locking of Lasers. *IEEE J. Sel. Top. Quant. Elect.* **2000**, *6*, 1173-1185.
617. Paschotta, R., *Field Guide to Laser Pulse Generation*. Society of Photo Optical: 2008.

618. Dobos, A.; Van Hoorick, J.; Steiger, W.; Gruber, P.; Markovic, M.; Andriotis, O. G.; Rohatschek, A.; Dubruel, P.; Thurner, P. J.; Van Vlierberghe, S.; al., e., Thiol–Gelatin–Norbornene Bioink for Laser-Based High-Definition Bioprinting. *Adv. Healthcare Mater.* **2019**, 1900752.
619. Dobos, A.; Steiger, W.; Theiner, D.; Gruber, P.; Lunzer, M.; Van Hoorick, J.; Van Vlierberghe, S.; Ovsianikov, A., Screening of Two-Photon Activated Photodynamic Therapy Sensitizers Using a 3D Osteosarcoma Model. *Analyst* **2019**, *144*, 3056-3063.
620. LaFratta, C. N.; Li, L., Chapter 9 - Making Two-Photon Polymerization Faster. In *Three-Dimensional Microfabrication Using Two-Photon Polymerization*, Baldacchini, T., Ed. William Andrew Publishing: Oxford, 2016; pp 221-241.
621. Sun, H.-B.; Takada, K.; Kim, M.-S.; Lee, K.-S.; Kawata, S., Scaling Laws of Voxels in Two-Photon Photopolymerization Nanofabrication. *App. Phys. Lett.* **2003**, *83*, 1104-1106.
622. Farsari, M.; Vamvakaki, M.; Chichkov, B. N., Multiphoton Polymerization of Hybrid Materials. *J. Opt.* **2010**, *12*, 124001.
623. Haske, W.; Chen, V. W.; Hales, J. M.; Dong, W.; Barlow, S.; Marder, S. R.; Perry, J. W., 65 Nm Feature Sizes Using Visible Wavelength 3-D Multiphoton Lithography. *Opt. Express* **2007**, *15*, 3426-3436.
624. Li, L.; Gattass, R. R.; Gershgoren, E.; Hwang, H.; Fourkas, J. T., Achieving $\lambda/20$ Resolution by One-Color Initiation and Deactivation of Polymerization. *Science* **2009**, *324*, 910-913.
625. Gan, Z.; Cao, Y.; Evans, R. A.; Gu, M., Three-Dimensional Deep Sub-Diffraction Optical Beam Lithography with 9 nm Feature Size. *Nat. Commun.* **2013**, *4*, 2061.
626. Lee, K.-S.; Kim, R. H.; Yang, D.-Y.; Park, S. H., Advances in 3D Nano/Microfabrication Using Two-Photon Initiated Polymerization. *Prog. Polym. Sci.* **2008**, *33*, 631-681.
627. Marino, A.; Filippeschi, C.; Genchi, G. G.; Mattoli, V.; Mazzolai, B.; Ciofani, G., The Osteoprint: A Bioinspired Two-Photon Polymerized 3-D Structure for the Enhancement of Bone-Like Cell Differentiation. *Acta Biomater.* **2014**, *10*, 4304-4313.
628. Alcântara, C. C. J.; Kim, S.; Lee, S.; Jang, B.; Thakolkaran, P.; Kim, J.-Y.; Choi, H.; Nelson, B. J.; Pané, S., 3D Fabrication of Fully Iron Magnetic Microrobots. *Small* **2019**, *15*, 1805006.
629. Larramendy, F.; Yoshida, S.; Maier, D.; Fekete, Z.; Takeuchi, S.; Paul, O., 3D Arrays of Microcages by Two-Photon Lithography for Spatial Organization of Living Cells. *Lab on a Chip* **2019**, *19*, 875-884.
630. Lölsberg, J.; Cinar, A.; Felder, D.; Linz, G.; Djeljadini, S.; Wessling, M., Two-Photon Vertical-Flow Lithography for Microtube Synthesis. *Small* **2019**, *15* (0), 1901356.
631. Tricinci, O.; Eason, E. V.; Filippeschi, C.; Mondini, A.; Mazzolai, B.; Pugno, N. M.; Cutkosky, M. R.; Greco, F.; Mattoli, V., Approximating Gecko Setae via Direct Laser Lithography. *Smart Mater. Struct.* **2018**, *27*, 075009.
632. Baker, R. D.; Montenegro-Johnson, T.; Sediako, A. D.; Thomson, M. J.; Sen, A.; Lauga, E.; Aranson, I. S., Shape-programmed 3D Printed Swimming Microtori for the Transport of Passive and Active Agents. *Nat. Commun.* **2019**, *10*, 4932.
633. Brown, T. E.; Anseth, K. S., Spatiotemporal Hydrogel Biomaterials for Regenerative Medicine. *Chem. Soc. Rev.* **2017**, *46*, 6532-6552.
634. Maruo, S.; Nakamura, O.; Kawata, S., Three-Dimensional Microfabrication with Two-Photon-Absorbed Photopolymerization. *Opt. Lett.* **1997**, *22*, 132-134.
635. Kawata, S.; Sun, H.-B.; Tanaka, T.; Takada, K., Finer Features for Functional Microdevices. *Nature* **2001**, *412*, 697-698.
636. LaFratta, C. N.; Fourkas, J. T.; Baldacchini, T.; Farrer, R. A., Multiphoton Fabrication. *Angew. Chem. Int. Ed.* **2007**, *46*, 6238-6258.
637. Yetisen, A. K.; Coskun, A. F.; England, G.; Cho, S.; Butt, H.; Hurwitz, J.; Kolle, M.; Khademhosseini, A.; Hart, A. J.; Folch, A.; al., e., Art on the Nanoscale and Beyond. *Adv. Mater.* **2016**, *28*, 1724-1742.
638. Klein, F.; Richter, B.; Striebel, T.; Franz, C. M.; Freymann, G. v.; Wegener, M.; Bastmeyer, M., Two-Component Polymer Scaffolds for Controlled Three-Dimensional Cell Culture. *Adv. Mater.* **2011**, *23*, 1341-1345.

639. Klein, F.; Striebel, T.; Fischer, J.; Jiang, Z.; Franz, C. M.; von Freymann, G.; Wegener, M.; Bastmeyer, M., Elastic Fully Three-Dimensional Microstructure Scaffolds for Cell Force Measurements. *Adv. Mater.* **2010**, *22*, 868-871.
640. Raimondi, M. T.; Eaton, S. M.; Nava, M. M.; Laganà, M.; Cerullo, G.; Osellame, R., Two-Photon Laser Polymerization: From Fundamentals to Biomedical Application in Tissue Engineering and Regenerative Medicine. *J. Appl. Biomater. Funct. Mater.* **2012**, *10*, 56-66.
641. Ovsianikov, A.; Schlie, S.; Ngezahayo, A.; Haverich, A.; Chichkov, B. N., Two-Photon Polymerization Technique for Microfabrication of CAD-Designed 3D Scaffolds from Commercially Available Photosensitive Materials. *J. Tissue Eng. Regen. Med.* **2007**, *1*, 443-449.
642. Ma, Z.; Koo, S.; Finnegan, M. A.; Loskill, P.; Huebsch, N.; Marks, N. C.; Conklin, B. R.; Grigoropoulos, C. P.; Healy, K. E., Three-Dimensional Filamentous Human Diseased Cardiac Tissue Model. *Biomaterials* **2014**, *35*, 1367-1377.
643. Marino, A.; Tricinci, O.; Battaglini, M.; Filippeschi, C.; Mattoli, V.; Sinibaldi, E.; Ciofani, G., A 3D Real-Scale, Biomimetic, and Biohybrid Model of the Blood-Brain Barrier Fabricated through Two-Photon Lithography. *Small* **2018**, *14*, 1702959.
644. Thompson, J. R.; Worthington, K. S.; Green, B. J.; Mullin, N. K.; Jiao, C.; Kaalberg, E. E.; Wiley, L. A.; Han, I. C.; Russell, S. R.; Sohn, E. H.; al., e., Two-Photon Polymerized Poly(Caprolactone) Retinal Cell Delivery Scaffolds and Their Systemic and Retinal Biocompatibility. *Acta Biomater.* **2019**, *94*, 204-218.
645. Melissinaki, V.; Gill, A. A.; Ortega, I.; Vamvakaki, M.; Ranella, A.; Haycock, J. W.; Fotakis, C.; Farsari, M.; Claeysens, F., Direct Laser Writing of 3D Scaffolds for Neural Tissue Engineering Applications. *Biofabrication* **2011**, *3*, 045005.
646. Koroleva, A.; Gill, A. A.; Ortega, I.; Haycock, J. W.; Schlie, S.; Gittard, S. D.; Chichkov, B. N.; Claeysens, F., Two-Photon Polymerization-Generated and Micromolding-Replicated 3D Scaffolds for Peripheral Neural Tissue Engineering Applications. *Biofabrication* **2012**, *4*, 025005.
647. Campagnola, P. J.; Delguidice, D. M.; Epling, G. A.; Hoffacker, K. D.; Howell, A. R.; Pitts, J. D.; Goodman, S. L., 3-Dimensional Submicron Polymerization of Acrylamide by Multiphoton Excitation of Xanthene Dyes. *Macromolecules* **2000**, *33*, 1511-1513.
648. Balčiūnas, E.; Baldock, S. J.; Dreizė, N.; Grubliauskaitė, M.; Coultas, S.; Rochester, D. L.; Valius, M.; Hardy, J. G.; Baltrikienė, D., 3D Printing Hybrid Organometallic Polymer-Based Biomaterials via Laser Two-Photon Polymerization. *Polymer Int.* **2019**, *68*, 1928-1940.
649. Wloka, T.; Czich, S.; Kleinstüber, M.; Moek, E.; Weber, C.; Gottschaldt, M.; Liefelth, K.; Schubert, U. S., Microfabrication of 3D-Hydrogels via Two-Photon Polymerization of Poly(2-Ethyl-2-Oxazoline) Diacrylates. *Eur. Polym. J.* **2020**, *122*, 109295.
650. Tudor, A.; Delaney, C.; Zhang, H.; Thompson, A. J.; Curto, V. F.; Yang, G.-Z.; Higgins, M. J.; Diamond, D.; Florea, L., Fabrication of Soft, Stimulus-Responsive Structures with Sub-Micron Resolution via Two-Photon Polymerization of Poly(Ionic Liquid)s. *Mater. Today* **2018**, *21*, 807-816.
651. Fonseca, R. D.; Correa, D. S.; Paris, E. C.; Tribuzi, V.; Dev, A.; Voss, T.; Aoki, P. H. B.; Constantino, C. J. L.; Mendonca, C. R., Fabrication of Zinc Oxide Nanowires/Polymer Composites by Two-photon Polymerization. *J. Polym. Sci. B Polym. Phys.* **2014**, *52*, 333-337.
652. Wang, J.; Xia, H.; Xu, B.-B.; Niu, L.-G.; Wu, D.; Chen, Q.-D.; Sun, H.-B., Remote Manipulation of Micronanomachines Containing Magnetic Nanoparticles. *Opt. Lett.* **2009**, *34*, 581-583.
653. Yasa, I. C.; Tabak, A. F.; Yasa, O.; Ceylan, H.; Sitti, M., 3D-Printed Microrobotic Transporters with Recapitulated Stem Cell Niche for Programmable and Active Cell Delivery. *Adv. Funct. Mater.* **2019**, *29*, 1808992.
654. Marino, A.; Barsotti, J.; de Vito, G.; Filippeschi, C.; Mazzolai, B.; Piazza, V.; Labardi, M.; Mattoli, V.; Ciofani, G., Two-Photon Lithography of 3D Nanocomposite Piezoelectric Scaffolds for Cell Stimulation. *ACS Appl. Mater. Inter.* **2015**, *7*, 25574-25579.
655. Lemma, E. D.; Spagnolo, B.; De Vittorio, M.; Pisanello, F., Studying Cell Mechanobiology in 3D: The Two-Photon Lithography Approach. *Trends Biotechnol* **2019**, *37*, 358-372.
656. Hippler, M.; Lemma, E. D.; Bertels, S.; Blasco, E.; Barner-Kowollik, C.; Wegener, M.; Bastmeyer, M., 3D Scaffolds to Study Basic Cell Biology. *Adv. Mater.* **2019**, *31*, 1808110.

657. Ovsianikov, A.; Ostendorf, A.; Chichkov, B. N., Three-Dimensional Photofabrication with Femtosecond Lasers for Applications in Photonics and Biomedicine. *Appl. Surf. Sci.* **2007**, *253*, 6599-6602.
658. Aksit, A.; Arteaga, D. N.; Arriaga, M.; Wang, X.; Watanabe, H.; Kasza, K. E.; Lalwani, A. K.; Kysar, J. W., In-Vitro Perforation of the Round Window Membrane via Direct 3-D Printed Microneedles. *Biomed. Microdev.* **2018**, *20*, 47.
659. Schizas, C.; Melissinaki, V.; Gaidukeviciute, A.; Reinhardt, C.; Ohrt, C.; Dedoussis, V.; Chichkov, B. N.; Fotakis, C.; Farsari, M.; Karalekas, D., On the Design and Fabrication by Two-Photon Polymerization of a Readily Assembled Micro-Valve. *Int. J. Adv. Manuf. Technol.* **2010**, *48*, 435-441.
660. Jiang, W.; Ma, L.; Xu, X., Recent Progress on the Design and Fabrication of Micromotors and Their Biomedical Applications. *Bio-des. Manuf.* **2018**, *1*, 225-236.
661. Serrano, P.; Decanini, D.; Leroy, L.; Couraud, L.; Hwang, G., Multiflagella Artificial Bacteria for Robust Microfluidic Propulsion and Multimodal Micromanipulation. *Microelec. Eng.* **2018**, *195*, 145-152.
662. Peters, C.; Costanza, V.; Pané, S.; Nelson, B. J.; Hierold, C. In *Superparamagnetic Hydrogels for Two-Photon Polymerization and Their Application for the Fabrication of Swimming Microrobots*, 18th International Conference on Solid-State Sensors, Actuators and Microsystems, 2015; pp 764-767.
663. Lee, S.; Kim, J.-y.; Kim, J.; Hoshidar, A. K.; Park, J.; Lee, S.; Kim, J.; Pané, S.; Nelson, B. J.; Choi, H., A Needle-Type Microrobot for Targeted Drug Delivery by Affixing to a Microtissue. *Adv. Healthcare Mater.* **2020**, *9*, 1901697.
664. Ceylan, H.; Yasa, I. C.; Yasa, O.; Tabak, A. F.; Giltinan, J.; Sitti, M., 3D-Printed Biodegradable Microswimmer for Theranostic Cargo Delivery and Release. *ACS Nano* **2019**, *13*, 3353-3362.
665. Bozuyuk, U.; Yasa, O.; Yasa, I. C.; Ceylan, H.; Kizilel, S.; Sitti, M., Light-Triggered Drug Release from 3D-Printed Magnetic Chitosan Microswimmers. *ACS Nano* **2018**, *12*, 9617-9625.
666. Wang, X.; Qin, X.-H.; Hu, C.; Terzopoulou, A.; Chen, X.-Z.; Huang, T.-Y.; Maniura-Weber, K.; Pané, S.; Nelson, B. J., 3D Printed Enzymatically Biodegradable Soft Helical Microswimmers. *Adv. Funct. Mater.* **2018**, *28*, 1804107.
667. Accardo, A.; Blatché, M. C.; Courson, R.; Loubinoux, I.; Vieu, C.; Malaquin, L., Two-Photon Lithography and Microscopy of 3D Hydrogel Scaffolds for Neuronal Cell Growth. *Biomed. Phys. Eng. Express* **2018**, *4*, 027009.
668. Zheng, Y.-C.; Zhao, Y.-Y.; Zheng, M.-L.; Chen, S.-L.; Liu, J.; Jin, F.; Dong, X.-Z.; Zhao, Z.-S.; Duan, X.-M., Cucurbit[7]uril-Carbazole Two-Photon Photoinitiators for the Fabrication of Biocompatible Three-Dimensional Hydrogel Scaffolds by Laser Direct Writing in Aqueous Solutions. *ACS Appl. Mater. Int.* **2019**, *11*, 1782-1789.
669. Ovsianikov, A.; Gruene, M.; Pflaum, M.; Koch, L.; Maiorana, F.; Wilhelmi, M.; Haverich, A.; Chichkov, B., Laser Printing of Cells Into 3D Scaffolds. *Biofabrication* **2010**, *2*, 014104.
670. Kufelt, O.; El-Tamer, A.; Sehring, C.; Schlie-Wolter, S.; Chichkov, B. N., Hyaluronic Acid Based Materials for Scaffolding via Two-Photon Polymerization. *Biomacromolecules* **2014**, *15*, 650-659.
671. Trautmann, A.; RÜth, M.; Lemke, H.-D.; Walther, T.; Hellmann, R., Two-Photon Polymerization Based Large Scaffolds for Adhesion and Proliferation Studies of Human Primary Fibroblasts. *Opt. Laser Technol.* **2018**, *106*, 474-480.
672. Florian, B.; Michel, K.; Steffi, G.; Nicole, H.; Frant, M.; Klaus, L.; Henning, S., MSC Differentiation on Two-Photon Polymerized, Stiffness and BMP2 Modified Biological Copolymers. *Biomed. Mater.* **2019**, *14*, 035001.
673. Paun, I. A.; Popescu, R. C.; Mustaciosu, C. C.; Zamfirescu, M.; Calin, B. S.; Mihailescu, M.; Dinescu, M.; Popescu, A.; Chioibas, D.; Soproniy, M.; al., e., Laser-Direct Writing by Two-Photon Polymerization of 3D Honeycomb-Like Structures for Bone Regeneration. *Biofabrication* **2018**, *10*, 025009.
674. Danilevicius, P.; Rezende, R. A.; Pereira, F. D. A. S.; Selimis, A.; Kasyanov, V.; Noritomi, P. Y.; da Silva, J. V. L.; Chatzinikolaidou, M.; Farsari, M.; Mironov, V., Burr-Like, Laser-Made 3D Microscaffolds for Tissue Spheroid Encagement. *Biointerphases* **2015**, *10*, 021011.
675. K p yl , E.; Aydogan, D. B.; Virjula, S.; Vanhatupa, S.; Miettinen, S.; Hyttinen, J.; Kellom ki, M., Direct Laser Writing and Geometrical Analysis of Scaffolds with Designed Pore Architecture for Three-Dimensional Cell Culturing. *J. Micromech. Microeng.* **2012**, *22*, 115016.

676. Do, A.-V.; Worthington, K. S.; Tucker, B. A.; Salem, A. K., Controlled Drug Delivery from 3D Printed Two-Photon Polymerized Poly(Ethylene Glycol) Dimethacrylate Devices. *Int. J. Pharmaceu.* **2018**, *552*, 217-224.
677. Gou, X.; Zheng, M.; Zhao, Y.; Dong, X.; Jin, F.; Xing, J.; Duan, X., Mechanical Property of PEG Hydrogel and the 3D Red Blood Cell Microstructures Fabricated by Two-Photon Polymerization. *Appl. Surf. Sci.* **2017**, *416*, 273-280.
678. Jhaveri, S. J.; McMullen, J. D.; Sijbesma, R.; Tan, L.-S.; Zipfel, W.; Ober, C. K., Direct Three-Dimensional Microfabrication of Hydrogels via Two-Photon Lithography in Aqueous Solution. *Chem. Mater.* **2009**, *21*, 2003-2006.
679. Hasselmann, N. F.; Hackmann, M. J.; Horn, W., Two-photon fabrication of hydrogel microstructures for excitation and immobilization of cells. *Biomedical Microdevices* **2017**, *20* (1), 8.
680. Ovsianikov, A.; Deiwick, A.; Van Vlierberghe, S.; Dubruel, P.; Möller, L.; Dräger, G.; Chichkov, B., Laser Fabrication of Three-Dimensional CAD Scaffolds from Photosensitive Gelatin for Applications in Tissue Engineering. *Biomacromolecules* **2011**, *12*, 851-858.
681. Ovsianikov, A.; Mühleder, S.; Torgersen, J.; Li, Z.; Qin, X.-H.; Van Vlierberghe, S.; Dubruel, P.; Holthöner, W.; Redl, H.; Liska, R.; al., e., Laser Photofabrication of Cell-Containing Hydrogel Constructs. *Langmuir* **2014**, *30*, 3787-3794.
682. Berg, A.; Wyrwa, R.; Weisser, J.; Weiss, T.; Schade, R.; Hildebrand, G.; Liefeth, K.; Schneider, B.; Ellinger, R.; Schnabelrauch, M., Synthesis of Photopolymerizable Hydrophilic Macromers and Evaluation of Their Applicability as Reactive Resin Components for the Fabrication of Three-Dimensionally Structured Hydrogel Matrices by 2-Photon-Polymerization. *Adv. Eng. Mater.* **2011**, *13*, B274-B284.
683. Kufelt, O.; El-Tamer, A.; Sehring, C.; Meißner, M.; Schlie-Wolter, S.; Chichkov, B. N., Water-Soluble Photopolymerizable Chitosan Hydrogels for Biofabrication via Two-Photon Polymerization. *Acta Biomater.* **2015**, *18*, 186-195.
684. Parkatzidis, K.; Chatzinikolaidou, M.; Kaliva, M.; Bakopoulou, A.; Farsari, M.; Vamvakaki, M., Multiphoton 3D Printing of Biopolymer-Based Hydrogels. *ACS Biomater. Sci. Eng.* **2019**, *5*, 6161-6170.
685. Rothhammer, M.; Heep, M.-C.; von Freymann, G.; Zollfrank, C., Enabling Direct Laser Writing of Cellulose-Based Submicron Architectures. *Cellulose* **2018**, *25*, 6031-6039.
686. Della Giustina, G.; Gandin, A.; Brigo, L.; Panciera, T.; Giullitti, S.; Sgarbossa, P.; D'Alessandro, D.; Trombi, L.; Danti, S.; Brusatin, G., Polysaccharide Hydrogels for Multiscale 3D Printing of Pullulan Scaffolds. *Mater. Design* **2019**, *165*, 107566.
687. Brigo, L.; Urciuolo, A.; Giullitti, S.; Della Giustina, G.; Tromayer, M.; Liska, R.; Elvassore, N.; Brusatin, G., 3D High-Resolution Two-Photon Crosslinked Hydrogel Structures for Biological Studies. *Acta Biomater.* **2017**, *55*, 373-384.
688. Qin, X.-H.; Ovsianikov, A.; Stampfl, J.; Liska, R., Additive Manufacturing of Photosensitive Hydrogels for Tissue Engineering Applications. *BioNanoMaterials* **2014**, *15*, 49-70.
689. McCall, J. D.; Anseth, K. S., Thiol-Ene Photopolymerizations Provide a Facile Method to Encapsulate Proteins and Maintain Their Bioactivity. *Biomacromolecules* **2012**, *13*, 2410-2417.
690. Roberts, J. J.; Bryant, S. J., Comparison of Photopolymerizable Thiol-Ene PEG and Acrylate-Based PEG Hydrogels for Cartilage Development. *Biomaterials* **2013**, *34*, 9969-9979.
691. Van Hoorick, J.; Gruber, P.; Markovic, M.; Rollot, M.; Graulus, G.-J.; Vagenende, M.; Tromayer, M.; Van Erps, J.; Thienpont, H.; Martins, J. C.; al., e., Highly Reactive Thiol-Norbornene Photo-Click Hydrogels: Toward Improved Processability. *Macromol. Rapid. Comm.* **2018**, *39*, 1800181.
692. Baudis, S.; Bomze, D.; Markovic, M.; Gruber, P.; Ovsianikov, A.; Liska, R., Modular Material System for the Microfabrication of Biocompatible Hydrogels Based on Thiol-Ene-Modified Poly(Vinyl Alcohol). *J. Polym. Sci. A Polym. Chem.* **2016**, *54*, 2060-2070.
693. Pitts, J. D.; Campagnola, P. J.; Epling, G. A.; Goodman, S. L., Submicron Multiphoton Free-Form Fabrication of Proteins and Polymers: Studies of Reaction Efficiencies and Applications in Sustained Release. *Macromolecules* **2000**, *33*, 1514-1523.

694. Pitts, J. D.; Howell, A. R.; Taboada, R.; Banerjee, I.; Wang, J.; Goodman, S. L.; Campagnola, P. J., New Photoactivators for Multiphoton Excited Three-Dimensional Submicron Cross-Linking of Proteins: Bovine Serum Albumin and Type 1 Collagen. *Photochem. Photobiol.* **2002**, *76*, 135-144.
695. Basu, S.; Rodionov, V.; Terasaki, M.; Campagnola, P. J., Multiphoton-Excited Microfabrication in Live Cells via Rose Bengal Cross-Linking of Cytoplasmic Proteins. *Opt. Lett.* **2005**, *30*, 159-161.
696. Connell, J. L.; Ritschdorff, E. T.; Whiteley, M.; Shear, J. B., 3D Printing of Microscopic Bacterial Communities. *Proc. Natl. Acad. Sci. U. S. A.* **2013**, *110*, 18380-18385.
697. Kaehr, B.; Allen, R.; Javier, D. J.; Currie, J.; Shear, J. B., Guiding Neuronal Development with in Situ Microfabrication. *Proc. Natl. Acad. Sci. U. S. A.* **2004**, *101*, 16104-16108.
698. Kaehr, B.; Shear, J. B., Multiphoton Fabrication of Chemically Responsive Protein Hydrogels for Microactuation. *Proc. Natl. Acad. Sci. U. S. A.* **2008**, *105*, 8850-8854.
699. Kaehr, B.; Shear, J. B., Mask-Directed Multiphoton Lithography. *J. Am. Chem. Soc.* **2007**, *129*, 1904-1905.
700. Basu, S.; Cunningham, L. P.; Pins, G. D.; Bush, K. A.; Taboada, R.; Howell, A. R.; Wang, J.; Campagnola, P. J., Multiphoton Excited Fabrication of Collagen Matrixes Cross-Linked by a Modified Benzophenone Dimer: Bioactivity and Enzymatic Degradation. *Biomacromolecules* **2005**, *6*, 1465-1474.
701. Cunningham, L. P.; Veilleux, M. P.; Campagnola, P. J., Freeform Multiphoton Excited Microfabrication for Biological Applications Using a Rapid Prototyping CAD-Based Approach. *Opt. Express* **2006**, *14*, 8613-8621.
702. Gebinoga, M.; Katzmann, J.; Fernekorn, U.; Hampl, J.; Weise, F.; Klett, M.; Löffert, A.; Klar, T. A.; Schober, A., Multi-Photon Structuring of Native Polymers: A Case Study for Structuring Natural Proteins. *Eng. Life Sci.* **2013**, *13*, 368-375.
703. Vining, K. H.; Mooney, D. J., Mechanical Forces Direct Stem Cell Behaviour in Development and Regeneration. *Nat. Rev. Mol. Cell Biol.* **2017**, *18*, 728-742.
704. Lutolf, M. P., Spotlight on Hydrogels. *Nat. Mater.* **2009**, *8*, 451-453.
705. Badeau, B. A.; Comerford, M. P.; Arakawa, C. K.; Shadish, J. A.; DeForest, C. A., Engineered Modular Biomaterial Logic Gates for Environmentally Triggered Therapeutic Delivery. *Nat. Chem.* **2018**, *10*, 251-258.
706. Theis, S.; Iturmendi, A.; Gorsche, C.; Orthofer, M.; Lunzer, M.; Baudis, S.; Ovsianikov, A.; Liska, R.; Monkowius, U.; Teasdale, I., Metallo-Supramolecular Gels that are Photocleavable with Visible and Near-Infrared Irradiation. *Angew. Chem. Int. Ed.* **2017**, *56*, 15857-15860.
707. García-Fernández, L.; Herbivo, C.; Arranz, V. S. M.; Warther, D.; Donato, L.; Specht, A.; del Campo, A., Dual Photosensitive Polymers with Wavelength-Selective Photoresponse. *Adv. Mater.* **2014**, *26*, 5012-5017.
708. Zhu, C.; Bettinger, C. J., Light-Induced Remodeling of Physically Crosslinked Hydrogels Using Near-IR Wavelengths. *J. Mater. Chem. B* **2014**, *2*.
709. Liu, Z.; Lin, Q.; Sun, Y.; Liu, T.; Bao, C.; Li, F.; Zhu, L., Spatiotemporally Controllable and Cytocompatible Approach Builds 3D Cell Culture Matrix by Photo-Uncaged-Thiol Michael Addition Reaction. *Adv. Mater.* **2014**, *26*, 3912-3917.
710. Brown, T. E.; Marozas, I. A.; Anseth, K. S., Amplified Photodegradation of Cell-Laden Hydrogels via an Addition-Fragmentation Chain Transfer Reaction. *Adv. Mater.* **2017**, *29*, 1605001.
711. Obata, K.; El-Tamer, A.; Koch, L.; Hinze, U.; Chichkov, B. N., High-Aspect 3D Two-Photon Polymerization Structuring with Widened Objective Working Range (WOW-2PP). *Light Sci. Appl.* **2013**, *2*, e116.
712. Chu, W.; Tan, Y.; Wang, P.; Xu, J.; Li, W.; Qi, J.; Cheng, Y., Centimeter-Height 3D Printing with Femtosecond Laser Two-Photon Polymerization. *Adv. Mater. Technol.* **2018**, *3*, 1700396.
713. He, F.; Xu, H.; Cheng, Y.; Ni, J.; Xiong, H.; Xu, Z.; Sugioka, K.; Midorikawa, K., Fabrication of Microfluidic Channels with a Circular Cross Section Using Spatiotemporally Focused Femtosecond Laser Pulses. *Opt. Lett.* **2010**, *35*, 1106-1108.
714. Saha, S. K.; Wang, D.; Nguyen, V. H.; Chang, Y.; Oakdale, J. S.; Chen, S.-C., Scalable Submicrometer Additive Manufacturing. *Science* **2019**, *366*, 105-109.

715. Manousidaki, M.; Papazoglou, D. G.; Farsari, M.; Tzortzakis, S., 3D Holographic Light Shaping for Advanced Multiphoton Polymerization. *Opt. Lett.* **2020**, *45*, 85-88.
716. Yang, D.; Liu, L.; Gong, Q.; Li, Y., Rapid Two-Photon Polymerization of an Arbitrary 3D Microstructure with 3D Focal Field Engineering. *Macromol. Rapid Commun.* **2019**, *40*, 1900041.
717. Vizsnyiczai, G.; Kelemen, L.; Ormos, P., Holographic Multi-Focus 3D Two-Photon Polymerization with Real-Time Calculated Holograms. *Opt. Express* **2014**, *22*, 24217-24223.
718. Richter, B.; Hahn, V.; Bertels, S.; Claus, T. K.; Wegener, M.; Delaittre, G.; Barner-Kowollik, C.; Bastmeyer, M., Guiding Cell Attachment in 3D Microscaffolds Selectively Functionalized with Two Distinct Adhesion Proteins. *Adv. Mater.* **2017**, *29*, 1604342.
719. Mayer, F.; Richter, S.; Westhauser, J.; Blasco, E.; Barner-Kowollik, C.; Wegener, M., Multimaterial 3D Laser Microprinting Using an Integrated Microfluidic System. *Sci. Adv.* **2019**, *5*, eaau9160.
720. Mačiulaitis, J.; Deveikytė, M.; Rekštytė, S.; Bratchikov, M.; Darinskas, A.; Šimbelytė, A.; Daunoras, G.; Laurinavičienė, A.; Laurinavičius, A.; Gudas, R.; al., e., Preclinical Study of SZ2080 Material 3D Microstructured Scaffolds for Cartilage Tissue Engineering Made by Femtosecond Direct Laser Writing Lithography. *Biofabrication* **2015**, *7*, 015015.
721. Gao, L.; Kupfer Molly, E.; Jung Jangwook, P.; Yang, L.; Zhang, P.; Da Sie, Y.; Tran, Q.; Ajeti, V.; Freeman Brian, T.; Fast Vladimir, G.; al., e., Myocardial Tissue Engineering With Cells Derived From Human-Induced Pluripotent Stem Cells and a Native-Like, High-Resolution, 3-Dimensionally Printed Scaffold. *Circ. Res.* **2017**, *120*, 1318-1325.
722. Jang, J.; Kim, J.-Y.; Kim, Y. C.; Kim, S.; Chou, N.; Lee, S.; Choung, Y.-H.; Kim, S.; Brugger, J.; Choi, H.; Jang, J. H., A 3D Microscaffold Cochlear Electrode Array for Steroid Elution. *Adv. Healthcare Mater.* **2019**, *8*, 1900379.
723. Hahn, M. S.; Miller, J. S.; West, J. L., Three-Dimensional Biochemical and Biomechanical Patterning of Hydrogels for Guiding Cell Behavior. *Adv. Mater.* **2006**, *18*, 2679-2684.
724. Lee, S.-H.; Moon, J. J.; West, J. L., Three-Dimensional Micropatterning of Bioactive Hydrogels via Two-Photon Laser Scanning Photolithography for Guided 3D Cell Migration. *Biomaterials* **2008**, *29*, 2962-2968.
725. Culver, J. C.; Hoffmann, J. C.; Poché, R. A.; Slater, J. H.; West, J. L.; Dickinson, M. E., Three-Dimensional Biomimetic Patterning in Hydrogels to Guide Cellular Organization. *Adv. Mater.* **2012**, *24*, 2344-2348.
726. Hoffmann, J. C.; West, J. L., Three-Dimensional Photolithographic Patterning of Multiple Bioactive Ligands in Poly(Ethylene Glycol) Hydrogels. *Soft Matter* **2010**, *6*, 5056-5063.
727. Ovsianikov, A.; Li, Z.; Torgersen, J.; Stampfl, J.; Liska, R., Selective Functionalization of 3D Matrices Via Multiphoton Grafting and Subsequent Click Chemistry. *Adv. Funct. Mater.* **2012**, *22*, 3429-3433.
728. DeForest, C. A.; Polizzotti, B. D.; Anseth, K. S., Sequential Click Reactions for Synthesizing and Patterning Three-Dimensional Cell Microenvironments. *Nat. Mater.* **2009**, *8*, 659-664.
729. Grim, J. C.; Brown, T. E.; Aguado, B. A.; Chapnick, D. A.; Viert, A. L.; Liu, X.; Anseth, K. S., A Reversible and Repeatable Thiol-Ene Bioconjugation for Dynamic Patterning of Signaling Proteins in Hydrogels. *ACS Central Sci.* **2018**, *4*, 909-916.
730. Gandavarapu, N. R.; Azagarsamy, M. A.; Anseth, K. S., Photo-Click Living Strategy for Controlled, Reversible Exchange of Biochemical Ligands. *Adv. Mater.* **2014**, *26*, 2521-2526.
731. Li, Z.; Stankevičius, E.; Ajami, A.; Račiukaitis, G.; Husinsky, W.; Ovsianikov, A.; Stampfl, J.; Liska, R., 3D Alkyne-Azide Cycloaddition: Spatiotemporally Controlled by Combination of Aryl Azide Photochemistry and Two-Photon Grafting. *Chem Comm.* **2013**, *49*, 7635-7637.
732. Seidlits, S. K.; Schmidt, C. E.; Shear, J. B., High-Resolution Patterning of Hydrogels in Three Dimensions using Direct-Write Photofabrication for Cell Guidance. *Adv. Funct. Mater.* **2009**, *19*, 3543-3551.
733. Luo, Y.; Shoichet, M. S., A Photolabile Hydrogel for Guided Three-Dimensional Cell Growth and Migration. *Nat. Mater.* **2004**, *3*, 249-253.
734. Wosnick, J. H.; Shoichet, M. S., Three-Dimensional Chemical Patterning of Transparent Hydrogels. *Chem. Mater.* **2008**, *20*, 55-60.

735. Rahman, N.; Purpura, K. A.; Wylie, R. G.; Zandstra, P. W.; Shoichet, M. S., The Use of Vascular Endothelial Growth Factor Functionalized Agarose to Guide Pluripotent Stem Cell Aggregates Toward Blood Progenitor Cells. *Biomaterials* **2010**, *31*, 8262-8270.
736. Wylie, R. G.; Ahsan, S.; Aizawa, Y.; Maxwell, K. L.; Morshead, C. M.; Shoichet, M. S., Spatially Controlled Simultaneous Patterning of Multiple Growth Factors in Three-Dimensional Hydrogels. *Nat. Mater.* **2011**, *10*, 799-806.
737. Aizawa, Y.; Shoichet, M. S., The Role of Endothelial Cells in the Retinal Stem and Progenitor Cell Niche Within a 3D Engineered Hydrogel Matrix. *Biomaterials* **2012**, *33*, 5198-5205.
738. Owen, S. C.; Fisher, S. A.; Tam, R. Y.; Nimmo, C. M.; Shoichet, M. S., Hyaluronic Acid Click Hydrogels Emulate the Extracellular Matrix. *Langmuir* **2013**, *29*, 7393-7400.
739. Mahmoodi, M. M.; Fisher, S. A.; Tam, R. Y.; Goff, P. C.; Anderson, R. B.; Wissinger, J. E.; Blank, D. A.; Shoichet, M. S.; Distefano, M. D., 6-Bromo-7-Hydroxy-3-Methylcoumarin (Mbhc) Is an Efficient Multi-Photon Labile Protecting Group for Thiol Caging and Three-Dimensional Chemical Patterning. *Org. Biomol. Chem.* **2016**, *14*, 8289-8300.
740. Aizawa, Y.; Wylie, R.; Shoichet, M., Endothelial Cell Guidance in 3D Patterned Scaffolds. *Adv. Mater.* **2010**, *22*, 4831-4835.
741. Wylie, R. G.; Shoichet, M. S., Two-photon micropatterning of amines within an agarose hydrogel. *Journal of Materials Chemistry* **2008**, *18* (23), 2716-2721.
742. Menge, C.; Heckel, A., Coumarin-Caged dG for Improved Wavelength-Selective Uncaging of DNA. *Org. Lett.* **2011**, *13*, 4620-4623.
743. Rodrigues-Correia, A.; Weyel, X. M. M.; Heckel, A., Four Levels of Wavelength-Selective Uncaging for Oligonucleotides. *Org. Lett.* **2013**, *15*, 5500-5503.
744. Fichte, M. A. H.; Weyel, X. M. M.; Junek, S.; Schäfer, F.; Herbivo, C.; Goeldner, M.; Specht, A.; Wachtveitl, J.; Heckel, A., Three-Dimensional Control of DNA Hybridization by Orthogonal Two-Color Two-Photon Uncaging. *Angew. Chem. Int. Ed.* **2016**, *55*, 8948-8952.
745. Becker, Y.; Unger, E.; Fichte, M. A. H.; Gacek, D. A.; Dreuw, A.; Wachtveitl, J.; Walla, P. J.; Heckel, A., A Red-Shifted Two-Photon-Only Caging Group for Three-Dimensional Photorelease. *Chem. Sci.* **2018**, *9*, 2797-2802.
746. Lee, T. T.; García, J. R.; Paez, J. I.; Singh, A.; Phelps, E. A.; Weis, S.; Shafiq, Z.; Shekaran, A.; del Campo, A.; García, A. J., Light-Triggered in Vivo Activation of Adhesive Peptides Regulates Cell Adhesion, Inflammation and Vascularization of Biomaterials. *Nat. Mater.* **2014**, *14*, 352-360.
747. Farrukh, A.; Paez, J. I.; del Campo, A., 4D Biomaterials for Light-Guided Angiogenesis. *Adv. Funct. Mater.* **2019**, *29*, 1807734.
748. Horváth, L.; Umehara, Y.; Jud, C.; Blank, F.; Petri-Fink, A.; Rothen-Rutishauser, B., Engineering an in Vitro Air-Blood Barrier by 3D Bioprinting. *Sci. Rep.* **2015**, *5*, 7974.
749. DaSilva-Arnold, S. C.; Kuo, C.-Y.; Davra, V.; Remache, Y.; Kim, P. C. W.; Fisher, J. P.; Zamudio, S.; Al-Khan, A.; Birge, R. B.; Illsley, N. P., ZEB2, A Master Regulator of the Epithelial-Mesenchymal Transition, Mediates Trophoblast Differentiation. *Mol. Hum. Reprod.* **2018**, *25*, 61-75.
750. Zhang, Y. S.; Davoudi, F.; Walch, P.; Manbachi, A.; Luo, X.; Dell'Erba, V.; Miri, A. K.; Albadawi, H.; Arneri, A.; Li, X.; Wang, X.; Dokmeci, M. R.; Khademhosseini, A.; Oklu, R., Bioprinted thrombosis-on-a-chip. *Lab on a Chip* **2016**, *16* (21), 4097-4105.
751. Cui, H.; Esworthy, T.; Zhou, X.; Hann, S. Y.; Glazer, R. I.; Li, R.; Zhang, L. G., Engineering a Novel 3D Printed Vascularized Tissue Model for Investigating Breast Cancer Metastasis to Bone. *Adv. Healthcare Mater.* **2019**, 1900924.
752. Liu, L.; Shadish, J. A.; Arakawa, C. K.; Shi, K.; Davis, J.; DeForest, C. A., Cyclic Stiffness Modulation of Cell-Laden Protein-Polymer Hydrogels in Response to User-Specified Stimuli Including Light. *Adv. Biosys.* **2018**, *2*.
753. Shadish, J. A.; Strange, A. C.; DeForest, C. A., Genetically Encoded Photocleavable Linkers for Patterned Protein Release from Biomaterials. *J. Am. Chem. Soc.* **2019**, *141*, 15619-15625.
754. Rapp, T. L.; DeForest, C. A., Visible Light-Responsive Dynamic Biomaterials: Going Deeper and Triggering More. *Adv. Healthcare Mater.* **2020**, *9*, 1901553.

755. Bryant, S. J.; Chowdhury, T. T.; Lee, D. A.; Bader, D. L.; Anseth, K. S., Crosslinking Density Influences Chondrocyte Metabolism in Dynamically Loaded Photocrosslinked Poly(ethylene glycol) Hydrogels. *Ann. Biomed. Eng.* **2004**, *32*, 407-417.
756. Bian, L.; Hou, C.; Tous, E.; Rai, R.; Mauck, R. L.; Burdick, J. A., The Influence of Hyaluronic Acid Hydrogel Crosslinking Density and Macromolecular Diffusivity on Human MSC Chondrogenesis and Hypertrophy. *Biomaterials* **2013**, *34*, 413-421.
757. Kwon, M. Y.; Wang, C.; Galarraga, J. H.; Puré, E.; Han, L.; Burdick, J. A., Influence of Hyaluronic Acid Modification on CD44 Binding Towards the Design of Hydrogel Biomaterials. *Biomaterials* **2019**, *222*, 119451.
758. Kirschning, A.; Dibbert, N.; Dräger, G., Chemical Functionalization of Polysaccharides—Towards Biocompatible Hydrogels for Biomedical Applications. *Chemistry* **2018**, *24*, 1231-1240.
759. Sriphutkiat, Y.; Kasetsirikul, S.; Ketpun, D.; Zhou, Y., Cell Alignment and Accumulation Using Acoustic Nozzle for Bioprinting. *Sci. Rep.* **2019**, *9*, 17774.
760. Chansoria, P.; Narayanan, L. K.; Schuchard, K.; Shirwaiker, R., Ultrasound-Assisted Biofabrication and Bioprinting of Preferentially Aligned Three-Dimensional Cellular Constructs. *Biofabrication* **2019**, *11*, 035015.
761. Parfenov, V. A.; Koudan, E. V.; Bulanova, E. A.; Karalkin, P. A.; Das Pereira, F.; Norkin, N. E.; Knyazeva, A. D.; Gryadunova, A. A.; Petrov, O. F.; Vasiliev, M. M.; al., e., Scaffold-Free, Label-Free and Nozzle-Free Biofabrication Technology Using Magnetic Levitational Assembly. *Biofabrication* **2018**, *10*, 034104.
762. Liu, T. K.; Pang, Y.; Zhou, Z. Z.; Yao, R.; Sun, W., An Integrated Cell Printing System for the Construction of Heterogeneous Tissue Models. *Acta Biomater.* **2019**, *95*, 245-257.
763. Shanjani, Y.; Pan, C. C.; Elomaa, L.; Yang, Y., A Novel Bioprinting Method and System for Forming Hybrid Tissue Engineering Constructs. *Biofabrication* **2015**, *7*, 045008.
764. Shim, J.-H.; Lee, J.-S.; Kim, J. Y.; Cho, D.-W., Bioprinting of a Mechanically Enhanced Three-Dimensional Dual Cell-Laden Construct for Osteochondral Tissue Engineering Using a Multi-Head Tissue/Organ Building System. *J. Micromech. Microeng.* **2012**, *22*, 085014.
765. Daly, A. C.; Kelly, D. J., Biofabrication of Spatially Organised Tissues by Directing the Growth of Cellular Spheroids Within 3D Printed Polymeric Microchambers. *Biomaterials* **2019**, *197*, 194-206.
766. Sugioka, K., Hybrid Femtosecond Laser Three-Dimensional Micro-and Nanoprocessing: A Review. *Int. J. Extrem. Manuf.* **2019**, *1*, 012003.
767. Brandenburg, N.; Lutolf, M. P., In Situ Patterning of Microfluidic Networks in 3D Cell-Laden Hydrogels. *Adv. Mater.* **2016**, *28*, 7450-7456.
768. Arakawa, C.; Gunnarsson, C.; Howard, C.; Bernabeu, M.; Phong, K.; Yang, E.; DeForest, C. A.; Smith, J. D.; Zheng, Y., Biophysical and Biomolecular Interactions of Malaria-Infected Erythrocytes in Engineered Human Capillaries. *Sci. Adv.* **2020**, *6*, eaay7243.
769. Gattass, R. R.; Mazur, E., Femtosecond Laser Micromachining in Transparent Materials. *Nat. Photon.* **2008**, *2*, 219-225.
770. Snyder, J.; Rin Son, A.; Hamid, Q.; Wang, C.; Lui, Y.; Sun, W., Mesenchymal stem cell printing and process regulated cell properties. *Biofabrication* **2015**, *7* (4), 044106.
771. Cook, C. C.; Fong, E. J.; Schwartz, J. J.; Porcincula, D. H.; Kaczmarek, A. C.; Oakdale, J. S.; Moran, B. D.; Champley, K. M.; Rackson, C. M.; Muralidharan, A.; McLeod, R. R.; Shusteff, M., Highly Tunable Thiol-Ene Photoreins for Volumetric Additive Manufacturing. *Advanced Materials* **2020**, *32* (47), 2003376.
772. Van Hoorick, J.; Dobos, A.; Markovic, M.; Gheysens, T.; Van Damme, L.; Gruber, P.; Tytgat, L.; Van Erps, J.; Thienpont, H.; Dubruel, P.; Ovsianikov, A.; Van Vlierberghe, S., Thiol-norbornene gelatin hydrogels: influence of thiolated crosslinker on network properties and high definition 3D printing. *Biofabrication* **2021**, *13* (1), 015017.
773. McCall, J. D.; Anseth, K. S., Thiol-Ene Photopolymerizations Provide a Facile Method To Encapsulate Proteins and Maintain Their Bioactivity. *Biomacromolecules* **2012**, *13* (8), 2410-2417.
774. Fairbanks, B. D.; Macdougall, L. J.; Mavila, S.; Sinha, J.; Kirkpatrick, B. E.; Anseth, K. S.; Bowman, C. N., Photoclick Chemistry: A Bright Idea. *Chemical Reviews* **2021**, *121* (12), 6915-6990.

775. Wolf, K.; te Lindert, M.; Krause, M.; Alexander, S.; te Riet, J.; Willis, A. L.; Hoffman, R. M.; Figdor, C. G.; Weiss, S. J.; Friedl, P., Physical limits of cell migration: Control by ECM space and nuclear deformation and tuning by proteolysis and traction force. *Journal of Cell Biology* **2013**, *201* (7), 1069-1084.
776. Van Den Bulcke, A. I.; Bogdanov, B.; De Rooze, N.; Schacht, E. H.; Cornelissen, M.; Berghmans, H., Structural and Rheological Properties of Methacrylamide Modified Gelatin Hydrogels. *Biomacromolecules* **2000**, *1* (1), 31-38.
777. Van Hoorick, J.; Gruber, P.; Markovic, M.; Rollot, M.; Graulus, G.-J.; Vagenende, M.; Tromayer, M.; Van Erps, J.; Thienpont, H.; Martins, J. C.; Baudis, S.; Ovsianikov, A.; Dubruel, P.; Van Vlierberghe, S., Highly Reactive Thiol-Norbornene Photo-Click Hydrogels: Toward Improved Processability. *Macromolecular Rapid Communications* **2018**, *39* (14), 1800181.
778. Yue, K.; Trujillo-de Santiago, G.; Alvarez, M. M.; Tamayol, A.; Annabi, N.; Khademhosseini, A., Synthesis, properties, and biomedical applications of gelatin methacryloyl (GelMA) hydrogels. *Biomaterials* **2015**, *73*, 254-71.
779. Leucht, A.; Volz, A. C.; Rogal, J.; Borchers, K.; Kluger, P. J., Advanced gelatin-based vascularization bioinks for extrusion-based bioprinting of vascularized bone equivalents. *Scientific Reports* **2020**, *10* (1), 5330.
780. Fan, L.; Liu, C.; Chen, X.; Zou, Y.; Zhou, Z.; Lin, C.; Tan, G.; Zhou, L.; Ning, C.; Wang, Q., Directing Induced Pluripotent Stem Cell Derived Neural Stem Cell Fate with a Three-Dimensional Biomimetic Hydrogel for Spinal Cord Injury Repair. *ACS Applied Materials & Interfaces* **2018**, *10* (21), 17742-17755.
781. Lee, B. H.; Shirahama, H.; Cho, N.-J.; Tan, L. P., Efficient and controllable synthesis of highly substituted gelatin methacrylamide for mechanically stiff hydrogels. *RSC Advances* **2015**, *5* (128), 106094-106097.
782. Muñoz, Z.; Shih, H.; Lin, C.-C., Gelatin hydrogels formed by orthogonal thiol-norbornene photochemistry for cell encapsulation. *Biomaterials Science* **2014**, *2* (8), 1063-1072.
783. Perera, M. M.; Ayres, N., Gelatin based dynamic hydrogels via thiol-norbornene reactions. *Polymer Chemistry* **2017**, *8* (44), 6741-6749.
784. Vlierberghe, S. V.; Schacht, E.; Dubruel, P., Reversible gelatin-based hydrogels: Finetuning of material properties. *European Polymer Journal* **2011**, *47* (5), 1039-1047.
785. Van Hoorick, J.; Declercq, H.; De Muyne, A.; Houben, A.; Van Hoorebeke, L.; Cornelissen, R.; Van Erps, J.; Thienpont, H.; Dubruel, P.; Van Vlierberghe, S., Indirect additive manufacturing as an elegant tool for the production of self-supporting low density gelatin scaffolds. *Journal of Materials Science: Materials in Medicine* **2015**, *26* (10), 247.
786. D'souza, A. A.; Shegokar, R., Polyethylene glycol (PEG): a versatile polymer for pharmaceutical applications. *Expert Opinion on Drug Delivery* **2016**, *13* (9), 1257-1275.
787. Readily3D. <https://readily3d.com/>.
788. Trappmann, B.; Baker, B. M.; Polacheck, W. J.; Choi, C. K.; Burdick, J. A.; Chen, C. S., Matrix degradability controls multicellularity of 3D cell migration. *Nature Communications* **2017**, *8* (1), 371.
789. Guo, X.; Mittelstaedt, R. A.; Guo, L.; Shaddock, J. G.; Heflich, R. H.; Bigger, A. H.; Moore, M. M.; Mei, N., Nitroxide TEMPO: A genotoxic and oxidative stress inducer in cultured cells. *Toxicology in Vitro* **2013**, *27* (5), 1496-1502.
790. Guo, X.; Seo, J.-E.; Bryce, S. M.; Tan, J. A.; Wu, Q.; Dial, S. L.; Moore, M. M.; Mei, N., Comparative Genotoxicity of TEMPO and 3 of Its Derivatives in Mouse Lymphoma Cells. *Toxicological Sciences* **2018**, *163* (1), 214-225.
791. Appiah, C.; Arndt, C.; Siemsen, K.; Heitmann, A.; Staubitz, A.; Selhuber-Unkel, C., Living Materials Herald a New Era in Soft Robotics. *Advanced Materials* **2019**, *31* (36), 1807747.
792. Fleischer, S.; Tavakol, D. N.; Vunjak-Novakovic, G., From Arteries to Capillaries: Approaches to Engineering Human Vasculature. *Advanced Functional Materials* **2020**, *30* (37), 1910811.
793. O'Grady, B. J.; Balotin, K. M.; Bosworth, A. M.; McClatchey, P. M.; Weinstein, R. M.; Gupta, M.; Poole, K. S.; Bellan, L. M.; Lippmann, E. S., Development of an N-Cadherin Biofunctionalized Hydrogel to Support the Formation of Synaptically Connected Neural Networks. *ACS Biomaterials Science & Engineering* **2020**, *6* (10), 5811-5822.

794. Liu, L.; Li, X.; Shi, X.; Wang, Y., Injectable alendronate-functionalized GelMA hydrogels for mineralization and osteogenesis. *RSC Advances* **2018**, *8* (40), 22764-22776.
795. Piluso, S.; Vukićević, R.; Nöchel, U.; Braune, S.; Lendlein, A.; Neffe, A. T., Sequential alkyne-azide cycloadditions for functionalized gelatin hydrogel formation. *European Polymer Journal* **2018**, *100*, 77-85.
796. Diba, M.; Camargo, W. A.; Brindisi, M.; Farbod, K.; Klymov, A.; Schmidt, S.; Harrington, M. J.; Draghi, L.; Boccaccini, A. R.; Jansen, J. A.; van den Beucken, J. J. J. P.; Leeuwenburgh, S. C. G., Composite Colloidal Gels Made of Bisphosphonate-Functionalized Gelatin and Bioactive Glass Particles for Regeneration of Osteoporotic Bone Defects. *Advanced Functional Materials* **2017**, *27* (45), 1703438.
797. Buie, T.; McCune, J.; Cosgriff-Hernandez, E., Gelatin Matrices for Growth Factor Sequestration. *Trends in Biotechnology* **2020**, *38* (5), 546-557.
798. Leung, C. M.; de Haan, P.; Ronaldson-Bouchard, K.; Kim, G.-A.; Ko, J.; Rho, H. S.; Chen, Z.; Habibovic, P.; Jeon, N. L.; Takayama, S.; Shuler, M. L.; Vunjak-Novakovic, G.; Frey, O.; Verpoorte, E.; Toh, Y.-C., A guide to the organ-on-a-chip. *Nature Reviews Methods Primers* **2022**, *2* (1), 33.
799. Qiu, Y.; Ahn, B.; Sakurai, Y.; Hansen, C. E.; Tran, R.; Mimche, P. N.; Mannino, R. G.; Ciciliano, J. C.; Lamb, T. J.; Joiner, C. H.; Ofori-Aquah, S. F.; Lam, W. A., Microvasculature-on-a-chip for the long-term study of endothelial barrier dysfunction and microvascular obstruction in disease. *Nature Biomedical Engineering* **2018**, *2* (6), 453-463.
800. Hsu, Y.-H.; Moya, M. L.; Hughes, C. C. W.; George, S. C.; Lee, A. P., A microfluidic platform for generating large-scale nearly identical human microphysiological vascularized tissue arrays. *Lab on a Chip* **2013**, *13* (15), 2990-2998.
801. Xie, R.; Zheng, W.; Guan, L.; Ai, Y.; Liang, Q., Engineering of Hydrogel Materials with Perfusable Microchannels for Building Vascularized Tissues. *Small* **2020**, *16* (15), 1902838.
802. Bernal, P. N.; Delrot, P.; Loterie, D.; Li, Y.; Malda, J.; Moser, C.; Levato, R., Volumetric Bioprinting of Complex Living-Tissue Constructs within Seconds. *Advanced Materials* **2019**, *31* (42), 1904209.
803. Bernal, P. N.; Bouwmeester, M.; Madrid-Wolff, J.; Falandt, M.; Florczak, S.; Rodriguez, N. G.; Li, Y.; Größbacher, G.; Samsom, R.-A.; van Wolferen, M.; van der Laan, L. J. W.; Delrot, P.; Loterie, D.; Malda, J.; Moser, C.; Spee, B.; Levato, R., Volumetric Bioprinting of Organoids and Optically Tuned Hydrogels to Build Liver-Like Metabolic Biofactories. *Advanced Materials* **2022**, *34* (15), 2110054.
804. Pradhan, S.; Keller, K. A.; Spurduto, J. L.; Slater, J. H., Fundamentals of Laser-Based Hydrogel Degradation and Applications in Cell and Tissue Engineering. *Advanced Healthcare Materials* **2017**, *6* (24), 1700681.
805. Schaffer, C. B.; Brodeur, A.; Mazur, E., Laser-induced breakdown and damage in bulk transparent materials induced by tightly focused femtosecond laser pulses. *Measurement Science and Technology* **2001**, *12* (11), 1784-1794.
806. Rayner, S. G.; Howard, C. C.; Mandrycky, C. J.; Stamenkovic, S.; Himmelfarb, J.; Shih, A. Y.; Zheng, Y., Multiphoton-Guided Creation of Complex Organ-Specific Microvasculature. *Advanced Healthcare Materials* **2021**, *10* (10), 2100031.
807. Mark, A. S.-S.; Man-Chi, L.; Yuelong, W.; Mehmet Fatih, Y. In *Multi-photon microfabrication of three-dimensional capillary-scale vascular networks*, Proc.SPIE, 2017; p 101150L.
808. Sarig-Nadir, O.; Livnat N Fau - Zajdman, R.; Zajdman R Fau - Shoham, S.; Shoham S Fau - Seliktar, D.; Seliktar, D., Laser photoablation of guidance microchannels into hydrogels directs cell growth in three dimensions. (1542-0086 (Electronic)).
809. Applegate, M. B.; Coburn, J.; Partlow, B. P.; Moreau, J. E.; Mondia, J. P.; Marelli, B.; Kaplan, D. L.; Omenetto, F. G., Laser-based three-dimensional multiscale micropatterning of biocompatible hydrogels for customized tissue engineering scaffolds. *Proceedings of the National Academy of Sciences* **2015**, *112* (39), 12052-12057.
810. Lee, B. L.-P.; Jeon, H.; Wang, A.; Yan, Z.; Yu, J.; Grigoropoulos, C.; Li, S., Femtosecond laser ablation enhances cell infiltration into three-dimensional electrospun scaffolds. *Acta Biomaterialia* **2012**, *8* (7), 2648-2658.

811. Enrico, A.; Voulgaris, D.; Östmans, R.; Sundaravadivel, N.; Moutaux, L.; Cordier, A.; Niklaus, F.; Herland, A.; Stemme, G., 3D Microvascularized Tissue Models by Laser-Based Cavitation Molding of Collagen. *Advanced Materials* **2022**, *34* (11), 2109823.
812. Liu, H.; Chansoria, P.; Delrot, P.; Angelidakis, E.; Rizzo, R.; Ruetsche, D.; Applegate, L. A.; Loterie, D.; Zenobi-Wong, M., Filamented Light (FLight) Biofabrication of Highly Aligned Tissue-engineered Constructs. *Advanced Materials* **2022**, *n/a* (n/a), 2204301.
813. Rackson, C. M.; Toombs, J. T.; De Beer, M. P.; Cook, C. C.; Shusteff, M.; Taylor, H. K.; McLeod, R. R., Latent image volumetric additive manufacturing. *Opt. Lett.* **2022**, *47* (5), 1279-1282.
814. Kewitsch, A. S.; Yariv, A., Self-focusing and self-trapping of optical beams upon photopolymerization. *Opt. Lett.* **1996**, *21* (1), 24-26.
815. Burgess, I. B.; Shimmell, W. E.; Saravanamuttu, K., Spontaneous Pattern Formation Due to Modulation Instability of Incoherent White Light in a Photopolymerizable Medium. *Journal of the American Chemical Society* **2007**, *129* (15), 4738-4746.
816. Biria, S.; Malley, P. P. A.; Kahan, T. F.; Hosein, I. D., Tunable Nonlinear Optical Pattern Formation and Microstructure in Cross-Linking Acrylate Systems during Free-Radical Polymerization. *The Journal of Physical Chemistry C* **2016**, *120* (8), 4517-4528.
817. Kip, D.; Soljagic, M.; Segev, M.; Eugenieva, E.; Christodoulides, D. N., Modulation Instability and Pattern Formation in Spatially Incoherent Light Beams. *Science* **2000**, *290* (5491), 495-498.
818. Scott, M. A.; Wissner-Gross, Z. D.; Yanik, M. F., Ultra-rapid laser protein micropatterning: screening for directed polarization of single neurons. *Lab on a Chip* **2012**, *12* (12), 2265-2276.
819. Broguiere, N.; Lüchtfeld, I.; Trachsel, L.; Mazunin, D.; Rizzo, R.; Bode, J. W.; Lutolf, M. P.; Zenobi-Wong, M., Morphogenesis Guided by 3D Patterning of Growth Factors in Biological Matrices. *Advanced Materials* **2020**, *32* (25), 1908299.
820. Rizzo, R.; Bonato, A.; Chansoria, P.; Zenobi-Wong, M., Macroporous Aligned Hydrogel Microstrands for 3D Cell Guidance. *ACS Biomaterials Science & Engineering* **2022**, *8* (9), 3871-3882.
821. Boyd, R. W.; Prato, D., *Nonlinear Optics*. Elsevier Science: 2008.
822. Becerra, J.; Andrades, J. A.; Guerado, E.; Zamora-Navas, P.; López-Puertas, J. M.; Reddi, A. H., Articular Cartilage: Structure and Regeneration. *Tissue Engineering Part B: Reviews* **2010**, *16* (6), 617-627.
823. Correa, D.; Lietman, S. A., Articular cartilage repair: Current needs, methods and research directions. *Seminars in Cell & Developmental Biology* **2017**, *62*, 67-77.
824. Temenoff, J. S.; Mikos, A. G., Review: tissue engineering for regeneration of articular cartilage. *Biomaterials* **2000**, *21* (5), 431-440.
825. Balakrishnan, B.; Banerjee, R., Biopolymer-Based Hydrogels for Cartilage Tissue Engineering. *Chemical Reviews* **2011**, *111* (8), 4453-4474.
826. Yang, J.; Zhang, Y. S.; Yue, K.; Khademhosseini, A., Cell-laden hydrogels for osteochondral and cartilage tissue engineering. *Acta Biomaterialia* **2017**, *57*, 1-25.
827. Chung, C.; Burdick, J. A., Engineering cartilage tissue. *Advanced Drug Delivery Reviews* **2008**, *60* (2), 243-262.
828. Liu, H.; Chansoria, P.; Delrot, P.; Angelidakis, E.; Rizzo, R.; Ruetsche, D.; Applegate, L. A.; Loterie, D.; Zenobi-Wong, M., Filamented Light (FLight) Biofabrication of Highly Aligned Tissue-Engineered Constructs. *Advanced Materials* **2022**, *n/a* (n/a), 2204301.
829. Öztürk, E.; Stauber, T.; Levinson, C.; Cavalli, E.; Arlov, Ø.; Zenobi-Wong, M., Tyrosinase-crosslinked, tissue adhesive and biomimetic alginate sulfate hydrogels for cartilage repair. *Biomedical Materials* **2020**, *15* (4), 045019.
830. Boschetti, F.; Pennati, G.; Gervaso, F.; Peretti, G. M.; Dubini, G., Biomechanical properties of human articular cartilage under compressive loads. *Biorheology* **2004**, *41*, 159-166.
831. Patel, J. M.; Wise, B. C.; Bonnevie, E. D.; Mauck, R. L., A Systematic Review and Guide to Mechanical Testing for Articular Cartilage Tissue Engineering. *Tissue Engineering Part C: Methods* **2019**, *25* (10), 593-608.

832. Robinson, D. L.; Kersh, M. E.; Walsh, N. C.; Ackland, D. C.; de Steiger, R. N.; Pandy, M. G., Mechanical properties of normal and osteoarthritic human articular cartilage. *Journal of the Mechanical Behavior of Biomedical Materials* **2016**, *61*, 96-109.
833. Guimarães, C. F.; Gasperini, L.; Marques, A. P.; Reis, R. L., The stiffness of living tissues and its implications for tissue engineering. *Nature Reviews Materials* **2020**, *5* (5), 351-370.
834. Shepherd, D. E. T.; Seedhom, B. B., Thickness of human articular cartilage in joints of the lower limb. *Annals of the Rheumatic Diseases* **1999**, *58* (1), 27.
835. Shah, R. F.; Martinez, A. M.; Padoia, V.; Majumdar, S.; Vail, T. P.; Bini, S. A., Variation in the Thickness of Knee Cartilage. The Use of a Novel Machine Learning Algorithm for Cartilage Segmentation of Magnetic Resonance Images. *The Journal of Arthroplasty* **2019**, *34* (10), 2210-2215.
836. Farr, J.; Yao, J. Q., Chondral Defect Repair with Particulated Juvenile Cartilage Allograft. *CARTILAGE* **2011**, *2* (4), 346-353.
837. Acosta, F. L.; Metz, L.; Adkisson, H. D.; Liu, J.; Carruthers-Liebenberg, E.; Milliman, C.; Maloney, M.; Lotz, J. C., Porcine Intervertebral Disc Repair Using Allogeneic Juvenile Articular Chondrocytes or Mesenchymal Stem Cells. *Tissue Engineering Part A* **2011**, *17* (23-24), 3045-3055.
838. Adkisson, H. D.; Martin, J. A.; Amendola, R. L.; Milliman, C.; Mauch, K. A.; Katwal, A. B.; Seyedin, M.; Amendola, A.; Streeter, P. R.; Buckwalter, J. A., The Potential of Human Allogeneic Juvenile Chondrocytes for Restoration of Articular Cartilage. *The American Journal of Sports Medicine* **2010**, *38* (7), 1324-1333.
839. Adkisson, H. D.; Milliman, C.; Zhang, X.; Mauch, K.; Maziarz, R. T.; Streeter, P. R., Immune evasion by neocartilage-derived chondrocytes: Implications for biologic repair of joint articular cartilage. *Stem Cell Research* **2010**, *4* (1), 57-68.
840. Ret, D.; Steiner, G.; Gentilini, S.; Knaus, S., Exact determination of the degree of substitution of high molar mass hyaluronan by controlling the conformation in solution. *Carbohydrate Polymers* **2019**, *204*, 124-130.
841. Cavalli, E.; Levinson, C.; Hertl, M.; Broguiere, N.; Brück, O.; Mustjoki, S.; Gerstenberg, A.; Weber, D.; Salzmann, G.; Steinwachs, M.; Barreto, G.; Zenobi-Wong, M., Characterization of polydactyly chondrocytes and their use in cartilage engineering. *Scientific Reports* **2019**, *9* (1), 4275.
842. Fu, J.; in het Panhuis, M., Hydrogel properties and applications. *Journal of Materials Chemistry B* **2019**, *7* (10), 1523-1525.
843. Ramiah, P.; du Toit, L. C.; Choonara, Y. E.; Kondiah, P. P. D.; Pillay, V., Hydrogel-Based Bioinks for 3D Bioprinting in Tissue Regeneration. *Frontiers in Materials* **2020**, *7*.
844. Lutzweiler, G.; Ndreu Halili, A.; Engin Vrana, N., The Overview of Porous, Bioactive Scaffolds as Instructive Biomaterials for Tissue Regeneration and Their Clinical Translation. *Pharmaceutics* **2020**, *12* (7).
845. De France, K. J.; Xu, F.; Hoare, T., Structured Macroporous Hydrogels: Progress, Challenges, and Opportunities. **2018**, *7* (1), 1700927.
846. Hamley, I. W., Small Bioactive Peptides for Biomaterials Design and Therapeutics. *Chemical Reviews* **2017**, *117* (24), 14015-14041.
847. Caballero Aguilar, L. M.; Silva, S. M.; Moulton, S. E., Growth factor delivery: Defining the next generation platforms for tissue engineering. *Journal of Controlled Release* **2019**, *306*, 40-58.
848. Huettner, N.; Dargaville, T. R.; Forget, A., Discovering Cell-Adhesion Peptides in Tissue Engineering: Beyond RGD. *Trends in Biotechnology* **2018**, *36* (4), 372-383.
849. Li, J.; Liu, Y.; Zhang, Y.; Yao, B.; Enhejirigala; Li, Z.; Song, W.; Wang, Y.; Duan, X.; Yuan, X.; Fu, X.; Huang, S., Biophysical and Biochemical Cues of Biomaterials Guide Mesenchymal Stem Cell Behaviors. *Frontiers in Cell and Developmental Biology* **2021**, *9*.
850. Qin, X.-H.; Wang, X.; Rottmar, M.; Nelson, B. J.; Maniura-Weber, K., Hydrogels: Near-Infrared Light-Sensitive Polyvinyl Alcohol Hydrogel Photoresist for Spatiotemporal Control of Cell-Instructive 3D Microenvironments (Adv. Mater. 10/2018). *Advanced Materials* **2018**, *30* (10), 1870070.
851. Schuldiner, M.; Yanuka, O.; Itskovitz-Eldor, J.; Melton, D. A.; Benvenisty, N., Effects of eight growth factors on the differentiation of cells derived from human embryonic stem cells. *Proceedings of the National Academy of Sciences* **2000**, *97* (21), 11307-11312.

852. Ma, J.; Huang, C., Composition and Mechanism of Three-Dimensional Hydrogel System in Regulating Stem Cell Fate. *Tissue Engineering Part B: Reviews* **2020**, *26* (6), 498-518.
853. Hersel, U.; Dahmen, C.; Kessler, H., RGD modified polymers: biomaterials for stimulated cell adhesion and beyond. *Biomaterials* **2003**, *24* (24), 4385-4415.
854. Heino, J., The collagen family members as cell adhesion proteins. *BioEssays* **2007**, *29* (10), 1001-1010.
855. Li, P.; Dou, X.; Feng, C.; Schönherr, H., Enhanced cell adhesion on a bio-inspired hierarchically structured polyester modified with gelatin-methacrylate. *Biomaterials Science* **2018**, *6* (4), 785-792.
856. Davidenko, N.; Schuster, C. F.; Bax, D. V.; Farndale, R. W.; Hamaia, S.; Best, S. M.; Cameron, R. E., Evaluation of cell binding to collagen and gelatin: a study of the effect of 2D and 3D architecture and surface chemistry. *Journal of Materials Science: Materials in Medicine* **2016**, *27* (10), 148.
857. Rose, J. C.; Gehlen, D. B.; Omidinia-Anarkoli, A.; Fölster, M.; Haraszti, T.; Jaekel, E. E.; De Laporte, L., How Much Physical Guidance is Needed to Orient Growing Axons in 3D Hydrogels? *Advanced Healthcare Materials* **2020**, *9* (21), 2000886.
858. Ledeck, C.; Villard, C., Cellular and Subcellular Contact Guidance on Microfabricated Substrates. *Frontiers in Bioengineering and Biotechnology* **2020**, *8*.
859. Gasiorowski, J. Z.; Murphy, C. J.; Nealey, P. F., Biophysical Cues and Cell Behavior: The Big Impact of Little Things. *Annual Review of Biomedical Engineering* **2013**, *15* (1), 155-176.
860. Kim, T. H.; An, D. B.; Oh, S. H.; Kang, M. K.; Song, H. H.; Lee, J. H., Creating stiffness gradient polyvinyl alcohol hydrogel using a simple gradual freezing–thawing method to investigate stem cell differentiation behaviors. *Biomaterials* **2015**, *40*, 51-60.
861. Guilak, F.; Cohen, D. M.; Estes, B. T.; Gimble, J. M.; Liedtke, W.; Chen, C. S., Control of Stem Cell Fate by Physical Interactions with the Extracellular Matrix. *Cell Stem Cell* **2009**, *5* (1), 17-26.
862. Engler, A. J.; Sen, S.; Sweeney, H. L.; Discher, D. E., Matrix Elasticity Directs Stem Cell Lineage Specification. *Cell* **2006**, *126* (4), 677-689.
863. Fereshteh, Z., 7 - Freeze-drying technologies for 3D scaffold engineering. In *Functional 3D Tissue Engineering Scaffolds*, Deng, Y.; Kuiper, J., Eds. Woodhead Publishing: 2018; pp 151-174.
864. Han, L.-H.; Yu, S.; Wang, T.; Behn, A. W.; Yang, F., Microribbon-Like Elastomers for Fabricating Macroporous and Highly Flexible Scaffolds that Support Cell Proliferation in 3D. *Advanced Functional Materials* **2013**, *23* (3), 346-358.
865. Gegg, C.; Yang, F., Spatially patterned microribbon-based hydrogels induce zonally-organized cartilage regeneration by stem cells in 3D. *Acta Biomaterialia* **2020**, *101*, 196-205.
866. Coogan, K. R.; Stone, P. T.; Sempertegui, N. D.; Rao, S. S., Fabrication of micro-porous hyaluronic acid hydrogels through salt leaching. *European Polymer Journal* **2020**, *135*, 109870.
867. Sokic, S.; Christenson, M.; Larson, J.; Papavasiliou, G., In Situ Generation of Cell-Laden Porous MMP-Sensitive PEGDA Hydrogels by Gelatin Leaching. *Macromolecular Bioscience* **2014**, *14* (5), 731-739.
868. Aubin, H.; Nichol, J. W.; Hutson, C. B.; Bae, H.; Sieminski, A. L.; Cropek, D. M.; Akhyari, P.; Khademhosseini, A., Directed 3D cell alignment and elongation in microengineered hydrogels. *Biomaterials* **2010**, *31* (27), 6941-6951.
869. Rose, J. C.; Cámara-Torres, M.; Rahimi, K.; Köhler, J.; Möller, M.; De Laporte, L., Nerve Cells Decide to Orient inside an Injectable Hydrogel with Minimal Structural Guidance. *Nano Letters* **2017**, *17* (6), 3782-3791.
870. Walls, H. J.; Caines, S. B.; Sanchez, A. M.; Khan, S. A., Yield stress and wall slip phenomena in colloidal silica gels. *Journal of Rheology* **2003**, *47* (4), 847-868.
871. Yang, M. C.; Scriven, L. E.; Macosko, C. W., Some Rheological Measurements on Magnetic Iron Oxide Suspensions in Silicone Oil. *Journal of Rheology* **1986**, *30* (5), 1015-1029.
872. Zhou, M.; Lee, B. H.; Tan, Y. J.; Tan, L. P., Microbial transglutaminase induced controlled crosslinking of gelatin methacryloyl to tailor rheological properties for 3D printing. *Biofabrication* **2019**, *11* (2), 025011.
873. Chansoria, P.; Shirwaiker, R., 3D bioprinting of anisotropic engineered tissue constructs with ultrasonically induced cell patterning. *Additive Manufacturing* **2020**, *32*, 101042.

874. Chansoria, P.; Asif, S.; Gupta, N.; Piedrahita, J.; Shirwaiker, R. A., Multiscale Anisotropic Tissue Biofabrication via Bulk Acoustic Patterning of Cells and Functional Additives in Hybrid Bioinks. *Advanced Healthcare Materials* **2022**, *n/a* (n/a), 2102351.
875. Ermis, M.; Antmen, E.; Hasirci, V., Micro and Nanofabrication methods to control cell-substrate interactions and cell behavior: A review from the tissue engineering perspective. *Bioactive Materials* **2018**, *3* (3), 355-369.
876. Abagnale, G.; Sechi, A.; Steger, M.; Zhou, Q.; Kuo, C.-C.; Aydin, G.; Schalla, C.; Müller-Newen, G.; Zenke, M.; Costa, I. G.; van Rijn, P.; Gillner, A.; Wagner, W., Surface Topography Guides Morphology and Spatial Patterning of Induced Pluripotent Stem Cell Colonies. *Stem Cell Reports* **2017**, *9* (2), 654-666.
877. Xue, X.; Hu, Y.; Wang, S.; Chen, X.; Jiang, Y.; Su, J., Fabrication of physical and chemical crosslinked hydrogels for bone tissue engineering. *Bioactive Materials* **2022**, *12*, 327-339.
878. Agüero, L.; Alpdagtas, S.; Ilhan, E.; Zaldivar-Silva, D.; Gunduz, O., Functional role of crosslinking in alginate scaffold for drug delivery and tissue engineering: A review. *European Polymer Journal* **2021**, *160*, 110807.
879. Berg, I.; Rizzo, R.; Lee, M.; Ren, Q.; Broguiere, N.; Zenobi-Wong, M., Factor XIII Cross-Linked Adhesive Chitosan Hydrogels. *ACS Biomaterials Science & Engineering* **2021**, *7* (6), 2198-2203.
880. Nikkhah, M.; Akbari, M.; Paul, A.; Memic, A.; Dolatshahi-Pirouz, A.; Khademhosseini, A., Gelatin-Based Biomaterials For Tissue Engineering And Stem Cell Bioengineering. *Biomaterials from Nature for Advanced Devices and Therapies* **2016**, 37-62.
881. Monteiro, N.; Thirivikraman, G.; Athirasala, A.; Tahayeri, A.; França, C. M.; Ferracane, J. L.; Bertassoni, L. E., Photopolymerization of cell-laden gelatin methacryloyl hydrogels using a dental curing light for regenerative dentistry. *Dental Materials* **2018**, *34* (3), 389-399.
882. Murphy, C. M.; Haugh, M. G.; O'Brien, F. J., The effect of mean pore size on cell attachment, proliferation and migration in collagen–glycosaminoglycan scaffolds for bone tissue engineering. *Biomaterials* **2010**, *31* (3), 461-466.
883. Loh, Q. L.; Choong, C., Three-Dimensional Scaffolds for Tissue Engineering Applications: Role of Porosity and Pore Size. *Tissue Engineering Part B: Reviews* **2013**, *19* (6), 485-502.
884. Qu, F.; Holloway, J. L.; Esterhai, J. L.; Burdick, J. A.; Mauck, R. L., Programmed biomolecule delivery to enable and direct cell migration for connective tissue repair. *Nature Communications* **2017**, *8* (1), 1780.
885. Lozinsky, V. I., Polymeric cryogels as a new family of macroporous and supermacroporous materials for biotechnological purposes. *Russian Chemical Bulletin* **2008**, *57* (5), 1015-1032.
886. Sahiner, N., Super macroporous poly(N-isopropyl acrylamide) cryogel for separation purpose. *Polymers for Advanced Technologies* **2018**, *29* (8), 2184-2191.
887. Dainiak, M. B.; Galaev, I. Y.; Kumar, A.; Plieva, F. M.; Mattiasson, B., Chromatography of Living Cells Using Supermacroporous Hydrogels, Cryogels. In *Cell Separation: Fundamentals, Analytical and Preparative Methods*, Kumar, A.; Galaev, I. Y.; Mattiasson, B., Eds. Springer Berlin Heidelberg: Berlin, Heidelberg, 2007; pp 101-127.
888. Gyarmati, B.; Mészár, E. Z.; Kiss, L.; Deli, M. A.; László, K.; Szilágyi, A., Supermacroporous chemically cross-linked poly(aspartic acid) hydrogels. *Acta Biomaterialia* **2015**, *22*, 32-38.
889. Karvinen, J.; Ihalainen, T. O.; Calejo, M. T.; Jönkkäri, I.; Kellomäki, M., Characterization of the microstructure of hydrazone crosslinked polysaccharide-based hydrogels through rheological and diffusion studies. *Materials Science and Engineering: C* **2019**, *94*, 1056-1066.
890. Nicol, E., Photopolymerized Porous Hydrogels. *Biomacromolecules* **2021**, *22* (4), 1325-1345.
891. Leal-Egaña, A.; Braumann, U.-D.; Díaz-Cuenca, A.; Nowicki, M.; Bader, A., Determination of pore size distribution at the cell-hydrogel interface. *Journal of Nanobiotechnology* **2011**, *9* (1), 24.
892. Cuccia, N. L.; Pothineni, S.; Wu, B.; Méndez Harper, J.; Burton, J. C., Pore-size dependence and slow relaxation of hydrogel friction on smooth surfaces. *Proceedings of the National Academy of Sciences* **2020**, *117* (21), 11247-11256.
893. Jain, R. K.; Au, P.; Tam, J.; Duda, D. G.; Fukumura, D., Engineering vascularized tissue. *Nature Biotechnology* **2005**, *23* (7), 821-823.

894. Richardson, S., On the no-slip boundary condition. *Journal of Fluid Mechanics* **1973**, *59* (4), 707-719.
895. Cidonio, G.; Glinka, M.; Dawson, J. I.; Oreffo, R. O. C., The cell in the ink: Improving biofabrication by printing stem cells for skeletal regenerative medicine. *Biomaterials* **2019**, *209*, 10-24.
896. Bae, Y. B.; Jang, H. K.; Shin, T. H.; Phukan, G.; Tran, T. T.; Lee, G.; Hwang, W. R.; Kim, J. M., Microfluidic assessment of mechanical cell damage by extensional stress. *Lab on a Chip* **2016**, *16* (1), 96-103.
897. Tanzeglock, T.; Soos, M.; Stephanopoulos, G.; Morbidelli, M., Induction of mammalian cell death by simple shear and extensional flows. *Biotechnology and Bioengineering* **2009**, *104* (2), 360-370.
898. Costantini, M.; Testa, S.; Fornetti, E.; Barbetta, A.; Trombetta, M.; Cannata, S. M.; Gargioli, C.; Rainer, A., Engineering Muscle Networks in 3D Gelatin Methacryloyl Hydrogels: Influence of Mechanical Stiffness and Geometrical Confinement. *Frontiers in Bioengineering and Biotechnology* **2017**, *5*.
899. Zhuang, P.; An, J.; Chua, C. K.; Tan, L. P., Bioprinting of 3D in vitro skeletal muscle models: A review. *Materials & Design* **2020**, *193*, 108794.
900. Khodabukus, A.; Prabhu, N.; Wang, J.; Bursac, N., In Vitro Tissue-Engineered Skeletal Muscle Models for Studying Muscle Physiology and Disease. *Advanced Healthcare Materials* **2018**, *7* (15), 1701498.
901. Cittadella Vigodarzere, G.; Mantero, S., Skeletal muscle tissue engineering: strategies for volumetric constructs. *Frontiers in Physiology* **2014**, *5*.
902. Schäfer, B.; Cai, A.; Ruhl, T.; Beier, J. P., Chapter 14 - Skeletal muscle tissue engineering. In *Tissue Engineering Using Ceramics and Polymers (Third Edition)*, Boccaccini, A. R.; Ma, P. X.; Liverani, L., Eds. Woodhead Publishing: 2022; pp 519-553.
903. Carnes, M. E.; Pins, G. D., Skeletal Muscle Tissue Engineering: Biomaterials-Based Strategies for the Treatment of Volumetric Muscle Loss. *Bioengineering* **2020**, *7* (3).
904. Gilbert-Honick, J.; Grayson, W., Vascularized and Innervated Skeletal Muscle Tissue Engineering. *Advanced Healthcare Materials* **2020**, *9* (1), 1900626.
905. Naranjo, J. D.; Dziki, J. L.; Badylak, S. F., Regenerative Medicine Approaches for Age-Related Muscle Loss and Sarcopenia: A Mini-Review. *Gerontology* **2017**, *63* (6), 580-589.
906. Cai, Z.; Liu, D.; Yang, Y.; Xie, W.; He, M.; Yu, D.; Wu, Y.; Wang, X.; Xiao, W.; Li, Y., The role and therapeutic potential of stem cells in skeletal muscle in sarcopenia. *Stem Cell Research & Therapy* **2022**, *13* (1), 28.
907. Wang, P.-Y.; Yu, H.-T.; Tsai, W.-B., Modulation of alignment and differentiation of skeletal myoblasts by submicron ridges/grooves surface structure. *Biotechnology and Bioengineering* **2010**, *106* (2), 285-294.
908. Liao, I. C.; Liu, J. B.; Bursac, N.; Leong, K. W., Effect of Electromechanical Stimulation on the Maturation of Myotubes on Aligned Electrospun Fibers. *Cellular and Molecular Bioengineering* **2008**, *1* (2), 133-145.
909. Azevedo, M.; Baylies, M. K., Getting into Position: Nuclear Movement in Muscle Cells. *Trends in Cell Biology* **2020**, *30* (4), 303-316.
910. Rozwadowska, N.; Kolanowski, T.; Wiland, E.; Siatkowski, M.; Pawlak, P.; Malcher, A.; Mietkiewski, T.; Olszewska, M.; Kurpisz, M., Characterisation of Nuclear Architectural Alterations during In Vitro Differentiation of Human Stem Cells of Myogenic Origin. *PLOS ONE* **2013**, *8* (9), e73231.
911. Roman, W.; Gomes, E. R., Nuclear positioning in skeletal muscle. *Seminars in Cell & Developmental Biology* **2018**, *82*, 51-56.
912. Espigat-Georger, A.; Dyachuk, V.; Chemin, C.; Emorine, L.; Merdes, A., Nuclear alignment in myotubes requires centrosome proteins recruited by nesprin-1. *Journal of Cell Science* **2016**, *129* (22), 4227-4237.
913. Li, L.; Scheiger, J. M.; Levkin, P. A., Design and Applications of Photoresponsive Hydrogels. *Advanced Materials* **2019**, *31* (26), 1807333.
914. del Barrio, J.; Sánchez-Somolinos, C., Light to Shape the Future: From Photolithography to 4D Printing. *Advanced Optical Materials* **2019**, *7* (16), 1900598.
915. Grigoryan, B.; Paulsen, S. J.; Corbett, D. C.; Sazer, D. W.; Fortin, C. L.; Zaita, A. J.; Greenfield, P. T.; Calafat, N. J.; Gounley, J. P.; Ta, A. H.; Johansson, F.; Randles, A.; Rosenkrantz, J. E.; Louis-Rosenberg,

- J. D.; Galie, P. A.; Stevens, K. R.; Miller, J. S., Multivascular networks and functional intravascular topologies within biocompatible hydrogels. *Science* **2019**, *364* (6439), 458-464.
916. Wang, M.; Li, W.; Hao, J.; Gonzales, A.; Zhao, Z.; Flores, R. S.; Kuang, X.; Mu, X.; Ching, T.; Tang, G.; Luo, Z.; Garciamendez-Mijares, C. E.; Sahoo, J. K.; Wells, M. F.; Niu, G.; Agrawal, P.; Quiñones-Hinojosa, A.; Eggen, K.; Zhang, Y. S., Molecularly cleavable bioinks facilitate high-performance digital light processing-based bioprinting of functional volumetric soft tissues. *Nature Communications* **2022**, *13* (1), 3317.
917. Ovsianikov, A.; Mironov, V.; Stampfl, J.; Liska, R., Engineering 3D cell-culture matrices: multiphoton processing technologies for biological and tissue engineering applications. *Expert Review of Medical Devices* **2012**, *9* (6), 613-633.
918. Torgersen, J.; Qin, X.-H.; Li, Z.; Ovsianikov, A.; Liska, R.; Stampfl, J., Hydrogels for Two-Photon Polymerization: A Toolbox for Mimicking the Extracellular Matrix. *Advanced Functional Materials* **2013**, *23* (36), 4542-4554.
919. Williams, C. G.; Malik, A. N.; Kim, T. K.; Manson, P. N.; Elisseeff, J. H., Variable cytocompatibility of six cell lines with photoinitiators used for polymerizing hydrogels and cell encapsulation. *Biomaterials* **2005**, *26* (11), 1211-1218.
920. Bryant, S. J.; Nuttelman, C. R.; Anseth, K. S., Cytocompatibility of UV and visible light photoinitiating systems on cultured NIH/3T3 fibroblasts in vitro. *Journal of Biomaterials Science, Polymer Edition* **2000**, *11* (5), 439-457.
921. Fedorovich, N. E.; Oudshoorn, M. H.; van Geemen, D.; Hennink, W. E.; Alblas, J.; Dhert, W. J. A., The effect of photopolymerization on stem cells embedded in hydrogels. *Biomaterials* **2009**, *30* (3), 344-353.
922. Ruskowitz, E. R.; DeForest, C. A., Proteome-wide Analysis of Cellular Response to Ultraviolet Light for Biomaterial Synthesis and Modification. *ACS Biomaterials Science & Engineering* **2019**, *5* (5), 2111-2116.
923. Nguyen, A. K.; Goering, P. L.; Elespuru, R. K.; Sarkar Das, S.; Narayan, R. J., The Photoinitiator Lithium Phenyl (2,4,6-Trimethylbenzoyl) Phosphinate with Exposure to 405 nm Light Is Cytotoxic to Mammalian Cells but Not Mutagenic in Bacterial Reverse Mutation Assays. *Polymers* **2020**, *12* (7).
924. Klán, P.; Šolomek, T.; Bochet, C. G.; Blanc, A.; Givens, R.; Rubina, M.; Popik, V.; Kostikov, A.; Wirz, J., Photoremovable Protecting Groups in Chemistry and Biology: Reaction Mechanisms and Efficacy. *Chemical Reviews* **2013**, *113* (1), 119-191.
925. Hoyle, C. E.; Bowman, C. N., Thiol–Ene Click Chemistry. *Angewandte Chemie International Edition* **2010**, *49* (9), 1540-1573.
926. Pelliccioli, A. P.; Wirz, J., Photoremovable protecting groups: reaction mechanisms and applications. *Photochemical & Photobiological Sciences* **2002**, *1* (7), 441-458.
927. Kloxin, A. M.; Kasko, A. M.; Salinas, C. N.; Anseth, K. S., Photodegradable Hydrogels for Dynamic Tuning of Physical and Chemical Properties. *Science* **2009**, *324* (5923), 59-63.
928. Badeau, B. A.; Comerford, M. P.; Arakawa, C. K.; Shadish, J. A.; DeForest, C. A., Engineered modular biomaterial logic gates for environmentally triggered therapeutic delivery. *Nature Chemistry* **2018**, *10* (3), 251-258.
929. DeForest, C. A.; Anseth, K. S., Cytocompatible click-based hydrogels with dynamically tunable properties through orthogonal photoconjugation and photocleavage reactions. *Nature Chemistry* **2011**, *3* (12), 925-931.
930. Liu, Z.; Lin, Q.; Sun, Y.; Liu, T.; Bao, C.; Li, F.; Zhu, L., Spatiotemporally Controllable and Cytocompatible Approach Builds 3D Cell Culture Matrix by Photo-Uncaged-Thiol Michael Addition Reaction. *Advanced Materials* **2014**, *26* (23), 3912-3917.
931. Paez, J. I.; Farrukh, A.; Valbuena-Mendoza, R.; Włodarczyk-Biegun, M. K.; del Campo, A., Thiol-Methylsulfone-Based Hydrogels for 3D Cell Encapsulation. *ACS Applied Materials & Interfaces* **2020**, *12* (7), 8062-8072.
932. Paez, J. I.; de Miguel-Jiménez, A.; Valbuena-Mendoza, R.; Rathore, A.; Jin, M.; Gläser, A.; Pearson, S.; del Campo, A., Thiol-Methylsulfone-Based Hydrogels for Cell Encapsulation: Reactivity Optimization

of Aryl-Methylsulfone Substrate for Fine-Tunable Gelation Rate and Improved Stability. *Biomacromolecules* **2021**, *22* (7), 2874-2886.

933. Baldwin, A. D.; Küick, K. L., Reversible maleimide–thiol adducts yield glutathione-sensitive poly(ethylene glycol)–heparin hydrogels. *Polymer Chemistry* **2013**, *4* (1), 133-143.

934. Weissman, M. R.; Winger, K. T.; Ghiassian, S.; Gobbo, P.; Workentin, M. S., Insights on the Application of the Retro Michael-Type Addition on Maleimide-Functionalized Gold Nanoparticles in Biology and Nanomedicine. *Bioconjugate Chemistry* **2016**, *27* (3), 586-593.

935. Frija, L. M. T.; Ismael, A.; Cristiano, M. L. S., Photochemical Transformations of Tetrazole Derivatives: Applications in Organic Synthesis. *Molecules* **2010**, *15* (5).

936. Maier, G.; Eckwert, J.; Bothur, A.; Reisenauer, H. P.; Schmidt, C., Photochemical Fragmentation of Unsubstituted Tetrazole, 1,2,3-Triazole, and 1,2,4-Triazole: First Matrix-Spectroscopic Identification of Nitrilimine HCNNH. *Liebigs Annalen* **1996**, *1996* (7), 1041-1053.

937. Sakai, S.; Kamei, H.; Mori, T.; Hotta, T.; Ohi, H.; Nakahata, M.; Taya, M., Visible Light-Induced Hydrogelation of an Alginate Derivative and Application to Stereolithographic Bioprinting Using a Visible Light Projector and Acid Red. *Biomacromolecules* **2018**, *19* (2), 672-679.

938. Yang, Y.; Zhou, Y.; Lin, X.; Yang, Q.; Yang, G., Printability of External and Internal Structures Based on Digital Light Processing 3D Printing Technique. *Pharmaceutics* **2020**, *12* (3).

939. Seo, J. W.; Kim, G. M.; Choi, Y.; Cha, J. M.; Bae, H., Improving Printability of Digital-Light-Processing 3D Bioprinting via Photoabsorber Pigment Adjustment. *International Journal of Molecular Sciences* **2022**, *23* (10).

940. Fukai, T.; Ushio-Fukai, M., Superoxide Dismutases: Role in Redox Signaling, Vascular Function, and Diseases. *Antioxidants & Redox Signaling* **2011**, *15* (6), 1583-1606.

941. Zelko, I. N.; Mariani, T. J.; Folz, R. J., Superoxide dismutase multigene family: a comparison of the CuZn-SOD (SOD1), Mn-SOD (SOD2), and EC-SOD (SOD3) gene structures, evolution, and expression. *Free Radical Biology and Medicine* **2002**, *33* (3), 337-349.

942. Landis, G. N.; Tower, J., Superoxide dismutase evolution and life span regulation. *Mechanisms of Ageing and Development* **2005**, *126* (3), 365-379.

943. Bresciani, G.; da Cruz, I. B. M.; González-Gallego, J., Chapter Four - Manganese Superoxide Dismutase and Oxidative Stress Modulation. In *Advances in Clinical Chemistry*, Makowski, G. S., Ed. Elsevier: 2015; Vol. 68, pp 87-130.

944. Wang, Y.; Branicky, R.; Noë, A.; Hekimi, S., Superoxide dismutases: Dual roles in controlling ROS damage and regulating ROS signaling. *Journal of Cell Biology* **2018**, *217* (6), 1915-1928.

945. Harris, Isaac S.; Treloar, Aislinn E.; Inoue, S.; Sasaki, M.; Gorrini, C.; Lee, Kim C.; Yung, Ka Y.; Brenner, D.; Knobbe-Thomsen, Christiane B.; Cox, Maureen A.; Elia, A.; Berger, T.; Cescon, David W.; Adeoye, A.; Brüstle, A.; Molyneux, Sam D.; Mason, Jacqueline M.; Li, Wanda Y.; Yamamoto, K.; Wakeham, A.; Berman, Hal K.; Khokha, R.; Done, Susan J.; Kavanagh, Terrance J.; Lam, C.-W.; Mak, Tak W., Glutathione and Thioredoxin Antioxidant Pathways Synergize to Drive Cancer Initiation and Progression. *Cancer Cell* **2015**, *27* (2), 211-222.

946. Morgan, M. J.; Liu, Z.-g., Crosstalk of reactive oxygen species and NF- κ B signaling. *Cell Research* **2011**, *21* (1), 103-115.

947. Frohlich, D. A.; McCabe, M. T.; Arnold, R. S.; Day, M. L., The role of Nrf2 in increased reactive oxygen species and DNA damage in prostate tumorigenesis. *Oncogene* **2008**, *27* (31), 4353-4362.

948. Liu, B.; Chen, Y.; St. Clair, D. K., ROS and p53: A versatile partnership. *Free Radical Biology and Medicine* **2008**, *44* (8), 1529-1535.

949. Allen, R. G.; Tresini, M., Oxidative stress and gene regulation. *Free Radical Biology and Medicine* **2000**, *28* (3), 463-499.

950. Fichte, M. A. H.; Weyel, X. M. M.; Junek, S.; Schäfer, F.; Herbivo, C.; Goeldner, M.; Specht, A.; Wachtveitl, J.; Heckel, A., Three-Dimensional Control of DNA Hybridization by Orthogonal Two-Color Two-Photon Uncaging. *Angewandte Chemie International Edition* **2016**, *55* (31), 8948-8952.

951. Yoshii, T.; Ikeda, M.; Hamachi, I., Two-Photon-Responsive Supramolecular Hydrogel for Controlling Materials Motion in Micrometer Space. *Angewandte Chemie International Edition* **2014**, *53* (28), 7264-7267.
952. Chen, T.-W.; Wardill, T. J.; Sun, Y.; Pulver, S. R.; Renninger, S. L.; Baohan, A.; Schreiter, E. R.; Kerr, R. A.; Orger, M. B.; Jayaraman, V.; Looger, L. L.; Svoboda, K.; Kim, D. S., Ultrasensitive fluorescent proteins for imaging neuronal activity. *Nature* **2013**, *499* (7458), 295-300.
953. Yang, Y.; Liu, N.; He, Y.; Liu, Y.; Ge, L.; Zou, L.; Song, S.; Xiong, W.; Liu, X., Improved calcium sensor GCaMP-X overcomes the calcium channel perturbations induced by the calmodulin in GCaMP. *Nature Communications* **2018**, *9* (1), 1504.
954. Boyden, E. S.; Zhang, F.; Bamberg, E.; Nagel, G.; Deisseroth, K., Millisecond-timescale, genetically targeted optical control of neural activity. *Nature Neuroscience* **2005**, *8* (9), 1263-1268.
955. Kandler, K.; Katz, L. C.; Kauer, J. A., Focal photolysis of caged glutamate produces long-term depression of hippocampal glutamate receptors. *Nature Neuroscience* **1998**, *1* (2), 119-123.
956. Wang, X.; Chen, X.; Yang, Y., Spatiotemporal control of gene expression by a light-switchable transgene system. *Nature Methods* **2012**, *9* (3), 266-269.
957. Rost, B. R.; Schneider-Warme, F.; Schmitz, D.; Hegemann, P., Optogenetic Tools for Subcellular Applications in Neuroscience. *Neuron* **2017**, *96* (3), 572-603.
958. Chou, C.; Young, D. D.; Deiters, A., A Light-Activated DNA Polymerase. *Angewandte Chemie International Edition* **2009**, *48* (32), 5950-5953.
959. Deiters, A.; Groff, D.; Ryu, Y.; Xie, J.; Schultz, P. G., A Genetically Encoded Photocaged Tyrosine. *Angewandte Chemie International Edition* **2006**, *45* (17), 2728-2731.
960. Dougherty, D. A., Unnatural amino acids as probes of protein structure and function. *Current Opinion in Chemical Biology* **2000**, *4* (6), 645-652.
961. Kloxin, A. M.; Tibbitt, M. W.; Anseth, K. S., Synthesis of photodegradable hydrogels as dynamically tunable cell culture platforms. *Nature Protocols* **2010**, *5*, 1867.
962. Burdick, J. A.; Murphy, W. L., Moving from static to dynamic complexity in hydrogel design. *Nature Communications* **2012**, *3* (1), 1269.
963. Strijbis, K.; Spooner, E.; Ploegh, H. L., Protein Ligation in Living Cells Using Sortase. *Traffic* **2012**, *13* (6), 780-789.
964. Pasqual, G.; Chudnovskiy, A.; Tas, J. M. J.; Agudelo, M.; Schweitzer, L. D.; Cui, A.; Hacohe, N.; Victora, G. D., Monitoring T cell–dendritic cell interactions in vivo by intercellular enzymatic labelling. *Nature* **2018**, *553* (7689), 496-500.
965. Theile, C. S.; Witte, M. D.; Blom, A. E. M.; Kundrat, L.; Ploegh, H. L.; Guimaraes, C. P., Site-specific N-terminal labeling of proteins using sortase-mediated reactions. *Nature Protocols* **2013**, *8* (9), 1800-1807.
966. Guimaraes, C. P.; Witte, M. D.; Theile, C. S.; Bozkurt, G.; Kundrat, L.; Blom, A. E. M.; Ploegh, H. L., Site-specific C-terminal and internal loop labeling of proteins using sortase-mediated reactions. *Nature Protocols* **2013**, *8* (9), 1787-1799.
967. Hasan, A.; Stengele, K.-P.; Giegrich, H.; Cornwell, P.; Isham, K. R.; Sachleben, R. A.; Pfeleiderer, W.; Foote, R. S., Photolabile protecting groups for nucleosides: Synthesis and photodeprotection rates. *Tetrahedron* **1997**, *53* (12), 4247-4264.
968. Bhushan, K. R.; DeLisi, C.; Laursen, R. A., Synthesis of photolabile 2-(2-nitrophenyl)propyloxycarbonyl protected amino acids. *Tetrahedron Letters* **2003**, *44* (47), 8585-8588.
969. Pirrung, M. C.; Dore, T. M.; Zhu, Y.; Rana, V. S., Sensitized two-photon photochemical deprotection. *Chemical Communications* **2010**, *46* (29), 5313-5315.
970. Furuta, T.; Wang, S. S. H.; Dantzker, J. L.; Dore, T. M.; Bybee, W. J.; Callaway, E. M.; Denk, W.; Tsien, R. Y., Brominated 7-hydroxycoumarin-4-ylmethyls: Photolabile protecting groups with biologically useful cross-sections for two photon photolysis. *Proceedings of the National Academy of Sciences* **1999**, *96* (4), 1193-1200.

971. Schönleber, R. O.; Bendig, J.; Hagen, V.; Giese, B., Rapid photolytic release of cytidine 5'-diphosphate from a coumarin derivative: a new tool for the investigation of ribonucleotide reductases. *Bioorganic & Medicinal Chemistry* **2002**, *10* (1), 97-101.
972. Hagen, V.; Bendig, J.; Frings, S.; Eckardt, T.; Helm, S.; Reuter, D.; Kaupp, U. B., Highly Efficient and Ultrafast Phototriggers for cAMP and cGMP by Using Long-Wavelength UV/Vis-Activation. *Angewandte Chemie International Edition* **2001**, *40* (6), 1045-1048.
973. Hagen, V.; Dekowski, B.; Nache, V.; Schmidt, R.; Geißler, D.; Lorenz, D.; Eichhorst, J.; Keller, S.; Kaneko, H.; Benndorf, K.; Wiesner, B., Coumarinylmethyl Esters for Ultrafast Release of High Concentrations of Cyclic Nucleotides upon One- and Two-Photon Photolysis. *Angewandte Chemie International Edition* **2005**, *44* (48), 7887-7891.
974. Hagen, V.; Dekowski, B.; Kotzur, N.; Lechler, R.; Wiesner, B.; Briand, B.; Beyermann, M., {7-[Bis(carboxymethyl)amino]coumarin-4-yl}methoxycarbonyl Derivatives for Photorelease of Carboxylic Acids, Alcohols/Phenols, Thioalcohols/Thiophenols, and Amines. *Chemistry – A European Journal* **2008**, *14* (5), 1621-1627.
975. Kotzur, N.; Briand, B.; Beyermann, M.; Hagen, V., Wavelength-Selective Photoactivatable Protecting Groups for Thiols. *Journal of the American Chemical Society* **2009**, *131* (46), 16927-16931.
976. Lyon, R. P.; Setter, J. R.; Bovee, T. D.; Doronina, S. O.; Hunter, J. H.; Anderson, M. E.; Balasubramanian, C. L.; Duniho, S. M.; Leiske, C. I.; Li, F.; Senter, P. D., Self-hydrolyzing maleimides improve the stability and pharmacological properties of antibody-drug conjugates. *Nature Biotechnology* **2014**, *32* (10), 1059-1062.
977. Mokotoff, M.; Mocarski, Y. M.; Gentsch, B. L.; Miller, M.; Zhou, J. H.; Chen, J.; Ball, E. D., Caution in the use of 2-iminothiolane (Traut's reagent) as a cross-linking agent for peptides. The formation of N-peptidyl-2-iminothiolanes with bombesin (BN) antagonist (d-Trp⁶,Leu¹³-ψ[CH₂NH]-Phe¹⁴)BN⁶⁻¹⁴ and d-Trp-Gln-Trp-NH₂. *The Journal of Peptide Research* **2001**, *57* (5), 383-389.
978. Lutolf, M. P.; Tirelli, N.; Cerritelli, S.; Cavalli, L.; Hubbell, J. A., Systematic Modulation of Michael-Type Reactivity of Thiols through the Use of Charged Amino Acids. *Bioconjugate Chemistry* **2001**, *12* (6), 1051-1056.
979. Kruger, R. G.; Otvos, B.; Frankel, B. A.; Bentley, M.; Dostal, P.; McCafferty, D. G., Analysis of the Substrate Specificity of the Staphylococcus aureus Sortase Transpeptidase SrtA. *Biochemistry* **2004**, *43* (6), 1541-1551.
980. Lawrence, M. S.; Phillips, K. J.; Liu, D. R., Supercharging Proteins Can Impart Unusual Resilience. *Journal of the American Chemical Society* **2007**, *129* (33), 10110-10112.
981. Tsai, P. S.; Blinder, P.; Migliori, B. J.; Neev, J.; Jin, Y.; Squier, J. A.; Kleinfeld, D., Plasma-mediated ablation: an optical tool for submicrometer surgery on neuronal and vascular systems. *Current Opinion in Biotechnology* **2009**, *20* (1), 90-99.
982. Eckardt, T.; Hagen, V.; Schade, B.; Schmidt, R.; Schweitzer, C.; Bendig, J., Deactivation Behavior and Excited-State Properties of (Coumarin-4-yl)methyl Derivatives. 2. Photocleavage of Selected (Coumarin-4-yl)methyl-Caged Adenosine Cyclic 3',5'-Monophosphates with Fluorescence Enhancement. *The Journal of Organic Chemistry* **2002**, *67* (3), 703-710.
983. Klausen, M.; Dubois, V.; Verlhac, J.-B.; Blanchard-Desce, M., Tandem Systems for Two-Photon Uncaging of Bioactive Molecules. *ChemPlusChem* **2019**, *84* (6), 589-598.
984. Ostuni, E.; Chapman, R. G.; Holmlin, R. E.; Takayama, S.; Whitesides, G. M., A Survey of Structure-Property Relationships of Surfaces that Resist the Adsorption of Protein. *Langmuir* **2001**, *17* (18), 5605-5620.
985. Levi-Montalcini, R., The Nerve Growth Factor 35 Years Later. *Science* **1987**, *237* (4819), 1154-1162.
986. Sarig-Nadir, O.; Seliktar, D., Compositional Alterations of Fibrin-Based Materials for Regulating In Vitro Neural Outgrowth. *Tissue Engineering Part A* **2008**, *14* (3), 401-411.
987. Schense, J. C.; Bloch, J.; Aebischer, P.; Hubbell, J. A., Enzymatic incorporation of bioactive peptides into fibrin matrices enhances neurite extension. *Nature Biotechnology* **2000**, *18* (4), 415-419.

988. Chan, C. C. M.; Roberts, C. R.; Steeves, J. D.; Tetzlaff, W., Aggrecan components differentially modulate nerve growth factor-responsive and neurotrophin-3-responsive dorsal root ganglion neurite growth. *Journal of Neuroscience Research* **2008**, *86* (3), 581-592.
989. Sakiyama-Elbert, S. E.; Panitch, A.; Hubbell, J. A., Development of growth factor fusion proteins for cell-triggered drug delivery. *The FASEB Journal* **2001**, *15* (7), 1300-1302.
990. Sakiyama-Elbert, S. E.; Hubbell, J. A., Controlled release of nerve growth factor from a heparin-containing fibrin-based cell ingrowth matrix. *Journal of Controlled Release* **2000**, *69* (1), 149-158.
991. Quinn, J. V., *Tissue Adhesives in Clinical Medicine*. BC Decker, Incorporated: 2005.
992. Mehdizadeh, M.; Yang, J., Design Strategies and Applications of Tissue Bioadhesives. *Macromol. Biosci.* **2013**, *13*, 271-288.
993. Spotnitz, W. D., Fibrin Sealant: The Only Approved Hemostat, Sealant, and Adhesive-a Laboratory and Clinical Perspective. *ISRN Surg* **2014**, *2014*, 203943-203943.
994. Kovalchuk, V.; Voronkina, A.; Binnewerg, B.; Schubert, M.; Muzychka, L.; Wysokowski, M.; Tsurkan, M. V.; Bechmann, N.; Petrenko, I.; Fursov, A.; Martinovic, R.; Ivanenko, V. N.; Fromont, J.; Smolii, O. B.; Joseph, Y.; Giovine, M.; Erpenbeck, D.; Gelinsky, M.; Springer, A.; Guan, K.; Bornstein, S. R.; Ehrlich, H., Naturally Drug-Loaded Chitin: Isolation and Applications. *Marine Drugs* **2019**, *17* (10).
995. Croisier, F.; Jérôme, C., Chitosan-Based Biomaterials for Tissue Engineering. *Eur. Polym. J.* **2013**, *49*, 780-792.
996. Francis Suh, J. K.; Matthew, H. W. T., Application of Chitosan-Based Polysaccharide Biomaterials in Cartilage Tissue Engineering: a Review. *Biomaterials* **2000**, *21*, 2589-2598.
997. Yadav, M.; Goswami, P.; Paritosh, K.; Kumar, M.; Pareek, N.; Vivekanand, V., Seafood Waste: a Source for Preparation of Commercially Employable Chitin/Chitosan Materials. *Bioresources and Bioprocessing* **2019**, *6*, 8.
998. Wysokowski, M.; Petrenko, I.; Stelling, A. L.; Stawski, D.; Jesionowski, T.; Ehrlich, H., Poriferan Chitin as a Versatile Template for Extreme Biomimetics. *Polymers* **2015**, *7* (2).
999. Muzychka, L.; Voronkina, A.; Kovalchuk, V.; Smolii, O. B.; Wysokowski, M.; Petrenko, I.; Youssef, D. T. A.; Ehrlich, I.; Ehrlich, H., Marine biomimetics: bromotyrosines loaded chitinous skeleton as source of antibacterial agents. *Applied Physics A* **2021**, *127* (1), 15.
1000. Khrunyk, Y.; Lach, S.; Petrenko, I.; Ehrlich, H., Progress in Modern Marine Biomaterials Research. *Marine Drugs* **2020**, *18* (12).
1001. Tsurkan, M. V.; Voronkina, A.; Khrunyk, Y.; Wysokowski, M.; Petrenko, I.; Ehrlich, H., Progress in chitin analytics. *Carbohydrate Polymers* **2021**, *252*, 117204.
1002. Mourya, V. K.; Nazma, N. I.; Tiwari, A., Carboxymethyl Chitosan and its Applications. *Adv. Mater. Lett.* **2010**, *1*, 11-33.
1003. Holme, K. R.; Perlin, A. S., Chitosan N-sulfate. A Water-Soluble Polyelectrolyte. *Carbohydr. Res.* **1997**, *302*, 7-12.
1004. Ruihua, H.; Bingchao, Y.; Zheng, D.; Wang, B., Preparation and Characterization of a Quaternized Chitosan. *Journal of Materials Science* **2012**, *47*, 845-851.
1005. Tang, H.; Zhang, P.; Kieft, T. L.; Ryan, S. J.; Baker, S. M.; Wiesmann, W. P.; Rogelj, S., Antibacterial Action of a Novel Functionalized Chitosan-Arginine Against Gram-Negative Bacteria. *Acta Biomater.* **2010**, *6*, 2562-2571.
1006. Zhao, D.; Yu, S.; Sun, B.; Gao, S.; Guo, S.; Zhao, K., Biomedical Applications of Chitosan and Its Derivative Nanoparticles. *Polymers* **2018**, *10*, 462.
1007. Anitha, A.; Sowmya, S.; Kumar, P. T. S.; Deepthi, S.; Chennazhi, K. P.; Ehrlich, H.; Tsurkan, M.; Jayakumar, R., Chitin and Chitosan in Selected Biomedical Applications. *Prog. Polym. Sci.* **2014**, *39*, 1644-1667.
1008. Vunain, E.; Mishra, A. K.; Mamba, B. B., 1 - Fundamentals of Chitosan for Biomedical Applications. In *Chitosan Based Biomaterials Volume 1*, Jennings, J. A.; Bumgardner, J. D., Eds. Woodhead Publishing: 2017; pp 3-30.
1009. Kean, T.; Thanou, M., Biodegradation, biodistribution and toxicity of chitosan. *Advanced Drug Delivery Reviews* **2010**, *62* (1), 3-11.

1010. M. Ways, T. M.; Lau, W. A.-O.; Khutoryanskiy, V. A.-O., Chitosan and Its Derivatives for Application in Mucoadhesive Drug Delivery Systems. *Polymers* **2018**, *10*, 267.
1011. Mati-Baouche, N.; Elchinger, P.-H.; de Baynast, H.; Pierre, G.; Delattre, C.; Michaud, P., Chitosan as an Adhesive. *Eur. Polym. J.* **2014**, *60*, 198-212.
1012. Baker, S.; Wiesmann, W. P.; Ryan, S. Chitosan-derivative compounds and methods of controlling microbial populations. 2012.
1013. Ehrbar, M.; Rizzi, S. C.; Schoenmakers, R. G.; San Miguel, B.; Hubbell, J. A.; Weber, F. E.; Lutolf, M. P., Biomolecular Hydrogels Formed and Degraded via Site-Specific Enzymatic Reactions. *Biomacromolecules* **2007**, *8*, 3000-3007.
1014. Lee, D. W.; Lim, C.; Israelachvili, J. N.; Hwang, D. S., Strong Adhesion and Cohesion of Chitosan in Aqueous Solutions. *Langmuir* **2013**, *29*, 14222-14229.
1015. Bajpayee, A. G.; Grodzinsky, A. J., Cartilage-targeting drug delivery: can electrostatic interactions help? *Nature Reviews Rheumatology* **2017**, *13* (3), 183-193.
1016. Hsueh, M. F.; Khabut, A.; Kjellström, S.; Önerfjord, P.; Kraus, V. B., Cartilage Permeability Assessment Based on Proteomic Analysis of Plasma Protein Penetration. *Osteoarthr. Cartil.* **2015**, *23*, A132-A133.
1017. Fei Liu, X.; Lin Guan, Y.; Zhi Yang, D.; Li, Z.; De Yao, K., Antibacterial Action of Chitosan and Carboxymethylated Chitosan. *J. Appl. Polym. Sci.* **2001**, *79*, 1324-1335.
1018. Liu, Z.-Q.; Deng, G.-M.; Foster, S.; Tarkowski, A., Staphylococcal Peptidoglycans Induce Arthritis. *Arthritis Res. Ther.* **2001**, *3*, 375.
1019. Johnson, C. T.; Sok, M. C. P.; Martin, K. E.; Kalelkar, P. P.; Caplin, J. D.; Botchwey, E. A.; García, A. J., Lysostaphin and BMP-2 Co-Delivery Reduces *S. aureus* Infection and Regenerates Critical-Sized Segmental Bone Defects. *Sci. Adv.* **2019**, *5*, eaaw1228.
1020. Ngo, D.-H.; Kim, S.-K., Chapter Two - Antioxidant Effects of Chitin, Chitosan, and Their Derivatives. In *Adv. Food Nutr. Res.*, Academic Press: 2014; Vol. 73, pp 15-31.
1021. Park, P.-J.; Je, J.-Y.; Kim, S.-K., Free Radical Scavenging Activity of Chitooligosaccharides by Electron Spin Resonance Spectrometry. *J. Agric. Food Chem.* **2003**, *51*, 4624-4627.
1022. Ong, S.-Y.; Wu, J.; Moochhala, S. M.; Tan, M.-H.; Lu, J., Development of a Chitosan-Based Wound Dressing with Improved Hemostatic and Antimicrobial Properties. *Biomaterials* **2008**, *29*, 4323-4332.
1023. Stricker-Krongrad, A.-H.; Alikhassy, Z.; Matsangos, N.; Sebastian, R.; Marti, G.; Lay, F.; Harmon, J. W., Efficacy of Chitosan-Based Dressing for Control of Bleeding in Excisional Wounds. *Eplasty* **2018**, *18*, e14-e14.
1024. Kinstlinger, I. S.; Calderon, G. A.; Royle, M. K.; Means, A. K.; Grigoryan, B.; Miller, J. S., Perfusion and endothelialization of engineered tissues with patterned vascular networks. *Nature Protocols* **2021**, *16* (6), 3089-3113.

Curriculum Vitae

Personal Information – Contact

Address	Otto-Stern-Weg 7, HPL J15.2, 8093 Zurich (CH)
Mail	riccardo.rizzo@hest.ethz.ch
Twitter	@RiccardoRizzo18
ORCID	0000-0001-8297-6776
Google Scholar	https://scholar.google.com/citations?hl=it&user=OuL7YnIAAAAJ

Education

11.2018	PhD – ETH Zürich (Switzerland) <ul style="list-style-type: none">• <u>Supervision</u>: Prof. Dr. Marcy Zenobi-Wong
12.2022	
10.2016	Master’s Degree in Nanobiotechnology – University of Trieste (Italy) <ul style="list-style-type: none">• <u>Final grade</u>: 110/110 <i>cum laude</i>• <u>Average grade</u>: 29.8/30
10.2018	
10.2013	Bachelor’s Degree in Biotechnology – University of Trieste (Italy) <ul style="list-style-type: none">• <u>Final grade</u>: 110/110 <i>cum laude</i>• <u>Average grade</u>: 29.3/30• <u>Admission test</u>: 1st overall placement
07.2016	

Employment History

11.2018	PhD – Tissue Engineering and Biofabrication Lab (ETH Zürich) <ul style="list-style-type: none">• <u>Project Manager</u> for Innosuisse funded project “Bioresins and processes for next-generation volumetric printing”• <u>Supervision of Master student</u> (Nika Petelinsek, ETH, D-CHAB) “Biocompatible Photoinitiator-Free Photoresins”• <u>Teaching activities</u>: responsible for 3D printing practical lab classes “Practical Methods in Biofabrication” and “Practical Methods in Tissue Engineering”
12.2022	
03.2018	MSc Internship – Carbon Nanobiotechnology Lab (CICBiomaGune, San Sebastian) <ul style="list-style-type: none">• <u>Supervision</u>: Prof. Dr. Maurizio Prato “Development of PDMS/multiwalled carbon nanotubes-based scaffolds for tissue engineering applications”
08.2018	
07.2018	MSc Internship – Carbon Nanotechnology Lab (University of Trieste) <ul style="list-style-type: none">• <u>Supervision</u>: Prof. Dr. Maurizio Prato
02.2018	

- | | |
|--------------------|---|
| 07.2015
12.2015 | BSc Internship – Biomat Lab (University of Trieste) <ul style="list-style-type: none"> • <u>Supervision</u>: Prof. Dr. Sergio Paoletti |
| 07.2012
08.2012 | HS Internship – National Cancer Institute (C.R.O., Aviano) <ul style="list-style-type: none"> • <u>Supervision</u>: Dr. Riccardo Spizzo |

Supervision of Junior Researchers

- | | |
|--------------------|---|
| 02.2021
07.2021 | Master’s student – Semester Project (ETH Zürich) <ul style="list-style-type: none"> • <u>Student</u>: Nika Petelinsek
“Biocompatible Photoinitiator-Free Photoresins” |
| 03.2020
05.2020 | Master’s students – Practical course project (ETH Zürich) <ul style="list-style-type: none"> • <u>Students</u>: Vasil Kecheliev, Golo Wytttenbach
“Biofabrication of an Intervertebral Disc” |
| 03.2019
05.2019 | Master’s students – Practical course project (ETH Zürich) <ul style="list-style-type: none"> • <u>Students</u>: Dünki Tomoya, Anna Scheeder
“Tissue-Engineered Trachea by Reinforced Hydrogel Scaffold” |

Prizes, Awards and Fellowships

- | | |
|------|---|
| 2022 | Gordon Research Conference – Poster Award
“Development of Novel Photoclick Bioresins: from Two-Photon Stereolithography to Volumetric Printing”

Chemistry Travel Award (ETH Zürich)
Swiss Academy of Sciences and Swiss Chemical Society

Global Young Scientist Summit – Winner Video Contest: Panel’s Choice Award
https://www.youtube.com/watch?v=lw5Lofj9MdQ |
| 2018 | Erasmus+ Traineeship Scholarship
EU Erasmus Program |
| 2017 | Top Merit Scholarship – Above 80th Percentile
University of Trieste

Top Merit Scholarship – BSc degree: 110/110 <i>cum laude</i>
University of Trieste |
| 2016 | Top Merit Scholarship – Above 80th Percentile
University of Trieste |

2015 **Top Merit Scholarship – Above 80th Percentile**
University of Trieste

Publications

- 2022 | R. Rizzo[†], D. Ruetsche[†], H. Liu, P. Chansoria, A. Wang, A. Hasenauer, M. Zenobi-Wong
“Multiscale Hybrid Fabrication: Volumetric Printing Meets Two-Photon Ablation”
Biorxiv 2022 (preprint)
- H. Liu., P. Chansoria, P. Delrot, E. Angelidakis, R. Rizzo, D. Rüttsche, L. A. Applegate, D. Loterie, M. Zenobi-Wong
“Filamented Light (FLight) Biofabrication of Highly Aligned Tissue-Engineered Constructs”
Advanced Materials 2022, 2204301
<https://doi.org/10.1002/adma.202204301>
- R. Rizzo[†], A. Bonato[†], P. Chansoria, M. Zenobi-Wong
“Macroporous Aligned Hydrogel Microstrands for 3D Cell Guidance”
ACS Biomaterials Science & Engineering 2022, 8, 9, 3871-3882
<https://doi.org/10.1021/acsbiomaterials.2c00370>
- 2021 | R. Rizzo, D. Ruetsche, H. Liu, M. Zenobi-Wong
“Optimized Photoclick (Bio)Resins for Fast Volumetric Bioprinting”
Advanced Materials 2021, 33, 2102900
<https://doi.org/10.1002/adma.202102900>
-Inside Front Cover (Illustration by R.Rizzo, see <https://doi.org/10.1002/adma.202170384>)
- I. Berg[†], R. Rizzo[†], M. Lee[†], Q. Ren, N. Broguiere, M. Zenobi-Wong
“Factor XIII Cross-Linked Adhesive Chitosan Hydrogels”
ACS Biomaterials Science & Engineering 2021, 7 (6), 2198-2203 -
<https://doi.org/10.1021/acsbiomaterials.1c00298>
- 2020 | M. Lee[†], R. Rizzo[†], F. Surmant[†], M. Zenobi-Wong[†]
“Guiding Lights: Tissue Bioprinting Using Photoactivated Materials”
Chemical Reviews 2020, 120 (19), 10950-11027 -
<https://doi.org/10.1021/acs.chemrev.0c00077>
- N. Broguiere, I. Luchtefeld[†], L. Trachselt[†], D. Mazunin[†], R. Rizzo[†], J. W. Bode, M. P. Lutolf,
M. Zenobi-Wong
“Morphogenesis Guided by 3D Patterning of Growth Factors in Biological Matrices”
Advanced Materials 2020, 32, 1908299
<https://doi.org/10.1002/adma.201908299>
-Back Cover (Illustration by R.Rizzo, see <https://doi.org/10.1002/adma.202070193>)

In preparation

- 2022 | R. Rizzo[†], A. Puiggali-Jou[†], A. Bonato, M. Zenobi-Wong
“Flight Biofabrication of Anisotropic Articular Cartilage with Zonal Architecture”
- P. Chansoria, D. Ruetsche, A. Wang, R. Rizzo, H. Liu, F. Surman, P. Weber, M. Zenobi-Wong
“Synergizing algorithmic design, photoclick chemistry and multi-materials volumetric printing for the rapid fabrication of complex structures”
- P. Chansoria, H. Liu, R. Rizzo, D. Ruetsche, P. Delrot, D. Loterie, M. Zenobi-Wong
“Fast and precise: Volumetric printing for rapid fabrication of complex structures”

In revision

- 2022 | R. Rizzo, N. Petelinsek, A. Bonato, M. Zenobi-Wong
“From Free-Radical to Radical-Free: A Paradigm Shift in Light-Mediated Biofabrication”
- R. Rizzo[†], D. Ruetsche[†], H. Liu, P. Chansoria, A. Wang, A. Hasenauer, M. Zenobi-Wong
“Multiscale Hybrid Fabrication: Volumetric Printing Meets Two-Photon Ablation”

Patents

- 2022 | H. Liu, P. Chansoria, R. Rizzo, M. Zenobi-Wong
“Light Beam Projection Guided Biofabrication of Aligned Tissues”
Patent application, eth209ep-b

Contributions to conferences

- 2023 | **Global Young Scientists Summit** – Singapore
Selected for participation
- 2022 | **Global Young Scientists Summit** – Singapore
Selected for participation
- Gordon Research Conference** – Ventura, California (USA)
Poster: “Development of Novel Photoclick Bioresins: from Two-Photon Stereolithography to Volumetric Printing”
- TERMIS-EU** – Krakow, Poland
Poster: “Photoinitiator- and Radical-free High Resolution Bioprinting”
- Swiss Society for Biomaterials and Regenerative Medicine** – Zürich, Switzerland

- Oral Presentation: “From Free-Radical to Radical-Free: A Biocompatible Paradigm Shift in Light Mediated Biofabrication”
- ETH Materials and Processes Graduate Symposium** – Zürich, Switzerland
Oral Presentation: “From Free-Radical to Radical-Free: A Biocompatible Paradigm Shift in Light Mediated Biofabrication”
- 2021 | **31st ESB - European Society for Biomaterials** - Porto, Portugal
Oral Presentation: “An Ideal Photoresin for Fast Volumetric Bioprinting Based on Thiol-Norbornene Photoclick Crosslinking”
- TERMIS World Congress** - Maastricht, Netherlands
Oral Presentation: “Aligned Microgels Constructs for 3D Physical Guidance of Muscle Tissue Development”
- 2018 | **ChemOnTubes** - Biarritz, France

Contribution as non-presenting author

- 2022 | **International Conference on Biofabrication** – Montecatini Terme, Italy
P. Chansoria, D. Ruetsche, A. Wang, R. Rizzo, M. Zenobi-Wong
“Algorithmic design and multi-material volumetric printing for the rapid fabrication of complex architectures”
- 32nd ESB - European Society for Biomaterials** – Bordeaux, France
D. Ruetsche, R. Rizzo, P. Chansoria, A. Wang, M. Zenobi-Wong
“Fabrication of vascularized 3D mammary gland model using hybrid volumetric bioprinting and photoablation”
- Swiss Society for Biomaterials and Regenerative Medicine** - Zürich, Switzerland
D. Ruetsche, R. Rizzo, P. Chansoria, A. Wang, M. Zenobi-Wong
“Fabrication of complex hierarchical 3D vascularized models using hybrid volumetric bioprinting and photoablation”
- 2021 | **TERMIS World Congress** – Maastricht, Netherlands
H. Liu, R. Rizzo, M. Zenobi-Wong
“Biofabrication of Photo-crosslinked Constructs with Highly Aligned Microstructure for Tissue Engineering”

Personal Skills

Digital Skills	Adobe Illustrator	●●●●●	Autodesk Fusion	●●●●○	ChemDraw	●●●●●
	Adobe Photoshop	●●●●●	GraphPad Prism	●●●●●	Power Point	●●●●●
	Adobe Lightroom	●●●●○	ImageJ Fiji	●●●●●	Word-Excel	●●●●●

Techniques	Confocal/Two-photon imaging	Microfluidics	Organic Chemistry
	SEM imaging	Cell culture	Analytical Chemistry
	Extrusion/FDM printing	2P-SL and VP	Polymer Chemistry

Soft Skills	<u>Leadership</u> : project manager for Innosuisse project, supervision and senior PhD experience
	<u>Independency / problem solving</u> : projects design and experiments conducted independently
	<u>Written and Verbal Communication</u> : numerous reports, articles, presentations in group meetings, departmental/institute meetings, teaching activities and international conferences
	<u>Social skills</u> : Frequently collaborating with colleagues on common projects, sharing ideas and offering feedbacks to one another.

Language	Italian (native)	Others	Sommelier (Level 1 – FISAR Milan)
	English (full professional proficiency)		Amateur Photographer
	Spanish (basic)		20+ years basketball player